

COMPUMAG 2003

Conference on the
Computation of
Magnetic Fields

Saratoga Springs, New York
July 13–17, 2003

Volume II

COMPUMAG

14th Conference on the Computation of Magnetic Fields

July 13-17, 2003

Saratoga Springs, New York USA

Record of the 14th COMPUMAG Conference
on the Computation of Magnetic Fields

Volume II: Tuesday, July 15

COMPUMAG 2003

14th Conference on the Computation of Magnetic Fields

Saratoga Springs, New York, USA

July 13-17, 2003

Compumag 2003 Committee:

Prof. Sheppard J. Salon, Chairman
Rensselaer Polytechnic Institute, Troy, NY USA
Philippe Wendling, Vice Chairman
Magsoft Corporation, Troy, NY USA
David Burow, Secretariat
Genfo, Inc., Troy, NY USA

Local Organizing Committee:

M. DeBortoli K. Sivasubramaniam
M. Lean M. Shah
I. Mayergoyz S. Babic
U. Deshpande

Editorial Board Chairmen:

J. Webb, McGill University, Montreal, Quebec Canada
D. Giannacopoulos, McGill University, Montreal, Quebec Canada
Email: edboard.compumag2003@mcgill.ca

Correspondence:

Compumag 2003
1223 Peoples Ave
Troy, NY 12180 USA
Email : secretariat@compumag2003.com

Lodging Arrangements Made By:

Sherie Klein, Carlson Wagonlit/Albany Travel
30 Corporate Drive, Clifton Park, NY 12065 USA
Phone: +1 (518) 292-9000
Email: corporate@albanytravel.com

COMPUMAG 2003 Chairman's Welcome

Welcome to COMPUMAG 2003, the 14th Conference on the Computation of Electric and Magnetic Fields!

In the 27 years since the first COMPUMAG Conference in 1976 at Oxford, we have seen the society and the conference continue to grow in numbers, in significance and in international renown and respect. We are honored, therefore, to carry on what has become a well-established tradition of presenting the leading research and thought in the area of computational electromagnetics.

Because of its high standards and rigorous review process, the Conference has become the place to present in our field. This year 429 papers were approved for presentation in 8 oral sessions and 32 poster sessions. The contributors represent 30 different countries. Our deep thanks go to the editorial board and to the co-chairs Jon Webb and Dennis Giannacopoulos, who did an outstanding job.

And welcome to Saratoga Springs, New York! Those of us fortunate to live and work in New York's Capital District can take advantage of some of the best opportunities in the United States for research and education; cultural, historical and recreational resources; and small cities and towns where neighbors still don't lock their doors. Nearby research institutions and universities include Rensselaer, GE Global Research Laboratories, Knolls Atomic Power Laboratory, IBM Research Laboratory and others. New York City, Boston, and Montreal, with their rich historical and cultural resources, are all within a few hours' drive. Finally, there is the peace and friendliness of smaller towns and villages, like Saratoga Springs, where you are sure to enjoy the activities we have planned; we hope you will also take time to explore on your own.

COMPUMAG 2003 offers lively scientific exchange to charm the intellect and convivial activities to warm the heart. Welcome!

Prof. Sheppard J. Salon
COMPUMAG 2003 Chairman



City of Saratoga Springs

Kenneth Klotz, Mayor

Hank Kuczynski, Deputy Mayor

July, 2003

Welcome!

On behalf of the entire City of Saratoga Springs, I would like to welcome the **14th Conference on the Computation of Electromagnetic Fields** to Saratoga Springs!

As you know, Saratoga Springs is a world-class resort destination, which offers cosmopolitan amenities without the drawbacks of a typical metropolitan area. Our city takes great pride in its hospitality to visitors. We offer world-class attractions, wonderful restaurants, unique shops and a host of related activities that your attendees are sure to enjoy!

Saratoga Springs looks forward to hosting the **14th Conference on the Computation of Electromagnetic Fields and its attendees.**

Once again, Welcome to our City, where we invite you to.....**Experience Saratoga!**

Sincerely,

Kenneth Klotz
Mayor

COMPUMAG 2003 Editorial Board

Chairmen: J. Webb, D. Giannacopoulos

Raffaele Albanese	Raymond Findlay	Raffaele Martone	Pierre Saguet
Salvatore Alfonzetti	Virgiliu Fireteanu	Daniel Mayer	Magdalena Salazar-Palma
Piergiorgio Alotto	Behzad Forghani	Isaak Mayergoyz	Carlos Sartori
Zoran Andjelic	Minya Gavrilovic	Steven McFee	Antonio Savini
Carlos F. Lemos Antunes	Dennis Giannacopoulos	Jan Melkebeek	Imre Sebestyén
Abdul-Rahman Arkadan	Andrew Gibson	Frantisek Melkes	Jan Sikora
Michel Aubourg	Roberto Graglia	Renato Mesquita	John Simkin
Zsolt Badics	Stanislaw Gratkowski	Gérard Meunier	Andrea Stella
Bernard Bandelier	Miklos Gyimesi	Pavel Mintchev	Saku Suuriniemi
Istvan Bardi	Johan Gyselinck	Osama A. Mohammed	Jan K. Sykulski
João P. Assumpção Bastos	Song-yop Hahn	Paolo Molfino	Toshiyuki Takagi
Jean Bigeon	Kay Hameyer	Giorgio Molinari	Norio Takahashi
Oszkar Bíró	Florea Ioan Hantila	Vikass Monebhurrin	Tadasu Takuma
Carlo Angelo Borghi	Nathan Ida	Francesco Carlo Morabito	Antonello Tamburrino
Frédéric Bouillault	Hajime Igarashi	Irina Munteanu	Renyuan Tang
Hartmut Brauer	Kazuhisa Ishibashi	Silvio Ikuyo Nabeta	Takashi Todaka
John R. Brauer	Amália Ivány	Ryszard Nawrowski	Bill Trowbridge
Noël Burais	Rick Janssen	Mario Nervi	Theodoros Tsiboukis
François Buret	Jianming Jin	Alain Nicolas	Igor Tsukerman
Andreas Cangelaris	Hyun-Kyo Jung	Laurent Nicolas	Larry R. Turner
Ermanno Cardelli	Manfred Kaltenbacher	Keijo Nikoskinen	Lalita Udpa
José Roberto Cardoso	Akihisa Kameari	Isoharu Nishiguchi	Satish Udpa
Zoltan Cendes	Yasushi Kanai	W Toby Norris	Hermann Uhlmann
Zhiguang Cheng	Manfred Kasper	Dzevat Omeragic	Ursula Van Rienen
Mario Chiampi	Yoshihiro Kawase	Jozsef Pavo	Patrick Vaudon
Charles T. M. Choi	Leo Kempel	Giuseppe Pelosi	Serge Verdeyme
Kyung Choi	Lauri Kettunen	Ilaria Perugia	Fabio Villone
Markus Clemens	Ahmed Kishk	Lionel Pichon	John L. Volakis
Enzo Coccorese	Fumio Kojima	Francis Piriou	Christian Vollaire
Jean-Louis Coulomb	Arnulf Kost	Milica Popovic	Shinji Wakao
Xiang Cui	Laurent Krähenbühl	Kurt Preis	Simon Walker
Kent R. Davey	Andrzej Krawczyk	Thomas William Preston	Zanming Wang
Herbert De Gersem	Patrick Kuo-Peng	Mirco Raffetto	Jonathan P. Webb
João A. De Vasconcelos	Stefan Kurz	Adroaldo Raizer	Thomas Weiland
Edward Deeley	Ioan E. Lager	Jaime Ramirez	Slawomir Wiak
Edward Della Torre	Hong Cheng Lai	Liyun Rao	Hideo Yamashita
Andrzej Demenko	Meng H. Lean	Adel Razek	Katsumi Yamazaki
Paolo Di Barba	Luiz Lebensztajn	Zhuoxiang Ren	Ivan Yatchev
Bernice Dillon	Robert Lee	Werner Renhart	Traianos Yioultis
Alistair Duffy	Jin-Fa Lee	Maurizio Repetto	Jiansheng Yuan
Fabrizio Dughiero	Paul John Leonard	Gilbert Reyne	Kazimierz Zakrzewski
Patrick Dular	Dominique Lesselier	Christopher Riley	Ping Zhou
Derek Dyck	David Lowther	Françoise Rioux-Damidau	
Romanus Dyczij-Edlinger	Valérie Madrangeas	Dave Rodger	
Chris R.I. Emson	Christian Magele	Guglielmo Rubinacci	
Mauro Feliziani	Yves Maréchal	Wolfgang M. Rucker	
Paolo Fernandes	Marlene Marinescu	Stephan Russenschuck	
Gilles Fillion	Iliana Marinova	Nelson Sadowski	

COMPUMAG 2003 Program at a Glance

	July 13 Sunday	July 14 Monday	July 15 Tuesday	July 16 Wednesday	July 17 Thursday
7:00		Continental Breakfast Buffet	Continental Breakfast Buffet	Continental Breakfast Buffet	Continental Breakfast Buffet
8:00		Formulations Saratoga Ballroom	Devices Saratoga Ballroom	Quasistatic Saratoga Ballroom	Inverse Problems Saratoga Ballroom
10:15		Coffee Break	Coffee Break	Coffee Break	Coffee Break
10:45		Numerical Techniques I Coupled Problems I Devices I Statics I	Numerical Techniques II Coupled Problems II Machines II Statics II	Numerical Techniques III Coupled Problems III Devices III Software	Numerical Techniques IV Coupled Problems IV Machines IV Devices IV
12:00		Lunch: Grand Ballroom – High Rock	Lunch: Grand Ballroom – High Rock	Lunch: Grand Ballroom – High Rock	Lunch: Grand Ballroom – High Rock
1:30		Optimization I Waves I Machines I Quasistatic I	Optimization II Waves II Devices II Quasistatic II	Optimization III EMC Machines III Materials I	Optimization IV Materials II Education – TEAM Quasistatic III
2:45		Afternoon Break	Afternoon Break	Afternoon Break	Afternoon Break
3:15	Registration* 2:00 – 6:00 p.m.	Methodologies Saratoga Ballroom	Materials Saratoga Ballroom	Waves Saratoga Ballroom	Optimization Saratoga Ballroom
5:30		Enjoy Saratoga!	5:00 Short Break (no refreshments)		Have a safe and pleasant journey home!
			5:15 Panel Session: Topic To Be Announced Saratoga Ballroom		
6:30	Evening Reception Saratoga Ballroom		6:15 Enjoy Saratoga!	Banquet at the Canfield Casino	6:30

* Registration will also be available each day from 7:00 AM to 12:00 noon and from 1:30 to 2:45 PM.

COMPUMAG 2003 Technical Program

Tuesday, July 15, 2003

	8:00 – 10:15
Oral Session	
	Devices Saratoga Ballroom
	10:45 – 12:00
Poster Session	
	Numerical Techniques II: Novel Methodologies
	Coupled Problems II: Deformations
	Machines II: Induction Motors
	Statics II: Magnetostatics
	1:30 – 2:45
Poster Session	
	Optimization II
	Waves II
	Devices II: NTD, Microwave Cavities
	Quasistatic II: Eddy Current
	3:15 – 5:00
Oral Session	
	Materials Saratoga Ballroom
	5:15 – 6:15
Panel Session	
	Topic To Be Announced Saratoga Ballroom

Devices	Chairman
Tuesday, July 15, 8:00am - 10:15am	Dr. José Cardoso

Fields, Focussing and Aberrations in Electrostatic Accelerator Tubes	II - 2
H.R. McK. Hyder, C.W. Trowbridge	P94805
<i>Vector Fields Ltd</i>	
<i>Oxford - UK</i>	

Finite Element Simulation of Head / Media Interactions in Perpendicular Recording	II - 4
Thomas Schrefl, Hermann Forster, Manfred E. Schabes, Byron Lengsfeld	P65497
<i>Vienna University of Technology - Solid State Physics</i>	
<i>Vienna - Austria</i>	

Scalar and vector potentials' coupling on nonmatching grids for the simulation of an electromagnetic brake	II - 6
B. Flemisch, Y. Maday, F. Rapetti, B.I. Wohlmuth	P41724
<i>Universite de Nice et Sophia-Antipolis - Laboratoire J.-A. Dieudonne</i>	
<i>Nice - France</i>	

Numerical Analysis of Frequency Characteristic Fluctuations of Semiconductor Devices Caused by Random Doping Fluctuations	II - 8
Isaak D. Mayergoyz, P. Andrei	P21591
<i>University of Maryland - Department of Electrical and Computer Engineering</i>	
<i>College Park, MD - USA</i>	

Propulsion and Guidance Simulation of HTS Bulk Ropeless Linear Elevator	II - 10
Kinjiro Yoshida, Hirokazu Matsumoto	P44560
<i>Kyushu University - Graduate School of Information Science and Electrical Engineering,</i>	
<i>Department of Electrical and Electronic Systems Engineering</i>	
<i>Fukuoka - Japan</i>	

Study of the Influence of Leakage Fields on the Inchworm Actuator	II - 12
Y. Bernard, Sheppard J. Salon, Philippe Bouchilloux	P15892
<i>Rensselaer Polytechnic Institute - ECSE Department</i>	
<i>Troy, NY - USA</i>	

Numerical Techniques II: Novel methodologies	Chairman
Tuesday, July 15, 10:45am - 12:00pm	Dr. Hajime Igarashi

Investigation of EEG Problems using the Superposition Principle in the Finite Volume Method	II - 14
Y.Q. Xie, X.S. Ma, J.S. Yuan, J. Zou	P94225
<i>Peking University</i>	
<i>Beijing - China</i>	

A Meshless Collocation Method based on Radial Basis Functions and Wavelets	II - 16
S.L. Ho, Shiyong Yang, H.C. Wong <i>Hong Kong Polytechnic University - Dept. of Electrical Engineering Kowloon - Hong Kong</i>	P61644
A Fast Volume Integral Equation Solver Based On A Novel 2-Level Dual Rank SVD Algorithm	II - 18
N.A. Ozdemir, J.F. Lee <i>Ohio State University - ElectroScience Lab. Columbus, OH - USA</i>	P31977
Research on Weighted Functions of Meshless Methods in Electromagnetic Field Analysis	II - 20
Jianxin Liu, Zhenhua Liu, Xiang Cui <i>North China Electric Power University Hebei - China</i>	P41278
Point Collocation Method Based on the FMLSrk Approximation for Electromagnetic Field Analysis	II - 22
D.W. Kim, H.K. Kim, Y.S. Kim <i>Korea Electrotechnology Research Institute(KERI) - Advanced Power Apparatus Group Changwon - South Korea</i>	P72397
The Natural Element Method for Electromagnetic Field Computation	II - 24
Hong-Kyu Kim, K.Y. Park, Chang-Hwan Im, Hyun-Kyo Jung <i>Korea Electrotechnology Research Institute(KERI) - Advanced Power Apparatus Group Changwon - South Korea</i>	P22398
Quasi-2D FE Analysis of Hybrid Stepping Motor(HSM)	II - 26
Ki-Bong Jang, Hyun-Hun Shin, Ju Lee <i>Hanyang University - Department of Electrical Engineering, Energy Conversion Lab. Seoul - Korea</i>	P83311
Isotropic and anisotropic electrostatic field computation by means of the cell method	II - 28
M. Bullo, F. Dughiero, M. Guarnieri, E. Tittone <i>Università degli Studi di Padova - Dipartimento di Ingegneria Elettrica Padova - Italy</i>	P23759
A Finite Element Method with Grouped Smooth Constraints	II - 30
Xixin Yan, Jianyun Chai <i>Tsinghua University - Department of Electrical Engineering Beijing - China</i>	P54979
Formulation of admittance boundary conditions for the solution of frequency domain problems by FIT	II - 32
Lorenzo Codecasa, Vito Minerva, Marco Politi <i>Politecnico di Milano - Dipartimento di Elettronica e Informazione Milan - Italy</i>	P45318

A New Multilevel Subgridding Scheme for Two-Dimensional FDTD method	II - 34
Charles T.M. Choi, Shu-Hai Sun	P65220
<i>I-Shou University - Department of Electrical Engineering Kaohsiung county - Taiwan, ROC.</i>	
A Subgridding Scheme for Two-Dimensional FDTD(2,4) Method	II - 36
Charles T.M. Choi, Shu-Hai Sun	P85721
<i>I-Shou University - Department of Electrical Engineering Kaohsiung County - Taiwan, ROC</i>	
Design of the Recording Head considering the Field Gradient in High Density Magnetic Recording	II - 38
H. Won, Gwan Soo Park, Y.Y. Kim, G.P. Han	P75832
<i>Korea Maritime University - Dept. Electrical Engineering Busan - South Korea</i>	
Closed-Form Approximation of Electromagnetic Green's Function for Layered Media with Variable Source Point	II - 40
Leonid B. Proekt, Andreas Cangelaris	P85166
<i>University of Illinois at Urbana-Champaign – Dept. of Electrical and Computer Engineering Urbana, IL - USA</i>	

Coupled Problems II: Deformation
Tuesday, July 15, 10:45am - 12:00pm

Chairman

Finite Element Simulation of Micro Electro Mechanical Systems (MEMS) by Strongly Coupled Electro Mechanical Transducers	II - 42
Miklos Gyimesi, Dale Ostergaard, Ilya Avdeev	P91303
<i>University of Pittsburgh - Department of Mechanical Engineering Pittsburgh, PA - USA</i>	
Magneto-mechanical strong coupling model and experiment for a giant magnetostrictive actuator	II - 44
Rongge Yan, Bowen Wang, Shuying Cao, Ling Weng, Fuigui Liu, Weili Yan	P71810
<i>Hebei University of Technology - School of Electrical Engineering Tianjin - China</i>	
Stability of augmented staggered method for electromagnetic and structural coupled problem	II - 46
Yoshikazu Tanaka, Syuji Furuki, Eiji Shintaku, Yukio Fujimoto	P12014
<i>Hiroshima University - System Safety Lab., Graduate School of Engineering Hiroshima - Japan</i>	
About the Implementation of Mechanical Flaking Effects Inside a Layer Structure During a Coupled Finite Element Analysis	II - 48
Christian Grabner, Erich Schmidt	P93705
<i>Graz University of Technology - Institute of Electrical Machines and Drives Graz - Austria</i>	

Finite Element Computation of the Deformation of Ferromagnetic Material taking into account Magnetic Forces and Magnetostriction	II - 50
Lieven Vandeveld, Johan Gyselinck, Marc A.C. De Wulf, Jan A.A. Melkebeek <i>Ghent University -- Electrical Energy Laboratory (EELAB)</i> <i>Gent - Belgium</i>	P94282
Investigation of Inverse Magnetostriction Effects in Electric Machinery	II - 52
O.A. Mohammed, S. Liu <i>Florida International University - Department of Electrical & Computer Engineering</i> <i>Miami, FL - USA</i>	P65339
Modelling of Magneto-Mechanical Phenomena by Using Shell Elements	II - 54
M. Hadjali, M. Besbes, F. Bouillault <i>LGEP - Supelec</i> <i>Gif-sur-Yvette - France</i>	P95281
Electromagnetic force density in a ferromagnetic material	II - 56
François Henrotte, Hans Vande Sande, Geoffrey Deliége, Kay Hameyer <i>Katholieke Universiteit Leuven, ESAT-ELECTA - Electrical Engineering Department</i> <i>Leuven-Heverlee - Belgium</i>	P45391

Machines II: Induction Motors

Chairman

 Tuesday, July 15, 10:45am - 12:00pm

Comparison of 2D and 3D Transient FEM Calculations of a Skewed Induction Machine	II - 58
Markus Johnen, Christian Kaehler, Gerhard Henneberger <i>Aachen University - Department of Electrical Machines</i> <i>Aachen - Germany</i>	P91570
Investigation of Induction Motor Zero Order Magnetic Stresses by a Finite Element Model	II - 60
Timothy McDevitt, David Jenkins, Michael Jonson <i>Penn State University - Applied Research Laboratory</i> <i>State College, PA - USA</i>	P41193
Calculation of Negative Torque Caused by Slot Ripples of Induction Motor	II - 62
Katsumi Yamazaki, Yoshihisa Haruishi, Takahiro Ara <i>Chiba Institute of Technology - Dept. of Electrical Engineering</i> <i>Tsudanuma - Japan</i>	P72617
Calculation of Force Excitations in Induction Machines with Centric and Excentric positioned Rotor using 2D Transient FEM	II - 64
Christoph Schlenzok, Gerhard Henneberger <i>Aachen University - Dept. of Electrical Machines</i> <i>Aachen - Germany</i>	P92227

Effects of saturation on the forces in induction motors with whirling cage rotor	II - 66
Asmo Tenhunen, Timo P. Holopainen, Antero Arkkio <i>Helsinki University of Technology - Laboratory of Electromechanics HUT - Finland</i>	P32699
Analysis of Voltage Distribution in Stator Windings of Induction Motor Driven by IGBT PWM Inverter	II - 68
Don-Ha Hwang, Dong-Sik Kang, Yong-Joo Kim, Sung-Woo Bae, Dong-Hee Kim <i>Korea Electrotechnology Research Institute (KERI) - Industry Applications Research Lab Changwon - Korea</i>	P23262
Loss Distribution of 3-phase Induction Motor with PWM Inverter drive	II - 70
Jeong-Jong Lee, Young-Kyun Kim, Kyung-Ho Ha, Jung-Pyo Hong, Don-Ha Hwang <i>Changwon National University - Dept. of Electrical Eng. Changwon - Korea</i>	P13189
A Discrete Fourier Transform Based Method to Compute Steady State Operation of Induction Motors Using Complex Finite Elements	II - 72
B. Laporte, S. Mezani, Norio Takorabet <i>GREEN - ENSEM - INPL Vandoeuvre-lès-Nancy - France</i>	P84722
Finite element analysis of a double winding induction motor with a special rotor bars topology	II - 74
A.M. Oliveira, P. Kuo-Peng, N. Sadowski, F. Rüncoş, R. Carlson, Patrick Dular <i>GRUCAD/EEL/CTC - UFSC Florianópolis - Brazil</i>	P35268
Calculation of the Rotor Bar Resistance and Leakage Inductance in a Solid Rotor Induction Motor with a One-Slot Model	II - 76
Lale T. Ergene, Sheppard J. Salon <i>Magsoft Corporation Troy, NY - USA</i>	P25278

Statics II: Magnetostatics

Tuesday, July 15, 10:45am - 12:00pm

Chairmen
Dr. Paul Leonard
Dr. Igor Tsukerman

The Mutual Inductance of Two Thin Coaxial Disk Coils in Air	II - 78
Slobodan Babic, Cevdet Akyel, Sheppard J. Salon <i>Ecole polytechnique de Montreal Montreal - Canada</i>	P21106

Two Mixed Hybrid Formulations For Magnetostatics in Unbounded Domains	II - 80
Leila Hamouda, Bernard Bandelier, Françoise Rioux-Damidau <i>Université Paris Sud - U2R2M Orsay - France</i>	P81515
Application of Spheroidal Functions in Magnetostatics	II - 82
Alexander V. Kildishev <i>Purdue University West Lafayette, IN - USA</i>	P91337
Magnetic field Analysis of Iron-Core Reactor Coils by Finite Volume Method	II - 84
J. Zou, Q. Huang, J.S. Yuan, X.S. Ma <i>Tsinghua University - Department of Electrical Engineering Beijing - China</i>	P11854
Solenoidal Current Flows for Filamentary Conductors	II - 86
Derek N. Dyck, J.P. Webb <i>McGill University - Dept. of Elec. and Comp. Engineering Montreal - Canada</i>	P11266
Discretisation of Boundary Integral Equations by Differential Forms on Dual Grids	II - 88
Stefan Kurz, Oliver Rain, Volker Rischmuller, Sergej Rjasanow <i>Robert Bosch GmbH Stuttgart - Germany</i>	P51972
Development of 3-D Read/Write Simulation System	II - 90
Naoya Fujiwara, Kiminari Shinagawa, Kohei Ashiho, Koji Fujiwara, Norio Takahashi <i>Okayama University - Dept. Electrical and Electronic Eng. Okayama - Japan</i>	P61879
Key problems in Element-Free Galerkin Method for Electromagnetic Field Computations	II - 92
Suzhen Liu, Qingxin Yang, Haiyan Chen, Weili Yan <i>Hebei University of Technology Tianjin - China</i>	P72666
Simplified Magnetic Moment Method Applied to Current Transformers Modeling	II - 94
Fleur Janet, Jean-Louis Coulomb, Christian Chillet, Patrick Mas <i>Laboratoire d'électrotechnique de Grenoble -- INPG/UJF-CNRS UMR 5529 ENSIEG Saint-Martin-d'Hères - France</i>	P12483

Computation of Voltage Driven, Current Dependent Ferrite Inductors using FEM	II - 96
W. Renhart, Christian Magele, K. Preis	P13466
<i>Graz University of Technology Graz - Austria</i>	
Hybrid Numerical Techniques for Power Transformer Modeling: A comparative analysis validated by measurements	II - 98
M. Tsili, Antonios G. Kladas, P. Georgilakis, A. Souflaris, C. Pitsilis, J. Bakopoulos, D. Paparigas	P73287
<i>National Technical University of Athens - Department of Electrical & Computer Engineering Athens - Greece</i>	
Computation of the magnetostatic field by means of a mixed analytical-numerical procedure	II - 100
Fabrizio Bellina, Enrico Serra	P54702
<i>Università di Udine - DIEGM Udine - Italy</i>	
Automatic Generation of Sizing Models for the Optimisation of Electromagnetic Devices using Reluctance Networks	II - 102
Augustin Delale, Laurent Albert, Frédéric Wurtz, Laurent Gerbaud	P54088
<i>Laboratoire d'Electrotechnique de Grenoble - (INPG/UJF - CNRS - UMR 5529), Saint-Martin-d'Hères - France</i>	
Computation of the strayfields generated by a magnetic core with air-gap	II - 104
R. Scorretti, Noël Burais, J.P. Masson	P75386
<i>Ecole Centrale de Lyon Ecully - France</i>	

Optimization II

Tuesday, July 15, 1:30pm - 2:45pm

Chairmen

Dr. Joao Pedro Bastos
Dr. Oszkár Bíró

A Novel Auto-tuning Algorithm for the Integrated RBF Network of Brushless D.C. Motor	II - 106
S.L. Ho, M.N. Fei, K.W.E. Cheng, H.C. Wong	P51848
<i>Hong Kong Polytechnic University - Dept. of Electrical Engineering Kowloon - Hong Kong</i>	
Optimal Design of Switched Reluctance Motor	II - 108
H. Zeroug, H. Sahraoui, H. A. Toliyat	P92512
<i>Texas A&M University - Electrical Engineering Department College Station, TX - USA</i>	
Pareto Optimality and Particle Swarm Optimization	II - 110
Ulrike Baumgartner, Bernhard Brandstätter, Christian Magele, W. Renhart	P53550
<i>Graz University of Technology Graz - Austria</i>	

Applying continuum design sensitivity analysis combined with standard EM software to shape optimisation in magnetostatic problems	II - 112
Dong-Hun Kim, K.S. Ship, Jan K. Sykulski	P13365
<i>University of Southampton - Department of Electronics and Computer Science Southampton - United Kingdom</i>	
3D optimal shape design of magnetic pole in permanent magnet assembly for MRI taking account of gradient coil field	II - 114
Yingying Yao, Chang Seop Koh, Dexin Xie	P33379
<i>Chungbuk National University - School of Electrical & Computer Engineering Chungbuk - Korea</i>	
Support Vector Machines - a Promising Tool for Optimal Design of Electromagnetic Devices	II - 116
Jacek Starzyński, Stanisław Osowski, Stanisław Wincenciak	P24137
<i>Warsaw University of Technology Warsaw - Poland</i>	
Design of Inserted Core Type Slotless PMLSM for Detent Force Minimization by using Neural Network	II - 118
Mi-Yong Kim, Jae-Yun Moon, Gyu-Tak Kim	P74649
<i>Changwon National University - Dept. of Electrical Engineering Changwon - Korea</i>	
A Pruning Method for Neural Networks and its Application for Optimization in Electromagnetics	II - 120
Frederico G. Guimaraes, Jaime A. Ramirez	P24556
<i>Universidade Federal de Minas Gerais -- Escola de Engenharia, Departamento de Engenharia Eletrica Belo Horizonte - Brazil</i>	
Optimal Designs of Roll-iron Core Transformers by Pareto Genetic Algorithm	II - 122
Yan Hu, Renyuan Tang, Xiulian Wang, Liangyun Zhao	P84662
<i>Shenyang University of Technology - School of electrical Engineering Shenyang - China</i>	
A new Tabu Search Method for Optimization with Continuous Parameters	II - 124
O. Hajji, S. Brisset, P. Brochet	P94585
<i>Ecole Centrale de Lille - Departement Genie Electric Villeneuve d'Ascq - France</i>	
Treating Constraints as Objectives in Multiobjective Optimization Problems using Niche Pareto Genetic Algorithm	II - 126
Douglas A.G. Vieira, Ricardo L.S. Adriano, Laurent Krähenbühl, João A. De Vasconcelos	P95729
<i>Federal University of Minas Gerais Belo Horizonte - Brazil</i>	

Extracting Sensitivity Information of Electromagnetic Device Models from a Modified ANFIS Topology **II - 128**

Douglas A.G. Vieira, Walmir M. Caminhas, Jaime A. Ramirez, João A. De Vasconcelos P65733

*Universidade Federal de Minas Gerais - Escola de Engenharia, Departamento de Engenharia Eletrica
Belo Horizonte - Brazil*

Design Optimization for Cogging Torque Minimization using Response Surface Methodology **II - 130**

J.T. Li, Z.J. Liu, M.A. Jabbar, X.K. Gao P55349

*Data Storage Institute
Singapore*

Waves II

Chairman

Tuesday, July 15, 1:30pm - 2:45pm

A high-order, high-frequency method for surface scattering by convex obstacles **II - 132**

Oscar P. Bruno, Christophe A. Geuzaine P71323

*California Institute of Technology - Applied & Computational Mathematics
Pasadena, CA - USA*

Computation of HF Currents in Opened Shells **II - 134**

Badr Kebaili, Bernard Bandelier, Françoise Rioux-Damidau P11031

*Université Paris Sud - U2R2M
Orsay - France*

Using star loop method of moment to model arbitrary shaped microstrip antennas **II - 136**

Kezhong Zhao, Jin-Fa Lee P41076

*ElectroScience Lab
Columbus, OH - USA*

Optimal Design of Planar Microwave Filter Structure of Arbitrary Shape by the FEM-GA Approach **II - 138**

Wen Wang, Yilong Lu, Jeffrey S. Fu P92403

*Nanyang Technological University - School of EEE
Singapore*

Rapid simulation of laser scattering from dielectric cylinders of arbitrary cross-section **II - 140**

Meng H. Lean P82068

*Palo Alto Research Center Inc
Palo Alto, CA - USA*

Finite Element Modelling for the Design of Microwave Filters	II - 142
S. Bila, D. Bariant, D. Baillargeat, M. Aubourg, S. Verdeyme, F. Seyfert, L. Baratchart, C. Boichon, F. Thevenon, J. Puech, C. Zanchi	P52080
<i>IRCOM - CDM, Faculté des Sciences et Techniques Limoges - France</i>	
3D Ray Tracing Propagation Model in Urban Environments	II - 144
A. Barabino, P. Girdinio, M. Nervi	P23221
<i>University of Genova Dept. Of Electrical Engineering Genova - Italy</i>	
EMIR-A Numeric Processor for the Analysis and Simulation of Radiated Electromagnetic Fields due to Electric Cabling Systems	II - 146
Carlos F.R. Lemos Antunes, António Paulo Coimbra	P33084
<i>University of Coimbra - Electrical Engineering Department Coimbra - Portugal</i>	
Multiobjective Optimization of Wire Antennas	II - 148
R.M. Ramos, R.R. Saldanha, R.H.C. Takahashi, F.J.S. Moreira	P94258
<i>Universidade Federal de Minas Gerais Minas Gerais - Brazil</i>	
Conceptual Framework for Numerical Wave Propagation Schemes	II - 150
Timo Tarhassari, Lauri Kettunen	P24463
<i>Tampere University of Technology -- Institute of Electromagnetics Tampere - Finland</i>	
Current and near field calculations for cellular base-station collinear array antennas	II - 152
Federico Delfino, Renato Procopio, Mansueto Rossi	P85661
<i>University of Genoa - Department of Electrical Engineering Genova - Italy</i>	
Finite Element Waveguide Solvers Revisited	II - 154
Ortwin Farle, Volker Hill, Romanus Dyczij-Edlinger	P26000
<i>Universitaet des Saarlandes - Lehrstuhl fuer Theoretische Elektrotechnik Saarbruecken - Germany</i>	
Microwave Drying of Cylindrical Products	II - 156
M.A. Saber	P46022
<i>Manama Town - State of Bahrain</i>	

Devices II: NTD and Microwave Cavities
Tuesday, July 15, 1:30pm - 2:45pm

Chairman
Dr. Francis Piriou

- Proposal of Detecting Method of Plural Cracks and Their Depth by Alternating Flux Leakage Testing - 3-D Nonlinear Eddy Current Analysis and Experiment** II - 158
Yuji Gotoh, Norio Takahashi P31625
Okayama University - Dept. of Electrical and Electronic Eng.
Okayama - Japan
- Eigenmode Simulation of Electromagnetic Resonator Cavities with Gyrotropic Materials** II - 160
Stefan Feigh, Markus Clemens, Rolf Schuhmann, Thomas Weiland P12921
TU Darmstadt - FG Theorie Elektromagnetischer Felder
Darmstadt - Germany
- Approximate Methods for the Calculation of the ECT Signal of a Crack in a Plate Coated by Conducting Deposit** II - 162
József Pávó P52854
Budapest University of Technology and Economics - Department of Electromagnetic Theory
Budapest - Hungary
- An Optimum Design and Analysis of A Multi-port Microwave Cavity using 3D FEM with a Sensitivity Method** II - 164
Pan-Seok Shin, Changyul Cheon, Sheppard J. Salon P72060
Hongik University - Electrical Eng. Department
Chungnam - S. Korea
- TLM and FEM Analysis of a Mode Stirred Chamber Excited by Wires** II - 166
D. Weinzierl, R. Jacobs, Arnulf Kost, Adroaldo Raizer P62777
Brandenburgische Technische Universitaet Cottbus - Lehrstuhl Allgemeine Elektrotechnik und Numerische Feldberechnung
Cottbus - Germany
- A Combined Method for Fast 3-D FEM Modeling of NDT Signal** II - 168
Lin Heyun, S.L. Ho, H.C. Wong P33144
Hong Kong Polytechnic University - Dept. of Electrical Engineering
Kowloon - Hong Kong
- Minimum Norm Reconstruction of Vicinal Defects in Magnetic Flux Leakage Pipeline Data** II - 170
Jens Haueisen, M. Seitz, T. Beuker, M.E. Bellemann P94064
University Jena -- Biomagnetic Center
Jena - Germany
- Analysis of the Velocity Induced Eddy Current in MFL Type NDT** II - 172
Gwan Soo Park, S.H. Park P95400
Korea Maritime Univ. - Dept. Electrical Engineering
Pusan - South Korea
-

Transmission Line Matrix Model for Detection of Local Changes in Permeability Using a Microwave Technique II - 174
 Razvan Ciocan, Nathan Ida P15557
The University of Akron - Department of Electrical Engineering
Akron, OH - USA

Extending the Operation of Mode Stirred Chambers to Low Frequencies II - 176
 Jose Perini, Lawrence S. Cohen P25773
Syracuse University - ECE Dept.
Daytona Beach Shores, FL - USA

Quasistatic II: Eddy Current
 Tuesday, July 15, 1:30pm - 2:45pm

Chairman
 Dr. Patrick Dular

Working Nonlinear Transient Eddy Current Problems with Time Harmonic Solutions II - 178
 Kent R. Davey P41338
American Maglev, Inc.
New Smyrna Beach, FL - USA

Numerical Analysis of Thin Skin Depth of 3-D Eddy Current Problems Using a Combination of Finite Element and Meshless Methods II - 180
 Shiyong Yang, S.L. Ho, Guangzheng Ni, H.C. Wong, Yuhuai Wang P91345
Hong Kong Polytechnic University -- Dept. of Electrical Engineering
Kowloon - Hong Kong

A Single-Source Surface Integral Formulation for Eddy-Current Problems II - 182
 Ioan R. Ciric, R. Curiac P51594
The University of Manitoba - Department of Electrical Engineering
Winnipeg - Canada

Performance of Surface Impedance Integral Equation for Quasistationary Field Analysis in Axisymmetric Systems II - 184
 Himal C. Jayatilaka, Ioan R. Ciric P51796
The University of Manitoba - Department of Electrical and Computer Engineering
Manitoba - Canada

The Weighted Wavelet-Based Multiresolution Time-Domain Analysis in the MOM Solutions for Transient Eddy Current Problems II - 186
 K.R. Shao, L.R. Li, J.D. Lavers P62500
Huazhong University of Science & Technology - Dept. of Electrical Engineering
Wuhan - China

Transient Eddy Current Analysis of Pulsed Eddy Current Testing by Finite Element Method II - 188
 Hajime Tsuboi, Norio Seshima, Imre Sebestyén, József Pávó, Szabolcs Gyimóthy, Antal Gasparics P32261
Fukuyama University - Dept. of Information Engineering
Fukuyama - Japan

Efficient Technique for 3-D Finite Element Analysis of Skin Effect in Current-Carrying Conductors	II - 190
Hong-Kyu Kim, K.Y. Park, Chang-Hwan Im, Hyun-Kyo Jung	P12996
<i>Korea Electrotechnology Research Institute(KERI) - Advanced Power Apparatus Group Changwon - South Korea</i>	
Algebraic MultiGrid Preconditioner for Harmonic Eddy Current Problems in 3D	II - 192
M. Kaltenbacher, S. Reitzinger	P43561
<i>University of Erlangen - Department of Sensor Technology Erlangen - Germany</i>	
Magnetic scalar potential formulation using a 3D complex permeability for proximity losses computation	II - 194
Michael Joan, Olivier Moreau, Gérard Meunier, Thierry Chevalier	P53063
<i>LEG - ENSIEG CNRS UMR 5529 Saint-Martin-d'Hères - France</i>	
Field-circuit coupling for time-harmonic models discretized by the finite integration technique	II - 196
Herbert De Gersem, Thomas Weiland	P34394
<i>Technische Universität Darmstadt -- Theorie Elektromagnetischer Felder Darmstadt - Germany</i>	
Experimental Validation for Numerical Simulation of Eddy Current in Iron Structures	II - 198
Tatsuei Nomura, Yoshihiro Tani	P55408
<i>Osaka Electro-Comm. Univ. Neyagawa - Japan</i>	
Time-domain analysis of proximity effect current driven problems	II - 200
M. Vitelli	P45922
<i>Seconda Università di Napoli - Dipartimento di Ingegneria dell'Informazione Aversa - Italy</i>	

Materials

Chairman

Tuesday, July 15, 3:15pm - 5:00pm

Simulation of a three-phase transformer using an improved anisotropy model	II - 202
Hans Vande Sande, T. Boonen, I. Podoleanu, François Henrotte, Kay Hameyer	P92706
<i>KULeuven - Dept. ESAT, Div. ELECTA Leuven-Heverlee - Belgium</i>	

A Time Domain Homogenisation Technique for Laminated Iron Cores in Three-Dimensional Finite Element Models	II - 204
Johan Gyselinck, Patrick Dular, W. Legros	P34697
<i>University of Liège - Department of Applied Electricity Liège - Belgium</i>	
Iron Losses Analysis in Magnetic Circuits supplied by PWM Converters	II - 206
Konstantinos V. Tatis, Antonios G. Kladas, John A. Tegopoulos	P93182
<i>National Technical University of Athens - Department of Electrical & Computer Engineering, Electric Power Division Athens - Greece</i>	
Field Errors in SC Magnets Due to Persistent Currents Generated by Arbitrary Field Changes in the Transverse Plane	II - 208
Martin Aleksa, Bernhard Auchmann, Stephan Russenschuck, Christine Vollinger	P93620
<i>CERN Geneva - Switzerland</i>	

Fields, Focussing and Aberrations in Electrostatic Accelerator Tubes

H.R.McK. Hyder

Department of Physics, Oxford University, Oxford

C.W.Trowbridge

Vector Fields Ltd, Oxford, OX5 1JE

Abstract – Electrostatic field distributions and particle trajectories have been computed using a standard software package for a number of geometries typical of the accelerator tubes used in modern electrostatic accelerators. The results have been used to investigate the focussing action and the effect of lens aberrations on the subsequent emittance and brightness of the beam. A novel aspect is the calculation of field distributions in the tube interior close to the edges of thick electrodes.

INTRODUCTION

Small electrostatic accelerators are in widespread use for research, material modification, ion implantation and analysis including carbon dating. The quality of the beam on target is critical to all these applications. It depends on the ion source and on the optical elements, the most critical of which is the accelerator tube. The first order focussing action of an accelerator tube is simple and well known [1]. Empirical corrections to the formula for an electrostatic immersion lens [2] result in prescriptions adequate for most purposes. But it has long been known that these simplified models overlook effects, such as aberration at the entrance to the tube, which cannot always be ignored.

Rose et al. [1] reported calculations of field distributions and particle trajectories that took into account the geometry of the entrance region and field variations inside the tube due to finite electrode thickness. They concluded that this effect might be significant in tubes with small bore diameters. However they did not compute the exact form of the longitudinal voltage ripple at different distances from the axis as a function of thickness, pitch and bore radius.

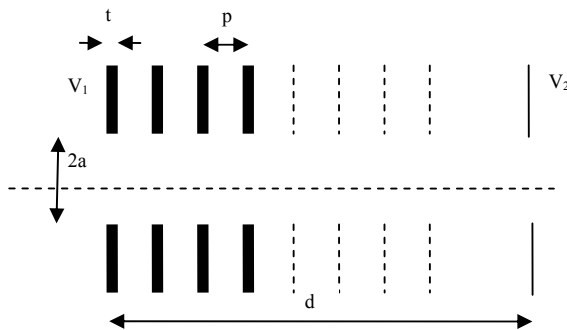


Fig. 1 Simple accelerator tube geometry

With the object of determining the mesh size and precision necessary to obtain reliable predictions of aberration and emittance growth, we have examined the optics of an accelerator tube consisting of a number $n+1$ of equispaced plane electrodes, of thickness t , bore radius a and pitch p , as shown in Fig. 1. At either end a region bounded by conductors at the potential of the first and last electrodes is sufficiently long not to perturb the field distribution extending beyond the tube proper. A cylindrical boundary of radius $a+2p$ extends from each electrode to its neighbour. A uniform field of $V/(p-t)$, where V is the

constant voltage between electrodes, defines the potential of these boundaries. The computational challenge is to calculate the fields to high accuracy so that sufficiently smooth values of higher derivatives can be obtained to evaluate aberration integrals [3]. The use of an analytic expression fitted to the numerical results enables third order ray tracing to be compared with general ray tracing to aid confidence in the numerical finite element solution.

ENTRANCE & EXIT LENS

The mesh size necessary in the field program for adequate precision over the region $r < a$ has been specified so that particle trajectories and the effects of third order aberrations can be found with confidence. The results for a series of rays originating from points on the axis, with varying values of initial energy eV_0 and initial transverse momentum, have been compared with data obtained from the field distribution derived from the analytic expression for the axial field.

An analytic model for the case without internal plates is obtained by superimposing the fields from two circular apertures for which Laplace's equation can be solved exactly using oblate spherical coordinates [3]. The resulting formula for the axial electric field distribution appropriate to Fig. 1 is:

$$V(z) = \frac{(V_2+V_1)}{2} + \frac{(V_2-V_1)}{\pi} \frac{a}{d} \left[\frac{z}{a} \arctan \frac{z}{a} - \frac{(z-d)}{a} \arctan \frac{(z-d)}{a} \right] \quad (1)$$

eV_1 is set equal to the energy of the incoming particle as is customary in electron optics and eV_2 the final energy. A comparison of the results from a FE computation ($t=0$) and (1) are shown in Fig. 2. In Table 1 the results for the optical properties of the tube are shown both by solving the particle equations of motion, truncated to third order expansions of the potentials defined in (1), and the general case based on the full FE solution.

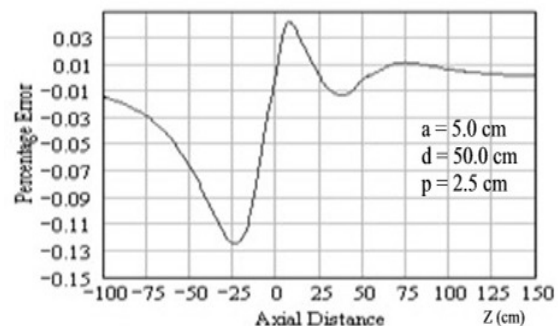


Fig. 2 FE Solution comparison to (1)

Table I suggests that the analytic representation can be used with confidence for the optical properties but for real tubes with thick electrodes a full solution will be necessary, see next section. The effect of aberration on the beam spot

in the image plane is shown by a phase space emittance diagram where the ray angle α is plotted versus radius at $z = Z_i$, see Fig. 3. The solid line is the image computed from the general ray tracing using the full FE solution and the dashed line uses the third order optical parameters.

TABLE I: COMPUTED OPTICAL PARAMETERS ($t=0$)

Optical Parameter	Paraxial	Third Order	General with no plates	General with Plates
Z_i	92.656	92.656	92.574	91.858
M	-0.418	-0.418	-0.418	-0.413
Ma	-0.721	-0.721	-0.722	-0.730
Cs -fitted		9114.0	8889.0	8988.0
Cs- [3]		9180.0		

Key: Length Unit is cm. Z_i Gaussian image plane, M linear magnification, Ma angular magnification and Cs spherical aberration coefficient. Columns 2 & 3 - third order using (1) for the fields, 4&5 using full FE solution. Cs computed both by using the classical formula based on third order perturbation theory [3] and by fitting a ray bundle in the object plane to $r'=C_s\alpha^3$.

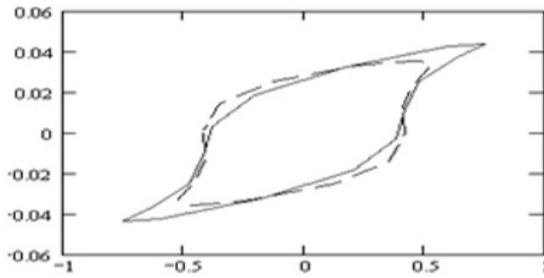


Fig. 3. Emittance plot in the image plane α (radians) vs r (cm)

RIPPLE

Field distributions inside tubes with finite electrode thicknesses have also been computed using an optimised mesh. Away from the ends of the tube the field distribution is periodic and is completely determined by the ratios t/a and t/p . The resulting periodic nature of E_z for values of r from 0 to $0.9a$ is indicated in Fig. 4 for typical values of t , a and p ($t=1$ mm, $a = 10$ mm, $p = 25$ mm). Near the axis the ripple is nearly sinusoidal, but as r increases the ripple amplitude increases, higher harmonics become important and aberrations and focussing are affected in consequence. For higher values of t/a , even the field on axis is no longer sinusoidal. Rose et al. [1] have suggested that the radial variation of ripple voltage can be approximately represented by an exponential dependence of amplitude on the ratio of bore radius to pitch and a sinusoidal variation with z . At fixed bore radius (a), the radial variation is expressed by a zero order Bessel function. The higher harmonics in the Fourier series which describes the z variation were neglected, but our data suggest that this may not be justified for large values of t/a .

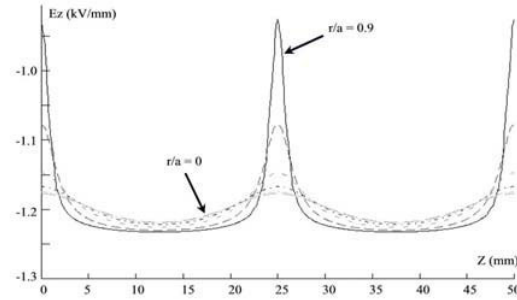


Fig. 4. Axial field E_z across two pitches for $r/a = 0, 0.2, 0.4, 0.6, 0.8, 0.9$. [$t/a = 0.1, t/p = 0.04, E_z(t=0) = 1.2$ kV/mm]

Using these calculated field distributions we have computed the trajectories for a range of particles. Trajectories for the extreme case of low energy particles (10 keV) traversing a tube with $t/a = 0.5$ and $t/p = 0.1$ are shown in Fig. 5. It is obvious that particles starting near the electrodes are strongly affected, those near the axis much less so. There is evidence of severe spherical aberration.

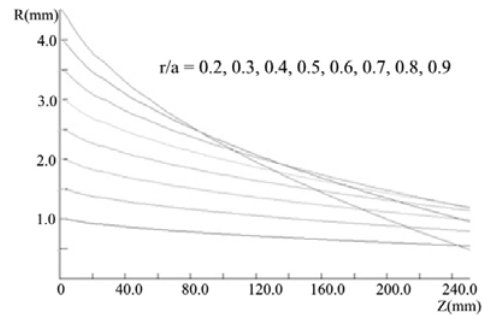


Fig. 5. Trajectories for 10 keV particles with zero initial transverse velocity in a tube with $t/a = 0.5, t/p = 0.1$.

SUMMARY

The modern computational techniques have been used to assess the accuracy of accelerator tube optical properties using a simple analytic model. We report, for the first time, accurate values of the fields close to the edges of thick electrodes and aberrations using a FE package. In the extended paper, the authors will discuss focussing and aberrations due to the inclined fields used to suppress secondary particles; in particular a full 3-D analysis will be applied to tubes with spiral and non-cylindrical geometries.

REFERENCES

- [1] A Galejs and P Rose, "Optics of Electrostatic Accelerator Tubes", *Focusing of Charged Particles*, Ed A Septier, Vol 2, A P, 1967.
- [2] P Stenning and C Trowbridge, "The Pathfinder Programme and its Application to Ion Optics, Rutherford Lab /Reading University RU/RL-1, 1968. Download from <http://www.trowbridge.org.uk/downloads.htm>
- [3] P Hawkes and E Kaspar, *Principles of Electron Optics*, Vol 1, page 142 & page 361, Eq 24.62, AP, 1996

Finite Element Simulation of Head / Media Interactions in Perpendicular Recording

Thomas Schrefl, Hermann Forster

Solid State Physics, Vienna University of Technology
Wiedner Haupstr. 8-10/138
A-1040 Vienna, Austria

thomas.schrefl@tuwien.ac.at, hermann.forster@tuwien.ac.at

Manfred E. Schabes, Byron Lengsfeld

IBM Almaden Research Center
650 Harry Road
San Jose, CA 95120 USA
manfred@almaden.ibm.com

Abstract—Finite element micromagnetics is combined with fast boundary element techniques to calculate the magnetostatic interactions between the recording head, the data layer, and the soft underlayer in perpendicular magnetic recording. The finite element method is highly suitable to model the physical microstructure of the media such as realistic grain shapes and intergranular phases. The fast boundary method provides an efficient and accurate means to simulate the mutual interactions between the moving magnetic parts. Fully time dependent simulations of the recording process treating both head and media micromagnetically and taking into account the moving head were performed.

INTRODUCTION

The design and optimization of ultra high density storage technologies requires a precise understanding of the magnetization processes that occur during the formation of the bit patterns. A possible route towards storage densities of one Tbit/in² is perpendicular recording [1,2]. A bit is stored by a small number of vertically magnetized grains. A weak exchange coupling between the grains may be beneficial to improve the thermal stability [3], but can decrease the switching speed [4]. Media models therefore have to take into account variable intergrain exchange interactions, in order to assist design optimization by micromagnetic simulations. The writer involves a write pole, a return pole, and the soft underlayer. The magnetic path between the write pole and the return pole is bridged by the soft underlayer which thus becomes an integral part of the recording head. The write field properties and the associated magnetization processes in the soft underlayer were calculated previously using finite difference techniques and finite element techniques [5].

A common approach to include moving parts into electromagnetic finite element simulations is the use of sliding grids and Mortar elements [6]. An alternative approach is the use of the use hybrid finite element / boundary element (FEM/BEM) techniques [7]. For magnetic recording simulations FEM/BEM methods have the advantage that no mesh is needed

between the different magnetic parts, and the magnetization dynamics can be calculated in the rest frame of each part.

In this paper we present a novel algorithm that combines the finite element method with fast boundary element techniques to simulate the fully integrated system: moving head, data layer, and soft underlayer. The microstructural features of the data layer can be taken into account in full detail using the finite element method. Different techniques to accelerate the boundary element method and to reduce the memory are compared.

COMPUTATIONAL TECHNIQUES

The basic equation describing magnetization dynamics is the stochastic Gilbert equation

$$\frac{\partial \mathbf{J}}{\partial t} = -|\gamma| \mathbf{J} \times (\mathbf{H}_{\text{eff}} + \mathbf{H}_{\text{th}}) + \frac{\alpha}{J_s} \mathbf{J} \times \frac{\partial \mathbf{J}}{\partial t}, \quad (1)$$

where \mathbf{J} is the magnetic polarization vector, γ the gyromagnetic ration, and α the Gilbert damping constant. The effective field \mathbf{H}_{eff} is the sum of the exchange field, the anisotropy field, the external field, and the magnetostatic field. \mathbf{H}_{th} is a random, thermal field that mimics the effect of thermal fluctuations at non-zero temperature.

Magnetostatic field calculation The magnetostatic field is computed from a magnetic scalar potential using a FEM/BEM formulation proposed by Fredkin and Koehler [8]: The potential is split into two parts $U = U_1 + U_2$. U_1 follows from the Poisson equation, and U_2 is a double layer potential given by the surface integral over a dipole sheet with density U_1 .

Media model Columnar grains are constructed from Voronoi cells. The grains are further subdivided into tetrahedral finite elements. The magnetization and the magnetic scalar potential are interpolated by linear shape functions. The exchange coupling between neighboring grains and the mag-

netostatic interactions across grain boundaries are modeled using special elements for narrow gaps [9].

Fast boundary method The discretization of the surface integral for the evaluation of U_2 leads to a fully populated matrix. Different methods were used to sparsify the BEM matrix and to accelerate the matrix vector multiplication. We compared hierarchical matrices [10] computed by adaptive cross approximation [11] and the Barnes and Hut tree code [12].

Time integration We apply a multiple time step method for the integration of (1). The effective field contains near field and far field contributions. The far field part is the potential U_2 that is generated from remote surface triangles. We found that it is sufficient to evaluate the far field every 10th time step only. In between U_2 is extrapolated linearly.

RESULTS

Fig. 1 shows a bit pattern as calculated from magnetic recording simulations. The data layer consists of 2048 grains. The total number of finite elements is $4 \cdot 10^5$. The head velocity was 20 m/s. Fig. 2 compares the memory requirements for the different BEM methods.

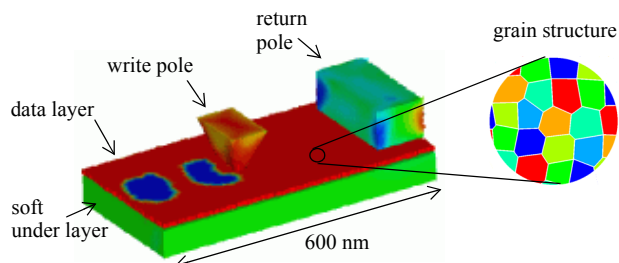


Fig. 1. Simulated bit patterns using a tapered write pole. On the left hand side the color code maps the magnetization direction. The right hand side shows a top view of the grain structure.

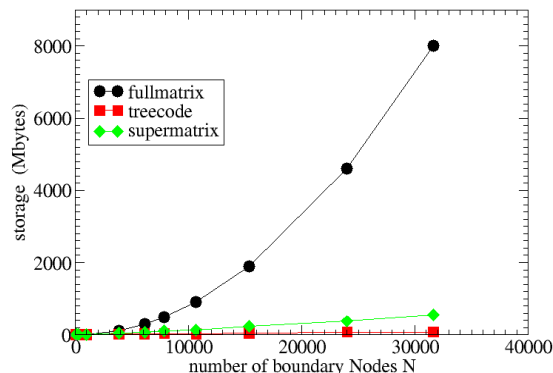


Fig. 2. Memory requirements for the BEM matrix versus the number of boundary nodes for the full matrix method, the tree code, and the supermatrix (hierarchical matrix method).

We compared the CPU time required for the setup phase and for the evaluation of U_2 (BEM matrix times a vector). The tree code requires the least memory and has the shortest setup phase. A fast setup is essential since the BEM data has to be computed every time step. The calculation of the tree code data takes only a quarter of the CPU time required to compute the supermatrix. However, the evaluation of the matrix vector product by walking the tree takes considerable more time than the hierarchical matrix method. This can be compensated using a multiple time step time integration scheme. The most promising approach is the use of hierarchical matrices for the self interactions within the data layer and the soft underlayer and the tree code for the interactions between the moving head and the media.

Work supported by the Austrian Science Fund (Y132PHY).

REFERENCES

- [1] M. Mallery, A. Torabi, and M. Benakli, "1 Tb/in² perpendicular recording conceptual design," *IEEE Trans. Magn.*, vol. 38, pp. 1719-1724, July 2002.
- [2] R. H. Victora, J. Xue, and M. Patwari, "Areal density limits for perpendicular magnetic recording," *IEEE Trans. Magn.*, vol. 38, pp. 1886-1891, September 2002.
- [3] H. Zhou, H. Neal Bertram, and M. E. Schabes, "Micromagnetic Analysis of the Effect of Intergranular Exchange on Thermal Stability in Magnetic Recording (III): Perpendicular Media," *IEEE Trans. Magn.*, vol. 38, pp. 1422-1428, March 2002.
- [4] M. Benakli, A. F. Torabi, M. L. Mallery, H. Zhou, and H. Neal Bertram, "Micromagnetic Study of Switching Speed in Perpendicular Recording Media," *IEEE Trans. Magn.*, vol. 37, pp. 1564-1566, July 2001.
- [5] M. E. Schabes, B. Lengsfeld, and T. Schrefl, "Micromagnetic Modeling of Soft Underlayer Magnetization Processes and Fields in Perpendicular Magnetic Recording," *IEEE Trans. Magn.*, vol. 38, pp. 1670-1675, July 2002.
- [6] A. Buffa, Y. Maday, F. Rapetti, "A sliding mesh-mortar method for a two dimensional eddy currents model of electric engines," *Meth. Math. en Anal. Num.*, Vol. 35, No. 2, pp. 191-228, 2001.
- [7] S. Kurz, J. Fetzer, G. Lehner, and W. M. Rucker, "Numerical analysis of 3D eddy current problems with moving bodies using BEM-FEM coupling," *Surveys on Mathematics for Industry*, vol. 9, pp. 131--150, 1999.
- [8] D. R. Fredkin, T. R. Koehler, "Hybrid method for computing demagnetizing fields," *IEEE Trans. Magn.*, vol. 26, pp. 415-417, March 1990.
- [9] C. Guérin, G. Tanneau, G. Meunier, X. Brunotte, J.-B. Albertini, "Three dimensional magnetostatic finite elements for gaps and iron shells using magnetic scalar potentials," *IEEE Trans. Magn.*, vol. 30, September 1994.
- [10] S. Börm, L. Grasedyck, and W. Hackbusch, "Introduction to hierarchical matrices with applications," *Mathematica Bohemica*, vol. 127, pp. 229-241, 2002.
- [11] S. Kurz, O. Rain, S. Rjasanow, "Application of the adaptive cross approximation technique for the coupled BE-FE solution of electromagnetic problems," *IEEE Trans. Magn.*, vol. 38, pp. 421-424, March 2002.
- [12] J. Barnes and P. Hut, "A hierarchical O(n log n) force calculation algorithm," *Nature*, vol. 324, pp. 446-449, 1986.

Scalar and vector potentials' coupling on nonmatching grids for the simulation of an electromagnetic brake

B. Flemisch¹, Y. Maday², F. Rapetti³, B.I. Wohlmuth¹

¹Inst. Ang. Analysis und Numer. Simulation, Univ. Stuttgart, Pfaffenwaldring 57, 70569 Stuttgart, DE

²Lab. J.-L. Lions, CNRS & Univ. Paris VI, 4 place Jussieu, 75252 Paris 05, FR

³Lab. J.-A. Dieudonné, CNRS & Univ. Nice et Sophia-Antipolis, Parc Valrose, 06108 Nice 02, FR

Abstract—We present a method for the simulation of the dynamical behavior of a coupled magneto-mechanical system. We consider a model based on the T - Ω formulation of the eddy currents problem for the magnetic part and on the motion equation of a moving rigid body for the mechanical part. The coupled system is solved with an iterative procedure.

INTRODUCTION

In a coupled magneto-mechanical system, the forces due to the magnetic field contribute to the free structure motion and the resulting variation in the structure configuration modifies the distribution of the magnetic field and so of the induced forces. To take simultaneously into account the electromagnetic and mechanical equations it is necessary to compute the global magnetic force acting on the moving part of the system, through the numerical evaluation of the magnetic field. Here, we study a system where, attached to an elastic spring suspended from the lid of a rigid box, a conductor of mass m oscillates within the magnetic field supported by a ferromagnet.

The algorithm we consider is based on an “explicit” coupling procedure: at each time step, the magnetic force obtained from the field solution is inserted in the mechanical equation to compute the displacement. The latter is imposed to the moving part for the next step of the magnetic field calculation. A finite difference scheme is adopted to discretize the ordinary differential equation which accounts for the conductor position. The magnetic field is computed by applying the finite element method to the T - Ω formulation of the eddy current problem. This formulation allows to use a scalar function (Ω) in the computational domain and a vector quantity (T) only in the conducting parts. We propose to approximate these two quantities on different meshes, in order to deal with moving conductors, and to couple them by means of the mortar element method [4], [5]. The proposed method is a valid alternative to remeshing or boundary elements.

THE MODEL

The mathematical model describing the eddy current problem in the conductors at low frequencies is given by the quasi-stationary Maxwell's equations [1]. In this paper, we restrict ourselves to the magnetic field approach. The space \mathbb{R}^3 is decomposed in the conducting region V_c and the external region $\mathbb{R}^3 \setminus V_c$. Denoting by H , B , J and E the magnetic field, the magnetic flux density, the current density and the electric field, respectively, the quasi-stationary Maxwell's equations in V_c read:

$$\nabla \times H = J, \quad \nabla \times E = -\partial_t B, \quad \nabla \cdot B = 0. \quad (1)$$

The densities and the fields are linked by the constitutive properties, i.e., $B = \mu H$, $J = \sigma E$, where $\mu > 0$ is the

magnetic permeability and $\sigma \geq \bar{\sigma} > 0$ stands for the electric conductivity. Moreover, we assume that the material parameters are time independent and associated with linear isotropic media, and that the given external source J_s is zero within the conducting regions. As a result, we obtain the following field equations in $\mathbb{R}^3 \setminus V_c$:

$$\nabla \times H = J_s, \quad \nabla \cdot B = 0, \quad B = \mu H. \quad (2)$$

The problem is well posed by adding regularity conditions at infinity and suitable interface conditions on ∂V_c . In particular, $[H]_c \times n_c = 0$, $[B]_c \cdot n_c = 0$, where n_c is the outer normal on ∂V_c , and $[v]_c$ stands for the jump of v on ∂V_c . Additionally to the boundary conditions, we have to impose suitable initial values for the vector fields at a given time t_0 . The initial condition on B has to satisfy $\nabla \cdot B = 0$ and $[B] \cdot n = 0$ at any interface. By introducing artificial boundary conditions, we can work on a bounded domain V . For simplicity, we assume that V_c is a simply connected polyhedral subdomain of V and $\bar{V}_c \subset V$. For the current density J , the condition $\nabla \cdot J = 0$ suggests the introduction of a vector potential \tilde{T} such that $J = \nabla \times \tilde{T}$. Then in V_c , the difference between the vector potential \tilde{T} and the magnetic field H can be written as the gradient of a scalar function $\tilde{\Omega}$, i.e., $H = \tilde{T} - \nabla \tilde{\Omega}$. A similar argument holds for the insulating region, where we assume knowing a vector potential T_s such that $J_s = \nabla \times T_s$.

We define a variational formulation based on the decomposition of H into $\tilde{T} - \nabla \tilde{\Omega}$ in V_c and $T_s - \nabla \tilde{\Omega}$ in $V \setminus V_c$. Choosing $\tilde{T} \in H_0(\text{curl}; V_c)$ and $\tilde{\Omega} \in H_0^1(V)$, \tilde{T} and $\tilde{\Omega}$ satisfy at each time step the interface conditions, i.e., $\tilde{\Omega}$ is continuous at ∂V_c and $[\tilde{T}]_c \times n_c = 0$. Note that, if $(\tilde{T}, \tilde{\Omega})$ is a solution of the variational problem, then $(\tilde{T} + \nabla \phi, \tilde{\Omega} + \phi)$, $\phi \in H_0^1(V_c)$, is a solution as well. In order to get uniqueness, we choose ϕ such that $\Omega = \tilde{\Omega} + \phi$ is harmonic on V_c . Using a stable implicit Euler scheme with time step δt , the variational problem reads: find $(T, \Omega) \in H_0(\text{curl}; V_c) \times H_0^1(V)$ such that

$$\begin{aligned} a(\Omega, v) + b_c(T, v) &= \int_{V \setminus V_c} f \nabla v, \quad \forall v \in H_0^1(V), \\ a_c(T, W) + b_c(W, \Omega) &= \int_{V_c} f_c W, \quad \forall W \in H_0(\text{curl}; V_c). \end{aligned} \quad (3)$$

Denoting with $\mathcal{H} : H^{\frac{1}{2}}(\partial V_c) \rightarrow H^1(V_c)$ the harmonic extension operator, the continuous bilinear forms in (3) are

$$\begin{aligned} b_c(W, v) &= -\int_{V_c} W \nabla \mathcal{H} v|_{\partial V_c}, \\ a(\Omega, v) &= \int_V \beta \nabla \Omega \nabla v, \\ a_c(T, W) &= \int_{V_c} (\alpha \nabla \times T \nabla \times W + T W), \end{aligned}$$

for all $\Omega, v \in H_0^1(V)$ and $T, W \in H_0(\text{curl}, V_c)$. The coefficients $\alpha, \beta > 0$ are assumed to be piecewise constant and

depend on the material parameters σ , μ as well as on the time step (e.g., $\alpha = \frac{\delta t}{\mu\sigma}$ in V_c). Note that the unknowns T and Ω denote the approximations at the current time step, f_c depends on the approximations of T and Ω at the previous time step, and f denotes the scaled source term depending on T_s . Problem (3) has a unique solution.

The domain V is associated with a quasi-uniform simplicial triangulation \mathcal{T}_H on which we use standard conforming finite elements of lowest order. The associated discrete space having zero boundary conditions on ∂V is called $S_{0;H}(V)$. For the discretization of the vector field T , we use edge elements, see [3], on a quasi-uniform simplicial triangulation \mathcal{T}_h of V_c . The associated discrete space is $X_h(V_c)$ and we set $X_{0;h}(V_c) = X_h(V_c) \cap H_0(\text{curl}; V_c)$. Finally, we denote by $S_h(V_c)$ the space of standard conforming finite elements of lowest order associated with \mathcal{T}_h on V_c , and its trace space on ∂V_c is called $W_h(\partial V_c)$.

In order to formulate the discrete version of problem (3), we have to replace the harmonic extension operator \mathcal{H} in the definition of $b_c(\cdot, \cdot)$ by a discrete one $\mathcal{H}_h : W_h(\partial V_c) \rightarrow S_h(V_c)$. The restriction of $v \in S_{0;H}(V)$ on ∂V_c is, in general, not an element in $W_h(\partial V_c)$. To overcome this difficulty, we introduce a projection operator $\Pi_h : S_{0;H}(V) \rightarrow W_h(\partial V_c)$ on the boundary ∂V_c which is well known in the mortar finite element context [2], [6]. In terms of \mathcal{H}_h and Π_h , the discrete variational problem reads: find $(T_h, \Omega_H) \in X_{0;h}(V_c) \times S_{0;H}(V)$ such that

$$\begin{aligned} a(\Omega_H, v) + b_h(T_h, v) &= \int_{V \setminus V_c} f \nabla v, \quad \forall v \in S_{0;H}(V), \\ a_c(T_h, W) + b_h(W, \Omega_H) &= \int_{V_c} f_c W, \quad \forall W \in X_{0;h}(V_c), \end{aligned} \quad (4)$$

where $b_h(W, v) = - \int_{V_c} W \nabla \mathcal{H}_h \Pi_h v$, for $v \in S_{0;H}(V)$ and $W \in X_{0;h}(V_c)$. This approach is characterized by an optimal error estimate and problem (4) can be solved efficiently by means of a Gauß-Seidel iterative scheme [6].

For the mechanical part, let ℓ be the distance between the two equilibrium positions of V_c which correspond to take or not to take into account the gravity force, respectively. We then denote by m the mass of V_c and by y the vertical position of the center of V_c at time t , with the initial conditions $y(0)$, $\dot{y}(0)$. Then at any given time, there are four forces acting on m : the gravity force $-mg$ pulling downward, the spring force $k(\ell - y)$, the damping force $-b\dot{y}$ and the external magnetic force $(F_m)_y$. Neglecting any movement in the x -direction, the Newton's law of motion for a point mass (the center of V_c) reads:

$$m\ddot{y} = -mg + k(\ell - y) - b\dot{y} + \left(\int_{V_c} (\nabla \times H) \times \mu H \right)_y. \quad (5)$$

If we write (5) at the equilibrium position, i.e. $y = 0$ and $F_m = 0$, we get $mg = k\ell$. Then, (5) simplifies into

$$m\ddot{y} + b\dot{y} + ky = \left(\int_{V_c} (\nabla \times H) \times \mu H \right)_y. \quad (6)$$

To discretize (6), we apply a second order explicit finite difference scheme of time step δt .

RESULTS AND DISCUSSION

We present some numerical results for problem (4) explicitly coupled with the discrete form of (6). Figure 1 shows the problem configuration (for a given $y \neq 0$) and the computational mesh, quadrilateral in V and triangular in V_c . The mechanical parameters are chosen to give

a damped oscillating system (i.e., $b^2 - 4km < 0$). Here, $m = 0.2$, $b = 0.05$, $k = 5$, $\delta t = 0.06$ s; with $y(0) = 0.2$ and $\dot{y}(0) = 0$, we perform 100 time iterations.

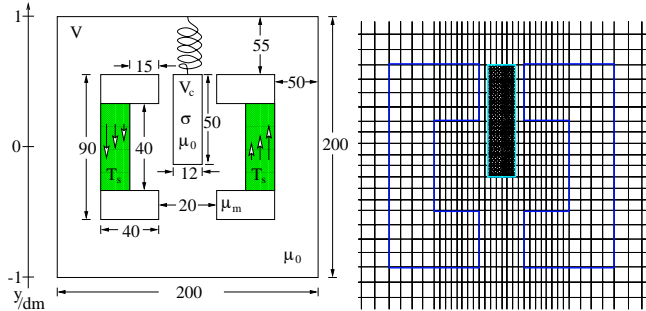


Fig. 1. (Left) Domain geometry and dimensions in cm. For the tests, $V = (-0.1m, 0.1m)^2$, $\sigma \geq 0$, $\mu_0 = 4\pi 10^{-7} \text{H/m}$, $\mu_m = 10^{-3} \text{H/m}$, $T_s = 3 \cdot 10^3 x \hat{e}_y$, $t > 0$. (Right) Nonmatching grids for V_c and V .

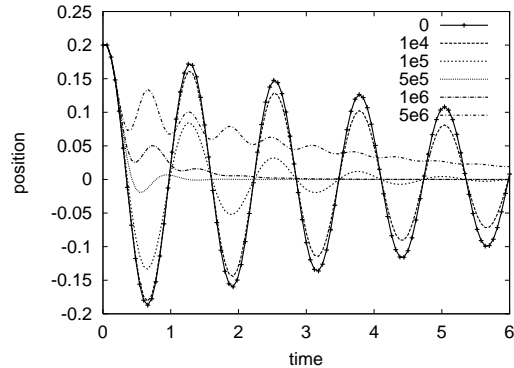


Fig. 2. Vertical position y of V_c for different values of σ .

Looking at Figure 2, we observe that, for $\sigma = 10^4 \text{ S/m}$, the resulting motion almost coincides with that described by the homogeneous form of (6). In this case, the magnetic force related to the induced currents in V_c is rather weak and it takes more than 6 s for the center of V_c to reach the equilibrium position. As soon as $\sigma \geq 10^5 \text{ S/m}$, the contrasting effect of the eddy currents to the motion is more visible: the amplitude of the oscillation decreases and the damping time interval as well as the oscillation period changes. For $\sigma \geq 10^6 \text{ S/m}$ some nonlinear effects occur: a resonance phenomenon appears and V_c goes through a transient equilibrium position different from $y = 0$.

REFERENCES

- [1] R. Albanese, G. Rubinacci, "Formulation of the eddy-current problem", *IEE Proc.*, A 137, 16-22 (1990).
- [2] C. Bernardi, Y. Maday, A. Patera, "A new nonconforming approach to domain decomposition: The mortar element method", *Nonlinear partial differential equations and their applications*, H. Brezis & J. Lions eds., Pitman, 1994, pp. 13-51.
- [3] A. Bossavit, *Computational Electromagnetism: Variational Formulations, Complementarity, Edge Elements*, 1st ed., Academic Press (1998).
- [4] B. Flemisch, Y. Maday, F. Rapetti, B.I. Wohlmuth, "Coupling scalar and vector potentials on nonmatching grids for eddy currents in a moving conductor", *Journal of Computational and Applied Mathematics* (2002) submitted.
- [5] Y. Maday, F. Rapetti, B.I. Wohlmuth, "Coupling between scalar and vector potentials by the mortar element method", *C. R. Acad. Sci. Paris, Ser. I* 334, 933-938 (2002).
- [6] B.I. Wohlmuth, "Discretization methods and iterative solvers based on domain decomposition", *Lecture Notes in Comp. Sciences and Engineering*, 17, Springer, Heidelberg, 2001.

Numerical Analysis of Frequency Characteristic Fluctuations of Semiconductor Devices Caused by Random Doping Fluctuations

I. D. Mayergoyz and P. Andrei

Department of Electrical and Computer Engineering, University of Maryland,
College Park, 20742 MD, USA
isaak@eng.umd.edu

Abstract — A novel technique for the numerical analysis of fluctuations of frequency characteristics of semiconductor devices induced by random doping fluctuations is presented. The basic idea of the technique is to linearize the transport equations with respect to the fluctuating quantities (state variables and doping). It can be shown that this technique yields information on the sensitivity of variances of frequency characteristics to different locations of doping fluctuations. This information can be directly used for the design of dopant fluctuation-resistant structures of semiconductor devices. The numerical implementation of this technique is discussed and numerous computational results are presented.

INTRODUCTION

The prevalent trends in the design of semiconductor devices are to increase the operational frequency and to reduce the power consumption of the devices. This can be achieved by deeply scaling down the semiconductor devices. It is well-known that such small devices will be very susceptible to random dopant fluctuations that are inevitably present due to the random nature of ion implantation and diffusion process. For this reason, an accurate statistical analysis of random dopant-induced effects is very important for the further progress in semiconductor technology, in general, and in mixed signal electronics, in particular.

One of the most important issues in the analysis of semiconductor devices is the frequency characterization of the devices. From a computational point of view, this is equivalent to (1) solving the transport equations that are Poisson and current continuity equations and (2) solving the linearized transport equations and find the frequency characteristics of the device (small-signal parameters, cut-off frequency, etc.). The statistical analysis of semiconductor devices usually requires to accumulate statistics for a large number of devices with different doping realizations and then to compute the variances of different quantities of interest. Most of the existing approaches to the analysis of random dopant-induced fluctuations [1,2] are related to the computation of standard deviation of threshold voltage of MOSFET devices and no effort have been made to study random dopant-induced fluctuations of frequency characteristics. In this paper, we develop an efficient technique to the computation of fluctuations of admittance matrix elements (y-parameters) of semiconductor devices. This technique is based on the linearization of transport equations with respect to the fluctuating quantities and it completely avoids computations for numerous doping realizations.

TECHNICAL DISCUSSION

The basic idea of the method as well as some numerical results for the variances of admittance matrix elements are presented below. The admittance matrix elements are very important for the small-signal ac device characterization and they can be used for direct calculations of other device parameters such as voltage gain, current gain, cutoff frequency, as well as to estimate the stability and noise behavior of semiconductor devices. The usual approach to the calculation of frequency characteristics is to linearize the spatially discretized transport equations [3] and write them in the form:

$$\frac{d}{dt} \mathbf{J}(\mathbf{X}) + \mathbf{F}(\mathbf{X}, \mathbf{D}, V_\alpha, V_\beta, \dots) = 0, \quad (1)$$

where \mathbf{F} is a nonlinear vector function of unknown “state” vector \mathbf{X} , doping vector \mathbf{D} , and terminal potentials V_α, V_β, \dots , while \mathbf{J} is a vector function which depends on \mathbf{X} only. In the drift-diffusion model, the state vector \mathbf{X} consists of three vectors $\boldsymbol{\varphi}$, \mathbf{n} , and \mathbf{p} , whose components are the mesh-point values of electric potential, electron and hole densities, respectively.

In order to find the admittance matrix elements, a sinusoidal voltage of infinitesimal amplitude v_α is applied to the α -terminal, $V_\alpha = V_{\alpha 0} + v_\alpha e^{j\omega t}$, while all other terminals are kept at constant dc potentials. This will induce an ac perturbation in the state variable $\mathbf{X} = \mathbf{X}_0 + \mathbf{x}_\alpha e^{j\omega t}$. The governing equations for \mathbf{x}_α can be found by linearizing equation (1) about the dc bias values \mathbf{X}_0 and $V_{\alpha 0}$:

$$(j\omega \hat{\mathbf{J}}_X + \hat{\mathbf{F}}_X) \mathbf{x}_\alpha + \mathbf{F}_{V_\alpha} v_\alpha = 0. \quad (2)$$

The doping fluctuates from point to point and from one device to another and can be treated as a random field [1]:

$$\mathbf{D} = \mathbf{D}_0 + \tilde{\mathbf{D}}, \quad \bar{\tilde{\mathbf{D}}} = 0, \quad (3)$$

where $\bar{\tilde{\mathbf{D}}}$ denotes the expected value of $\tilde{\mathbf{D}}$, and \mathbf{D}_0 is the average value of the doping. This will induce fluctuations $\tilde{\mathbf{X}}_0$ and $\tilde{\mathbf{x}}_\alpha$ in the dc and ac components of the state variable, respectively. It can be shown (details will be provided in the full paper) that these fluctuations satisfy the following linear system of equations:

$$\begin{cases} \hat{\mathbf{F}}_X \tilde{\mathbf{X}}_0 = -\hat{\mathbf{F}}_D \tilde{\mathbf{D}}, \\ \hat{\mathbf{A}} \tilde{\mathbf{x}}_\alpha + \hat{\mathbf{B}} \tilde{\mathbf{X}}_0 = 0, \end{cases} \quad (4)$$

where the following matrix notations have been introduced:

$$\hat{\mathbf{A}} = j\omega \hat{\mathbf{J}}_X + \hat{\mathbf{F}}_X, \quad (5)$$

$$\hat{\mathbf{B}} = \sum_{i=1}^{3N} (j\omega \hat{\mathbf{J}}_{X,X_i} + \hat{\mathbf{F}}_{X,X_i}) x_{\alpha,i}. \quad (6)$$

Here: $\hat{\mathbf{J}}_{X,X_i} = \frac{\partial \hat{\mathbf{J}}_X}{\partial X_i}$, $\hat{\mathbf{F}}_{X,X_i} = \frac{\partial \hat{\mathbf{F}}_X}{\partial X_i}$, while X_i and $x_{\alpha,i}$ denote the i -th component of vectors \mathbf{X} and \mathbf{x}_α , respectively. Both matrices $\hat{\mathbf{A}}$ and $\hat{\mathbf{B}}$ are computed at dc bias point $(\mathbf{X}_0, \mathbf{D}_0, V_{\alpha 0})$.

The fluctuations of admittance matrix elements are caused by $\tilde{\mathbf{x}}_\alpha$, and it can be shown that, in the first order approximation, they can be evaluated as a linear combination of the fluctuations of doping at different mesh-points:

$$\tilde{y}_{\beta\alpha} = \sum_{i=1}^N \gamma_{\beta\alpha}^i \tilde{D}_i, \quad (7)$$

where $\gamma_{\beta\alpha}^i$ are some ‘‘superposition’’ coefficients and N is the total number of mesh points. Assuming that \tilde{D}_i are independent Poisson random variables, the variance of $y_{\beta\alpha}$ is:

$$\sigma_{y_{\beta\alpha}}^2 = \sum_{i=1}^N (\gamma_{\beta\alpha}^i)^2 \sigma_{D_i}^2 = \sum_{i=1}^N (\gamma_{\beta\alpha}^i)^2 \frac{D_{0i}}{\Delta V_i} = \sum_{i=1}^N S_{\beta\alpha}^i \Delta N_{0i}, \quad (8)$$

where ΔN_{0i} is the expected number of doping ions in volume ΔV_i and $S_{\beta\alpha}^i$ are the ‘‘sensitivity’’ coefficients which are defined as:

$$S_{\beta\alpha}^i = \left(\frac{\gamma_{\beta\alpha}^i}{\Delta V_i} \right)^2. \quad (9)$$

These coefficients show how sensitive the standard deviation of admittance matrix elements is to different locations of doping fluctuations. Therefore, they are very instrumental in the design of dopant fluctuation-resistant structures. The problem of the computation of variances of y -parameters is reduced to the computation of superposition coefficients. In order to find all N superposition coefficients, one has to solve N times the linear systems (4). It turns out that there exists a mathematical trick that substantially simplifies these computations and reduces them to the solution of only one linear system of equations equivalent to (4). This trick will be fully described in the paper.

Numerical codes have been developed and extensively used to study the dependence of variances of admittance matrix elements of MOSFET devices on frequency, doping concentration, channel width and oxide thickness. Figure 1 presents the computed values of real and imaginary parts of y_{21} . In the above simulations, the oxide thickness $t_{ox} = 3$ nm, the channel width $W = 50$ nm, the channel length $L = 50$ nm, the operating frequency $f = 10$ GHz, while the average

doping concentration is $D_0 = 10^{18}$ cm⁻³. Numerous other numerical results will be presented in the full paper.

Figure 2 shows the sensitivity coefficients of the gate capacitance $C_{GG} = \text{Im}(y_{GG})/2\pi f$ as a function of the spatial locations of doping fluctuations. The channel extends between 100nm and 150nm, while the drain and the source regions correspond to $x > 150$ nm and $x < 100$ nm, respectively. One can see that the main contribution to the fluctuation of the gate capacitance is given by fluctuations of the doping at the drain-channel and source-channel junctions, and in the direct proximity to the oxide-semiconductor interface. As it will be shown in the paper, this case is different from the cases of fluctuations of other admittance matrix elements, where also exists a significant contribution from fluctuations of the doping localized deeper inside the device.

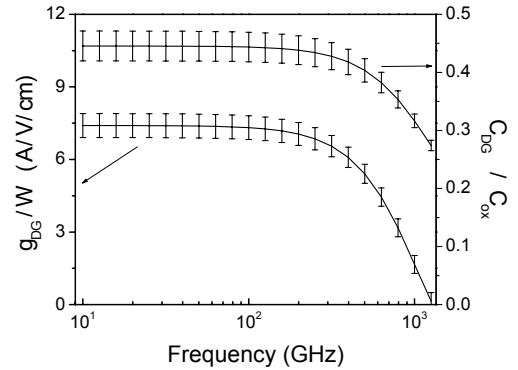


Fig. 1. Real and imaginary parts of y_{21} (continuous line) and their standard deviation (vertical bars).

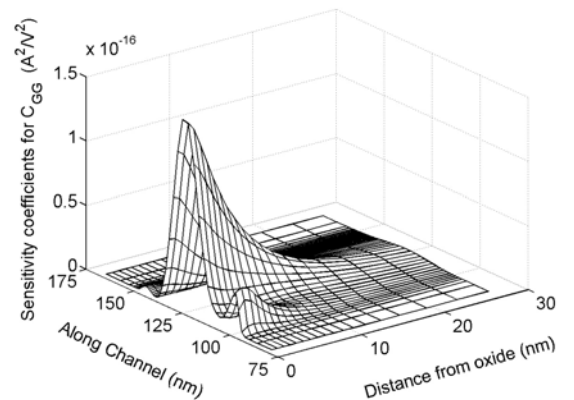


Fig. 2. Sensitivity coefficients for the gate capacitance.

REFERENCES

- [1] A. Asenov and S. Saini, IEEE Trans. Electron Devices. **46**, 1718 (1999).
- [2] I. D. Mayergoyz and P. Andrei, J. Appl. Phys. **90**, 3019 (2001).
- [3] S. Selberherr, *Analysis and Simulation of Semiconductor Devices* (Springer-Verlag, 1984).

Propulsion and Guidance Simulation of HTS Bulk Ropeless Linear Elevator

Kinjiro Yoshida and Hirokazu Matsumoto

Kyushu University

6-chome 10-1 Hakozaki Higashi-ku Fukuoka 812-8581, JAPAN

yoshida@ees.kyushu-u.ac.jp

Abstract It is possible that high temperature superconducting (HTS) bulk linear synchronous motor (LSM) is propelled contactlessly with no guidance and levitation control. Its design and dynamic simulation are based on very complicated analysis of HTS bulk. This paper proposes HTS bulk LSM applied to ropeless linear elevator (RLE) analyzed numerically taking into account E-J characteristic in finite element method (FEM). The LSM can be propelled following command motion pattern with PID control and produce stable guidance force without its control.

INTRODUCTION

HTS bulk can be levitated stably on a track which consist of permanent magnets of the same polarity by maintaining magnetic flux in HTS bulk. We have proposed a new LSM theory which is based on an idea of this characteristic as synchronizing force in using current-carrying-armature-winding instead of permanent magnets [1, 2]. By using this method, HTS bulk LSM can be propelled without guidance and levitation control.

This paper proposes vertical type HTS bulk LSM which is applied to ropeless linear synchronous motor for elevator. HTS RLE is analyzed numerically taking into account E-J characteristic in FEM. The LSM propulsion motion is simulated following command motion pattern with PID feedback control, together with combined guidance simulation without its control.

HTS LSM MODEL

Figure 1 shows the model of HTS LSM applied to RLE. The armature guideway of RLE in our laboratory is used as that of this simulation model. The x -axis and z -axis denote a direction of propulsion and guidance. The x -directed cage position is x_2 , and the z -directed cage position is z_2 . HTS bulk is cooled at $x_2=0$ and $z_2=0$, where the cage is located in the center of armatures for starting.

The cage has ten pieces of HTS bulk on each side of the armature. The shape of bulk is a rectangular parallelepiped. The size is 40 mm in length and 10 mm in thickness with 40 mm in width in the y -direction. These bulks are arranged 2 poles in the x -direction. At $z_2 = 0$, the mechanical clearance between cage

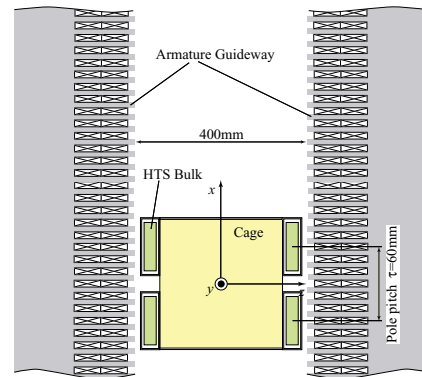


Fig. 1 Model of HTS LSM applied to RLE

and armature is 5 mm. The weight of the cage is assumed 9 kg.

SIMULATION METHOD

Simulation is based on 2D FEM calculation. According to Maxwell equations, electromagnetic phenomena in HTS bulk are described by using the magnetic vector potential A as:

$$\nabla \times \frac{1}{\mu} (\nabla \times A) = -\sigma_{sc} \left(\frac{\partial A}{\partial t} + \nabla \phi \right) \quad (1)$$

$$\nabla \cdot \sigma_{sc} \left(\frac{\partial A}{\partial t} + \nabla \phi \right) = 0 \quad (2)$$

where σ_{sc} is electrical conductivity in HTS bulk and ϕ is electric potential. It is simulated by using E-J characteristic as follow[3]:

$$E = E_c \left(\frac{J}{J_c} \right)^n \quad (3)$$

where J_c is the critical current density 5.0×10^7 A/m², $E_c = 1.0 \times 10^{-4}$ V/m and $n=30$ [3]. Ohm's law is supposed in HTS bulk and by using Eq. (3) σ_{sc} is expressed as:

$$\sigma_{sc} = \frac{J_c}{E} \left(\frac{E}{E_c} \right)^{\frac{1}{n}} \quad (4)$$

σ_{sc} in Eq. (4) is applied to Eq. (1), (2), and magnetic force is calculated from solving numerically the nonlinear eddy-current FEM problem.

Making use of symmetry of LSM shown in Fig. 1, FEM model is considered on one side of the cage. HTS bulk is cooled in magnetic field produced by DC armature current $I_1=40$ A. At

time $t = 0$ s, the cage starts at $I_1=40$ A.

Combined propulsion and guidance motion to go up along the armature guideway of HTS LSM is simulated by adapting to close loop. In the close loop, equation expressing between LSM mechanical load angle x_0 and F_x is needed to obtain x_0 from demanded magnetic force F_x^* .

The formulated equation is given by

$$\left. \begin{aligned} 0 \leq x_0 \leq 0.015 \\ F_x = 9.70 \times 10^3 (x_0 - 1.50 \times 10^{-2}) + 40.4 \\ 0.015 \leq x_0 \leq 0.03 \\ F_x = 4.45 \times 10^6 x_0^3 - 1.91 \times 10^5 x_0^2 + 6.78 \times 10^3 x_0 - 33.4 \end{aligned} \right\} (5)$$

In order to follow the command propulsion patterns, the control law for x_0 based on PID regulator is given by

$$x_0 = K_P (v_{20} - v_2) + K_I (x_{20} - x_2) + K_D (a_{20} - a_2) + x_0^* \quad (6)$$

where x_0^* and x_0 are the demand and actual mechanical load angle. x_{20} , v_{20} , a_{20} and x_2 , v_2 , a_2 represent the command and actual position, speed and acceleration of the cage, respectively. K_P , K_I and K_D are feedback gains.

SIMULATION RESULT

The command motion pattern is as follows. Propulsion and guidance simulation of HTS LSM with using close loop control is carried out. At 0-6 s, the cage went up with a variety velocity up to 0.2 m/s. During 4 s from 6 to 10 s, the cage is stopped at $x_2=0.8$ m. After 10 s, the cage went down. At 3 s, z-directed disturbance force 10 N is given the cage.

Figure 2 (a), (c) show x-directed and z-directed position. The x-directed position follows the command pattern very well. Though z-directed disturbance force is given at 3 s, changes are not seen clearly. The z-directed position oscillates. The oscillation is stable and decreases gradually for 13 s, but the oscillation could not be converged in the short operating times.

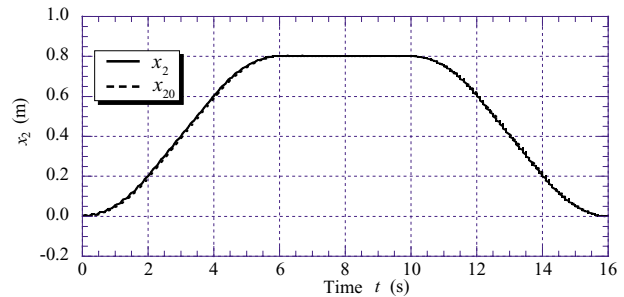
Figure 2 (b), (d) show x_0 -dependence of x-directed force and z_2 -dependence of z-directed force. F_x for 12-16 s is weaker than one for 0-4 s. z-directed position is proportional to z_2 .

CONCLUSION

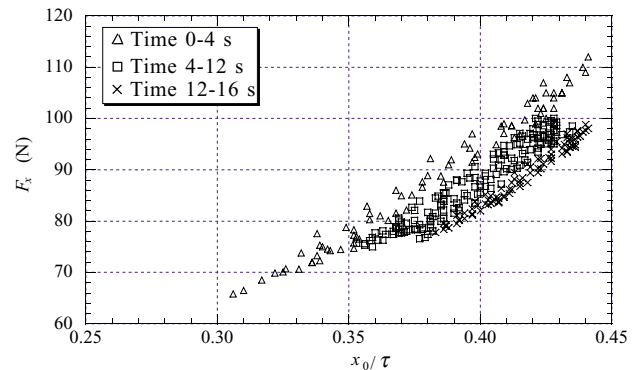
This paper presents combined propulsion and guidance simulation of HTS bulk LSM applied to RLE. By using the formulated equation of thrust force, a precise position control can be carried out. A stable guidance oscillation is decayed gradually but will be able to be converged quickly with feedback control.

REFERENCES

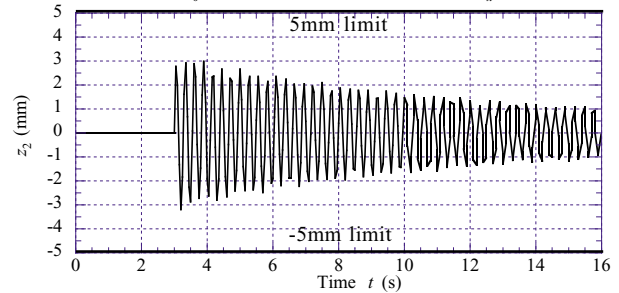
- [1] K. Yoshida, H. Takami, M. Kanehiro, S. Arima: "A New HTSC-Bulk Motor", Advances in Superconductivity IX, Vol.2, 1996, pp.1369-1372.
- [2] K. Yoshida, H. Matsumoto: "Design and simulation of HTS bulk linear motor", Physica C 378-381, 2002, pp.833-837
- [3] H. Yamasaki, Y. Mawatari: "Current-voltage characteristics and flux creep in melt-textured $YBa_2Cu_3O_{7-\delta}$ ", Supercond. Sci. Technol. 13, 2000, pp.202-208



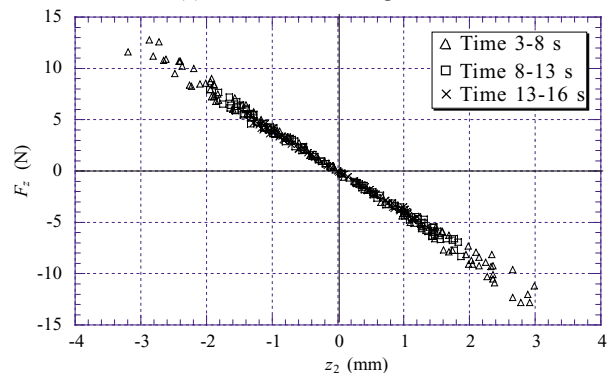
(a) x-directed cage position



(b) x_0/τ -dependence of thrust force F_x



(c) z-directed vehicle position



(d) z_2 -dependence of normal force F_z

Fig. 2 Simulation results

Study of the Influence of Leakage Fields on the Inchworm Actuator

Y. BERNARD** S. SALON*, P. BOUCHILLOUX***

*Rensselaer Polytechnic Institute
TROY, New York, USA
e-mail : salons@rpi.edu

**Laboratoire de Génie Electrique de Paris - UMR 8507 CNRS - SUPELEC - Universités Paris XI et VI
Plateau de Moulon, F-91192 Gif-sur-Yvette Cedex, France

e-mail: bernard@lgep.supelec.fr

*** Adaptronics Inc.
Troy, New York 12180

Abstract? In this article we study the design parameters and especially the influence of leakage electric fields on the performance of a piezoelectric inchworm actuator. We consider the deformation of the central piezoelectric element caused by the leakage fields produced by exciting the end electrodes. A range of possibilities for minimizing this deformation is proposed. Particularly we study the effect of the thickness of insulating disks which separate the piezoelectric elements.

INTRODUCTION

Piezoelectric actuators are currently being considered for medical application due to their small size, high force density production, precision and low-speed controllability. An inchworm device is now being considered which has three piezoelectric elements adjacent to one another. These three elements are excited independently (one at a time) and successively to achieve the desired motion. We would like these to act independently. If there is a deformation of one of the active elements due to the excitation of the adjacent element, we must correct the excitation to compensate for this or build into the design isolation from the electric fields.

DESCRIPTION OF THE DEVICE

The device considered is a piezoelectric inchworm actuator. It is made of 6 elements illustrated in Figure 1. The piezoelectric rings (1 and 3) contract and expand around a core (5) by application of a voltage on electrodes attached to these elements. The tube (2) is also piezoelectric and expands and contracts along the core. The disks (4) isolate elements 1 and 3 from element 2.

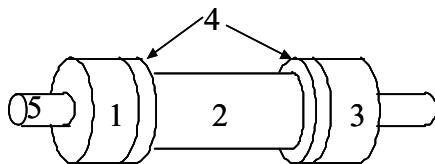
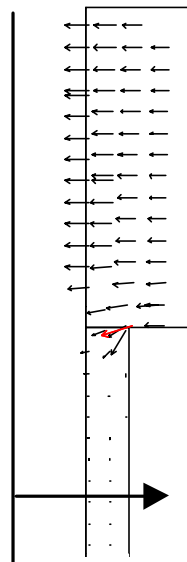


Fig. 1. The Inchworm Actuator

The sequence of excitation of the actuator is composed of six steps. First element 1 contracts squeezing the central rod while element 3 is in the expanded state. Then we expand element 2 in the longitudinal direction. The third step is the contraction of element 3, squeezing the rod. Element 1 is then released and then element 2 contracts. We then expand element 3 and have gone through a full cycle. At each cycle the core moves along the rod a distance equal to the displacement of element 2.

MODELING AND ACCOUNTING FOR FRINGING FLUX

The geometry of the actuator and the nature of the sources allows us to model the device axisymmetrically. Figure 2 shows the electric field vectors in the piezoelectric elements 1 and 2 when only element 1 is excited. There is no insulating disk in this case. The figure illustrates that there is electric flux penetrating element 2, which will cause an undesirable deformation. The leakage flux penetrating element 2 is due to its proximity to element 1.



EFFECT OF THE LEAKAGE FLUX ON THE ACTUATOR

The penetration of the leakage flux on the central element will result in the deformation of this element and could affect the performance of the actuator.

Fig. 2 : Electric Field Vectors with Element 1 Excited.

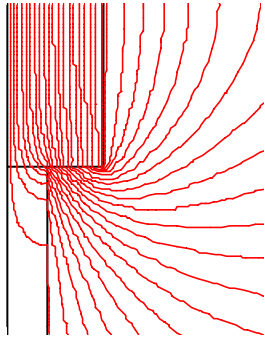


Figure 3: Equipotential Lines (elements 1 and 2) With No Insulating Disk

The insulating disks will not prevent leakage or fringing flux but will reduce the coupling between elements 1 and 3 and element 2. We see in Fig. 3 and 4 the equipotential lines with no insulating disk and with an insulating disk. Clearly the coupling is reduced because of the insulation.

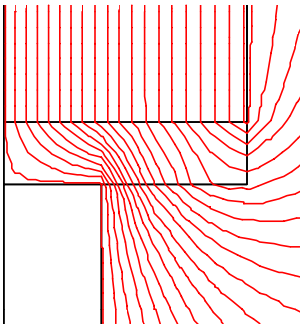


Fig. 4 : Equipotential Lines (elements 1 and 2) With An Insulating Disk.

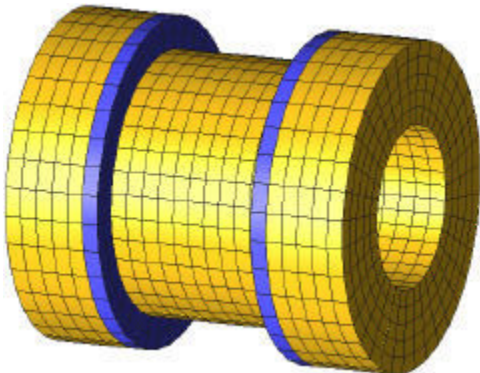


Fig. 5: Undeformed Device

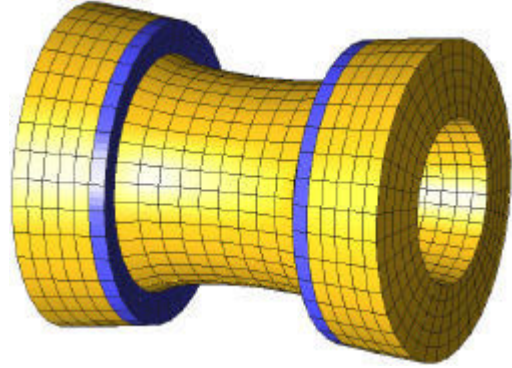


Fig 6 : Deformed Device

The analysis of the device in the deformed and undeformed state is shown in Figs. 5-6. The analysis was done using a coupled electric field and deformable material formulation. In the case shown we have included an insulating disk and the elements are therefore isolated.

CONCLUSIONS

The applications anticipated for this actuator includes the precision positioning. The modeling of the inchworm actuator using Flux2D and Atila allows us to find a geometry in which the excitation of the different electrodes do not have an appreciable effect on the adjacent elements. We have studied the use of an insulating disc to reduce the coupling effect. It is clear that numerical methods are necessary to study these effects and that these effects must be minimized.

Solutions to this problem have been proposed and studies have been done to quantify the coupling effects. The advantages and disadvantages have been studied and will be presented in the extended paper.

REFERENCES

- [1] T. Sashida, K. Kenjo, *An Introduction to Ultrasonic Motors*, Clarendon Press, Oxford 1993
- [2] FLUX2D User Guide, Magsoft Corporation 2001
- [3] Atila User Guide, Magsoft Corporation 2001

Investigation of EEG Problems using the Superposition Principle in the Finite Volume Method*

Y. Q. Xie, X. S. Ma, J. S. Yuan, J. Zou

Department of Electrical Engineering, Tsinghua University, Beijing, 100084, China

yaoqin98@mails.tsinghua.edu.cn

Abstract—A novel finite volume method is proposed to investigate the EEG forward problem using the superposition principle. The current continuity is satisfied and the calculation accuracy is enhanced. The realistic head model is simulated. Calculation results indicate that FVM is a powerful numerical tool for simulating the realistic head model with anisotropic conductivity.

INTRODUCTION

The finite volume method (FVM) possesses some advantages in the calculation of curved anisotropic problems. The electroencephalogram (EEG) is a current field problem generated by point sources or dipole sources. The EEG problem with anisotropic conducting media can be solved conveniently by FVM. The principle of superposition is used in FVM to satisfy the current continuity equation.

METHOD

Suppose a dipole source is positioned in a conducting region, the potential distribution in the region can be expressed by the current continuity equation [1], i.e.,

$$I = \oiint_S \vec{J} \cdot d\vec{S} = -\oiint_S (\sigma \nabla \varphi) \cdot d\vec{S}, \quad \square \square$$

where S is the surface of each control volume, σ is the conductivity of the media, I is the total current through the closed surfaces. The boundary condition specifies that no current flows into the air, i.e., $\sigma \partial \varphi / \partial n = 0$ (n is the normal of the boundary).

To describe the discretization of the field domain, let us take a sphere for instance as shown in Fig. 1. The sphere is divided into homocentric spheres and the surface of the sphere is divided into a large number of triangles. Connecting all the vertices of the triangles to the spherical center, a large number of curved triangular prisms are constructed. The potentials φ_i at the vertices or mesh nodes are taken as the unknown to be solved. To obtain the FVM equation system, a closed surface around each node is

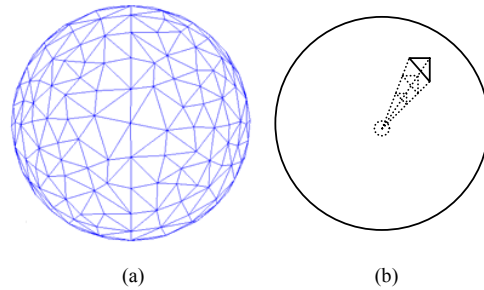


Fig. 1. Mesh generation of a spherical model. (a) triangles on the spherical surface; (b) the triangular prism in the sphere.

defined as the integral surface in (1).

To simplify the description, let us first consider the two-dimensional case as shown in Fig. 2. Let M_{i0} be the node under consideration, O_M is the barycentre of the triangle $M_{i0} M_{i1} M_{i2}$. M_{i01} and M_{i02} are the middle points of the edges $M_{i0} M_{i1}$, $M_{i0} M_{i2}$ of triangles. If all the barycentres of triangles around M_{i0} are connected with the middle points of their edges respectively, a closed region is formed, as shown hatched in Fig. 2. Now generalize the two-dimensional case to the three-dimensional case, as in Fig. 3. Triangle $M_{i0} M_{i1} M_{i2}$ is the interface of two adjacent triangular prisms. Other five triangles surrounding point M_{i0} as shown in Fig. 2 can be defined in a similar way as the interfaces of other triangular prisms. We then displace the hatched region of Fig. 2 to the central section of the upper and lower triangular prisms respectively, which compose the

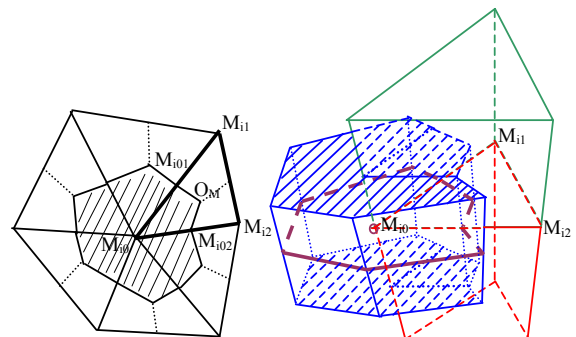


Fig. 2. Closed surface in the two dimensional case

Fig. 3. Definition of the polygonal prism around node M_{i0} .

*Project 59877009 supported by National Natural Science Foundation of China.

top and the bottom faces of the closed surface surrounding point M_{i0} . Other parts of the closed surfaces are the rectangular surfaces as shown in Fig. 3.

Suppose the number of the surface segments of the polygonal prism is N . By taking the surface of the prism as the integral surface in (1), we can get an equation as:

$$I = -\sum_{i=1}^N \iint_{S_i} \sigma \nabla \varphi \cdot d\vec{S}_i = -\sum_{i=1}^N \iint_{S_i} \sigma \nabla_{n_i} \varphi dS_i, \quad (2)$$

where n_i is the normal of the surface segment i .

Equation (2) involves the surface integration of the normal potential gradient on the closed surface. However, they should be expressed by potentials on each node. The calculation of the current flux is developed based on the principle of superposition, as shown in Fig. 4, where “1” represents that the potential of the point is considered in the calculation of the current flux and “0” represents that the potential of the point is ignored in the calculation of the current flux. The current flux of the closed surface is equal to the summation of the current flux generated by each vertex of triangles. Let us take point A for instance, as shown in Fig. 5. If the potential of point A is considered, but the potential of point B and C are 0, it is equivalent that a parallel plane field is set up in the region of the triangle, as shown in Fig. 5(b). Suppose the media in the triangle is homogeneous, σ is a constant. Since the field intensity is homogeneous in the parallel plane field, so the current flux is homogeneous. To calculate the flux of OP is equivalent to calculate the flux of OP_1 , which is the projection of OP to BC . Therefore, the current density on each surface is obtained by superimposing current fluxes of these three parts in Fig. 4. Consequently, the current flux is obtained. Because the calculation of the current flux of the surface inside is the same as the calculation of the current flux of the surface outside, it is obvious that the current flux satisfies the current continuity equation.

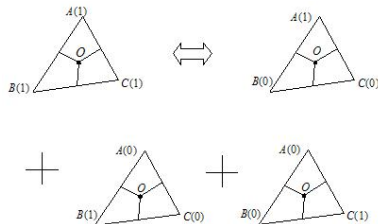


Fig. 4. Superimposing of the current flux.

NUMERICAL EXAMPLES

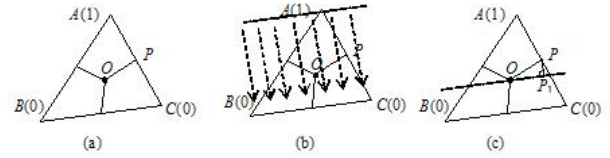


Fig. 5. Calculation of the current flux based on the superimposing principle.

The approaches above are extended to the realistic head model. The mesh generation on the head surface is shown in Fig. 6(a). The head model is divided into four layers, including the cortex, cerebrospinal fluid (CSF), skull and scalp. The conductivity of the cortex, CSF and scalp are isotropic. They were adapted from Zhou and Oosterom [2]. The conductivities are $0.33 (\Omega\text{m})^{-1}$, $1.0 (\Omega\text{m})^{-1}$, $0.33 (\Omega\text{m})^{-1}$, respectively. While the conductivity of the skull is anisotropic, the normal conductivity is $0.0042 (\Omega\text{m})^{-1}$, and the tangential conductivity is $0.042 (\Omega\text{m})^{-1}$. Totally 71617 mesh nodes were employed. The potential distribution on the outer surface is shown in Fig. 6, in which (b) is the one dipole case and (c) is the five dipoles case. In the figures the bright regions represent high potential.

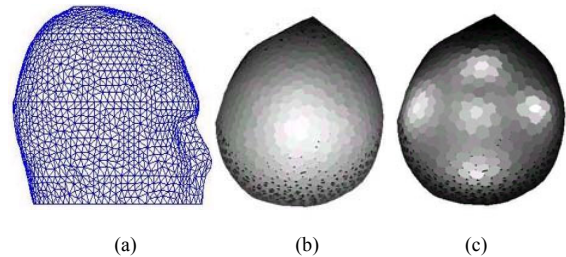


Fig. 6. Realistic head model. (a) mesh generation on the surface of the realistic head model; (b) potential distribution on the scalp; (c) potential distribution on the cortex.

CONCLUSION

In this paper, a novel FVM is developed to solve EEG forward problems. Compared with the conventional structured meshes of FVM, the geometrical singularity is overcome using triangular prism meshes. The superposition principle satisfies the current continuity equation, which increases the calculation accuracy. As described above, FVM is a powerful numerical tool for simulating the realistic head model with the anisotropic conductivity.

REFERENCES

- [1] R. D. Pascual-Marqui et al. "Low resolution electromagnetic tomography: a new method for localizing electrical activity in the brain", *Inter. Journal of Psychophysiology*, vol.18, pp.49-55, 1994.
- [2] Hong Zhou, A. V. Oosterom, "Computation of the potential distribution in a four layer anisotropic concentric spherical volume conductor," *IEEE Trans. BME*. vol.39, pp. 154-158, Feb. 1992.

A Meshless Collocation Method based on Radial Basis Functions and Wavelets

S. L. HO¹, Shiyu YANG², H.C WONG³, Guangzheng NI²

¹EE Department, ³Industrial Center, The Hong Kong Polytechnic University, Hong Kong

²EE College, Zhejiang University, China

Email : eeslho@polyu.edu.hk

Abstract—A meshless method based on the collocation with Radial Basis Functions (RBF) and wavelets is proposed. It is shown that the proposed method makes full advantages of both RBFs and Wavelets. The bridging scales are employed to preserve the mathematical properties of the entire bases in terms of consistency and linear independence. A numerical example used to validate the proposed method is reported.

MESHLESS COLLOCATION METHOD BASED ON RBFs AND WAVELETS

The study of meshless methods has now become a topical area for computational electromagnetics since meshless methods can eliminate the tedious and difficult mesh generating process in traditional numerical methods when solving boundary value problems. However, the inherent inefficiency in imposing boundary and interface conditions of meshless methods often undermine the usefulness of these methods in many engineering applications. Consequently, some meshless methods based on the collocation with RBFs are proposed [1]. Moreover, it should be noted that by using some compactly supported RBFs, one might avoid the need for the full coefficient matrix in traditional globally supported RBFs. However such approach will result in significant errors when one interpolates the derivatives on the boundary [1]. To address the problem and, more specifically, to take full advantages of both RBFs and wavelets, a meshless collocation method using RBF interpolation to enforce the boundary conditions is proposed. To keep the required mathematical properties, such as the consistency and linear independence, of the shape functions of the proposed method, the bridge scales are generalized and used in the proposed algorithm. Computer simulations are conducted and the numerical results are reported to validate and demonstrate the advantages of the proposed method.

Wavelet Approximations

For any function $u(x,y) \in \Omega$, its approximation using wavelets can be given as

$$u(x,y) = \sum_{i,j} c_{i,j} \phi_{i,j}^J(x,y) \quad (1)$$

where J is the resolution or scale parameter, $\phi_{i,j}^J(x,y) = \phi_i^J(x)\phi_j^J(y)$, $\phi_i^J(z) = 2^{J/2} \phi(2^J z - i)$ is the one dimensional scale function of the wavelets, and it can be determined from the following two scale relation

$$\phi(x) = \sum_{k=0}^{L-1} p_k \phi(2x - k) \quad (2)$$

In the proposed algorithm, the Daubechies' scale function is used, hence L is an even integer.

Interpolation Using Radial Basis Function

Since the RBF interpolation is only used for enforcing boundary conditions in the proposed method, the globally supported RBFs will be used in this paper because of their high interpolation accuracies. The interpolation of a function $u(x,y): D \rightarrow R$ on the basis of its values u_i at some scattered data points $X_i = (x_i, y_i) \in D (i = 1, 2, \dots, N)$ in terms of some radial basis function H is

$$u(X) = \sum_{j=1}^N d_j H(\|X - X_j\|) \quad (3)$$

where, $\|\bullet\|$ is the Euclidean norm.

The radial basic function used in this paper is

$$h(r) = (r^2 + 0.1)^{0.04}, \quad (4)$$

which has been reported as the optimal RBFs [2].

In the numerical implementation, a transformation is used to consider the difference in the dimensions of the coordinate directions, i.e.,

$$r = \|X\| = \sqrt{\left(\frac{x}{k_x}\right)^2 + \left(\frac{y}{k_y}\right)^2} \quad (5)$$

Combined Interpolation of RBFs and Wavelets

For the proposed algorithm to work in a more general form, the entire domain of the problem is divided into three sub-regions (Fig. 1): Ω_R is where only the RBF interpolation is present, Ω_w is where only the wavelets contribute to the approximation of the solution variable, Ω_R^w is where both RBFs and wavelets have influences. In region Ω_R or Ω_w , the interpolation of the solution variable is the standard form of (3) or (1), respectively. To develop a general interpolation formula in region Ω_R^w for the solution variable $u(x,y)$ using both RBFs and wavelets, one begins with

$$u(X) = \sum_{j=1}^N d_j H(\|X - X_j\|) + \sum c_{i,j} \phi_{i,j}^J(X) \quad (6)$$

To ensure the required mathematical properties of the entire bases such as the consistency and the linear independence are retained, the bridging scale concept is used to modify the wavelets [3]. Thus, in region Ω_R^w , (6) becomes:

$$u(X) = \sum_{j=1}^N d_j H(\|X - X_j\|) + \sum_{i,j} c_{i,j} \bar{\phi}_{i,j}^J(X) \quad (7)$$

where, $\bar{\phi}_{i,j}^J(X)$ is the modified wavelet based on the bridging

scales, and is defined as

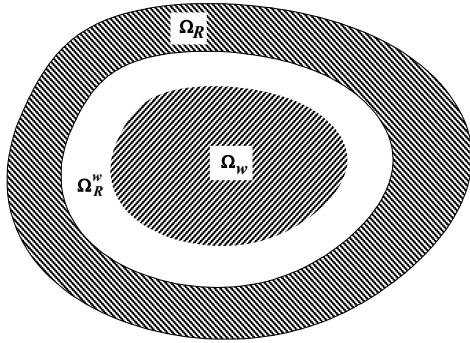


Fig. 1. The Schematic diagram of the division of the solution domain

$$\bar{\phi}_{j,k}^J(X) = \phi_{j,k}^J(X) - \sum_i H_i(X) \phi_{j,k}^J(X_i) \quad (8)$$

Discrete Mathematical Model

Without loss of generality, one considers the following 2-D Poisson's equation on the domain Ω bounded by boundary $\Gamma = \Gamma_D \cup \Gamma_N$

$$\Omega: Lu = -f/\beta \quad (9)$$

$$\Gamma_D: u = u_0 \quad (10)$$

$$\Gamma_N: Du = q/\beta \quad (11)$$

where, $L = \frac{\partial^2}{\partial x^2} + \frac{\partial^2}{\partial y^2}$, $D = \frac{\partial}{\partial n}$.

Based on the collocation method, and substituting (7) into (9)-(11), one obtains the discrete equations as

$$\begin{bmatrix} L[H] & L[\Phi] \\ H & \Phi \\ D[H] & D[\Phi] \end{bmatrix} \begin{Bmatrix} d \\ c \end{Bmatrix} = \begin{Bmatrix} -\frac{f}{\beta} \\ u_0 \\ \frac{q}{\beta} \end{Bmatrix} \quad (12)$$

NUMERICAL APPLICATION

To validate and to demonstrate the advantages of the proposed method, it is used to analyze the magnetic fields of a typical U-magnet as shown in Fig.2 (a). Due to the geometrical symmetry, only half of the physical region, i.e., the region enclosed by ABCD in Fig. 2 (a) needs to be studied. The boundary value problem can be formulated as

$$\frac{\partial^2 A}{\partial x^2} + \frac{\partial^2 A}{\partial y^2} = -\mu J \quad (13)$$

In the numerical implementation, the solution domain is divided into two different sub-regions with i) very thin layers near the essential boundaries where both RBFs and wavelets have common influences, and ii) the residual of the solution domain where only wavelets contribute to the interpolation (Fig. 2 (b)). The node arrangement of the proposed method is also shown in Fig. 2. (b). The computed flux density

distribution by using the proposed method is shown in Fig. 3, which is almost identical to those obtained by using a FE method as reported in [4]. In other words, these numerical results positively confirm the feasibility of using the proposed numerical method in finding the solutions of practical field problems. It should also be pointed out that even when compared to other meshless methods, the proposed one needs to discretize some very thin layers near the boundaries only, resulting in significant reductions in the number of total nodes, thereby offering high flexibility in dealing with 3-D problems in which traditional methods such as the FEM are awkward because of the tedious meshing requirements.

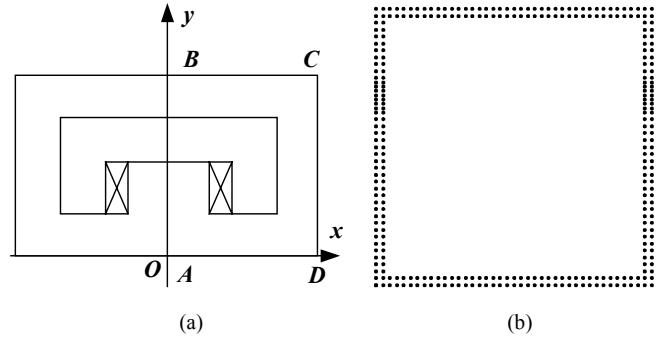


Fig. 2. (a) The U-Magnet and (b) The node arrangement of the proposed method

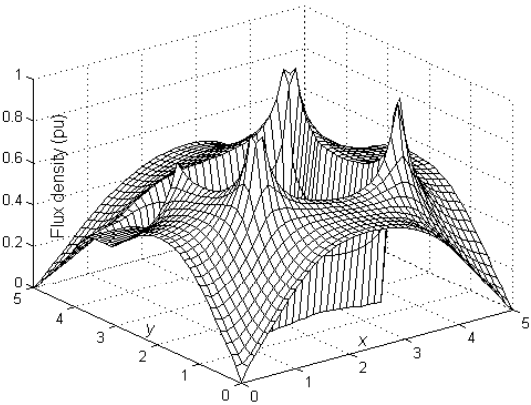


Fig. 3. The distribution of the computed magnetic flux density

REFERENCES

- [1] X. Zhang, K.Z. Song, X. Liu, " Meshless methods based on collocation with radial basis functions, " *Computational Mechanics*, vol. 26, pp. 333-343, 2000.
- [2] T. Ishikawa, Y. Tsuke and M. Matsunami, "A combined method for global optimization using radial basis function and deterministic approach, " *IEEE Trans. Magn.*, vol. 35, pp. 1730-1733, 1999.
- [3] G.J. Wagner J., W.K. Liu, "Hierarchical enrichment for bridging scales and mesh-free boundary conditions, " *International Journal for Numerical Methods in Engineering*, vol. 50, pp. 507-524, 2001.
- [4] S.Y. Yang, G.Z. Ni, S.L. Ho, J.M. Machado et al., "Wavelet-Galerkin method for computations of electromagnetic fields—computations of connection coefficients, " *IEEE Trans. Magn.*, vol. 36, pp. 644-648, 2000.

**A Fast Volume Integral Equation Solver Based on
A Novel 2-Level Dual Rank SVD Algorithm**

N. A. Ozdemir, J.F. Lee

ElectroScience Lab., Electrical Engineering Dept.

The Ohio State University

1320 Kinnear Road, OH 43212

ozdemir.5@osu.edu

Abstract— Electromagnetic scattering from arbitrarily shaped inhomogeneous dielectric bodies has been an interesting topic due to its importance to problems that include propagation through inhomogeneities. This type of problems can be formulated in the form of a volume integral equation and solved by the method of moments (MoM). However, solving large scale electromagnetic problems by MoM suffers from $O(N^2)$ numerical complexity of memory requirement and CPU time both to assemble and solve the system matrix, where N is the number of basis functions. This paper presents a novel 2-level dual rank SVD algorithm that efficiently compresses the system matrix to reduce the memory requirement and CPU time for both matrix assembly and solution to $O(N^{3/2})$.

I. VOLUME INTEGRAL EQUATION FORMULATION

Volume integral equation (VIE) is obtained through mixed potential integral equation. Let V denote the volume of a scatterer characterized by its relative permittivity $\epsilon(\bar{r})$ and relative permeability $\mu(\bar{r})$, which are continuous inside V . Applying the volume equivalence principle and the continuity equation, the scatterer can be replaced with equivalent electric current and charge densities [1]:

$$\bar{J}(\bar{r}) = j\omega\kappa(\bar{r})\bar{D}(\bar{r}) \quad (1a)$$

$$\rho(\bar{r}) = -\nabla\kappa(\bar{r}) \cdot \bar{D}(\bar{r}) - \kappa(\bar{r})\nabla \cdot \bar{D}(\bar{r}) \quad (1b)$$

where $\kappa(\bar{r}) = \frac{\epsilon(\bar{r}) - \epsilon_0}{\epsilon(\bar{r})}$ is the contrast ratio. Decomposing

the total field into incident and scattered fields we have

$$\bar{E}(\bar{r}) = \bar{E}^i(\bar{r}) + \bar{E}^s(\bar{r}) \quad (2)$$

where

$$\bar{E}^s = -j\omega\bar{A}(\bar{r}) - \nabla\phi(\bar{r}) \quad (3)$$

$$\bar{A}(\bar{r}) = \frac{\mu_0}{4\pi} \int_V \bar{J}(\bar{r}') \frac{e^{-jk_0|\bar{r}-\bar{r}'|}}{|\bar{r}-\bar{r}'|} dv' \quad (4a)$$

$$\phi(\bar{r}) = \frac{\mu_0}{4\pi} \int_V \rho(\bar{r}') \frac{e^{-jk_0|\bar{r}-\bar{r}'|}}{|\bar{r}-\bar{r}'|} dv'. \quad (4b)$$

Discretization of the volume by tetrahedral elements and interpolation of $\bar{D}(\bar{r})$ by the first order divergence conforming vector basis functions followed by testing of Equation (2) with the basis function chosen leads to a system of linear equations:

$$\langle \bar{D}/\epsilon, \bar{f}_m \rangle + \langle j\omega\bar{A}, \bar{f}_m \rangle + \langle \nabla\phi, \bar{f}_m \rangle = \langle \bar{E}^i, \bar{f}_m \rangle \quad (5)$$

$m = 1, 2, \dots, N$
where $\langle \nabla\phi, \bar{f}_m \rangle = \int_S \phi \bar{f}_m \cdot \hat{n} ds - \int_V \phi \nabla \cdot \bar{f}_m dv$ and S is the surface that bounds the volume V [2].

II. DUAL RANK SVD ALGORITHM

The dual rank SVD algorithm is based on the rank deficiency feature of the integral equation for well-separated groups of basis functions [3]. The algorithm factorizes the local matrix $Z_{m \times n}^{ij}$ due to the groups i and j into $Q_{m \times r}^{ij}$ and $R_{r \times n}^{ij}$ matrices without a priori knowledge of $Z_{m \times n}^{ij}$, where m and n are the number of receiving and transmitting basis functions, respectively, and r is the rank of interaction:

$$Z_{m \times n}^{ij} = \begin{bmatrix} z_1 & z_2 & \dots & z_n \end{bmatrix} = \begin{bmatrix} v_1 \\ v_2 \\ \dots \\ v_m \end{bmatrix} \approx Q_{m \times r}^{ij} \times R_{r \times n}^{ij} \quad (6)$$

Here, z_p is the column vector due to the p^{th} transmitter and v_q is the row vector due to the q^{th} receiver.

Assuming the average number of basis functions in each group is m , the number of groups is $N_g = N/m$. If average rank r is also assumed to be constant for all non-self group interactions, the numerical complexity for the memory requirement and matrix-vector multiplication can be estimated by

$$C = N_g m^2 + (N_g^2 - N_g) 2rm = Nm + 2rN^2/m - 2rN \quad (7)$$

C can be optimized by choosing m proportional to \sqrt{N} . With this choice of m the numerical complexity is $O(N^{3/2})$. The numerical complexity of the matrix assembly may also be shown to be $O(N^{3/2})$, albeit with a large scale factor.

V. NUMERICAL RESULTS

A numerical example is presented in this section to demonstrate both the accuracy and efficiency of the dual rank SVD algorithm for solving the volume integral equation of electromagnetic scattering. As shown in Figure 1, far field patterns calculated using the dual rank SVD algorithm is compared with the direct MoM implementation for a dielectric sphere. The sphere has radius of $0.75\lambda_0$ and the dielectric constant is $\epsilon_r = 4.0$. The incident wave is 1.125 GHz at $\theta = 180^\circ$. The sphere is discretized into 4901 tetrahedron elements with 10162 unknowns. The generalized minimum residual (GMRES) is used to solve the matrix equation iteratively. In Figure 2, CPU time and memory requirements for generating the matrices of homogeneous dielectric spheres of radius 0.5, 0.75, 1, 1.25 λ_0 are plotted.

VI. CONCLUSION

The dual rank SVD algorithm has been applied for solving volume integral equation. Due to the reduction of the computational complexity the method presented in this paper can be applied to solve electromagnetic scattering problems with electrically larger dielectrics.

REFERENCES

- [1] A. F. Peterson, S. L. Ray, and R. Mittra, *Computational Methods for Electromagnetics*. Piscataway, NJ: IEEE Press, 1998.
- [2] D. H. Schaubert, D.R. Wilton, and A. W. Glisson, "A tetrahedral modeling method for electromagnetic scattering by arbitrarily shaped inhomogeneous dielectric bodies," *IEEE Trans. Antennas and Propagat.*, vol. 32, no.1, pp 77-85, Jan. 1984.
- [3] S. Kapur, D. E. Long, "IES³: A Fast Integral Equation Solver for Efficient 3-Dimensional Extraction," *ICCAD 1997*, pp.448-455.

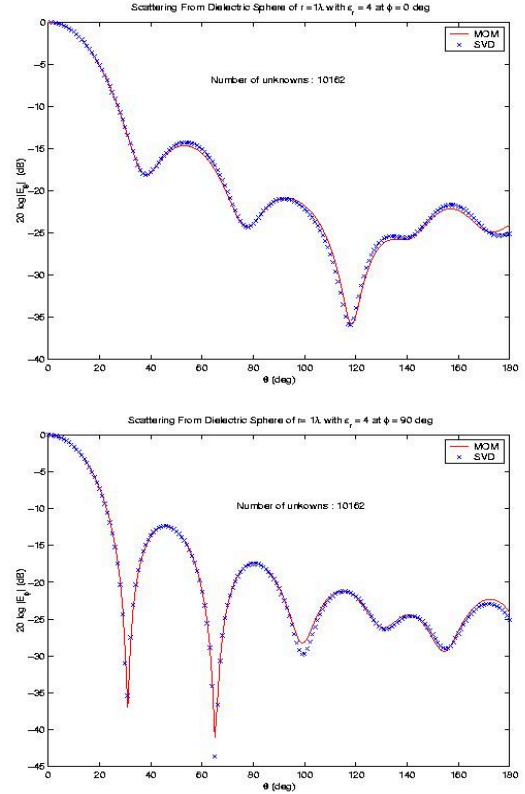


Figure 1: Comparison of MoM and SVD results

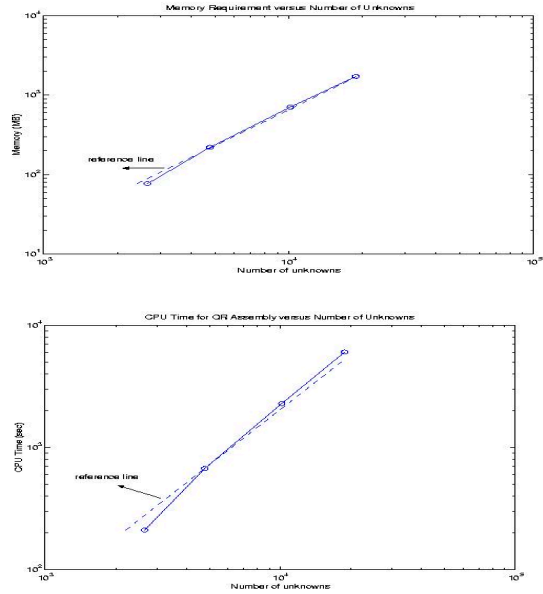


Figure 2: Numerical complexity of SVD

Research on Weighted Functions of Meshless Methods in Electromagnetic Field Analysis

Liu Jianxin, Liu Zhenhua, Cui Xiang

North China Electric Power University, Baoding, Hebei, 071003, China

bull_lzh@hotmail.com

Abstract—The meshless method theory and its' application to the electrostatic problems are discussed. The selection of the weighted functions is the key of this method. Therefore, the computing speeds and precisions are compared by the different weighted functions. With help of the 2D electrostatic field models, according to the principles of weighted functions' selection, the parameters' range of each weighted functions and the adaptive weighted function for solution of electrostatic field are found.

INTRODUCTION

Meshless methods, which originated about twenty years ago and is developed speedily in recent ten years, was used firstly to analyze electromagnetic field on 1998. As the method is based on moving least squares (MLS), it can provide the any order continuity shape functions. Weighted function, the core of MLS, determines the continuity of the field function, precision of results and speed of computing. Nowadays, We have found many kinds of weighted functions, which can be used in MLS. Unfortunately, there are not principles on weighted function selection

In this paper, the meshless method in electrostatic field was discussed based on the experience of mechanics research. We compare the results of two-dimension electrostatic field under different weighted functions, then, draw the conclusion of some regulations of weighted functions' selection in electromagnetic field analyzing.

FORMULATION

The essential formulations of meshless method and MLS can be obtained easily [1]. To make the theory clearer, we consider two-dimensional electrostatic problems, which are governed by the equation

$$\begin{cases} \Omega: \nabla \cdot \beta \nabla \mathbf{u} = -\mathbf{f} \\ \Gamma_1: \mathbf{u} = \mathbf{u}_0 \\ \Gamma_2: \partial \mathbf{u} / \partial \mathbf{n} = 0 \end{cases}$$

The weighted functions have to satisfy the following conditions:

- a) Nonnegative;
- b) Continuity and derivativeness;
- c) Monotonically decreasing, and the value equal to zeros outside the sub-domains.

The weighted functions are the commonly used in engineering as follow:

- a) Exponential \square

$$w(s) = \begin{cases} e^{-(s/\alpha)} & s \leq 1; \\ 0 & s > 1 \end{cases}$$

- b) Exponential \square

$$w_I(r_I^{2k}) = \begin{cases} \frac{e^{-(r_I/c)^{2k}} - e^{-(r_{ml}/c)^{2k}}}{(1 - e^{-(r_{ml}/c)^{2k}})} & r_I \leq r_{ml}; \\ 0, & r_I > r_{ml} \end{cases}$$

- c) Cubic Spline

$$w(s) = \begin{cases} 2/3 - 4s^2 + 4s^3 & s \leq 1/2 \\ 4/3 - 4s + 4s^2 - 4s^3/3 & 1/2 < s \leq 1; \\ 0 & s > 1 \end{cases}$$

- d) Quartic Spline

$$w(s) = \begin{cases} 1 - 6s^2 + 8s^3 - 3s^4 & s \leq 1; \\ 0 & s > 1 \end{cases}$$

- e) Quintic Spline

$$w(s) = \begin{cases} 1 - 10s^3 + 15s^4 - 6s^5 & s \leq 1; \\ 0 & s > 1 \end{cases}$$

- f) Rational Formula

$$w(s) = \begin{cases} (1 - s^2)^k / (s^2 + \zeta^2) & s \leq 1; \\ 0 & s > 1 \end{cases}$$

- g) Conical Function

$$w(s) = \begin{cases} 1 - s^{2k} & s \leq 1; \\ 0 & s > 1 \end{cases}$$

Among the three rules, the vital condition is the second one (continuity and derivativeness). To obtain results as exact as possible, weighted functions must satisfy continuity and derivativeness, the parameters of weighted functions should be chosen properly. Two of exponential functions and conical function are not of strict continuity and derivativeness, but the results worked out from them in proper parameters are acceptable.

CALCULATING

Some electrostatic field models are given and computed by meshless method with above weighted functions, and the results are compared. As in the general case of meshless methods, the application of essential boundary conditions is very complicated and difficult since the shape functions do not satisfy the Kronecker delta criterion. In this paper, the penalty function method is adopted to deal with the essential boundary conditions.

The boundless parallel-plate capacitor, which is the simplest two-dimension model, is analyzed under the 7 weighted functions respectively, the errors and the CPU time are compared in TABLE I. Obviously, the results by weighted functions a)—g) are better than ones by weighed function f), it is because the properties of the continuity and derivativeness among them are different.

As an example, the parallel-plate capacitor considering of outside region is analyzed by the quadratic spline weighted function and quadratic basis. The field-strength and the voltage distribution are showed in Fig.1. The result is valid.

The weighted functions' selection is quite important and difficult in meshless method. The three rules, especially the second one, have to be obeyed in order to ensure the rational results. Further more, the weighted functions must be agree with the practical engineering, because the engineering problems are so complicated that it is not easy to catch.

TABLE I. ERROR OF THE RESULTS UNDER THE DIFFERENT WEIGHTTTED FUNCTIONS

Weighted Function	Absolute Max Value of Relative Error□%□	Mean Square Quantization Error□%□	CPU(s)
Exponential □	5.32E-06	5.75E-06	24.94
Rational Formula	2.76E-06	6.80E-06	26.58
Cubic Spline	5.62E-06	1.22E-05	29.00
Exponential □	6.46E-06	1.34E-05	25.87
Quartic Spline	2.19E-05	6.33E-05	26.41
Quintic Spline	6.12E-05	9.22E-05	26.47
Conical	6.14E-04	1.50E-03	24.77

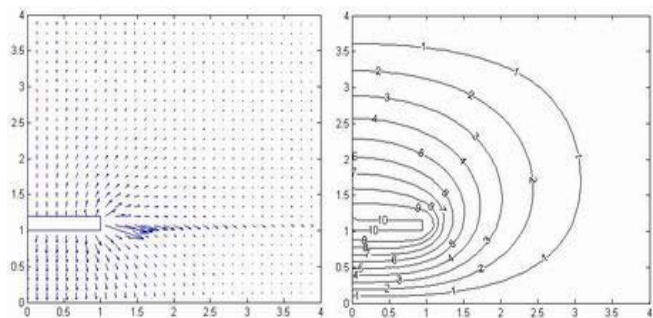


Fig.1 1/4 region of the parallel-plate capacitor taking into account fringe effect, field-strength and voltage distribution

REFERENCES

- [1]. T. Belytschko, Y. Y. LU, L. GU, "Element free Galerkin methods," *International Journal for Numerical Methods in Engineering*, vol. 37, pp. 229-256, 1994.
- [2]. T. Belytschko, Y. Krongauz, D. Organ, M. Fleming, P. Krysl, "Meshless method: An overview and recent developments," *Computer Methods in Applied Mechanics and Engineering*, vol. 139, pp. 3-47, 1996.
- [3]. S. L. Ho, S. Yang, J. M. Machado, and H. C. Wong, "Application of a Meshless Method in Electromagnetics," *IEEE Transactions on Magnetics*, vol. 37, no. 5, pp. 3198-02, 2001 □
- [4]. Vlatko Cingoski, Naoki Miyamoto, Hideo Yamashita, "Element-Free Galerkin Method for Electromagnetic Field Computations," *IEEE Transactions on Magnetics*, vol. 34, no. 5, pp. 3236-39, 1998.

Point Collocation Method Based on the FMLSrk Approximation for Electromagnetic Field Analysis

D.W. Kim¹, H.K. Kim² and Y.S. Kim³

¹Dept. of Mathematics, Sunmoon Univ., 100 Kalsan-ri, Tangjeong-myeon Asan-si, Chungnam, 336-708, South Korea

²Advanced Power Apparatus Group, KERI, P.O. Box 20, Changwon, 641-600, South Korea

³Dept. of Mathematics, Yonsei Univ., 134, Seoul 120-749, South Korea

E-mail : ¹dwkim@sunmoon.ac.kr ; ²kimhk@keri.re.kr ; ³yskim67@yonsei.ac.kr

Abstract — This paper presents the description of the point collocation method and its application to the electromagnetic field computation. The interpolation scheme is based on the fast moving least square reproducing kernel approximation. In the method, the integration cell is not needed and the essential boundary conditions can be enforced directly. Numerical simulations on 1-D and 2-D problems are carried out to validate the method.

INTRODUCTION

Some kinds of mesh-free methods have been successfully applied to the analysis of the electromagnetic field problems [1,2,3]. The shape functions for most of mesh-free methods are derived from the moving least square approximation [2,3]. Because the shape functions for conventional mesh-free methods do not have the Kronecker delta function property, special treatment for imposing the essential boundary conditions is required [4]. In this paper, the point collocation method based on the fast moving least square reproducing kernel (FMLSrk) approximation is presented. The method does not require the integration cells for the numerical integration and the derivative of the shape function is much faster than that of the conventional moving least square approximation. By some numerical experiments, the rate of convergence and the accuracy of the method are shown.

FAST MOVING LEAST SQUARE REPRODUCING KERNEL METHOD

Let Ω be a bounded domain in \mathbf{R}^n and $u(\mathbf{x})$ be a continuous function defined in $\Omega \subset \mathbf{R}^n$. We also let $\Lambda = \{x_I \in \bar{\Omega} \mid I = 1, \dots, NP\}$ be a set of distributed nodes both in Ω and on its boundary. When $\alpha = (\alpha_1, \dots, \alpha_n)$ is an n -tuple of non-negative integers and $\mathbf{x} = (x_1, x_2, \dots, x_n) \in \mathbf{R}^n$, we define

$$\mathbf{x}^\alpha \equiv x_1^{\alpha_1} x_2^{\alpha_2} \dots x_n^{\alpha_n}, \quad D_{\mathbf{x}}^\alpha \equiv \partial_{x_1}^{\alpha_1} \partial_{x_2}^{\alpha_2} \dots \partial_{x_n}^{\alpha_n}. \quad (1)$$

Now let us introduce the vector of complete basis polynomials in \mathbf{R}^n of order less than or equal to m such that

$$\mathbf{P}_m(\mathbf{x}) = (\mathbf{x}^{\beta_1}, \mathbf{x}^{\beta_2}, \dots, \mathbf{x}^{\beta_L})^T, \quad L = \frac{(n+m)!}{n!m!} \quad (2)$$

where β_k 's are all multi-indices of n -tuples in lexicographical order and $|\beta_k| \leq m$. For example, if $n = 2$ and $m = 2$, then the multi-indices are arranged in order of $(0,0), (1,0), (0,1), (2,0), (1,1)$ and $(0,2)$ and thus $\mathbf{P}_m(\mathbf{x})$ is $(1, x, y, x^2, xy, y^2)^T$.

Using a compactly supported continuous non-negative window function $\Phi(y)$, the resulting shape functions of FMLSrk are defined as the following [5]:

$$\Psi_I^{[\alpha]}(\mathbf{x}) = \frac{\alpha!}{\rho^{|\alpha|}} \mathbf{e}_\alpha^T \mathbf{M}^{-1}(\mathbf{x}) \mathbf{P}_m\left(\frac{\mathbf{x}_I - \mathbf{x}}{\rho}\right) \Phi\left(\frac{\mathbf{x}_I - \mathbf{x}}{\rho}\right) \quad (3)$$

where $|\alpha| \leq m$, \mathbf{e}_α^T is the α -th unit vector in $\mathbf{R}^{\frac{(n+m)!}{n!m!}}$ and $\mathbf{M}(\mathbf{x})$ is the moment matrix defined by

$$\mathbf{M}(\mathbf{x}) \equiv \sum_{x_I \in \Lambda} \mathbf{P}_m\left(\frac{\mathbf{x}_I - \mathbf{x}}{\rho}\right) \mathbf{P}_m^T\left(\frac{\mathbf{x}_I - \mathbf{x}}{\rho}\right) \Phi\left(\frac{\mathbf{x}_I - \mathbf{x}}{\rho}\right). \quad (4)$$

In this study, we use the window function of $\Phi(\mathbf{y}) = (1 - \|\mathbf{y}\|)^4$ for $\|\mathbf{y}\| < 1$.

The functions $\Psi_I^{[\alpha]}(\mathbf{x})$'s can be defined as the solution of the following matrix equation.

$$\mathbf{M}(\mathbf{x}) \begin{pmatrix} \frac{\rho^{|\beta_1|}}{\beta_1!} \Psi_I^{[\beta_1]}(\mathbf{x}) \\ \vdots \\ \frac{\rho^{|\beta_L|}}{\beta_L!} \Psi_I^{[\beta_L]}(\mathbf{x}) \end{pmatrix} = \mathbf{P}_m\left(\frac{\mathbf{x}_I - \mathbf{x}}{\rho}\right) \Phi\left(\frac{\mathbf{x}_I - \mathbf{x}}{\rho}\right) \quad (5)$$

We call $\Psi_I^{[\alpha]}(\mathbf{x})$ the α -th shape function associated with the window function Φ [5]. Note that $\Psi_I^{[0]}(\mathbf{x})$'s are standard shape functions of mesh-free methods.

POINT COLLOCATION SCHEME BASED ON FMLSrk APPROXIMATION

We will propose a point collocation scheme in some general sense. In order to obtain the mesh-free numerical solution of a partial differential equation (PDE), we first interpolate the solution $u(\mathbf{x})$ of the PDE such that

$$u(\mathbf{x}) \approx U(\mathbf{x}) = \sum_{x_I \in \Lambda} u_I \Psi_I^{[0]}(\mathbf{x}) \quad (6)$$

where the nodal values u_I should be determined later from the governing equations. The derivatives of $u(\mathbf{x})$ in the PDE and on the boundary conditions are replaced with the following approximated derivatives

$$D^\beta u(\mathbf{x}) \approx D_m^{\mathbf{h}, \beta} U(\mathbf{x}) = \sum_{x_I \in \Lambda} u_I \Psi_I^{[\beta]}(\mathbf{x}) \quad (7)$$

for $0 < |\beta| \leq m$.

In order to expose a point collocation scheme, we consider the following Poisson problem.

$$-\Delta u = f \quad \text{in } \Omega \quad (8)$$

$$u = g \quad \text{on } \Gamma_D \quad \text{and} \quad \frac{\partial u}{\partial n} = h \quad \text{on } \Gamma_N \quad (9)$$

We propose the point collocation discretization of the Poisson problem using the approximations (6) and (7) as follows:

$$u(\mathbf{x}) = \sum_{\mathbf{x}_j \in \Lambda} u_j \Psi_j^{[(0,0)]}(\mathbf{x}) \quad (10)$$

$$-\sum_{\mathbf{x}_j \in \Lambda} u_j (\Psi_j^{[(2,0)]}(\mathbf{x}^i) + \Psi_j^{[(0,2)]}(\mathbf{x}^i)) = f(\mathbf{x}^i) \quad (11)$$

$$\sum_{\mathbf{x}_j \in \Lambda} u_j \Psi_j^{[(0,0)]}(\mathbf{x}^d) = g(\mathbf{x}^d) \quad (12)$$

$$\sum_{\mathbf{x}_j \in \Lambda} u_j (\Psi_j^{[(1,0)]}(\mathbf{x}^n), \Psi_j^{[(0,1)]}(\mathbf{x}^n)) \cdot \mathbf{n}(\mathbf{x}^n) = h(\mathbf{x}^n) \quad (13)$$

$$\mathbf{x}^i \in \Lambda_i, \mathbf{x}^d \in \Lambda_d, \mathbf{x}^n \in \Lambda_n \quad (14)$$

where Λ_i, Λ_d and Λ_n are sets of interior nodes, Dirichlet boundary nodes and Neumann boundary nodes, respectively. Here $\mathbf{n}(\mathbf{x}^n)$ is the outward unit normal vector at $\mathbf{x}^n \in \Lambda_n$.

NUMERICAL SIMULATIONS

To validate the method, one-dimensional problem with the analytical solution is solved at first. The model problem is

$$-\frac{d^2 u}{dx^2} = x \quad (0 < x < 1) \quad (15)$$

$$u(0) = 0 \quad \text{and} \quad u'(1) = 0. \quad (16)$$

Fig. 1 shows the comparison between the numerical and analytic solutions. The numerical results are obtained using the second and third order scheme ($m=2$ and 3 respectively) with five nodes. For the third order case, the numerical result is nearly the same as the analytic solution only with five nodes.

Next numerical test problem is for the study of convergence rate of the method. The governing equations are

$$\Delta u = f \quad \text{in } \Omega = [0,1] \times [0,1] \quad (17)$$

$$u = g \quad \text{on } \partial\Omega, \quad (18)$$

where f and g are obtained from the solution of $u(x,y) = (x+2y)^5$.

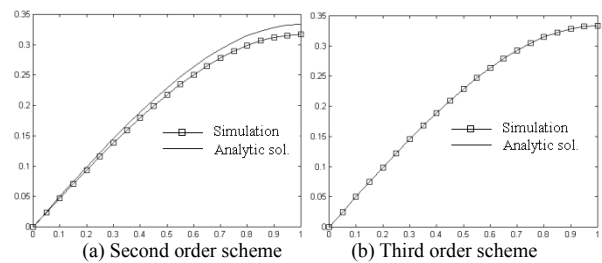
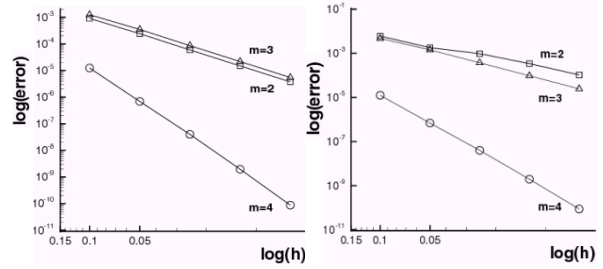
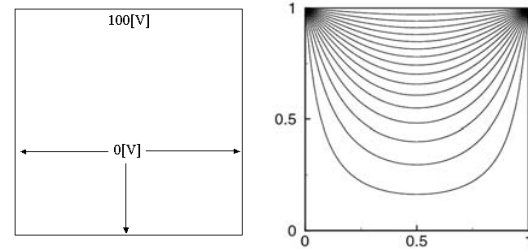


Fig. 1. Comparison between numerical and analytic solutions.



(a) Relative L^∞ error for u (b) Relative L^∞ error for $\partial u / \partial x$
Fig. 2. Convergence rate with respect to nodal distance h .



(a) Boundary condition (b) Plot of equi-potential lines
Fig. 3. Analysis of electrostatic problem

Fig. 2 shows the plot of the relative error in L^∞ -norm when a uniform h -refinement is used. For the case $m = 4$, the convergence rate is observed to be better than that of the case $m = 2$ or $m = 3$.

The proposed method is also applied to the electrostatic problem. Fig. 3(a) shows the analysis domain and boundary condition and (b) shows the plot of computed equi-potential lines. Quite accurate solution can be obtained for this problem.

CONCLUSIONS

The point collocation method proposed in this paper is a very promising mesh-free method and has many merits compared with other mesh-free methods. Therefore the proposed method is applicable to many applications such as optimization problems, 3-D problems, moving boundary problems and so on.

REFERENCES

- [1] S.L. Ho, S.Yang, J.M. Machado and H.C. Wong, "Application of a Meshless Method in Electromagnetics," *IEEE Trans., Magn.*, Vol.37, No.5, pp.3198-3202, September 2001.
- [2] S. A. Viana and R.C. Mesquita, "Moving Least Square Reproducing Kernel Method for Electromagnetic Field Computation," *IEEE Trans., Magn.*, Vol. 35, No.3, pp.1372-1375, May 1999.
- [3] V. Cingoski, N.Miyamoto, K.Kaneda, H.Yamashita, "Element-Free Galerkin Method for Electromagnetic Field Computation," *COMPUMAG*, Rio de Janeiro, 209-210, November 1997.
- [4] C. Herault and Y. Marechal, "Boundary And Interface Conditions In Meshless Methods," *IEEE Trans., Magn.*, Vol. 35, No.3, pp.1450-1453, May 1999.
- [5] D.W. Kim and Y.S. Kim, "Point Collocation Methods Using the Fast Moving Least Square Reproducing Kernel Approximation," *Int. J. Numer. Meth. Engng.*, pp.1-38,2001.

The Natural Element Method for Electromagnetic Field Computation

H.K. Kim¹, K.Y. Park¹, C.H. Im² and H.K. Jung²

Advanced Power Apparatus Group, KERI, P.O. Box 20, Changwon, 641-600, South Korea¹

E-mail : kimhk@keri.re.kr

Electromechanics Lab., School of Electrical Engineering, Seoul National University, San 56-1,

Shinrimdong, Seoul, 151-742, South Korea²

Abstract — The natural element method is a kind of meshless Galerkin method. The shape function is derived from the natural neighbor co-ordinates interpolation scheme. During assembling the system matrix, the numerical integration is carried out using the Delaunay triangles as the background cells. The method is applied to the test problems and simulation results show that the natural element method can give accurate solutions for the electromagnetic field problems.

INTRODUCTION

Recently, many meshless methods have been developed in solving the electromagnetic field problems [1,2]. These methods do not need mesh generation and only data set for node distribution and description of the boundaries are required. Most of the meshless methods - for example, Element-Free Galerkin (EFG) method [3] - employ the moving least square (MLS) approximation to compute the shape function. The natural element method (NEM) is a kind of meshless method employing the Galerkin scheme for the solution of partial differential equations. The difference from other meshless methods is that the trial functions are constructed using natural neighbor coordinates. In this paper, the description of the NEM and the application of the method to the electromagnetic field problems are presented.

VORONOI DIAGRAM AND DELAUNAY TESSELLATION

The Voronoi diagram and Delaunay tessellation are widely used in the field of computational geometry in constructing the geometries. For Euclidean space \mathbf{R}^2 , consider a set of distinct points $P = \{ p_1, p_2, \dots, p_N \}$. The Voronoi polygon of p_n is defined as follows:

$$T_n = \{ x \in \mathbf{R}^2 : d(x, x_n) < d(x, x_m) \quad \forall m \neq n \} \quad (1)$$

where $d(x_m, x_n)$ is the distance between x_m and x_n . Each T_n is the intersection of finitely many open half-spaces, each being delimited by the perpendicular bisector. The Voronoi polygon can be viewed as the locus of all points closer to p_n than to any other nodes. The Voronoi diagram for a set of nodes divides the plane into a set of regions, one for each node, such that any point in a particular region is closer to that region's node than to any other node. The Delaunay triangles are constructed by connecting the nodes whose Voronoi cells have common boundaries(edges). Therefore Delaunay triangulation and Voronoi diagram are dual structures.

NATURAL NEIGHBOR INTERPOLATION

If T_n and T_m have a common boundary, p_n and p_m are considered as neighbors. The notion of a set of neighboring nodes is generalized by the definition of natural neighbor nodes. The natural neighbors of any node are those in the neighboring Voronoi cells, or equivalently, those to which the node is connected by the sides of the Delaunay triangle [4,5].

If the sampling point x in the Delaunay triangulation is given, the natural neighbors of x are the set of nodes which are connected to it. The number of natural neighbors is a function of position x and depends on the local nodal density. Consider an interpolation scheme for a function $u(x)$ in the form of (2).

$$u^h(x) = \sum_{I=1}^n \phi_I(x) u_I \quad (2)$$

where u_I ($I=1, 2, \dots, n$) is the function value at neighboring node I , and $\phi_I(x)$ is the weight associated with each node.

The weight $\phi_I(x)$ in the NEM is taken as the natural neighbor coordinates of the point x in the plane. Fig.1 shows an example of the Voronoi cells. In Fig. 1(a), a point x is introduced into the Voronoi diagram and it is observed that x has four natural neighbors, namely nodes 1-4. If a point x is added, then a new Voronoi cell is placed around x as shown in Fig. 1(b). The natural neighbor coordinates of x with respect to a natural neighbor I is defined as the ratio of the area of their overlapping Voronoi cells to the total area of the Voronoi cell for x .

$$\phi_I(x) = A_I(x) / A(x) \quad (3)$$

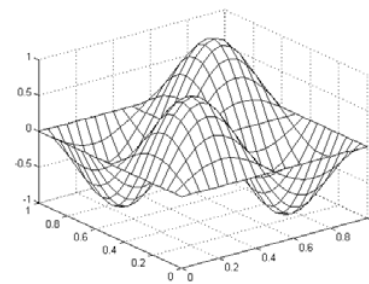
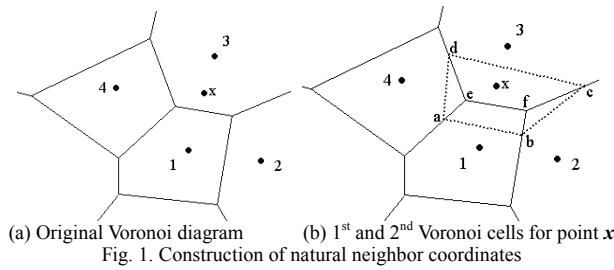
where $I = 1, 2, \dots, n$, and $A(x) = \sum_{J=1}^n A_J(x)$.

For example, in Fig. 1, the four regions composing the closed polygon $abcd$ are called the second-order cells and their union (polygon $abcd$) is a first-order Voronoi cell. The natural neighbor coordinates or shape function $\phi_1(x)$ for node 1 is given by (4).

$$\phi_1(x) = A_{abfe} / A_{abcd} \quad (4)$$

From the definition of $\phi_1(x)$, the shape function has following properties [4]:

$$0 \leq \phi_I(x) \leq 1, \quad \phi_I(x_j) = \delta_{IJ}, \quad \sum_{I=1}^n \phi_I(x) = 1 \quad (5)$$



The Kronecker-delta property of (5) is one of the main different properties compared with moving least square approximation scheme. In one-dimension, the shape function by the natural neighbor interpolation is precisely the same as the 1-D linear finite element shape function [5].

IMPLEMENTATION OF NEM

The implementation of the NEM is similar to that of FEM or other Galerkin procedure-based meshless methods. The major feature of the NEM is in the construction of the shape function and their derivatives. The system matrix and forcing vector by the NEM are assembled on a nodal basis. For the numerical integration, the integration cells are needed. In this paper, the Delaunay triangles themselves are used as the integration cells. The essential boundary conditions can be directly enforced like the finite element procedure because the shape function has Kronecker delta property and the trial function of NEM is strictly linear between two nodes that belong to an edge of a Delaunay triangle on the boundary of the convex hull [4]. Generally the system matrix from the NEM is symmetric and sparse but not necessarily banded.

NUMERICAL RESULTS

First example is the 2-D simple test problem to validate the NEM. The equation to be solved and the exact solution are given by:

$$\Delta u = -8\pi^2 \sin(2\pi x)\sin(2\pi y) \quad (6)$$

$$u(x, y) = \sin(2\pi x)\sin(2\pi y) \quad (7)$$

In performing the numerical integration, the three-point Gauss quadrature is used for each Delaunay triangle. The numerical solution of $u(x,y)$ by the NEM is plotted in Fig. 2 when the node distribution of 21×21 grid with regular node-spacing is used in the simulation. In this case, the maximum relative error of u compared with the exact solution for each node is less than 1[%]. Next numerical example of the NEM is the application to the electrostatic problem. The problem definition is shown in Fig. 3(a) and nodal discretization for analysis is shown in Fig. 3(b). Fig. 4 shows the comparison of the NEM results with FEM ones. As shown in the figure, the NEM results show very good agreement with FEM ones. However, the computational cost of the NEM is somewhat higher because the NEM requires the more steps for Delaunay tessellation, searching for natural neighbors and so on.

Fig.2. Plot of numerical solution of (6).

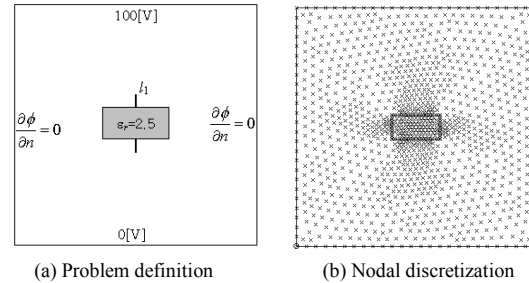


Fig.3. Application of NEM to electrostatic problem

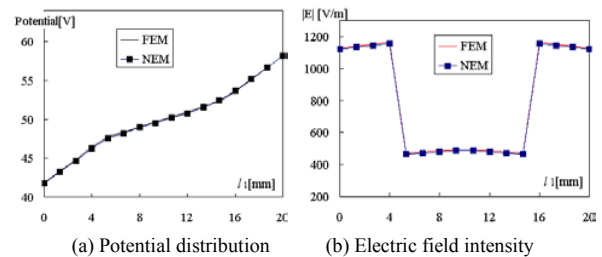


Fig.4. Comparison of NEM results with FEM ones along line l_1 (Line l_1 is defined in Fig. 3(a) and thickness of dielectric material is 10[mm])

CONCLUSIONS

In this paper, the description of the NEM and the application to the electromagnetic field problems are presented. The shape function of the NEM has many common properties compared with that of FEM. Therefore, the NEM is very promising numerical method for electromagnetic field computation.

REFERENCES

- [1] S.L. Ho, S.Yang, J.M. Machado and H.C. Wong, "Application of a Meshless Method in Electromagnetics," *IEEE Trans., Magn.*, Vol.37, No.5, pp.3198-3202, September 2001.
- [2] S. A. Viana and R.C. Mesquita, "Moving Least Square Reproducing Kernel Method for Electromagnetic Field Computation," *IEEE Trans., Magn.*, Vol. 35, No.3, pp.1372-1375, May 1999.
- [3] V. Cingoski, N.Miyamoto, K.Kaneda, H.Yamashita, "Element-Free Galerkin Method for Electromagnetic Field Computation," *COMPUMAG*, Rio de Janeiro, 209-210, November 1997.
- [4] N. Sukumar, b. Moran and T. Belytschko, "The Natural Element Method in Solid Mechanics," *Int. J. Numer. Meth. Engng.*, 43:pp.839-887, 1998.
- [5] N. Sukumar, B. Moran, A.Yu Semenov and V.V. Belikov "Natural neighbor Galerkin methods," *Int. J. Numer. Meth. Engng.*, 50:pp.1-27, 2001.

Quasi-2D FE Analysis of Hybrid Stepping Motor(HSM)

Ki-Bong Jang, Hyun-Hun Shin, and Ju Lee
Energy Conversion Lab.,
Department of Electrical Engineering, Hanyang University,
Haengdang 1-dong Seongdong-gu, 133-791, SEOUL, KOREA
e-mail: kebin70@ihanyang.ac.kr

Abstract—The Hybrid Stepping Motor (HSM) is described. Though full 3D FEA is the proper method to analyze the HSM, this paper used Quasi - 2D FEA for the axial cross section to save computation time. For the purpose of quasi-2D FEA, the virtual magnetic barrier and equivalent permanent magnet model of HSM are proposed

The step angle of this motor is 1.8° , the period of cogging torque is 3.6° and the airgap length is 0.005mm. Further details are shown in table 1.

GENERAL

Hybrid Step Motors (HSM) are commonly used for the most part in the industry because HSM has high torque and resolution advantages with comparing with other types of stepping motor.

Since HSM has a great number of small-teeth on the stator and rotor surface and very small air gap, the magnetic saturation in the teeth becomes severe with increasing the flux density in the air gap. In addition, both radial and axial flux is produced because of axially magnetized permanent magnet and geometric characteristic. These make the analysis of HBM more difficult, the 3D Finite Element Analysis (FEA) is one of solutions for non-linear analysis of HBM under this situation, but a large amount of computation time is necessary. This paper introduces the virtual magnetic barrier and the virtual equivalent permanent magnet magnetized in radial direction for the 2D FEA of HBM.

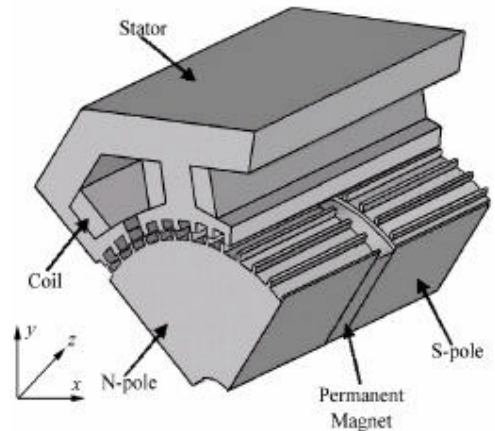


Fig. 1 The basic construction of a 2-phase HSM

QUASI -2D FE ANALYSIS

ANALYSIS MODEL

Fig. 1 show the basic construction of a 2-phase HSM having 8 stator poles with 6 teeth per pole and 50 teeth on the rotor. The permanent magnet is magnetized in z-direction.

TABLE I. SPECIFICATION OF HSM

Stator		Rotor	
Pole number	8	Teeth number	50
Teeth number per pole	6	Outer diameter	12.95 (mm)
Phase number	2	Permanent magnet thickness	2 (mm)
Turns per phase	38	Residual flux density	1.2 (T)
Inner diameter	13 (mm)	Airgap length	0.05 (mm)
Outer diameter	21 (mm)		

Though full 3D FEA is the proper method to analyze the HSM, we used 2D FEA for the axial cross section to save computation time. In order to calculate the torque of HSM with 2D analysis, the permanent magnet in the HSM is replaced to equivalent virtual magnet which is axially magnetized and virtual magnetic barrier on both sides make the magnetic flux oriented to radial direction. This new approach produces correct flux distribution.

Fig.2 shows flux distribution in the pole of HBM as a result of 2D FEA using virtual magnet barrier. Although the flux route of 2D model is different from that of real situation, the flux distribution in the air gap is very similar to that of real one. That is due to virtual magnetic barrier placed at the both sides of magnet and the virtual equivalent permanent magnet in radial direction.

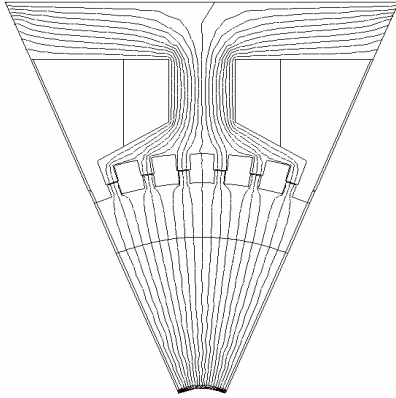


Fig. 2 Flux distribution by 2D FEA

EXPERIMENTAL AND RESULTS

In order to get detent and hold torque of HSM, the experimental setup is composed of a pulley, a string, a weight, and position detector with DSP based measurement system like Fig.3.

The resolution of position detector is 0.036° . Only one fourth of period can be successfully measured by above referred method

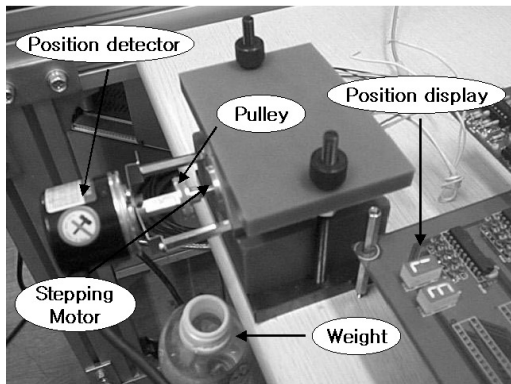


Fig. 3 Flux distribution

Fig.4 shows the cogging torque of HBM, which is calculated by 2D analysis. This result is compared with that of a 3D analysis, considered as reference result. A few typical results are also compared with measurements. Accuracy is sufficient to assess that the suggested method, considering magnetic saturation, realize a good compromise between simulation time and precision

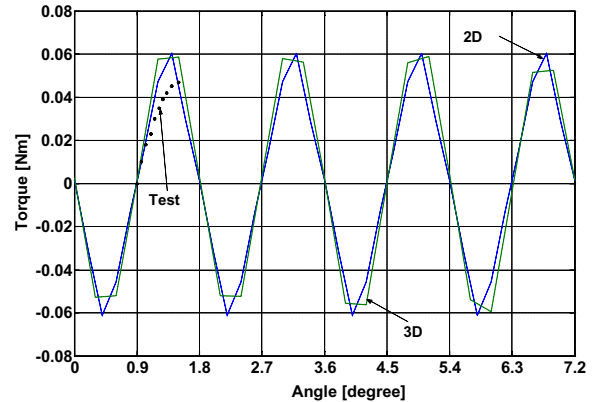


Fig. 2 Detent Torque of HSM

REFERENCES

- [1] M. K. Jenkins, D. Howe, and T. S. Brich, "An improved design procedure for hybrid stepper motors", IEEE Trans. Magn., vol, 26, pp. 2535-2537, 1990
- [2] Takashi Kosaka and Nobuyuki Matsui. "Simple non-linear magnetic analysis for three-phase hybrid stepping motors", IEEE IA Conference. vol 1, pp. 126-131, 2000

Isotropic and anisotropic electrostatic field computation by means of the cell method

M. Bullo, F. Dughiero, M. Guarnieri and E. Tittonel

Università degli Studi di Padova
Via G. Gradenigo 6/A
35131 – Padova – Italy
e-mail: massimo.guarnieri@unipd.it

Abstract – The paper presents two different approaches for the computations of isotropic and anisotropic electrostatic problems by means of the cell method. The results obtained by this technique are compared with those obtained by a first order FEM based algorithm.

INTRODUCTION

The finite formulation of the electromagnetism developed by E. Tonti [1,2] employs the field equations in their integral form and doesn't require mathematical differential operators (gradient, curl, divergence). The peculiarity of this technique is the use of two tessellation systems (called *primal simplicial* and *dual simplicial meshes*) to write the integral equations. The primal grid constitutes, by means of its own domains, namely the nodes, the support of the configuration variable (in our case the electrical scalar potential V) while the dual grid constitutes, by its own volumes, the support of source variable (the electrical charge Q). Configuration and source variables are correlated by the constitutive equations which contain the material properties and the metrical notions. By imposing also each finite volume of the dual grid to satisfy the balance equations (i.e. Gauss electric law), an algebraic system is obtained whose solution provides the unknown values of the configuration variables.

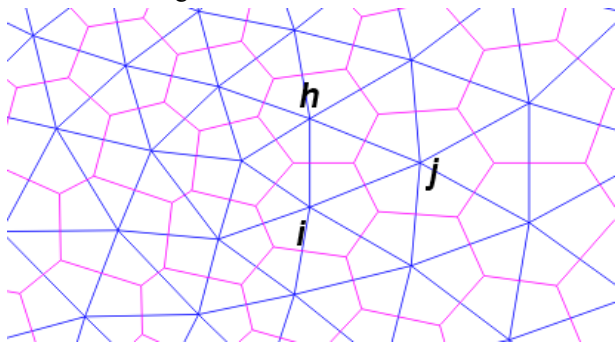


Fig. 1. Detail of the Delaunay (primal) – Voronoi (dual) tessellation used in the following application.

ISOTROPIC PROBLEM

In the following the mathematical formulation developed for the numerical analysis of a 2-dimensional axisymmetric, non homogeneous and isotropic problem is presented.

The analysis domain is discretized in a Delaunay (primal grid) and Voronoi (dual grid) tessellation (Fig. 1): this kind of mesh can be applied to regions of every shape and the constitutive equation can be directly written on its domains.

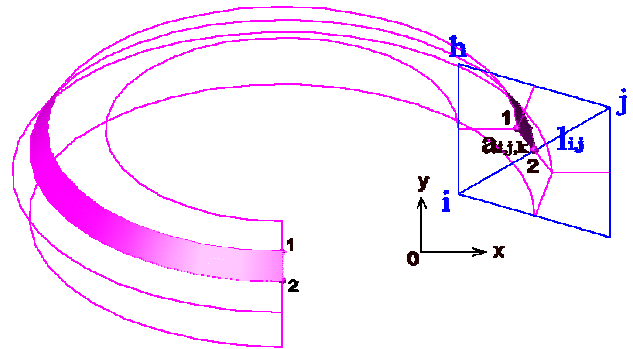


Fig. 2. Axisymmetric revolution.

The finite quantities used to define the problem are the electric charge Q , the electrical scalar potential V and the electrical flux Ψ through the dual grid surfaces. Due to the axisymmetric geometry (Fig. 2), each one of these surfaces $A_{i,j,k}$, is obtained by revolution of the line $a_{i,j,k}$ along a circular path so becoming the lateral surface of a frustum of cone:

$$A_{i,j,k} = \pi(x_1 + x_2) \cdot a_{i,j,k} \quad (1)$$

Fig. 2 also shows the metric distance l_{ij} between the primal grid nodes i and j (perpendicular to the $A_{i,j,k}$ surface).

The electrical quantities V and Ψ are related each other through the constitutive equation which is written for isotropic materials of the primal k^{th} cell:

$$\Psi_{i,j,k} = \varepsilon_k \frac{A_{i,j,k}}{l_{i,j}} (V_i - V_j) \quad (2)$$

where the value of the dielectric constant ε is considered.

The usual boundary condition on the symmetry axis (i.e. Neumann condition) is naturally obtained imposing the electric flux variable Ψ with a null value.

Adding the Gauss law, written for each dual cell:

$$\sum_i \Psi_i = Q_i \quad (3)$$

a complete equation system is obtained (corresponding to the “fundamental system” of the FEM) in the unknown variables V which is solved by means of the Gauss elimination method.

ANISOTROPIC PROBLEM

In order to solve anisotropic problems the previous formulation is not suitable. Let's consider instead that the scalar potential V can be expressed, inside each primal cell, by the following linear function:

$$\begin{bmatrix} l_{i,j,x} & l_{i,j,y} \\ l_{i,h,x} & l_{i,h,y} \end{bmatrix} \begin{bmatrix} E_x \\ E_y \end{bmatrix} = \begin{bmatrix} V_i - V_j \\ V_i - V_h \end{bmatrix} \quad (4)$$

where $[l]$ is the metrical distance matrix, $[E]$ the column vector of electric field components (which are the coefficients of the linear function of V) and $[V]$ is the column vector containing the potential differences between two of the three vertex of a primal cell indicated by i , j and h . The flux through the surfaces $A_{i,j,k}$ and $A_{i,h,k}$ can be expressed as:

$$\Psi_{i,k} = [A_{i,j,k} + A_{i,h,k}] [\varepsilon_k] [E_k] \quad (5)$$

where ε_k is the permittivity tensor of the primal k^{th} cell and $[E]$ is the column vector of the electric field components. Using (4) (5) in relation (3), a complete system is obtained, which results the same of the first order FEM method [3].

The two procedures have been implemented in Matlab environment which has been interfaced with a mesh generator specifically developed for producing the dual complex cells.

EXAMPLE OF APPLICATION

The previous mathematical formulations have been used to compute the electrical quantities of the configuration shown in Fig. 3, axisymmetric around A-B axis.

A voltage of 1000 Volt is applied between the two plates: in a first case the dielectric was considered isotropic ($\varepsilon_r=100$), in a second case it was assumed anisotropic:

$$\begin{bmatrix} \varepsilon_{x,x} & \varepsilon_{x,y} \\ \varepsilon_{y,x} & \varepsilon_{y,y} \end{bmatrix} = \begin{bmatrix} 100 & 0 \\ 0 & 200 \end{bmatrix} \quad (6)$$

The analysis domain was meshed by a Delaunay triangular grid made up of 1682 nodes and 3208 elements.

At the aim of comparison, the same problems were solved with a first order FEM algorithm using the same unstructured triangular grid; table I reports the maximum discrepancy between the computed scalar potential V values: the very low difference found in the anisotropic case is due to machine round error.

Fig. 4. shows electrical quantities computed with the cell numerical method in the anisotropic case.

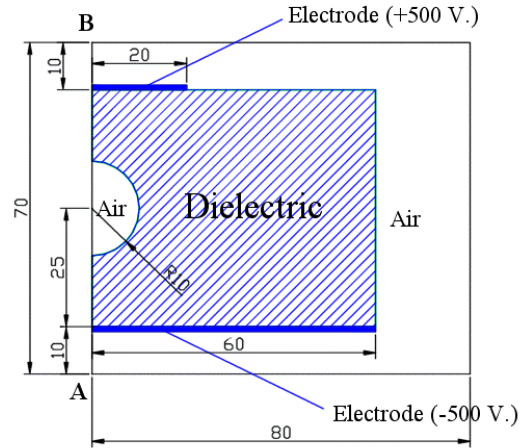


Fig. 3. Geometry used in the example (linear dimensions in mm).

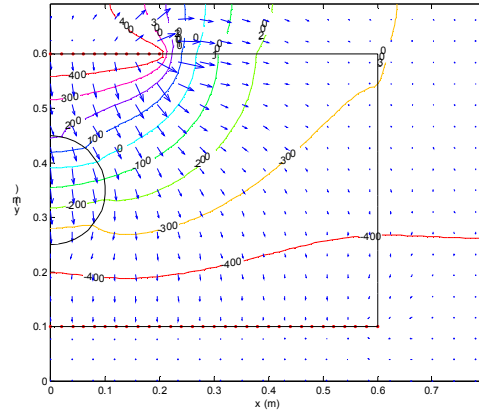


Fig. 4. Electrostatic field values computed by the cell method in the anisotropic case.

TABLE I COMPUTED VALUES AND DISCREPANCY		
	Isotropic problem	Anisotropic problem
Node number	1672	1462
Node coordinates (m)	0; 0.62	0.21; 0.582679
FEM potential (V)	483.6357	269.7878
Cells potential (V)	483.2615	269.7878
Discrepancy (V)	0.3742	$4.77 \cdot 10^{-12}$

REFERENCES

- [1] E. Tonti, “Finite Formulation of the Electromagnetic Field”, *ICS Newsletter*, Vol. 9, No. 4, pp. 5-11.
- [2] E. Tonti, “Algebraic topology and Computational Electromagnetism”, *Fourth International Workshop on the Electric and Magnetic fields*, Marseille, 1998, pp. 284-294.
- [3] E. Tonti, “Formulazione finita delle equazioni di campo: il metodo delle celle”, *Internal report*.

A Finite Element Method with Grouped Smooth Constraints

YAN Xixin, CHAI Jianyun

Tsinghua University, Beijing 100084, China

chaijy@tsinghua.edu.cn

Abstract – The accurate calculation of the potential derivatives is a key process in computing electromagnetic field by finite element method (FEM). According to the continuity of electromagnetic field, we propose a modified FEM formula, in which a high order polynomial function conquering all nodal potentials in a group of neighboring elements is taken as a smooth constraint to the FEM functional. Compared with the traditional FEM, the method, can considerably improve the field calculation accuracy, and reduce the scale of the FEM stiff matrix. Numerical experiments show that the errors of the computed field vectors are reduced by one or two orders.

I. INTRODUCTION

The Finite Element method (FEM) has been applied to a variety of electromagnetic problems. The variables used in the FEM solutions are often the potentials on nodes or edges. In order to obtain the physical field values, it is necessary to find the derivatives of the potentials. Thus, the accurate calculation of the potential derivatives becomes a key step in the computation of electromagnetic field by FEM.

There are two ways that had been explored to improve the numerical field results. The first approach is to refine the mesh adaptively according to the field distribution that considerably increases the scale of computation; the second method is to employ high order interpolation in the elements. High order element leads to more complex integrations in deducing the FEM stiff matrix and sometimes even the numerical integrations have to be used.

In this paper, we propose a new FEM algorithm in which elements are grouped into a patch and the potentials in the patch are constrained by a flexible smooth function. The constraint equations can be easily dealt with as a linear transformation to the standard FEM equations. Therefore the derivatives of the potentials can be obtained analytically in the patch, while the linear interpolation in elements is remained as in the usual FEM.

II. SMOOTH FITTING OF POTENTIALS

According to the continuity of electromagnetic field, the potential and the field vectors are of at least second order derivatives in the interior region of a continued medium. Although the potentials used in FEM are assumed piecewise continuity, no great accuracy losses occur in the accumulated energy functional. But for finding the potential derivatives, good accuracy cannot be expected if only the information of nodes in one

element is used. So it is desirable that the approximation in terms of potential used in the energy computation and used in the differentiation should be different.

Consider a group of neighboring elements, called an element patch. If the potential of field is smooth enough, then the nodal potential values in FEM solutions should belong to a continued and smooth expression which is valid over the element patch. Assuming that the expression takes the form of polynomial expansion,

$$u_h^* = \mathbf{p}\mathbf{a} \quad (1)$$

where the vector \mathbf{P} consists of the base terms of polynomials and the vector \mathbf{a} is a set of parameters to be determined. For two dimensional cases we can use the quadratic expansion as,

$$\mathbf{p} = [1, x, y, x^2, xy, y^2]$$

Given a set of nodal potential values u_h within an element patch, a smooth potential surface can be fitted by means of LSM method, so that the best parameters of the surface are obtained.

III. FEM WITH GROUPED SMOOTH CONSTRAINTS

The smooth fitting of potentials is only a post-processing of FEM, which does not enrich the information of FEM itself. If we consider the smooth continuity be an inherent characteristic of the field, then the nodal potential values u_h in the element patch can be replaced by the smooth function u_h^* . That is to say (1) can be taken as a smooth constraint equation to the FEM functional. This constraint brings additional information into the FEM.

The constraint of all the nodal potential within the element patch can be assembled in matrix notation

$$\mathbf{u}_h = \mathbf{P}\mathbf{a} \quad (2)$$

where $\mathbf{P}_{ij} = \mathbf{p}_j(x_i, y_i)$ for 2D cases, $j=1,2,\dots,m$, $i=1,2,\dots,n_1$, and n_1 is the number of nodes within the element patch.

The energy functional of FEM is of the form as

$$E(\mathbf{u}) = \frac{1}{2} \mathbf{u}^T \mathbf{K} \mathbf{u} - \mathbf{u}^T \mathbf{f} \quad (3)$$

where, \mathbf{K} and \mathbf{f} denote the stiff matrix and the exciting force vector respectively, the vector \mathbf{u} represents the nodal potentials on the mesh.

With the constraint of (2), the components of \mathbf{u} are not independent each other. Let the indexes of the nodes within the patch begin with 1 and other nodes begin with $n_1 + 1$, then a new vector \mathbf{u}' can be constructed as,

$$\mathbf{u} = \mathbf{M}\mathbf{u}' \quad (4)$$

where $\mathbf{M} = \begin{bmatrix} \mathbf{P} & \mathbf{0} \\ \mathbf{0} & \mathbf{I} \end{bmatrix}$

$$\mathbf{u}'_j = \begin{cases} \mathbf{a}_j, & j = 1, 2, \dots, m \\ \mathbf{u}_{j-m+n_1}, & j = m, m+1, \dots, n-n_1+m \end{cases}$$

and \mathbf{I} is the identity matrix.

Substitute (4) for the vector \mathbf{u} in (3), we get

$$E(\mathbf{u}) = E(\mathbf{u}') = \frac{1}{2} (\mathbf{u}')^T \mathbf{M}^T \mathbf{K} \mathbf{M} \mathbf{u}' - (\mathbf{u}')^T \mathbf{M} \mathbf{f}$$

From the minimization of the above functional, the equation of the FEM with smooth constraints is obtained.

$$\mathbf{M}^T \mathbf{K} \mathbf{M} \mathbf{u}' = \mathbf{M} \mathbf{f} \quad (5)$$

It can be seen that the transformed stiff matrix $\mathbf{M}^T \mathbf{K} \mathbf{M}$ is also symmetrical and positively definite; therefore the standard FEM equation solver can be directly applied to it. It should be noted that in order to avoid the under determination problem, the number of nodes in an element patch should be greater than the number of polynomial items used in that patch, namely $n_1 > m$. Thus the scale of the transformed stiff matrix will be reduced.

IV. EXAMPLES

We calculated a 2D magnetic field in a transformer window shown in Fig.1 by the proposed method and by the standard FEM respectively. The flux densities in and between the primary and secondary windings are examined. The region boundary made of iron core is assumed being of infinite permeability, and the node K at the left-bottom corner on the boundary is set as reference. There exists an analytical solution for this field problem.

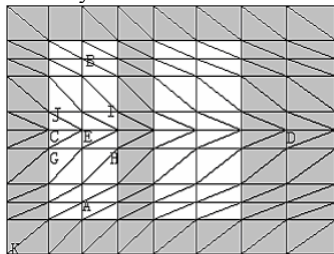


Fig.1. 2D FEM model of a magnetic field

In order to make the comparison more clear, we take only one check point at once. Simple element patch is constructed by the elements around the check point. For instance, the patch of the node E consists of the elements in the rectangle JHGG. And quadratic polynomial expansion is adopted in the patch.

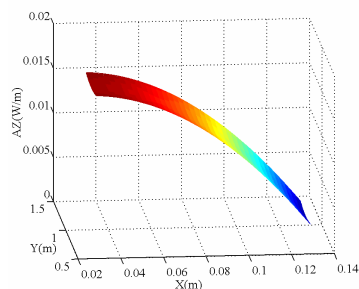


Fig.2. calculated potential surface in JHGGJ by the new method

Fig.2 shows the potential surface calculated by the proposed method in JHGGJ. It can be seen that the potential is smooth not only in every element but also between the elements in the patch.

We also tested the two FEM when their mesh around the check point is locally refined as in Fig.3.

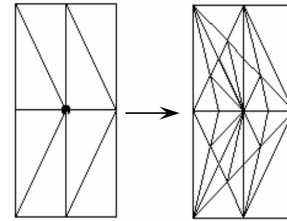


Fig.3. mesh refinement around a node

The relative errors of the flux density calculated by these methods at seven nodes along the segment AB in Fig.1 are illustrated in Fig.4. It is evident that the refinement of the mesh does improve the accuracy of the FEM field computation, while the FEM with grouped smooth constraint proposed here can improve the accuracy more considerably. The relative errors of the computed flux density are reduced by one or two orders.

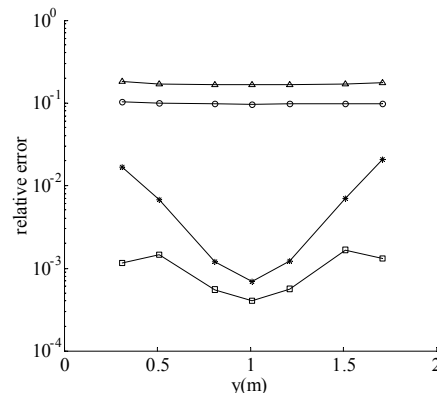


Fig.4 The relative errors of the flux density on the nodes along AB: Δ traditional FEM, \circ FEM with local mesh refinement, * new FEM, \square new FEM with local mesh refinement

V. CONCLUSION

This paper proposed a novel FEM with grouped smooth constraints. Compared with the traditional FEM, it gives smoother and more reasonable calculation results of electromagnetic field. The relative errors of the computed flux density can be reduced by one or two orders.

REFERENCES

- [1] N.Ida and J.P.A.Bastos, *Electromagnetics and Calculation of Fields*, Springer Verlag, New York, 1997.
- [2] O. C. Zienkiewicz and J. Zhu, "The superconvergent patch recovery and a posteriori error estimates. Part I: The recovery technique," *International Journal for Numerical Methods in Engineering*, vol. 33, pp. 1331-1364, 1992.
- [3] P. P. Silvester and D. Omeragic, "A two-dimensional Zhu-Zienkiewicz method for gradient recovery from finite element solutions", *COMPEL*, vol. 12, pp. 191-204, 1993.

Formulation of admittance boundary conditions for the solution of frequency domain problems by FIT

Lorenzo Codecasa, Vito Minerva, Marco Politi

Dipartimento di Elettronica e Informazione
Politecnico di Milano
Piazza Leonardo da Vinci, 32
20133 Milan, Italy
{codecasa, minerva, politi}@elet.polimi.it

Abstract— In this paper it is shown that admittance boundary conditions for electromagnetic boundary value problems in the frequency domain can be formulated for the Finite Integration Technique using augmented dual grids. The details are presented both for orthogonal dual grids and for barycentric dual grids composed either of (oblique) parallelepipeds, (oblique) triangular prisms or tetrahedra.

I. INTRODUCTION

It is well known that the solution of an electromagnetic boundary value problem can be numerically approximated by means of the Finite Integration Technique (FIT) [1], [2], [3]. Precisely, firstly the τ region in which the problem is considered is discretized by means of a primal grid \mathcal{G} and a dual grid $\tilde{\mathcal{G}}$. Then the electromagnetic field is discretized over the dual grids \mathcal{G} and $\tilde{\mathcal{G}}$. Lastly the Maxwell's equations and the constitutive relations are discretized.

In the FIT however the discretization of boundary conditions is not explicitly considered. In particular the FIT equations, as reported in [1], [2], [3], implicitly assume magnetic wall boundary conditions. In [4] it is shown that properly augmenting the dual grid $\tilde{\mathcal{G}}$ with nodes, edges and faces on the boundary $\partial\tau$ and discretizing the electromagnetic field over the augmented dual grid, discretized boundary conditions can be introduced.

In this paper, for electromagnetic boundary value problems in the frequency domain, the discretization of admittance boundary conditions is formulated using augmented dual grids. Firstly, orthogonal dual grids \mathcal{G} and $\tilde{\mathcal{G}}$ are considered, such that the edges and faces of the primal grid \mathcal{G} are orthogonal to the corresponding faces and edges of the dual grid $\tilde{\mathcal{G}}$. In this case, it is shown that, using augmented dual grids, admittance boundary conditions can be naturally discretized similarly to the discretization of constitutive relations. Barycentric dual grids are then considered, such that the primal grid \mathcal{G} is composed of either (oblique) parallelepipeds, (oblique) triangular prisms or tetrahedra and the dual grid $\tilde{\mathcal{G}}$ is the barycentric subdivision [5] of $\tilde{\mathcal{G}}$. For such dual grids a general formulation of the FIT is given in [6]. It is shown that, using augmented dual grids, the discretization of the admittance boundary conditions can be deduced, similarly to the discretization of constitutive relations in [6]. A first numerical results is also presented.

II. DISCRETIZATION OVER AUGMENTED DUAL GRIDS

In order to discretize boundary conditions, augmented dual grids are introduced as in [6]. Precisely the intersection with $\partial\tau$ of each volume, face and edge of $\tilde{\mathcal{G}}$ defines respectively one face, edge and node added to $\tilde{\mathcal{G}}$. These added faces, edges and nodes constitute the dual grid $\tilde{\mathcal{G}}_b$ of the primal grid \mathcal{G}_b constituted by the nodes, edges and faces of \mathcal{G} that belong to $\partial\tau$. Therefore the elements of $\tilde{\mathcal{G}}_b$ are oriented as the corresponding elements of \mathcal{G}_b . The union of the $\tilde{\mathcal{G}}$ and $\tilde{\mathcal{G}}_b$ grids defines the augmented dual grid $\tilde{\mathcal{G}}_a$, for which volume-face, face-edge and edge-node incidence matrices can be introduced as for the grid $\tilde{\mathcal{G}}$.

The discretization of the electromagnetic field is completed, discretizing over the elements of the $\tilde{\mathcal{G}}_b$ dual grid. In particular, it is introduced the $\tilde{\mathbf{f}}_b$ vector of the line integrals of the $\mathbf{h}(\mathbf{r})$ magnetic field along the edges of $\tilde{\mathcal{G}}_b$. The elements of this vector correspond to the elements of the \mathbf{v}_b vector of the line integrals of the $\mathbf{e}(\mathbf{r})$ electric field along the edges of \mathcal{G}_b .

Maxwell's equations are naturally discretized in terms of the incidence matrices of the primal grid \mathcal{G} and of the augmented dual grid $\tilde{\mathcal{G}}_a$, instead of the dual grid $\tilde{\mathcal{G}}$. In this way discretized Maxwell's equations exactly include the contribution of the electromagnetic field on the $\partial\tau$ boundary. Discretized constitutive relations do not change using the augmented dual grid $\tilde{\mathcal{G}}_a$ instead of the dual grid $\tilde{\mathcal{G}}$. Thus they can be written both for orthogonal dual grids as in [1], [2], [3] and for barycentric dual grids as in [6].

Discretized boundary conditions have to be introduced in order to complete the formulation of the discretized electromagnetic boundary value problem. If either the tangent component of the electric field $\mathbf{e}(\mathbf{r})$ or the tangent component of the magnetic field $\mathbf{h}(\mathbf{r})$ are imposed over $\partial\tau$, discretized boundary conditions can be exactly written, imposing the values of either the \mathbf{v}_b vector or the $\tilde{\mathbf{f}}_b$ vector. More generally, admittance boundary conditions are expressed at each \mathbf{r} over $\partial\tau$ by the condition

$$(\mathbf{n}(\mathbf{r}) \times \mathbf{h}(\mathbf{r})) \times \mathbf{n}(\mathbf{r}) = \mathbf{Y}(\mathbf{r}) (\mathbf{n}(\mathbf{r}) \times \mathbf{e}(\mathbf{r})) \quad (1)$$

where $\mathbf{n}(\mathbf{r})$ is the outward unit vector normal to $\partial\tau$ at \mathbf{r} , and $\mathbf{Y}(\mathbf{r})$ is the admittance at \mathbf{r} . In the hypothesis that $\mathbf{Y}(\mathbf{r})$ is constant within each face of \mathcal{G}_b , boundary conditions can be approximated both for orthogonal and barycentric dual grids.

III. ORTHOGONAL DUAL GRIDS

For orthogonal dual grids, the faces of $\tilde{\mathcal{G}}$ are, by construction, orthogonal to the corresponding edges of \mathcal{G} . Therefore also the edges of $\tilde{\mathcal{G}}_b$ are orthogonal to the corresponding edges of \mathcal{G}_b .

As a consequence of (1), at each \mathbf{r} over $\partial\tau$, the component of $\mathbf{e}(\mathbf{r})$ tangent to $\partial\tau$ and the component of $\mathbf{h}(\mathbf{r})$ tangent to $\partial\tau$ form, together to the $\mathbf{n}(\mathbf{r})$ outward unit vector normal to $\partial\tau$, a right tern of axes, and the ratio of their moduli is $\mathbf{Y}(\mathbf{r})$. Thus, locally approximating the $\mathbf{e}(\mathbf{r})$ electric field and the $\mathbf{h}(\mathbf{r})$ magnetic field with constant vectors, admittance boundary conditions are naturally approximated by equation

$$\tilde{\mathbf{f}}_b \approx \mathbf{Y}_b \mathbf{v}_b \quad (2)$$

in which \mathbf{Y}_b is a diagonal matrix, whose i -th diagonal element is the product of the admittance times the length of the i -th edge of $\tilde{\mathcal{G}}_b$ divided by the length of i -th edge of \mathcal{G}_b . This relation is exact when the $\mathbf{e}(\mathbf{r})$ electric field and the $\mathbf{h}(\mathbf{r})$ magnetic field are spatially constant.

IV. BARYCENTRIC DUAL GRIDS

For any primal grid \mathcal{G} and augmented dual grid $\tilde{\mathcal{G}}_a$, if the relation between $\tilde{\mathbf{f}}_b$ and \mathbf{v}_b is approximated by (2) by means of a \mathbf{Y}_b matrix, then twice the flux of Poynting's vector across $\partial\tau$,

$$\int_{\partial\tau} (\mathbf{n}(\mathbf{r}) \times \mathbf{e}(\mathbf{r})) \cdot (\mathbf{Y}(\mathbf{r}) (\mathbf{n}(\mathbf{r}) \times \mathbf{e}(\mathbf{r})))^* d\sigma, \quad (3)$$

is approximated by

$$\mathbf{v}_b^T \cdot (\mathbf{Y}_b \mathbf{v}_b)^*. \quad (4)$$

In fact (4) converges to (3) for finer and finer discretizations, under mild assumptions, as proved in [4]. The converse approach is here considered, as in [6]: if matrix \mathbf{Y}_b is such that (4) approximates (3), does (2) approximate the relation between $\tilde{\mathbf{f}}_b$ and \mathbf{v}_b ? Hereafter a sufficient condition is given when the primal grid \mathcal{G} is composed either by (oblique) parallelepipeds, (oblique) triangular prisms or tetrahedra and the dual grid $\tilde{\mathcal{G}}$ is the barycentric subdivision of \mathcal{G} , as in [6],

Let the component of the $\mathbf{e}(\mathbf{r})$ electric field tangent to $\partial\tau$ be approximated by

$$(\mathbf{n}(\mathbf{r}) \times \mathbf{e}(\mathbf{r}, t)) = \sum_1^{l_b} v_{b_i} (\mathbf{n}(\mathbf{r}) \times \mathbf{w}_i^e(\mathbf{r})) \quad (5)$$

in which v_{b_i} is the i -th element of the \mathbf{v}_b vector and $\mathbf{w}_i^e(\mathbf{r})$ is the i -th weight function of $\mathbf{e}(\mathbf{r}, t)$, defined as in [6]. Using (5) for $\mathbf{e}(\mathbf{r})$, it results

$$\begin{aligned} \mathbf{v}_b^T \mathbf{Y}_b \mathbf{v}_b(t) &= \\ &= \int_{\partial\tau} (\mathbf{n}(\mathbf{r}) \times \mathbf{e}(\mathbf{r})) \cdot (\mathbf{Y}(\mathbf{r}) (\mathbf{n}(\mathbf{r}) \times \mathbf{e}(\mathbf{r})))^* d\sigma, \end{aligned}$$

where the element at the i -th row and j -th column of \mathbf{Y}_b is

$$\int_{\partial\tau} (\mathbf{n} \times \mathbf{w}_i^e(\mathbf{r})) \cdot (\mathbf{Y}(\mathbf{r}) (\mathbf{n}(\mathbf{r}) \times \mathbf{w}_j^e(\mathbf{r})))^* d\sigma.$$

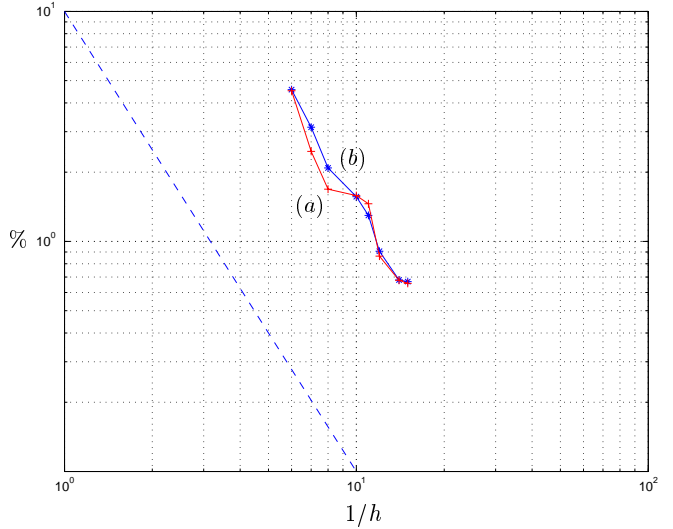


Fig. 1. Per cent error in the energy norm at $\omega/\omega_c = 1.5$ as a function of h . (a) orthogonal dual grids. (b) barycentric dual grids.

This \mathbf{Y}_b matrix approximates the relation between $\tilde{\mathbf{f}}_b$ and \mathbf{v}_b . In fact the following necessary and sufficient condition is satisfied

$$\int_{\partial\tau} (\mathbf{n}(\mathbf{r}) \times \mathbf{w}_i^e(\mathbf{r})) d\sigma = \int_{\tilde{\gamma}_i} \mathbf{t}(\mathbf{r}) d\gamma,$$

in which $\tilde{\gamma}_i$ is the i -th edge of $\tilde{\mathcal{G}}_b$, of tangent $\mathbf{t}(\mathbf{r})$.

V. NUMERICAL RESULTS

The field inside a matched section rectangular waveguide, under TE_{10} excitation, has been evaluated as a simple test case. The analyses have been performed at different normalized angular frequencies ω/ω_c , using a primal grid \mathcal{G} composed of triangular prisms. The resulting error in the norm of the energy [4] is shown in Fig. 1, as a function of the maximum diameter h of the volumes of \mathcal{G} , both for orthogonal and barycentric dual grids.

VI. CONCLUSION

In this paper admittance boundary conditions for the solution of electromagnetic boundary value problems in the frequency domain by FIT, have been formulated using augmented dual grids. The derivation has been carried out both for orthogonal dual grids and barycentric dual grids.

REFERENCES

- [1] K.S. Yee, "Numerical Solution of Initial Boundary Value Problems Involving Maxwell's Equations in Isotropic Media", *IEEE Tran. Antennas Propag.*, vol. 14, p. 302, 1966.
- [2] T. Weiland, A Discretization Method for the Solution of Maxwell's Equations for Six-Component Fields, *Electronic and Communication (AEÜ)*, vol. 31, p. 116, 1977
- [3] E. Tonti, "Finite formulation of electromagnetic field", *IEEE Trans. Magn.*, vol. 38, p. 333, 2002.
- [4] L. Codecasa, M. Politi "Consistent Spatial Discretization of Electromagnetic Boundary Value Problems Through Augmented Dual Grids", submitted to *IEEE Tran. Antennas Propag.*
- [5] A. Bossavit, *Computational Electromagnetism*, Academic Press (Boston), 1998.
- [6] L. Codecasa, V. Minerva, M. Politi "Extension of FIT to barycentric dual grids", submitted to *COMPUMAG 2003*.

A New Multilevel Subgridding Scheme for Two-Dimensional FDTD method

Charles T. M. Choi and Shu-Hai Sun

Department of Electrical Engineering

I-Shou University

1, section 1, Hsueh Cheng Road, Ta-Hsu Hsiang

Kaohsiung county, TAIWAN, ROC.

Email: c.t.choi@ieee.org

Abstract—A multilevel subgridding scheme with a different interpolation scheme is presented. In order to model a structure with fine components using FDTD method, the accuracy of the results can be improved by utilizing multilevel subgridding scheme. In this scheme, the fields on the boundary between neighbor subgridding regions are coupled using simple interpolations. The validation of the scheme is tested by computing the resonant frequencies of a cavity, and the results are compared with uniform grid FDTD and another multilevel subgridding scheme solutions.

I. INTRODUCTION

FDTD method was presented by K. S. Yee in 1966[1]. It is a useful numerical method to analyze the propagation of electromagnetic wave. In FDTD method, Maxwell's curl equations are discretized by utilizing central-difference equations with second-order accuracy. Since the solution resolution is influenced by the grid size, the accuracy can be improved by using finer grids to discretize the computational space, but the memory and computation requirements are also increased.

To reduce the memory requirement, small size components are discretized by subgrids, and the remaining volume is filled with coarse grids. In this subgridding scheme, the coarse-grid region and the subgrid region are also computed by FDTD method. In [2], the size of a coarse grid is 4 that of a subgrid, and the fields in the subgridding region and on the boundary between coarse grids and subgrids need to be updated four times for every time step of coarse-grid region. The fields on the boundary between coarse grids and subgrids are coupled using temporal and spatial interpolations. Zivanovic *et al.* [3] analyzed problems using a 2:1 grid-subgrid size ratio, and discussed the interpolations of both electric and magnetic fields. M. W. Chevalier *et al.* [4] discussed a subgridding scheme, which allowed conducting materials to traverse the boundary, while keeping the grid-subgrid ratio to 3 : 1. C.-C. Chang and S.-K. Jeng [5] developed a multilevel subgridding scheme, and verify the scheme by solving scattering and cavity problems. In this paper, we developed a multilevel subgridding scheme with a similar interpolation as in [4], and compare the results of solving a cavity problem with uniform grid FDTD and the results from [5].

II. METHOD

The multilevel subgridding scheme in this paper is developed utilizing the similar interpolations as [4]. To take two-level subgridding scheme as an example, we name the original subgridding region as the first-level subgridding region, and set the second-level subgridding region in the first-level subgridding region. When the size of a coarse grid is 3 that of a first-level subgrid, and the size of a first-level subgrid is 3 that of a second-level subgrid, the fields in the first-level subgrids and on the boundary between the coarse grid and the first-level subgrids need to be updated three times for every time step of coarse grid, and the fields in the second-level subgrids and on the boundary between the first-level subgrids and the second-level subgrids need to be updated three times for every time step of the first-level subgrid. A brief description of the procedure is given in Fig. 1. In Fig. 1, when e_2 and h_2 are computed three time steps of the second-level subgrid, the h_2 that have collocated h_1 need to be transferred to first-level subgrids. Similarly for the first-level subgrids, h_1 need to be transferred to coarse grids.

III. RESULTS

We illustrate the accuracy of the multilevel subgridding scheme by solving a cavity problem. A cavity with perfect conductor walls and a perfect conductor fin is analyzed. The specifications of the structure are shown in Fig. 2. The thickness of walls is 2mm, and the cavity is filled with air. For the cavity shown in Fig. 2, if we don't consider the fin, the first and second resonant frequencies are about 2.0 GHz and 3.3 GHz for TM mode. We set the coarse grid size to 2 mm, which is 1/20 wavelength (λ) at 7.5 GHz. Five simulations were performed by using 1) uniform coarse FDTD with a grid size of 2 mm, 2) uniform fine FDTD with a grid size of 2/3 mm, 3) two-level subgridding scheme in [5], 4) one-level subgridding scheme for FDTD with a coarse grid cell size of 2 mm, and subgrid size of 2/3 mm, and 5) two-level subgridding scheme for FDTD with a coarse grid cell size of 2 mm, first-level subgrid size of 2/3 mm, and second-level subgrid size of 2/9 mm. The first-level subgridding region is set 25*13 coarse grids when using one-level subgridding scheme, and add second-level subgridding region of 33*27 first-level subgrids when using two-level subgridding scheme. Fig. 3. shows the normalized Ez field at the observation point in time domain.

Manuscript received November 15, 2002.

After finishing the iteration for our subgridding scheme, we performed a 24000-points FFT to compute the resonant frequencies of the cavity. The results of five simulations are listed in Table I. In case 2, it is found that the first and second resonant frequencies are 2.425 GHz and 3.775 GHz, respectively. Comparing with case 3, case 4 has a more accurate 2nd resonant frequency, and case 5 has a more accurate 2nd resonant frequency than case 4. When comparing with the results from cases 1 and 3, results from cases 4 and 5 have a better solution accuracy. Since we had not optimized our program, the flops require for an optimized scheme should be less than the results given in Table I.

IV. CONCLUSIONS

A multilevel subgridding scheme with an interpolation similar to [4] has been presented. It has been shown that this multilevel subgridding scheme can improve the accuracy of results. Besides, the variation of fields in time are stable after six thousands of time-steps for two-level subgridding scheme.

V. REFERENCES

- [1] K. S. Yee, "Numerical solutions of initial boundary value problems involving Maxwell's equations in isotropic media," *IEEE Trans. Antennas Propagat.*, vol. AP-14, pp. 302-307, May 1966.
- [2] I. S. Kim and W. J. R. Hoefer, "A local mesh refinement algorithm for the time domain-finite difference method using Maxwell's curl equations," *IEEE Trans. Microwave Theory Tech.*, vol. 38, pp. 812-815, June 1990.
- [3] S. S. Zivanovic, K. S. Yee, and K. K. Mei, "A subgridding method for the time-domain finite-difference method to solve Maxwell's equations," *IEEE Trans. Microwave Theory Tech.*, vol. 39, pp. 471-479, Mar. 1991.
- [4] M. W. Chevalier and R. J. Luebbers, "FDTD local grid with material traverse," *Antennas and Propagation Society International Symposium*, vol. 2, pp. 116-119, 1996.
- [5] C.-C. Chang and S.-K. Jeng, "A multilevel subgridding scheme for two-dimensional finite-difference time-domain method," *Asia Pacific Microwave Conference*, 2001.

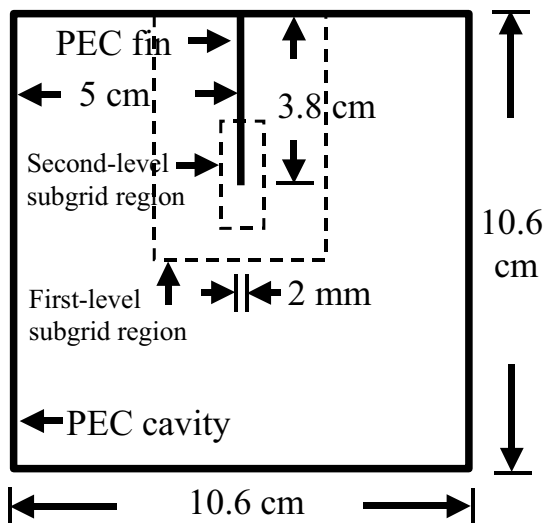


Fig. 2. A cavity with a PEC fin.

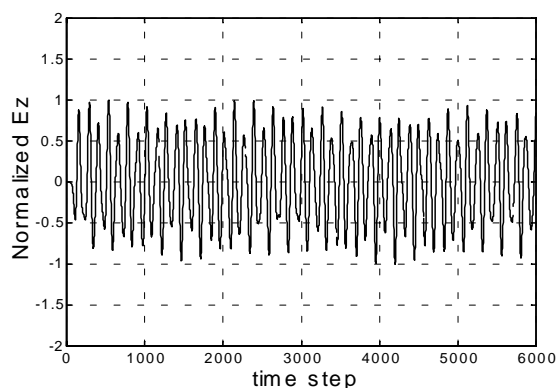


Fig. 3. Normalized E_z field at the observation point in time domain.

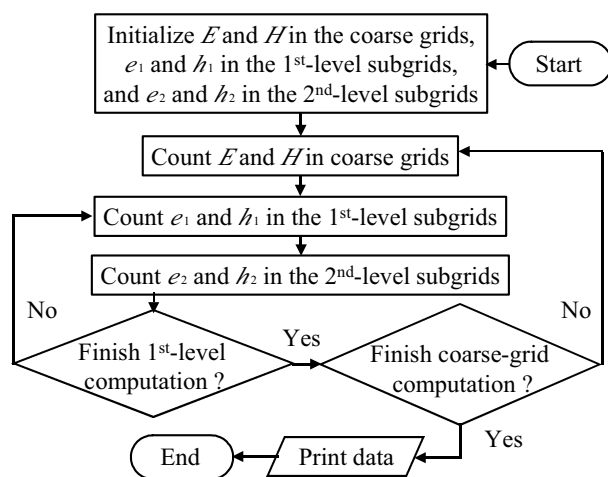


Fig. 1 The flow-chart for new multilevel subgridding scheme.

TABLE I
RESONANT FREQUENCIES AND FLOPS USED

Case	Resonant frequency (GHz)		Flops (M flops)
	First	Second	
1	2.375	3.700	350
2	2.425	3.775	2768
3	2.4125	3.7125	-----
4	2.4125	3.7250	1664
5	2.4125	3.7375	5451

A Subgridding Scheme for Two-Dimensional FDTD(2,4) Method

Charles T. M. Choi and Shu-Hai Sun

Department of Electrical Engineering

I-Shou University

1, section 1, Hsueh Cheng Road, Ta-Hsu Hsiang

Kaohsiung county, TAIWAN, ROC.

Email: c.t.choi@ieee.org

Abstract—A second-order accurate in time and fourth-order accurate in space FDTD(2,4) subgridding scheme is presented. By using subgridding scheme at fine components in a structure, the necessary resolution can be obtained. Some error introduced in the second-order central difference approach can be reduced by using FDTD(2,4) method. The accuracy of the scheme is tested by computing the resonant frequencies of a cavity, and the results are compared with uniform mesh FDTD solutions.

I. INTRODUCTION

The finite difference time domain (FDTD) method is a useful technique to analyze electromagnetic wave propagation [1]. In FDTD method, Yee discretized Maxwell's curl equations by utilizing central-difference equations with second-order accuracy. In order to reduce the numerical dispersion, utilizing a scheme with high-order accuracy to analyze problems is a useful alternative. T. Deveze *et al.* in [2] developed a fourth order scheme for the FDTD algorithm, and considered the dispersion and the stair case problems. They discretized Maxwell's curl equations by utilizing central-difference equations with fourth-order accuracy. M. F. Hadi *et al.* in [3] developed the second-order difference in time and fourth-order difference in space FDTD scheme, and used the scheme to model electrically structures that were thousands of wavelengths large.

Beside reduce the numerical dispersion, reducing the memory usage is also important. Since numerical dispersion is controlled by the grid size, the solution accuracy can be improved by using finer grids to discretize the volume, but the memory and computation requirement are increased accordingly. Solving electromagnetic problems utilizing a FDTD subgridding scheme is an approach to reduce the memory usage by controlling the distribution of the degrees of freedom. In a subgridding scheme, small size components in a structure are discretized by subgrids, and the residual of the volume is filled with coarse grids. The coarse-grid region and the subgrid region are also computed by FDTD method and are kept in time step. The fields on the boundary between coarse-grid region and subgridding region are coupled using temporal and spatial interpolations. In [4], the size of a coarse grid is 4 that of a subgrid, and the fields in the subgridding region and on the boundary between coarse grids and subgrids need to be updated four times for every time step of coarse-grid region. Zivanovic *et al.* [5] analyzed problems for a 2:1

grid-subgrid size ratio, and discussed the interpolations of both electric and magnetic fields. M. W. Chevalier *et al.* in [6] discuss a subgridding scheme, which allows conducting materials to transverse the boundary. The grid-subgrid ratio in [6] is 3 : 1. Georgakopoulos *et al.* in [7] developed a hybrid fourth-order FDTD utilizing a second-order FDTD subgrid. They analyzed an electromagnetic problem for a subgridding scheme, with coarse grids are computed using the FDTD(2,4) method and subgrids are computed for traditional FDTD method.

In this paper, we developed a subgridding scheme for FDTD(2,4) method. For this subgridding scheme, coarse grids and subgrids are computed for FDTD(2,4) method. The accuracy of this scheme is compared with traditional FDTD method, FDTD(2,4), and the subgridding scheme in [7] by solving resonant frequencies of a cavity.

II. METHOD

The subgridding scheme used in this paper is utilizing a similar interpolations as in [6]. Comparing with the scheme in [7], the accuracy of the solution is improved by applying FDTD(2,4) method to the subgrids. For the central-difference equations with fourth-order accuracy in [2], $E^n(r)$ can be obtained by $E^n(r+0.5)$, $E^n(r-0.5)$, $E^n(r+1.5)$, and $E^n(r-1.5)$. Unfortunately, the fields in subgrids close to the boundary between coarse grids and subgrids cannot be obtained by utilizing central-difference equations to maintain the fourth-order accuracy. In this paper, forward and backward difference equations are used to compute the fields close to the boundary between coarse grids and subgrids to bypass this problem.

When the size of a coarse grid is 3 times that of a subgrid, the fields in the subgrids and on the boundary between coarse grids and subgrids need to be updated three times for every time step of coarse grid, where the fields in the subgrids close to the boundary between coarse grids and subgrids can be obtained by utilizing forward and backward difference equations. The fields in the residual subgrids can be obtained by utilizing central-difference equations. The fields on the boundary between coarse grids and subgrids can be computed by utilizing the interpolations in [6].

III. RESULTS

We illustrate the accuracy of the subgridding scheme for

FDTD(2,4) method by solving a cavity problem. A cavity with perfect conductor walls and a perfect conductor fin is analyzed. The specifications of the structure are shown in Fig. 1. The thickness of walls is 4mm, and the cavity is filled with air. For the cavity shown in Fig. 1, if we don't consider the fin, the first and second resonant frequencies are about 2.0 GHz and 3.3 GHz for the TM mode. We set the coarse grid size to 2 mm, which is $1/20$ wavelength (λ) at 7.5 GHz. Five simulations were performed by using 1) traditional FDTD method with a grid size of 2 mm, 2) traditional FDTD method with a grid size of $2/3$ mm, 3) uniform FDTD(2,4) method with a grid size of 2 mm, 4) the subgridding scheme in [7] with a coarse grid size of 2 mm, and a subgrid size of $2/3$ mm, and 5) the subgridding scheme for FDTD(2,4) method with a coarse grid size of 2 mm, and a subgrid size of $2/3$ mm. The subgridding region is set 25×11 coarse grids. Fig. 2. shows the normalized E_z field at the observation point in time domain. After finishing the iteration of 12000 time steps of coarse grid, we utilize the fast Fourier transform (FFT) to compute the resonant frequencies of the cavity. The results of five simulations are listed in Table I. In case 2, it is found that the first and second resonant frequencies are 2.45 GHz and 3.775 GHz. In case 4 and 5, it is found that the resonant frequencies are identical. Comparing with case 1, case 3 has more accurate resonant frequencies, and case 4 and 5 have more accurate resonant frequencies than case 1. Our program can be optimized to reduce the computational requirement to less than the results given in Table I.

IV. CONCLUSIONS

A subgridding scheme based on FDTD(2,4) method has been presented. It has been shown that this subgridding scheme can improve the accuracy of the results. The variation of fields in time are stable after twelve thousands time-steps.

V. REFERENCES

- [1] K. S. Yee, "Numerical solutions of initial boundary value problems involving Maxwell's equations in isotropic media," *IEEE Trans. Antennas Propagat.*, vol. AP-14, pp. 302-307, May 1966.
- [2] T. Devez, L. Beaulieu, and W. Tabbara, "A fourth order scheme for the FDTD algorithm applied to Maxwell's equations," *IEEE APS int. Symp. Proc.*, pp. 346-349, July 1992.
- [3] M. F. Hadi and M. Picket-May, "A modified FDTD(2,4) scheme for modeling electrically large structures with high-phase accuracy," *IEEE Trans. Antennas Propagat.*, vol. 45, pp. 254-264, Feb. 1997.
- [4] I. S. Kim and W. J. R. Hofer, "A local mesh refinement algorithm for the time domain-finite difference method using Maxwell's curl equations," *IEEE Trans. Microwave Theory Tech.*, vol. 38, pp. 812-815, June 1990.
- [5] S. S. Zivanovic, K. S. Yee, and K. K. Mei, "A subgridding method for the time-domain finite-difference method to solve Maxwell's equations," *IEEE Trans. Microwave Theory Tech.*, vol. 39, pp. 471-479, Mar. 1991.
- [6] M. W. Chevalier and R. J. Luebbers, "FDTD local grid with material traverse," *Antennas and Propagation Society International Symposium*, vol. 2, pp. 116-119, 1996.
- [7] S. V. Georgakopoulos, R. A. Renaut, and C. A. Balanis, "A hybrid fourth-order FDTD utilizing a second-order FDTD subgrid," *IEEE Microwave and Wireless Components Letters*, vol. 11, pp. 462-464, Nov. 2001.

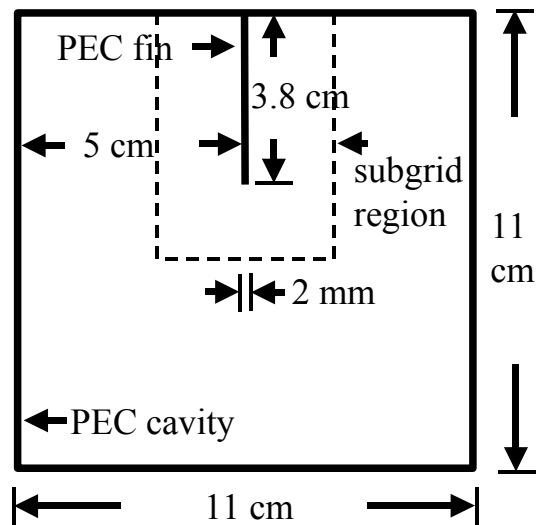


Fig. 1. A cavity with a PEC fin.

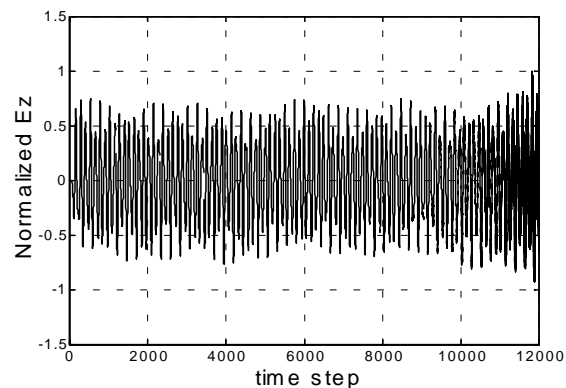


Fig. 2. Normalized E_z at the observation point in time domain.

TABLE I
RESONANT FREQUENCIES AND FLOPS USED

Case	Resonant frequency (GHz)		Flops (M flops)
	First	Second	
1	2.375	3.700	350
2	2.450	3.775	2768
3	2.400	3.725	851
4	2.425	3.750	2137
5	2.425	3.750	3445

Design of the Recording Head considering the Field Gradient in High Density Magnetic Recording

H. Won, G. S. Park

Dept. Electrical Engineering, Korea Maritime Univ.,
Youngdo-Ku, Dongsam-Dong, Busan 606-791
e-mail: gspark@hanara.kmaritime.ac.kr

Y. Y. Kim, G. P. Han

New Function Information Device Team,
Electronics and Telecommunications Research Institute
e-mail: yykim3@etri.re.kr

Abstract— The gap size of the write head in magnetic recording system is so small compared to head size, which causes the difficulties in numerical analysis and design. In this paper, two step of the analysis is presented. After the analysis of the full size head by using conventional 3D FEM, the field gradient of the small gap region is computed by Laplacian analysis. Write field and field gradient of the Longitudinal and perpendicular head are to be computed effectively. By using this algorithm, optimum shapes of the write head in high density recording system could be designed.

I. INTRODUCTION

The recording density in magnetic recording system is represented by multiplying the bit density and track density. To increase the recording density, not only the magnitude of the magnetic field but also the field gradient of the recording head are need to be high. In general, the track density of the magnetic recording is depended on the width of the write head and the linear density is mainly depended on the field gradient in down track direction. So, the magnitude of the head field at the gap recording region is needed to be high enough to overwrite the high coercive recording media, and together, magnetic field gradient of the write head is needed to be high enough to increase the linear density in the data track.

The size of the head gap is very small compared to head size, and recording is occurred in the small gap region. So, if the number of the mesh is not sufficient, field gradient is not computed correctly. If the number of mesh is increased so as to compute field gradient, total number of the mesh is too big to solve.

In this paper, two step to solve this problem is presented. The magnitude of the magnetic field is computed by the conventional 3D FEM, and then, field gradient of the write head in the gap region by using Laplacian.

II. COMPUTATION OF THE FIELD GRADIENT OF THE WRITE HEAD

The relative permeability of the recording region is considered to be 1 because that of the recording media is small compared to the high permeable head material. In this

case, magnetic field in the gap region could be analyzed by Laplacian analysis. Magnetic field of the head by using conventional non-linear FEM is as following. From the Maxwell equation,

$$\nabla \times H = J \tag{1}$$

$$B = \mu_0(H + M) \tag{2}$$

$$B = \nabla \times A \tag{3}$$

So, the system equation is as follows,

$$H = \nu B - \nu_r M \tag{4}$$

$$\nabla \times (\nu \nabla \times A) = J + \nu_r \nabla \times M \tag{5}$$

$$-(\nabla \cdot \nu \nabla) A = J + \nu_r \nabla \times M \tag{6}$$

In this equation, susceptibility is not a constant so that (6) need to be solved iteratively.

In the recording region, the relative permeability is considered to be 1. So, the following Laplacian analysis could be applied to compute magnetic field gradient around the recording region.

$$\nabla^2 \phi = \frac{\delta^2 \phi}{\delta x^2} + \frac{\delta^2 \phi}{\delta y^2} + \frac{\delta^2 \phi}{\delta z^2}$$

$$\cong \frac{\frac{x_1}{l_1} + \frac{x_2}{l_2} + \frac{y_1}{l_3} + \frac{y_2}{l_4} + \frac{z_1}{l_5} + \frac{z_2}{l_6}}{\frac{1}{l_1} + \frac{1}{l_2} + \frac{1}{l_3} + \frac{1}{l_4} + \frac{1}{l_5} + \frac{1}{l_6}} \tag{7}$$

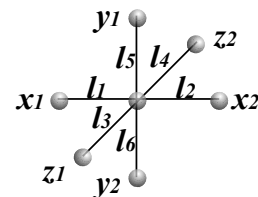


Fig. 1. The lattice to compute the Laplacian in gap region.

Fig. 2 (a) shows the contour plot of the magnetic potential around the recording region of the magnetic recording head by using conventional FEM. In the result, the mesh is not enough to compute magnetic field gradient. After the Laplacian calculation by using boundary interpolations, magnetic head field and field gradient could be obtained as in Fig. 2(b).

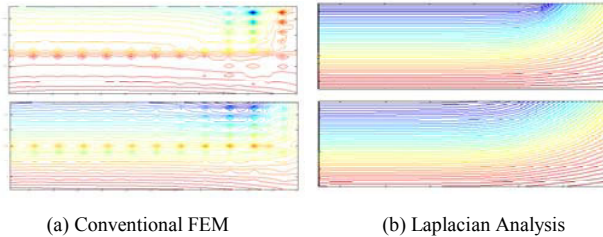


Fig. 2. Contour plot of the magnetic potential around the recording region.

III. WRITE HEAD FIELD AND FIELD GRADIENT

Fig. 3 shows the longitudinal and perpendicular head to computed field with field gradient in down track direction.

Magnetic field and field gradient of the longitudinal and perpendicular write head is in Fig. 4 and Fig. 5, respectively. The width and length of the head foot is 80 nm x 80nm. Maximum field strength of the write head is about 7600 Oe in longitudinal head and 6900 Oe in Perpendicular head. Recording field in down track direction and cross track direction is obtained in Fig. 6.

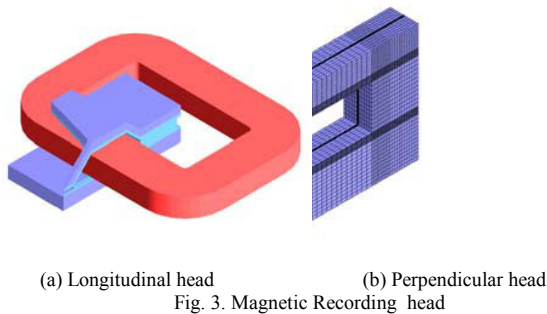


Fig. 3. Magnetic Recording head

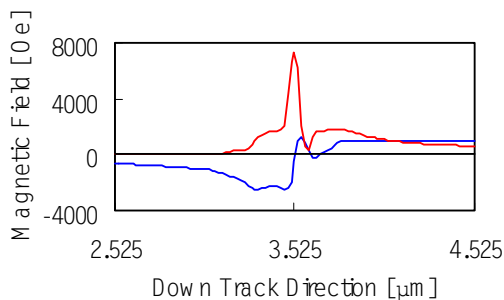


Fig. 4. Magnetic field strength of the longitudinal write head

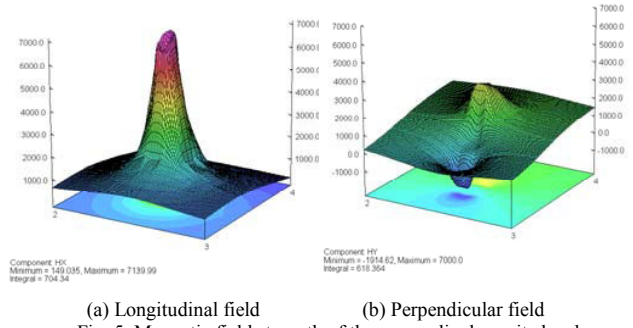


Fig. 5. Magnetic field strength of the perpendicular write head

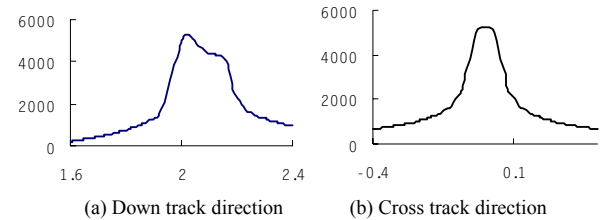


Fig. 6. Perpendicular head Field

IV. CONCLUSIONS

There are numerical difficulties to analyze and design of the recording head because the size of the head gap is very small compared to head size. In this paper, magnetic field and field gradient in the region of the recording around the head gap could be obtained by Laplacian analysis based on the conventional FEM results. Magnetic field and field gradient of the Longitudinal and Perpendicular head could be obtained in the analysis. In the size 80 nm x 80 nm, 7600 Oe and 6900 Oe is achieved in the longitudinal and perpendicular head, respectively. Presented algorithm opens the possibility to perform the optimum design of the write head.

V. REFERENCES

- [1] W. P. Jayasekara, S. Khizroev, M. H. Kryder, W. Weresin, P. Kasiraj and J. Fleming, "Inductive Write Heads Using High Moment FeAlN Poles", IEEE Trans. on Magn., Vol. 35, No. 2, pp. 613 -618, 1999. 3.
- [2] Thomas Chang, "Modeling Assessment of Side Writing Properties of a Notch Write Head", IEEE Trans. on Magn., Vol. 33, No. 5", pp. 2842 - 2843, 1997. 10.
- [3] S.X.Wang and P.R.Webb, "Modeling of Submicron Track Width Inductive Write Head Designs", IEEE Trans. on Magn., Vol. 31, No. 6, pp 2687 - 2689, November 1995.
- [4] Mark H.Kryder and Weng-Yew Lai, "Modeling of Narrow Tracks Thin Film Write Head Fields", IEEE Trans. on Magn., Vol. 30, No. 6, November 1994.
- [5] Kai-Zhong Gao an JH. Neal Bertram, "Write Field Analysis and Write Pole Design in Perpendicular Recording", IEEE Trans. on Mag, Vol.38, No. 5, pp3521 - 3527 September 2002

Closed-Form Approximation of Electromagnetic Green's Function for Layered Media with Variable Source Point

Leonid B. Proekt, Andreas Cangellaris

Electrical and Computer Engineering Department of The University of Illinois at Urbana - Champaign
1406 West Green Street,
Urbana, IL, 61801-2991, USA
proekt@uiuc.edu, cangella@uiuc.edu

Abstract — A novel method is presented for the development of an approximate closed-form electromagnetic Green's function for layered media, where the coordinates of the source are considered as independent variables. The analysis of its accuracy along with its numerical implementation and validation are presented also.

Index Terms – Novel Methodologies, error estimation.

I. INTRODUCTION

THIS papers concerns itself with the well-known problem of fast and efficient calculation of electromagnetic Green's functions in planar layered media. Of particular interest is the availability of closed-form expressions that expedite iterative solution of electromagnetic integral equation-based solution of electromagnetic interference in high-density, multi-layered planar circuits.

Recently, a new technique for the development of a closed-form approximation of the Green's function has been put forward [1]. This methodology leads to a semi-analytical approximation of the Green's function in the form of a truncated series over poles of its spectrum. The analysis of this approximation reveals certain issues to be elaborated upon:

- i. It can be shown that the disturbance of the computational solution of the integral equation, which is due to the approximation of the Green's function G , is minimized if G is approximated with respect to H_1 rather than L_2 norm.
- ii. The Green's function is defined over the product of the scalar fields ($R_3 \times R_3$). That is why, when approximating the Green's function, it is essential to consider the coordinates of the source as independent variables.

In this paper, the methodology in [1] is modified in accordance with these two items. In Section II a brief account of the method of the semi-analytical approximation of the Green's function is presented, and the proposed solution through the finite element method is discussed. Section III presents the accuracy analysis of the derived Green's function. Finally, numerical results from its application are presented.

II. SEMI-ANALYTICAL APPROXIMATION OF THE GREEN'S FUNCTION

Assuming multi-layered dielectric planar media, the development of the electromagnetic Green's function for both cases of the vertical and horizontal orientation of a dipole source involves the application of the Fourier-Bessel transform to reduce the problem to the solution of one-

dimensional scalar differential equations for the Green's function spectrum [1],[4]. These are of the form,

$$\frac{d}{dx} \left(\varepsilon^{-1} \frac{dg_\lambda}{dx} \right) + (1 - \varepsilon^{-1} \lambda^2) g_\lambda = \delta(x, x_0) \quad (1)$$

Note, that for the case of reciprocal media the Green's function is symmetric,

$$g_\lambda(x, x_0) = g_\lambda(x_0, x) \quad (2)$$

Thus, (1) is equivalent to its symmetric analog,

$$\frac{d}{dx} \left(\varepsilon^{-1}(x) \frac{dg_\lambda}{dx} \right) + \frac{d}{dx_0} \left(\varepsilon^{-1}(x_0) \frac{dg_\lambda}{dx_0} \right) + \left\{ 2 - \left[\varepsilon^{-1}(x) + \varepsilon^{-1}(x_0) \right] \lambda^2 \right\} g_\lambda = 2\delta(x, x_0) \quad (3)$$

In (1) (and (3)) the spectrum $g_\lambda(x, x_0)$ is considered as a function of two independent variables $\{x, x_0\}$. We define the standard finite element space over the field $R_2 = R_1 \times R_1$ and rewrite (1) in the weak form

$$\int dx dx_0 \left\{ \varepsilon^{-1} \partial g / \partial x \partial \varphi_n / \partial x + (1 - \varepsilon^{-1} \lambda^2) g \varphi_n \right\} = \int dx \varphi_n, \quad (4)$$

where $\varphi_n(x, x_0)$ is the basis of the approximating space. Following standard finite element procedures we seek the approximation $\hat{g}_\lambda(x, x_0)$ of the spectral function $g_\lambda(x, x_0)$ as a linear combination of functions $\{\varphi_n(x, x_0)\}$:

$$\hat{g}_\lambda(x, x_0) = \sum_n C_n(\lambda) \varphi_n(x, x_0) \quad (5)$$

Substitution of (5) into (4) leads to the system of algebraic equations that in matrix form can be written as

$$(M - A_\varepsilon - \lambda^2 \tilde{M}_\varepsilon) C(\lambda) = F \quad (6)$$

In (6) the matrix A_ε stands for the stiffness matrix associated with the first term of the integrand in the left-hand side of the equation (4), M and \tilde{M}_ε are mass matrices corresponding to the second and third terms in the integrand and F is associated with the right-hand side of (4).

Introducing the eigen value decomposition of the matrix $S \equiv \tilde{M}_\varepsilon^{-1}(M - A_\varepsilon)$,

$$S = U \Lambda U^{-1} \quad (7)$$

the following truncated expansion $\hat{g}_\lambda(x, x_0)$ of the spectral function $g_\lambda(x, x_0)$ over its poles is obtained,

$$\hat{g}_\lambda(x, y) = \sum_{k,m,n} \left\{ U_{km} \left[\frac{U_{mn}^{-1}}{\Lambda_m - \lambda^2} \{ \tilde{M}_\varepsilon^{-1} F \}_n \right] \right\} \varphi_k(x, y) \quad (8)$$

The inverse Fourier Bessel transform of (8) yields the desired closed-form approximation of the Green's function,

$$\tilde{G} = \sum_{k,m} U_{km} \left\{ H_0^{(1)} \left(\sqrt{\Lambda_m} (\rho - \rho_0) \right) R_m \right\} \varphi_k(x, x_0) \quad (9)$$

where it is, $R_m = \sum_n U_{mn}^{-1} \{ \tilde{M}_\varepsilon F \}_n$.

III. ACCURACY

The accuracy of the approximation in (9) is quantified through the energy norm of the error $\|G - \tilde{G}\|_{H_1}$. This error can be represented as the norm of the inverse Bessel-Fourier transform $F_{\lambda \rightarrow \rho}^{-1}$ of the function $\varepsilon_\lambda(x, x_0) = \{g_\lambda(x, x_0) - \hat{g}_\lambda(x, x_0)\}$:

$$\begin{aligned} \|G - \tilde{G}\|_{H_1}^2 &= \|F_{\lambda \rightarrow \rho}^{-1}[\varepsilon_\lambda(x, x_0)]\|_{H_1}^2 \leq \|J_0\|_{L_2}^2 \int d\lambda \|\varepsilon_\lambda\|_{L_2(x, x_0)}^2 + \\ &\int d\lambda \left(C_1 \|\varepsilon_\lambda\|_{L_2(x, x_0)}^2 + C_2 \|\nabla \varepsilon_\lambda\|_{L_2(x, x_0)}^2 \right) \leq C \int d\lambda \|\varepsilon_\lambda\|_{H_1(x, x_0)}^2 \end{aligned} \quad (10)$$

Here $\{C_i\}$ are constants associated with the norm of the Bessel function J_0 .¹ This result connects the accuracy of the approximation in (9) with that of the finite element approximation $\hat{g}_\lambda(x, x_0)$ of the spectrum of the Green's function. It can be shown that $g_\lambda(x, x_0)$, as a function of the complex parameter λ , is meromorphic with simple poles. Moreover, if the wavelength is larger than the characteristic size of the structure, all poles of this function are purely imaginary, located on only one of the semi-planes of the complex λ -plane. Since as λ tends to infinity the function $g_\lambda(x, x_0)$ goes to zero, $g_\lambda(x, x_0)$ can be represented in a form analogous to (8),

$$g_\lambda(x, x_0) = \sum_{m=1}^{\infty} \frac{C_m(x, x_0)}{\lambda - \lambda_m} \quad (11)$$

Rewriting (8) as

$$\hat{g}_\lambda(x, x_0) = \sum_{m=1}^M \frac{\hat{C}_m(x, x_0)}{\lambda - \sqrt{\Lambda_m}}, \quad M = \dim(S), \quad (12)$$

the following result is obtained [5]²

$$\|\varepsilon_\lambda\|_{H_1(x, x_0)}^2 \leq Ph^{2\gamma} \sum_{m=0}^M \frac{\|C_m\|^2 |\lambda + \lambda_m|^2}{|\lambda - \lambda_m|^4} + \sum_{m=M}^{\infty} \frac{\|C_m\|^2}{|\lambda - \lambda_m|^2}, \quad (13)$$

where P is a constant that is independent of λ ; h is the maximum size of the finite element mesh; γ is defined by the order of finite elements [5]; the eigen values $\{\lambda_m\}$ are ordered,

$$|\lambda_1| < |\lambda_2| < \dots < |\lambda_M| < \dots < |\lambda_\infty|.$$

Substitution of (13) into (10) and use of the fact that $\{\lambda_m\}$ are purely imaginary, leads to the following result for the error estimate,

$$\|G - \tilde{G}\|_{H_1}^2 = O \left\{ h^2 \pi \sum_{m=0}^M \frac{\|C_m\|^2}{|\lambda_m|} + \pi \sum_{m=M}^{\infty} \frac{\|C_m\|^2}{|\lambda_m|} \right\} \quad (14)$$

IV. NUMERICAL EXAMPLE

The following example studies are for the case of the Green's function of a vertical electric dipole inside a parallel-plate waveguide with its perfectly conducting plates parallel to the yz -plane and with multiple planar dielectric interfaces. Magnitudes of normalized Green's functions versus x and z for a given source position and on the plane of the source are depicted in Figs. 2 and 3.

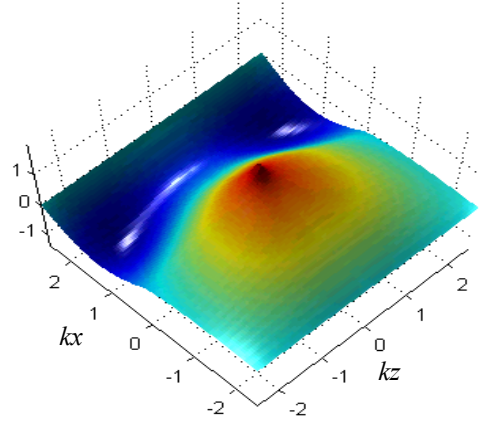


Fig.1 Two-layered structure ($\varepsilon_1=1$; $\varepsilon_2=3$)

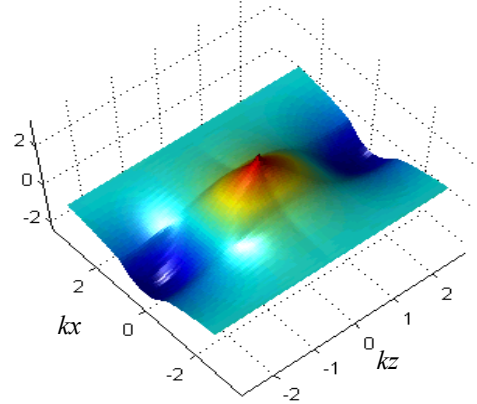


Fig.3 Three-layered structure ($\varepsilon_1=1$; $\varepsilon_2=3$, $\varepsilon_3=1$)

V. REFERENCES

- [1] Okhmatovski V., Cangellaris, A., "A new Technique for the Derivation of Closed-Form Electromagnetic Green's Function for Unbounded Planar Layered Structure", IEEE Transactions on Antennas and Propagation, Vol. XX, N5, May 2000
- [2] Hsiao G., Klenman, R., "Mathematical Foundations for Error Estimation in Numerical Solutions of Integral Equations in Electromagnetics," IEEE Transactions on Antennas and Propagation, V. 45, N3, March 1997
- [3] Duatray R., "Mathematical Analysis and Numerical Methods for Science and Technology", V.2, Springer-Verlag
- [4] Wait J. "Geo-Electromagnetism", Academic Press, 1982
- [5] Ciarlet, P., "The finite element method for elliptic problems", North-Holland 1978

¹ Proof of the result (4.1) is given in the full version of the paper

² This estimation is derived in the full version of the paper.

Finite Element Simulation of Micro Electro Mechanical Systems (MEMS) by Strongly Coupled Electro Mechanical Transducers

Miklos Gyimesi and Dale Ostergaard

ANSYS, Inc.

275 Technology Dr.

Canonsburg, PA 15317, U.S.A.

miklos.gyimesi@ansys.com

Ilya Avdeev

University of Pittsburgh, Department of Mechanical Engineering

B72B Benedum Engineering Hall

Pittsburgh, PA 15261, U.S.A.

ivast@pitt.edu

Abstract—The paper introduces a new methodology using novel electromechanical transducers for the strongly coupled finite element (FE) simulation of micro electro mechanical systems (MEMS).

INTRODUCTION

The increasing functionality of the micro electro mechanical systems (MEMS) leads to complex geometrical configurations of MEMS, which requires new efficient finite element (FE) modeling techniques to solve coupled electromechanical problems. Lumped models are no longer applicable for the devices, where fringing electrostatic fields are dominant, such as combdrives or electrostatic motors. There have been several numerical methods proposed for the more accurate treatment of electromechanical systems: FE or boundary element methods using sequential physics coupling; strongly coupled but reduced order methods using fully lumped or mechanically distributed but electrically lumped 1D, multi-dimensional or modal-space transducers. All these methods need some extra meshing or morphing, introduce simplifying assumptions and may not be convenient to use.

This paper introduces and describes a distributed strongly coupled electromechanical transducer finite element with internal meshing/morphing for full and accurate modeling the underlying physical phenomena. The new transducer can be used with both lumped and solid mechanical models.

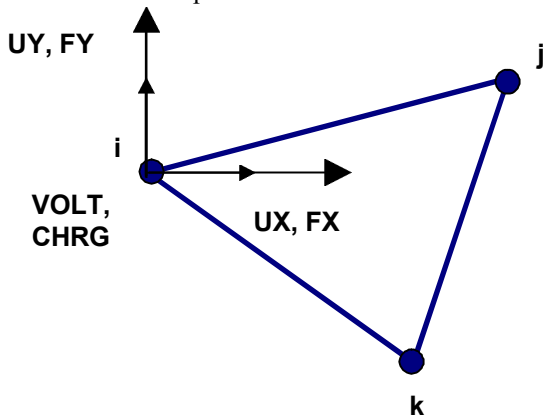


Fig. 1. Degrees of freedom and forces of the transducer FE

FORMULATION

For the sake of simplicity, the principle of the new strongly coupled transducer is shown in 2D (see Fig. 1), but it could be applied to 3D. A transducer has a regular FE shape with electrical potential (VOLT) and structural displacement (UX and UY in 2D; UX, UY and UZ in 3D) degrees of freedom. The reaction solutions are electrical charge (CHRG) and mechanical forces (FX and FY in 2D; FX, FY and FZ in 3D). The support is meshed by regular mechanical FE; the air region between electrodes is meshed by transducers.

The total energy is the sum of electrostatic and elastic energies. Mechanical elements store elastic energy, the transducers store electrostatic energy. The energy change due to potential and displacement distribution changes produces forces. The FE formulation of the transducer follows standard Ritz - Galerkin variational energy principles, which ensures compatibility with regular mechanical FE. The electrostatic energy, W , is

$$W = \frac{1}{2} \mathbf{v}^T \mathbf{C} \mathbf{v} \quad (1)$$

In (1), \mathbf{v} is the vector of nodal voltages, superscript T denotes transpose, and \mathbf{C} is the element capacitance matrix. The nodal electrostatic charge vector, \mathbf{q} , can be obtained as

$$\mathbf{q} = \mathbf{C} \mathbf{v} \quad (2)$$

The capacitance matrix, \mathbf{C} , depends on the element geometry. The nodal electrostatic reaction force, \mathbf{f} , can be calculated by the virtual work principle:

$$\mathbf{f} = \frac{dW}{d\mathbf{u}} \quad (3)$$

In (3), \mathbf{u} is the vector of nodal displacements. At equilibrium, forces between transducers and mechanical elements balance each other. The mesh, including the air region, deforms to reach force equilibrium. The mesh is morphed, which means that no new nodes or elements are created, but the displacements of the original nodes are constantly updated according to the electro-structural force equilibrium. This procedure is highly non-linear and huge displacements are allowed for arbitrary uneven mesh.

Fig. 2 shows a MEMS combdrive modeled using the new transducer element. The deforming comb is meshed by regular mechanical FE. The air region is meshed by the transducers. Contact and electrical features can be captured by adding regular contact and electric elements to the model. The mesh is refined near the edges of comb fingers in order to accurately calculate fringing fields. After applying electrical potential over the electrodes, electrostatic force develops and deforms the structure. Details of the original and deformed FE mesh are shown in Fig. 2. The potential distribution over the deformed structure is depicted in Fig. 3. The theoretical and computed values of the driving electrostatic force and deformations are within 1% of margin.

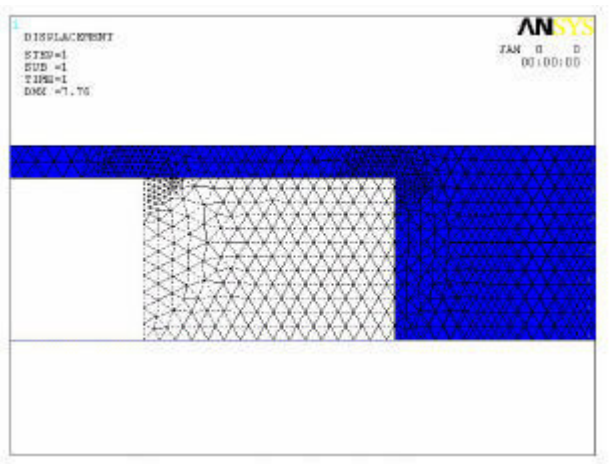


Fig. 2. Original and deformed mesh

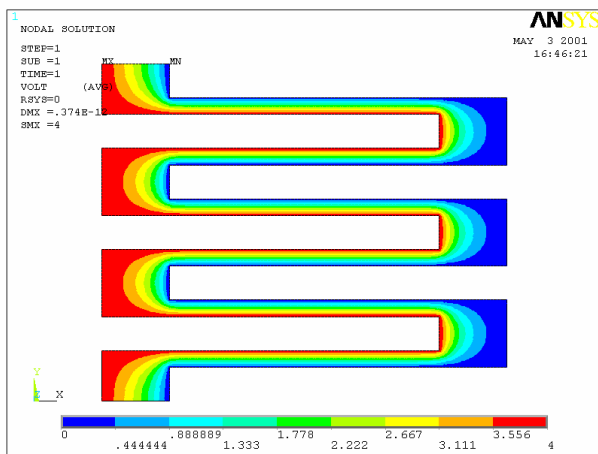


Fig. 3. Potential on deformed combdrive

For a second example, the new transducer element is used to efficiently solve the pull-in/release hysteric beam-bending problem with contact. This problem is difficult numerically because of the bifurcation of static equilibrium, which may lead to stability issues. The tip vertical displacement (in μm) vs. potential drop is depicted in Fig. 4. Lacking analytical

solution, the new transducer is verified against methods using sequentially coupled procedure. The computed results show good agreement whereas the solution with the new transducers converges more robustly and quickly.

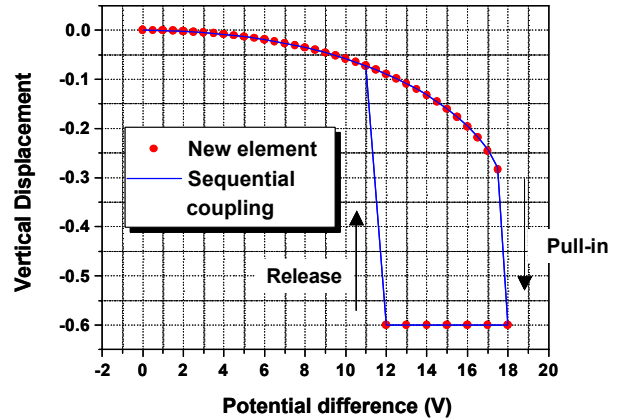


Fig. 4. Hysteresis loop (pull-in/release)

In a third example, the transducer is applied for a transient analysis, such as simulation of the parallel plate drive with a current impulse load. The results agree very well with and Runge – Kutta time integration (see Fig. 5). Note, that the transducer works robustly with charge, voltage, force or displacement load.

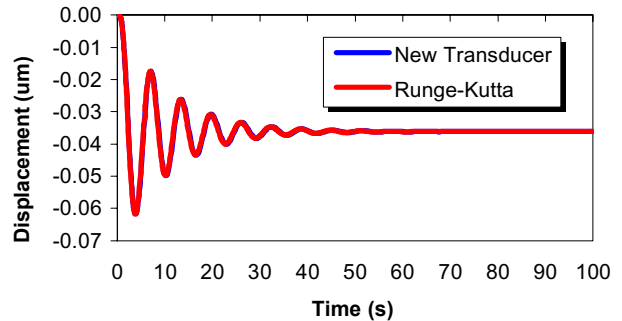


Fig. 5. Transient response of the parallel-plate electrode

CONCLUSIONS

The paper introduced a strongly coupled distributed electromechanical transducer that is compatible with regular solid and lumped FE. Its application range is as general as the sequentially coupled procedure, but converges more robustly with about an order of magnitude smaller number of iteration. The new transducers apply internal morphing: a new mesh is automatically created in the air domain, according to mechanical deformations of the supporting electrodes. The morphing allows the mesh density to be different across the domain permitting accurate modeling of fringing effects.

Magneto-mechanical strong coupling model and experiment for a giant magnetostrictive actuator

Yan Rongge, Wang Bowen, Cao Shuying, Weng Ling, Liu Fuigui and Yan Weili
Hebei University of Technology, Tianjin 300130, China
yanrg@eyou.com

Abstract—Magneto-mechanical strong coupling model for a giant magnetostrictive actuator was founded, based on the energy functional theory. The input current dependence of output displacement for the actuator was calculated according to the model by means of the finite element method. A comparison between the calculating result and experimental one for the actuator was carried out and it was found that they were in a good agreement. This indicates that the model can express the relation between the input current and the output displacement for the actuator.

INTRODUCTION

The rare earth-iron compounds are known to exhibit a large magnetostriction and there has been interest in the development of magneto-mechanical actuators and sensors. In order to design an actuator, it is necessary to know the relation between the input current and output displacement [1]. Dapino et al. [2] described a computed model of magnetostriction according to technical magnetization theory and analyzed the relation between the magnetostriction and the magnetization. Calkins et al [3] using the above model analyzed magnetostriction characteristic of the materials under AC magnetic field excitation. In this paper, the strong coupling model has been founded and the output displacement for the actuator has been calculated by means of the finite element method.

MAGNETO-MECHANICAL STRONG COUPLING MODEL AND FINITE ELEMENT METHOD COMPUTATION

Fig. 1 shows the schematic diagram for our manufacturing actuator. Axis-symmetric geometry is well adapted and an axis-symmetric reference (r,θ,z) can be used. The computed domains of magnetic field and mechanical one are shown in Fig.2 and Fig.3, respectively. u_r and u_z are radial and axial displacement components, respectively.

The total energy of the actuator is equal to the sum of magnetic energy, elastic energy, work of external forces, potential energy of current, potential energy of magnetic boundary, magnetoelastic energy and

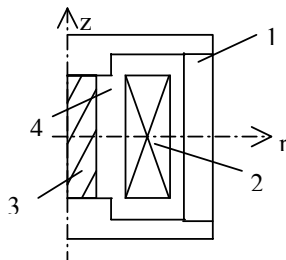


Fig.1 schematic diagram of magnetostrictive actuator
1 magnetic yoke, 2 coil, 3 magnetostrictive rod 4 air

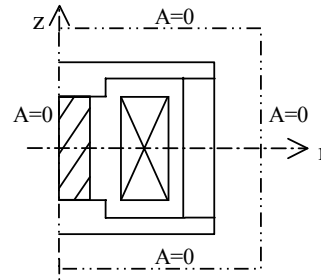


Fig.2 The computed domain of the magnetic domain Ω_1 (dash dot line strands for boundary)

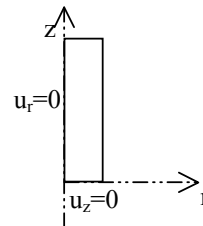


Fig.3 The computed domain of the mechanical domain Ω_2

magneto-crystalline anisotropy energy. If the magnetostrictive material is considered isotropic, the anisotropy energy is negligible. Introducing the magnetic vector potential A via $\mathbf{B} = \nabla \times \mathbf{A}$ and supposing $\nabla \cdot \mathbf{A} = 0$, the energy functional can be expressed as:

$$I = \int_{\Omega_2} \left(\int_0^{\epsilon} \boldsymbol{\sigma} \cdot d\boldsymbol{\epsilon} \right) d\Omega - \int_{\Gamma_2} \mathbf{f}^T \cdot \mathbf{u} d\Gamma - \int_{\Omega_2} \mathbf{f}^v \cdot \mathbf{u} dV + \int_{\Omega_1} \left(\int_0^B \mathbf{H} \cdot d\mathbf{B} \right) d\Omega - \int_{\Omega_1} \left(\int_0^A \mathbf{J} \cdot d\mathbf{A} \right) d\Omega + \int_{\Omega_2} \mathbf{S} \cdot \mathbf{T} d\Omega$$

(1)

where $\boldsymbol{\sigma}$ and $\boldsymbol{\epsilon}$ are stress tensor and strain tensor, respectively.

$\mathbf{f}^T, \mathbf{f}^v$ are the external surface force density and the external volume force density separately. \mathbf{u} denotes displacement vector. Γ_2 is the boundary of mechanical domain Ω_2 . \mathbf{B} and \mathbf{H} denote the magnetic flux density and the magnetic field intensity, respectively. \mathbf{J}, \mathbf{A} being the current density and the magnetic vector potential, respectively. \mathbf{S}, \mathbf{T} are the strain and stress of magnetostrictive rod induced by application magnetic field, respectively.

Substituting the discrete magnetic vector potential $A(r,z)$ and displacement components $\mathbf{u}(r,z)$ to equation (1), the variation problem of I is converted to a multivariate function extremum problem. Magnetic and mechanical unknown quantities are now solved simultaneously. The non-linearity is taken into account by an iterative method and the Newton-Raphson process.

CALCULATING AND EXPERIMENTAL RESULTS

The above-mentioned procedure has been realized by a computer program. According to the experimental curve of the flux density and the magnetic field intensity for the giant magnetostrictive materials, the Young modulus and the Poisson's ratio given in reference [4], the input current dependence of output displacement for the actuator was calculated and the calculating result is shown in Fig.4. The input current dependence of output displacement for the actuator was measured and the result is also shown in Fig.4. It is found that the experimental result is in a good agreement with calculating one. This indicates that the model can express the relation between the input current and the output

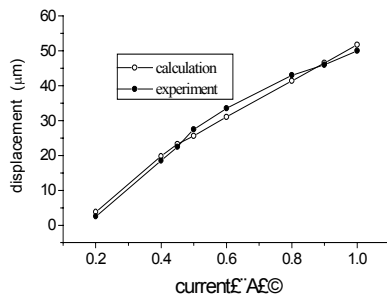


Fig. 4 Validation of the model: comparison between experimental and computed displacement for the actuator

displacement for the actuator and it can be used to design an actuator.

ACKNOWLEDGMENT

This work is supported by the Natural Science Foundation of Hebei Province.

REFERENCES

- [1] Christophe Body, Gilbert Reyne and Gérard Meunier "Nonlinear finite element modeling of magneto-mechanical phenomenon in giant magnetostrictive thin films," *IEEE Transactions on Magnetics*, vol.33, pp.1620-1623, 1997.
- [2] Marcelo J. Dapino, Ralph C. Smith and Alison B. Flatau, "Structural magnetic strain model for magnetostrictive transducers," *IEEE Transactions on Magnetics*, vol.36, pp.545-556, 2000.
- [3] F.T. Calkins, R.C. Smith and A.B. Flatau, "Energy-based hysteresis model for magnetostrictive transducers," *IEEE Transactions on Magnetics*, vol.36, pp.429-439, 2000.
- [4] A.E. Clark, *Magnetostrictive rare earth-Fe₂ compounds*, in *Ferromagnetic material*, volume 1, edited by E.P. Wohlfarth, North-Holland Publishing Company, 1980, 531.

Stability of augmented staggered method for electromagnetic and structural coupled problem

Yoshikazu Tanaka, Syuji Furuki, Eiji Shintaku, Yukio Fujimoto

System Safety Lab., Graduate School of Engineering, Hiroshima University,
1-4-1, Kagamiyama, Higashihiroshima, Hiroshima 739-8527, Japan
E-mail : yoshi@naoe.hiroshima-u.ac.jp

Abstract— Numerical instability occurs in an analysis of an electromagnetic and structural coupled problem or a magnetically damped vibration by solving the matrix equations of structure and eddy current alternatively. In this paper, the augmented staggered method is presented. Using the characteristic equation obtained from the recurrence relation of its time integration scheme, it is confirmed that this method for first mode is unconditionally stable even if the magnetic field and the time increment are large.

INTRODUCTION

In analysis of the electromagnetic and structural coupled problem or the magnetically damped vibration, there are some methods: one is the simultaneous method in which the simultaneous linear equations, which combined the equation of an eddy current and a structure, are solved, and the others are staggered methods in which these equations are solved alternatively. Although the latter methods are attractive in computing cost rather than the former method, the results of the latter methods diverge as a result of numerical instability under some analysis conditions of magnetic fields and time increments. Therefore, it is important to stabilize the staggered methods.

As for the research of the numerical stability, T. Niho et al have examined the stability of the staggered method evaluating the electromotive force with velocity of previous time step using finite element in time [1]. T. Horie et al have examined the stability of some staggered methods using the characteristic equation obtained from the recurrence relation of time integration scheme [2]. But, the stabilized staggered methods for this coupled problem have not been proposed yet.

In the fluid-structure interaction analysis, K. C. Park et al have shown that the staggered methods constructed by the reformulated governing equations are unconditionally stable [3]. Thus, in this paper, the staggered method applied the idea of K. C. Park et al is proposed and its numerical stability is also discussed.

ANALYSIS METHOD OF THE COUPLED PROBLEM

Modal Equations for the Coupled Problem

In the analysis of the electromagnetic and structural coupled problem, combining the finite element equations of motion and eddy current is needed. The equation of motion in the modal coordinate $\{\xi\}$ is expressed using the normal component $\{\mathbf{T}\}$ of the current vector potential as

$$\{\ddot{\xi}\} + [\Omega] \{\xi\} = [\Phi] [\mathbf{C}] \{\mathbf{T}\} + [\Phi] \{\mathbf{f}\} \quad (1)$$

where $[\mathbf{C}] \{\mathbf{T}\}$ is the electromagnetic force. Similarly, the equation of eddy current in the modal coordinate $\{\zeta\}$ is also expressed using the displacement $\{\mathbf{x}\}$ as

$$\{\dot{\zeta}\} + [\Gamma] \{\zeta\} = [\Phi] [\mathbf{C}] \{\dot{\mathbf{x}}\} + [\Phi] \{\dot{\mathbf{b}}\} \quad (2)$$

where $[\mathbf{C}] \{\dot{\mathbf{x}}\}$ is the electromotive force. Matrix $[\Omega]$ in (1) is the stiffness matrix diagonalized by the modal matrix $[\Phi]$, and $[\Gamma]$ in (2) is the resistance matrix diagonalized by the modal matrix of the eddy current $[\Phi]$.

Conventional Staggered Methods

In the conventional staggered methods, Newmark's β method is applied to (1), and Crank-Nicolson method is applied to (2). To construct the staggered methods, the electromotive force in (2) is estimated using the velocity of previous time step or the approximated velocity using forward difference. Iterations for each time step may be added [2].

Augmented Staggered Method

Based on the idea of K. C. Park et al [3], the equations of the augmented staggered method are obtained. Solving (2) about ζ , and substitution of it into (1) yields

$$\begin{aligned} \{\ddot{\xi}\} + [\Omega] \{\xi\} - [\Phi] [\mathbf{C}] [\Phi] [\Gamma]^{-1} [\Phi] [\mathbf{C}] [\Phi] \{\dot{\xi}\} \\ = -[\Phi] [\mathbf{C}] [\Phi] [\Gamma]^{-1} \{\dot{\zeta}\} \\ + [\Phi] [\mathbf{C}] [\Phi] [\Gamma]^{-1} [\Phi] \{\dot{\mathbf{b}}\} + [\Phi] \{\mathbf{f}\}. \end{aligned} \quad (3)$$

In this paper, the staggered method combining (3) and (2) is referred as the augmented staggered method.

ANALYSIS OF COUPLED PROBLEM

Analysis Model

Fig. 1 shows the analysis model which is a copper plate with bending motion in a steady magnetic field B [4]. By changing B and time increment Δt , the numerical stability is discussed. To obtain the deflection at the free end of the plate, the first mode in vibration modes and all eddy current modes are used for the analyses.

Analysis Results

Fig. 2 shows the deflection by the augmented staggered method. The result of the staggered method using the previous time step velocity for electromotive force evaluation, which is referred as the simple method below, and that of the simultaneous method are also shown for comparison. According to

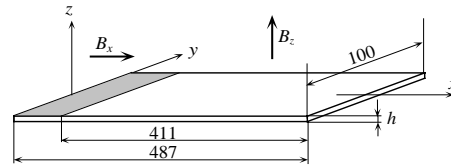


Fig. 1. Schematic diagram of a bending plate in a steady magnetic field B

this figure, though the result of the simple method shows a numerical instability, that of the augmented method is stable.

Fig. 3 is the results of the augmented staggered method with large time increments. The critical time increment for stable analysis of the staggered method with one iteration, which is the stables of all staggered methods have already been examined, is 7.480 [msec] for $B = 2.0$ [T]. In the augmented method, the numerical instability does not appear if the time increments larger than 7.480 [msec] are used. Thus, this method is stabler than the staggered method with one iteration.

STABILITY OF AUGMENTED STAGGERED METHOD

Stability Analysis Method

According to the previous section, the results of the augmented staggered method are stable. Then, the stability of this method is discussed using the recurrence relation of time integration scheme. For each vibration mode and eddy current mode, the recurrence relation is expressed as

$$\begin{Bmatrix} \ddot{x}_{+\Delta t} \\ \dot{x}_{+\Delta t} \\ x_{+\Delta t} \\ T_{+\Delta t} \end{Bmatrix} = [\mathbf{A}] \begin{Bmatrix} \ddot{x} \\ \dot{x} \\ x \\ T \end{Bmatrix} + \mathbf{L}_1 f_{+\Delta t} + \mathbf{L}_2 \dot{B}_{+\Delta t}. \quad (4)$$

The stability of time integration scheme is determined by investigating the eigenvalue λ of the integration operator $[\mathbf{A}]$. For $|\lambda| > 1$, results diverge by means of the numerical instability, while stable results are obtained for $|\lambda| \leq 1$ [2].

Characteristics Equation

For a vibration mode and an eddy current mode, (1) and (2) reduce to

$$\ddot{x} + \frac{k}{m}x = \frac{C}{m}T \quad (5)$$

and

$$\dot{T} + \frac{R}{U}T = \frac{C}{U}\dot{x} - \frac{1}{U}\dot{b} \quad (6)$$

with neglecting the external force. Solving (6) about T , and substitution of it into (5) yields

$$\ddot{x} + \frac{k}{m}x - \frac{C}{mR}\dot{x} = -\frac{C}{m}\frac{U}{R}\dot{T} - \frac{C}{mR}\dot{b}. \quad (7)$$

Applying Crank-Nicolson method or backward difference to (6) with substituting the velocity of previous time step into \dot{x} and applying Newmark's β method to (7), the recurrence relation

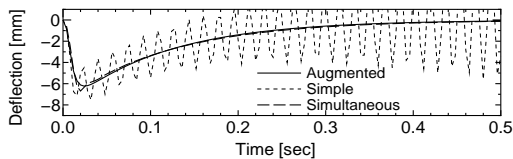


Fig. 2. Deflection at the free end of the plate under the condition of $B = 2.0$ [T] and $\Delta t = 4$ [msec]

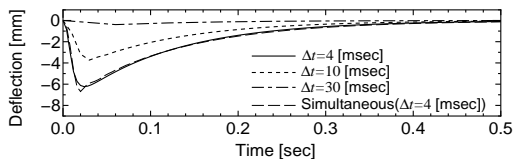


Fig. 3. Deflection by the augmented staggered method under the conditions of $B = 2.0$ [T] and different time increments

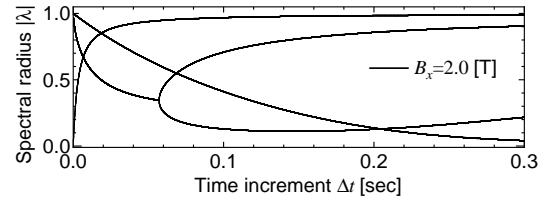


Fig. 4. Change of spectral radius $|\lambda|$ with time increment Δt

of the augmented staggered method such as (4) is obtained. From the recurrence relation, the characteristic equation is obtained as

$$\lambda^4 + c_3\lambda^3 + c_2\lambda^2 + c_1\lambda + c_0 = 0 \quad (8)$$

where c_3 , c_2 , c_1 and c_0 are the function of $-\frac{e^{-s}}{s}$, Δt and θ . $\theta = 1/2$ for Crank-Nicolson method and $\theta = 1$ for backward difference. Since the parameters $-\frac{e^{-s}}{s}$ and $-\frac{e^{-s}}{s}$ can be expressed as the function of young's modulus E , mass density ρ , electric conductivity κ , plate thickness h and steady magnetic field B , the solution λ of (8) can be treated as the function E , ρ , κ , h , B and Δt [5].

Discussion of Stability

Fig. 4 shows the relationship between Δt and $|\lambda|$ of the first mode for the coupled problem shown in Fig. 1 under the condition of $\theta = 1/2$ and $B = 2.0$ [T]. Since $|\lambda|$ is smaller than 1 for $\Delta t = 300$ [msec], the numerical instability does not occur as shown in Fig. 3. When $\Delta t \rightarrow \infty$ or $B \rightarrow \infty$ in (8), $|\lambda| \leq 1$ is obtained whenever $\theta = 1$ and $\theta = 1/2$. Thus, it is confirmed that the augmented staggered method for the first mode is unconditionally stable even if the time increment and the magnetic field are large.

CONCLUSION

In this paper, the augmented staggered method is presented for the electromagnetic and structural coupled problem or the magnetically damped vibration. Using the analysis results and the characteristic equation obtained from the recurrence relation of its time integration scheme, it is confirmed that this method about first mode is unconditionally stable even if the magnetic field and the time increment are large.

REFERENCES

- [1] T. Niho, T. Horie and Y. Tanaka, "Numerical instability of magnetic damping problem of elastic plate", *IEEE Transactions on Magnetics*, Vol. 36, No. 4, pp. 1373-1376, July 2000.
- [2] Tomoyoshi Horie, Yoshikazu Tanaka, Tomoya Niho, "Stability analysis of staggered methods for electromagnetic and structural coupled problem", *Computational Mechanics(New Frontiers for the New Millennium)*, pp. 1335-1340, November 2001.
- [3] K. C. Park, C. A. Felippa, eds., *Partitioned analysis of coupled systems*. Computational methods for transient analysis, Amsterdam: North-Holland, 1983.
- [4] L. R. Turner and T. Q. Hua, "Results for the cantilever beam moving in crossed magnetic fields", *COMPEL*, Vol. 9, No. 3, pp.205-216, September 1990.
- [5] T. Horie, T. Niho and T. Kawano, eds., *Coupling intensity parameter and its dependence for magnetic damping problem*. JSAEM Studies in Applied Electromagnetics, 4 Electromagnetic Phenomena Applied to Technology, Tokyo: JSAEM, 1995.

About the Implementation of Mechanical Flaking Effects Inside a Layer Structure During a Coupled Finite Element Analysis

Christian Grabner

Institute of Electrical Machines and Drives
Graz University of Technology
Kopernikusgasse 24, A-8010 Graz, Austria
grabner@ema.tu-graz.ac.at

Erich Schmidt

Institute of Electrical Drives and Machines
Vienna University of Technology
Gusshausstraße 25-29, A-1040 Vienna, Austria
erich.schmidt@tuwien.ac.at

Abstract—The mechanical problem of flaking can appear at the interface of a compressed but primary loose adjoining layer structure during a coupled mechanical and electromagnetic field calculation. Two different mechanical states, whereby either of them is generated from the other continuously due to rising electromagnetic forces, are included in the proposed computation due to the application of floating potentials. The evaluation of the intermediate state between the primary compressed structure and the occurring flaking effect between some structural layers requires only the knowledge of a subset of the usually total number of unknown degrees of freedom, which are obtained from both the mechanical and the electromagnetic field results. Therefore, the usage of static condensation enables us to solve each problem with a reduced number of degrees of freedom in an efficient way.

I. INTRODUCTION

The main disadvantage within the solution process of a coupled nonlinear electromagnetic and linear mechanical problem is given due to the fact that the mechanical mesh has in generally not the ability to break apart at specific locations within the performed investigations. This basic necessity may occur especially at the interface between different loose adjoining and compressed layers for some constellations of acting electromagnetic forces.

The proposed numerical computation method for the intermediate state requires only a subset of the degrees of freedom from the complete solution of the coupled field problem. Thus, the application of static condensation has the main advantage to obtain only the necessary subset of unknown degrees of freedom from the governing mechanical and electromagnetic field equations.

II. THE USAGE OF FLOATING POTENTIALS AND STATIC CONDENSATION

In order to take use of floating potentials in the mechanical and the electromagnetic part of the coupled field calculation, the necessary common continuous finite element mesh of our problem must be divided into several sub domains as exemplary shown in Fig.1.

All partitioned subdivisions have the ability to be connected together at the boundaries by the usage of floating potentials. Those potentials can only be applied to several nodes which are laying on different subdivisions.

The coupled electromagnetic and mechanical finite element calculation of the compressed adjoining layer structure is performed with varying electrical loads but with an default mechanical pre-load. The application of floating potentials allows to take into account the mechanical dissociation of parts inside a primarily compressed structure due to continuous rising electromagnetic force magnitudes in an efficient way.

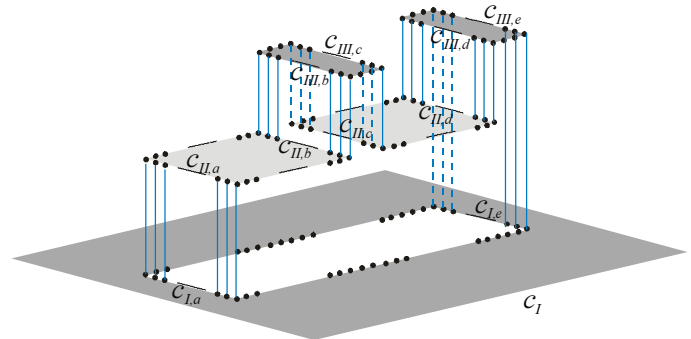


Fig. 1. Connections of the mechanical floating potentials representing the compressed structure.

A. Coupled electromechanical problem

The interconnection between the applied constant mechanical pre-load and the electromagnetic forces of arbitrary magnitude governs the common mechanical behavior of the layer structure in case of an interrelated structure according to [1,2]

$$K^c U^c = F^{a,c} + F^{r,c} \quad (1)$$

With the included mechanical floating potentials according to the Fig.1,

$$FP^m := \begin{cases} u^m|_{c_{I,a}} = u^m|_{c_{II,a}}, u^m|_{c_{II,b}} = u^m|_{c_{III,b}}, u^m|_{c_{III,c}} = u^m|_{c_{III,e}}, \\ u^m|_{c_{II,d}} = u^m|_{c_{III,d}}, u^m|_{c_{I,j}} = u^m|_{c_{III,j}} \end{cases} \quad (2)$$

the partitioning of (1) can be performed by means of

$$\begin{bmatrix} K_{ii}^c & K_{ie}^c \\ K_{ei}^c & K_{ee}^c \end{bmatrix} \begin{bmatrix} U_i^c \\ U_e^c \end{bmatrix} = \begin{bmatrix} F_i^{a,c} \\ F_e^{a,c} \end{bmatrix} + \begin{bmatrix} F_i^{r,c} \\ F_e^{r,c} \end{bmatrix} \quad (3)$$

The applied mechanical pre-load

$$U_i^c := U_i^m, \quad (4)$$

and the predetermined forces of electromagnetic origin [3]

$$F_e^{a,c} := \begin{cases} F_e^c & \text{on } A_{II,a}, A_{II,b}, c_{I,a}, c_{II,f}, c_{II,g}, c_{III,h} \text{ and } c_{III,i} \\ 0 & \text{else} \end{cases} \quad (5)$$

additionally with the non-existing nodal electromagnetic forces

$$F_i^{a,c} = 0, \quad (6)$$

and the vanishing reaction forces at all nodes with free varying nodal displacement values

$$F_e^{r,c} = 0, \quad (7)$$

allow to determine the unknown mechanical nodal reaction force values from

$$\left(K_{ii}^c - K_{ie}^c (K_{ee}^c)^{-1} K_{ei}^c \right) U_i^c + K_{ie}^c (K_{ee}^c)^{-1} F_e^{a,c} = F_i^{r,c}. \quad (8)$$

The mechanical solution of the coupled system (8) is only valid while no flaking occurs within the structure.

Flaking will demand other mechanical floating potentials in order to describe the mechanical behavior sufficiently.

Furthermore, a primary performed mechanical computation of a reference distribution

$$\left(K_{ii}^m - K_{ie}^m (K_{ee}^m)^{-1} K_{ei}^m \right) U_i^m = F_i^{r,m} \quad (9)$$

without any current excitation is necessary.

Afterwards, the computation of the intermediate state between the compressed structure and the case of flaking can be established with (9) and (10) as

$$F_i^{r,c} + F_i^{r,m} > 0. \quad (10)$$

The limiting condition (10) enables us to determine the minimal necessary electromagnetic nodal force magnitudes, which may cause flaking within the compressed structure. From (9) and (10), we obtain with the identity $K^c = K^m$ the condition

$$F_e^{a,c} > 2 U_i^m \left(K_{ei}^m - K_{ee}^m (K_{ii}^m)^{-1} K_{ii}^m \right). \quad (11)$$

The applied electromagnetic nodal force values are used for the necessary comparison (11) with the obtained mechanical quantities in an efficient way.

III. MECHANICAL STRESS DISTRIBUTIONS OBTAINED FROM THE PROPOSED COMPUTATION

The mechanical behavior of the investigated structure in Fig.2 mainly depends on the mechanical pre-load and the impressed electrical current [4,5].

The mechanical pre-load prevents the effect of flaking within vanishing electrical current magnitudes. But there exists the possibility to cause a loosening of the slot wedge due to continuous rising electromagnetic forces inside the conductors of both bars.

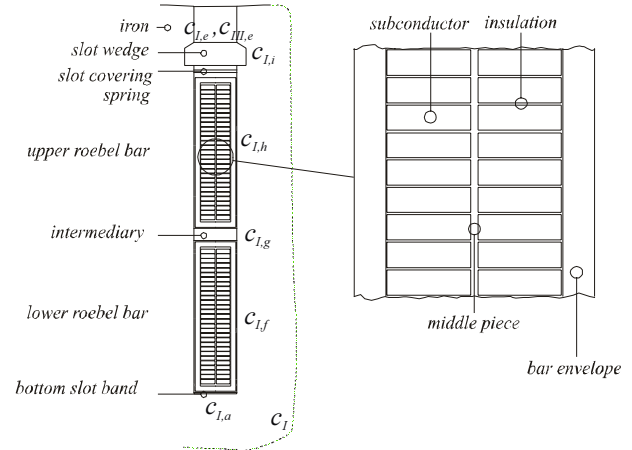


Fig. 2. Investigated mechanical Roebel bar structure inside a single slot.

For an applied slot wedge pre-load and the case of rated electrical current of 1pu, we receive a compressive stress situation inside the slot for the investigated assembly of Roebel bar composites.

Contrarily electrical current magnitudes up to 15pu will lead to flaking with the same assembly. The flaking effect can be identified in Fig.3 due to vanishing mechanical stress values between both adjoining layers at $x=0$ along the slot width.

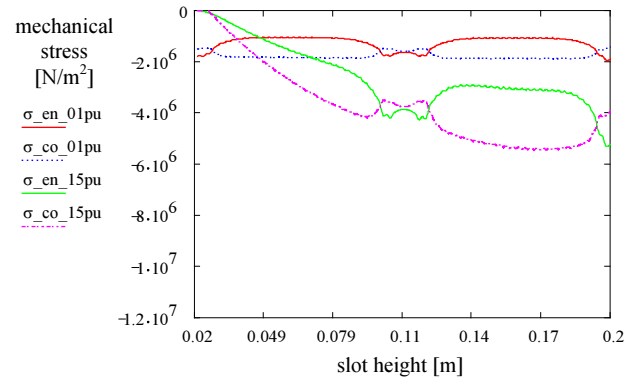


Fig. 3. Mechanical stress courses (σ) for inphase currents of 1pu and 15pu depicted along the bar envelope (en) and copper regions (co) versus slot height starting from the slot wedge up to the slot bottom.

REFERENCES

- [1] K. J. Bathe, *Finite Element Procedures*. New Jersey: Prentice Hall, 1996.
- [2] G. A. Holzapfel, *Nonlinear solid Mechanics*. Chichester: John Wiley & Sons, 2000.
- [3] C. Grabner, E. Schmidt " Numerical Computation of Electromagnetic Force Densities at Iron Boundaries Regarding Magnetic Saturation, " *10th IGTE Symposium on Numerical Field Calculation in Electrical Engineering*, September 2002.
- [4] C. Grabner, H. Köfler, E. Schmidt " Mechanical Stress Situations at Slot Wedge and Slot Bottom of Large Synchronous Machines, " *15th International Conference on Electrical Machines*, August 2002.
- [5] S. G. Lekhnitskii, *Theory of Elasticity of an Anisotropic Body*. Moscow: MIR Publisher, 1981.

Finite Element Computation of the Deformation of Ferromagnetic Material taking into account Magnetic Forces and Magnetostriction

Lieven Vandeveldel¹, Johan J. C. Gyselinck², Marc A. C. De Wulf¹ and Jan A. A. Melkebeek¹

¹ Electrical Energy Laboratory (EELAB)
Department of Electrical Energy, Systems, and Automation (EESA), Ghent University
Sint-Pietersnieuwstraat 41, B-9000 Ghent, Belgium
e-mail: lieven.vandevelde@rug.ac.be

² Montefiore Institute, Department of Electrical Engineering
University of Liège
Sart Tilman B28, B-4000 Liège, Belgium
e-mail: johan.gyselinck@ulg.ac.be

Abstract – This paper presents a method for computing the deformation of ferromagnetic material due to magnetic forces and magnetostriction by using the finite element method. Also the experimental determination of the magnetoelastic properties is discussed.

INTRODUCTION

In previous papers, a general method for modelling magnetic forces and magnetostriction in ferromagnetic material has been presented [1, 2].

The present paper deals with the computation of the deformation due to magnetic forces and magnetostriction by using the finite element method. Furthermore, the experimental determination of the magnetoelastic characteristics used in the numerical model, is discussed.

MAGNETIC FORCES AND MAGNETOSTRICTION

For the sake of clarity, the magnetic and magnetoelastic behaviour of the material is assumed to be reversible.

Mechanical and Magnetic Equivalent Stress Tensors

In deformable magnetized material, the free energy density depends on both the magnetization \mathbf{M} and the deformation, represented by the strain tensor $\boldsymbol{\varepsilon}$. By assuming a particular form of this free energy density, the magnetic and mechanical phenomena may be separated by defining a *mechanical equivalent stress tensor* $\boldsymbol{\tau}^*$ on the one hand and a *magnetic equivalent stress tensor* \mathbf{T}_m^* on the other hand.

The mechanical equivalent stress tensor $\boldsymbol{\tau}^*$ is related to the strain tensor according to Hooke's law :

$$\boldsymbol{\tau}^* = \boldsymbol{\varepsilon} : \mathbf{E} \quad (1)$$

where \mathbf{E} is the elasticity tensor.

The magnetic equivalent stress tensor \mathbf{T}_m^* represents magnetic forces and magnetostriction and is given by:

$$\mathbf{T}_m^* = \mathbf{T}^c + \boldsymbol{\alpha}^c - \frac{1}{2} \mathbf{e} \cdot \mathbf{c}^c \quad (2)$$

It consists of three parts:

- The tensor \mathbf{T}^c is given by an analytical expression of the magnetic quantities:

$$\mathbf{T}^c = \mathbf{B}\mathbf{H} - \frac{\mu_0}{2} H^2 \mathbf{I} \quad (3)$$

and determines the total force acting on a magnetized body.

- The symmetric tensor $\boldsymbol{\alpha}^c$ is given by a constitutive law in terms of the magnetization \mathbf{M} and the strain tensor $\boldsymbol{\varepsilon}$:

$$\boldsymbol{\alpha}^c = \boldsymbol{\alpha}^c(\mathbf{M}, \boldsymbol{\varepsilon}) \quad (4)$$

and represents the magnetoelastic (magnetostrictive) behaviour of the material.

- The tensor $-\frac{1}{2} \mathbf{e} \cdot \mathbf{c}^c$ represents the couple density \mathbf{c}^c :

$$\mathbf{c}^c = \mathbf{e} : \mathbf{T}^c = \mu_0 \mathbf{M} \times \mathbf{H} \quad (5)$$

where \mathbf{e} is the permutation tensor.

On the basis of this tensor we can define the *magnetic equivalent volume force density* \mathbf{f}_m^* as follows:

$$\mathbf{f}_m^* = \nabla \cdot \mathbf{T}_m^* \quad (6)$$

which displays a singularity at material boundaries (material-air interfaces), i.e. a *magnetic equivalent surface traction* \mathbf{t}_m^* given by:

$$\mathbf{t}_m^* = \frac{\mu_0}{2} M_n^2 \mathbf{n} - \mathbf{n} \cdot \left(\boldsymbol{\alpha}^c - \frac{1}{2} \mathbf{e} \cdot \mathbf{c}^c \right) \quad (7)$$

where \mathbf{n} is the outward normal unit vector of the material boundary, M_n is the normal component of the magnetization \mathbf{M} and the magnetic quantities are evaluated just inside the material.

The equations of motion can then be written in the following form:

$$\rho \mathbf{a} = \mathbf{f}_m^* + \mathbf{f}_{ex} + \nabla \cdot \boldsymbol{\tau}^* \quad \text{inside the material} \quad (8)$$

$$\mathbf{n} \cdot \boldsymbol{\tau}^* = \mathbf{t}_m^* + \mathbf{t}_{ex} \quad \text{on material boundaries} \quad (9)$$

where ρ , \mathbf{a} , \mathbf{f}_{ex} and \mathbf{t}_{ex} are the mass density, the acceleration, and possible external volume forces (such as gravity) and external surface tractions respectively.

The deformation can thus be calculated by using the standard equations of elasticity, i.e. the equations of motion (8)-(9) in terms of the mechanical equivalent stress tensor τ^* , which satisfies Hooke's law (1), and where the applied forces consist of the equivalent magnetic forces f_m^* (6) inside the material, the equivalent magnetic surface traction t_m^* (7) on material boundaries, and the external forces f_{ex} and t_{ex} .

Reciprocity

Due to the reciprocity, the deformation will affect the magnetic behaviour. It can be shown that the constitutive law for H , corresponding with the magnetic equivalent stress tensor T_m^* (2), is given by

$$H(M) = \tilde{H}(M) + \frac{1}{\mu_0} \frac{d\alpha^c}{dM} : \varepsilon \quad (10)$$

where $\tilde{\cdot}$ indicates the constitutive law in the undeformed state.

NUMERICAL IMPLEMENTATION

The 2D and 3D finite element method are used for computing the magnetic field and the ensuing deformation of electromagnetic devices. As the mechanical and magnetic phenomena are coupled (e.g. due to the reciprocity), an iterative procedure consisting of consecutive field, force and deformation computations, has been adopted (*weak coupling*).

For the numerical implementation, the tensor α^c is written in the following form:

$$\alpha^c = -\alpha_1 \mu_0 M M - \alpha_2 \mu_0 M^2 I \quad (11)$$

where α_1 and α_2 are dimensionless parameters which may depend on both the magnetization and the deformation (or mechanical stress) and which have to be determined experimentally.

Both static and dynamic computations are carried out. Fig. 1 shows some results of a 2D field, force and deformation computation in an induction motor stator. Other applications, such as 3D FE computations of the magnetic equivalent force distribution and the ensuing vibrations of transformer cores, will be presented in the extended paper.

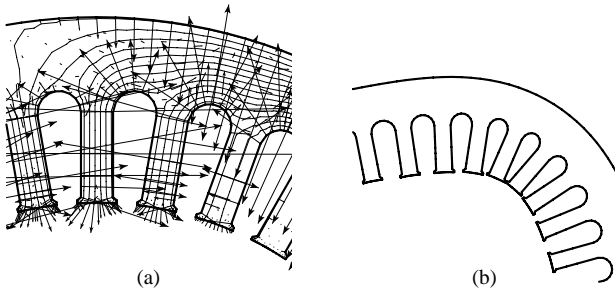


Fig. 1: The stator of an induction motor: (a) magnetic flux and magnetic equivalent force distribution (nodal forces representing f_m^* and t_m^*); (b) deformation (strongly magnified)

For the determination of the constitutive law $\alpha_c(M, \varepsilon)$, i.e. the determination of $\alpha_1(M, \varepsilon)$ and $\alpha_2(M, \varepsilon)$ when the expression (11) is used, accurate strain measurements are required. Therefore, several measurement techniques (e.g. strain gauges, optical techniques) and geometries of the samples and the excitation are investigated. For instance, for isotropic material, a ring core with strain gauges can be used. In that case the magnetic equivalent force distribution is (approximately) reduced to a surface traction t_m^* given by:

$$t_m^* \approx -n \cdot \alpha^c \quad (12)$$

which is illustrated in Fig. 2 for a ring core with outer and inner diameter of 188 mm and 158 mm respectively. As the magnetization and thus the magnetostriction is approximately constant in this core, the tensor α^c can be easily computed on the basis of the measured strain ε according to:

$$\alpha^c = -E : \varepsilon \quad (13)$$

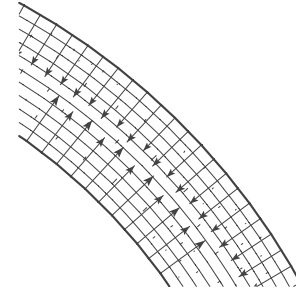


Fig. 2: Magnetic flux and magnetic equivalent force distribution (surface traction t_m^*) in a ring core

ACKNOWLEDGEMENTS

The work has been carried out in the frame of the Interuniversity Attraction Pole IAP P5/34, funded by the Belgian federal government and of the STWW-project "Electrical Steel" supported by the Institute for the Promotion of Innovation by Science and Technology in Flanders (IWT), Brussels, Belgium.

L. Vandeveld is a Postdoctoral Fellow of the Fund for Scientific Research – Flanders (Belgium) (F.W.O.-Vlaanderen).

REFERENCES

- [1] L. Vandeveld and J. Melkebeek, "Modeling of Magnetoelastic Material," *IEEE Transactions on Magnetics*, vol. 38, pp. 993–996, March 2002.
- [2] L. Vandeveld and J. Melkebeek, "Computation of deformation of ferromagnetic material," *IEE Proceedings – Science, Measurement and Technology*, vol. 149, pp. 222–226, September 2002.

Investigation of Inverse Magnetostriction Effects in Electric Machinery

O. A. Mohammed, Fellow *IEEE*, and S. Liu, Member, *IEEE*

Department of Electrical and Computer
Florida International University
10555 W. Flagler Street, Miami, FL 33174
mohammed@fiu.edu

Abstract---The Inverse Magnetostriction Effect is considered in the magnetoelastic-coupled analysis. From the magnetic field side, it reflects the changes of the ferromagnetic permeability at different stress levels. From the mechanical side, an additional force due to the inverse magnetostriction effect should be added to the magnetic forces. Virtual Work principle is adopted for the force calculation. It indicates that the magnetic force density distributes everywhere in the ferromagnetic material due to the inverse magnetostriction effect. A PM surface mounted motor is used for the implementation. The magnetic forces acted on the stator iron and the corresponding deformations of the stator iron with and without magnetostriction effects are compared.

INTRODUCTION

Study of the effects of magnetostriction on electrical machines is one of the topics in magnetoelastic-coupled analysis. Related papers published present different way of dealing with magnetostriction effects. In [1], the author deduced the magnetic force due to the magnetostriction origin and implemented it to coupled field analysis.

In this paper, we are focusing on the effects of the inverse magnetostriction phenomenon in electric machine numerical models. First, the method of measuring the magnetization property at various stress levels is presented. Second, a brief review of the formulation for the magnetoelastic-coupled analysis including magnetostriction effects is given. Third, the implementation on a PM surface-mounted motor is performed and some interesting conclusions are obtained..

INVERSE MAGNETOSTRICTION EFFECT MEASUREMENT

The structure of the sample, which is made of one piece of electrical steel sheet M_19, is shown in Fig. 1. At the two sides of the sample, pulling forces are applied so as to obtain the required stress inside the sample.

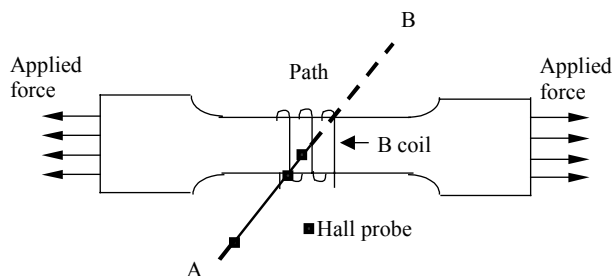


Fig. 1 Sample and measure method

The measurement is performed according to ASTM Standard V3.04 A341. B-coils were used for measuring the flux density inside the sample. As the sample is one sheet of

electrical steel, it is impossible to put any sensor inside it for field strength measuring. Instead, hall probes are put next to it at different distances along the line perpendicular to the sample to measure the field strength outside the sample. Extrapolation is used to determine the field strength at any point inside the sample.

FORMULATION REVIEW

Virtual work method is used for the force calculation of the magneto-mechanical coupled problems. The element contributions to the force are as follows:

$$F^e = - \int_{R_e} [(H^T \cdot \frac{\partial B}{\partial U}) \det(G) + (\int_0^B H^T \cdot dB) \frac{\partial(\det(G))}{\partial U}] + (\int_0^B \frac{\partial}{\partial \sigma} (H^T \cdot dB) \frac{\partial \sigma}{\partial U} \det(G)) dudv \quad (1)$$

Where R_e is the element region, G is the local Jacobian derivatives matrix of the element and $\det(G)$ is the determinate of G . u and v are the local coordinate system adopted for force evaluation by using virtual work principle. B is the flux density and H is the field strength.

The first two terms are reluctance forces and the third term is the magnetic force due to magnetostriction origin. It can be expanded as:

$$F_{ms}^e = - \int_{R_e} \left[\left(\int_0^B \frac{\partial}{\partial \sigma} (H^T \cdot dB) \right) \left(\frac{E}{(1+\nu)(1-2\nu)} \right) \det(G) \right] dudv \quad (2)$$

Where E is the Young's modulus; ν is the Poisson's ratio.

In eq. (2), the variation of the permeability with mechanical stress is taken into consideration in this term. Compared with the first two terms of eq. (1), it can be found that the derivatives of the nodal coordinates are not required for the third term force calculation. Therefore, besides the nearest air layer to the ferromagnetic region, its internal elements also give contributions to the total magnetic force. In other words, this force density distributes everywhere in the ferromagnetic region due to the inverse magnetostriction effect.

IMPLEMENTATION AND CONCLUSION

Magnetostrictive effects are taken into account in both magnetic field and mechanical field analysis. It is included in field equations by assuming the ferromagnetic material is

inhomogeneous. That is, it is composed of different magnetic materials with their corresponding magnetization properties, as shown in Fig. 2. First using the initial magnetization property, perform nonlinear magneto-mechanical FEM analysis to obtain the stress of each element. According the element stress value, determine which BH curve should be used for the next step for material property iteration. A nonlinear magneto-mechanical FEM analysis is performed again till the stored energy of the iron region stops changing.

For the mechanical field analysis, the third term force, in eq. (1), is calculated based on eq. (2). The calculation of $\partial v/\partial \sigma$ is given in eq. (3) and explained in Fig. 2.

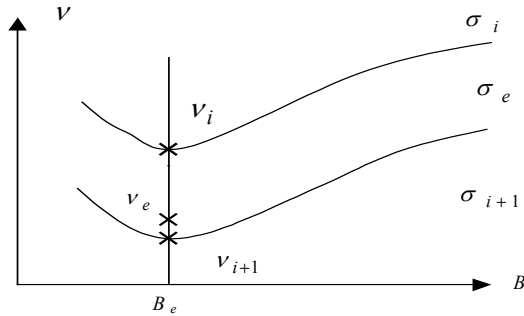


Fig. 2. Derivative of element permeability to stress

$$\partial v_e / \partial \sigma_e = (v_e - v_{i+1}) / (\sigma_e - \sigma_{i+1}) \quad (3)$$

The two curves are the reluctivity versus flux density properties at stress level σ_i and σ_{i+1} . Where, v_e and σ_e are element permeability and the stress is obtained by one step of coupled FEM analysis.

A six-pole surface mounted PM motor is used as an example. Its stator is made of non-oriented ferromagnetic material. Since non-oriented ferromagnetic materials also exhibits anisotropic magnetization properties under rotating magnetic fields [3], an anisotropic reluctivity tensor is included. In order to show the effects of magnetostriction, both the 2D coupled analysis with and without magnetostriction effects are performed. Below are part results.

Fig. 3 shows the deformed stator at the same rotor position and under same excitation conditions. It can be seen that the symmetric deformation becomes unsymmetrical if the magnetostriction effects is considered.

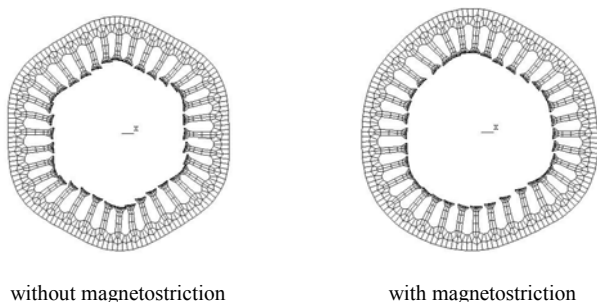


Fig. 3 Stator deformation

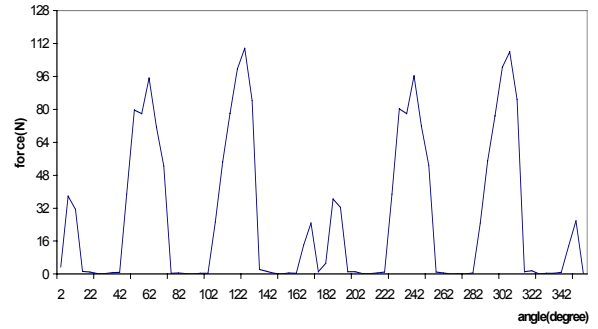


Fig. 4 Force density at teeth shank part with magnetostriction effects

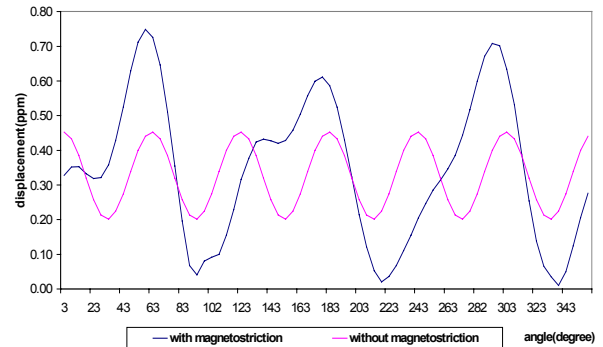


Fig. 5 Comparison of back iron displacement with and without magnetostriction effects

The virtual work principle is used for the force calculation. The reluctance forces at the teeth shank only distribute on the teeth boundary. And usually are so small and can be neglected. Fig. 4 shows that the magnetic force due to magnetostriction origin is significant. In the back iron, only the force density resulted by the magnetostriction effects exists. From fig. 5, it can be seen that magnetostriction effects cause more displacements and are not symmetric compared with those without considering magnetostriction effects.

When taking into account the magnetostriction effects, the magnetic force density distributes everywhere in the ferromagnetic region. Its value depends on the flux density and reluctivity property. The higher the flux density, the higher the force density due to the magnetostriction origin. Anisotropic reluctivity cause asymmetric magnetic force distribution.

REFERENCES

- [1] O. A. Mohammed, "Coupled magnetoelastic finite element formulation including anisotropic reluctivity tensor and magnetostriction effects for machinery applications," *IEEE Transactions on Magnetics*, vol. 37, No. 5, pp. 3388-3392, September 2001.
- [2] J. L. Coulomb, "A Methodology for the determination of global electromechanical quantities from finite element analysis and its application to the evaluation of magnetic forces, torque and stiffness," *IEEE Transactions on Magnetics*, vol. 19, No.6, pp.2514-2519, November 1983.
- [3] M. Enokizono, T. Todaka, and S. Kanao, "Two-dimensional magnetic properties of silicon steel sheet subjected to a rotating field," *IEEE Transactions on Magnetics*, vol. 29, no. 6, pp.3550-3552, November 1993.

Modelling of Magneto-Mechanical Phenomena by Using Shell Elements

M. Hadjali, M. Besbes and F. Bouillault

LGEP, Supelec Plateau de Moulon, 91192 Gif-sur-Yvette, France

mondher.besbes@lgep.supelec.fr

Abstract — This paper deals with the modelling of the magneto-mechanical phenomena for a ferromagnetic plate having weak thickness. In order to avoid problems in the mesh operation, we use shell elements. With such elements, one computes magnetic field, magnetic forces and deformations. In this work, we explain the different formulations and the main results obtained of the studied example.

INTRODUCTION

The finite element modelling of weak thickness domain needs a very fine mesh. This implies an important computing time on one hand, and on another hand leads to an ill-conditioned algebraic system. This problem is met in many applications using thin film materials (particularly in case of micro-systems), or in eddy current calculation for conducting plates of weak thickness (for non-destructive testing), or more in electromagnetic systems with a weak air-gap. The use of shell elements allows to set free of the fine mesh of thin weakness domains. It consists to use degenerated elements of quadrangle (in 2D case) and prisms or hexahedron (in 3D case) to lead in each configuration to line elements and respectively triangular or quadrangular elements [1, 2]. The main of this work is to perform the different formulations to compute magnetic fields and forces in the static case in order to determine the deformations of a ferromagnetic plate. The aimed application is the study of magneto-elastic behaviour of a magnetostrictive plate used in a micro-actuator.

FIELD CALCULATION AND FINITE ELEMENT FORMULATION

According to the physical nature of the thin domain and according to magnitude to be determined, we can use different kinds of shell elements. In this work, we are interested to use shell elements with potential jump. In this case, the potential is not constant along the thickness of the thin domain and the unknown variables are doubled in each node of a shell element. We have chosen a formulation based on a magnetic scalar potential Φ because it yields to reduce number of freedom degree compared to a formulation based on a magnetic vector potential. For this study, we consider, in the 3D case, a surface element such as a triangular element and, in the 2D case, a line element with a potential jump (as shown in Fig. 1). The nodes are doubled but geometrically overlapped. The shape functions are analytically integrated along the weakness.

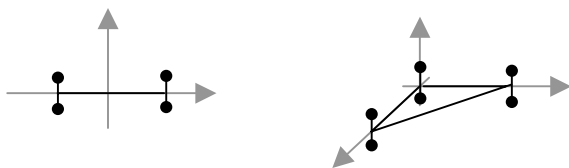


Fig. 1. 2D and 3D shell elements.

The variational formulation, in terms of magnetic scalar potential and associated to the problem as shown in Fig. 2, is expressed, for the side of Ω_1 , as follows [2]:

$$\int_{\Omega_1} \mu_1 \text{grad} w_i \text{grad} \Phi_1 d\Omega_1 + \int_{\Gamma} \frac{\delta \mu}{3} \text{grad}_s \lambda_i \text{grad}_s \Phi_1 d\Gamma + \int_{\Gamma} \frac{\delta \mu}{6} \text{grad}_s \lambda_i \text{grad}_s \Phi_2 d\Gamma + \int_{\Gamma} \frac{\mu}{\delta} \lambda_i \Phi_1 d\Gamma - \int_{\Gamma} \frac{\mu}{\delta} \lambda_i \Phi_2 d\Gamma = 0 \quad (1)$$

where w are shape functions of tetrahedral elements, λ are shape functions of triangular elements, Ω is a thin ferromagnetic domain, Ω_1 and Ω_2 represent the neighbour regions.

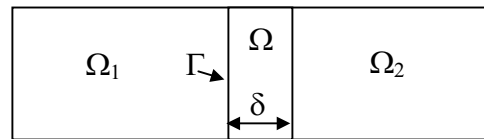


Fig. 2. Different domains of study.

The force calculation is based on the use of virtual work principle. This method presents a great advantage to be directly applicable in a finite element modelling. The forces are computed in both volume elements and shell ones. We use so an approach based on the local application of the virtual work principle which can be described by the variation of co-energy where the magnetic field circulation is held constant along an edge. This is identical to the variation of the magnetic scalar potential between two nodes of a given edge. In the linear case, the elementary force (relative to the contribution of one element) at node k of element e , is described by [3]:

$$F_k^e = \frac{1}{2} \Phi_{eT} (\partial_k^T S_e) \Phi_e \quad (2)$$

where S is the magnetic stiffness matrix composed by the different terms of (1). Let define :

$$S_1 = \alpha \delta \mu \int_{\Gamma} \text{grad}_s^T \lambda \text{grad}_s \lambda d\Gamma \quad \text{with } \alpha = \frac{1}{3} \text{ or } \frac{1}{6},$$

$$S_2 = \frac{\beta \mu}{\delta} \int_{\Gamma} \lambda^T \lambda d\Gamma \quad \text{with } \beta = \pm 1,$$

their derivatives versus displacement u , when using first order elements, are equal to:

$$\partial_u S_1 = \alpha \delta \mu \int_{\Gamma} \text{grad}_s^T \lambda \partial_u (j^{-T} \cdot j^{-1}) \text{grad}_s \lambda d\Gamma + |j|^{-1} \partial_u (|j|) S_1,$$

$$\text{and } \partial_u S_2 = |j|^{-1} \partial_u (|j|) S_2,$$

with $\hat{\Gamma}$ the reference element, j the jacobian matrix of the shell element and $|j|$ its determinant.

The mechanical problem is solved by using shell or plate elements which have as degree of freedom, associated to each node, displacements at each direction. In this case, the strain tensor is decomposed into shearing tensor and twisting one.

STUDIED EXAMPLE

The proposed example is composed of a magnetic circuit with a permanent magnet, an iron yoke and a ferromagnetic plate which has a constant permeability μ and a weak thickness. This latter is imbedded on edges and will be deformed by the action of magnetic forces.

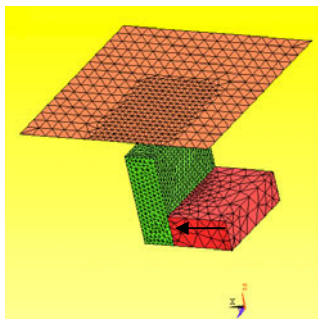


Fig. 3. Forth geometry of the example and its mesh.

The plot of iso-potentials is presented in figure 4 for a plate with thickness of 0.1mm. One can observe that iso-potentials on the permanent magnet are perpendicular to the magnetisation vector. The ferromagnetic plate canalises the majority of the lines of magnetic field. Consequently, the forces are practically located on one side of the plate as shown in Fig. 5. The plate mesh has been refined lightly on the part of the plate towards the magnetic circuit (yoke, permanent magnet) in order to reduce errors when computing magnetic forces.

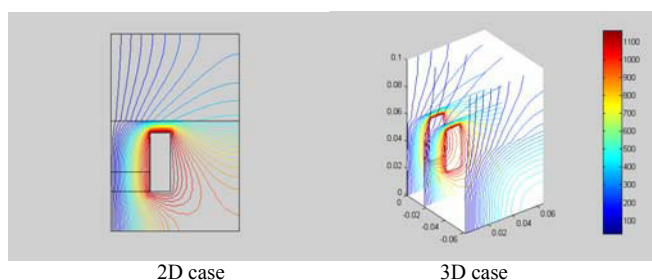


Fig. 4. Isovalue of magnetic scalar potential.

We notice that magnetic forces are important neighbour the air-gap between the plate and the iron yoke. When we compare the forces on the iron and the plate, we remark that these forces are comparable. The plate is completely imbedded on its sides, so the studied domain is limited to the forth of the plate. According to the magnetic force

distribution, the mechanical boundary conditions are as follows:

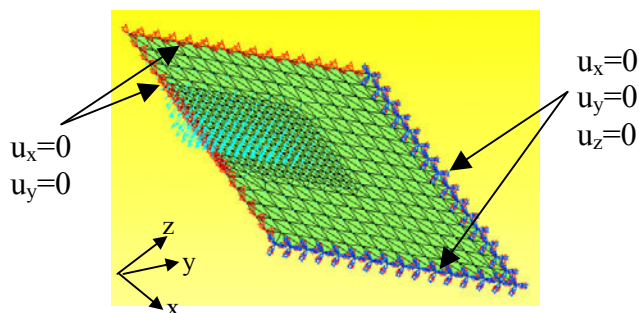


Fig. 5. Magnetic force distribution on the plate and the BC for mechanical problem.

The computed nodal forces are directly integrated in the mechanical computation by using shell or plate elements. The resulted strain is presented in Fig. 6. The calculation is realised with the forth of the plate but the result is rebuilt in the all domain by symmetry operation.

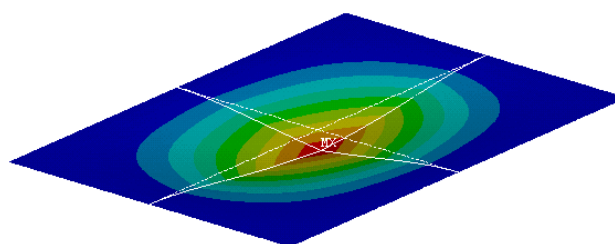


Fig. 6. Strain of the ferromagnetic plate.

CONCLUSION

In this paper, we have presented the interest of the shell elements in modelling of magnetic and deformable thin domain. In fact, these elements allows to set free of a hard step to perform the mesh. They make easy the parametric study and optimisation when the thickness is considered as a tested parameter, without remesh the domain. We have worked particularly in the magnetostatic case with a formulation in term of magnetic scalar potential. Our aim is to develop the theoretical aspect for the formulation of the problem associated to the determination of the magnetic field in thin domain, the produced forces and the induced deformations. The presented example illustrates the methodology of studying the coupled magneto-mechanical phenomena of structures with weak thickness.

REFERENCES

- [1] D. Rodger, P. J. Leonard, H. C. Lai, 'Surface element for modelling 3D fields around thin iron sheets', IEEE Trans Magn, Vol. 29, N°2, pp. 1483-1486, march 1993
- [2] Ch. Guérin, G. Tanneau, G. Meunier, X. Brunotte and J. B. Albertini, 'Three dimensional magnetostatic finite elements for gaps and iron shells using magnetic scalar potentials', IEEE Trans on Mag, Vol, 30, N° 5, sept 1994
- [3] Z. Ren and Z. Cendes, 'Shell elements for the computation of magnetic forces', IEEE Trans on Mag, Vol, 37, N° 5, sept 2001.

Electromagnetic force density in a ferromagnetic material

François Henrotte, Hans Vande Sande, Geoffrey Delière, Kay Hameyer

Abstract—A very simple but realistic model for ferromagnetic materials is proposed under the form of a functional to minimise. This functional is then used to derive the corresponding expression of the Maxwell stress tensor.

I. INTRODUCTION

IN a recent paper, a systematic derivation of the electromagnetic (EM) force density from the expression of the EM energy density was presented by the authors. It was applied to air (no magnetisation) and permanent magnet materials (magnetisation is independent of the magnetic field). In this paper, it is intended to make one step further and to apply the same procedure to saturable ferromagnetic materials (reversible case).

As the forces are directly derived from the knowledge of the EM energy density, the problem is simply to find a satisfactory expression of the latter. The classical expression is

$$\rho^\Psi(\vec{b}, \varepsilon) = \int_0^{\vec{b}} \vec{h}(\vec{b}, \varepsilon) \cdot d\vec{b}, \quad (1)$$

which has the nice *formal* property that

$$\delta \rho^\Psi|_{\delta \varepsilon=0} = \vec{h} \cdot \delta \vec{b}. \quad (2)$$

The idea is then to collate measurements of $\vec{h}(\vec{b}, \varepsilon)$ and to integrate them. This approach has however the following drawbacks.

Firstly, it does not rely on a real material model. The expression of the EM energy density is on the contrary *induced* from empirical constitutive laws, i.e. which are obtained from measurements. But measurements gives only a partial view on the complexity of the electromechanical behaviour of a real material, because of the limited number of measurements and the unavoidable experimental errors. Moreover, only *global quantities* (magnetic fluxes, displacements) are measured, whereas the constitutives laws are in terms of the corresponding *local quantities* (\vec{b} and ε), and the required transposition from *global* to *local* is not trivial in practice and full of pitfalls and simplifying assumptions.

Secondly, the integral with vector-valued bounds in (1) requires a mathematical definition in order to be useable. A suitable definition is

$$\rho^\Psi(\vec{b}, \varepsilon) = \int_0^{\vec{b}} \vec{h}(\vec{b}_t(u), \varepsilon_t(u)) \cdot \dot{\vec{b}}_t(u) du, \quad (3)$$

The authors are with the Katholieke Universiteit Leuven, Dept ESAT / ELECTA, Leuven, Belgium (email: francois.henrotte@esat.kuleuven.ac.be)

This text presents research results of the Belgian programme on Interuniversity Poles of Attraction initiated by the Belgian State, Prime Minister's Office, Science Policy Programming.

where $\vec{b}_t(t)$ and $\varepsilon_t(t)$ represent paths starting from a reference state and verifying $\vec{b}_t(t) = \vec{b}$ and $\varepsilon_t(t) = \varepsilon$. The energy density is properly defined if the integral in (3) is independent of the chosen paths, which gives integrability conditions that are not easy to fulfill in practice.

II. FERROMAGNETIC MATERIAL

For these reasons, a completely different approach is proposed in this paper. Instead of basing the material description upon constitutive laws, as is usually done, we shall define a simplified but realistic model for the ferromagnetic materials.

Ferromagnetic materials are substances with permanent atomic magnetic moments that are coupled by long-range exchange forces of quantum-mechanical origin. Therefore, they line up with each other and create an intense magnetic moment density. On the other hand, in order to minimize the overall magnetic energy, a macroscopic ferromagnetic sample tends to break up into several domains, called Weiss domains. The magnetic moment density is homogeneous within each domain but its orientation varies from one domain to the next, so that the total magnetic moment of the sample vanishes if no external field is applied. Because of anisotropy and provided the material is not highly saturated, the magnetic moments of the domains are preferably oriented along one of the easy-axes of magnetisation of the crystal. These are the mechanisms we are going to implement in our material model.

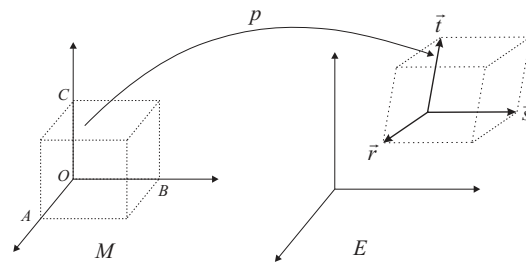


Fig. 1. Euclidean placement of a small piece of ferromagnetic material.

A small piece of ferromagnetic material M is considered at an intermediary scale between the microscopic structure of the ferromagnet (Weiss domains, ...) and the characteristic macroscopic dimensions of the system. The placement map p determines in the euclidean space E a parallelepiped region $p(M)$ spanned by the vectors \vec{r} , \vec{s} and \vec{t} . The volume of $p(M)$ is $V = (\vec{r} \times \vec{s}) \cdot \vec{t}$. Let N be the number of magnetic moments in M and \mathcal{M}_0 their magnitude. These are constant numbers. Let us assume a 2D monocrystal, with two easy-axes of magnetisation, respectively aligned with the α and β

directions. There are then 4 possible states for each atomic moment, i.e. $\pm\alpha$ and $\pm\beta$. Let a, b, c and d be their relative populations, with $a, b, c, d \in [0, 1]$ and $a + b + c + d = 1$. This has the pictorial representations showed at Fig. 2.

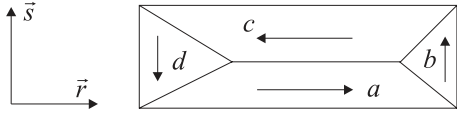


Fig. 2. A simple ferromagnetic material model.

In order to calculate forces, one needs to express the induction \vec{b} in $p(M) \subset E$ explicitly as a function of the fluxes across the facets of M . Since the induction \vec{b} is a differential form of 2d degree, one has in 2D (See [3], [4])

$$\vec{b}(\phi_i, \vec{r}_j) = \phi_{OBC} \frac{\vec{r}}{V} + \phi_{OCA} \frac{\vec{s}}{V}. \quad (4)$$

with ϕ_{OBC} and ϕ_{OCA} the fluxes across the facet OBC et OCA in Fig 1. On the other hand, if the $\rho^{\vec{M}}$ is assumed to be a differential form of 1st degree, (See [4] for a discussion of this assumption), it is represented in E by

$$\rho^{\vec{M}}(\vec{r}_j, a_k) = N\mathcal{M}_0 \left[(a-c) \frac{\vec{s} \times \vec{t}}{V} + (b-d) \frac{\vec{t} \times \vec{r}}{V} \right]. \quad (5)$$

Let us now define the energy density of our ferromagnetic material, subjected to an induction \vec{b} , by

$$\rho^\Psi = \frac{|\vec{b}|^2}{2\mu_0} - \vec{b} \cdot \rho^{\vec{M}} + C \frac{(N\mathcal{M}_0\xi)^2}{2} \quad (6)$$

with \vec{b} given by (4), $\rho^{\vec{M}}$ given by (5) and

$$\xi^2 = (b-a)^2 + (c-b)^2 + (d-c)^2 + (a-d)^2. \quad (7)$$

The first two terms in (6) are classical. The third one is a tentative expression for the internal energy of the sample. It is interpreted as follows. As shown at Fig. 2, the four domains can be considered as forming a magnetic circuit. Each imbalance between two successive moments in that circuit creates a kind of leakage field, which generates magnetostatic energy in the surroundings. This assumption is of course somewhat rudimentary, but we shall see it gives already very important and nicely general results.

III. MATERIAL MODEL

The material model we are seeking for is given by the minimisation of the energy density functional (6). In order to get rid of the constraint $a + b + c + d = 1$, independent internal variables $\zeta, \eta, \theta \in [0, 1]$ are defined, such that $a = \zeta \eta$, $b = (1 - \zeta) \theta$, $c = \zeta (1 - \eta)$ and $d = (1 - \zeta) (1 - \theta)$. Equation (7) becomes

$$\xi^2 = 2 - 4\zeta^2\eta(1 - \eta) - 4(1 - \zeta)^2\theta(1 - \theta) - 6\zeta(1 - \zeta). \quad (8)$$

Using (8), the energy density functional ρ^Ψ can be written in terms of the independent thermodynamic variables ϕ_i, \vec{r}_j and ζ_k . The material model is now defined by the minimisation

$$\zeta_k^*(\phi_i, \vec{r}_j) \equiv \min_{\zeta_k \in [0,1]} \rho^\Psi(\phi_i, \vec{r}_j, \zeta_k) \quad (9)$$

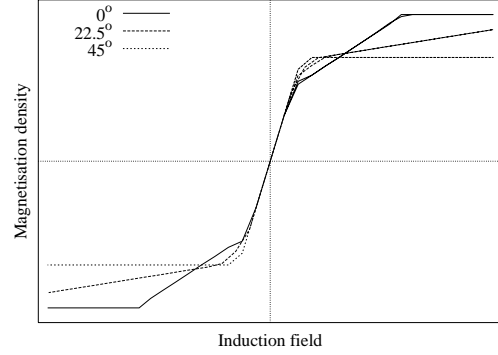


Fig. 3. Magnetisation curves as a function of the orientation of the magnetic field with respect to \vec{r} .

with respect to the internal variables ζ_k .

This simple model of a ferromagnetic material, which involves only one free parameter C , is already able to represent saturation and a certain kind of anisotropy, as shown at Fig. 3. In this case, the value of C is related with the susceptibility of the material, i.e. the slope at zero-field of the magnetisation curve. In general, the value of the free parameters are determined by matching the constitutive laws derived from the material model with measurements.

IV. ELECTROMAGNETIC FORCES

The advantage of having a real material model is that it directly gives an expression for the energy density, from which forces are directly derived by

$$\delta \{ V \rho^\Psi(\phi_i, \vec{r}_j, \zeta_k^*(\phi_i, \vec{r}_j)) \} |_{\delta\phi=0} = V \vec{\nabla} \vec{u} : \sigma \quad (10)$$

where σ is by definition the Maxwell stress tensor and $\vec{\nabla} \vec{u}(\vec{r}_j, \delta \vec{r}_j)$ is the gradient of the displacement field obtained by perturbing the \vec{r}_j vectors (virtual displacement). The total variation of energy is

$$\delta \{ V \rho^\Psi \} = \delta V \rho^\Psi + V \frac{\partial \rho^\Psi}{\partial \phi_i} \delta \phi_i + V \frac{\partial \rho^\Psi}{\partial \vec{r}_j} \delta \vec{r}_j + V \frac{\partial \rho^\Psi}{\partial \zeta_k} \delta \zeta_k. \quad (11)$$

The second term at the r.h.s. plays no role for forces because $\delta\phi = 0$ in (10). The fourth term does not play a role either, because (9) implies that either $\frac{\partial \rho^\Psi}{\partial \zeta_k} = 0$ or $\delta\zeta_k = 0$ at equilibrium. The only thing that remains to do now, is to factorize the two remaining terms into the form of the r.h.s. of (10). This will be done in the full paper.

REFERENCES

- [1] G. A. Maugin, *Continuum mechanics of electromagnetic solids*. North Holland, 1988.
- [2] S. Chikazumi, *Physics of magnetism*. John Wiley & Sons, 1966.
- [3] F. Henrotte and K. Hameyer, *Electromagnetic force densities in a continuous medium*, submitted at SCEE'2002, Eindhoven, The Netherlands, June 2002.
- [4] F. Henrotte and K. Hameyer, *Computation of electromagnetic force densities: Maxwell stress tensor vs virtual work principle*, submitted at ACOMEN'2002, Liège, Belgium, May 2002.

Comparison of 2D and 3D Transient FEM Calculations of a Skewed Induction Machine

Markus Johnen, Christian Kaehler, and Gerhard Henneberger
Department of Electrical Machines (IEM), Aachen University (RWTH),
Schinkelstrasse 4, D-52056 Aachen, Germany
markus.johnen@iem.rwth-aachen.de

Abstract— The Finite-Element Method (FEM) allows for the calculation of the magnetic field distribution and the torque in electrical machines. Transient vector formulations are utilized to compute the torque of a skewed induction machine. In the two-dimensional approach three slices are calculated to take the skew of the rotor into account. Both approaches, the two-dimensional (2D) and the three-dimensional (3D), consider the movement of the rotor geometry of the machine and calculate the currents in the rotor bars. The 2D calculation is preferred because of its time efficiency. The aim of the presented paper is to examine, whether the two-dimensional calculation provides sufficiently accurate results in comparison to the expensive 3D computation.

Index Terms— Transient FEM Computation, Skewed Induction Machine, Induced Currents, Rotor Movement, Comparison 2D - 3D

I. INTRODUCTION

Induction machines are used for all kinds of actuation in industry and are therefore also matter of research. A main problem of all electrical machines is the noise evaluation. To predict the noise radiation of an electrical drive, the magnetic force and the torque of the machine, both exiting the vibrations, have to be calculated exactly.

Due to higher harmonics in the noise evaluation a transient calculation has to be conducted with a high time resolution. To take the skew of the rotor into account, a 3D approach has to be employed. 3D FEM calculations are very expensive concerning calculation time and memory effort. Therefore, a sufficiently exact 2D FEM approach has to be preferred.

Corresponding to the 2D approach it is not possible to take the skew of the machine directly into account. Hence, three slices of the machine are calculated. For the slice positioned in the middle of the machine, a transient computation is applied in which the currents in the rotor bars are determined. With these currents, two static FEM calculations are performed on the two remaining slices. In comparison with the middle slice of the machine, the rotor in the other slices is turned according to the skew of the machine.

For the interpretation of the results, the torque of the three-dimensional and the two-dimensional calculations are compared. To evaluate the torque of the 2D calculations the results of the three slices are superposed.

In order to calculate the machine in 2D and 3D numerical tools for the design process have been developed. In this paper the 2D and the 3D approaches are outlined, the FEM models are described and the results of the calculations are compared.

II. THEORY OF THE TRANSIENT SOLVERS

The applied solvers are parts of an object-oriented solver package [1]. They apply a transient FEM formulation taking the rotational movement into account.

The node-based 2D \vec{A} -approach applies the magnetic vector potential in all regions. The following equation (already in Galerkin formulation) is solved in all regions Γ [2]:

$$\int_{\Gamma} \left(\nabla \cdot \alpha_i \cdot \nu \cdot \nabla \cdot A_z(t) + \alpha_i \cdot \sigma \frac{\partial}{\partial t} A_z(t) \right) d\Gamma = \int_{\Gamma} (\alpha_i \cdot J_{z0}(t)) d\Gamma \quad (1)$$

The material parameters ν and σ represent the non-linear reluctance and the linear conductivity, respectively. α_i defines the shape function of an element (in this solver triangles). $J_{z0}(t)$ describes the z-component of the given coil current density $\vec{J}_0(t)$. Note, that $\vec{J}_0(t) > \vec{0}$ only applies for $\sigma = 0$.

The edge-based 3D \vec{A} -approach applies also the magnetic vector potential \vec{A} in all regions Ω . The following equation (again in Galerkin formulation) is solved [3]:

$$\int_{\Omega} \left(\nabla \times \vec{\alpha}_i \cdot \nu \nabla \times \vec{A}(t) + \alpha_i \cdot \sigma \frac{\partial}{\partial t} \vec{A}(t) \right) d\Omega = \int_{\Omega} (\vec{\alpha}_i \cdot \vec{J}_0(t)) d\Omega \quad (2)$$

$\vec{\alpha}_i$ defines the shape function of a 3D edge element (in this solver tetrahedra).

The time-stepping algorithm interpolates the time-dependent variables linearly:

$$\begin{aligned} \vec{A}(t) &= \tau \cdot \vec{A}_{n+1} + (1 - \tau) \vec{A}_n \quad \text{ditto for } \vec{J}_0; \\ \frac{\partial}{\partial t} \vec{A}(t) &= \frac{1}{\Delta t} (\vec{A}_{n+1} - \vec{A}_n) \quad , \end{aligned} \quad (3)$$

where n represents the number of the transient step, Δt the time in between transient steps and τ the relaxation factor. The relaxation factor used in between transient steps is chosen as $\tau = \frac{2}{3}$ (Galerkin scheme) [4].

The magnetic flux density \vec{B} and the eddy-current density \vec{J} are computed from the magnetic vector potential as follows:

$$\vec{B} = \nabla \times \vec{A}, \quad \vec{J} = -\sigma \frac{A_{n+1} - A_n}{\Delta t} \quad (4)$$

The resulting global matrix of both approaches is symmetric, thus allowing the storage as lower or upper triangular matrix and the use of the Cholesky-CG combination [5] of the ITL package [6]. Saturation effects are computed with an overlaying Newton-Raphson procedure for each transient step.

In the 2D approach, the rotor mesh of the machine is turned and the air-gap is remeshed for each transient step. The benefit of the remeshing strategy lies in a time stepping independent of the mesh of the machine and thus an arbitrary rotation angle.

To represent the rotational movement in the 3D model a lock-step method is utilized. In this method the movement is purely virtual. Boundary conditions are used which pair edges in a sliding area mesh. In each step a search function connects the edges in this area depending on the displacement in between the transient steps, while the mesh remains stationary [7]. Thus, the flux is coupled between moving and stationary regions.

III. FINITE-ELEMENT MODELS

Only magnetically relevant components of the induction machine are modelled. Since the geometry of the machine is symmetric, antiperiodic boundaries reduce the FEM model to one pole pitch or 90° .

The 3D model of the induction machine is depicted in Fig. 1 on the right with translucent iron regions. With this model the torque of the machine is determined and compared to the results of the 2D calculations on the model in Fig. 1 on the left.

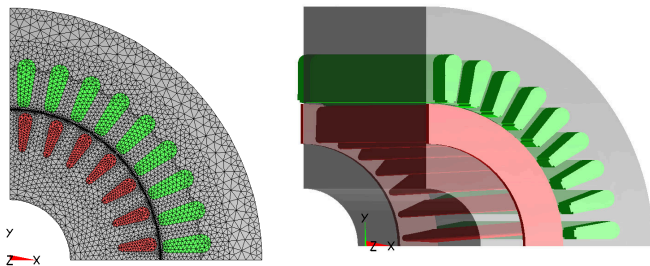


Fig. 1

2D AND 3D MODELS OF THE INDUCTION MACHINE

IV. CALCULATIONS AND RESULTS

All calculations are conducted at a constant speed of $n = 970$ rpm. The mechanical step angle amounts to $\alpha = 4^\circ$, leading to $\Delta t = 0.68728$ ms in between transient steps. The three-phase current of $I = 472$ A is impressed into the stator coils. The material conductivity of aluminum $\sigma = 1.834 \cdot 10^7 [\Omega m]^{-1}$ at material temperature $T = 200^\circ\text{C}$ is used for the massive aluminum regions of the rotor cage.

The rotor-bar currents are automatically induced by the electro-magnetic field in the 2D calculation of the middle slice and in the 3D calculation. In the other slices the computed rotor-bar currents are applied. The end ring of the rotor cage is taken into consideration as well.

The 2D calculated torque in time and frequency domain is depicted in Fig. 2 (time domain for middle slice). The resulting torque is generated by superposition of the torque values of all slices (frequency domain for superposition). The results of the 3D computation are shown in Fig. 3.

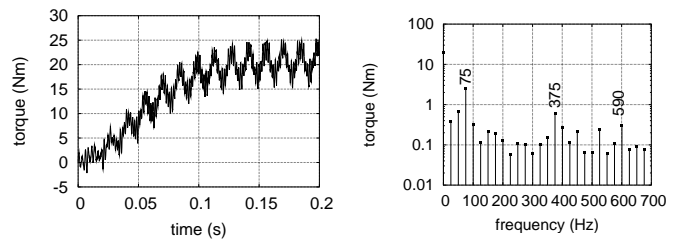


Fig. 2

TORQUE OF THE 2D CALCULATION

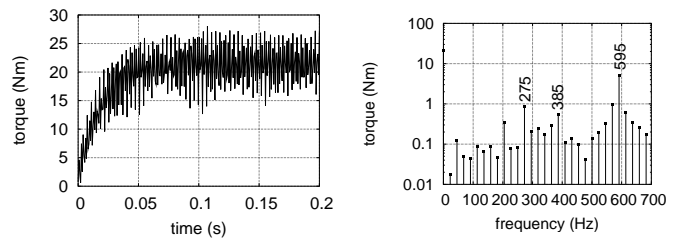


Fig. 3

TORQUE OF THE 3D CALCULATION

The frequency spectra of the 2D and the 3D calculations correspond rather good in the stationary value of the torque. Additionally both calculations show leading amplitudes at frequencies of approximately $f = 390$ Hz and $f = 600$ Hz.

V. CONCLUSION

In this paper a two-dimensional and a three-dimensional approach for the calculation of a skewed induction machine are compared. In the full paper 2D calculations with more than three slices of the machine will be presented and compared with the three-dimensional calculation. Additionally, the differences in the frequency domain will be investigated.

REFERENCES

- [1] Guido Arians, Thomas Bauer, Christian Kaehler, Wolfgang Mai, Christoph Monzel, Dirk van Riesen, and Christoph Schlenzok, "Innovative modern object-oriented solving environment - iMOOSE," Available: <http://imoose.sourceforge.net>, [Online].
- [2] Guido Arians and Gerhard Henneberger, "Object oriented analysis and design of transient finite element solvers applied to coupled problems," in *Digest of the 9th Conference on Electromagnetic Field Computation*. CEFC, 2000, p. 449.
- [3] Christian Kaehler, Dirk van Riesen, Dietmar Albertz, and Gerhard Henneberger, "Comparison of the $\vec{A} - \vec{A}, \vec{T}$ - and the \vec{A} -formulation for the computation of transient eddy-current field problems with edge elements," in *Proceedings of the 10th International IGTE Symposium on Numerical Field Calculation in Electrical Engineering*, Graz, Austria, September 2002, IGTE.
- [4] O. C. Zienkiewicz and R. L. Taylor, *The Finite Element Method*, McGraw-Hill Book Company, London, New York, 1991.
- [5] A. Kameari and K. Koganezawa, "Convergence of ICCG method in FEM using edge elements without gauge condition," *IEEE Transactions on Magnetics*, vol. 33, no. 2, pp. 1223–1226, March 1997.
- [6] Andrew Lumsdaine, Jeremy Siek, and Lie-Quan Lee, "The iterative template library - itl," Available: <http://www.lsc.nd.edu/research/itl>, [Online].
- [7] Christian Kaehler and Gerhard Henneberger, "Eddy-current computation on a one pole-pitch model of a synchronous claw-pole alternator," in *Conference Record of the 15th International Conference on Electrical Machines*, Brugges, Belgium, August 2002, ICEM.

Investigation of Induction Motor Zero Order Magnetic Stresses By a Finite Element Model

Timothy McDevitt, David Jenkins, and Michael Jonson
Applied Research Laboratory, the Pennsylvania State University,
P.O. Box 30, State College, PA U.S.A.
tem4@psu.edu

Abstract – A finite element analysis is conducted to provide radial stresses in an induction motor. An approach is implemented to find the primary contributors and likely causes of the zero order peaks in the radial magnetic stress spectrum for an ideal case.

INTRODUCTION

One of the most acoustically efficient low order circumferential vibration modes for cylinder-like structures is the “breathing mode” where k , the circumferential wavenumber, is zero [1]. This describes a circumferentially uniform vibration amplitude. This motion can be caused by zero order peaks in the magnetic forcing function. Zero order excitation can also cause vibration with mode numbers just above $k=0$, “low order modes” which also radiate well. This situation can occur in structures with non-periodic discontinuities such as supports. The focus of this study is to gain some insight into some of the origins of $k=0$ magnetic excitation in an induction motor

BACKGROUND

If two flux density waves in the air gap are represented as $B_1 \cos(k_1 \theta + \omega_1 t)$ and $B_2 \cos(k_2 \theta + \omega_2 t)$ then, by use of a trigonometric identity, their product (proportional to the air gap stress wave) becomes $[B_1 B_2] / 2 \cos[(k_1 + k_2) \theta + (\omega_1 + \omega_2) t] + \cos[(k_1 - k_2) \theta + (\omega_1 - \omega_2) t]$. Consequently a stress wave with zero mode number results any time the cross product of two flux density waves yields $(k_1 + k_2) = 0$ or $(k_1 - k_2) = 0$.

DESCRIPTION OF ANALYSIS AND PROCEDURE

The finite element model, shown in Fig. 1, represents a single pole of a twelve pole, Y-connected, three phase 240 V induction motor.

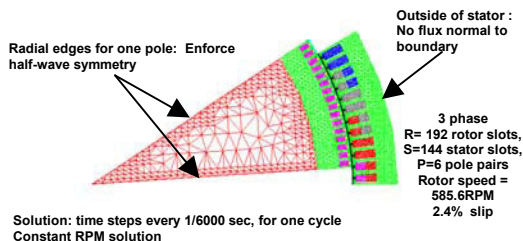


Figure 1. The Finite Element Model

The supply frequency is 60Hz. Ideal conditions are assumed, i.e. pure sinusoidal and fully balanced phase voltages and no rotor eccentricity. After the startup transient settled out, a one cycle simulation was conducted with time steps every 1/6000 second to capture forcing function variations up to 3 kHz. There were one thousand points along the arc in the air gap at which the flux densities were calculated for each time step.

A MATLAB 2D FFT routine was applied to the spatially sampled air gap radial flux density distribution over all simulation time steps. The radial stress was then approximated for each time step using a B-squared approach. (Outside the startup transient this normally provides results similar to the Maxwell stresses [2]). A 2D FFT was then applied to this result. Finally a MATLAB routine was written to match up flux density waves with the same wavenumbers which when multiplied would yield a $k=0$ stress wave. Flux density wavenumbers up to 600 were investigated over the entire frequency range of zero to 3 KHz. A table of flux density waves which played a role in the $k=0$ stress wave formation was then obtained.

RESULTS

Fig.2 illustrates the frequency spectrum for the zero wavenumber radial stresses. The frequencies of a few of the peak stress waves are flagged in the spectrum.

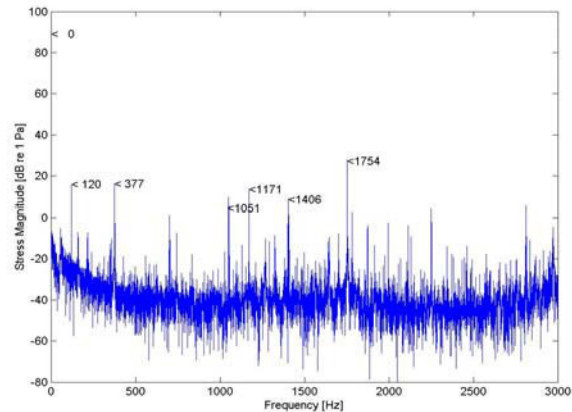


Figure 2. Spectrum of the “B-squared” Stresses for $k=0$.

We will focus on the strongest component in the $k=0$ stress spectrum; the wave at 1754Hz. There are numerous pairs of flux density waves whose product results in a stress wavenumber of zero at this frequency. The MATLAB output shows there are at least fourteen such pairs. The vector sum of these fourteen stress waves comprises the net amplitude shown in the spectrum above. There are three wave pairs however, which make up the most of the contribution. Table I, a very small portion of the total MATLAB results, shows these three stress waves. Each column represents a different stress wave followed by the two component flux density waves from which it originates.

Frequency (Hz)	1754.4	1754.4	1754.4
Amplitude (Pascals)	14.98	10.39	4.56
Phase (radians)	2.138	2.447	2.34
Frequency 1 (Hz)	1814.4	1814.4	1814.4
Amplitude 1 (Tesla)	0.021	0.00055	0.002826
Phase 1 (radians)	-0.856	1.421	2.603
Frequency 2 (Hz)	60.0	60.0	60.0
Amplitude 2 (Tesla)	0.00179	0.04750	0.004061
Phase 2 (radians)	-2.99	-1.0252	0.263
k	-186	-150	-42

Table I. Radial stress waves contributing to peak at 1754 Hz shown with their respective flux density components

The top three rows are the characteristics of the stress waves. The next three rows are the characteristics of one of the flux density waves while the following three rows are those for the second. The wavenumber of the two contributing flux density waves is listed in the last row. These three stress waves contribute 29dB, or practically all the amplitude at the 1754 Hz peak.

The overall MATLAB output shows that flux density pairs contributing to 1754Hz all have 60Hz and a 1814 Hz components with but varying wavenumber. For the three flux density wave pairs shown above, the negative wavenumbers (with positive frequencies) indicate that each flux density wave is moving in the direction of rotor rotation. (The same wave could be indicated by a negative frequency and positive wavenumber). In the overall MATLAB table we find that every pair of flux density waves has the two moving in the same direction. The highest amplitude stress wave has flux density waves with mode number at -186. The 1814 Hz wave in this case is likely a wave due to rotor slotting with a mode number of (R-P) and a frequency of $(\omega-RN)$. The 60Hz wave in this case, may be a fairly high stator m.m.f. harmonic with a mode number of -31P [3].

The second flux density pair consists of waves having mode numbers of -150. For the wave at 60Hz, this is

equivalent to a mode number of (S+P), having a frequency of $-\omega$ (due to the interaction of the fundamental m.m.f. with the stator slot induced permeance variations). The wave at 1814 Hz appears to be a slot ripple harmonic at $\{2*f*n*(R/p)*(1-s) - 1\}*f$ where f is the line frequency, R = number of rotor teeth, p =number of poles, s = slip, n = harmonic number equal to 1 here [4].

The third flux density pair has $k=-42$. The “60 Hz” wave is the 7th phase belt (stator winding m.m.f.) flux density harmonic having a mode number of 7P pairs or 42 and a frequency of -60Hz. The 1814 Hz wave is a slot flux density harmonic with a mode number of (S-R+P) or minus 42 and a frequency of $-(\omega-RN)$ rad/sec or plus 1814 Hz (N here is the rotor speed in radians/second).

SUMMARY AND DISCUSSION

This approach reveals that the resultant stress wave of a given wavenumber can have its origins in several (if not numerous) contributing stress waves which in turn are composed of various flux density wave pairs. A similar approach, which may be useful from a design standpoint, is to switch this process and scan the wavenumbers at a given frequency. However it is likely that multiple contributors, rather than a single dominating source will be found.

From a more general perspective, we note that high wavenumber flux density waves can contribute to $n=0$ and can contribute with relatively strong amplitude. Additionally we note that a high number of pole pairs, while ensuring against the “low” order mode excitation, may not help with zero order modes. Finally, these same zero order radial excitation modes may relate directly to unsteady torque modes as well [4].

ACKNOWLEDGMENTS

This work was sponsored by the Applied Research Laboratory Electric Drive Initiative.

REFERENCES

- [1] F. Fahy, *Sound and Structural Vibration*, Academic Press Limited, 1985 San Diego, CA
- [2] S.J. Salon, C.J. Slavik, M.J. DeBortoli and G. Reyne, “Analysis of Magnetic Vibrations in Rotating Electric Machines”, In *Finite Elements, Electromagnetics, and Design*, ed. S. RatnajeevanH., Hoole, chpt.4pp.116-178Elsevier Science, Amsterdam 1995.
- [3] K.J Binns, and E.Schmid, “Some Concepts Involved in the Analysis of the Magnetic Field in Cage Induction Machines,” Proc. IEE, Vol. 122, No. 2, pp 169-175, February 1975.
- [4] M.J. DeBortoli, “Extensions to the Finite Element Method for the Electromechanical Analysis of Electric Machines,” PhD Thesis, Rensselaer Polytechnic Institute, May, 1992.

Calculation of Negative Torque Caused by Slot Ripples of Induction Motor

Katsumi Yamazaki^{*1}, Yoshihisa Haruishi^{*1} and Takahiro Ara^{*2}

*1: Dept. of Electrical Eng., Chiba Institute of Tech., 2-17-1, Tsudanuma, Chiba 275-0016, Japan (yamazaki@pf.it-chiba.ac.jp)

*2: Dept. of Electrical Eng., Polytechnic University, 4-1-1, Hashimoto, Kanagawa 229-1196, Japan (ara@uitech.ac.jp)

Abstract — A method to calculate torque of induction motor considering the effects of harmonic iron losses is proposed. The negative torque caused by the eddy current and the hysteresis phenomena in the stator and the rotor core is calculated from the time-variation of the magnetic field distribution obtained by the nonlinear time-stepping finite element analysis. The calculated negative and the total torques agree well with the experimental results. It is clarified that the negative torque is not negligible in case of the analyzed motor and that the accuracy of the torque calculation is improved by the proposed method.

I. INTRODUCTION

It is well known that the magnetic fields in induction motors include much time-harmonics even if the motors are driven by sinusoidal voltage sources. Especially, the stator and the rotor slot harmonics cause relatively large harmonic losses at the stator and the rotor core. It can be considered that the harmonic fields also cause breaking force, which may decrease the torque of the motors. But there are few reports which estimate this effect using the electromagnetic field analyses because the direct consideration of the eddy current and the hysteresis phenomena in the laminated core requires vast of computer resources

From these points of view, we introduce the method to calculate the negative torque approximately from the time-variation of the electromagnetic field obtained by the finite element method. The measurement of the negative and the total torque of the induction motor are also carried out to examine the validity of the calculation.

II. CALCULATION METHOD

Fig.1 shows the outline of the negative and the total torque calculation. The calculation method consists of two steps.

First, the electromagnetic field of the motor is analyzed by the nonlinear time-stepping finite element analysis coupled with the primary voltage equation. Combined 3D-2D formulation [1] is applied to consider the end-effects. At this step, the conventional result of the torque T_0 , which neglects the effects of the harmonic core losses ΔW_c , is obtained. The harmonics copper losses ΔW_1 , ΔW_2 , which are the losses at the primary winding and the rotor cage, are also obtained directly by the finite element analysis.

Second, the harmonic losses of the stator and the rotor core ΔW_c are calculated approximately from the time-variation of the flux density obtained by the first step [2]-[4]. Although there are many kinds of harmonics caused by the stator and the rotor magnetic motive force, the slips of them can be considered as nearly 1.0 at the rating condition. Thus, the negative torque caused by the harmonic fields can be calculated approximately from the harmonics losses and the rotational speed ω due to the classical theory. The total torque can be also calculated by subtracting the effect of the harmonic core losses from the conventional result T_0 .

III. MEASUREMENT METHOD

Fig.2 shows the system for the measurement of the negative torque of the induction motor at synchronous speed. First, the induction motor is rotated without the power supply using the synchronous permanent magnet motor. At this moment, the input power of the permanent magnet motor includes not only the own losses but also the mechanical loss of the induction motor. Next, the power is supplied to the induction motor. The input power of the permanent magnet motor increases according to the voltage of the induction motor. It can be considered that this increase corresponds to the negative torque generated by the induction motor.

The total torque of the induction motor at the load condition is also measured using the torque detector with the analyzing recorder. The average torque is obtained from the 32000 data at steady rotation with the sampling time 100 μ s.

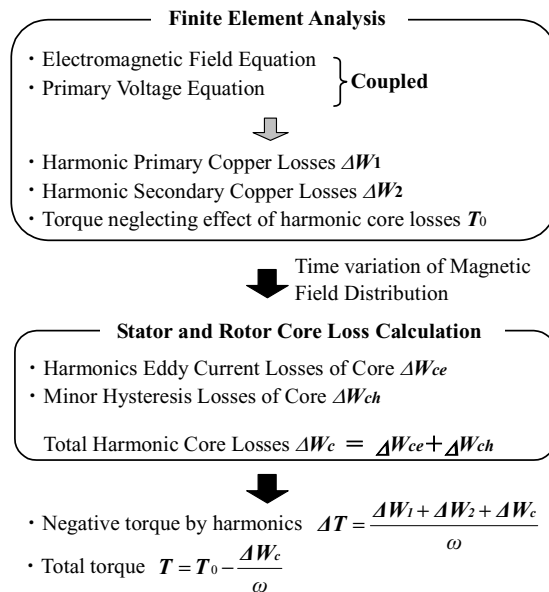


Fig.1. Outline of calculation method

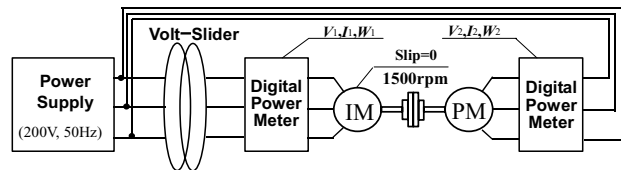


Fig.2. System for measurement of negative torque at synchronous speed.

IV. RESULTS AND DISCUSSION

A 400W cage induction motor with semi-closed stator and rotor slots is measured and analyzed.

Fig.3 shows the space and the time variation of flux density and the loss distribution of the motor at synchronous speed. The time variation of the flux density at the stator teeth top (b) includes much time-harmonics, which is caused by the rotor slot ripples due to the movement of the rotor. On the other hand, the time variation at the rotor teeth top (d) also includes much time-harmonics caused by the stator slot ripples. As a result, the loss concentrates at the stator and the rotor surface. Fig.4 shows the measured and the calculated negative torques at synchronous speed. Fig.5 shows the measured and calculated total torque due to the load. The calculated result by the conventional method is also shown. It is clarified that

the accuracy of the calculation is improved by the proposed method. The negative torque is nearly 5% of the rating torque.

REFERENCES

- [1] K. Yamazaki, "Induction Motor Analysis Considering both Harmonics and End Effects Using Combination of 2D and 3D Finite Element Method," *IEEE Trans. Energy Conversion*, vol.14, no.3, 698, 1999.
- [2] S. L. Ho, W. N. Fu and H. C. Wong: "Estimation of Stray Losses of Skewed Rotor Induction Motors Using Coupled 2-D and 3-D Time Stepping Finite Element Methods," *IEEE Trans. Magn.*, vol.34, No.5, 3102, 1998.
- [3] N. Sadowski, J. P. A. Bastos, M. V. Ferreira Da Luz, P. Kuo-Peng and M. Lajoie-Mazenc, "The Rain-Flow Method for Evaluation of Iron Losses in Electrical Machines," *IEEE Trans. Magn.*, vol.36, no.4, 1923, 2000.
- [4] K. Yamazaki, "Efficiency Analysis of Induction Motors for Ammonia Compressors Considering Stray Load Losses Caused by Stator and Rotor Slot Ripple", *Conference Record of the 2001 IEEE Industry Applications Conference 36th Annual Meeting*, 2001.

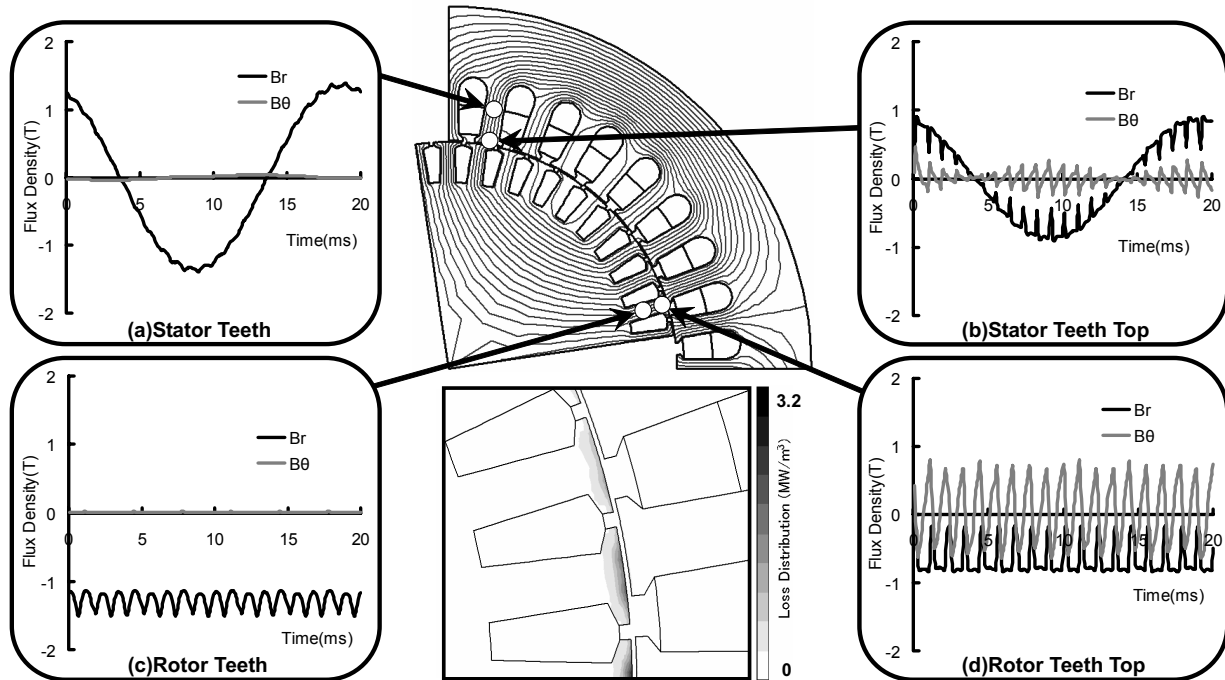


Fig.3. Space and time-variation of flux density and loss distribution of motor with semi-closed rotor slots at synchronous speed ($s=0$).

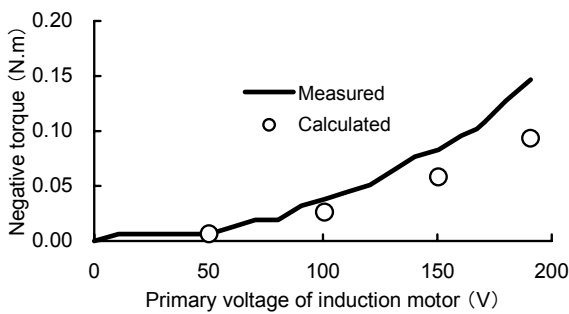


Fig.4. Measured and calculated negative torque at $s=0$.

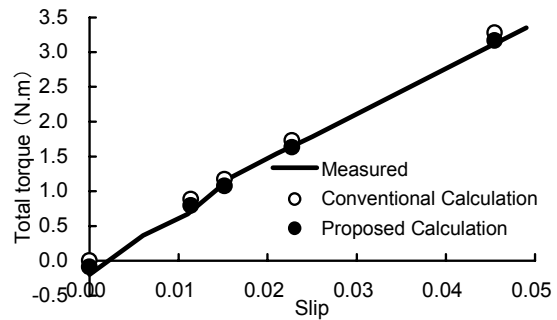


Fig.5. Measured and calculated total torque at 190V.

Calculation of Force Excitations in Induction Machines with Centric and Excentric positioned Rotor using 2D Transient FEM

Christoph Schlensok and Gerhard Henneberger
Department of Electrical Machines (IEM), Aachen University (RWTH),
Schinkelstraße 4, D-52056 Aachen, Germany
Christoph.Schlensok@iem.rwth-aachen.de

Abstract—The calculation of induction machines with squirrel cages using the Finite-Element Method (FEM) requires a transient solving process. The rotation has to be taken into account. Therefore a rotating air gap is implemented. The formulation for the transient solver is given. Finite-element models of an induction machine with centric and excentric positioned rotor are calculated. The formulation for the computation of the surface-force density on the stator teeth is presented. For both variants of the induction machine the forces are calculated and compared.

Index Terms—Transient 2D FEM Calculation, Excentricity, Induction Machine, Surface-Force Density

I. INTRODUCTION

Due to fabrication tolerances the rotors of electrical machines are usually not positioned central. In case of an induction machine used as a power-steering drive this has strong effect on the acoustic behaviour and therefore on the customer satisfaction. In order to estimate the effect of excentricity the force densities on the stator teeth have to be calculated.

In this paper two variants of an induction machine are compared. The rotor of the first variant is positioned centric. In case of the second variant the rotor is shifted radially but still rotated around the stator axis. Both variants are calculated with a 2D-transient solver and afterwards the force excitations on the stator teeth are computed.

II. FORMULATION OF THE TRANSIENT SOLVER

The applied solver is part of an object-oriented solver package [1]. The transient FEM formulation takes the rotational movement into account and two finite-element meshes have to be handled. The 2-dimensional \vec{A} -approach is node-based. The magnetic vector potential is used in all regions. The equation

$$\int_{\Gamma} \left(\nabla \cdot \alpha_i \cdot \nu \cdot \nabla \cdot A_z(t) + \alpha_i \cdot \sigma \cdot \frac{\partial}{\partial t} A_z(t) \right) d\Gamma = \int_{\Gamma} (\alpha_i \cdot J_{z0}(t)) d\Gamma \quad (1)$$

has to be solved in the complete model Γ and is given in Galerkin formulation [2]. The material parameters ν and σ represent the non-linear reluctivity and the linear conductivity. The shape function of an element is defined by α_i . Triangular

shaped elements are used. $J_{z0}(t)$ describes the z-component of the given coil current-density as the only excitation.

For linear interpolation of the time-dependent variables the first order time-step algorithm is applied and $A(t)$ can be written as function of time:

$$A(t) = (1 - \Theta) A_n + \Theta A_{n+1} \quad (2)$$

$$\Theta = \frac{t - t_n}{t_{n+1} - t_n} = \frac{t - t_n}{\Delta t}; \quad 0 \leq \Theta \leq 1. \quad (3)$$

Θ is the weighting parameter and is set to $\Theta = \frac{2}{3}$ according to the Galerkin scheme [3].

III. FORMULATION OF THE SURFACE FORCES

With the Maxwell stress tensor

$$\vec{\sigma} = \frac{1}{2} \vec{n}_{12} [B_n (H_{1n} - H_{2n}) - (w'_1 - w'_2)] \quad (4)$$

an expression for the local surface-force density is given [4]. The index n stands for the normal components of the vectors \vec{B} and \vec{H} . \vec{n}_{12} is the normal vector of the boundary surface from region 2 to 1. w'_1 and w'_2 are the magnetic-coenergy densities of these regions.

IV. FINITE-ELEMENT MODELS

For the regarded application investigations have shown that an induction machine with 24 stator slots and 26 rotor bars is a very good variant [5]. The lamination is shown in Fig. 1.

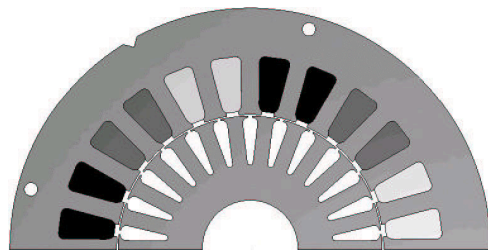


Fig. 1

LAMINATION OF THE INDUCTION MACHINE, TWO POLE PITCHES

Although only two pole pitches are depicted, the machine is modelled as a 360° -model since the number of elements is small for 2D-calculation in general. The models have about 25.000 elements and 12.500 nodes.

In Fig. 2 closeups of the airgaps of the centric and the excentric model are opposed. To the left the centric model is depicted. The airgap has a constant value of $\delta = 0.3$ mm. Next to it the excentric model is shown. The airgap differs between $\delta_{min} = 0.2$ mm and $\delta_{max} = 0.4$ mm. The maximal airgap is depicted.

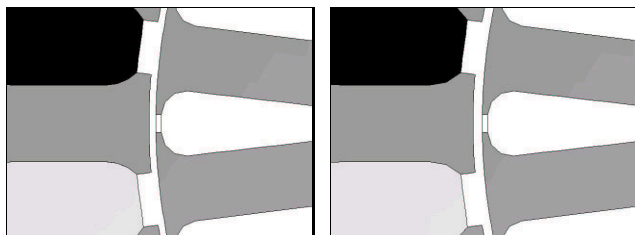


Fig. 2
CLOSEUPS OF CENTRIC AND EXCENTRIC MODEL

V. 2D-TRANSIENT FEM CALCULATION

In a first step the two variants are calculated with the 2D-transient solver. The operation point is at $n = 1200 \text{ min}^{-1}$ with $f_1 = 50.2 \text{ Hz}$. The sinusoidal stator current densities are sampled with 64 steps per period. The resulting time step is $\Delta t = 311 \mu\text{s}$. The torque of which the time-dependent behaviour is depicted in Fig. 3 and the overall force are computed.

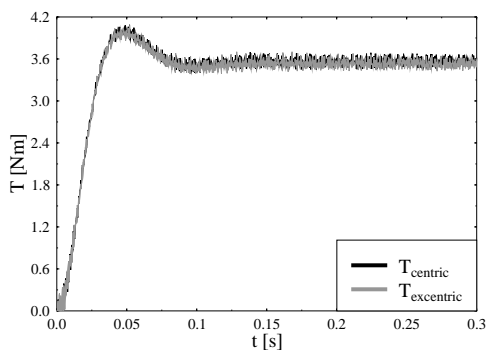


Fig. 3
TIME-DEPENDENT TORQUE BEHAVIOUR

The average torque is not affected by the excentricity [6]. Its value is $T = 3.56 \text{ Nm}$. But for the overall forces on the rotor the excentricity has very strong effect. The average value increases from $F_{centric} = 0.012 \text{ N}$ to $F_{excentric} = 101.4 \text{ N}$.

VI. SURFACE-FORCE DENSITY CALCULATION

Equation (4) is used to calculate the surface-force density on the stator teeth. The force density is only computed towards the airgap since the forces between the lamination and the copper winding is much smaller. The main excitation will appear in

radial direction towards the rotor. Usually the normal forces are about 10 to 100 times the tangential.

Fig. 4 shows the surface-force densities for one certain time step for both variants. In case of the centric variant the forces which occur on the one stator side are compensated on the opposite side. If compared with the force excitation for the same time step in the excentric case the forces have no longer the same value on the opposite sides. Consequently they are not compensated. The stator is excited asymmetrically with the rotor frequency.

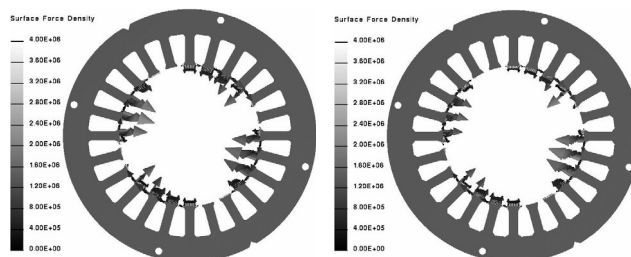


Fig. 4
SURFACE-FORCE DENSITIES FOR BOTH VARIANTS

VII. CONCLUSION

In this paper an induction machine with squirrel cage as power-steering drive is calculated with a 2D-transient solver. The machine geometry is varied by placing the rotor centrically and excentrically. The torque and the overall force on the rotor is computed and compared. Although the average torque and its behaviour are not significantly affected by the excentricity the overall forces rise strongly.

In a next step the surface-force densities on the stator teeth are calculated. It can be noted that the excentricity has strong effect onto the surface-force density distribution. The forces on the one side of the machine are not compensated on the other side any longer. The stator teeth are excited asymmetrically. It is obvious that this will generate extra noise.

Beyond this the deformation of the stator will be discussed and further results will be presented in the full paper.

REFERENCES

- [1] Guido Arians, Thomas Bauer, Christian Kaehler, Wolfgang Mai, Christoph Monzel, Dirk van Riesen, and Christoph Schlensok, "Innovative modern object-oriented solving environment - iMOOSE," Available: <http://imoose.sourceforge.net>, [Online].
- [2] Guido Arians and Gerhard Henneberger, "Object oriented analysis and design of transient finite element solvers applied to coupled problems," in *9th Conference on Electromagnetic Field Computation*, Milwaukee, USA, 2000, CEFC.
- [3] O. C. Zienkiewicz and R. L. Taylor, *The finite element method*, pp. 346–361, McGraw-Hill Book Company, London, 1989.
- [4] Ingo Ramesohl, Stefan Küppers, Wilfried Hadrys, and Gerhard Henneberger, "Three dimensional calculation of magnetic forces and displacements of a claw-pole generator," *IEEE Transactions on Magnetics*, vol. 32, no. 3, pp. 1685–1688, May 1996.
- [5] Christoph Schlensok and Gerhard Henneberger, "Torque behaviour in induction machines due to skewing," in *3rd international seminar on Vibrations and acoustic Noise of Electric Machinery*, Łódź, Poland, October 2002, VANEM.
- [6] Jan Rusek, "Effect of static plus dynamic excentricity on static and dynamic behaviour of induction machines," in *3rd international seminar on Vibrations and acoustic Noise of Electric Machinery*, Łódź, Poland, October 2002, VANEM.

Effects of saturation on the forces in induction motors with whirling cage rotor

Asmo Tenhunen, Timo, P. Holopainen*, Antero Arkkio

Laboratory of Electromechanics
Helsinki University of Technology
P.O. Box 3000, FIN-02015 HUT, Finland
Asmo.Tenhunen@hut.fi

*VTT Industrial Systems
Technical Research Centre of Finland
P.O. Box 1705, FIN-02044 VTT, Finland
Timo.Holopainen@vtt.fi

Abstract — The effects of magnetic saturation on the radial magnetic force in induction machines when the rotor is performing cylindrical circular whirling motion are studied in this paper. Impulse method in the finite element analysis is used to calculate the forces and the eccentricity harmonics from both, the air gap flux density and rotor currents. The forces are studied as a function of supply voltage in order to find out the effects of the saturation on them. The maximum radial force is found to be limited by saturation and saturation also couples the eccentricity harmonics together.

INTRODUCTION

An electromagnetic force acts between the rotor and stator if the rotor is performing cylindrical circular whirling motion with respect to the stator [1]. The magnetic saturation influences on the amplitude and the direction of the force.

The effects of saturation are quite difficult to take into account analytically and the analytical models give only an approximation of the saturation effects [2]. In the numerical studies of rotor eccentricity, some results of the effects of saturation are presented in [1,3].

In this study, the effects of saturation are studied using impulse method in finite element analysis. The forces are calculated as a function of whirling frequency and supply voltage at no load and rated load. The effects are also considered from the air-gap flux density and rotor current harmonics.

METHODS

The calculation of the magnetic field is based on the time-stepping, finite element analysis. The magnetic field is supposed to be two-dimensional and the laminated iron core is treated as a non-conducting magnetically nonlinear medium, which is modeled by a single-valued magnetization curve (Fig. 1). For a comparison, the forces were also calculated for a linearized motor which has a constant relative permeability $\mu_r = 1000$.

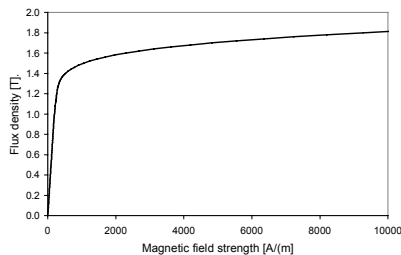


Fig. 1. The single-valued magnetization curve used.

The impulse method [4] is utilized in the analysis. The basic idea of the impulse method is to move the rotor from its central position for a short period of time. The displacement excitation produces the flux density harmonics into the air gap. The harmonics, in their turn, induce the equalizing currents into the rotor bars and cause forces between the rotor and stator. During the time-stepping analysis, the harmonics of order $p \pm 1$ (p is number of pole pairs of the motor) from rotor currents and air gap flux density distribution are calculated at each time step. The forces are calculated by a method, based on the principle of the virtual work [5]. Using spectral analysis techniques the frequency response of the harmonics and forces is calculated using the excitation and response signals.

RESULTS

A four-pole 15 kW induction motor was chosen for test motor. The parameters of the motor are given in [4]. In the analysis, the length of the cosine-type displacement pulse was 0,01 s and the amplitude 11% of the air gap length. The total simulation time was 1 s with a constant time-step of 0.05 ms. In the spectral analysis, the number of sample points was 8192 and the length of the signal 4 s, by adding the zero level at the end of the sample to increase the frequency resolution.

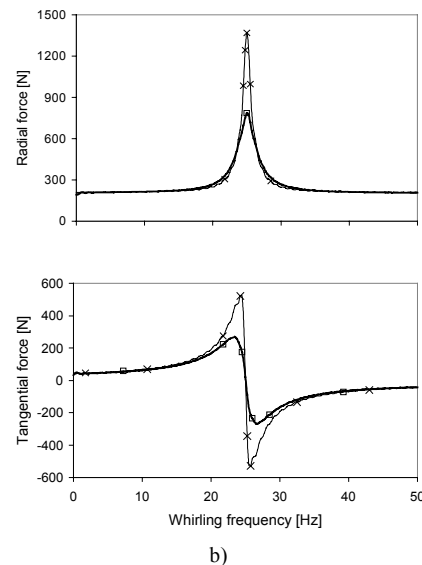


Fig. 2. The radial and tangential component of the force as a function of whirling frequency at no load. \circ - normal and \times - the linearized motor.

If the forces are divided into a radial component in the direction of the shortest air gap and a tangential component perpendicular to the radial one, the components are almost independent on time.

Fig. 2 shows the radial and tangential components of the force as a function of the whirling frequency at no load and supplied by the rated voltage 380 V for both normal and linearized motor.

Fig. 3 shows the radial and tangential components of the force as a function of the supply voltage at whirling frequencies 5 Hz and 25 Hz. At no-load condition, the maximum force occurs at 25 Hz for the four-pole motors. Fig. 3 shows that the maximum force is reached near to 300 V and for bigger values of supply voltages the amplitude of the force is decreased. At a 5 Hz whirling frequency, the flux density harmonics are strongly damped by rotor currents and the radial component of the force behaves like in the linearized case.

The ratio of the tangential and radial force components changes with the voltage. This means that the saturation also affects the direction of the force.

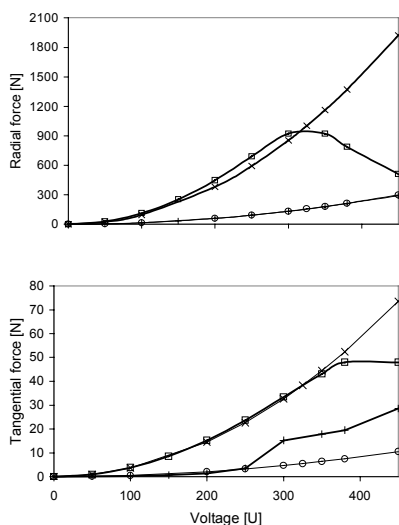


Fig. 3. The amplitudes of the force components as a function of supply voltage at no load. Marking: X - linearized 25 Hz, □ - normal 25 Hz, ○ - linearized 5 Hz and + - normal 5 Hz.

Fig. 4 shows the behaviour of the flux density harmonics $p \pm 1$ as a function of supply voltage at whirling frequencies 5 Hz and 25 Hz at no load and voltage level 380 V.

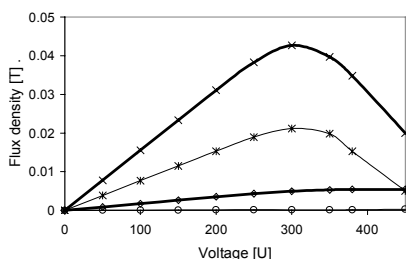


Fig. 4. The flux density harmonics ($p \pm 1$) as a function of supply voltage at rated load. Marking: X - $p \pm 1$ at 25 Hz, * - $p - 1$ at 25 Hz, ◇ - $p \pm 1$ at 5 Hz and ○ - $p - 1$ at 5 Hz.

The effects of saturation can be seen easily from the flux density harmonics versus voltage behaviour. The amplitudes of the harmonics start to decrease approximately at the same voltage as the forces.

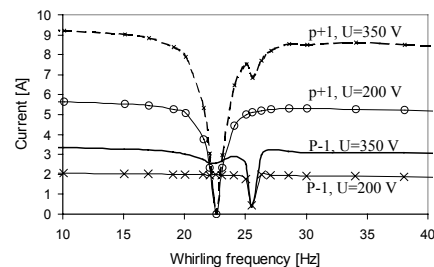


Fig 5. $p \pm 1$ harmonics of the rotor currents at rated load at 350 V and 200 V.

Since now, we have discussed the results calculated at no load. At rated load, the behavior of the forces and flux density harmonics is similar as at no load, except that the frequency response of the forces has two peaks, because the slip differs from zero at the rated load. Then the maximum force and also the maximum value of flux density harmonics occur at different whirling frequencies. Respectively, the minimum of the rotor current harmonics occurs at different whirling frequencies. Fig. 5 presents the calculated rotor current harmonics $p \pm 1$ as a function of whirling frequency at rated load and at supply voltages 200 V and 350 V. The coupling of the harmonics due to the saturation can be seen from figure. At 350 V, the motor core is saturated and the current harmonics seem to influence each other. At 200 V, the motor core is not saturated and no coupling can be found.

CONCLUSIONS

The effects of saturation on the electromagnetic forces in induction machines with rotor eccentricity are studied. The forces and harmonics of flux density and rotor currents are calculated using impulse method in finite element analysis. The results show that the magnetic saturation limits the maximum force and influences also on the direction of the force.

REFERENCES

- [1] A. Arkkio, M. Antila, K. Pokki, A. Simon and E. Lantto, "Electromagnetic force on a whirling cage rotor", *IEE Proc. Elect. Power Appl.*, vol. 147, pp. 353-360, September 2000.
- [2] D. G. Dorrell, "Experimental behaviour of unbalanced magnetic pull in 3-phase induction motors with eccentric rotors and the relationship with tooth saturation", *IEEE Transactions on Energy Conversion*, vol. 14, pp. 304-309, September 1999.
- [3] A. Arkkio and O. Lindgren, "Unbalanced magnetic pull in a high-speed induction motor with an eccentric rotor", *Proceedings of ICEM'94*, Paris, France, 5-8 September 1994, pp. 53-58.
- [4] A. Tenhunen, T. P. Holopainen and A. Arkkio, "Impulse method to calculate the frequency response of the electromagnetic forces on whirling cage rotors", Accepted to be published in *IEE Proc. Elect. Power Appl.*
- [5] J. L. Coulomb, "A methodology for the determination of global electro-mechanical quantities from a finite element analysis and its application to the evaluation of magnetic forces, torques, and stiffness", *IEEE Transactions on Magnetics*, vol. 19, pp. 2514-2519, November 1983.

Analysis of Voltage Distribution in Stator Windings of Induction Motor Driven by IGBT PWM Inverter

Don-Ha Hwang, Dong-Sik Kang, Yong-Joo Kim

Industry Applications Research Laboratory,
Korea Electrotechnology Research Institute (KERI),
P.O. Box 20, Changwon, Gyeongnam,
641-600, Korea
dhhwang@keri.re.kr

Sung-Woo Bae, Dong-Hee Kim

School of Electrical & Electronic Engineering,
Yeungnam University,
214-1, Daedong, Gyeongsan, Gyeongbuk,
712-749, Korea
sungwoobae@koreamail.co.kr

Abstract – IGBT PWM inverter has been concerned that insulation breakdown and irregular voltage distribution on stator winding due to high rate of voltage rise (dv/dt) caused by high-frequency switching and impedance mismatches between inverter and motor.

In this paper, voltage distribution in stator windings of induction motor driven by IGBT PWM inverter is studied. To analyze the irregular voltage of stator winding, high frequency parameter is computed by using finite element method (FEM). Electro-magnetic transient program (EMTP) analysis of the whole system, induction motor and PWM inverter, is proposed. An induction motor, 50 [HP], with taps from one phase and a switching surge generator were built to consider the voltage distribution.

I. INTRODUCTION

Insulated gate bipolar transistor (IGBT) PWM inverter has been concerned that insulation breakdown and irregular voltage distribution on stator winding due to high rate of voltage rise (dv/dt) caused by high-frequency switching and impedance mismatches between inverter and motor. These steep pulses and irregular voltage of stator winding lead to occur partial discharge and eventually premature insulation breakdown [1-3].

In this paper, voltage distribution in each turn of stator windings of induction motor driven by IGBT PWM inverter is studied. In order to calculate the parameter, resistance, inductance and capacitance among turns of end-line coil, a high frequency equivalent circuit model of inverter-cable-motor was proposed and analyzed with finite element method (FEM). Also, by using the electro-magnetic program (EMTP), the whole system of stator winding for induction motor driven by IGBT PWM inverter is modeled.

Finally, for experiment of voltage distribution, a switching surge generator as pulse voltage source and the induction motors tapped from initial turn to fifth turn were built and analyzed. Various rise time, frequency, and different cable lengths were applied to an induction motor.

II. THE SLOT MODELING OF 50 [HP] INDUCTION MOTOR

In order to analyze voltage distribution in stator winding of low voltage induction motors fed by IGBT PWM inverter, the induction motor, 50 [HP], 380 [V], is applied. The stator slots are 48, and the rotor slots are 40. The wires of 1.2 [mm] × 3 and 1.1 [mm] × 1 are connected total 96 turns as parallel.

One slot out of stator slots 48 and rotor slots 40 are modeled to calculate the parameters as shown in Fig. 1 by

using Maxwell 2D which is finite element method (FEM) program [4-5].

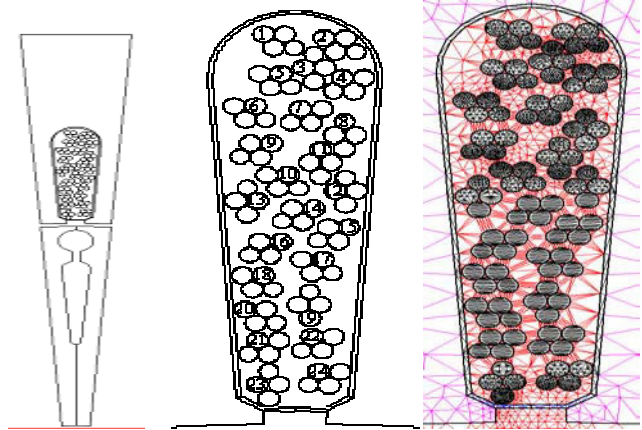


Fig. 1. Cross section of slot model and mesh diagram for FEM analysis

It is essential that first turn to fifth turn should be expressed distributed parameter circuit as shown in Fig. 2. The other turns are applied concentrated constant circuit.

It can be known that the resistance increases and the inductance decreases according to rising the frequency due to skin effect as shown Fig. 3.

III. SIMULATION OF SURGE EQUIVALENT CIRCUIT

In order to analyze the voltage distribution in stator winding of low-voltage induction motor driven by IGBT PWM inverter, electromagnetic transient program (EMTP) analysis is performed, because voltage distribution of stator appears as unbalanced voltage [6].

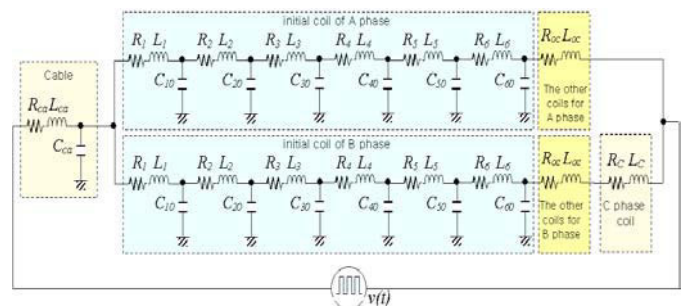


Fig. 2. Equivalent circuit of whole induction motor system

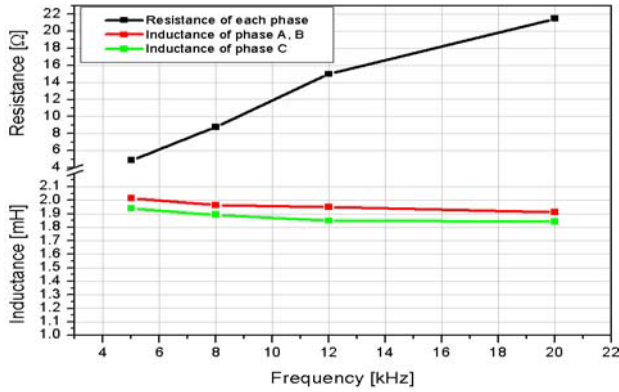


Fig. 3. Resistance and inductance as increasing frequency

Turn to turn voltage distribution is shown Fig. 4 as increasing cable length when frequency is 20 [kHz], and rise time is 150 [ns]. First turn voltage is much higher than the other turns.

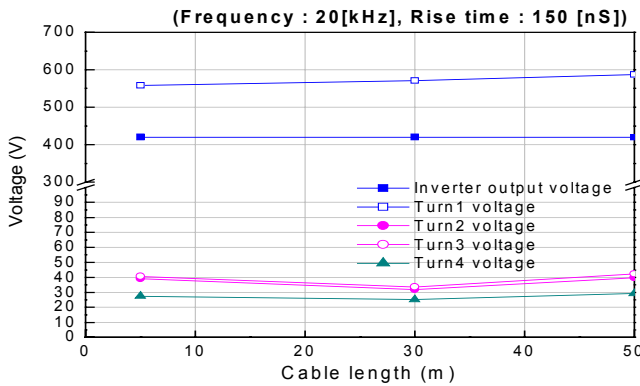


Fig. 4. Turn to turn voltage distribution

IV. EXPERIMENTAL RESULT

The stator winding was insulated by standard varnish impregnation and taped first turn to fifth turn from one phase for measurement of the voltage distribution as shown in Fig. 5. In order to prevent the insulation breakdown in weld part, KAPTON insulation type that is superior to insulation characteristics in spite of over 200 °C was used.

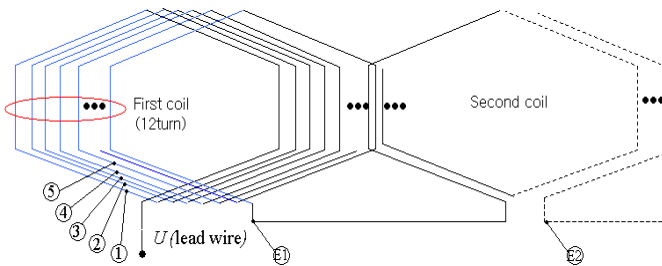


Fig. 5. The tap for measurement of the voltage distribution

Fig. 6 shows the example of experiment voltage waveform between first turn and ground when rise-time of inverter has

150 [ns], the length of cable is 100 [m], and switching frequency is 20 [kHz]. As shown in Fig. 6, the surge voltage occurred in initial turn of stator winding. This over-voltage causes to voltage reflection phenomena due to impedance mismatches among the inverter, cable, and motor. This surge voltage results in premature insulation failure of induction motor driven by IGBT PWM inverter.

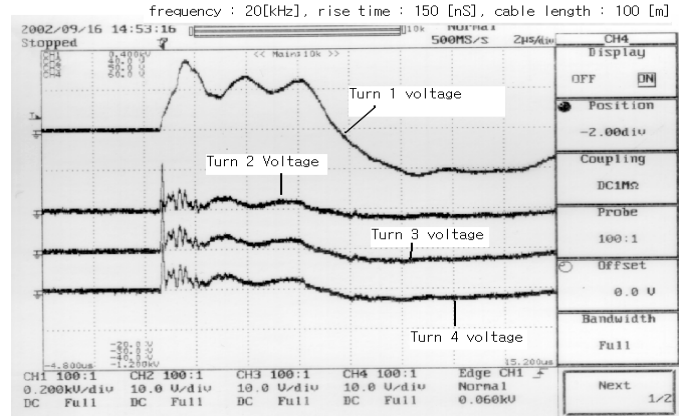


Fig. 6. Example of turn to turn voltage waveform

V. CONCLUSION

In this paper, the voltage distribution of in stator winding of low-voltage induction motor driven by IGBT PWM inverter is analyzed. To analyze the voltage distribution, slot model and equivalent circuit of one coil is proposed. The tap for voltage measurement experiment is built in induction motor. The characteristics of voltage distribution by the simulation and experiment is that the voltage of first turn is generally higher than that of the other turns and as rise-time become fast, the magnitude of voltage is increased. Furthermore, according to increase the cable length between inverter and motor, the voltage of induction motor is increased. When this results are considered, induction motor that is able to endure surge voltage is needed.

REFERENCES

- [1] R. J. Kerkman and D. Leggate, "Interaction of drive modulation and cable parameters on AC motor transients", *IEEE Transactions on Industry Applications*, Vol. 33, No. 3, pp. 722-731, May/June 1997.
- [2] M. Kaufhold, H. Auinger, M. Berth, J. Speck, and M. Eberhardt, "Electrical stress and failure mechanism of the winding insulation in PWM-inverter-fed low-voltage induction motors", *IEEE Transactions on Industrial Electronics*, Vol. 47, No. 2, pp. 396-402, Apr. 2000.
- [3] E. Persson, "Transient effects in application of PWM inverters to induction motors", *IEEE Transactions on Industry Applications*, Vol. 28, No. 5, pp. 1095-1101, Sep./Oct. 1992.
- [4] Maxwell 2D Field Simulator, *User's Reference, Release Notes Version 6.4*, Ansoft Corporation, 1997
- [5] S. Cristina and M. Feliziani, "A finite element technique for multi-conductor cable parameters calculation", *IEEE Transactions on Magnetics*, Vol. 25, No. 4, pp. 2986-2988, July 1989.
- [6] ATP Rule Book, *ATP Solford Version of EMTP, Volume 1 and 2*, Leuven EMTP Center, 1987.

Loss Distribution of 3-phase Induction Motor with PWM Inverter Drive

Jeong-Jong Lee, Young-Kyun Kim, Kyung-Ho Ha, Jung-Pyo Hong, *Senior Member, IEEE*
Don-Ha Hwang*

Department of Electrical Engineering, Changwon National University, #9, Sarim-dong, Changwon, Gyeongnam, 641-773, Korea
Industry Applications Research Lab., Korea Electrotechnology Research Institute, P.O. Box 20, Changwon, Gyeongnam, 641-600, Korea*
E-mail: wave95@korea.com

Abstract— This paper presents the analysis of loss distribution in 3-phase induction motor using PWM (Pulse-Width Modulated) inverter drive. The analysis is based on the time-stepping finite element method. The loss of induction motor is separated into mechanical loss, conductor loss, and iron loss. The iron loss is evaluated by the frequency analysis of flux density using DFT (Discrete Fourier Transforms) and the data of iron loss curves. The iron loss curve data is provided by manufacturing company. In order to calculate loss distribution of PWM inverter fed, voltage profiles are performed. The result is compared with the sinusoidal drive loss distribution. The validity of this method is verified by the comparison of the estimated values with measured one.

INTRODUCTION

In recent years, PWM inverter drive is mainly used as the input of motor rather than sinusoidal voltage. The average voltage of the inverter output is equal to that of sinusoidal input, but it causes current ripple. And the high frequency current ripple decreases the motor performance [1]. The iron loss and conductor loss are changed in PWM waveforms. There is a need for the quantitative analysis, because it leads to improvement of motor performance. In traditional ac machine theory, the core loss is viewed as being caused mainly by the fundamental frequency variation of the magnetic field, which is not sufficiently accurate. Nick Stranges, Raymond D. Findly studied the method for predicting rotational iron losses in three phase induction motor stators [2].

In this paper, the loss distribution of induction motor is calculated considering the various frequency PWM methods. The analysis is based on the time stepping FEM (Finite Element Method). The voltage of inverter output is described according to time, and transient FEM is performed, where the time is changed on the each analysis step. And the simulation results, which are the iron loss, conductor loss, and the current, are compared with test result.

ANALYSIS MODEL AND METHODS

The 3-phase Induction Motor

The stator has 48 slots and the rotor is consisted of 40 conductor bars. Fig. 1. show the quarter cross-section of the induction motor and Table I describes main specification of

the motor. In order to compare sinusoidal voltage with PWM inverter output voltage, voltage profiles are shown in Fig. 2. Sinusoidal frequency is 60 [Hz], and PWM frequency is variable from 2-12 [kHz].

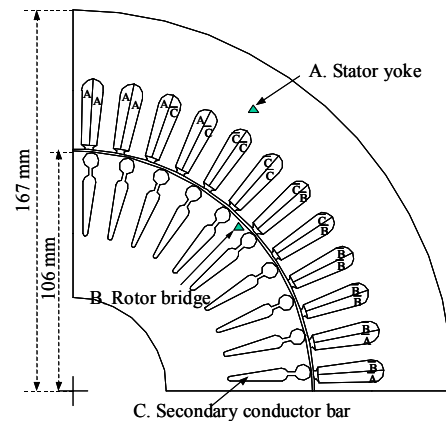


Fig. 1. Analysis model

Table I. Specifications of the induction motor

Specification	Value
Input voltage	380 (line-to-line)
Rated Output	35 (kW)
Frequency	60(Hz)

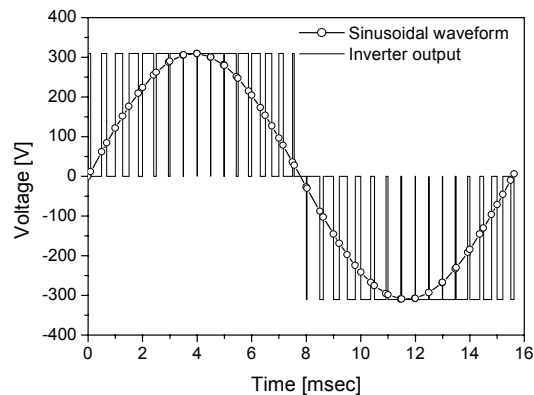


Fig. 2. The voltage profile when PWM frequency is 2 [kHz], sinusoidal frequency is 60 [Hz]

Analysis Methods

The loss of induction motor is separated into mechanical loss, conductor loss and iron loss. The mechanical loss is ignored in simulation. The conductor loss is separated into the primary winding conductor loss and secondary winding eddy current conductor loss. It is possible to calculate the conductor loss with FEA result, and the method is described in this paper. Iron loss is divided into the hysteresis loss and eddy current loss. It is difficult to estimate the eddy current loss of iron. In this paper, iron loss is calculated by the frequency analysis of flux density using DFT and iron loss data sheet [3]. The iron loss sheet is provided by core manufacturer company. Flux density of iron core is analyzed by each element harmonic component, and iron loss is calculated by the harmonic component of each element considering the magnitude of flux density and frequency. The proposed method is shown in Fig. 3.

ANALYSIS RESULTS AND CONCLUSION

Table II shows the loss distribution according to drive method. The sinusoidal current and PWM inverter drive current are shown in Fig. 4. The effect of PWM inverter is high frequency current. That current increases the conduction loss, and iron loss. When driving with PWM inverter, iron loss and conductor loss are greater than sinusoidal voltage. The flux density waveforms of elements in stator yoke and rotor bridge are shown in Fig. 5.

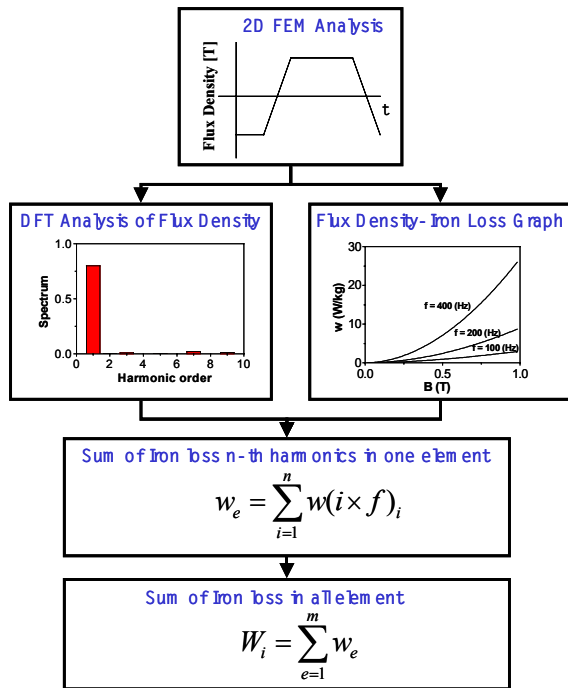


Fig. 3. Flow chart of iron loss computation

This paper presents the loss distribution of 3-phase induction motor comparing PWM inverter and sinusoidal drive. The proposed analysis method and experimental result will be reported in extend paper in detail. And the proposed method is expected that can be applied to other motors.

REFERENCES

- [1] Hyuk Nam, et al, "A Study on Iron Loss Analysis Method Considering the Harmonics of the Flux Density Waveform Using Iron Loss Curves of Epstein Samples," *Digest of CFCE 2002*, pp. 107, June 2002
- [2] Nick Stranges, Raymond D. Findly, "Methods for Predicting Rotational Iron Losses in Three Phase Induction Motor Stators," *IEEE Transactions on Magnetics*, Vol. 36, No. 6, pp. 3112-3114, September, 2000.
- [3] Fang Deng, "An Improved Iron Loss Estimation for Permanent Magnet Brushless Machines," *IEEE Transactions on Energy Conversion*, Vol. 14, No. 4, pp. 1391-1395, December, 1999.

Table II. Loss distributions

Power & Loss	Sinewave	PWM (8kHz)
Input power	43163	38135
Primary conductor loss	1190	988
Secondary conductor loss	637	818
Iron loss	640	882
Output power	39640	34391
Efficiency	91.37 %	90.60 %

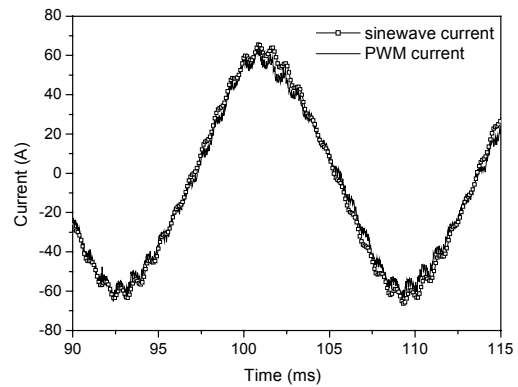


Fig. 4. Current display according to voltage profiles.

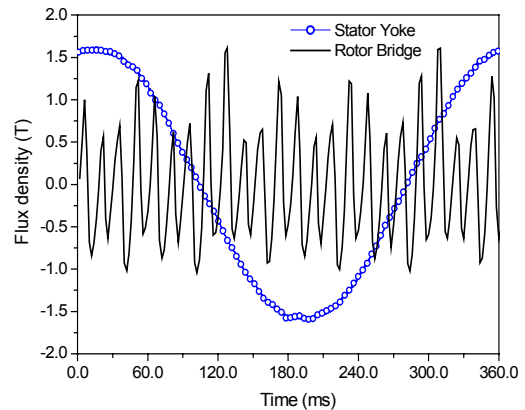


Fig. 5. The flux density waveforms of the stator yoke and the rotor bridge.

A Discrete Fourier Transform Based Method to Compute Steady State Operation of Induction Motors Using Complex Finite Elements

B. Laporte, S. Mezani, N. Takorabet
GREEN, UMR CNRS 7037 - ENSEM - INPL
02, avenue de la Forêt de Haye
Vandœuvre-lès-Nancy 54516 France
E-mail : smail.mezani@ensem.inpl-nancy.fr

Abstract- The authors propose a method to compute induction motors with consideration of space harmonics. The idea is based on computing the spectrum of the slot's currents using a discrete Fourier transform. We use the double air gap method together with complex finite elements to compute elementary problems corresponding to a harmonic order. Finally, superposition permits the determination of the electromagnetic field distribution in the whole machine. An application example is given to show the reliability of the method.

INTRODUCTION

The common methods used for analyzing induction machines with consideration of space harmonics derive from the per-phase chain equivalent circuit [1]. Finite element based methods dealing with space harmonics consist on computing once the stator source problem, i.e. field due to stator current, and to use a Fourier analysis to determine the air gap harmonic fields. Then, each of these harmonic fields is used in a second step for the coupling with a rotor problem. Finally, superposition permits the computation of the overall field in the machine [2].

In this paper, the authors propose an alternative method to compute induction machines with consideration of space harmonics. Instead of a spectral decomposition of the air gap field, we have focussed our attention on the stator currents whose spectrum is calculated using a Discrete Fourier Transform (DFT).

SLOT CURRENTS DECOMPOSITION

Let us consider a 3-phase induction motor with a spatial period of $2\pi/r$. Each period consists of N_s stator slots numbered from 0 to N_s-1 . The machine is supplied from a balanced 3-phase sinusoidal system of currents whose complex phasors are:

$$\bar{I}_q = \left(\bar{I} \exp(-j2\pi(q-1)/3) ; q = 1,3 \right) \quad (1)$$

This leads to a discrete and periodic distribution of the slot currents that forms a sequence of N_s discrete values \bar{J}_k , $k=0 \dots N_s-1$. The DFT of \bar{J}_k is:

$$\bar{Y}_n = \sum_{k=0}^{N_s-1} \bar{J}_k \exp(jnk2\pi/N_s) ; n = 0 \dots N_s-1 \quad (2)$$

It is well known that for 3-phase winding, the space harmonics are of the form $n=r \times (1 \pm 3m)$, $m \geq 0$. In the case of a p pair pole machine and integral slot winding the periodicity of the machine is $r=p$ and the harmonics reduce to $n=p \times (1 \pm 6m)$. The total stator slots being $p \times N_s$. The sequence

\bar{Y}_n states for the forward wave. Using the DFT properties, the backward wave DFT (corresponding to \bar{J}_k^*) is given by:

$$\bar{X}_n = \bar{Y}_{N_s-n}^* \quad (3)$$

The harmonic order for \bar{X}_n takes negative values.

The sequence \bar{J}_k is called the inverse DFT of the sequence \bar{Y}_n . The formula for the inverse DFT is:

$$\bar{J}_k = \frac{1}{N_s} \sum_{n=0}^{N_s-1} \bar{Y}_n \exp(-jkn2\pi/N_s) ; k = 0 \dots N_s-1 \quad (4)$$

This implies that for a harmonic order n corresponds a stator current distribution in the slots given by:

$$\bar{J}_{nk} = \bar{Y}_n \exp(-jkn2\pi/N_s) / N_s ; k = 0 \dots N_s-1 \quad (5)$$

Equation (4) naturally suggests the use of superposition to solve the multi-harmonic problems considered here. Of course, saturation can be incorporated in an average sense but this is technically incompatible with superposition principle.

ELECTROMAGNETIC MODELING

Let us consider two domains D_s and D_r of an induction machine, Fig.1. The air gap D_e is included both in D_s and D_r . The relevant Maxwell's equations under a 2D approximation and the use of a time harmonic formulation lead to the following magnetic vector potential (mvp) equations (for the n th harmonic order):

$$\nabla \cdot (\nu_s \nabla \bar{A}_{sn}) + \bar{\gamma}_{sn} = 0 \quad \text{in } D_s \quad (6)$$

$$\nabla \cdot (\nu_r \nabla \bar{A}_{rn}) - j s_n \omega_s \sigma_r \bar{A}_{rn} = 0 \quad \text{in } D_r \quad (7)$$

where ν is the magnetic reluctivity, σ the electric conductivity, s_n the slip for n th harmonic, ω_s the time pulsation and $\bar{\gamma}_{sn}$ the stator current density.

The mvp \bar{A}_{sn} and \bar{A}_{rn} must coincide in the air gap D_e . So, because they are harmonic functions, the following relations arise:

$$\bar{A}_{sn}(R_r, \theta) = \bar{A}_{rn}(R_r, \theta) \quad \text{on } \Gamma_r \quad (8)$$

$$\bar{A}_{sn}(R_s, \theta) = \bar{A}_{rn}(R_s, \theta) \quad \text{on } \Gamma_s \quad (9)$$

R_r and R_s are the radius of Γ_r and Γ_s respectively.

To determine the distribution of the mvp in the machine, we use the method described in [3] which consists on considering only the n th harmonic mvp in (8) and (9) when computing the n th harmonic problem.

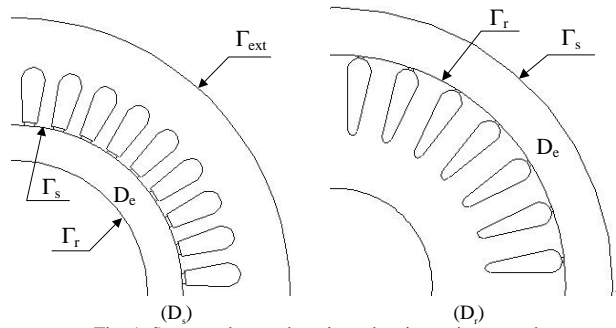


Fig. 1. Stator and rotor domains - the air gap is zoomed

The whole procedure may be described in terms of the following sequence of steps:

Step 1 Impose 3-phase complex unitary currents in the stator winding, i.e. $\bar{I}=1$ in (1) and compute the slot current DFT using (2) and (3). This allows the determination of the spectrum \bar{Y}_n and hence the significant harmonics.

Then for the n th harmonic order, proceed as follows:

Step 2 Compute the inverse DFT using (4), (5) and solve (6) using finite elements by setting $\bar{A}_{sn}=0$ on both Γ_r and Γ_{ext} . The n th mvp harmonic is computed on Γ_s .

Step 3 The stator winding is not supplied, i.e. $\bar{I}=0$ in (1). We solve (6) by setting $\bar{A}_{sn}=0$ on Γ_{ext} and $\bar{A}_{sn}(R_r, \theta) = \exp(jn\theta)$ on Γ_r . This step corresponds to the armature reaction. The n th mvp harmonic on Γ_s is then computed.

Step 4 We set $\bar{A}_m(R_s, \theta) = \exp(jn\theta)$ on Γ_s and we solve (7). The n th mvp harmonic on Γ_r is then determined.

Step 5 The mvp in the whole machine for the n th harmonic is then obtained using the coupling relations (8), (9) and the computed mvp in steps 2, 3, 4.

Step 6 Determine the total per phase flux using superposition and calculate the phase operational impedance \bar{Z}_o . The absorbed current is obtained by adding to \bar{Z}_o the stator phase resistance r_s and the end-winding phase reactance x_{ew} that is evaluated using classical formulas:

$$\bar{I} = \bar{V} / (\bar{Z}_o + r_s + jx_{ew}) \quad (10)$$

where \bar{V} is the phase terminal voltage.

For each considered harmonic order, the final value of the mvp is obtained by multiplying the actual mvp value by the stator current \bar{I} since we have assumed the linearity of the magnetic materials.

APPLICATION EXAMPLE

The method described above has been applied to compute a 3-phase, 4-pole ($p=2$), 2.2 kW, 380V, 50 Hz induction motor for which we have some experimental data. The full pitch stator winding with 3 slots per pole and phase is distributed in 36 slots. The spectrum of the slot's currents obtained in step 1 is shown in Fig. 2.

As expected for this integral slot winding, the significant harmonics are of the form $n=p \times (1 \pm 6m)$, with $m \geq 0$.

The torque/speed characteristics are shown in Fig. 3. A good agreement can be seen between the computed total torque and the experimental data. The starting torque is overestimated if we consider only the first space harmonic. The asynchronous crawling is clearly illustrated by the dip in the total torque characteristic near the synchronous speed of each space harmonic.

CONCLUSION

A novel DFT based method to compute induction motors with consideration of space harmonics has been presented in this paper. The use of complex finite elements allows a significant reduction of the computation time. The presented results reveal the effectiveness of the method when tracking steady state operation.

REFERENCES

- [1] P. L. Alger, *Induction machines - Their behavior and uses*, Gordon and Breach Science Publishers, 3rd edition, 1995.
- [2] H. De Gerssem, K. Hamayer and T. Weiland, "Time-harmonic finite element machine analysis including higher harmonic air gap fields," *Proc. ICEM*, Brugge, Belgium, August 2002.
- [3] G. Vinsard and B. Laporte, "A new formulation for induction machine computation," *IEEE Transactions on Magnetics*, vol. 30, no. 5, pp. 3693-3696, 1994.

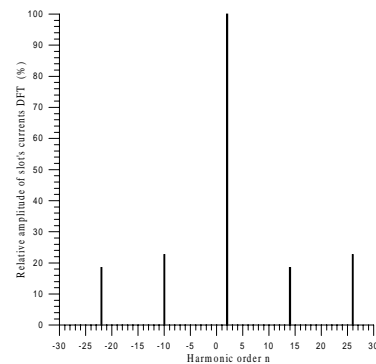


Fig. 2. Spectrum of slot's currents obtained by means of a DFT

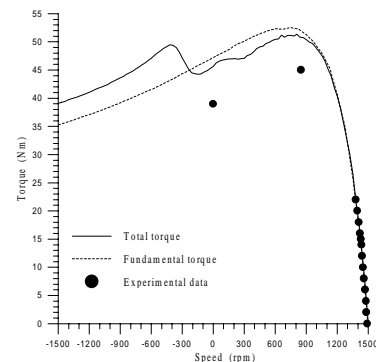


Fig. 3. Speed - torque characteristics

Finite element analysis of a double winding induction motor with a special rotor bars topology

A.M. Oliveira¹, P. Kuo-Peng¹, N. Sadowski¹, F. Rüncoş², R. Carlson¹, P. Dular³

¹ GRUCAD-EEL-CTC-UFSC, C.P. 476, 88040-900 – Florianópolis-SC-Brazil

² WEG Indústrias Ltda, Jaraguá do Sul-SC-Brazil

³ ELAP - Institut Montefiore, B. 28, 4000 – Liège-Belgium
goga@grucad.ufsc.br

Abstract— A model allowing the simulation of induction machines with different rotor bars configurations is presented. The electrical machine is modelled by using 2D FEM and its equations are directly coupled with the circuit ones. A general and new contribution is added for the consideration of special rotor bars topologies. The movement is taken into account by means of the Moving Band technique, the Maxwell stress tensor and the mechanical oscillation equation. The model is applied to a double winding induction motor with a special rotor bars configuration.

INTRODUCTION

Double winding induction motors are usually used in wind energy generation. Its performance when it is double supplied presents certain features of practical interest [3]. By using appropriate drive, it is possible to control the induction machine to operate as generator working above the synchronous speed as well as under the synchronous speed. This is especially convenient when a variable speed-constant frequency is required. In this article a double winding induction machine with a special rotor bar topology is modeled using the finites elements method.

METHODOLOGY

The electrical machine is modeled in a 2D domain, using the Maxwell equations to formulate the field behavior and the FEM to discretize the domain. The formulation uses the magnetic vector potential as unknown, the Galerkin method to obtain the set of equations to be solved numerically, the Euler recurrence method to discretize the temporal derivatives and the Newton-Raphson method to consider the non-linear characteristic of magnetic materials. This, arise to the equation below:

$$\mathbf{M}(\mu) \cdot \mathbf{A}(t) + \mathbf{N} \cdot p\mathbf{A}(t) - \mathbf{P} \cdot \mathbf{I}_f(t) - \mathbf{P}' \cdot \mathbf{U}_t(t) = \mathbf{D} \quad (1)$$

In (1) \mathbf{A} is the magnetic vector potentials; \mathbf{I}_f , the electric currents in the thin conductors; \mathbf{U}_t , the electric voltages in the thick conductors; \mathbf{M} , the matrix related to permeability; \mathbf{N} , the matrix related to electric conductivity; \mathbf{P} , the matrix that relates the thin current elements and its nodes; \mathbf{P}' , the matrix that relates the thick voltage elements and its nodes; \mathbf{D} , the vector related to permanent magnet contributions and p , the time derivative operator.

Thin conductors fed by external electric circuit, as static converters, form the machine windings. The direct-coupled equations that describe this connection are [2]:

$$\begin{aligned} \mathbf{Q} \cdot p\mathbf{A}(t) + \mathbf{R} \cdot \mathbf{I}_f(t) + \mathbf{L} \cdot p\mathbf{I}_f(t) &= \mathbf{G}_4 \cdot \mathbf{X}(t) + \mathbf{G}_5 \cdot \mathbf{E}(t) + \mathbf{G}_6 \cdot \mathbf{I}_f(t) \\ \mathbf{G}_1 \cdot \mathbf{X}(t) + \mathbf{G}_2 \cdot \mathbf{E}(t) + \mathbf{G}_3 \cdot \mathbf{I}_f(t) &= p\mathbf{X}(t) \end{aligned} \quad (2)$$

where \mathbf{Q} is the matrix associated with flux linkage; \mathbf{R} and \mathbf{L} correspond respectively to diagonal matrix representing the resistances and end windings inductances matrices; \mathbf{X} , the circuit state variables vector; \mathbf{E} , the independent electric sources vector and \mathbf{G}_1 to \mathbf{G}_6 , matrices that depend on the circuit topology. If semi-conductors are present in the circuit, their commutation are automatically determined and \mathbf{G}_1 to \mathbf{G}_6 , automatically actualized.

Different combinations of thick conductors connections can be taken into account. We can consider and describe them by:

$$\begin{aligned} \mathbf{Q}' \cdot p\mathbf{A}(t) - \mathbf{1} \cdot \mathbf{U}_t(t) + \mathbf{R}' \cdot \mathbf{I}_t(t) &= \mathbf{0} \\ \mathbf{C}_1 \cdot \mathbf{U}_t(t) + \mathbf{C}_2 \cdot \mathbf{I}_t(t) &= \mathbf{E}_t \end{aligned} \quad (3)$$

where \mathbf{Q}' is the matrix associated with flux linkage; $\mathbf{1}$, the identity matrix; \mathbf{R}' , a diagonal matrix representing thick conductors resistances; \mathbf{E}_t , the independent voltage sources vector; \mathbf{C}_1 and \mathbf{C}_2 , matrices depending of thick conductors connection. The most common topologies found in practical applications are series (Fig. 1) and parallel (Fig. 2) connections.

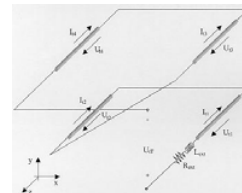


Fig. 1. Series connection of thick conductors.

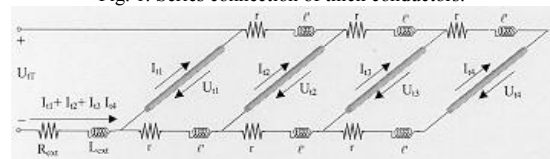


Fig. 2. Parallel connection of thick conductors.

For a series configuration we can write:

$$\begin{bmatrix} +1 & -1 & +1 & \dots & -1 \\ 0 & 0 & 0 & \dots & 0 \\ 0 & 0 & 0 & \dots & 0 \\ \vdots & \vdots & \vdots & \ddots & \vdots \\ 0 & 0 & 0 & \dots & 0 \end{bmatrix} \begin{bmatrix} U_{t1} \\ U_{t2} \\ U_{t3} \\ \vdots \\ U_{tm} \end{bmatrix} + \begin{bmatrix} Z_{ext} & 0 & 0 & \dots & 0 \\ 1 & 1 & 0 & \dots & 0 \\ 0 & 1 & 1 & \dots & 0 \\ \vdots & \vdots & \vdots & \ddots & \vdots \\ 0 & 0 & 0 & \dots & 1 \end{bmatrix} \begin{bmatrix} I_{t1} \\ I_{t2} \\ I_{t3} \\ \vdots \\ I_{tm} \end{bmatrix} = \begin{bmatrix} U_{tT} \\ 0 \\ 0 \\ \vdots \\ 0 \end{bmatrix} \quad (4)$$

where $Z_{ext} = R_{ext} + j\omega L_{ext}$ can be an external resistance and inductance or a resistance and an inductance related to the end windings. U_{IT} is an external voltage feeding source, which is equal to 0 if the coil is short-circuited.

For a parallel configuration, we have:

$$\begin{bmatrix} +1 & 0 & 0 & \dots & 0 \\ -1 & +1 & 0 & \dots & 0 \\ 0 & -1 & +1 & \dots & 0 \\ \vdots & \vdots & \vdots & \ddots & \vdots \\ 0 & 0 & 0 & \dots & +1 \end{bmatrix} \begin{bmatrix} U_{I1} \\ U_{I2} \\ U_{I3} \\ \vdots \\ U_m \end{bmatrix} + \begin{bmatrix} Z_{ext} & Z_{ext} & Z_{ext} & \dots & Z_{ext} \\ 0 & z & z & \dots & z \\ 0 & 0 & z & \dots & z \\ \vdots & \vdots & \vdots & \ddots & \vdots \\ 0 & 0 & 0 & \dots & z \end{bmatrix} \begin{bmatrix} I_{I1} \\ I_{I2} \\ I_{I3} \\ \vdots \\ I_m \end{bmatrix} = \begin{bmatrix} U_{IT} \\ 0 \\ 0 \\ \vdots \\ 0 \end{bmatrix} \quad (5)$$

where $z = 2r + 2\ell p$ are the resistance and inductance associated to end-winding parameters.

A particular case of parallel connection is the squirrel-cage of the induction motors (Fig. 3) [1].

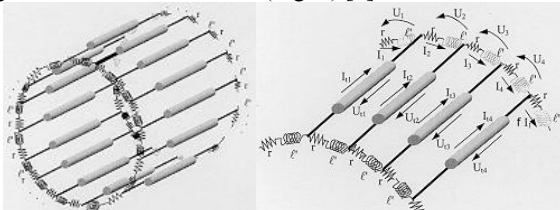


Fig. 3. Squirrel-cage: parallel connected and thick conductors short-circuited.

For this case we can write:

$$\begin{bmatrix} z & 0 & 0 & \dots & 0 \\ 0 & z & 0 & \dots & 0 \\ 0 & 0 & z & \dots & 0 \\ \vdots & \vdots & \vdots & \ddots & \vdots \\ 0 & 0 & 0 & \dots & z \end{bmatrix} \begin{bmatrix} U_{I1} \\ U_{I2} \\ U_{I3} \\ \vdots \\ U_m \end{bmatrix} + \begin{bmatrix} -1 & 0 & 0 & \dots & f \\ +1 & -1 & 0 & \dots & 0 \\ 0 & +1 & -1 & \dots & 0 \\ \vdots & \vdots & \vdots & \ddots & \vdots \\ 0 & 0 & 0 & \dots & -1 \end{bmatrix} \begin{bmatrix} I_{I1} \\ I_{I2} \\ I_{I3} \\ \vdots \\ I_m \end{bmatrix} = \begin{bmatrix} 0 \\ 0 \\ 0 \\ \vdots \\ 0 \end{bmatrix} \quad (6)$$

where f equals to 1 for periodicity condition and -1 if we have antiperiodic conditions.

The Moving Band technique is chosen to consider the movement during the field calculation [4].

The multi-slice technique can be used to consider the skewing of stator slots. In this technique, the motor is divided into M slices uniformly distributed along its axis [1]. In each slice the magnetic potential and the electric currents have only an axial component. The strong coupling between all slices is imposed by the continuity of the currents flowing through them.

RESULTS

The method is applied to a double winding induction motor with a special rotor bars configuration (Fig. 4). This motor has 72 stator slots and 50 rotor bars. Its windings are distributed into four layers, the two inner layer occupied by the main 8 poles winding and the outer ones by the auxiliar 12 poles winding. The rotor bars are connected in a 10 poles configuration containing series and parallel connections, as shown in Fig. 4b. Table I shows the main characteristics of the motor.

Stator diameters	350 – 480 mm	Rotor diameters	122 – 347.5 mm
Inertia	5.6 kg.m ²	Depth	420 mm
Voltage	380 V _{RMS}	Frequency	60 Hz

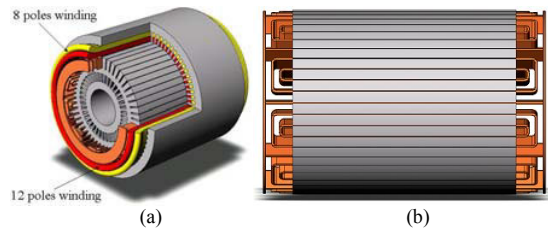


Fig. 4. (a) Double winding induction motor, (b) Rotor bars configuration

The 8 poles winding is fed by a three-phase sinusoidal source and the 12 poles winding is short-circuited. Both windings are Y connected and have no electric connection with each other. Fig. 5 and 6 shows some simulation results obtained for this configuration and Fig. 7 shows the magnetic flux distribution in steady-state operation.

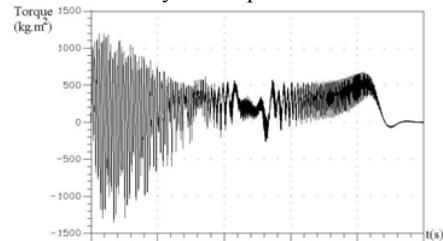


Fig. 5. Torque (kg.m²) transient waveforms.

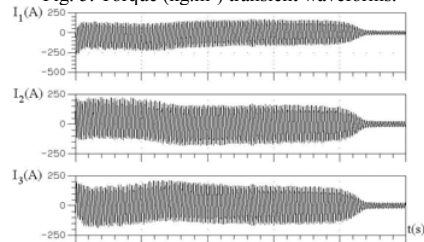


Fig. 6. 8 poles winding currents (A) waveform transient.

Fig. 7. Flux distribution in steady-state operation.

CONCLUSIONS

A method coupling directly the electromagnetic field, the external circuit and the movement equations is presented. Consideration of different thick conductors connection is made allowing the analysis with several topologies. The methodology is used in the simulation of a non-conventional induction machine.

REFERENCES

[1] A. Tenhunen, A. Arkkio, "Modelling of induction machines with skewed rotor slots", IEE Proc.-Electr. Power Application, Vol. 148, No. 1, pp. 45-50, January 2001.
 [2] A. M. Oliveira, P. Kuo-Peng, M. V. Ferreira da Luz, N. Sadowski, J. P. A. Bastos, "Generalization of coupled circuit-field calculation for polyphase structures", IEEE Trans. On Magn., Vol. 37, No. 5, pp. 3444-3447, September 2001.
 [3] Luca De Camillis, Marco Matuonto, Antonello Monti, Alberto Vignati, "Optimizing current control performance in double winding asynchronous motors in large power inverter drives", IEEE Trans. On Power Electronics, Vol. 16, No. 5, pp. 676-685, September 2001.
 [4] N. Sadowski, Y. Lefevre, M. Lajoie-Mazenc, J. Cros, "Finite element torque calculation in electrical machines while considering the movement", IEEE Trans. on Magn., Vol. 28, No. 2, pp. 1410-1413, March 1992.

Calculation of the Rotor Bar Resistance and Leakage Inductance in a Solid-Rotor Induction Motors with a One Slot Model

L. T. Ergene¹, S.J.Salon², Y.Akiyama³

¹ Magsoft Corporation
Peoples Avenue Troy NY 12180

Phone: +1 518 271 1352 – fax: +1 518 271 8366 - e-mail: lal@magsoft-flux.com

² Rensselaer Polytechnic Institute
ECSE Department
110 8th Street Troy NY 12180 USA
e-mail: salons@rpi.edu

³ Small Motors Laboratory
Heiwa Plaza #305 8-12 Toyooka Tsurumi-Ku
Yokohama-Shi 230-0062 Japan
e-mail: office@sml-nb.co.jp

Abstract—This paper presents a one slot finite element model of a specific type of induction motor, a solid rotor induction motor. This machine will have eddy currents and extra losses inside the rotor since the rotor doesn't have the lamination. The reason for creating a one-slot model of the solid rotor induction motor is to simplify the model and reduce the computational time while still retaining the ability to compute the rotor bar resistance and the leakage reactance. The paper shows how to model one slot at the low frequency applications and gives the comparison between one slot and the entire induction motor results.

Index terms—solid rotor induction motor, active power losses, one-slot model, rotor bar resistance and leakage inductance.

I. INTRODUCTION

The Finite Element Method has many advantages compared to the other numerical methods such as handling complex geometries, nonlinearity etc. [1]. Since the rotor body and rotor bars are made of conducting material in the solid rotor induction motor, the eddy current problem would arise. In that case, the Finite Element Model will be based on the nodal solution of the nonlinear/linear diffusion equations. One slot gives the smaller model compare to the entire machine and this helps to reduce computation time significantly. This approach has been used to calculate rotor bar resistance, leakage inductance, end ring resistance and inductance for the conventional type of induction motors previously [2],[3].

II. THEORY

To define appropriate boundary conditions for this model is the most critical point. Since a one-slot model is used, periodic boundary conditions will be imposed along the radial boundaries. The radial boundaries show that the one slot model is just one portion of the complete machine which carries 2p pole MMF distribution. The motor section with the regions is shown in Figure 1. The magnetic vector potential relationship between the radial sides of the boundary is given by equation 1:

$$\vec{A}_2 = \vec{A}_1 e^{-j\alpha p} \quad (1)$$

In the equation α and p denote rotor slot pitch and number of pole pairs, respectively.

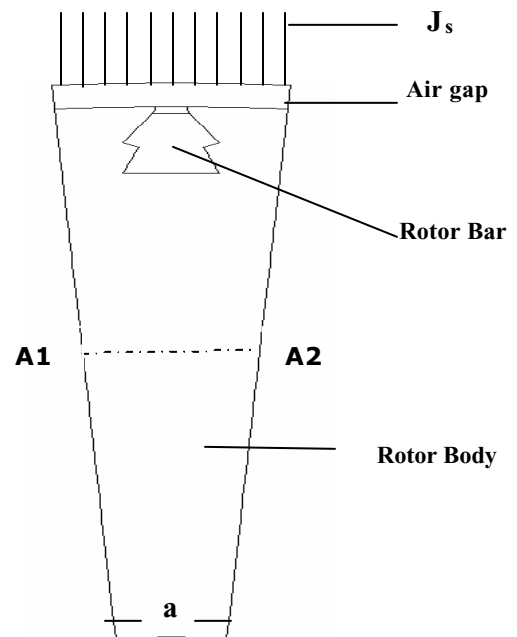


Fig. 1. The rotor tooth-pitch model of the solid rotor induction motor.

The inner arc portion is assumed to be impermeable to flux, so the vector potential value is defined as a constant, which is the Dirichlet boundary condition. The outer radial boundary of the one-slot pitch model is defined as an MMF source representing the stator equivalent current sheet. This value should give the same fundamental airgap flux density as the actual stator. The harmonics due to stator slotting and phase belts are not included. The outer boundary corresponding to the stator bore has been defined as a line or shell region to impose a current sheet (or vector potential) along that arc.

III. IMPLEMENTATION

The stator phase current is obtained from the AC steady state (magneto-dynamic) solution. The use of the phase current on the line region will not satisfy the required boundary conditions, so the total ampere-turn equivalent current for the one slot pitch of the motor is applied on that surface. The current is distributed along the arc by taking into account the phase angle. Figure 2,3,4 show the one slot model results for different low frequency levels. The flux lines are getting more concentrated to the air gap when the frequency increases as expected.

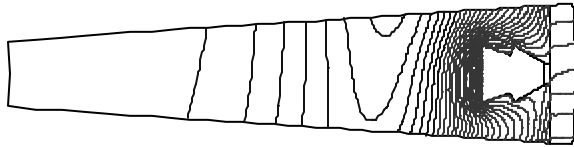


Fig. 2. The equi-flux lines at 1 Hz.

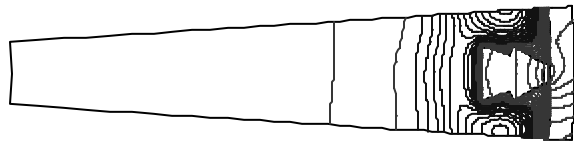


Fig. 3. The equi-flux lines at 8 Hz.

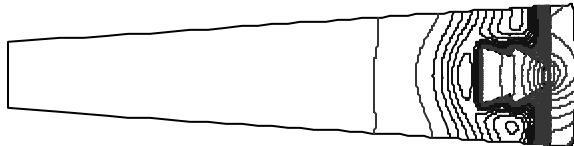


Fig. 4. The equi-flux lines at 16 Hz.

The equivalent ac resistance of the bar is computed by equating the Joule loss.

$$R_{ac} = \frac{\int J_r \cdot J_r^* ds}{s I_r^2} \quad (2)$$

The rotor leakage inductance is due to the entire rotor driven flux which crosses the slot. By using the stored energy in the rotor bar, the equivalent inductance can be calculated as follows:

$$L_{slot} = \frac{l_b}{\mu_0 I^2} \int_s |B|^2 ds \quad (3)$$

IV. RESULTS

Table 1 shows the rotor bar resistance and the leakage reactance comparison between the analytical and Finite Element results for the one slot model.

TABLE I THE ROTOR BAR RESISTANCE AND LEAKAGE INDUCTANCE

	Inductance (H)	Resistance (Ohm)
Finite Element	1.58E-6	6.1e-4
Analytical	1.56 e-6	6.1e-4

Figure 5 and 6 shows the resistance and leakage inductance of the bar as a function of the rotor frequency.

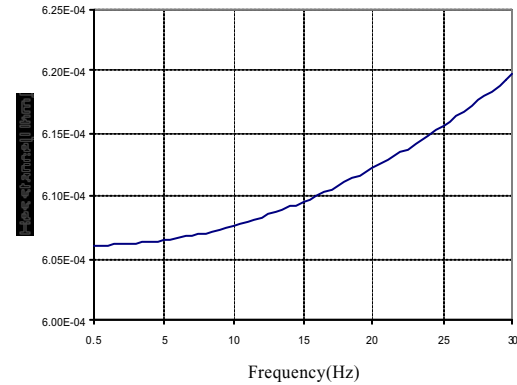


Fig. 5. The resistance of the rotor bar.

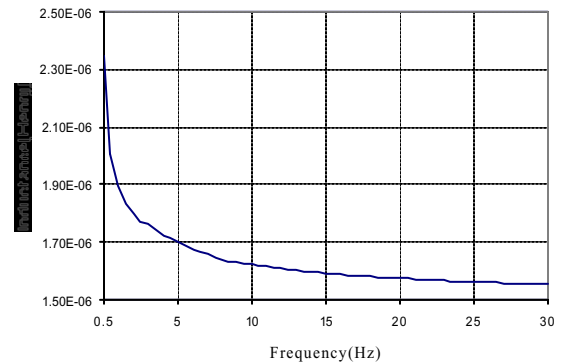


Fig. 6. The inductance of the rotor bar.

V. CONCLUSION

This paper gives the basic concepts, the finite element formulation and implementation strategies of the one slot model. The rotor bar resistance and the leakage inductance can be computed for that specific type of the motor. The future work is going to show how to extract magnetizing reactance value from the total reactance at the one slot model. The paper also will include how the rotor conductivity affects the results.

REFERENCES

- [1] Chari, M.V.K., Salon, S.J. "Numerical Methods in Electromagnetism". Academic Press, 2000.
- [2] Williamson, S. "Calculation of the bar resistance and Leakage Reactance of Cage Rotors with Closed Slots". IEE Proceedings, Vol.132, Pt.B, No.3, May 1985.
- [3] Flux2D User's Guide. Version 7.6. CEDRAT/ MAGSOFT, January 2002.

The Mutual Inductance of Two Thin Coaxial Disk Coils in Air

*Slobodan Babic, *Cevdet Akyel, *Member, IEEE* and **Sheppard Salon, *Fellow, IEEE*
*École Polytechnique, Département de Génie Électrique et Informatique, H3C 3A7 Montréal, Québec, Canada
e-mail: babics@grmes.polymtl.ca; akyel@grmes.polymtl.ca
**Rensselaer Polytechnic Institute, Troy, New York, 12180-3590, USA
e-mail: salons@rpi.edu

Abstract— This paper deals with two efficient approaches for determining the mutual inductance between two thin coaxial disk coils in air. In the first approach we give new expressions for calculating the mutual inductance of these configurations. These results are expressed in terms of the complete elliptical integrals of the first and second kind, Heuman's Lambda function and some terms that must be evaluated numerically. Another approach is based on the filament method where all conductors are approximated by a set of Maxwell's coils. These new expressions are accurate and simple. All results obtained by the two approaches are in excellent agreement. Also we compare these results to those obtained by laboratory measurements.

I. INTRODUCTION

CIRCULAR coils are widely used in various electromagnetic applications such as coil guns, tubular linear motors, single layer coils and current reactors. The mutual inductance as a fundamental electrical engineering parameter for a coil can be computed by applying the Biot - Savart law directly or using other alternate methods ([1] -[5]). Today FEM and BEM methods are routinely used for magnetostatic problems, but these methods have accuracy problems near sharp surface discontinuities unless a high density of elements is used, [6]. Exact methods based on elliptic integral solutions for current loops have existed since at least the time of Maxwell but were laborious without computers. In [2] expressions are given for calculating the mutual inductance of two thin disk coils in the same plane. The purpose of this article is to present an elliptic integral-based solution for two coaxial disk coils that are separated. This calculation leads to very accurate expressions obtained in terms of the complete elliptical functions of the first and second kind, Heuman's Lambda function and some terms that have to be evaluated using numerical integration. These terms must be solved numerically because the analytical solutions do not exist and kernel functions are not always smooth and continuous functions. Also, we give an other approach based on filament method, [3] where some modifications lead to very simple procedures for calculating the mutual inductance of two thin disk coils using the well-known formula for Maxwell's coils [4], [5]. It will be useful to compare the accuracy and the computational cost of both proposed methods.

II. CALCULATION METHOD

In [2] a basic formula from which the mutual inductance is derived for two thin coaxial circular disk coils with constant current density (see Fig. 1) is given by,

$$M = \frac{\mu_0 N_1 N_2}{(R_2 - R_1)(R_4 - R_3)} \int_0^{\pi} \int_{R_1}^{R_2} \int_{R_3}^{R_4} \frac{\cos \theta r_1 r_2 dr_1 dr_2 d\theta}{r_{QN}} \quad (1)$$

where

$$r_{QN} = \sqrt{z_Q^2 + r_1^2 + r_2^2 - 2r_1 r_2 \cos \theta}, \quad z_Q = z_2 - z_1$$

and N_1, N_2 are total number of turns.

In (1) we integrate over r_1, r_2 and θ respectively. The mutual inductance of the system thin disk coil - thin disk is

$$M = \frac{\mu_0 N_1 N_2}{3(R_2 - R_1)(R_4 - R_3)} \sum_{n=1}^{n=4} (-1)^{n-1} T_n \quad (2)$$

where

$$\begin{aligned} T_n = & -\frac{2l_n \rho_n \sqrt{l_n \rho_n}}{k_n} E(k_n) + k_n \sqrt{l_n \rho_n} [z_Q^2 - l_n^2 - \rho_n^2 \\ & + \rho_n \sqrt{\rho_n^2 + z_Q^2} + l_n \sqrt{l_n^2 + z_Q^2}] K(k_n) \\ & - \pi |z_Q| \left| \frac{\rho_n \sqrt{\rho_n^2 + z_Q^2}}{2} [1 - \Lambda_0(\theta_{1n}, k_n) - \operatorname{sgn}(\sqrt{\rho_n^2 + z_Q^2} - l_n) \right. \\ & \times (1 - \Lambda_0(\theta_{2n}, k_n))] - \pi |z_Q| \left| \frac{l_n \sqrt{l_n^2 + z_Q^2}}{2} [1 - \Lambda_0(\theta_{3n}, k_n) \right. \\ & \left. - \operatorname{sgn}(\sqrt{l_n^2 + z_Q^2} - \rho_n) \times (1 - \Lambda_0(\theta_{4n}, k_n))] \right| \\ & - \frac{z_Q^3}{2} J_{1n} + \rho_n^3 J_{2n} + l_n^3 J_{3n} \end{aligned}$$

$$\rho_1 = \rho_2 = R_1; \rho_1 = \rho_2 = R_2; l_1 = l_4 = R_3; l_2 = l_3 = R_4$$

$$r_{QN}^+ = \sqrt{l_n^2 + \rho_n^2 + z_Q^2 + 2l_n \rho_n \cos(\beta)}, \quad r_{QN}^- = \sqrt{l_n^2 + \rho_n^2 + z_Q^2 - 2l_n \rho_n \cos(\beta)}$$

$$\begin{aligned} f(\beta) = & \frac{1}{\sin(\beta)} \left[a \tan \frac{z_Q^2 \cos(\beta) + \rho_n l_n \sin^2(\beta)}{z_Q \sin(\beta) r_{QN}^-} \right. \\ J_{1n} = & \int_0^{\pi/2} f(\beta) d\beta, \\ & \left. - a \tan \frac{z_Q^2 \cos(\beta) - \rho_n l_n \sin^2(\beta)}{z_Q \sin(\beta) r_{QN}^+} \right] \end{aligned}$$

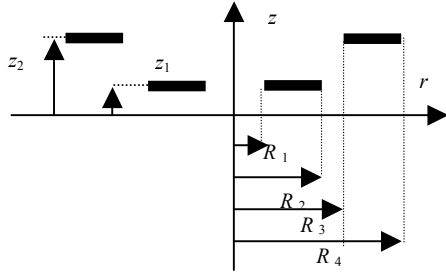


Fig 1. Thin coaxial disk coils

$$J_{2n} = \int_0^{\pi/2} a \sinh \frac{l_n + \rho_n \cos 2\beta}{\sqrt{\rho_n^2 \sin^2(2\beta) + z_Q^2}} d\beta, \quad k_n^2 = \frac{4\rho_n l_n}{(l_n + \rho_n)^2 + z_Q^2}$$

$$J_{3n} = \int_0^{\pi/2} a \sinh \frac{\rho_n + l_n \cos 2\beta}{\sqrt{l_n^2 \sin^2(2\beta) + z_Q^2}} d\beta, \quad m_n = \frac{2\rho_n}{\sqrt{\rho_n^2 + z_Q^2} + \rho_n}$$

$$p_n = \frac{2l_n}{\sqrt{l_n^2 + z_Q^2} + l_n}, \quad \theta_{1n} = \arcsin \frac{|z_Q|}{\sqrt{\rho_n^2 + z_Q^2} + \rho_n}$$

$$\theta_{2n} = \arcsin \sqrt{\frac{1-m_n^2}{1-k_n^2}}, \quad \theta_{3n} = \arcsin \frac{|z_Q|}{\sqrt{l_n^2 + z_Q^2} + l_n}, \quad \theta_{4n} = \arcsin \sqrt{\frac{1-p_n^2}{1-k_n^2}}$$

It is important to mention that the function $f(\beta)$ is not a smooth function at one of its ends and has a singularity.

III. EXAMPLES

To verify the validity of presented expressions let us solve the following problem.

The coil dimensions are as follows:

New approach :

$R_1 = 10$ (cm), $R_2 = 20$ (cm), $R_3 = 30$ (cm), $R_4 = 40$ (cm),

$z_Q = 10$ (cm), $N_1=100$, $N_2=100$

Filament method :

$R_1 = 15$ (cm), $R_{II} = 35$ (cm), $a = b = 10$ (cm), $N_1 = 100$, $N_2 = 100$, $c = 10$ (cm).

The new approach gives the mutual inductance (using the Gaussian numerical integration) as,

$$M_{\text{This work}} = 1,22625644 \text{ (mH)}$$

Execution time was 0.1099 seconds.

TABLE I
COMPARISON OF COMPUTATIONAL EFFICIENCY

N/n subdivisions	M_{Filament} (mH)	Computational Time (Seconds)	Error (%)
10/10	1,22613781	0,28	0,00967416
50/50	1,22625131	5,22	0,00041835
100/100	1,22625515	20,54	0,00010520
500/500	1,22625639	604,12	0,00000408
1000/1000	1,22625643	2568,48	0,00000008

In Table I we find the values of the mutual inductance using the filament method, [3]. Also the corresponding computational time and the absolute error of calculation regarding to the exact values are given. From Table I one can conclude that all results obtained using the two approaches are in good agreement. Nevertheless, one has to make more subdivisions using the filament method, thus somewhat increasing the computational cost (the case of 500/500 subdivisions and more). We tested three types of numerical integrations (Gaussian, Simpson and Lobatto) to solve the integrals J_{1n} , J_{2n} and J_{3n} . These quadratures have been tested because all kernel functions are not smooth functions and could have oscillations on the interval of integration.

Next example is the system of two duplicate disk-shaped coils, [8] for which $R_1 = 7,62$ (cm), $R_2 = 15,94$ (cm), $R_3 = 7,62$ (cm), $R_4 = 15,94$ (cm), $z_Q = 4,68$ (cm), $N_1=516$, $N_2=516$. The formula for the mutual inductance given in [5] has been checked by a laboratory measurement on these disk coils. The measured value of the mutual inductance was 0,0374 (H). The calculated value given in [5] is 0,0366 (H). The mutual inductance found by the new method was 0,03655608 (H), and by the filament method 0,03655629 (H). We can see that results are in very good agreement.

IV. CONCLUSION

New accurate mutual-inductance expressions for two thin disk coils are derived and presented in this paper. This proposed approach has been verified by the filament method and laboratory measurements. The results are obtained in terms of complete elliptic integrals of the first, second kind, Heuman's Lambda function and three terms, which have to be solved numerically using the single integration. We tested three types of numerical integrations because to evaluate the accuracy and the computational cost. Even though one might think that the proposed method is 'tedious' because of special elliptic integrals and some terms that have to be solved using one of the numerical integrations schemes, we have developed fast procedures to easily calculate the mutual inductance of the treated configurations. The results are in very good agreement with already published data.

V. REFERENCES

- [1] S.Babic, C.Akyel and S. J. Salon, "New Procedures for Calculating the Mutual Inductance of the system: Filamentary Circular Coil-Massive Circular Solenoid", CEFC Conference on Electromagnetic Field Computation, 16-20 June, 2002, Perugia, Italy.
- [2] S. Babic and C. Akyel, "An Improvement in Calculation of the Self- and Mutual Inductance of Thin-Wall Solenoids and Disk Coils", *IEEE Transactions on Magnetics*, Vol. 36, No.4, pp. 1970-1975, July 2000.
- [3] Ki-Bong Kim, E. Levi, Z. Zabar and L. Birenbaum, "Mutual Inductance of Noncoaxial Circular Coils with Constant Current Density", *IEEE Transactions On Magnetics*, Vol. 33, No. 5, pp. 3916-3921, September 1997.
- [4] F. W. Grover, "Inductance Calculations", New York: Dover, 1964
- [5] H. B. Dwight, "Electrical Coils as Conductors", McGraw-Hill Book Company, INC. New York, 1945.
- [6] J.T.Conway, "Exact Solutions for the Magnetic Fields of Axisymmetric Solenoids and Current Distributions", *IEEE Transactions On Magnetics*, Vol. 37, No.4, pp. 2977-2988, July 2001..

Two Mixed Hybrid Formulations for Magnetostatics in Unbounded Domains

Leila Hamouda, Bernard Bandelier, Françoise Rioux-Damidau,
U2R2M, Université Paris XI, UMR CNRS 8081, Bat 220, 91405 Orsay - France
E-mail: Bernard.Bandelier@u2r2m.u-psud.f

Abstract—We present two mixed hybrid formulations for magnetostatics in an unbounded domain. The first one (HMH) is H-oriented, the second one (BMH) is B-oriented. Inside each finite element we use edge elements for H and facet elements for B but we do not impose any continuity at the interelement boundaries. Lagrange multipliers are introduced in order to relax the tangential continuity of H in HMH and the normal continuity of B in BMH. The “mass matrix” obtained is then block-diagonal and the linear system is solved more easily. The two methods are compared.

INTRODUCTION

The mixed formulations are becoming increasingly popular [1], [2]. However, their discretization by means of a finite element method yields to a linear system, the matrix of which is indefinite and ill-conditioned. Several methods are generally used to solve this linear system. Another technique is the use of Lagrangian multipliers in order to impose normal or tangential continuity at the interelement boundaries. Then, a symmetric and definite positive system has to be solved instead of the indefinite one. This method was studied theoretically in [3] where it was shown that Lagrange multipliers provide a better accuracy than that obtained directly.

In previous papers, we established two mixed formulations. In the first one, the principal unknown was the magnetic field while the auxiliary unknown was a vector potential [4]. In the second one, the principal unknown was the flux density, a scalar potential being the auxiliary unknown [5].

In this paper, we propose a hybridation technique for each of these two methods by introducing Lagrangian multipliers at the interelement boundaries. The magnetic field is expanded with edge functions inside each finite element and then its tangential continuity is no longer imposed by the shape functions but by mean of a vectorial Lagrange multiplier. The same technique is used for the B-oriented method. The flux density is expanded with facet functions inside each finite element and its normal continuity is satisfied thanks to a scalar Lagrange multiplier. We then obtain a greater number of unknowns, but the matrices are block diagonal.

MIXED HYBRID VARIATIONAL FORMULATION

We consider a domain Ω made of materials having a permeability $\mu = \mu_0 \mu_r$. Γ denotes its boundary. Ω is

divided into N sub-domains Ω_i (generally the finite elements), each one having a boundary $\partial\Omega_i$. Ω is imbedded in a static magnetostatic source H^s .

In the H-oriented mixed hybrid formulation, magnetic field H in Ω and reduced potential φ on Γ are the principal unknowns; vector potential A in Ω is an auxiliary unknown. Moreover, a vectorial Lagrange multiplier ξ is introduced on the $\partial\Omega_i$ to force the H tangential component continuity. The H-oriented mixed hybrid formulation (HMH) is so written:

For a given source field H^s , find (H, φ, A, ξ) such that:

$$\begin{aligned} \int_{\Omega} \mu H \cdot H' d\Omega - \mu_0 \int_{\Gamma} \frac{\partial \varphi}{\partial n} \varphi' d\Gamma - \sum_{i=1, N} \int_{\Omega_i} A \cdot \text{curl } H' d\Omega \\ + \sum_{i=1, N} \int_{\partial\Omega_i} \xi \cdot H' \times n dS = \mu_0 \int_{\Gamma} H^s \cdot n \varphi' d\Gamma, \\ \sum_{i=1, N} \int_{\Omega_i} \text{curl } H \cdot A' d\Omega = 0, \\ \sum_{i=1, N} \int_{\partial\Omega_i} \xi' \cdot H \times n dS = 0. \end{aligned}$$

In the B-oriented mixed hybrid formulation, the flux density B is the principal unknown and the scalar reduced potential φ is an auxiliary unknown, both in Ω . In order to force the B normal component continuity on boundaries $\partial\Omega_i$, a scalar Lagrange multiplier λ is introduced on each $\partial\Omega_i$. The B-oriented mixed hybrid formulation (BMH) is then:

For a given source field H^s , find (B, φ, λ) such that:

$$\begin{aligned} \sum_{i=1, N} \int_{\Omega_i} \nu B \cdot B' d\Omega - \int_{\Gamma} \varphi B' \cdot n d\Gamma \\ + \sum_{i=1, N} \int_{\Omega_i} \varphi \text{div } B' d\Omega + \sum_{i=1, N} \int_{\partial\Omega_i} \lambda B' \cdot n dS \\ = \sum_{i=1, N} \int_{\Omega_i} H^s \cdot B' d\Omega, \\ \sum_{i=1, N} \int_{\Omega_i} \text{div } B \varphi' d\Omega = 0, \\ \sum_{i=1, N} \int_{\partial\Omega_i} \lambda' B \cdot n dS = 0. \end{aligned}$$

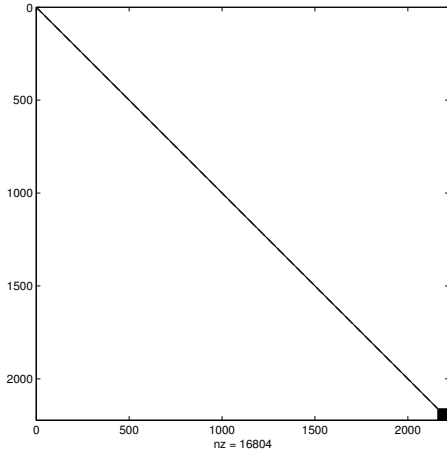


Fig. 1. Matrix M for a mixed hybrid method

DISCRETIZATION

Domain Ω is meshed into N tetrahedra Ω_i and boundary Γ is meshed into triangles.

H-oriented method (HMH)

Magnetic field H is expanded with edge elements, scalar potential φ with nodal elements and vector potential A with facet elements. Lagrange multiplier ξ is discretized by means of vectorial functions associated to facets. For each facet f , having i, j, k as vertices, they are the 3 functions $w_{ij} \times n, w_{jk} \times n, w_{ki} \times n$ where w_{ij}, w_{jk}, w_{ki} are the edge functions and n the normal vector to f .

After discretization, HMH formulation provides the following system:

$$\begin{pmatrix} M & P & Q \\ P^t & 0 & 0 \\ Q^t & 0 & 0 \end{pmatrix} \begin{pmatrix} h \\ A \\ \xi \end{pmatrix} = \begin{pmatrix} f \\ g \\ 0 \end{pmatrix}$$

where h denotes the unknowns (H, φ) .

B-oriented method (BMH)

Flux density B is expanded with facet elements and scalar potential φ with functions constant per tetrahedron. Scalar Lagrange multiplier λ is taken as constant on each facet of the meshing. The linear system obtained has the the same form as the one given by HMH method.

Resolution

The more difficult is the inversion of matrix M . But, for both methods HMH and BMH, matrix M is block-diagonal and symmetrical (Fig. 1). Each block is 6x6 for HMH and 4x4 for BMH with the exception of the ones

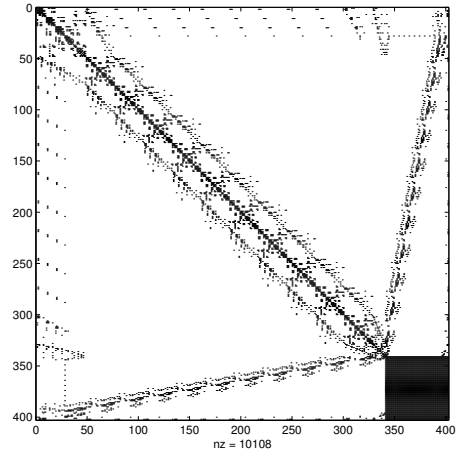


Fig. 2. Matrix M for a classical mixed method

corresponding to the boundaries integrals on Γ . The system is then easily solved though the number of unknowns and the number nz of non zero matrix elements is greater than with a classical mixed method (Fig. 2).

NUMERICAL RESULTS

Numerical results are given in Table 1 for a sphere of permeability $\mu_r = 100$, meshed with 360 tetrahedra. We have computed the error on the magnetic field by comparison with analytical values. These results are obtained

TABLE I. Numerical results for HMH and BMH

Method	CPU	err %	iter
HMH	44.4	2.7	484
BMH	6.0	6.6	145

with a SGI-Origin 2000. The CPU time is shorter for BMH, but the precision appears better for HMH.

Numerical results and comparisons with other formulations will be given in the full paper.

REFERENCES

- [1] F. Brezzi and D. Marini, "A Survey On Mixed Finite Element Approximations" *IEEE Transactions on Magnetics*, vol. 30, pp. 3547-3551, Sept. 1994.
- [2] A. Bossavit, "Mixed-Hybrid Methods in Magnetostatics: Complementarity in One Stroke" *CEFC 2002, The Tenth Biennial Conference on Electromagnetic Field Computation, Perugia*, Proceedings p. 1.
- [3] F. Brezzi and M. Fortin, "Mixed and Hybrid Finite Element Methods", *Springer-Verlag* 1991.
- [4] B. Bandelier and F. Rioux-Damidaou, "Mixed Finite element Method for Magnetostatics in \mathbb{R}^3 ," *IEEE Transactions on Magnetics*, vol. 34, pp 2473-2476, Sept. 1998.
- [5] B. Bandelier and F. Rioux-Damidaou, "A Mixed B-Oriented FEM for Magnetostatics in Unbounded Domains", *IEEE Transaction on Magnetics*, vol. 38, pp. 373-376, March 2002.

Application of Spheroidal Functions in Magnetostatics

Alexander V. Kildishev

School of Electrical and Computer Engineering, Purdue University
1285 EE Building
West Lafayette IN 47907-1285 U.S.A.
a.v.kildishev@ieeee.org

Abstract—We briefly outline the use of spheroidal functions in extrapolation of the external field of magnetic sources. The extrapolation is carried out by means of spatial harmonic analysis, in which the expansion functions are the spheroidal harmonics. An efficient method for computing external spheroidal harmonic functions of magnetostatic problems has been developed. The method can be utilized to the spatial harmonic characterization of magnetic sources in the prolate and oblate spheroidal coordinates. The new approach minimizes numerical imprecision in a wide range of parameters by using the Wronski determinant as a recurrence basis.

INTRODUCTION

The effort has been motivated by difficulties in accurate and efficient calculation of the spheroidal harmonics in naval and spacecraft magnetics [1, 2]. The difficulties have also been predicted by F. E. Baker and S. H. Brown [3].

Select a coordinate system defined by the semi-focal distance (f) and the prolate spheroidal coordinates (PSC) $\xi \in [1, \infty[$, $\eta \in [-1, 1]$, $\phi \in [0, 2\pi]$.

For an oblate spheroidal domain, select another coordinate system characterized by the semi-focal distance (\hat{f}) and the oblate spheroidal coordinates (OSC) $\hat{\xi} \in [0, \infty[$, $\hat{\eta} \in [-1, 1]$, $\hat{\phi} \in [0, 2\pi]$.

Laplace's equation $\nabla^2 U = 0$ defines the scalar magnetic potential U of the conservative magnetic field, which is generated by the internal source outside the boundary encapsulating the source. In the PSC (or OSC) U outside the boundary $\xi = \xi_i$ (or $\hat{\xi} = \hat{\xi}_i$) is given by [4]

$$U = \sum_{n=1}^{\infty} \sum_{m=0}^n (c_n^m F_c^{n,m} + s_n^m F_s^{n,m}) \quad (1)$$

where the harmonic coefficients c_n^m , s_n^m determine the spheroidal multipole image (MI) of the source, and $F_c^{n,m}$, $F_s^{n,m}$ are the spheroidal harmonic functions of the n -th degree and m -th order.

The External Spheroidal Harmonics

The harmonics $F_c^{n,m}$, $F_s^{n,m}$ in (1) are defined as

$$\text{PSC: } Q_n^m(\xi) P_n^m(\eta) \cos(m\phi), Q_n^m(\xi) P_n^m(\eta) \sin(m\phi) \quad (2)$$

$$\text{OSC: } q_n^m(\hat{\xi}) P_n^m(\hat{\eta}) \cos(m\hat{\phi}), q_n^m(\hat{\xi}) P_n^m(\hat{\eta}) \sin(m\hat{\phi}), \quad (3)$$

In addition to the associated Legendre functions of the first

and second kind (P_n^m , Q_n^m) in (2), the modified associated Legendre function of the second kind $q_n^m(\hat{\xi}) = i^{n-2m+1} Q_n^m(i\hat{\xi})$ is used in (3) to avoid complex functions and arguments of standard notations. Note, that we define $P_n^m(\eta)$, $Q_n^m(\xi)$ as:

$$P_n^m = (1 - \eta^2)^{\frac{m}{2}} \frac{d}{d\eta} P_n, Q_n^m = (\xi^2 - 1)^{\frac{m}{2}} \frac{d}{d\xi} Q_n.$$

CALCULATION OF THE EXTERNAL SPHEROIDAL HARMONIC FUNCTIONS

This paper focuses on practical algorithms for computing the spheroidal harmonics; the emphasis is on the associated Legendre functions of the second kind ($Q_n^m(\xi)$).

The most advanced computational schemes for $Q_n^m(\xi)$ are built on continuous fractions (CF). This approach provides stable algorithms valid for a wider range of the parameters and with higher precision. Herndon, [5, 6], and Gautschi created an extended set of procedures for P_n^m and Q_n^m [7], which is similar to the most advanced modern implementations [8, 9]. The most efficient CF approach is demonstrated by Gil and Segura in [8], [9] and [10], where the Wronski determinant links of the dominant solution P_n^m to the minimal solution Q_n^m . As a result, the application of forward recurrence relations for P_n^m provides good accuracy performance.

Our method uses a series representation instead of computation of continuous fractions. Unfortunately, the hypergeometric series [11] is limited to $\xi > \frac{3}{4}\sqrt{2} \approx 1.061$ (it also demonstrates oscillating behavior for certain combinations of n , m and ξ). The other hypergeometric series [12], which is valid for smaller ξ , converges very slowly and its use is impractical.

To overcome these drawbacks of hypergeometric series, an analog of the Wronski determinant is used as a recurrence basis. The initial step was mainly influenced by a classical Hobson example for zonal ($m = 0$) functions $Q_n(\xi)$ [13]:

$$Q_n = (-1)^m P_n \sum_{\nu=n}^{\infty} ((\nu+1)P_{\nu+1}P_{\nu})^{-1}. \quad (4)$$

A new series generalizes (4) for any $Q_n(\xi)$:

$$Q_n^m = (-1)^m P_n^m \sum_{\nu=n}^{\infty} (\nu+m)! / ((\nu-m+1)! P_{\nu+1}^m P_{\nu}^m). \quad (5)$$

Since, $P_n^m(\xi)$ values are increasing with increase of n , the above series converges, and it converges rather quickly. As a result, a controllable computational scheme can be used as an alternative to the CF algorithms.

Consider the ratios $\Omega_n^m(\xi) = Q_n^m(\xi)/P_n^m(\xi)$ and $\mathfrak{R}_{\nu,n}^m(\xi) = (-1)^m (n + \nu + m)! / ((n + \nu - m + 1)! P_{n+\nu+1}^m P_{n+\nu}^m)$,

then (5) can be rewritten as $\Omega_n^m(\xi) = \sum_{\nu=0}^N \mathfrak{R}_{\nu,n}^m(\xi)$, where N is a number of terms in the truncated infinite series.

The computation starts with consequent calculation of $P_{m+\nu}^m(\xi)$ for $\nu \in [0, (n_{\max} - m)]$ using [14] ($\nu = n - m$):

$$(\nu + 1)P_{m+\nu+1,m} = (2m + 2\nu + 1)\xi P_{m+\nu,m} - (2m + \nu)P_{m+\nu-1,m}. \quad (6)$$

The recurrence (6) is stable for an increasing range of $n \in [m, n_{\max}]$, differing to the analog of (6) for $Q_n^m(\xi)$. Since (6) is not valid for $n = m$, the initializing values are given by $P_0^m(\xi) \equiv 1$ and the relation

$$P_{m+1}^{m+1} = (2m + 1)\sqrt{\xi^2 - 1}P_m^m, \text{ which is tailored for } \xi > 1 \text{ as a direct succession of [15].}$$

The number of terms (N) is adaptively adjusted to reach a given accuracy of the initial ratio of the highest degree (n_{\max}): $\Omega_{n_{\max}}^m$. Once a desired accuracy is achieved, all terms of the Q_n^m set are computed consequently as $Q_{n_{\max}}^m = \Omega_{n_{\max}}^m P_{n_{\max}}^m$, $Q_{n_{\max}-1}^m = \Omega_{n_{\max}-1}^m P_{n_{\max}-1}^m, \dots, Q_m^m = \Omega_m^m P_{n_{\max}-1}^m, (\Omega_{n-1}^m = \Omega_n^m + \mathfrak{R}_{n-1,0}^m)$.

The approach also works for $q_n^m(\xi)$ and can be used in computing of the spheroidal harmonics in the OSC.

$$q_n^m = (-1)^{n-m} P_n^m \sum_{\nu=n}^{\infty} (-1)^\nu (\nu + m)! / ((\nu - m + 1)! P_{\nu+1}^m P_\nu^m),$$

where the modified Legendre function of the first kind is defined as $p_n^m(\xi) = i^{-n} P_n^m(i\xi)$.

SAMPLE RESULTS AND FURTHER ENHANCEMENTS

A calculated example of $q_n^m(\xi)$ for $n = 10$ is shown in Table 1. The sample results are consistent with [16].

TABLE 1 - SAMPLE RESULTS FOR $q_{10}^m(\xi)$

ξ	$m = 0$	$m = 1$	$m = 2$
0.1	1.350137559350E-01	-1.425930470817E+00	1.513528392267E+01
0.5	2.324708238053E-03	-2.495041703345E-02	2.780342376073E-01
0.9	6.775688269903E-05	-7.345287333435E-04	8.436004730834E-03

A more advanced test includes the use of the addition theorems. The test demonstrates relative errors of order 10^{-15} for the parameter ranges required by our applications, i.e. $\xi = [1.001, 3]$, $n = 1 \dots 200$, and $m = 0 \dots 20$.

Further enhancements are perhaps associated with fast

numerical algorithms for the direct computation of the field components. For example, the axial component of the field (PSC) is given by the following series ($w_k^{n,m}$ is a coefficient)

$$(\mu_0/f) \sum_{n=1}^{\infty} \sum_{m=0}^n \left(c_n \sum_{k=0}^{\infty} w_k^{n,m} F_s^{n+2k+1,m} + s_n \sum_{k=0}^{\infty} w_k^{n,m} F_s^{n+2k+1,m} \right),$$

where the successive use of same harmonic terms in the expansion induces a controllable computational scheme for B_x .

ACKNOWLEDGMENT

Thanks to Michael Morgan and his warning regarding possible difficulties with $Q_n(\xi)$, which motivated the development of the efficient algorithms. Thanks to Walter Gautschi for a concise discussion on continuous fractions. The author is also grateful to José Javier Segura Sala, who kindly provided us with his original Fortran code to test our results. The author would like to thank Ron Radlinski for his continuous support and encouragement during the study of the esoteric functions.

This work was supported by the ONR under the Grant N00014-00-1-0117.

REFERENCES

- [1] A. V. Kildishev, J. A. Nyenhuis, and A. V. Hetman, "Zonal Magnetic Signatures in Spherical and Prolate Spheroidal Analysis", *MARELEC'99*, Brest, France, 1999, pp. 231-242.
- [2] A. V. Kildishev and S. A. Volokhov, "Sense coils and selective functions for tesseral multipole determination by integral transforms of magnetic signatures", *Space Science and Technology*, Vol. 2, No 5-6, 1996, pp. 26-30.
- [3] F. E. Baker and S. H. Brown, "Magnetic induction of ferromagnetic pro-late spheroidal bodies and infinitesimally thin current bands," *Journal of Applied Physics*, Vol. 53, Issue 6, June 1982, pp. 3991 - 3996.
- [4] P. Moon, D. E. Spencer, "Field theory handbook; including coordinate systems, differential equations and their solutions," Springer-Verlag, 1961, pp. 28 -29, and pp. 31-33.
- [5] J. R. Herndon, "Algorithm 62 - A set of associated Legendre polynomials of the second kind", *Comm. ACM* 4, July 1961, pp. 320-321.
- [6] J. R. Herndon, "Remark on Algorithm 62", *Comm. ACM* 4, December 1961, p. 544.
- [7] W. Gautschi, "Algorithm 259 - Legendre functions for arguments larger than one", *Communications of the ACM*, vol. 8, no. 8 (1965), p. 488.
- [8] A. Gil, J. Segura, "Evaluation of Legendre functions of argument greater than one", *Comput. Phys. Comm.*, No 105, 1997, p. 273-283.
- [9] A. Gil, J. Segura, "A code to evaluate prolate and oblate spheroidal harmonics", *Comput. Phys. Comm.*, Vol. 108, 1998, p. 267 - 278.
- [10] J. Segura and A. Gil, "Evaluation of associated Legendre functions off the cut and parabolic cylinder functions", *Electronic Transactions on Numerical Analysis*, Volume 9, 1999, pp. 137-146.
- [11] E. W. Hobson, *The theory of spherical and ellipsoidal harmonics*, Chelsea Publishing Company, New York, 1955, p. 286, Eq. 158.
- [12] *ibid*, p. 286, Eq. 158.
- [13] *ibid*, p. 73, Example 10.
- [14] I. S. Gradshteyn, I. M. Ryzhik, *Table of integrals, series, and products*, edited by Alan Jeffrey, Translated from the Russian, *Academic Press*, 1980, Formula 8.731.
- [15] *ibid*, Formulae 8.755.2 and 8.752.1.
- [16] *Tables of Associated Legendre Functions*, NBS; Columbia University Press, New York, 1945, 303 pp.

Magnetic field Analysis of Iron-Core Reactor Coils by Finite Volume Method

J. Zou, Q. Huang, J. S. Yuan, X. S. Ma

Department of Electrical Engineering, Tsinghua University, Beijing, 100084, China

zoujun@tsinghua.edu.cn

X. Cui

Department of Electrical Engineering, North China Electric Power University, Baoding, Hebei, 071003, China

hjbdcuix@heinfo.net

Abstract—An accurate evaluation of the magnetic field of the iron-core reactor coils by the finite volume method (FVM) is presented. The calculation scheme of FVM, with the control volume connected by the circumcenter of each triangular element, is developed. The numerical results are compared with those obtained by the finite element method. Good agreement is obtained. The main advantage of the approach proposed is that the formation of coefficient matrix is very straightforward without needing the complicated mathematical derivation.

INTRODUCTION

The accurate analysis of the power frequency magnetic field inside and outside large substation iron-core reactor coils is essential for solving the problem associated with the reactor coil design and management of power system magnetic filed distribution. In the past years, the finite element method is widely used in many engineering applications. However, there are few papers to report analysis of the magnetic field of reactor by the finite volume method (FVM)[1]. In this paper, the magnetic field of iron-core reactor is calculated by FVM. The results obtained by FVM are compared with those calculated by ANSYS software with a 2D axisymmetric finite element method. Good agreement is obtained.

PRINCIPLE

Fig.1 is the model of the iron-core reactor. Due to the axisymmetric property of reactor structure, a cylindrical coordinate system of (r, α, z) is set up. Because the current

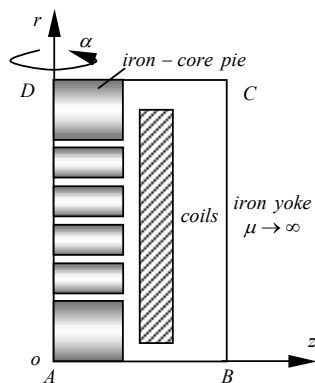


Fig.1 Model of the iron-core reactor

flowing in the coils has only α^0 component, the boundary value problem concerned can be expressed by the vector magnetic potential $A_\alpha(r, z)\alpha^0$ as follows.

$$\begin{cases} \nabla^2 A_\alpha(r, z) = J_\alpha \\ A_\alpha(r, z)|_{AD} = 0, \frac{\partial A_\alpha(r, z)}{\partial n}|_{AB, BC, CD} = 0 \end{cases} \quad (1)$$

The field region $ABCD$ is discreted by a number of triangular elements. The control volume can be defined by connecting the circumcenter of each triangular element and the central point of each segment line in an orderly way. For example, the control volume with respect to P_0 as shown in Fig.2(a) is $M_1Q_1M_2 \cdots M_6Q_6M_1$. The control volume equation is based on the following identical equation

$$\oint_{\Gamma_{K_P}^i} \frac{1}{\mu} \nabla \times A_\alpha(r, z) \cdot dl = \iint_{K_P^i} J_\alpha(r, z) ds \quad (2)$$

Referring to Fig.2 (a), (2) can be rewritten as

$$\sum_i \int_{\Gamma_{K_P}^i} \frac{1}{\mu} \frac{\partial}{\partial n} (r A_\alpha) dl = - \sum_i \iint_{K_P^i} J_\alpha \cdot ds \quad (3)$$

where $J_\alpha(r, z)$ is the current density of element i , $\Gamma_{K_P}^i$ is the integral path within element i (saying $M_1Q_1M_2$) and K_P^i is the area surrounding by $\Gamma_{K_P}^i$ and P_0 . Similar with the approach in the finite element method, one can calculate

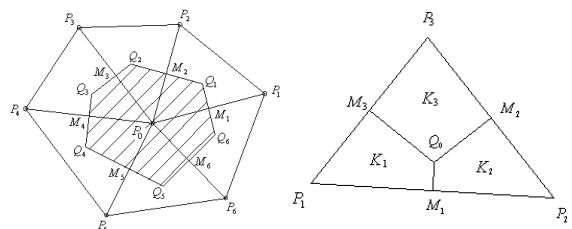


Fig.2 Definition of control volume elements

the coefficient of control volume in terms of the conception of the second element [1]. For example, the second element K_1 with respect to the node P_1 of element $P_1P_2P_3$, shown in Fig.2(b), can be calculated in the following way.

$$\int_{L_1+L_2} \frac{1}{\mu} \frac{1}{r} \frac{\partial u}{\partial n} ds = \int_{M_1Q_0} \frac{1}{\mu} \frac{1}{r} \frac{\partial u}{\partial n} ds + \int_{Q_0M_3} \frac{1}{\mu} \frac{1}{r} \frac{\partial u}{\partial n} ds$$

$$= \frac{1}{\mu} \frac{|M_1Q_0|}{r_1} \frac{u_{P_2} - u_{P_1}}{|P_2P_1|} + \frac{1}{\mu} \frac{|Q_0M_3|}{r_2} \frac{u_{P_3} - u_{P_1}}{|P_3P_1|}$$

$$= k_{P_1} u_{P_1} + k_{P_2} u_{P_2} + k_{P_3} u_{P_3} = [k] \cdot [u]$$

where u represents $rA(r, z)$ for convenience, \bar{r}_1 and \bar{r}_2 are the distance between P_1 and the central point of M_1Q_0 and M_3Q_0 respectively. By using (4), the left term of coefficient matrix can be formed easily. The right term of FVM equation group is

$$-I = -J_\alpha S_{K1} = -\frac{1}{2} J_\alpha (|P_1P_2| |M_1Q_0| + |P_1P_3| |Q_0M_3|) \quad (5)$$

By using (4) and (5), summing up the contribution of all elements, one can obtain the equation group of FVM, i.e.,

$$KU = -I \quad (6)$$

After solving (6), the vector magnetic potential of each node is obtained and $B = \nabla \times A$.

NUMERICAL EXAMPLES

The geometrical dimension and parameter of the iron-core reactor can be summarized as follows: the radius of iron-core is 115 mm; the window height is 460 mm; the center distance is 390 mm; the number of air gap is 5; the length of air gap is 10.5 mm; the length of core pie is 50 mm; the inner radius of coil is 132 mm; the outer radius of coil is 186.5 mm; the turn of coil is 68. Because the finite element method can give an accurate result, the results obtained by FEM are used as the reference data. In FEM, a 2D axisymmetric finite element model at 50 Hz was used. The ANSYS field simulator was utilized to obtain the pertinent results. The distribution of the magnetic induction intensity B inside the iron-yoke by 2D FVM is plotted in Fig.3, and the reactance calculated by FEM and FVM respectively are listed in Tab. I. It can be seen from the Tab.I that the error of reactance is only 0.5% taking the result by ANSYS as a reference, so the agreement is very good.

Tab. I Comparison of FVM and FEM

terms	FEM (ANSYS)	FVM
Reactance (Ω)	1.5754	1.5670

Further, the error of FVM is defined as the following way

$$\varepsilon = \frac{A_{FVM} - A_{ANSYS}}{A_{ANSYS}} \times 100\% \quad (7)$$

In the field region, the error distribution is plotted in Fig.4. According to Fig.4, the maximal error is 5% and the mean error is only 0.6%. The maximal error takes place at the points with $r \rightarrow 0$. Obviously, the reason of such kind of error is too small \bar{r}_i in (4) to obtain the accurate numerical value.

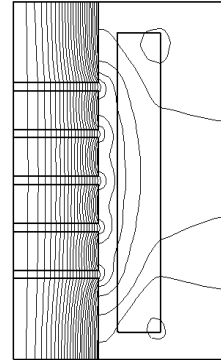


Fig. 3 Distribution of the magnetic induction intensity

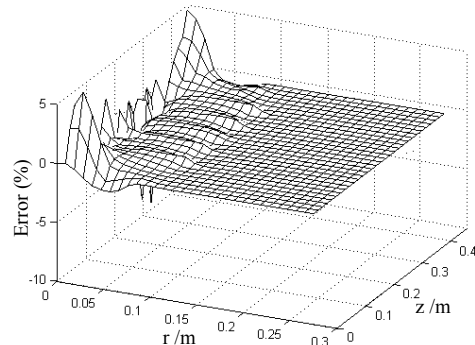


Fig.4 Error distribution of calculated region

CONCLUSION

The magnetic field distribution and parameter of iron-core reactor is calculated by FVM. The main advantage of FVM is that it holds the mathematical simplicity like the finite difference method and also can calculate the complex field region with the different media and boundary like the finite element method. It should be noted that the quadratic scheme of FVM is omitted in purpose because of the length restriction of the paper. The quadratic scheme of FVM can give more accurate results than that proposed here and will be reported in the extended paper.

REFERENCES

- [1] M. Rosenfeld, R. Tanami, and S. Abboud "Numerical solution of the potential due to dipole sources in volume conductors with arbitrary geometry and conductivity", *IEEE transactions on biomedical engineering*, Vol.43. No.7 pp.679-688, July 1996.

Solenoidal Current Flows for Filamentary Conductors

D. N. Dyck

Infolytica Corporation
Place du Parc, 300 Léo-Pariseau, Suite 2222
Montreal, H2X 4B3, Canada
derek@infolytica.com

J. P. Webb

Department of Electrical and Computer Engineering
McGill University, 3480 University Street
Montreal, H3A 2A7, Canada
jon.webb@mcgill.ca

Abstract—The “uniform” current density inside a filamentary (stranded) conductor must be found by a pre-processing step before the magnetic field produced by it can be computed. A previously-published method [1] for achieving this is very general, but gives a current density that is not solenoidal. Here, an algorithm is described for generating a solenoidal current density. The densities before and after applying the algorithm are separately used as the source in the computation of the magnetostatic field of a square coil. The non-solenoidal source leads to significant field errors; the corrected source gives the expected field.

INTRODUCTION

Filamentary conductors (conductors or coils made of a large number of fine filaments or strands) are widely used to generate magnetic fields, and the accurate prediction of those fields requires, in general, an accurate modeling of the conductor currents. This is particularly the case with devices such as deflection yokes, where the electron beam deflection may be quite sensitive to variations in the current distribution. A general-purpose magnetic field analysis program should, therefore, provide an accurate treatment of the currents in filamentary conductors.

On the face of it, since the current density in each strand is well defined, there would appear to be no difficulty in specifying the current density vector \mathbf{J} throughout a filamentary conductor. However, there are usually far too many filaments to be individually modeled. Instead, the overall shape of the conductor is defined, together with two cross-sectional planes (“terminals”). The current flows in a “uniform” fashion from one terminal to the other, without, of course, passing out of any other surfaces of the conductor. Note that this “uniform” distribution is *not* the same as the current pattern in a solid conductor (i.e. with no strands). For example, in the latter case the current density is greater on the inside of a curve than on the outside; no such inequality occurs in the filamentary case.

How can the “uniform” current density be determined? For certain simple cases, such as a straight length of conductor with constant cross-section, the answer is trivial. However, a general-purpose program must be able to handle arbitrary conductor shapes, and an algorithm is needed for this case. There may, in fact, be no unique solution. However, the method proposed in [1] seems to be very practical. An electrostatic problem is solved within the conductor, imposing a potential difference between the terminal planes.

The resulting equipotential surfaces provide natural cross-sections along the conductor, and are used to generate a current density that is uniform in magnitude over the cross-section, and parallel to the static electric field.

However, a problem with the current density computed in this way is that it is not necessarily solenoidal. Certainly it is in an integral sense, because the net current flow is the same through each of the equipotential surfaces used in its construction. Also, within each element the current density in [1] is taken to be uniform, hence solenoidal. Between elements, however, there is no guarantee that the normal component of \mathbf{J} is continuous.

Why does this matter? Finite element methods for computing the quasi-static magnetic field solve the equation:

$$\nabla \times \mathbf{H} = \mathbf{J} \quad (1)$$

for the magnetic field (together with the divergence equation for flux density). This equation *requires* that \mathbf{J} is solenoidal. Starting with a non-solenoidal \mathbf{J} makes the magnetic field problem fundamentally ill-posed, and leads to unpredictable results. Whether the inaccuracies caused by this are large or small depends on the formulation chosen and on the particular nature of the problem being solved, but it is clearly unwise to base any general purpose program on the unreliable foundation of a non-solenoidal current density.

Here we propose an algorithm for generating a solenoidal current density for an arbitrarily-shaped stranded conductor represented by tetrahedral elements.

THEORY

The starting point for the algorithm is a current density \mathbf{J}_0 , such as might be generated by the method of [1]. It is uniform in each tetrahedron but non-solenoidal, i.e. its normal component is not continuous from one element. Next we define a space of solenoidal current densities on the same set of elements. These are also uniform in each tetrahedron, but are normally continuous. Such a space can be constructed from the curl of the Whitney edge functions:

$$\mathbf{J} = \sum_i h_i \nabla \times \mathbf{w}_i \quad (2)$$

where w_i is the Whitney function [2] associated with the i^{th} edge and the summation is over all edges of the mesh. However, in (2) there are too many degrees of freedom because (a) the boundary conditions on the surfaces of the conductor are not enforced and (b) many linear combinations of the w_i are irrotational and hence correspond to zero \mathbf{J} . The degrees of freedom are reduced in two steps, using a tree-cotree approach [3]. First, a tree of the edges on the *surface* of the conductor is formed, and the h_i corresponding to these tree edges are set to zero. The h_i of the cotree edges are found iteratively from a knowledge of the current flow through each boundary face (either zero for the side walls or a known nonzero value for the terminals). Second, a tree of the edges in the interior *volume* of the conductor is formed, and again the h_i for these edges are set to zero. The result is an expression for \mathbf{J} in terms of some known, nonzero, cotree values on the surface, and many unknown cotree values in the interior.

In the final step, the unknown cotree values are determined by minimizing this functional:

$$\int_V (\mathbf{J} - \mathbf{J}_o)^2 dV \quad (3)$$

This results in a sparse matrix problem, solved by the conjugate gradient method with preconditioning.

RESULTS

Figure 1 shows one quarter of a square conductor, enclosed in a box of air for the purposes of computing the magnetic field. The boundary condition on all walls of the box is that the normal component of flux density vanishes.

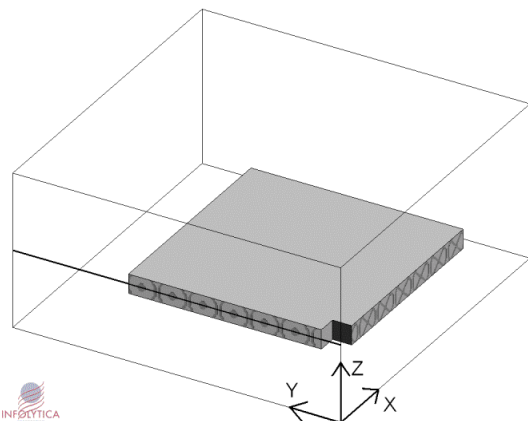


Fig. 1. Quarter of a square filamentary conductor.

For a conductor of this shape, with a tight inner corner, there is quite a large difference between the current density that would flow if the conductor were treated as solid and the current density of the filamentary conductor. It is therefore

necessary to compute a current density \mathbf{J}_0 using the method of [1], rather than relying on the “solid” current distribution. However, if \mathbf{J}_0 is used as the source for the magnetic field, large errors in the field can result. Fig. 2 shows the three components of flux density along a symmetry line (the thick line in Fig. 1) when a reduced scalar potential method [4] is used to calculate the magnetostatic field, with \mathbf{J}_0 is the source. The x - and y -components should be zero, by symmetry, yet they are not, and the B_z curve is unreasonably jagged. By contrast, also plotted is the B_z found by the same method starting from the solenoidal \mathbf{J} , obtained from \mathbf{J}_0 using the algorithm described above. The x - and y -components in this case were negligible.

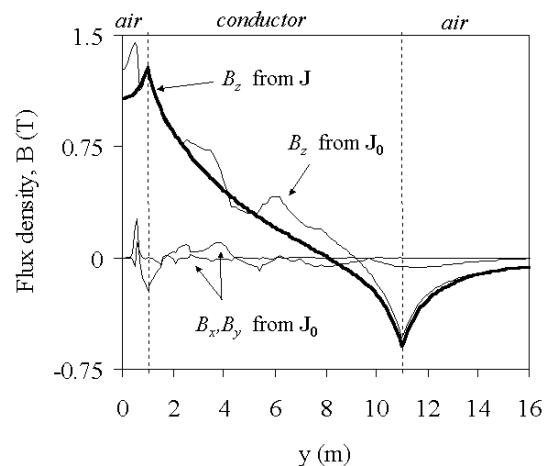


Fig. 2. Flux density of the square conductor, along one line.

CONCLUSIONS

An algorithm has been described that can generate an exactly solenoidal current density that nearly matches a given, non-solenoidal one. Solenoidality is necessary to avoid substantial errors in computed magnetic fields.

REFERENCES

- [1] Chang-Hwan Im, Hong-Kyu Kim, Hyun-Kyo Jung, “Novel technique for current density distribution analysis of solidly modeled coil”, *IEEE Trans. on Magnetics*, vol. 38, no. 2, part 1, pp.505-508, March 2002.
- [2] A. Bossavit, “A rationale for ‘edge-elements’ in 3-D fields computations”, *IEEE Trans. Magnetics*, vol. 24, pp.74-79, 1988.
- [3] R. Albanese, G. Rubinnaci, “Solution of 3-dimensional eddy-current problems by integral and differential methods”, *IEEE Trans. on Magnetics*, vol. 24, no. 1, pp.98-101, January 1988.
- [4] J.P. Webb, B. Forghani, “A $T-\Omega$ method using hierarchal edge elements”, *IEE Proc. Sci. Meas. Tech.*, vol. 142, no. 2, pp.133-141, 1995.

Discretisation of Boundary Integral Equations by Differential Forms on Dual Grids

Stefan Kurz*, Oliver Rain*, Volker Rischmüller*, Sergej Rjasanow†

*Robert Bosch GmbH, Postfach 10 60 50, 70049 Stuttgart, Germany

†Universität des Saarlandes, Fachbereich Mathematik, 66041 Saarbrücken, Germany

Abstract— In this paper some integral equations of electromagnetics are reformulated in terms of differential forms. The integral kernels become double forms. These are forms in one space with coefficients that are forms in another space. The results correspond closely to the usual treatment, but are clearer and more intuitive. Since differential forms possess discrete counterparts, the discrete differential forms, such schemes lend themselves naturally to discretisation. As an example, a boundary integral equation for the double curl operator is considered. The discretisation scheme generalises the well-known collocation technique by using de Rham maps.

Index terms— Boundary element methods, differential forms, integral equations.

I. INTRODUCTION

In the recent years, a remarkable amount of papers has been published that treat continuous and discrete electromagnetics in terms of differential forms (DF). For a good account on this topic see e.g. [1]. However, most of these papers focus on (generalised) finite difference and finite element methods (FEM). There are only rare papers that deal with the boundary element method (BEM) [2]–[4]. The aim of the present paper is to show how the integral equations of electromagnetics can be expressed in the language of DFs. Since DFs possess discrete counterparts, the discrete DFs, such schemes lend themselves naturally to discretisation. We restrict ourselves to the static case. Similar schemes can be derived for time dependent problems.

Let $\Omega \subset E_3$ be an open domain of the three-dimensional affine-Euclidean space E_3 whose sufficiently smooth boundary is denoted by Γ . We consider the generic second order equation

$$\delta d\alpha = *\eta \quad \text{in } \Omega, \quad (1)$$

where α is a p -Form, η is a $(3-p)$ -Form, $p=0, \dots, 2$. Moreover, d denotes the exterior derivative, δ the coderivative, $\delta\omega = (-1)^{\deg \omega} * d*\omega$, and $*$ the Hodge operator of the Euclidean metric. The boundary conditions shall be represented by trace operators $\gamma_D^- \alpha = \mathbf{t}^- \alpha = \beta$, $\gamma_N^- \alpha = \mathbf{t}^- * d\alpha = \gamma$, where γ_D^- , γ_N^- are the interior Dirichlet and Neumann traces, respectively, \mathbf{t}^- is the standard interior trace operator, and β , γ are the Dirichlet and

Neumann data. Note that β is a p -form and γ is a $(2-p)$ -form that are defined on Γ .

For $p=0$, (1) is the Laplace equation, and we can identify α with the electric scalar potential, β with its value on Γ , $-\varepsilon_0\gamma$ with the normal component of the electric displacement on Γ , and $\varepsilon_0\eta$ with the charge density. In contrast, $p=1$ yields the double curl equation, where α can be seen as the magnetic vector potential, β as its tangential component on Γ , γ/μ_0 as the tangential component of the magnetic field on Γ , and η/μ_0 as the current density.

By applying the exterior derivative to the Neumann data and taking into account (1) we find

$$d\gamma = d\mathbf{t}^- * d\alpha = \mathbf{t}^- d* d\alpha = (-1)^{p+1} \mathbf{t}^- \eta. \quad (2)$$

This condition is fulfilled trivially for $p=0$, since there are no non-trivial 3-forms on surfaces. For $p=1$ (2) means that a possible normal current density $\mathbf{t}^- \eta/\mu_0$ through Γ must be consistent with the tangential magnetic field γ/μ_0 such that Ampère's law is satisfied.

At this point it is useful to introduce double forms [5]. These are forms in one space with coefficients that are forms in another space, or DF-valued DFs [6]. The double forms to be used here are associated with $E'_3 \times E_3$, where E'_3 is the observation space and E_3 is the source space. Subsequently, all operators which refer to the space E'_3 are denoted by a prime. A double form can be used as a transformation kernel. If we fix a double p -form K_p , we have the transformation from E_3 to E'_3 given by the volume integral $\omega' = \int_{E_3} K_p \wedge * \omega$, where ω is a p -form and ω' is the transform of ω due to the kernel K_p , provided that the integral exists.

The Green double form G_p for (1) satisfies $\delta d G_p = I_p$, where I_p is the identity kernel [6]. By pre-multiplying (1) by G_p , integrating over Ω and performing integration by parts twice we end up with the following representation formula

$$\alpha' = \int_{\Gamma} (\gamma_D^- G_p) \wedge \gamma - (-1)^p \int_{\Gamma} (\gamma_N^- G_p) \wedge \beta + \int_{\Omega} G_p \wedge \eta. \quad (3)$$

The first integral is the single layer potential $\Psi_{SL}(\gamma)$, the second one the double layer potential $\Psi_{DL}(\beta)$, and the last one the Poisson integral. Eq. (3) encompasses the usual scalar and vector representation formulas known from literature.

For the sake of simplicity, we restrict ourselves to $\eta=0$. By applying γ_D^- to (3) and taking into account the defini-

tions $V = \gamma_D^- \circ \Psi_{SL}$ and $K = \frac{1}{2}(\gamma_D^- + \gamma_D^+) \circ \Psi_{DL}$ we obtain the boundary integral equation

$$\frac{1}{2}\beta'(\mathbf{x}') = V(\gamma)(\mathbf{x}') - K(\beta)(\mathbf{x}') \quad (4)$$

for smooth boundary points \mathbf{x}' , where γ_D^+ is the exterior Dirichlet trace [7]. Eq. (4) can be generalised to the non smooth case as well.

II. DISCRETIZATION

It is well known that Ampère’s and Faraday’s law might be discretised on dual grid systems, and that the coupling of these is accomplished by material matrices, which can be seen as discrete Hodge operators [1, Sect. 3.3]. Each time a hodge operator is applied this should be associated with a change of the grid on the discrete level. We therefore state that α and β should be allocated on one grid, but γ and η on the other. Note that the discrete counterparts of the exterior derivative and of the trace operator \mathbf{t} act on identical grids, respectively.

In this paper, we wish to highlight a discretization by so called de Rham maps [3]. Technically, this simply means that (4) is integrated over nodes ($p=0$, point evaluation) or edges ($p=1$) of the grid that is associated with β . Applying the appropriate de Rham map to (4), where the unknown surface DF is taken from a space of Whitney forms, instantly provides us with a discretization, see Table I. The boundary integral operators give rise to matrices V_h, K_h . Moreover, the matrix applied to the d.o.f. vector of the unknown quantity turns out to be square. We observe that V_h provides a mapping between dual grids, while K_h acts on the same grid.

For $p=0$ we obtain the well known collocation technique. This gives a geometrical explanation for the common practice to use piecewise linear shape functions (Whitney-0-forms) for the Dirichlet data but piecewise constant shape functions (Whitney-2-forms) for the Neumann data.

For $p=1$ the de Rham maps generalise the collocation technique. Considering the Neumann problem, β is discretised by Whitney-1-forms, i.e. linear edge elements, and (4) is enforced for the integrals over the primal edges. Regarding the Dirichlet problem, it can be shown that

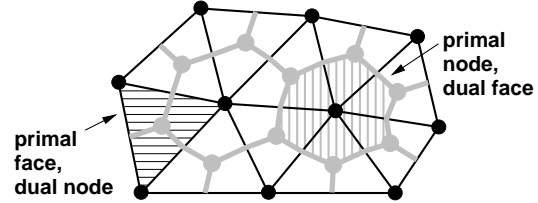


Fig. 1. Barycentric dual grid systems for the discretisation of the Dirichlet problem (black: primal grid, grey: dual grid).

the condition (2) has to be included into the construction of the space for γ . Otherwise the operator V fails to be elliptic and convergence cannot be taken for granted any more [8]. We restrict ourselves to the case $\eta = 0$, where the condition (2) reduces to $d\gamma = 0$, i.e. γ is a closed DF.

One possibility to remedy this problem is the introduction of a scalar magnetic potential ψ defined on Γ [8]. In case of a trivial topology, $d\gamma = 0$ implies $\gamma = d\psi$. On the discrete level, γ is represented by the discrete surface gradients of Whitney-0-forms. On the dual side, we propose to restrict the collocation to closed 1-chains, i.e. cycles, and these can be obtained similarly as the boundaries of dual faces, see Fig. 1 right. Physically, this means that the residual flux through any surface on Γ which is composed of dual faces vanishes. In case of a nontrivial topology additional basis forms and basis cycles related to the first (co-)homology group of Γ have to be augmented [9].

As an example, a permeable sphere in the field of a circular current loop will be considered. For $\mu \rightarrow \infty$ (respectively $\mu \rightarrow 0$) this yields an exterior Neumann (respectively Dirichlet) problem of the double curl equation, where an analytical solution is available as a reference.

REFERENCES

- [1] R. Hiptmair, “Finite elements in computational electromagnetism,” *Acta Numerica*, pp. 237–339, 2002.
- [2] A. Bossavit, “On the representation of differential forms by potentials in dimension 3,” in *Scientific Computing in Electrical Engineering*, U. van Rienen, M. Günther, and D. Hecht, Eds., vol. 18 of *Lecture Notes in Computational Science and Engineering*, pp. 97–104. Springer-Verlag, Berlin, 2001.
- [3] C. Geuzaine, T. Tarhasaari, L. Kettunen, and P. Dular, “Discretization schemes for hybrid methods,” *IEEE Transactions on Magnetics*, vol. 37, no. 5, pp. 3112–3115, Sept. 2001.
- [4] A. Bossavit, “The ‘scalar’ Poincaré Steklov operator and the ‘vector’ one: Algebraic structures which underlie their duality,” in *Domain Decomposition Methods for Partial Differential Equations*, R. Glowinski et al., Ed., chapter 2, pp. 19–26. SIAM, 1991.
- [5] G. de Rham, *Differentiable Manifolds*, Springer-Verlag, Berlin, 1984.
- [6] K.F. Warnick and D.V. Arnold, “Electromagnetic Green functions using differential forms,” *Journal of Electromagnetic Waves and Applications*, vol. 10, no. 3, pp. 427–438, 1996.
- [7] W. McLean, *Strongly Elliptic Systems and Boundary Integral Equations*, Cambridge University Press, Cambridge, UK, 2000.
- [8] R. Hiptmair, “Boundary element methods for eddy current computation,” Tech. Rep. 166, SFB 382, Universität Tübingen, Sept. 2001.
- [9] R. Hiptmair and J. Ostrowski, “Generators of $H_1(\Gamma_h, \mathbb{Z})$ for triangulated surfaces: Construction and classification,” Tech. Rep. 160, SFB 382, Universität Tübingen, Mar. 2001.

TABLE I
DISCRETISATION OF THE BOUNDARY INTEGRAL EQUATION ON DUAL GRID SYSTEMS BY DE RHAM MAPS.

Problem type	Dirichlet	Neumann
Operator to be inverted	Single layer V	Double layer K
Unknown data on primal grid	Neumann γ	Dirichlet β
$p=0$	face based	nodal based
$p=1$	edge based (closed)	edge based
de Rham map (collocation) on	dual grid	primal grid
$p=0$	nodes	nodes
$p=1$	edges (cycles)	edges

Development of 3-D Read/Write Simulation System for Higher Areal Recording Density

Naoya Fujiwara¹⁾, Kiminari Shinagawa¹⁾, Kohei Ashiho²⁾, Koji Fujiwara²⁾ and Norio Takahashi²⁾

1)Faculty of Science, Toho Univ., Funabashi 274-8510, Japan {fujiwara, shinagawa}@ph.sci.toho-u.ac.jp

2)Dept. Electrical and Electronic Eng., Okayama Univ. Okayama 700-8530, Japan
{ashiho, fujiwara, norio}@eplab.elec.okayama-u.ac.jp

Abstract —Recently, higher areal recording density of hard disk drive(HDD) is achieved by increasing not only linear density(BPI) but also track density(TPI). Then, 3-D read/write(R/W) simulation is necessary in order to design high-density recording system by utilizing magnetic field analysis. In this paper, 3-D R/W simulation system using the edge-based finite element method is developed by introducing the 3-D medium hysteresis model based on the ensemble of the Stoner-Wohlfarth (S-W) particles. As it is not easy to apply the Newton-Raphson method for the nonlinear analysis of S-W model, an under-relaxation iteration method is used. The effectiveness of the 3-D R/W simulation system is illustrated by applying to the magnetic field analysis of a SPT(single-pole-type) head/DL(double-layer) medium perpendicular recording system.

I. INTRODUCTION

The increase in areal density of magnetic recording for HDD is remarkable over the last several years. In order to develop higher density recording system, CAD utilizing the magnetic field analysis is indispensable. As the higher areal recording density is achieved by increasing not only BPI but also TPI, 3-D R/W simulation is necessary to calculate the flux distribution in the track direction[1].

In this paper, 3-D R/W simulation system using the edge-based finite element method is developed by introducing the 3-D medium hysteresis model using the Stoner-Wohlfarth (S-W) particles[2]. The problems in developing 3-D analysis is examined, and the application is shown to the analysis of a SPT head/DL medium perpendicular recording system.

II. SIMULATION METHOD

The 3-D R/W simulation system was developed by solving the Maxwell's equation for the head-medium system using the edge-based finite element method[3] and a hysteresis model of the medium based on the ensemble of the Stoner-Wohlfarth (S-W) particles[2]. In the S-W model, the easy axis of each particle is distributed according to a Gaussian distribution in 3-D space, and the M-H loops for the medium was calculated by taking account of the history of each S-W particle(switced or unswitched). Since it is not easy to apply the Newton-Raphson method to the nonlinear analysis of the medium, the Newton-Raphson method was employed only for the head, and an under-relaxation iteration method was applied for the medium.

The flow chart of the 3-D R/W system developed is shown in Fig.1. First, the whole domain of the model is discretized using a hexahedral element, and the material parameters and their initial values are set for the head-medium system. Then, a linear equation system for the model is made using a finite element method. After that, the linear equation system is solved using the Newton-Raphson method for the head, and an under-relaxation method for the medium. In the write process, the calculation process is repeated by shifting the medium and the recording current until the last step is reached. Furthermore, removing the head after the last step, an extra-calculation is carried out to obtain the final recorded magnetization. On the other hand, in the read process, the recorded magnetization is set at the first step instead of the recording current, and the similar calculation is repeated and the magnetic flux through the MR sensor element is calculated to obtain the read voltage waveform for the recorded magnetization.

III. RESULTS AND DISCUSSION

In order to test the 3-D R/W simulation system developed, the R/W simulation was performed on a SPT head/DL medium perpendicular recording system shown in Fig.2. The SPT head is composed of the main pole of 0.4 μ m thickness and 0.1 μ m track width. The thicknesses of the recording layer and the soft magnetic under-layer of the DL medium are 20 nm and 100 nm, respectively. Furthermore, the spacing between the head and the medium is assumed to be 15 nm and the recording density is about 3.5 Gb/in².

Fig.3 shows the M-H loops for the recording layer used for the R/W simulation calculated by the S-W model assuming the Gaussian distribution of an average anisotropy field $H_k = 477$ kA/m and its standard deviation $\Delta H_k = 40$ kA/m. Fig.4 shows the 3-D mesh for the SPT head used in the present simulation. The number of elements is 30636 for the write process and 25200 for the read one in total.

Fig.5 shows the recording current waveform and the recorded bit pattern. As shown in Fig.5, the magnetization is recorded perpendicularly bit by bit. Fig.6 shows the reproduced voltage waveform for the recorded magnetization with MR head. The CPU time for this R/W simulation is about 4 hours in the write process and about 1.5 hours in the read process(41 steps) using the Pentium 2.53 GHz with 1GB

memory of PC(OS Windows XP).

ACKNOWLEDGEMENT

This work is partly supported by SRC(Storage Research Consortium).

REFERENCES

- [1] Z.Zhang and G.Tarnopolsky, "Properties of longitudinal recording process at 100Gb/in² and higher areal densities", *IEEE Trans. Magn.*,vol.37, pp.1260-1263, 2001.
- [2] I.A.Beardsley, "Self-consistent recording model for perpendicularly oriented media", *J.Appl.Phys.*,vol.53, pp.2572-2587, 1982.
- [3] T.Nakata, N.Takahashi and K.Fujiwara, "Solution of 3-D eddy current problems by finite elements", *Finite Elements, Electromagnetics and Design*(Ed.S.R.H.Hoole),pp.37-72,Elsevier,1995.

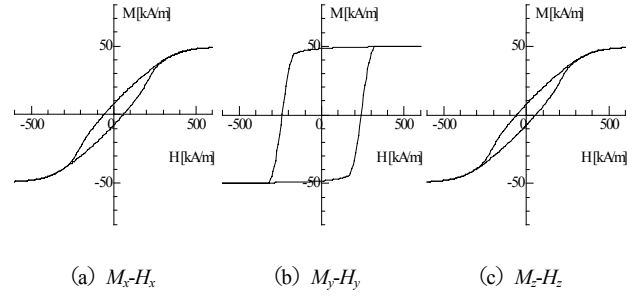


Fig.3 Hysteresis loops of a medium.

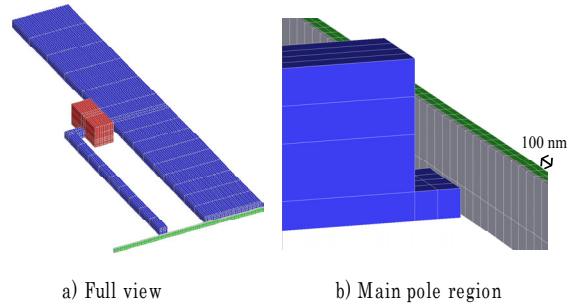


Fig.4 Mesh for SPT head model.

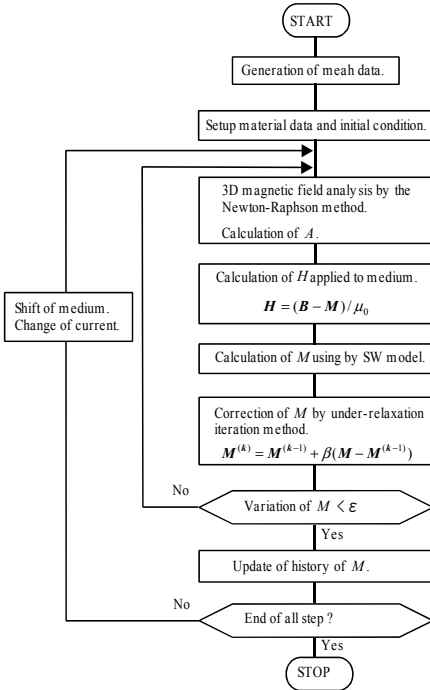


Fig.1 Flow chart of 3D Read/Write simulation system.

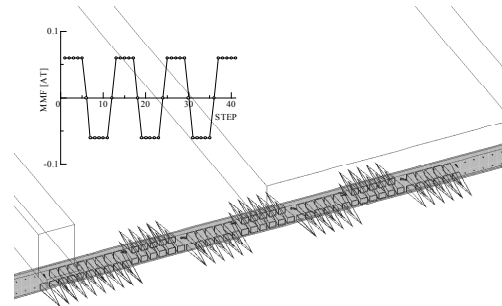
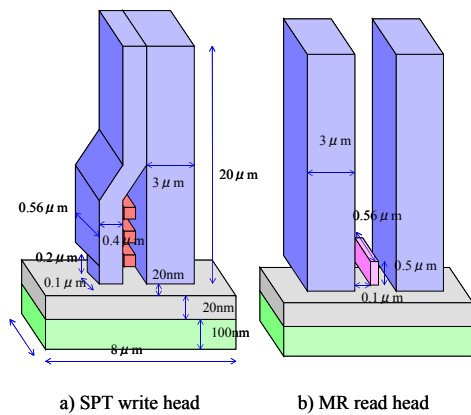


Fig.5 Recording current waveform and recorded bit pattern.

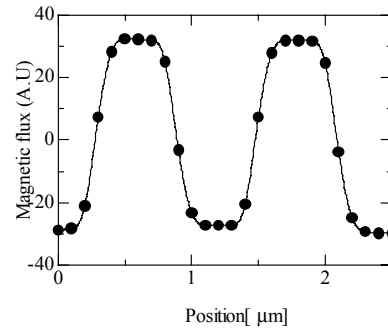


Fig.6 Output waveform for the recorded bit pattern in Fig.5

Key problems in Element-Free Galerkin Method for Electromagnetic Field Computations

Suzhen Liu, Qingxin Yang, Haiyan Chen, Weili Yan

Hebei University of Technology, Tianjin, 300130, China

E-mail: liu_suzhen@eyou.com

Abstract – In this paper, an improved formulation of the Element Free Galerkin method (EFGM) is proposed for electromagnetic field computation. Detailed research is conducted on some key problems, such as the selection of the weight function, the treatment of imposing boundary conditions and interface conditions. Finally, numerical examples are cited for demonstration.

I. INTRODUCTION

In the finite element method (FEM), mesh generation is a far more time-consuming and expensive task than the assembly and solution of the finite element equations. Moreover, there are certain classes of problems for which the finite element method (FEM) is difficult, or even impossible to be applied. For example, in electromagnetic field computation, with regard to thin plate problems, narrow air gap problems, moving conductors, cracks, etc., FEM usually requires remeshing in order to insure equality. Therefore, the huge computation time can be experienced during numerical analysis. For such problems, developments of advanced methods that do not rely on meshing are very advantageous.

The Element Free Galerkin Method (EFGM) is a method to obtain differentiable approximate function in the domain using known function values on discrete points through weighted least squares fitting. In this paper, the authors present successful complements of the element-free Galerkin method for electromagnetic field computation. First, a weight function suited electromagnetic field is given. Second, a penalty function is constructed in order to deal with essential boundary conditions. Thirdly, the treatment of interface between regions with different materials is also discussed. Finally, an application of the EFGM is presented and the numerical results are also given.

II. CHOICE OF WEIGHT FUNCTION

The weight function plays an important role in the performance of the method. It can exert a tremendous influence on the accuracy of solution, the amount of computation and the rate of convergence. In this paper, the weight function is selected as follows:

$$w_i(r_i) = \begin{cases} \frac{r_{mi}^2}{r_i^2 + \xi^2 r_{mi}^2} \left(1 - \frac{r_i}{r_{mi}}\right)^k, & (r_i \leq r_{mi}) \\ 0, & (r_i > r_{mi}) \end{cases}, \quad (1)$$

where $r_i = \|\mathbf{x} - \mathbf{x}_i\|$ is the distance between the two points \mathbf{x}_i and \mathbf{x} ; r_{mi} is the influence radius of \mathbf{x}_i ; ξ is a small positive value; k is a positive integer.

Moreover, if the weight function $w_i(\mathbf{x})$ is continuous together with its $(k-1)$ derivatives, the shape function $N_i(\mathbf{x})$ is also continuous together with its $(k-1)$ derivatives.

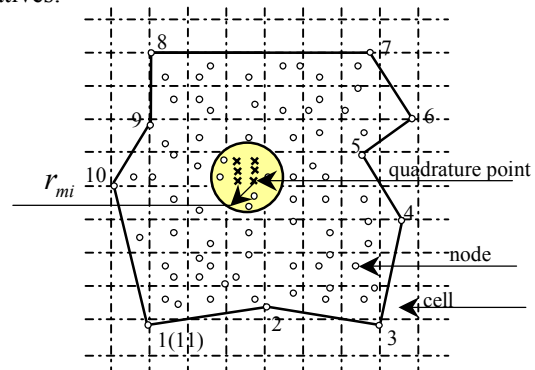


Fig. 1. Cell structure for quadrature in EFGM and domains of quadrature points

As can be seen in Fig. 1., the cells do not depend on the node disposition and they are simpler than the ordinary finite element mesh. On the other side, the integration is performed at each integration point of a simple integration cell. The radii of influence r_{mi} define the domain of influence of each integration point.

III. PENALTY FUNCTION

One of the biggest problems in the implementation of EFGM resides in that the used approach is not an interpolation. This implies that imposing the essential boundary conditions is very difficult. Some methods provide a means of overcoming the inherent difficulties, such as Lagrange multipliers^[1], modified variational principles^[2], coupling with finite element^[3]. However, Lagrange multipliers pose difficulties in that the resulting stiffness matrix is not

This work was supported in part by the natural science foundation of Hebei province of China under Grant No. 599017.

longer positive definite or banded. Modified variational principles are less accurate and rather inconvenient. Coupling with finite elements can result in discontinuities in the derivatives of the approximations.

In this paper, a penalty function for electromagnetic field computation is first given. With the penalisation method, we can obtain positive definite and banded stiffness matrix, which the size of problems is decreased. Further more, the results are very accurate.

We consider the following two-dimensional problem on the domain Ω bounded by Γ :

$$\begin{cases} \Omega : \nabla \cdot \beta \nabla \mathbf{u} = -f \\ \Gamma_1 : \mathbf{u} = \mathbf{u}_0 \\ \Gamma_2 : \frac{\partial \mathbf{u}}{\partial \mathbf{n}} = 0 \end{cases} \quad (2)$$

The equivalent variation form of the above equation is posed as follows:

$$\begin{cases} \Omega : \mathbf{I}(\mathbf{u}) = \int_{\Omega} \frac{1}{2} \beta (\nabla \mathbf{u})^2 d\Omega - \int_{\Omega} \mathbf{f} \mathbf{u} d\Omega = \min \\ \Gamma : \mathbf{u} = \mathbf{u}_0 \end{cases} \quad (3)$$

We would add to the above original functional the term

$$\begin{aligned} \pi &= \int_{\Gamma_k} \frac{1}{2} C [\bar{U}^2 - u(\mathbf{x})]^2 d\Gamma \\ &= \int_{\Gamma_k} \frac{1}{2} C [\bar{U}^2 + u^2(\mathbf{x}) - 2\bar{U} u(\mathbf{x})] d\Gamma \end{aligned} \quad (4)$$

With regard to two-dimensional problems, \bar{U} is the potential on one surface, $u(\mathbf{x})$ is the potential at the point \mathbf{x} and C is a penalty number, then the energy in the domain can be expressed as follows:

When π reaches its minimum, $u(\mathbf{x})$ approximates to \bar{U} .

Therefore, the total potential energy of the domain can be expressed as follows:

$$\begin{aligned} \mathbf{I}(\mathbf{u}) &= \int_{\Omega} \frac{1}{2} \beta (\nabla \mathbf{u})^2 d\Omega - \int_{\Omega} \mathbf{f} \mathbf{u} d\Omega \\ &\quad + \int_{\Gamma_k} \frac{1}{2} C [\bar{U}^2 + u^2(\mathbf{x}) - 2\bar{U} u(\mathbf{x})] d\Gamma \end{aligned} \quad (5)$$

Based on the law of minimum potential energy, the final discrete equations can be obtained through the derivative of function $\mathbf{I}(\mathbf{u})$ with respect to \mathbf{u}_i :

$$\mathbf{S}\mathbf{U} = \mathbf{F} \quad (6)$$

It should be pointed that this penalty function term is first put forward in electromagnetic field computation.

IV. INTERFACE CONDITION APPROXIMATION

Electromagnetic problems generally involve interfaces between different materials. This results in discontinuities of the magnetic induction tangential components when passing from a material to another. Therefore, it is necessary to introduce these discontinuities in the weight function. In this

paper, the visibility criterion is used. The effort to implement this technique is not very big, as can be seen in [4].

V. APPLICATIONS

Fig.2 shows the geometry of a simple two-dimensional magnetic problem. This problem has analytical solution and it is used to evaluate the EFGM precision. Which, $\mu_1 = 10\mu_0$, $\mu_2 = 10000\mu_0$, $\phi_1 = 200$, $\phi_2 = 100$. We can solve easily the magnetic potential (ϕ), and the results are given in Table I.

Although the example is simple, it tests some essential characteristics of EFGM, such as the treatment of essential boundary conditions and the interface between regions with different materials.

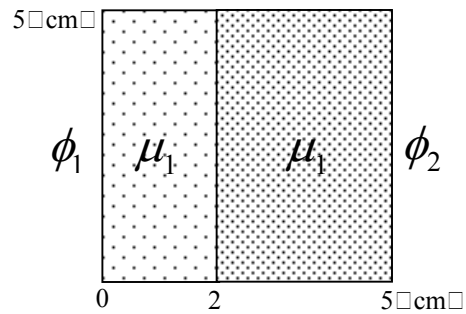


Fig.2 2D field domain with nonhomogeneous media

TABLE I. COMPARISON OF NUMERICAL SOLUTIONS BY EFGM WITH ANALYTICAL SOLUTION

Point (cm)	Analytical solution	EFGM solution
(1.0,0.0)	150.0749	150.075
(2.0,0.0)	100.1498	100.15
(3.0,0.0)	100.0999	100.1
(4.0,0.0)	100.0493	100.05

VI. CONCLUSION

As an effective complement method to FEM, EFGM can solve problems that FEM cannot solve effectively, such as the tiny gap problems and the thin board problems. Furthermore, being a potential method, EFGM will be widely applied to solving the electromagnetic problems along with the further study.

VII. REFERENCES

- Belytschko T., Lu Y.Y. and Gu L. Element-free Galerkin methods. *Int. J. for Num. Methods in Engrg.*, 1994, 37,229-256
- C. Herault, Y. Marechal. Boundary And Interface Conditions In meshless methods, *IEEE Transactions on Magnetics*, 1999,35(4):1450~1453
- T. Belytschko, D. Organ, and Y. Krongauz. A coupled finite element-element-free Galerkin method. *Computational Mathematics*, 17:186-195,1995
- Lu Y Y, Belytschko T, Gu L. A new implementation of the element free Galerkin method. *Comput Methods Appl Mech Engrg*, 1994, 113:397~414

Simplified Magnetic Moment Method Applied to Current Transformers Modeling

Fleur Janet⁽¹⁾⁽²⁾, Jean-Louis Coulomb⁽¹⁾, Christian Chillet⁽¹⁾, Patrick Mas⁽²⁾

⁽¹⁾Laboratoire d'Électrotechnique de Grenoble - INPG/UJF-CNRS UMR 5529 ENSIEG,
BP 46, 38402 St Martin d'Hères - France

⁽²⁾Schneider Electric, S2, avenue des Jeux Olympiques, 38100 Grenoble – France

Abstract – The aim of the study is to find a method to model electromagnetic devices which generate consequent magnetic leakage. Classical methods have proved to be efficient but time consuming. The method proposed in this article is based on the Magnetic Moment Method (MMM). We first introduce MMM and present a comparison with Finite Element Method in transient conditions. Then, a methodology to obtain a simplified MMM model is described. Beside the respectable accuracy, the simplicity of the model makes it possible to consider more complicated studies with reasonable resolution times.

INTRODUCTION

The study aims to contribute to the modeling of electromagnetic devices containing closed magnetic circuits, in particular current transformers. The difficulty of the problem is the quick saturation caused by high primary currents.

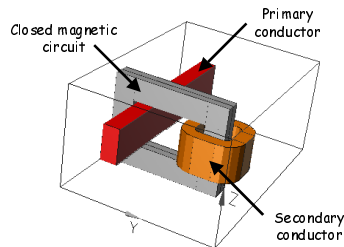


Fig. 1–Description of the studied device with closed magnetic circuit : a current transformer

The Finite Element Method (FEM) applied to such devices gives results with a good accuracy [1]. However, the method is time consuming. The Reluctance Network Method [2] has also been tested but is limited by the appearance of 3D magnetic leakage which is difficult to determine and to describe in a reluctance network (RNM) [3]. For these reasons, the study was then focused on another method, which gathers speed of simulation and saturation compatibility : the Magnetic Moment Method (MMM) [4].

After a short introduction to MMM, transient state results and comparison with FEM are presented so as to validate the application to current transformers. Then, a non conventional coupling between MMM and Reluctance Network Method is presented in order to generate a simple model of our sensor.

INTRODUCTION TO MAGNETIC MOMENT METHOD

Principle

Let us consider N ferromagnetic elements with uniform

magnetization vectors \mathbf{M}_i ($i=1,2..N$) and call \mathbf{H}_i the field strength in the center of the i^{th} element. \mathbf{H}_i is the superposition of an external field $\mathbf{H}_{ex,i}$ (created by inductors for example) and of the magnetic field produced by each element. We can write [5]:

$$\mathbf{H}_i = \sum_{j=1}^N g_{i,j} (\mathbf{M}_j) + \mathbf{H}_{ex,i} \quad i=1,2..N \quad (1)$$

where $g_{i,j}$ defines the matrix relation between the field in the center of the object i , created by the object j , and the magnetization vector of the object j .

Concurrently, in a ferromagnetic element, magnetization vector \mathbf{M}_i evolves relatively to the magnetic field \mathbf{H}_i . The relation is given by the material characteristic :

$$\mathbf{M}_i = f(\mathbf{H}_i) \quad i=1,2..N \quad (2)$$

Eqs. (1) and (2) describe the studied problem. Their simultaneous resolution with a relaxation procedure leads to the solution.

The restriction of the modeling to the sources and ferromagnetic elements of the problem has a consequent effect on computing time and facilitate parameterization

RADIA software, which is developed by researchers of the ESRF, has been chosen for the study. Radia [6] is a powerful 3D magneto-static implementation of the MMM .

Magnetic Moment Method Application

The pertinent information when studying current transformers is the secondary coil response $I_2(t)$ to a primary excitation $I_1(t)$. As Radia implementation of MMM is limited to static simulations, MMM secondary current signals are reconstructed using a response surface approach [7]. Due to configuration, eddy currents are neglected.

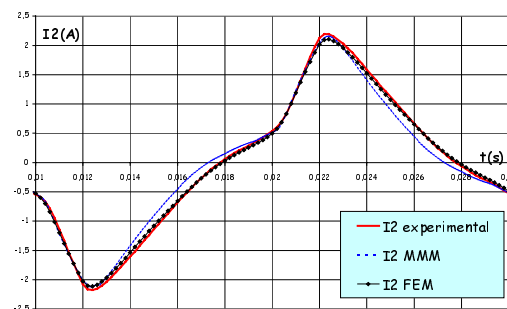


Fig. 2– Temporal secondary current signal for a saturating magnetic circuit. Comparison between experimental, FEM generated and MMM coupled with response surface generated signals.

Fig. 2 compares experimental temporal secondary current with MMM and FEM. As can be seen, MMM reconstructed signal gives fair results.

SIMPLIFIED MAGNETIC MOMENT METHOD COUPLED WITH RELUCTANCE NETWORK METHOD

Principle

The aim of this part is to generate a simplified magnetic moment method based model with very few elements.

This approach is tested on the studied transformer which is subdivided in four elements (due to symmetry). Magnetic field in the center of each bloc can be expressed as follows :

$$H_i = \sum_{k=1}^4 \alpha_{ik} \cdot M_k + \sum_{j=1}^2 \beta_{ij} \cdot I_j \quad i=1,2..4 \quad (3)$$

where coupling coefficients α_{ik} and β_{ij} define the relation between one source (I or M) and its effect in the studied element. These coefficients can be calculated with analytical formulas. Authors prefers FEM resolutions as a first step.

Concurrently, magnetization vector M_k in an element can be deduced from magnetic field by using the material characteristic curve $M_k(H_k)$ (4).

Simultaneous resolution of equations (3) and (4) with a relaxation process makes it possible for a given couple of currents (I_1, I_2) to determine a magnetic state of the device, for which can be deduced the flux under the secondary coil.

Reconstruction of the secondary signal employing this simple method is presented on Fig. 3. Results are very interesting relatively to the simplicity of the model.

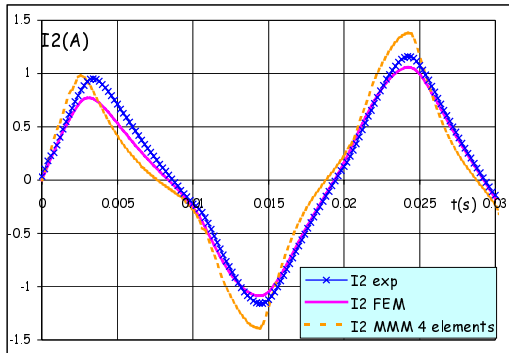


Fig. 3– Temporal secondary current signal for a saturating magnetic circuit. Comparison between experimental, FEM generated and four element MMM coupled with response surface generated signals.

However, reducing the number of elements used by MMM implies the non-respect of magnetization uniformity hypothesis in each bloc and induces error. Even though this error is small when studying static saturated devices, it is necessary to correct the model so as to have reliable results in other cases.

The idea is to use Reluctance Network Method, well-known for its accuracy in linear cases, to adjust the model.

Results

Fig. 4 presents variations of induction in the center of one element when I_1 varies and I_2 is kept to zero. We can verify that the correction of MMM parameters with RNM makes it possible to correct MMM results for linear use.

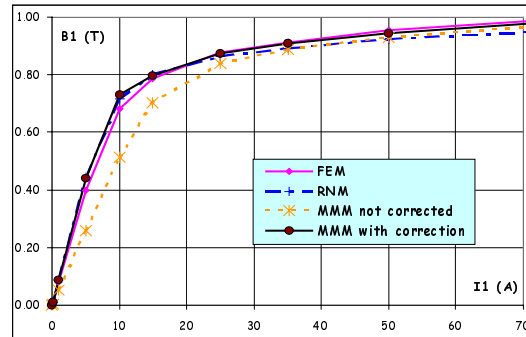


Fig. 4– Induction in the center of the first element of the model versus primary current ($I_2=0$) for corrected MMM static resolutions. Comparison with non corrected MMM, RNM and FEM.

CONCLUSIONS AND PERSPECTIVES

This paper presents an application of Magnetic Moment Method to current transformers. The method proves to be appropriate for steady state modeling of closed magnetic circuits. Moreover, resolution times are much shorter than with Finite Element Method.

The originality of the last part of the work is MMM and RNM coupling approach in order to generate simple static MMM based models. Very encouraging results can be obtained with a four element model corrected with RNM.

ACKNOWLEDGEMENT

The authors wish to thank Joël Chavanne and Sebastien Buffat for their support to this work.

V. REFERENCES

- [1] Y. Le Floch , G. Meunier, C.Guérin, P.Labie, X.Brunotte, D.Boudaud "Coupled Problem Computation of 3D Multiply Connected Magnetic Circuits and Electric Circuits", published in proc. of CEFC2002.
- [2] H. C. Roters, "Electromagnetic Devices", John Wiley & Sons Inc, pp.116-140, 1941.
- [3] D. Boudaud, "Modélisation Comportementale et Simulation des Capteurs de Courant, Optimisation Globale des Déclencheurs Electroniques dans les Disjoncteurs Industriels Basse Tension", Thèse de doctorat de l'UJF, Grenoble, juin 1999.
- [4] O. Chadebec, L.L. Rouve., J.L. Coulomb, J.P. Bongiraud, "New Method for a Fast and Easy Computation of Stray Fields Created by Wound Rods", COMPUMAG 2001, Lyon-Evian (France), July 2-5, 2001
- [5] P. Elleaume, O. Chubar, J. Chavanne, "Computing 3D Magnetic Field from Insertion Devices", proc. of the PAC97 Conference.
- [6] For more information, see : http://www.esrf.fr/machine/groups/insertion_devices/Codes/software.html
- [7] F.Janet, J.L.Coulomb, C.Chillet, P.Mas, "Magnetic Moment Method Applied to the modeling of current transformers", published in proc. of CEFC2002.

Computation of Voltage Driven, Current Dependent Ferrite Inductors using FEM

W. Renhart, C. Magele and K. Preis

Institute for Fundamentals and Theory in Electrical Engineering, Graz University of Technology
Kopernikusgasse 24/3
Graz 8010 Austria
werner.renhart@tugraz.at

Abstract— Ferrite inductors in practice will be excited very often by an impressed voltage of known signal form, while general the inductance values depend strongly on the current flowing during operation. Due to the non-linear behaviour of such magnetic devices, the arising current enforced by the driving voltage is not known in advance. A way how to find the associated currents with the aid of FEM-computations will be shown in this paper. On a lifelike ferrite inductor the proposed way will be demonstrated. Once the u/i-characteristic has been found, the inductor can be implemented in a network model to simulate any kind of operating state.

INTRODUCTION

Non-linear inductor devices find a large application area. Especially, the voluminous and lossy transformers in mains adapters have been replaced by switch-mode power supply devices. Numerously, its operating range runs from nearly no-load condition to full load. The basic principle of a switch-mode power supply is shown in Fig. 1.

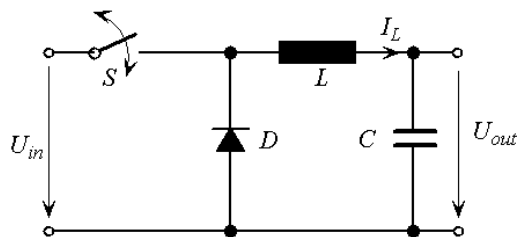


Fig. 1. Basic principle of a switch-mode power supply.

The switch S controls the output voltage U_{out} by varying the ratio between switching-time on and off, t_{on} and t_{off} , according to (1):

$$U_{out} = U_{inp} \frac{t_{on}}{t_{on} + t_{off}}. \quad (1)$$

In case of the switch S to be closed (t_{on}), the current I_L through the inductor increases, depending on the inductance value L . After switching off, the current flows over the diode D (during t_{off}). Thereby a large inductance value L limits the decrease of I_L . This is important, especially for low load conditions. To avoid a current flow interruption, a large value of L is required. So we need an inductor with large L -values at low currents.

Generally, magnetic circuits with small air gaps show high inductance coefficients at low magnetic excitation.

Due to the saturation of the core the L -values decrease very rapidly at higher currents. Curve 1 in Fig. 2 shows this behaviour. Devices with large air gaps have more or less constant but low L -values over a wide range of the current I , as indicated in curve 2. To get an inductor with the above mentioned requirements a combination of curve 1 and curve 2, like curve 3 in Fig. 2 is in demand.

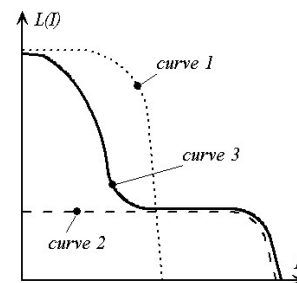


Fig. 2. $L(I)$ -Characteristic of magnetic circuits with different air gaps.

In order to achieve an inductor with an $L(I)$ -characteristic like curve 3, the ferrite core of an inductor may be manufactured as shown in Fig. 3. Two identi-

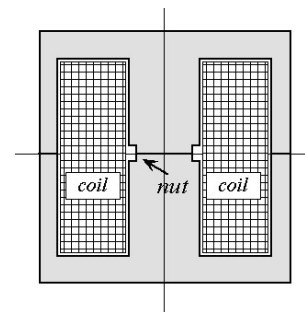


Fig. 3. Magnetic core with demanded $L(I)$ -characteristic.

cal halves of a mantle shaped core may be fitted together without air gap. In the middle of the core carrying the main magnetic flux, a nut can be inserted. The vicinity of this region will be saturated distinctly earlier than the remaining core. Designing size and shape of the nut may be a matter of an optimization process.

A 3D-FE model of the magnetic circuit shown in Fig. 3 has been developed. A static magnetic field formulation with the magnetic scalar potential Ψ [1],[2] and the reduced magnetic vector \vec{A}_r [3] has been applied. \vec{A}_r has been used to describe the field in the coil region and the core region, whereas the field elsewhere will be expressed with the magnetic scalar Ψ . The field quantities can be expressed by:

$$\vec{H} = \frac{1}{\mu} \nabla \times (\vec{A}_r + \vec{A}_e), \quad (2)$$

with the vector potential \vec{A}_e coming from the current running through the coil. For the remaining region in air follows

$$\vec{H} = -\nabla \Psi. \quad (3)$$

The reason for using the magnetic vector potentials can be found in the necessity of computing the voltage induced in the coil without derivating the computed quantities. Following Faraday's Law yields to

$$u = \oint_s \vec{E} \cdot d\vec{s} = -\frac{\partial}{\partial t} \oint_s (\vec{A}_r + \vec{A}_e) \cdot d\vec{s}. \quad (4)$$

Now, being able to compute the voltage induced of the non-linear magnetostatic problem, a step by step procedure can be applied to find the current enforced by the driving voltage.

STEP BY STEP PROCEDURE

The magnetic non-linearity enforces a discretization of the voltage signal in time, as shown in Fig. 4. For each

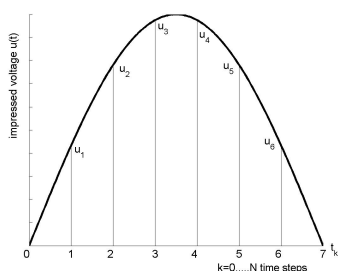


Fig. 4. Time discretization of the driving voltage.

time step k , a current I_k through the coil must be assumed and the non-linear field problem has to be solved by finite elements. Afterwards, the voltage induced has to be computed, according to (4). Now the computed value can be compared with the given voltage value u_k at t_k . The assumption for I_k must be adjusted until a predefined accuracy has been achieved. Thereafter the next time step $k + 1$ can be considered. Additionally, the current dependency of the non-linear inductance $L(I_k)$ can be found by

evaluating Faraday's Law

$$u(t_k) = L(I_k) \frac{\Delta I(t_k)}{\Delta t}. \quad (5)$$

NUMERICAL RESULTS

The ferrite core shown in Fig. 2 has been investigated whereby the procedure suggested above has been applied. Fig. 5 shows the obtained dependency $L(I_k)$. A slightly

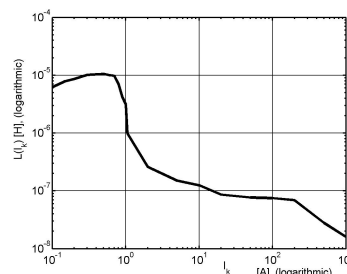


Fig. 5. $L(I_k)$ -characteristic of the core investigated.

corrugated run of the curve must be observed. It can be smoothed by selecting smaller intervals Δt so that the increments $\Delta I(t_k)$ in (5) become smaller as well. The $B-H$ -characteristic corresponds to a ferrite material N67 at an ambient temperature of 20° Centigrade and is taken from [4]. Wideness and depth of the nut immersed in the core of 9 mm of diameter amount to 1.75 mm and 1.95 mm, respectively.

CONCLUSION

The quite frequently case of the voltage excitation of magnetic non-linear devices has been treated. Special attention has been focused on finding the currents associated to the driving voltage. Therefore a step by step time scheme for the FE-computations has been discussed. In addition the non-linear dependence of the inductance L from the current could be constituted. Once this characteristic has been found, the non-linear behaviour of the ferrite inductance can be implemented in a network, in order to simulate the wide range of operating conditions. On a ferrite core the procedure suggested has been proven.

REFERENCES

- [1] O. Bir, K. Preis, K.R. Richter: "On the use of the magnetic vector potential in nodal and finite element analysis of 3D magnetostatic problems" IEEE Trans. Magn., vol. 32, No. 3, pp 651-654, 1996.
- [2] Preis K., I. Bardi, C. Magele, W. Renhart, Richter K.R., G.Vrisk: "Numerical analysis of 3D magnetostatic fields" IEEE Trans. Magn., vol. 27, pp 3798-3803, 1991.
- [3] W. Renhart, H. STgner, K. Preis: "Calculation of 3D eddy current problems by finite element method using either an electric or a magnetic vector potential", IEEE Trans. Magn., vol. 24, pp 122-125, 1988.
- [4] Siemens, "Ferrite data book", pp. 48, 1990/91.

Hybrid Numerical Techniques for Power Transformer Modeling: A comparative analysis validated by measurements

M. Tsili¹, A. Kladas¹, P. Georgilakis², A. Souflaris², C. Pitsilis², J. Bakopoulos², D. Paparigas²

¹Electric Power Division,
Department of Electrical & Computer Engineering
National Technical University of Athens
9, Iroon Polytechniou Street, 15780 Athens, Greece
e-mail: kladasel@central.ntua.gr

²Schneider Electric S.A.,
Elvim Plant
32011 Inofyta Viotia, Greece

Abstract— Power transformer analysis and design focussing on the equivalent circuit parameter evaluation by magnetic field numerical calculation is presented. The proposed method adopts a particular reduced scalar potential formulation enabling 3D magnetostatic problem solution. This method, necessitating no source field calculation, in conjunction with a mixed finite element –boundary element technique, results in a very efficient 3D numerical model for power transformer design office use. Computed results are validated through measurements. Such a methodology is very promising for investigation concerning losses and short circuit voltage variations with the main geometrical parameters.

MODELING TECHNIQUES

Numerical modeling techniques are now-a-days well established for power transformer analysis and enable representation of all important features of these devices [1,2]. More particularly, techniques based on finite elements present interesting advantages for nonlinear characteristics simulation. The leakage inductance evaluation has been extensively analyzed [10], as well as eddy current loss in transformer tank walls [7,8], iron lamination characteristics and design considerations [9]. Moreover, the combination of boundary and finite elements is widely used for electromagnetic problems since the electromagnetic field is not only confined to the conductors but it expands over extensive parts of air, where the use of a boundary element representation can significantly decrease the computational effort [5,6].

In the present paper a particular scalar potential formulation has been developed, enabling the 3D magnetostatic field analysis. According to our method the magnetic field strength H is conveniently partitioned to a rotational and an irrotational part as follows [3]:

$$\mathbf{H} = \mathbf{K} - \nabla\Phi \tag{1}$$

where Φ is a scalar potential extended all over the solution domain while \mathbf{K} is a vector quantity (fictitious field distribution), defined in a simply connected subdomain comprising the conductor, that satisfies Ampere's law and is perpendicular on the subdomain boundary.

The boundary element method is derived through discretization of an integral equation that is mathematically equivalent to the original partial differential equation. The boundary integral equation corresponding to Laplace equation is of the form:

$$c(s)\Phi(s) + \oint_{\Gamma} \left[\Phi(s') \frac{\partial G(s',s)}{\partial n} - G(s',s) \frac{\partial \Phi(s')}{\partial n'} \right] ds' = 0 \tag{2}$$

where s is the observation point, s' is the boundary Γ coordinate, n' is the unit normal and G the fundamental solution of Laplace equation in free space. Therefore, the matrix form of the equations corresponding to a coupled finite element/boundary element solution domain is of the form [5,6]:

1 . . . r	r+1 . . . m	m+1 . . . N _k	N _k +1 . . . N	N+1 . . . N+k	N+k+1 . . . N+n-k	N+n-k+1 . . . N+n	Φ ₁	=	O
.	Φ _r		
r+1	Φ _{r+1}		
.	Φ _m		
m+1	Φ _{m+1}		
.	Φ _{N_k }}		
N _k +1	Φ _{N_k+1 }}		
.	Φ _N		
N+1	0Φ _{r+1}		
.	0n		
N+k	0Φ _m		
.	0n		
N+k+1	0Φ _{m+1}		
.	0n		
N+n-k	0Φ _{N_k }}		
.	0n		
N+n-k+1	0Φ _{N_k+1 }}		
.	0n		
N+n	0Φ _N		
.	0n		

where $[S]$ and $[F]$ are the FEM matrices, $[H]$ and $[G]$ the BEM matrices while T_{ij} are the terms used to link the FEM to the BEM region.

RESULTS AND DISCUSSION

The proposed reduced scalar potential formulation has been applied in the 3D numerical analysis of a transformer under short circuit for its leakage reactance calculation. The case of the one phase part of a 1000 kVA, two tap 20-15kV / 400V

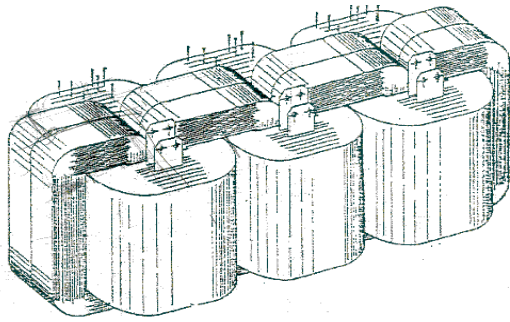


Fig. 1. Active part configuration of the three phase shell type distribution transformer considered.

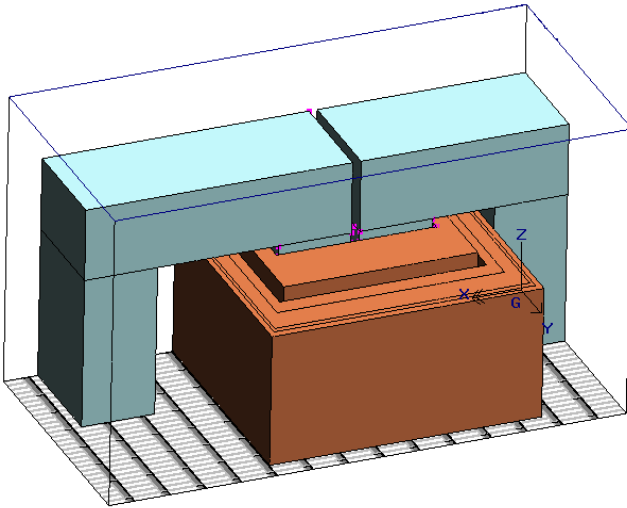


Fig. 2. Perspective view of the one phase transformer part modelled.

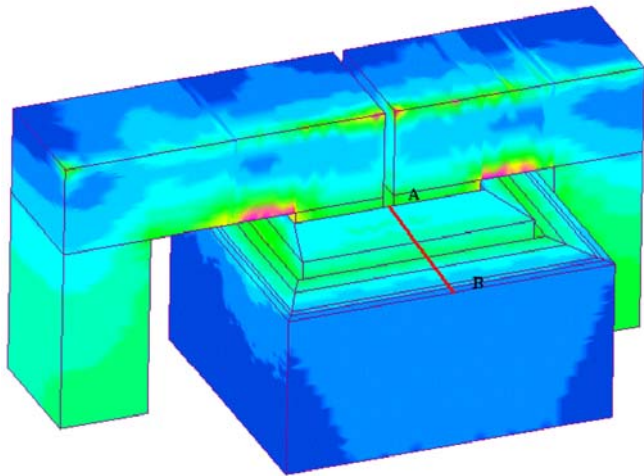


Fig. 3. Magnetic flux density magnitude distribution during short-circuit test

three phase shell type power transformer, shown in Fig. 1, has been considered. Fig. 2 illustrates the perspective view of the one-phase transformer part modeled.

The field values computed by the proposed 3D formulation have been compared to those measured by a Hall effect probe during short-circuit test. Fig. 4 gives the variation of the perpendicular flux density component B_n along the line AB,

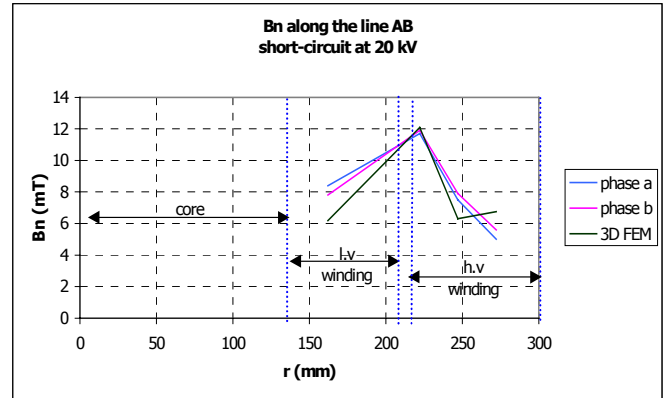


Fig.4. Comparison of measured and computed field values along the line AB.

positioned as shown in Fig. 2, in case of short-circuit with the high voltage winding connections corresponding to 20 kV voltage supply. This figure illustrates the good correlation of the simulated results with the local leakage field measurements.

REFERENCES

- [1] P. Georgilakis, N. Hatzigiorgiou, D. Pappas, "AI Helps Reduce Transformer Iron Losses", *IEEE Computer Applications in Power*, Vol. 12, Nr. 4, 1999, pp. 41-46.
- [2] P.S. Georgilakis, N.D. Doulamis, A.D. Doulamis, N.D. Hatzigiorgiou, S.D. Kollias, "A Novel Iron Loss Reduction Technique for Distribution Transformers Based on a Combined Genetic Algorithm - Neural Network Approach", *IEEE Trans. on Systems, Man, and Cybernetics, Part C, Applications and Reviews*, Vol. 31, Nr. 1, Feb. 2001, pp. 16-34.
- [3] A.G. Kladas, M.P. Papadopoulos, J.A. Tegopoulos, "Leakage Flux and Force Calculation on Power Transformer Windings under short-circuit: 2D and 3D Models Based on the Theory of Images and the Finite Element Method Compared to Measurements", *IEEE Trans. on Magnetics*, Vol. 30, Nr. 5/2, Sept. 1994, pp. 3487-3490.
- [4] Z.X. Feng, "The treatment of singularities in calculation of magnetic field by using integral method", *IEEE Trans. on Magnetics*, Vol. 21, Nr. 6, Nov. 1985, pp. 2207-2210.
- [5] G. Meunier, J.L. Coulomb, S.J. Salon, L. Krahenbul, "Hybrid Finite Element Boundary Element Solutions for three dimensional scalar potential problems", *IEEE Trans. on Magnetics*, Vol. 22, Nr. 5, Sept. 1986, pp. 1040-1042.
- [6] S.J. Salon, J. D'Angelo, "Applications of the hybrid finite element - boundary element method in electromagnetics", *IEEE Trans. on Magnetics*, Vol. 24, Nr. 1, Jan. 1988, pp. 80-85.
- [7] A. J. Moses, "Comparison of transformer loss prediction from computed and measured flux density distribution", *IEEE Trans. on Magnetics*, Vol. 34, Nr. 4, 1998, pp. 1186-1188.
- [8] C. Lin, C. Xiang, Z. Yanlu, C. Zhingwang, Z. Guoqiang, Z. Yinhan, "Losses calculation in transformer tie plate using the finite element method", *IEEE Trans. on Magnetics*, Vol. 34, Nr. 5, 1998, pp. 3644-3647.
- [9] I.L. Nahas, B. Szabados, R.D. Findlay, M. Poloujadoff, S. Lee, P. Burke, D. Perco "Three dimensional flux calculation on a three-phase transformer", *IEEE Trans. on Power Delivery*, Vol. 1, Nr. 3, 1986, pp. 156-160.
- [10] K. Zakrzewski, B. Tomczuk, "Magnetic field analysis and leakage inductance calculation in current transformer by means of 3D integral method", *IEEE Trans. on Magnetics*, Vol. 32, Nr. 3, 1996, pp. 1637-1640.

Computation of the magnetostatic field by means of a mixed analytical-numerical procedure

Fabrizio Bellina, Enrico Serra

Università di Udine, Dipartimento di Ingegneria Elettrica, Gestionale e Meccanica,
via delle Scienze 208, I 33100 Udine (Italy)

Fabrizio.bellina@uniud.it, Serra.enrico@spes.uniud.it

Abstract– The paper deals with a procedure for the computation of the magnetostatic field in vacuum. A very short summary of the most currently used methods for the field computation is given first, and their limits of applicability and drawbacks are recalled, then a mixed analytical-numerical method is presented which makes use of the analytical solution of Biot-Savart’s integral for simple elementary geometries. The method permits to obtain an accurate solution for a wide set of field source geometries even when the field is computed inside the sources.

I. INTRODUCTION

In a wide set of magnetostatic problems, in presence of a uniform magnetic permeability, the magnetic induction \mathbf{B} , or the vector potential \mathbf{A} can be determined straightforwardly solving the Biot-Savart’s integrals:

$$\mathbf{A} = \frac{\mu_0}{4\pi} \int_{\tau} \frac{\mathbf{J}}{r} d\tau \quad (1)$$

$$\mathbf{B} = \frac{\mu_0}{4\pi} \int_{\tau} \frac{\mathbf{J} \times \mathbf{r}}{r^3} d\tau \quad (2)$$

Where τ is the field source volume, i.e. the space domain where the current density vector \mathbf{J} is present. In a computer code, the direct numerical integration of (1) or (2) can be very time consuming, due to the large number of sample points sometimes required, and can lead to unacceptable errors when the field is computed inside the source, due to the well-known singularity of the integrand function. This last aspect can be critical, especially when the self and mutual inductance coefficients between field sources, or the self-field electromagnetic forces are computed.

For some types of source geometry and current density distribution, τ can be approximated as a set of adjacent space regions for which an analytical solution of these two integrals exist. Some formulas give the field generated by these simple elementary source geometries, as reported for instance in [1], [2], [3]. In this case the total field is a simple sum of the finite contributions of these elementary sources.

Another approach is reported in [4], where the volume integral (2) is replaced by a surface integral over the source boundary.

Again, for some elementary geometries, an analytical expression of this surface integral exists, therefore (2) can be replaced by a sum of the contributions from a finite number of elementary boundary surfaces. To the author’s knowledge, no transformation of the volume integral (1) in a surface integral is available, therefore this procedure is not applicable when, for instance, the self and mutual inductance coefficients between coils are to be computed.

When the field sources have a non uniform current density, or their geometry does not permit an efficient representation in terms of elementary sources, the numerical integration is the only way left. In some cases, however, a mixed analytical-numerical approach can still be followed: the field is computed starting from the contribution of monodimensional or bidimensional source subdomains of τ (like filaments or thin sheets), for which an analytical solution exists; this contribution is then numerically integrated, to complete the volume integration. Compared with the direct integration of (1) and (2), the advantage of this procedure is that, usually, in this way not only a shorter computation time is needed, but also a lower singularity level, or no singularity at all is present for the integrand function, when the point P is inside the source.

II. FIELD GENERATED BY A UNIFORM CURRENT DENSITY DISTRIBUTION

In order to develop an automatic computer procedure for the 3D magnetic field computation, we started our analysis with a general approach, considering the magnetic vector potential \mathbf{A} generated by a general-shaped space region τ^* in which a uniform current density \mathbf{J} is present. This region can be mono-, bi- or three-dimensional, and the physical dimension of vector \mathbf{J} changes accordingly. Within this hypothesis, (1) becomes:

$$\mathbf{A}(P) = \mathbf{J} \frac{\mu_0}{4\pi} \int_{\tau^*} \frac{1}{r} d\tau = \frac{\mu_0}{4\pi} \mathbf{J} \cdot \mathfrak{S}(\tau^*, P) \quad (3)$$

$\mathfrak{S}(\tau^*, P)$ is a function of the location P where the field is to be computed and the location, geometry and orientation of the source, τ^* . From (3), the magnetic induction in P can be easily obtained:

$$\mathbf{B}(P) = -\frac{\mu_0}{4\pi} \mathbf{J} \times \mathbf{grad}_P [\mathfrak{S}(\tau^*, P)] \quad (4)$$

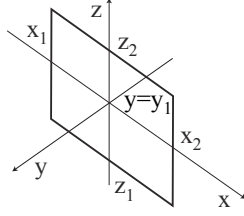


Fig. 1. 2D rectangular current slab. The current density vector \mathbf{J} can have whatever orientation with respect to XYZ axes.

The gradient in this formula is to be computed with respect to the point P coordinates.

To achieve enough flexibility of the sources representation, we found the analytical expression of $\mathfrak{Z}(\tau^*, P)$ and its gradient for a set of important elementary geometries. As an example, for the 2D rectangular thin slab represented in Fig. 1, for which a 2D current distribution is assumed, $\mathbf{grad}[\mathfrak{Z}(\tau^*, P)]$ is:

$$\mathbf{grad}[\mathfrak{Z}(\tau^*, P)] = \sum_{k=1}^2 \sum_{i=1}^2 (-1)^{i+k} \begin{bmatrix} -\log|w_k + r_{ik}| \\ \tan^{-1}\left(\frac{u_i w_k}{v_1 r_{ik}}\right) \\ -\log|u_i + r_{ik}| \end{bmatrix} \quad (5)$$

where $P \equiv (x, y, z)$, $u_i = x_i - x$, $w_k = z_i - z$, $v_1 = y_1 - y$ and $r_{ik}^2 = u_i^2 + v_1^2 + w_k^2$, as defined in [3]. When the current density \mathbf{J} is parallel to z axis, one can find from (4) the expression of \mathbf{B} reported in [3].

The analytical expression of $\mathfrak{Z}(\tau^*, P)$ for a source subdomain, can be numerically integrated along the other coordinate(s). As an example, if the source segment highlighted in Fig. 2A is considered, in which a uniform current density is supposed to be present, the field can be computed considering the 2D source cross-sections, whose contribution is numerically integrated along the longitudinal source coordinate s^1 , as sketched in Fig. 2B. At each s^1 value, the cross-section sizes and orientation change, as well as the angle between the current density and the surface.

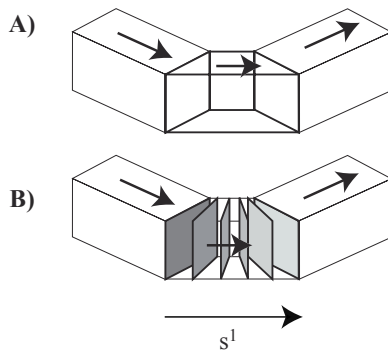


Fig. 2. A): 3D source segment with a uniform current density. B): view of the surfaces considered for the computation of $\mathfrak{Z}(\tau, P)$.

III. APPLICATIONS

A computer code has been developed for the magnetostatic field computation, in which the formulas of $\mathfrak{Z}(\tau^*, P)$ and $\mathbf{grad}[\mathfrak{Z}(\tau^*, P)]$ for a set of important elementary geometries have been implemented so far. The code is presently under full development and it is being used for the simulation of the behaviour of the superconducting magnets built with *cable-in-conduit conductors* (CICC). This type of conductor is made by several superconducting strands, wound together in some consecutive stages, to form larger and larger bundles made up to more than one thousand strands. The behaviour of these conductors strongly depends on the magnetic coupling between the strands, and the resistive contacts between them, distributed along the cable. Non homogeneous current distributions can take place within these CICC, with possible local overloadings and final magnet quench. The code permits a relatively accurate geometrical description of the complex CICC geometry and this model is used mainly for two main purposes. The first is the simulation of the current distribution within the CICC, based on a lumped inductive-resistive network model [5]. The other model application is the inverse problem of the identification of the current distribution inside the CICC: the current density distribution is determined starting from the signals given by sets of Hall probes suitably located around the CICC [6].

IV. CONCLUSIONS

A mixed analytical-numerical procedure has been outlined in this short version, which permits an accurate computation of the magnetic field generated by sources with uniform current density in air. Under certain hypotheses, it is possible to use the analytical expressions also in presence of a non uniform current density, as it is for example in a thick coil. In the full paper, the formulas for a set of elementary sources will be given, as well as the details of their application in a computer procedure.

REFERENCES

- [1] B. Azzerboni, E. Cardelli, A. Tellini, "Computation of the Magnetic Field in Massive Conductor Systems," *IEEE Trans. on Magnetics*, Vol. 25, pp. 4462-4473, Nov. 1989.
- [2] L. Urankar, "Vector Potential and Magnetic field of Current-Carrying Finite Arc Segment in Analytical Form, Part IV: General Three-Dimensional Current Density," *IEEE Trans. on Magnetics*, Vol. 20, pp. 2145-2150, Nov. 1984.
- [3] L. Urankar, "Vector Potential and Magnetic field of Current-Carrying Finite Arc Segment in Analytical Form, Part II: Thin sheet approximation," *IEEE Trans. on Magnetics*, Vol. 18, pp. 911-917, 1982.
- [4] M. Gyimesi, D. Lavers, T. Pawlak, D. Ostergaard, "Biot-Savart Integration for Bars and Arcs", *IEEE Trans. on Magnetics*, Vol. 29, pp. 2389-2391, Nov. 1993.
- [5] F. Bellina, P. Bettini, F. Trevisan, "Electromagnetic analysis of superconducting cables and joints in transient regime", presented at the Tenth Biennial IEEE Conference on Electromagnetic Field Computation, Perugia, Italy, June 16-19, 2002.
- [6] F. Bellina, P. Bettini, F. Trevisan, "Optimisation analyses of the magnetic measurements on multistrand SC cables", *IEEE Trans. on Applied Superconductivity*, Vol. 12, pp. 1651-1654, March 2002.

Automatic Generation of Sizing Models for the Optimisation of Electromagnetic Devices using Reluctance Networks

Augustin Delale, Laurent Albert, Frédéric Wurtz and Laurent Gerbaud

Laboratoire d'Electrotechnique de Grenoble (INPG/UJF - CNRS - UMR 5529),
ENSIEG, B.P. 46,38402 Saint Martin d'Hères Cedex, FRANCE
e-mail : frederic.wurtz@leg.ensieg.inpg.fr

Abstract — Models for the sizing of electromagnetic devices using reluctance network approach are very interesting especially for the sizing and the optimisation. Unfortunately, too often, designer do not use this approach because it is time consuming to use, mainly because of the need to write and to solve the network equations. We have developed a tool that automates all those symbolic operations. We also generate software components that allow to use those models very efficiently in an optimisation process by providing the formal right sensitivity. The methodology and the software will be presented as well as their application on examples.

INTRODUCTION

A designer can use different kinds of numerical models in order to size and to optimise a device. Some of them, like the FEM or the boundary element method, can be very precise, but need large computation time that limits the number of parameters and constraints that can be taken into account. So the designer should also use, especially in the first step of the design when he has to size a high number of parameters with many constraints, a more macroscopic approach like the reluctance network approach [1], [2]. Unfortunately, This approach is often neglected because it is time consuming to implement: as soon as the designer has a network topology in mind, a lot of work has to be done to generate the equations and to implement them in a programming language, especially when saturating materials are used. This leads to write implicit equations and to solve them by using numerical methods. This paper describes solutions that could radically change this state of the art for the designer. We have indeed developed software methodologies and tools that automatically make this job for the designer. Some similar environments have still been developed [3], [4], but the originality of this work is that we have a solution to generate the right symbolic sensitivity of the output parameters of the network even in the case of non linear behaviours due to saturating materials.

AN AUTOMATIC GENERATOR OF SIZING MODELS USING RELUCTANCE NETWORK

The aim of this paper is the realization of an automatic sizing model generator using reluctance network (see Fig. 2). We have called this software SolvReluct. The designer has to provide:

The reluctance network of his device: This network has to be build by the designer. For this purpose, the designer can use his knowledge. He can also have made some fine simulations, by using for instance a FEM approach, in order to understand how the flux propagates in his device and what

could be the topology of the reluctance network able to simulate the behaviour of the device [5].

The expression of the reluctance: It can be a reluctance in air (1), in linear magnetic material (2) or in saturating magnetic material (3).

$$R = \frac{L}{\mu_0 \cdot S} \quad (1) \quad R = \frac{L}{\mu_0 \cdot \mu_r \cdot S} \quad (2) \quad R(\phi) = H\left(\frac{\phi}{S}\right) \cdot \frac{L}{\phi} \quad (3)$$

Some particular reluctances, like the one of Fig. 1 extracted from [2], can also be considered.

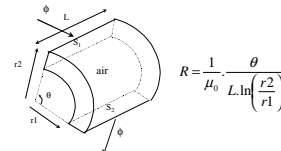


Fig. 1. A particular reluctance in air

Geometric relations: These relations connect the global geometric input parameters of the devices to the particular geometric parametric used in the expression of the reluctances (parameters L, S of (1), (2) and (3)).

Magnetic laws: it corresponds to the functions $H(B)=H(\phi/S)$ used in (3).

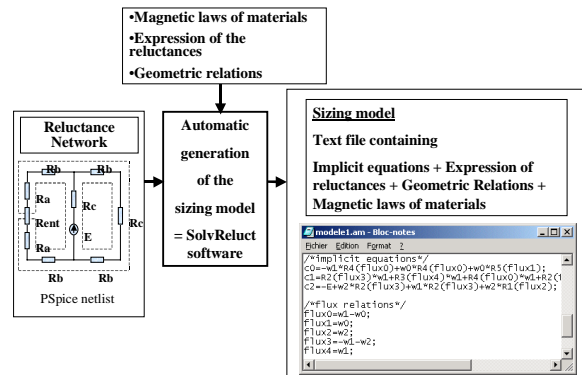


Fig. 2. Inputs and outputs of the sizing model generator

THE METHODOLOGY FOR THE AUTOMATIC GENERATION OF THE EQUATIONS OF THE SIZING MODEL

An algorithm has been used for the automatic symbolic generation of the equations. Fig. 3 illustrates it on a simple example. Let b to be the number of reluctances of the network. The goal is to generate the equations that allow to compute the b fluxes $\phi_j, j \in [1, b]$ of each reluctance. In fact we work with a reduced system. Starting from the netlist, given in the PSpice format, a node matrix N is built. A

number m of independent loops is defined by $m = b - n + 1$ and n is the number of nodes of the network. This allows to build a loops matrix S . The vector of the magneto-motive forces F of each loops, correctly oriented, is also built as well as the diagonal matrix R containing the reluctances. The following vector I is built:

$$I = F - S \cdot R \cdot S^T \cdot \psi \quad (4) \quad \text{with } \phi = S^T \psi \quad (5)$$

Ψ_i , $i \in [1, m]$ will be called the loops fluxes. The reluctances stored in R may depend on the fluxes ϕ that themselves depend on the loops fluxes ψ .

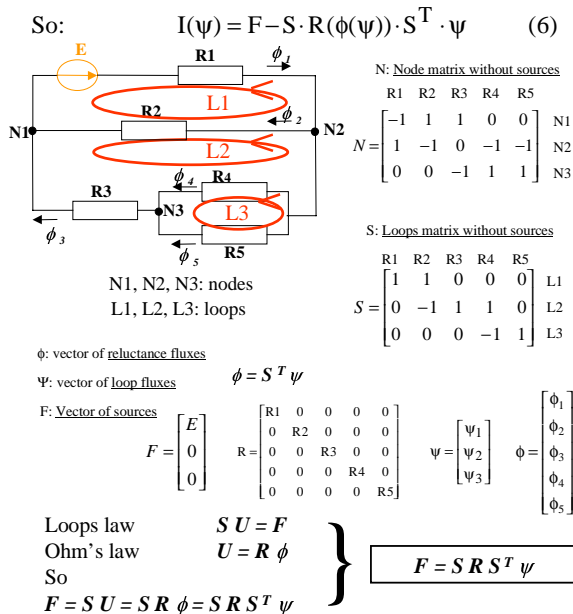


Fig. 3. Generation of the implicit equation on a simple example

The vector $I(\psi)$ is symbolically built. All the $I(\psi)_i$, constrained to be equal to 0, provide the implicit equations to solve in order to find the values of the Ψ_i . Then (5) is used to generate b symbolic expressions $\phi_i(\Psi_i)$.

The SolvReluct software implements this method. It has been entirely developed in Java language. We will describe its structure as well as all the procedures that automate the symbolic manipulation of the equations.

PROGRAMMING OF THE FORMAL RIGHT SENSITIVITY OF THE MODEL

In order to use efficiently the sizing model in an optimisation process, two approaches are adopted to manage the implicit equations $I(\psi)_i = 0$. They are exhaustively explained and compared in [6].

In the first one, the equations are generated with the SolvReluct software in a first mode. They are then automatically programmed in a software component equivalent to the one shown on the left part of Fig. 4. This programming is done with an automatic generator developed in our lab. and that is now commercially available¹. This

¹ : <http://www.designprocessing.com>

component has then to be integrated in an optimisation process in which the b constraints $I(\psi)_i = 0$ will have to be solved by the optimisation algorithm and the Ψ_i will be managed as degrees of freedom of the optimisation.

In the second one, the equations generated by SolvReluct and the automatic generator allows to create the software component shown on the right part of Fig. 4. In this case a numerical algorithm is internally used in the component in order to solve the implicit equations.

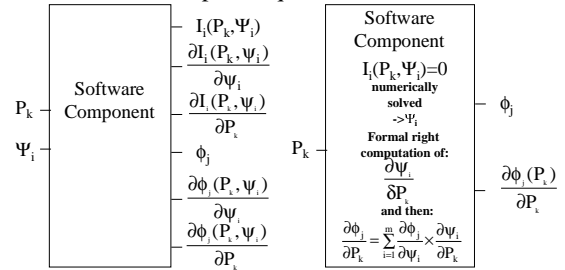


Fig. 4. The two kinds of software component generated for an use in an optimisation process (P_k , $k \in [1, r]$ are the input parameters of the reluctance network)

In order to show the efficiency of the tools developed, we will detail how they work on two examples. The first one is the example of a coil. The second one is a more complicated example of a claw pole alternator.

CONCLUSION

Thanks to a tool like SolvReluct, the designer has no symbolic operations or programming to do in order to use a reluctance network approach. This is certainly a key point to use such an approach especially for the sizing and optimising of devices when many parameters have to be considered. Another advantage is that the designer can test very easily new topologies and new variations of the reluctance network to use, before adopting the one he will use for his optimisation process. We also provide two approaches to generate the right partial derivatives of the output parameters of the network, which is another key point for the success of the optimisation process.

REFERENCES

- [1] J. Turowski, "Reluctance Networks", in Computational Magnetics, Edited by Jan K. Sykulski, chapter 4, Chapman & Hall Edition, ISBN 0-412-58570-7
- [2] H.C. Roters, "Electromagnetic Devices", New York: Wiley, 1941
- [3] M. E. H. Latreche, "modélisation magnétique et thermique des machines électriques par schémas équivalents", Thèse de l'Institut National Polytechnique de Toulouse, juillet 1987
- [4] A. Gentilhomme, A.; Bignon, J.; Coulomb, J.L.; Lauraire, "An expert system for preliminary design of contactors", IEEE Transactions on Magnetics, Volume: 28 Issue: 2, March 1992 Page(s): 1763-1766
- [5] C. Chillet, J.-Y. Voyant, "Design-oriented analytical study of a linear electromagnetic actuator by means of a reluctance network", IEEE Transactions on Magnetics, Volume: 37 Issue: 4 Part: 2, July 2001 Page(s): 3004-3011
- [6] C. Coutel, F. Wurtz, J. Bignon, "A comparative study of two methods for constrained optimisation with analytical models dealing with implicit parameters", IEEE Transactions on Magnetics, Volume: 35, No: 3, May 1999, Page(s): 1738-1741

Computation of the strayfields generated by magnetic a core with air-gap

R. Scorretti, N. Burais, J.P. Masson
CEGELY – UMR CNRS 5005 - Ecole Centrale de Lyon
69134 Ecully– France
e-mail : riccardo.scorretti@eea.ec-lyon.fr

Abstract – A quick method to compute the field generated by a magnetic circuits is presented. The method, based on the equivalence between a magnetized material and a distribution of fictive charges, allows to compute at the same time the flux inside the core, and the magnetic field in the surrounding air.

INTRODUCTION

We investigate the magnetic field generated in the air by electrical devices. Some classical numerical methods, like FEM or BEM, can be used to compute strayfields, but they generally lead to huge matrix systems, and require a detailed description of the geometry. On the other hand, the method of reluctances provides a simple way to perform an analytical computation of the flux inside a magnetic circuit, but it cannot be used to compute the surrounding field, since it is founded on the hypothesis of no-leakage flux. In [1] a simple method is proposed, but it cannot be applied to magnetic cores. We propose a numerical method to compute approximately both the flux inside a magnetic circuit, and the surrounding field. The method takes into account only the essentials features of the geometry of the system.

FORMULATION

Let Ω be the volume occupied by the core, and $\Gamma = \partial\Omega$ the boundary of Ω . The flux density is written as the sum of a term \vec{B}_{exc} due to the coils, and the reaction field \vec{B}_r . This one can be further decomposed[2] as the sum of the field $\mu_o \vec{E}^* = -\mu_o \overline{\text{grad}} V^*$ generated by a distribution of fictive charges, plus a term proportional to the magnetization \vec{M} :

$$\vec{B} = \vec{B}_{exc} + \mu_o (\vec{E}^* + k\vec{M}) \quad \text{with } k = \begin{cases} 1 & \text{inside } \Omega \\ 1/2 & \text{on } \Gamma \\ 0 & \text{in the air} \end{cases} \quad (1)$$

The volume (ρ^*) and surface (σ^*) fictive charge densities which generate the scalar potential V^* are given respectively by : $\rho^* = -\mu_o \text{div } \vec{M}$ and $\sigma^* = \mu_o \vec{M} \cdot \vec{n}$.

The core is represented by a discrete path of N elements $\{E_n\}_{n=1}^N$, connected by M sections $\{S_m\}_{m=1}^M$. Let

Φ_m be the magnetic flux through the section S_m , and Ξ be the set of the boundary sections (air-gaps).

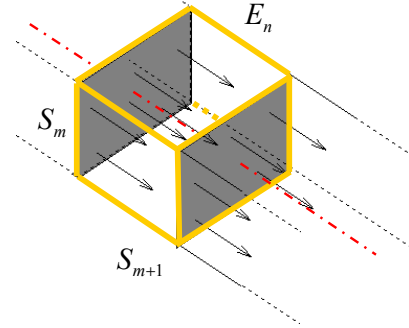


Figure 1: sketch of an element

The model is founded on the following four assumptions :

- A1** inside Ω , the flux density \vec{B} is parallel to the axis of the core, and uniform over each perpendicular section.
- A2** the core is made of a uniform, linear, isotropic, insulating magnetic material.
- A3** the magnetic flux Φ varies linearly in each element
- A4** the whole amount of charge in each element can be localized in the center of the element

A1 and A2 are classical assumptions. A1+A3 implies that ρ^* is constant in each element, and σ^* is zero in all the sections, excepted those on the boundary (that is $S_m \in \Xi$). A4 allows to simplify the numerical computations.

It can be shown easily that the total fictive charge over the elements E_n and sections $S_m \in \Xi$ is given respectively by :

$$q_{E(n)}^* = \frac{\mu_r - 1}{\mu_r} \left(\sum_{\text{inward } E(n)} \Phi - \sum_{\text{outward } E(n)} \Phi \right) \quad (2)$$

$$q_{S(m)}^* = \frac{\mu_r - 1}{\mu_r} \Phi_{\text{outward } S(m)} \quad (3)$$

Thus the potential V^* depends only upon the flux through the sections $\{\Phi_m\}_{m=1}^M$, which is taken as the unknown.

Substituting $\vec{M} = (\mu_r - 1)/(\mu_r \mu_o) \vec{B}$ in eq. 1, one finds :

$$\vec{B} = \begin{Bmatrix} \mu_r \\ 2\mu_r / (\mu_r + 1) \\ 1 \end{Bmatrix} (\vec{B}_{exc} + \mu_o \vec{E}^*) \quad (4)$$

where the value of the prefactor depends upon the coefficient k in eq. 1. The integration of eq. 4 over each section leads to:

$$\Phi_m = \left\{ \begin{array}{c} \mu_r \\ 2\mu_r / (\mu_r + 1) \\ 1 \end{array} \right\} (\Phi_{exc} + \mu_o \Phi_m^*) \quad (5)$$

where $\Phi_{exc} = \iint_{S_m} \vec{B}_{exc} \cdot \vec{n} ds$ is known, and the term

$\Phi_m^* = \iint_{S_m} \vec{E}^* \cdot \vec{n} ds$ is a linear combination of $\{\Phi_m\}_{m=1}^M$ whose

weights depends only upon the geometry of the core. Thus eq. 5 leads to a linear system, which can be solved to compute the flux through the sections Φ_m . Once $\{\Phi_m\}_{m=1}^M$ has been computed, the flux density is straightway computed in the air by eq. 4.

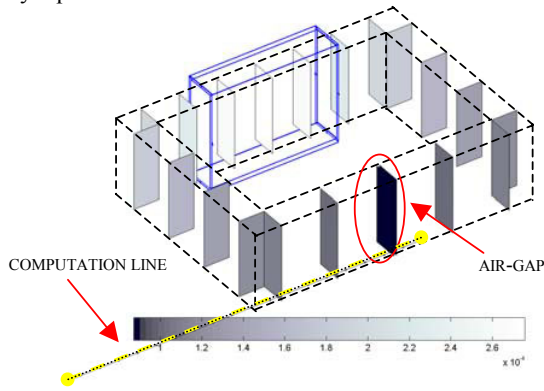


Figure 2 : flux density on the 21 sections used for the computation

IMPROVEMENT OF THE ACCURACY

In order to improve the accuracy of the solution, the Ampère's law is added as a strong constraint :

$$\oint \vec{H} \cdot d\vec{l} = \sum \frac{\pm \Phi_m}{\mu_o \mu_r S_m} L_n = NI \quad (6)$$

where L_n is the length of the n-th element and S_m is the surface of the m-th section. The sign of Φ_m depends upon the orientation of the m-th section. The linear system is then solved in the mean square sense using the Lagrange's multipliers method, and leads to a better solution.

It's worthful to remark that eq. 6 alone is the classical reluctance method. Indeed our formulation is a generalization of the reluctance method, where the no-leakage hypothesis (Φ constant in each element) has been replaced by the weaker assumptions A3 and A4.

We checked the effectiveness of the method on a simple magnetic circuit composed of a core ($\mu_r=100$, $80 \times 110 \times 30$ mm), a rectangular coil ($I=0.5$ A.turns) and an air-gap of 1 mm. In fig. 2 we plot the flux density in the core, computed using 21 sections. The same problem has been solved with the finite-elements software FLUX3D using 123876 first-order elements. In fig. 3 the flux density computed in the air along a straight line (the dotted line in fig. 2) is plotted as a function of the distance from the core. A good agreement is found between our method and FLUX3D.

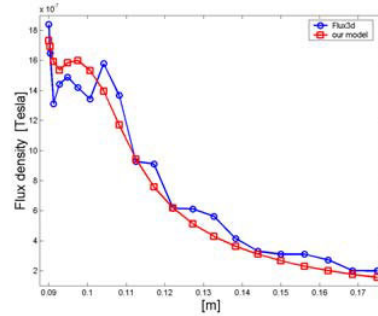


Figure 3 : flux density computed along the dotted line (see fig. 2)

CONCLUSION

The proposed method allows to easily compute the flux density generated by a linear magnetic circuit. The accuracy of the result is not as good as in some classical methods like FEM or BEM. This may be due to the fact that some of the assumptions begin to fail in proximity of the edges of the core. However this is acceptable when one takes into account the low computational effort required. More details about the limits of the model will be given in the full paper.

REFERENCES

[1] O. Chadebec, L-L. Rouve, J-L. Coulomb and J-P. Bongiraud, *New method for a fast and easy computation of stray fields created by wounds rods*
 [2] E. Durand, *"Magnétostatique"*, 1968, Masson, Paris

A Novel Auto-Tuning Algorithm for the Integrated RBF Network of Brushless D.C. Motor

S. L. Ho¹, M.N. Fei², K.W.E. Cheng¹ and H.C. Wong³

¹Department of Electrical Engineering, ³Industrial Centre, The Hong Kong Polytechnic University, Hong Kong

²Department of Automation, Shanghai University, Shanghai 200072, P. R. China

Email : eeslho@polyu.edu.hk

Abstract—Integrated Radial Basis Function (IRBF) network was reported to be efficient in the performance study of brushless dc motors. However such algorithm cannot be implemented readily since it is difficult to auto-tune or even to find the undetermined coefficients in the integrated RBF network. In this paper, a novel auto-tuning algorithm that can effectively guarantee the automatic implementation of the integrated RBF network of brushless dc motor is reported.

INTRODUCTION

The circuit-field (or field-circuit) coupled model of the brushless dc motor is more accurate, albeit computationally less efficient, than its circuit counterpart in studying the output characteristics of brushless dc motors. Hence, circuit-field coupled model is generally limited to off-line simulations only. To develop an on-line algorithm, an efficient RBF technique using artificial neural network based techniques is proposed to simulate and control the electric machines [1].

The outputs of the stator phase currents i_A, i_B, i_C and the motor torque T are dependent on the inputs of the normalized stator voltages u_A, u_B, u_C and the rotor position θ in a highly nonlinear manner. However changes of outputs against the impressed stator voltage u_m or the rotor speed ω can be regarded as virtually linear within a limited range. Hence, the IRBF network, which can be applied in the control and design optimisation of brushless dc motor with the same computational efficiency and accuracy as that in magnetic field computation using finite element modeling (FEM), has been proposed [2]. However, it is well-known that the undetermined coefficients in the IRBF network cannot be found accurately and automatically. In this paper a novel auto-tuning algorithm of the undetermined coefficients in the IRBF network of the brushless dc motor is reported.

INTEGRATED RBF NETWORK PRINCIPLE

Radial Basis Function (RBF) network has a linear output layer and a simple structure with a nonlinear hidden layer to synthesis the local approximations corresponding to the nonlinear input-output mapping of the brushless dc motor as:

$$\begin{cases} i_A = f_A(u_A, u_B, u_C, \theta, \omega, u_m) \\ i_B = f_B(u_A, u_B, u_C, \theta, \omega, u_m) \\ i_C = f_C(u_A, u_B, u_C, \theta, \omega, u_m) \end{cases} \quad (1)$$

$$T = f_T(i_A, i_B, i_C, \theta, \omega, u_m) \quad (2)$$

The basic idea of the IRBF network [2] is that, by using an approximate piecewise-linear assumption within a certain

range, one should model the centre point ($u_m = u_{mc}$ and $\omega = \omega_c$) by an adaptive RBF network. The adjacent and basic points ($u_m = u_{mb1}, u_{mb2}, \dots$ and $\omega = \omega_{b1}, \omega_{b2}, \dots$) could be modeled by the RBF network group with the same number of hidden layer nodes and parameters as the Gaussian based functions.

Both the adaptive RBF network to model the centre point and the RBF network group to model the basic points are dependent on the training data from the circuit-field coupled time stepping FEM computation [3]. Hence the IRBF network for modeling other points within a certain range (see Fig. 1) requires no additional training data for the same hidden layer.

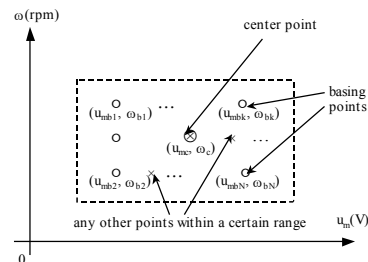


Fig.1. The diagrammatic sketch of integrated RBF network mechanics

To construct the IRBF network $w_{ij}^{(I)}$, however, the weighting matrixes $w_{ij}^{(k)}$ of the linear layer of the RBF network group are used as the bases of the IRBF network. In order to reduce undetermined coefficients and to implement the auto-tuning algorithm efficiently, the main equations of the IRBF network are given as follows,

$$y_i^{(I)} = \sum_{j=1}^n w_{ij}^{(I)} O_j^{(I)}(x) \quad (3)$$

$$w_{ij}^{(I)} = \sum_{k=1}^{N_b} \mu_k^{(I)} w_{ij}^{(I)k} \quad (4)$$

$$\mu_k^{(I)} = c_{\omega}^{(I)} \exp\left(-\left(\frac{\omega - \omega_{bk}}{\omega_c - \omega_{bkmax}}\right)^2\right) + c_{um}^{(I)} \exp\left(-\left(\frac{u_m - u_{mbk}}{u_{mc} - u_{mbkmax}}\right)^2\right) \quad (5)$$

where $y_i^{(I)}$ is the output of the IRBF network, the superscript (I) refers to the network of current output or torque output, n is number of nodes in the hidden layer, N_b is the number of basis points, and c_{ω} and c_{um} are the undetermined coefficients. Usually, it is difficult to find suitable values of c_{ω} and c_{um} in the IRBF network.

AUTO-TUNING PRINCIPLE

In order to find the optimized values of the undetermined coefficients c_{ω} and c_{um} automatically, the quadratic object

function of any specific point in an approximately linear range is defined as follows:

$$J = \sum_{i=1}^N [y_i^{d(i)} - y_i^{(i)}]^2 \quad (6)$$

that is

$$J = \sum_{i=1}^N \left[y_i^{d(i)} - \sum_{k=1}^{N_b} \mu_k y_i^{(i)k} \right]^2 \rightarrow \min \quad (7)$$

where $y_i^{d(i)}$ is the output of the circuit-field coupled time stepping FEM computation, $y_i^{(i)k}$ is the output of the RBF network group, N is the total length of the output series.

Assuming that $\frac{\partial J}{\partial \hat{c}_\omega} = 0, \frac{\partial J}{\partial \hat{c}_{um}} = 0$, then the optimized solutions c_ω and c_{um} are obtained as follows:

$$\begin{cases} \hat{c}_\omega^{(i)} = \frac{A_{uu}^{(i)} B_\omega^{(i)} - A_{u\omega}^{(i)} B_u^{(i)}}{A_{\omega\omega}^{(i)} A_{uu}^{(i)} - A_{\omega u}^{(i)} A_{u\omega}^{(i)}} \\ \hat{c}_{um}^{(i)} = \frac{A_{\omega\omega}^{(i)} B_u^{(i)} - A_{\omega u}^{(i)} B_\omega^{(i)}}{A_{\omega\omega}^{(i)} A_{uu}^{(i)} - A_{\omega u}^{(i)} A_{u\omega}^{(i)}} \end{cases} \quad (8)$$

where $A_{uu}, A_{\omega u}, A_{u\omega}, A_{\omega\omega}$ and B_u, B_ω are measurable functions as given below:

$$A_{\omega\omega}^{(i)} = \sum_{i=1}^N \left[\sum_{k=1}^{N_b} \exp \left(- \left(\frac{\omega - \omega_{bk}}{\omega_c - \omega_{bk \max}} \right)^2 \right) y_i^{(i)k} \right]^2 \quad (9)$$

$$A_{\omega u}^{(i)} = \sum_{i=1}^N \left\{ \left[\sum_{k=1}^{N_b} \exp \left(- \left(\frac{\omega - \omega_{bk}}{\omega_c - \omega_{bk \max}} \right)^2 \right) y_i^{(i)k} \right] \cdot \left[\sum_{k=1}^{N_b} \exp \left(- \left(\frac{u_m - u_{mbk}}{u_{mc} - u_{mbk \max}} \right)^2 \right) y_i^{(i)k} \right] \right\} = A_{u\omega}^{(i)} \quad (10)$$

$$A_{uu}^{(i)} = \sum_{i=1}^N \left[\sum_{k=1}^{N_b} \exp \left(- \left(\frac{u_m - u_{mbk}}{u_{mc} - u_{mbk \max}} \right)^2 \right) y_i^{(i)k} \right]^2 \quad (11)$$

$$B_\omega^{(i)} = \sum_{i=1}^N \left[y_i^{d(i)} \sum_{k=1}^{N_b} \exp \left(- \left(\frac{\omega - \omega_{bk}}{\omega_c - \omega_{bk \max}} \right)^2 \right) y_i^{(i)k} \right] \quad (12)$$

$$B_u^{(i)} = \sum_{i=1}^N \left[y_i^{d(i)} \sum_{k=1}^{N_b} \exp \left(- \left(\frac{u_m - u_{mbk}}{u_{mc} - u_{mbk \max}} \right)^2 \right) y_i^{(i)k} \right] \quad (13)$$

These equations are available if the auto-tuning algorithm works at a limited range near the specific point that builds a quadratic object function. Moreover, instead of eq. (6), eqs. (7)-(13) can be modified with the quadratic object function about some specific points being constructed as follows:

$$J = \sum_{i=1}^{N_a} \sum_{i=1}^N [y_{i,i}^{d(i)} - y_{i,i}^{(i)}]^2 \quad (14)$$

where N_a is the number of specific points used in the auto-tuning algorithm.

Note that even though additional training data from some points are required by the IRBF algorithm when compared to that of the trial-and-error method, the IRBF network with the auto-tuning algorithm can effectively build as well as compute all the points accurately within a certain range without calling upon the time consuming FEM computation.

The auto-tuning algorithm has been used to automatically evaluate the undetermined coefficients c_ω and c_{um} of the IRBF network of a multi-pole PM brushless dc motor as shown in Fig.2 (200 W / 12 V, 22 poles, 24 stator slots, with Nd-Fe-B magnets). The training data used to build the frame of IRBF network as well as to optimize its undetermined coefficients are produced by FEM computations with a mesh of about 6000 nodes.

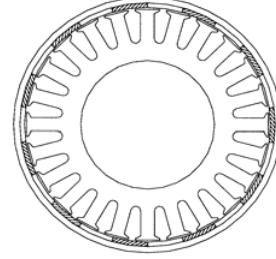


Fig. 2. A 3-phase motor with 22 poles and 24 slots

The experimental conditions are within the range of $|\omega - 220| < 20$ rpm and $|u_m - 10| < 1$ V. The target error $\sqrt{\sum_{i=1}^N [y_i^{(i)} - y_i^{d(i)}]^2 / \sum_{i=1}^N [y_i^{d(i)}]^2}$ is 0.05. The experiment results show that the auto-tuning algorithm can effectively guarantee a fully automatic modeling of the IRBF network.

CONCLUSIONS

In order to ensure the undetermined coefficients are found quickly, accurately and automatically, a novel auto-tuning algorithm in the IRBF network of the brushless dc motor is proposed. The fully automatic implementation of the IRBF network should be very valuable for practical and industrial applications. Based on the IRBF network of the brushless dc motor and its auto-tuning algorithm mentioned above, further investigations can also be carried out to extend the range of the impressed stator voltage u_m and the rotor speed ω for a given error tolerance for the simulation results obtained between the circuit-field coupled time stepping FEM computation and the IRBF network.

REFERENCES

- [1] P. Vas, "Recent trends and development in the field of machines and drives, application of fuzzy, neural and other intelligent techniques," Workshop on a.c. motor drives technology, *IEEE/IAS/PELS*, Vicenza, 1996, pp.55-74.
- [2] S.L. Ho, M.R. Fei, W.N. Fu et al., "Integrated RBF Network Based Estimation Strategy of Output Characteristics in Brushless D.C. Motors," *IEEE Trans. on Mag.*, Vol.38, No.2, March, 2002, pp. 1033-1036.
- [3] S.L. Ho, W.N. Fu, "A comprehensive approach to the solution of direct-coupled multislice model of skewed rotor induction motors using time-stepping eddy-current finite element method," *IEEE Trans. on Mag.*, vol. 33, no. 3, May, 1997, pp.2265-2273.
- [4] M.R. Fei, S.L. Ho, "Progress in on-line adaptive, learning and evolutionary strategies for fuzzy logic control," in *Proc. of IEEE PEDS*, Hong Kong, July, 1999, pp.1108-1113.

Optimal Design of Switched Reluctance Motor Drive

H. Zeroug*, H. Sahraoui**, and H. A. Toliyat***

*Electrical Engineering Department,
Institute of Electronics
U. S. T.H.B, BP32 El-Alia
16111, Algiers, Algeria.
Email: zeroughoucine@hotmail.com

** Electrical Engineering Department
National Polytechnic School
10, Rue Hacem Badi, El-Harrach
Algiers, Algeria
Email: houriasahraoui@hotmail.com

***Department of Electrical Engineering
Texas A&M University
College Station, TX 77843-3128
Fax: (979) 845-6259
Email: toliyat@ee.tamu.edu

Abstract- The paper describes investigations for the optimal design of Switched reluctance Motor (SRM). The approach focuses on the maximization of the average torque while minimizing torque ripple. The prediction of the average torque and torque ripple characteristics is based on FEM for several motor configurations where stator and rotor geometry parameters are varied, considering mainly the stator and rotor teeth. Prior to optimization, interpolation of the data was performed through function approximation using both least square method and neural network based on generalized radial basis function. Both approximation function results are very close and further show the higher accuracy of the neural network approach. The optimum parameters are obtained and confirmed by numerical field solutions.

INTRODUCTION

In this paper a switched reluctance motor with four phase regular 8/6 design optimization is performed. Usually, the criteria of optimization are maximization of average torque while reducing the torque ripple to the minimum, particularly for low speed operation. For this purpose, machine structure geometry and switching parameters are varied to achieve the optimum design [1,2,3]. In his paper, investigations on the significant geometry parameters are made. These are β_s and β_r , stator and the rotor pole arcs. In order to account for the geometry as well for the non-linearity of materiel utilized finite element method is used and solutions are obtained for several configurations corresponding to a set of (B_s , B_r), but limited to a region of the plane, called the feasible triangle [1]. Field solutions are used to determine the static torque characteristics.

In order to carry out shape optimization with sufficient accuracy, numerous field solutions are required. But this approach can be time consuming and require to adjust the meshing at each iteration; a task which is difficult to achieve. Interpolation techniques are therefore sought. The interpolation using non-linear least square method was implemented to produce a suitable function approximation. However, this has shown limitations as the error can become significant and hence the optimization may not be accurate. Another approach was explored for function approximation. This is neural network based using the generalized radial basis function [4]. After data training, a network is used to approximate the objective function. An optimization procedure was then performed using the data produced by the neural network approach.

POLE ARCS DESIGN CONSIDERATIONS

In order to produce an unidirectional torque, there must be an overlap between of the rotor and the poles of the excited stator phase. The overlap angle should be greater than the step angle, otherwise there will be 'gaps' where no torque is produced. Moreover, in order to get the largest possible variation of phase inductance with rotor position, the interpolar arc of the rotor must exceed the stator pole arc. A further constraint on the pole arcs is that usually the stator pole is made slightly smaller than the rotor pole arc. This permits slight increase in the slot area, the copper winding cross-section, and the align/unaligned inductance ratio. These constraints on the pole arcs can be expressed graphically in Fig, in which the 'feasible triangle' [1] define the range of combinations normally permissible. Of course, the variation in performance of SRM defined by different points in these triangle is considerable. But depends on various factors; torque ripple, the starting torque and the effects of saturation.

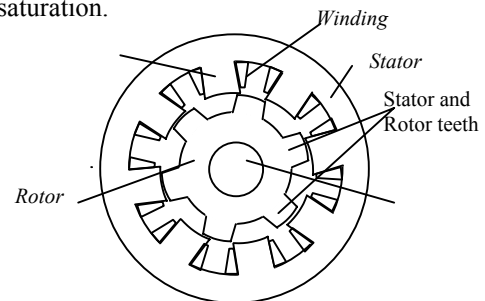


Fig 1. SRM Structure

FINITE ELEMENT MODELLING

The electromagnetic modeling of the machine is established from the meshing of the structure. A high mesh density in the air gap was undertaken. The distance between two positions was taken equal to 2.5 mechanical degrees. This increment was found sufficient to allow motor parameter determination with small error [3]. Fields solutions were used to determine the static torque with respect to rotor position, when three stator winding are excited in sequence. This characteristic is presented in Fig 2. The torque ripple is given by (1):

$$\text{Torque.ripple}(\%) = \frac{C_{\max} - C_{\min}}{C_{\max}} \cdot 100 \quad (1)$$

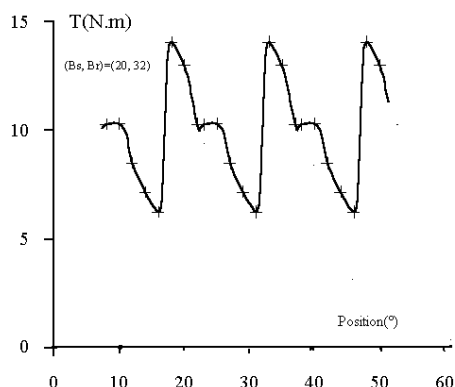


Fig.2 Variation of static Torque with position

Various configurations of SRM were considered, where both Bs and Br were varied, taking into account the constraints above. The table 1 summarizes the values of the average torque and torque ripple. It shows the effect of Bs and Br on machine characteristics. However, this effect is less significant with regard to the average torque.

Tableau 1 Values of average torque and torque ripple

(Bs, Br) (deg)	Average Torque (Nm)	Torque ripple (%)
15 16	8.86	74.41
15 20	9.13	71.93
15 24	9.18	71.93
15 28	9.20	71.93
15 32	9.19	71.93
15 36	9.16	72.75
15 40	9.09	73.45
20 24	9.85	55.76
20 28	9.95	55.58
20 32	9.96	55.66
20 36	9.94	55.77
20 40	9.85	56.00
25 28	9.83	55.47
25 32	9.86	55.46

OPTIMIZATION USING NEURAL NETWORK

Application of neural network

In this method, an interpolation using neural network was performed. based on the generalized radial basis function (GRN)[4]. After data training, a network is used to approximate the objective function. The trained GRN network appears to produce satisfactory output results for tested data that were not subject to training. Fig. 3 and 4 show the variation of the average torque and torque ripple with respect to (Bs, Br). Then, an optimization procedure was

carried out for the search of maximum torque and minimum ripple. This has led to the optimal structure with the following configuration: (Bs, Br)=(25, 32).

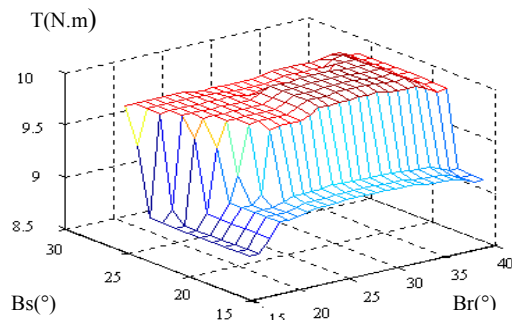


Fig. 3. Variation of Average Torque with Bs and Br

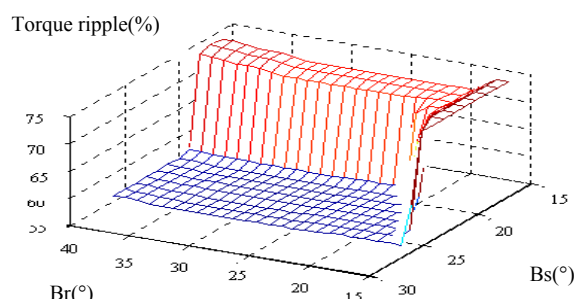


Fig. 4. Variation of torque ripple ratio with Bs and Br and Br

CONCLUSION

The paper describes investigations for the optimal design of Switched reluctance Motor (SRM). The approach focuses on the maximization of the average torque and minimization of torque ripple. Prior to optimization, interpolation of the data was performed through function approximation using both least square method and neural network based on generalized radial basis function. Both approximation function results are very close and further show the higher accuracy of the neural network approach. The optimum parameters are obtained. These are confirmed by numerical field solutions using FEM.

REFERENCES

- [1] Lawrenson P.J., Stephenson J.M, Blenkinson P.T., Corda J., Fulton N.N: Variable speed switched reluctance motors, IEE Proc,B, July 1980, no 127, pp 253-265.
- [2] Brisset S. and Brochet P.: Optimization of Switched Reluctance Motors using Deterministic Methods with Static and Dynamic Finite Element Simulations', IEEE Trans on Magnetics, Vol. 34. No. 5, Sept 1998, pp. 2853-2856.
- [3] Sahraoui H., Zeroug H.: 'Torque Analysis in a Switched Reluctance Motor Drive', Record of the 13th Compumag Conference on the Computation of Electromagnetic Fields, Vol II, July 2001, pp. 172-173.
- [4] Haykin S.: Neural Networks: A comprehensive Foundation, Prentice Hall, 1999.

Pareto Optimality and Particle Swarm Optimization

U. Baumgartner, B. Brandstätter, Ch. Magele, W. Renhart

Institute for Fundamentals and Theory in Electrical Engineering, Graz University of Technology

Kopernikugasse 24/3

Graz 8010 Austria

ulrike.baumgartner@tugraz.at

Abstract— Real world optimization problems often require to minimize/maximize more than one objective which, in general, are conflicting each other. These problems (multiobjective optimization problems, vector optimization problems) are usually treated by using weighted sums or other decision making schemes. An alternative way is to look for the Pareto Optimal Front. In this paper the Particle Swarm algorithm is modified to detect the Pareto Optimal Front.

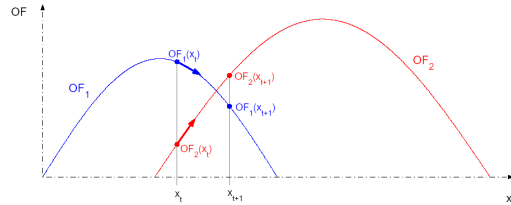


Fig. 1. Pareto optimal point - One dimension

INTRODUCTION

Stochastic optimization methods have successfully been applied to scalar and vector optimization problems. In the latter case, the different objectives, which are in general conflicting each other have to be transferred into a single scalar objective function. This is usually done by normalizing and processing the contributions to the objective function (weighted sums, fuzzy membership functions, ...) [1].

An alternative approach is to find the Pareto optimal front which summaries all Pareto optimal solutions [2]. A Pareto optimal solution is, by definition, the best that could be achieved for one objective without disadvantaging at least one other objective.

Particle Swarm Optimization (PSO) [3], a stochastic method imitating the social behaviour of a bird flock, can easily be adapted to perform this task. To test both performance and reliability of PSO a plain low pass filter with two conflicting objectives was chosen. In the extended version a shape optimization problem of an electromagnet will be presented.

PARETO OPTIMALITY

The solution to a multiobjective problem is, as a rule, not a particular value, but a set of values of optimization variables such that, for each element in this set, none of the objective functions can be further increased without a decrease of some of the remaining object functions (every such value of an optimization variable is referred to as pareto-optimal).

The simplest way illustrating this behaviour is shown in Fig. 1. The point x_t is pareto optimal because (1) (or (2)) is true (OF ... objective function value).

$$OF_1(x_{t+1}) < OF_1(x_t) \quad \& \quad OF_2(x_{t+1}) > OF_2(x_t) \quad (1)$$

$$OF_1(x_{t+1}) > OF_1(x_t) \quad \& \quad OF_2(x_{t+1}) < OF_2(x_t) \quad (2)$$

PARTICLE SWARM OPTIMIZATION

In the population-based search procedure σ particles fly around in a multidimensional search space. After initialization within a range $[x_{min}, x_{max}]$ each particle adjusts its position x_t and velocity v_t according to its own experience and the position of the best of all particles. The discrete ordinary differential equation controlling the motion of a single swarm member is given in (3).

$$v_{t+1} = \left(1 - \frac{\sqrt{\kappa\phi}}{2}\right) v_t + \kappa\phi (x_t^{best} - x_t)$$

$$x_{t+1} - x_t = \left(1 - \frac{\sqrt{\kappa\phi}}{2}\right) v_t + (1 - \kappa\phi) (x_t^{best} - x_t) \quad (3)$$

with

x_t^{best}	... current swarm leader
$\phi = [0, 1]$... random number
$\kappa = 0.8$... swarm movability control

The procedure is stopped if the the whole swarm can be found within a certain region which is defined by the swarm radius ϵ .

The Standard PSO Algorithm Two conflicting objectives OF_1 and OF_2 are transferred into n weighted sums

$$OF_{wk} = \lambda_k OF_1 + (1 - \lambda_k) OF_2 \quad k = 1, 2, \dots, n \quad (4)$$

and an optimal point is calculated for each of them. The resulting n solutions obtained form the Pareto optimal front.

The Pareto PSO Algorithm For each swarm member both objectives OF_1 and OF_2 are calculated separately and n weighted sums (4) are evaluated. For each of these sums the particle yielding the best objective function value becomes the leader $x_{t,k}^{best}$ of the sub-swarm, which

is formed by dividing the complete swarm into n equal parts. The n sub-swarms then evolve independently from each other following (3).

The major modification compared to the standard algorithm is the detection of Pareto optimal solutions. To speed up the algorithm this process is two fold. The first step (preliminary pareto decision) is narrowing down the choice by testing all swarm members against the simple Pareto formulations (1) and (2).

This procedure is followed by a substantially stricter selection process (main pareto decision), taking the slope information into account.

If a particle is recognized to be Pareto optimal, it has reached its final position and is removed from the swarm. If the number of remaining swarm members has reached a prescribed threshold or the maximum number of iterations max_{it} has been exceeded, the algorithm stops.

NETWORK EXAMPLE

Two different pairs R_1 and R_2 ($R_1^{(1)} = 30\Omega, R_2^{(1)} = 50\Omega; R_1^{(2)} = 700\Omega, R_2^{(2)} = 100\Omega$) were used to set up the frequency response of the amplitude ration $\mathbf{H}^{(1)}(j\omega) = \frac{\mathbf{U}_o}{\mathbf{U}_i}$ and of the phase angle $\theta^{(2)}(j\omega)$ of a cascaded low pass filter (Fig. 2). All other values were kept constant: $R_i = 50\Omega$, $R_L = 100\Omega$ and $C_1 = C_2 = 3.39\mu F$.

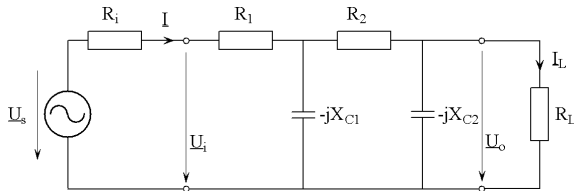


Fig. 2. Example circuit - complex representation

Optimization problem The task was to set up a single circuit which approximates best the magnitude $\mathbf{H}^{(1)}(j\omega)$ and the phase $\theta^{(2)}(j\omega)$. The two conflicting objectives are given in a least square sense in (5).

$$\begin{aligned} OF_1 &= \sum_{i=1}^m \left(|\mathbf{H}^{(1)}(j\omega_i)| - |\mathbf{H}(j\omega_i)| \right)^2 \\ OF_2 &= \sum_{i=1}^m \left(\theta^{(2)}(j\omega_i) - \theta(j\omega_i) \right)^2 \end{aligned} \quad (5)$$

Optimization results The results and performance of the Pareto PSO algorithm are compared to the solutions obtained from the standard PSO algorithm. The number of weighted sums was varied from $n = 3$ to $n = 15$, and the weights λ were in the range $\lambda = [0 : (n - 1) : 1]$. Furthermore, the initial swarm size was varied between $\sigma = 50$ and $\sigma = 100$ swarm members. The standard PSO algorithm was run for each weight λ , while the Pareto PSO algorithm was only run once. To be able to obtain mean values, each task was solved ten times.

The resulting mean values are displayed Tab. I. It can be observed that the number of total function calls is significantly lower for the Pareto PSO algorithm.

TABLE I. FUNCTION CALLS COMPARISON

n	$\sigma = 50$		$\sigma = 100$	
	pareto	weighted sums	pareto	weighted sums
3	2639	8430	5085	17670
6	2548	8285	3953	34020
9	2228	24640	3921	53000
12	2259	32660	3811	66790
15	2646	40685	3761	84280

Fig. 3 displays the Pareto optimal front obtained from both methods for $n = 3$ and $n = 15$ weighted sums. It can be seen that even in the case with only a few weighted sums the Pareto PSO models the Pareto front much better than it can be done with the final solutions of the standard PSO.

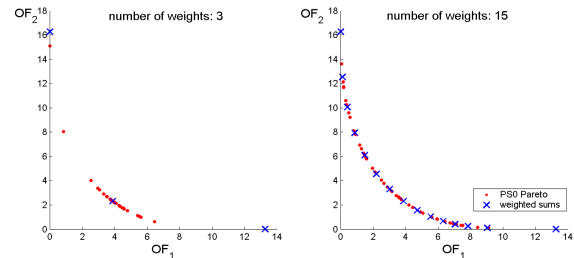


Fig. 3. OF_1 and OF_2

CONCLUSION

The particle swarm optimization algorithm was applied to a simple multiobjective optimization problem with two conflicting objectives. The algorithm revealed an excellent performance concerning the number of solutions of forward problems and completed with a very reliable representation of the Pareto optimal front. Further investigations will be made to increase both the number of optimization parameters (increasing the dimensionality) and the number of conflicting objectives. Based on the results obtained an satisfactory behavior can also be expected for real world applications.

REFERENCES

- [1] Alotto P.G., Brandstätter B., Cela E., Fürntratt G., Magele Ch., Molinari G., Nervi M., Preis K., Repetto M. and Richter K.R.: "Stochastic Algorithms in Electromagnetic Optimization" IEEE Trans. Magn., vol. 34, No. 5, pp 3674-3684, 1998
- [2] Barba P. Di, Farina M., Savini A.: "An improved technique for enhancing diversity in Pareto evolutionary optimization of electromagnetic devices" A COMPEL: Int J for Computation and Maths. in Electrical and Electronic Eng.; vol. 20 No. 2; 2001
- [3] Brandstätter B., Baumgartner U.: "Particle swarm optimization - mass-spring system analogon" Magnetics, IEEE Transactions on , Volume: 38 Issue: 2 Part: 1, March 2002

Applying Continuum Design Sensitivity Analysis combined with standard EM software to Shape Optimisation in Magnetostatic Problems

Dong-Hun Kim, K. S. Ship and J. K. Sykulski
Department of Electronics and Computer Science
University of Southampton
SO17 1BJ, UK
Email: jks@ecs.soton.ac.uk

Abstract—The paper introduces a technique of incorporating a Continuum Design Sensitivity Analysis (CDSA) into an existing finite element software package to obtain an optimum shape of electro-mechanical devices. In the continuum approach the design sensitivity is evaluated using an analytical formula with numerical solutions of the primary system and its corresponding adjoint system. The sensitivity coefficients were evaluated through Application Program Interface (API) between the command codes based on continuum sensitivity analysis and the electromagnetic software used. The applicability of this method is demonstrated by optimising the salient pole face shape of a high temperature superconducting (HTS) synchronous generator.

INTRODUCTION

Design optimisation of electromechanical devices using existing finite-element (FE) analysis packages has proven to be successful in terms of both accuracy and time efficiency. Optimisation methods such as stochastic techniques, approximated polynomial evolution strategies, response surface methodology and genetic algorithms have been used in the design process. However, when practical electro-mechanical devices are considered, these techniques are often not suitable due to the number of design variables. Such optimisation would simply require unacceptable computing times as the number of design variables increases. In an attempt to reduce the computing burden we have developed a methodology that combines CDSA with existing EM software (OPERA-2d Static Solver by Vector Fields Ltd).

Accurate information on design sensitivity may be obtained analytically from the formula derived in [1]. This method is based on the adjoint variable method and continuum mechanics in which the shapes as well as the dimensions of a design object are considered. The core of the program lies in building an adjoint system from the primary system. The proposed method enables designers to consider all foreseeable shape designs of magnetostatic problems because the computing times required to find an optimal solution are not affected by the number of design variables.

PROGRAM STRUCTURE

The design program consists of two modules as shown in Fig. 1. The first module, known as the Optimal Design Module, controls the overall optimization procedure and calculates several crucial values such as objective function, adjoint load term, design sensitivity, etc, relevant to the CDSA. The second module is related to the implementation of the software package, in our case OPERA-2d, where the

pre-processor, solver and post-processor are involved. The two modules are constantly communicating with each other exchanging information about design variables, regions of interest and state variables.

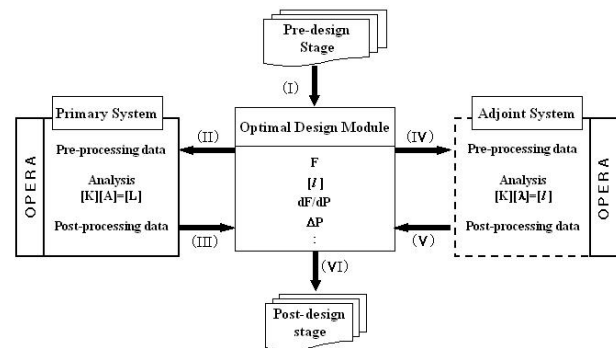


Fig. 1. Flow chart of CDSA in conjunction with the OPERA-2d.

In general, the adjoint system has the same geometry, material properties and boundary conditions as the primary system. The only difference between the two systems is the source distribution. During the iterative process, the primary system equations are solved and the continually updated results are used to construct the adjoint system equations. Based on the post-processing results, the sensitivity coefficients are evaluated and coordinate information on design variables is updated.

Usually the CDSA working in conjunction with FE software needs the full process mentioned above. However, in special cases, when the objective function is expressed in terms of energy, the adjoint system can be ignored. The reason is that the values of the adjoint state variables are exactly half of those in the primary system.

NUMERICAL IMPLEMENTATION

The design sensitivity coefficients can be easily evaluated by the following procedure (see also Fig. 1):

- (I) Read data about design variables, constraints and region of interest defined in pre-design stage;
- (II) Transfer the design data to the pre-processor and solve the primary system;
- (III) Output the analysis data to the optimal design module and calculate the objective function;

(IV) Compute the adjoint load and transfer it to the pre-processor;

(V) Solve the adjoint system and output its analysis results to the optimal design module;

(VI) Evaluate sensitivity coefficients from the sensitivity formula [1] and update the design data.

EXAMPLE

The proposed design method has been successfully applied to shape optimisation of a salient pole rotor of a HTS synchronous generator [2]. The stator of the generator has 48 slots and a balanced two-pole three-phase star-connected stator winding. Due to symmetry and under no-load condition, a quarter of the generator is analysed using nonlinear FEM. In order to minimise the effect of the undesirable harmonics of the air-gap flux density, an optimal design of the pole face shape is required. To achieve this goal, the following objective function is evaluated over a 90° arc at a 160 mm radius.

$$F = \int_{\Omega_f} (B_{ri} - B_{rio})^2 d\Omega, \quad B_{rio} = 0.7 \sin(\theta) \quad (1)$$

where B_{ri} is the radial component of the air-gap flux density comprised of odd harmonics order up to 19th and θ is the angle between 0° and 90°. A total of 53 grids forming the outline of the rotor pole have been selected as the design variables and allowed to move in the radial direction whose base point is located at (0,89).

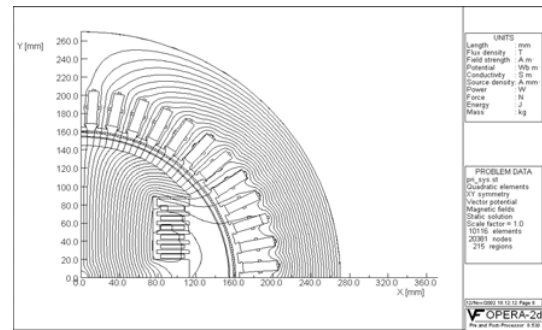
The flux lines of the primary and the adjoint systems are examined in Fig. 2 before the iteration process. As expected, the flux distribution for the two systems is different due to the applied sources. After only 23 iterations, the optimal pole shape of Fig. 3 was obtained. The magnitudes of the flux density at different positions before and after the optimisation are shown in Fig. 4.

CONCLUSIONS

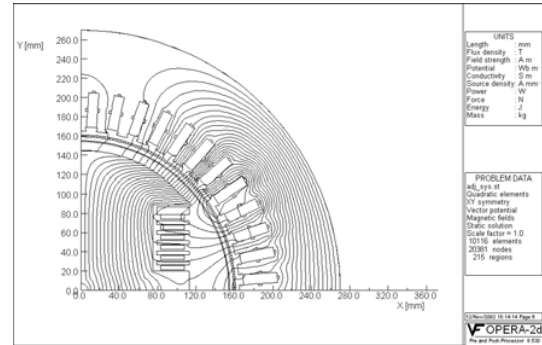
The computing times needed to reach an optimal solution can be reduced considerably by incorporating the optimisation technique into the existing finite element (FE) software package without compromising the accuracy. Moreover, using CDSA, the system equations are solved only twice regardless of the number of design variables.

REFERENCES

- [1] Dong-Hun Kim, Se-Hee Lee, Il-Han Park and Joon-Ho Lee, "Derivation of a general sensitivity formula for shape optimization of 2-D magnetostatic systems by continuum approach," *IEEE Transactions on Magnetics*, vol. 38, pp.1125-1258, March 2002.
- [2] Al-Mosawi M. K., Beduz C., Goddard K., Sykulski J. K., Yang Y., Xu B., Ship K. S., Stoll R., And Stephen N. G., "Design of a 100 kVA high temperature superconducting demonstration synchronous generator", *Physica C Superconductivity*, vol. 372-376, part 3, pp. 1539-1542, August 2002.



(a) Primary system.



(b) Adjoint system.

Fig. 2. Comparison of flux lines between the primary and the adjoint systems before starting the iterative design procedure.

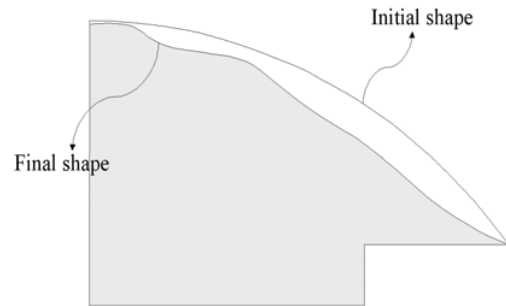


Fig. 3. Pole face shape optimisation.

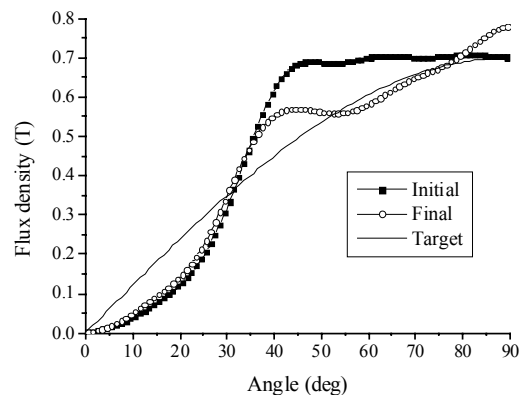


Fig. 4. Comparison of the air-gap flux density.

3D Optimal Shape Design of Magnetic Pole in Permanent Magnet Assembly for MRI Taking Account of Gradient Coil Field

Yingying Yao, Chang Seop Koh*, Dexin Xie

School of EE, Shenyang University of Technology, Shenyang, Liaoning 110023, P.R.China. yaoying62@hotmail.com

* School of ECE, Chungbuk National University, Cheongju, Chungbuk, 361-763, Korea. kohcs@chungbuk.ac.kr

Abstract—The ferromagnetic pole pieces of permanent magnet assembly for MRI(magnetic resonance imaging) is optimally designed taking account of the pulse excited gradient coil field. In the design, the transient design sensitivity analysis is combined with 3D finite element method to give a search direction. The effects of the eddy currents, induced on the ferromagnetic pole pieces, on the main magnetic field strength and homogeneity in diameter of spherical volume(DSV) are also investigated.

I. INTRODUCTION

The permanent MRI magnet is a viable alternative to the resistive and superconducting MRI magnet because it has the advantages of compact assembly, small leakage flux and low operating cost [1]. When the permanent MRI magnet works, the eddy current induced by the pulse excited gradient fields on the magnetic pole plates, which are made of steel, changes the homogeneity of the average magnetic fields, and causes a delay of build-up of the gradient fields, which may result in resolution degradation in the computed image. In this reasons, the pulse excited gradient coil currents should be taken account in the design of permanent MRI magnet [2].

However, most of the researches on the design of permanent MRI magnet have been confined to simplified 2D model, or 3D linear magnetostatic model [2,3].

In this paper, the magnetic pole shape of the permanent MRI magnet is optimized considering the gradient coil current in order to get uniform magnetic fields in the working space by using A, ϕ - A finite element method and transient design sensitivity analysis combined with steepest descent method.

II. FIELD ANALYSIS AND DESIGN SENSITIVITY FOR 3D TRANSIENT EDDY CURRENT PROBLEM

The governing equation for the 3D electromagnetic system with dynamic excitation is given as

$$\nabla \times (\nu \nabla \times A) - \nabla (\nu \nabla \cdot A) + \sigma \frac{\partial A}{\partial t} + \sigma \nabla \phi = 0 \quad \text{in } V_1 \quad (1)$$

$$\nabla \cdot \left(-\sigma \frac{\partial A}{\partial t} - \sigma \nabla \phi \right) = 0$$

$$\nabla \times (\nu \nabla \times A) - \nabla (\nu \nabla \cdot A) = J_s + \nu_0 \nabla \times B_s \quad \text{in } V_2 \quad (2)$$

where V_1 and V_2 present the conducting and non-conducting regions, respectively. Apply finite element method to (1) and (2), a differential matrix equation is obtained as follows:

$$[K][A] + [M][\dot{A}] = [f] \quad (3)$$

where $\dot{}$ denotes the time derivative.

In the 3D transient eddy current problems, the optimal shape

design problem, in general, can be defined as follows[4]:

$$\text{Minimize } F(p) = \int_0^T G(p, A, \dot{A}) dt \quad (4)$$

$$\text{Subject to } [p]^L \leq [p] \leq [p]^U$$

Where G is arbitrary differentiable function, $[p]$ is the design variable vector. The design sensitivity is derived as follows:

$$\frac{dF}{dp} = \frac{\partial G}{\partial A} \frac{\partial A}{\partial p} \Big|_{t=T} + \int_0^T \left\{ \left[\frac{\partial G}{\partial A} - \frac{d}{dt} \left(\frac{\partial G}{\partial \dot{A}} \right) \right] \frac{\partial A}{\partial p} + \frac{\partial G}{\partial p} \right\} dt \quad (5)$$

Differentiating the both sides of (3) with respect to p , introducing an adjoint variable $[\lambda]$ and integrating from 0 to T , it becomes

$$\int_0^T \left\{ \left(\lambda^T K - \dot{\lambda}^T M \right) \frac{\partial X}{\partial p} - \frac{\partial}{\partial p} \lambda^T (f - KX - MX) \right\} dt + \lambda^T M \frac{dX}{dp} \Big|_{t=T} = 0 \quad (6)$$

If $[\lambda]$ is chosen so that the coefficients of terms involving $\partial X / \partial p|_{t=T}$ and $\partial X / \partial p$ in (5) and (6) are equal, the following equations are satisfied,

$$[M]^T \lambda(T) = \left[\frac{\partial G}{\partial X} \right]^T (T) \quad (7)$$

$$[K]^T \lambda - [M]^T \dot{\lambda} = \left[\frac{\partial G}{\partial X} - \frac{d}{dt} \left(\frac{\partial G}{\partial \dot{X}} \right) \right]^T \quad (8)$$

The design sensitivity in (5) can be written as,

$$\frac{dF}{dp} = \int_0^T \left\{ \frac{\partial G}{\partial p} + \lambda^T \frac{\partial}{\partial p} \left[[f] - ([K] + [M])[\tilde{X}] \right] \right\} dt \quad (9)$$

where $[\tilde{X}]$ is the solution of (3) by using time stepping method,

$$\left(\theta K^{n+1} + \frac{M}{\Delta t} \right) \tilde{X}^{n+1} = \theta f^{n+1} + (1-\theta) f^n + \left(\frac{M}{\Delta t} - (1-\theta) K^n \right) \tilde{X}^n \quad 0 \leq \theta \leq 1; n = 1, \dots, T \quad (10)$$

and $[\lambda]$ is the solution of (7) and (8) from

$$\left(K^T (1-\theta) + \frac{M^T}{\Delta t} \right) \lambda^{n-1} = \left(\frac{M^T}{\Delta t} - \theta K^T \right) \lambda^n + q^n \theta + (1-\theta) q^{n-1} \quad (11)$$

where, $q = \frac{\partial G}{\partial X} + \frac{1}{\Delta t} \left(\frac{\partial G}{\partial \dot{X}} \Big|_n - \frac{\partial G}{\partial \dot{X}} \Big|_{n-1} \right)$; $0 \leq \theta \leq 1$; $n = T, \dots, 1$.

The stiff matrix of (10) and (11) are exactly same when $\theta = 0.5$.

III. Design RESULTS AND DISCUSSION

Fig.1 shows a model of permanent MRI magnet. The yoke consists of four columns at each corner and two ferromagnetic pole pieces, and made of steel(SS400) whose conductivity is 51×10^6 S/m. The NdFeB permanent magnet, the source of main magnetic field, has the residual magnetic flux density of 1.21T, and a hole of $\phi 60$ at center. The gradient coil has 15 turns is located on each pole piece, and excited by pulse current shown in Fig.1.

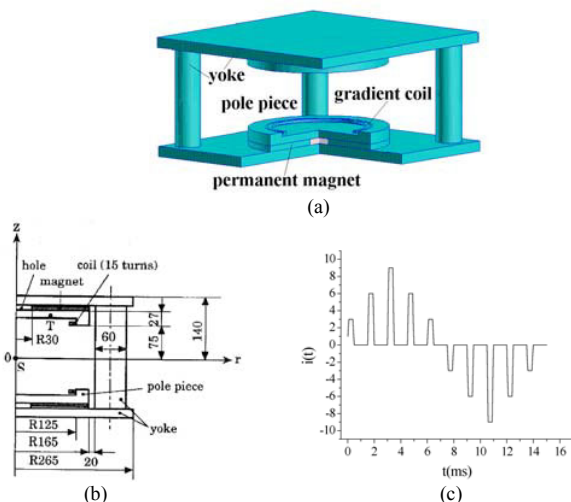


Fig.1. Model of permanent MRI magnet. (a) whole view, (b) cross section, (c) gradient coil currents.

The design target is to find a smooth optimum pole shape that gives uniform magnetic field distribution within 100mm DSV on $z=0$ plane. The initial shape of the pole is assumed to be flat. As the design variables, z coordinates of 202 nodal points on the pole surface near gradient coil are taken and allowed to move in z direction. The objective function is

$$F = \sum_{i=1}^{N_{target}} \left(\frac{1}{T} \int_0^T B_i dt - B_0 \right)^2$$

where B_0 is uniform field value; N_{target} is the number of nodes within target region.

After the design variables are updated using the computed transient sensitivity, the Bezier spline with 9th order is used to get a smooth shape along the radial axis.

After 36 iterations, the average uniformity of the magnetic fields in DSV is reduced, as shown in Fig.2, from 1775.367ppm to 349.401ppm. Fig.3 compares the final optimized shape with the initial one. With initial pole shape, the magnetic field at the center point is shown in Fig.4(a), where it is clear that the set-up

of the gradient field is delayed due to eddy current. Fig.4(b) shows the magnetic field distribution on symmetric surface.

The results indicate that it is necessary for the pole shape design of permanent MRI magnet to take account the eddy currents.

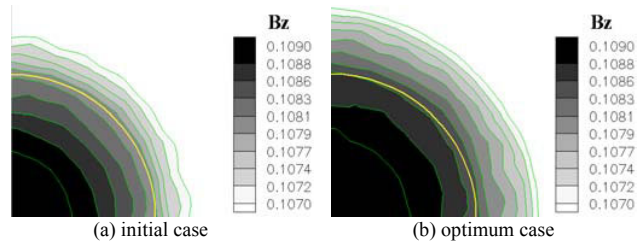


Fig.2 The magnetic field distribution in DSV.

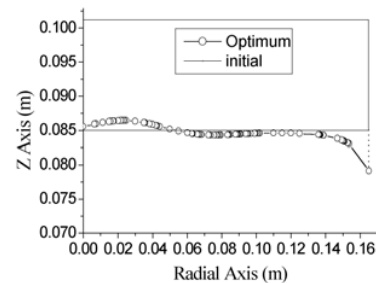


Fig.3 Initial and optimum shape of pole piece.

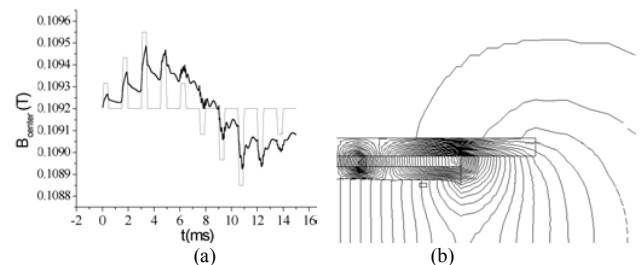


Fig.4. Magnetic field distribution. (a) at the center of DSV, (b) on symmetric surface.

REFERENCES

- [1] T.Miyamoto, et.al., "A development of a permanent magnet assembly for MRI devices using Nd-Fe-B material," IEEE Trans. On Magn., Vol.25, No.5, pp.3907-3909, Sept., 1989.
- [2] Koji Miyata, et. al., "Analysis of magnetic characteristics of permanent magnet assembly for MRI devices taking account of hysteresis and eddy current", IEEE Trans. on Magn., vol.34, No.5, pp.3556-3559, September 1998
- [3] Dong-Hun Kim, et. al., "3D optimal shape design of ferromagnetic pole in MRI magnet of open permanent-magnet type", IEEE Trans. on Magn., vol.12, No.1, pp.1467-1470, March 2000
- [4] Il-han Park, "Design sensitivity analysis for transient eddy current problems using finite element discretization and adjoint variable method", IEEE Trans. on Magn., vol.32, No.3, pp.1242-1245, May 1996

Support Vector Machines – a Promising Tool for Optimal Design of Electromagnetic Devices

Jacek Starzyński, Stanisław Osowski and Stanisław Wincenciak,
Chair of the Theory of Electrical Engineering, Warsaw University of Technology,
ul. Koszykowa 75, 00-661 Warsaw, Poland,
e-mail: *jstar@iem.pw.edu.pl*

Abstract—The paper presents application of support vector machines (SVM) for inverse problems of electromagnetics. SVM is a new approach to neural network learning, in which the learning task is transformed to the solution of the quadratic problem with linear constraints. The well known solutions of such problems lead to the global minimum of the cost function. SVM were reported to be extremely effective for classification and regression. Results of our numerical experiments prove that this technique can be also successfully adapted to solve optimization problems of electromagnetics.

INTRODUCTION

Many different types of the ANN have already been proposed for solving inverse problems of electromagnetics and no one seems to be superior. We like to focus your attention on support vector machine (SVM), a new approach to neural network learning which, compared to other ANNs, shows several important advantages.

In the full paper we will show application of SVM for design of excitation coil for an electromagnetic flow meter based on 3D numerical model. This problem is, however, too complicated for short paper, so here we only briefly present the methodology on a known example shown in Fig. 1 [1, 2]. The goal is to design the lower edge of the air gap (A-A'

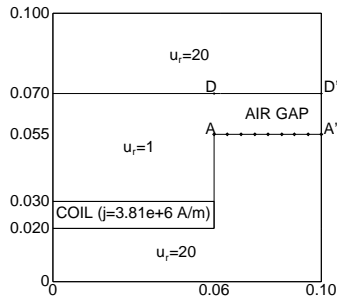


Fig. 1. Geometry of the sample problem

in Fig. 1) to obtain the uniform distribution of y -component of the flux density on the upper edge of the air gap (D-D' in Fig. 1). The y -coordinates of the N points marked with small diamonds in Fig. 1 form $\mathbf{d} = (y_1 \dots y_N)$ —the vector of the design parameters, and the target can be defined as follows

$$\min_{\mathbf{d} \in \mathbf{A}} \left(\sum_{k=1}^M |B_{y,k}(\mathbf{d}) - \hat{B}_{y,k}| \right) \quad (1)$$

where \mathbf{A} is domain of allowed shapes of the A-A' segment, $B_{y,k}$ is the computed and $\hat{B}_{y,k}$ is the desired value of the y -component of the magnetic flux density \vec{B} in k -th of M points chosen on the D-D' segment, where magnetic flux density is

controlled. Later we will use $\mathbf{b} = (B_{y,1}, \dots, B_{y,M})$ for values of flux density corresponding to given \mathbf{d} .

The ANN approach to inverse problem requires to solve many forward problems, when test shapes, represented by vectors of design variables \mathbf{d}_i are tried and the database used later for teaching ANN is collected. This database consists of corresponding pairs $(\mathbf{b}_i, \mathbf{d}_i)$. Having database ready one can train neural network to approximate the unknown function $\mathbf{d} = f(\mathbf{b})$. Trained network feeded with $(\hat{B}_{y,1}, \dots, \hat{B}_{y,M})$ should respond with the optimal shape.

SUPPORT VECTOR MACHINES

SVM has only one output [3], and thus to find the whole vector \mathbf{d} we need N networks. However, this demerit is compensated by the low numerical cost per one SVM.

Each SVM should approximate given function $d(\mathbf{b})$ on set $(\mathbf{b}, d(\mathbf{b}))$ where $\mathbf{b} \in \mathbf{R}^M$ and $d(\mathbf{b}) \in \mathbf{R}$ is one of the N design parameters. Teaching data (\mathbf{b}_i, d_i) are approximated with

$$y(\mathbf{b}) = \sum_{j=0}^K w_j \varphi_j(\mathbf{b}) = \mathbf{w}^T \boldsymbol{\varphi}(\mathbf{b}), \quad (2)$$

where unknown weight vector $\mathbf{w} = (w_0, w_1, \dots, w_K)^T$ contains polarity (w_0) and $\varphi_j(\mathbf{b})$ are known basis functions. For sake of effectiveness and to transform the problem into quadratic programming we shall adapt error function for learning with some tolerance ε [3, 4]:

$$L_\varepsilon(d, y(\mathbf{b})) = \begin{cases} |d - y(\mathbf{b})| - \varepsilon & \text{for } |d - y(\mathbf{b})| \geq \varepsilon, \\ 0 & \text{for } |d - y(\mathbf{b})| < \varepsilon. \end{cases} \quad (3)$$

The goal of the teaching process is to find values of w_j , number of the basis functions $\varphi_j(\mathbf{b})$ and their parameters which will minimize the cost function defined as

$$E = \frac{1}{p} \sum_{i=1}^p L_\varepsilon(d_i, y(\mathbf{b}_i)) \quad (4)$$

with constrain for the value of weights: $\|\mathbf{w}\|^2 < C_0$, where C_0 is given constant.

Introducing complementary variables ξ_i and ξ'_i we can transform the above problem to the more global form of minimization of the new cost function

$$\phi(\mathbf{w}, \xi, \xi') = C \left[\sum_{i=1}^p (\xi_i + \xi'_i) \right] + \frac{1}{2} \mathbf{w}^T \mathbf{w}, \quad (5)$$

with the following constrains

$$d_i - \mathbf{w}^T \boldsymbol{\varphi}(\mathbf{b}_i) \leq \varepsilon + \xi_i, \quad (6)$$

$$\mathbf{w}^T \boldsymbol{\varphi}(\mathbf{b}_i) - d_i \leq \varepsilon + \xi'_i, \quad (7)$$

$$\xi_i \geq 0, \quad \xi'_i \geq 0. \quad (8)$$

Note that ξ and ξ' are chosen such, that $|d_i - \mathbf{w}^T \boldsymbol{\varphi}(\mathbf{b}_i)| - (\varepsilon + \xi_i) \leq 0$ what assures $L_{\varepsilon+\xi} = 0$, what in turn minimizes cost function E .

The constant C in (5) can be explained as an regularization parameter setting compromise between the value of the tolerance (set by ε , ξ and ξ') and value of weights.

For problem formulated by (5)-(8) we can define the following Lagrange function

$$J(\mathbf{w}, \boldsymbol{\xi}, \boldsymbol{\xi}', \boldsymbol{\alpha}, \boldsymbol{\alpha}', \boldsymbol{\gamma}, \boldsymbol{\gamma}') = C \left[\sum_{i=1}^p (\xi_i + \xi'_i) \right] + \frac{1}{2} \mathbf{w}^T \mathbf{w} + \sum_{i=1}^p \alpha_i [\mathbf{w}^T \boldsymbol{\varphi}(\mathbf{b}_i) - d_i + \varepsilon + \xi_i] + \sum_{i=1}^p \alpha'_i [d_i - \mathbf{w}^T \boldsymbol{\varphi}(\mathbf{b}_i) + \varepsilon + \xi'_i] - \sum_{i=1}^p [\gamma_i \xi_i + \gamma'_i \xi'_i], \quad (9)$$

where the Lagrange multipliers α_i and α'_i are responsible for the functional constrains and γ_i and γ'_i are responsible for holding $\xi_i \geq 0$, $\xi'_i \geq 0$. The goal of optimization is to minimize J with respect to weights \mathbf{w} , ξ_i and ξ'_i (primary problem) and to maximize it with respect to α_i , α'_i , γ_i and γ'_i (dual problem). The methods for solving quadratic problem are well known and there is no place here to present this solution in detail [3, 4, 5], so we will just show the final result: after the Lagrange multipliers α_{i0} , α'_{i0} are calculated, the weight vector can be obtained as

$$\mathbf{w} = \sum_{i=1}^{N_s} (\alpha_{i0} - \alpha'_{i0}) \boldsymbol{\varphi}(\mathbf{b}_i), \quad (10)$$

where N_s is the number of non-zero Lagrange multipliers and respective \mathbf{b}_i are called support vectors [4]. Moreover the response signal can be described as

$$y(\mathbf{b}) = \sum_{i=1}^{N_s} (\alpha_{i0} - \alpha'_{i0}) K(\mathbf{b}, \mathbf{b}_i) + w_0, \quad (11)$$

where $K(\mathbf{b}_i, \mathbf{b}_j) = \boldsymbol{\varphi}^T(\mathbf{b}_i) \boldsymbol{\varphi}(\mathbf{b}_j)$ is so called kernel function. The most know kernels are radial Gaussian, polynomial or sigmoidal functions. It has been shown [6] that use of this kernel function instead of neurons activation functions leads to great reduction of the computational cost in learning and testing as well. The number of numerical operations becomes independent on the dimension of input vector.

NUMERICAL RESULTS

A SVM toolbox designed in our group was used to solve the problem shown in Fig. 1. In earlier publications we have used this test to compare different algorithms of shape optimization [2]. SVM has proved to be much more

effective than other ANNs. We have trained the radial kernel SVM using the learning base of only 50 test shapes \mathbf{d} and corresponding distributions of flux density \mathbf{b} . Then SVM was used to find shape which will assure the uniform $B_y = 80\text{mT}$. The obtained shape and corresponding flux density are shown in Fig.2. Those results are the best we have obtained with

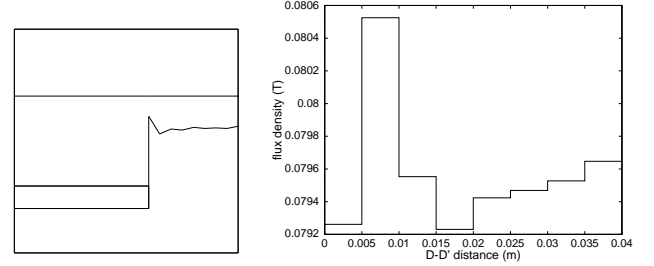


Fig. 2. SVM solution of the sample problem: the optimal shape (left inset) and the distribution of flux density along DD' (right inset)

any ANN. The learning database was rather small—previous experiments have shown that multilayer perceptrons needed at least ten times more learning patterns [1, 2]. It is an important feature when ANN is to be used to solve an inverse problem of electromagnetics where evaluation of each learning pattern can be computationally very expensive.

CONCLUSION

The experiments have shown that SVM can be a very effective tool for many problems of optimal design. It has many advantages: SVM needs relatively small learning database, learning process is very fast and it leads to the global minimum and last but not least the complication of the problem (usually measured by the number of design variables and the number of controlled quantities) practically does not influence the complication of the SVM network.

These hypotheses were verified by another test problem which will be used in the full paper: 3D design of the excitation coil of the electromagnetic flow meter [7]. This problem is too complicated to be explained here, but conclusion is the same: SVM network can be successfully applied to solve even huge, 3D inverse problem at reasonable computational cost.

REFERENCES

- [1] Ishikawa T., Tsukui Y., and Matsunami M. Optimization of electromagnetic devices using artificial neural network with quasi-newton algorithm. *IEEE Transactions on Magnetics*, 32(3):1226–1229, May 1996.
- [2] Ratajewicz-Mikołajczak E., Sikora J., Starzyński J. and Wincenciak S. Comparison of Optimal Shape Design Algorithms. *Proceedings of Compunag '97, Sapporo, Japan, Oct. 1999*, pp. 162-163
- [3] Vapnik V. *Statistical learning theory*. Wiley, N.Y., 1998
- [4] Haykin S. *Neural networks, comprehensive foundation*. Prentice Hall, 1999, New Jersey
- [5] Smola A., Scholkopf B. A tutorial on support vector regression. NeuroColt Technical Report NV2-TR-1998-030, 1998, <http://www.neurocolt.com>
- [6] Burges C.. A tutorial on support vector machines for pattern recognition. (in *Knowledge discovery and data mining*, ed. Usama Fayyad), Kluwer, 2000, pp. 1-43
- [7] Michalski A., Starzyński J., Wincenciak S. Electromagnetic Flowmeters for Open Channels - A Review. *IEEE Sensors Journal*, Vol. 1, Nr 1, June 2001, pp. 52-61.

Design of Inserted Core Type Slotless PMLSM for Detent Force Minimization by using Neural Network

Mi-Yong Kim, Jae-Yun Moon and Gyu-Tak Kim

Dept. of Electrical Engineering, Changwon National University, Changwon, Kyungnam, 641-773, Korea
e-mail: miyongkim@mail.changwon.ac.kr, 1835616@hanmail.net, gtkim@sarim.changwon.ac.kr

Abstract— This paper shows the minimization technique of detent force in inserted core type slotless Permanent Magnet Linear Synchronous Motor (PMLSM) by using neural network. In general, detent force affected in noise and vibration on Permanent Magnet (PM) linear machine. The width of coil and that of permanent magnet were adjusted to reduce detent force. Optimum value was calculated by neural network. It could be also easily calculated without time-consuming efforts. The results with neural network well corresponded to those of 2 Dimensions Finite Element Method (2D-FEM).

considerably increased energy density from decreasing magnetic air gap due to inserted core.

Table 1 shows dimension and specification of inserted core model

Table 1. Dimension and specification of analysis model

Parameter	Values[Unit]	Parameter	Values[Unit]
Number of poles	12	Turns / Phase	650 [turns]
Br	1.2 [T]	Height of coil	11 [mm]
Height of PM	12 [mm]	Width of coil	12 [mm]
Length of PM	73.5 [mm]	Distance of coil	12 [mm]
Width of PM	26 [mm]	Phase current(max)	2.66 [A]
Pole pitch	28.5 [mm]	Length of air-gap	2 [mm]

GENERAL INFORMATION

Slotless PMLSM has no detent force and low normal force, so it is suited for precision instruments requiring accurate controlling, but it has a disadvantage of lower power density than slotted type. On the contrary, slotted PMLSM has relatively high power density but strong detent force, so it has lower control performance than slotless type one.[1]

Thus, this paper adopted a complementary method to enhance output by inserting core between windings of each phase in slotless type PMLSM, while adjusting the width of coil and PM so as to detent force minization.

Neural network was introduced to calculate the optimum value of design. This paper used back-propagation neural network model on multi-layer feed-forward neural network [2]. The neural network was led to learning by the results of FE analysis. Variables in input design include the width of coil and PM, while variables in output include thrust, detent force and its 6th order harmonics component.

The optimum values obtained from neural network were compared with the results of FE analysis. By using neural network, the calculation time to get the optimum value of design could be remarkably shortened.

ANALYSIS RESULTS

Optimum values

Fig. 2 shows the results of analysis by neural network. When the width of coil is 6mm and the width of PM is 26mm, the optimum values by neural network are shown as table 2. Also, table 2 shows analysis results by FEM.

Detent force mostly consists of 6th order harmonics component as slotted harmonics. Thus, the minimization of 6th order harmonics component indicates same results as that of detent force.

Table 2. Specification of analysis model

Analysis method	Thrust[N]	Detent force[N]	Ratio of 6th order harmonics component of the thrust[%]
Neural network	993.6	5.2	0.2
FEM	993.7	4.996	0.36

ANALYSIS MODEL

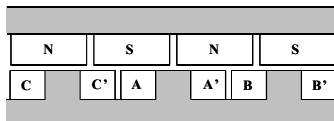
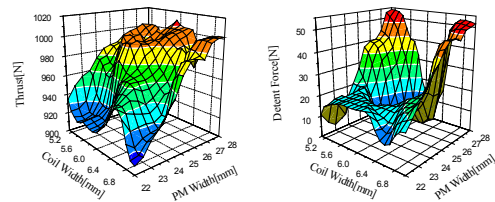


Fig.1. The analysis model of inserted core type slotless PMLSM

Fig. 1 shows the analysis model for inserted core type slotless PMLSM. Compared to slotless model, this had



(a) Thrust (b) Detent force
Fig. 2. Calculation results using neural network

Back-E.M.F and Inductance

Back electromotive force(emf) was calculated with variation of linkage flux. As a result of analysis, it was found

that Root Mean Square (RMS) value of back emf increased from 49.03[V] to 117.19[V] after inserting core. For an optimum model, this value increased up to 132.71[V]. This means that magnetic air gap was more decreased, since the width of inserted core was increased in optimum model.

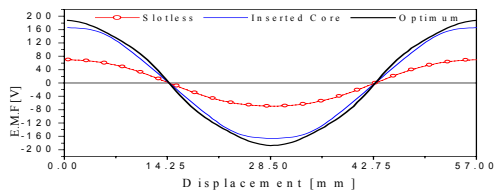


Fig. 3. Back-E.M.F (v=2m/s)

In this study, inductance was calculated by Energy Perturbation method. Table 3 shows the analysis results for each model

Table 3. Comparison of Inductance in each model

Inductance		Self [mH]	Mutual [mH]
Experiment	Slotless	29.38	-
	Slotless	30.86	9.08
Analysis	Inserted core	69.45	24.42
	Optimum	119.89	54.76

Detent force and Thrust

The detent force was calculated with Maxwell stress tensor. The analysis results for each model are shown in Fig. 4. The detent force corresponds to the 6th order harmonics component of thrust and the slot harmonics by teeth-slot structure. For inserted core model, the maximum value amounted to 55.96[N], while it decreased considerably down to 4.996[N] for optimum model.

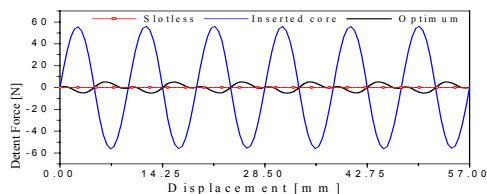


Fig. 4. Detent force

Fig. 5 shows the thrust for each model. As shown in this figure, inserted core model has double or more thrust than slotless model. As a result of analysis, it was found that thrust increased from 427.86[N] to 1004.27[N] after inserting core. For an optimum model, this value increased up to 1142.32[N].

Fig. 6 shows the analysis results for harmonics of thrust. It can be found that the 6th harmonics as slot harmonics were considerably more reduced in optimum model than in inserted core model.

Fig. 7 shows the characteristics of thrust upon steady state operation for each model. Inserted core model has double or more thrust than slotless model. Meanwhile, ripple ratio

reached 11.68[%] in inserted core model, while it decreased remarkably down to 3.92[%] in optimum model.

These results have little influences on operational characteristics of motor.

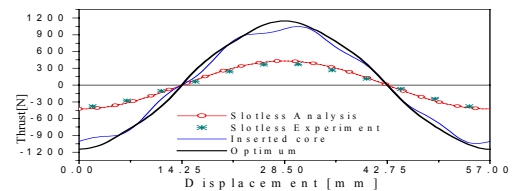


Fig. 5. Thrust

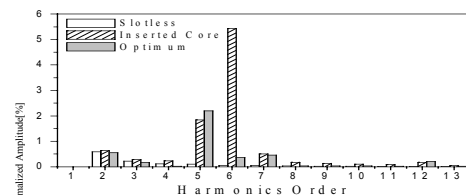


Fig. 6. Higher harmonic of thrust in each model

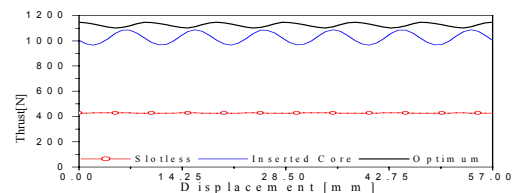


Fig. 7. Steady state thrust

CONCLUSION

In this paper, optimum value was calculated with neural network so as to maximize the thrust of inserted core type PMLSM and minimize detent force. For maximization of the thrust and minimization of detent force, the width of coil and that of PM were adjusted respectively. Optimum values were examined by FE analysis, and almost correspondent results could be obtained. It was noted that using neural network could save more time and efforts than FEM process.

REFERENCES

- [1] K. C. Lim, J. K. Woo, G. H. Kang, J. P. Hong, G. T. Kim, "Detent Force Minimization Techniques in Permanent Magnet Linear Synchronous Motors", IEEE Trans. Mag, Vol. 38, No. 2, pp.1157-1160, 2002
- [2] G.Tsekouras S. Kiartzis, A. Kladas, and J. A. Tegopoulos, "Neural Network Approach Compared to Sensitivity Analysis Based on Finite Element Technique for Optimization of Permanent Magnet Generators", IEEE Trans. Mag, Vol. 37, No. 5, pp.3618-3621, 2001

A Pruning Method for Neural Networks and its Application for Optimization in Electromagnetics

Frederico G. Guimarães and Jaime A. Ramírez

Universidade Federal de Minas Gerais

Departamento de Engenharia Elétrica, Av. Antônio Carlos, 6627

Belo Horizonte, MG, 31270-010, Brazil

e-mail: jramirez@cpdee.ufmg.br

Abstract— In this paper we propose a method for the exact computation of the Hessian matrix of the training error function for a multilayer perceptron network. The Hessian matrix is divided in small sub matrices, calculated independently, and then obtained by assembling these sub matrices. We developed a new pruning technique using the Hessian to estimate the error deviation due to the elimination of connections in the net. The method proposed is applied in the optimization of a loudspeaker's magnet problem consisting of seven design variables. The number of input variables is reduced whilst achieving the objective of the problem at an acceptable computational time.

Introduction

Given a data set consisting of input-output pair samples, one may train an artificial neural network to obtain an approximate objective function, which substitutes for the real model in the optimization process. This methodology is useful when the objective function is not available or demands high computational cost [1].

However, it is difficult to determine the exact topology for a neural network in an specific problem. To overcome this difficult, one may use pruning techniques. These techniques consists of systematically eliminate connections in the trained network, aiming to reduce its topology and obtain a minimum network size with good generalization performance.

Another motivation for using pruning is to investigate if the input space dimension may be reduced. If, after pruning the network, all or almost all connections of a given input variable are eliminated, we may remove this input and, hence, reduce the complexity of the problem. This type of analysis is interesting in diagnostic problems, fail detection, and also in optimization problems.

In this paper we propose a method for the exact calculation of the Hessian matrix of the error function for a multilayer perceptron network. A methodology for selecting weights for pruning is derived. The technique is applied to an optimization problem. The number of input variables of a loudspeaker's magnet design problem is reduced using the described approach.

Computation of the Hessian Matrix

Applying first derivatives to the training error function, we can get the gradient vector, which is the basis for training multiplayer perceptron networks. Rumelhart developed

this procedure in his error backpropagation algorithm [2]. Applying second derivatives, we can obtain the Hessian matrix. The following equations determine completely each element of the Hessian matrix for a generic network topology.

If both weights belong to the same neuron:

$$\frac{\partial}{\partial w_{ji}^{(l)}} \left(\frac{\partial \xi}{\partial w_{jg}^{(l)}} \right) = -h_j^{(l)} x_g^{(l)} x_i^{(l)}, \quad l = 1, \dots, k \quad (1)$$

where w represents a weight, superscript indicates the layer index, first subscript indicates neuron index in a layer, second subscript indicates weight index in a neuron, k is the number of layers. x represents a given input for a layer, and ξ is the error function. Furthermore:

$$\begin{aligned} h_j^{(l)} &= f'' \left(u_j^{(l)} \right) e_j + \left[f' \left(u_j^{(l)} \right) \right]^2 (-1), \quad l = k \\ h_j^{(l)} &= f'' \left(u_j^{(l)} \right) \sum_r \delta_r^{(l+1)} w_{rj}^{(l+1)} \\ &+ \left[f' \left(u_j^{(l)} \right) \right]^2 \sum_r h_r^{(l+1)} w_{rj}^{(l+1)} w_{rj}^{(l+1)}, \quad l < k \end{aligned} \quad (2)$$

where δ is the local gradient, u is the weighted sum of the inputs in a neuron, e is the error of a neuron in the output layer, and $f(\cdot)$ is the transfer function. $h_j^{(l)}$ is the local hessian of the j th neuron in the l th layer.

If both weights belong to different neurons in the same layer:

$$\frac{\partial}{\partial w_{ji}^{(l)}} \left(\frac{\partial \xi}{\partial w_{hg}^{(l)}} \right) = -h_{hj}^{(l)} x_g^{(l)} x_i^{(l)}, \quad l = 1, \dots, k \quad (3)$$

with:

$$\begin{aligned} h_{jh}^{(l)} &= 0, \quad l = k \\ h_{jh}^{(l)} &= f' \left(u_j^{(l)} \right) f' \left(u_h^{(l)} \right) \sum_r h_r^{(l+1)} w_{rj}^{(l+1)} w_{rh}^{(l+1)}, \quad l < k \end{aligned} \quad (4)$$

Finally, if the two weights belong to different neurons in different layers:

$$\frac{\partial}{\partial w_{ji}^{(l)}} \left(\frac{\partial \xi}{\partial w_{hg}^{(l-p)}} \right) = -h_{hj}^{(l-p,l)} x_g^{(l-p)} x_i^{(l)}, \quad l = 2, \dots, k; p < l \quad (5)$$

with:

$$\begin{aligned} h_{jh}^{(l,l-p)} &= f' \left(u_h^{(l-p)} \right) h_j^{(l)} w_{jh}^{(l)}, \quad p = 1 \\ h_{jh}^{(l,l-p)} &= f' \left(u_h^{(l-p)} \right) \sum_r h_{rj}^{(l-p+1,l)} w_{rh}^{(l-p+1)}, \quad p > 1 \end{aligned} \quad (6)$$

We may extend (1), (3) and (5) to matricial form, giving:

$$H_j^{(l)} = -h_j^{(l)} \vec{x}^{(l)} \vec{x}^{(l)T} \quad (7)$$

$$H_{jh}^{(l)} = -h_{jh}^{(l)} \vec{x}^{(l)} \vec{x}^{(l)T} = H_{hj}^{(l)} \quad (8)$$

$$H_{jh}^{(l,p)} = -h_{jh}^{(l,p)} \vec{x}^{(l)} \vec{x}^{(l-p)T} = H_{hj}^{(l-p,l)T} \quad (9)$$

With the submatrices above, we can assemble the Hessian matrix:

$$H^{(l)} = \begin{bmatrix} H_{11}^{(l)} & \dots & H_{1N}^{(l)} \\ \vdots & & \vdots \\ H_{N1}^{(l)} & \dots & H_{NN}^{(l)} \end{bmatrix} \quad (10)$$

considering that the l th layer has N neurons. Also:

$$H^{(l,l-p)} = \begin{bmatrix} H_{11}^{(l,l-p)} & \dots & H_{1N}^{(l,l-p)} \\ \vdots & & \vdots \\ H_{M1}^{(l,l-p)} & \dots & H_{MN}^{(l,l-p)} \end{bmatrix} = H^{(l-p,l)T} \quad (11)$$

considering that the l th layer has M neurons and $(l-p)$ layer has N neurons. Finally, using (10) and (11):

$$H = \begin{bmatrix} H^{(1)} & \dots & H^{(1,L)} \\ \vdots & & \vdots \\ H^{(L,1)} & \dots & H^{(L)} \end{bmatrix} \quad (12)$$

considering that the network has L layers.

The Pruning Technique

Having the Hessian matrix and using the Taylor series expansion, we can estimate the variation caused in the error function when a connection is eliminated. We consider that the weights are eliminated after training the net. In this way, we expect that the weight vector be in a local or global minimum. Hence, we may consider a quadratic approximation and we may neglect the gradient vector, which gives:

$$\Delta \xi_{mean} = \xi(\vec{w} + \Delta \vec{w}) - \xi(\vec{w}) \approx \frac{1}{2} \Delta \vec{w}^T H(\vec{w}) \Delta \vec{w} \quad (13)$$

Therefore, we may estimate variation in the error function due to a disturbance $\Delta \vec{w}$ in the weight vector. This disturbance is selected in a such way to eliminate a set of weights.

Results

We analyze the design of a loudspeaker's magnet, Fig. 1, consisting of seven geometric variables, given in Table I. The objective is to maximize the magnetic flux in the air-gap, which is established using the finite element method.

A 243 point data set is obtained by random sampling in the feasible region [3]. This data set is required for training a multilayer perceptron network. The initial topology

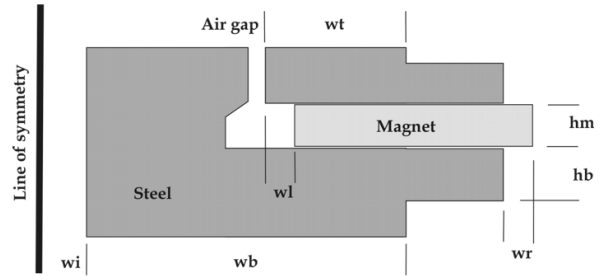


Fig. 1. The loudspeaker problem configuration.

TABLE I
LIMITS FOR THE 7 PARAMETERS

Var	w_i	w_t	w_l	w_r	w_b	h_m	h_b
Unit	mm	mm	mm	mm	mm	mm	mm
Min	3	5	1	1	1	3	2
Max	12	15	4	7	4	12	7

of the network was 7:50:1. A mean squared error (MSE) of 0.0023 was reached by the training process. After training, we computed the Hessian matrix using the method proposed. Table II presents the predicted error variation, by using (13), and the real variation for each variable when it is rejected by eliminating its corresponding input connections.

TABLE II
MSE VARIATION

Var	Predicted variation	Real variation
w_i	0.0021	0.0018
w_t	0.0789	0.0822
w_l	0.0199	0.0167
w_r	0.0043	0.0063
w_b	0.0018	0.0001
h_m	0.0313	0.0311
h_b	0.0178	0.0157

We see that the error function is less sensitive to w_i and w_b , hence we may remove these variables from the seven variable problem and thus reduce complexity of the optimization process. Eliminating the less significant variables the problem was reduced to one of five variables and was solved using a hybrid method. The result found gives a magnetic flux density of 1.5424 T, which is in agreement with the literature. Details of the problem will be discussed in the full paper.

References

- [1] M. Bazan, M. Aleksa, and S. Russenschuck, "An Improved Method Using Radial Basis Function Neural Networks to Speed Up Optimization Algorithms," IEEE Transactions on Magnetics, vol. 38, no. 2, pp. 1081-1084, March 2002.
- [2] D. E. Rumelhart and J. L. McClelland, eds., *Parallel Distributed Processing: Explorations in the Microstructure of Cognition*. Cambridge, MA: MIT Press, 1986.
- [3] K. Rashid, J. A. Ramirez, and E. M. Freeman, "A General Approach for Extracting Sensitivity Analysis from a Neuro-Fuzzy Model," IEEE Transactions on Magnetics, vol. 36, no. 4, pp. 1066-1070, July 2000.

Optimal Designs of Roll-iron Core Transformers by Pareto Genetic Algorithm

Hu Yan, Tang Renyuan, Wang Xiulian, and Zhao Liangyun
School of electrical Engineering, Shenyang University of Technology
58 Xinghua South Street, Tiexi District
Shenyang, 110023, China
huyansy@eyou.com

Abstract— Pareto theory and stochastic method are used to optimize multi-objective functions in the paper. The combination method of Pareto genetic algorithm and electromagnetic field numerical calculation is proposed to optimize a roll-iron core transformer. The transformer designers can obtain different optimal schemes emphasizing particularly on different objective functions from the Pareto optimal sets.

optimal designs of microwave absorbers and airplane airfoils [1,2]. In the paper, the combination method of Pareto genetic algorithm (PGA) and the electromagnetic field numerical calculation is proposed to optimize the roll-iron core transformer in the paper.

INTRODUCTION

The no load loss of a roll-iron core transformer is much lower than laminated core, as there is no any joint or less joints. However, magnetic flux distribution in the core isn't proportioned, thanks to the special core structure of the roll-iron core transformer. For avoiding the stronger magnetic flux density in some regions, the core diameter can't be designed to be too small. And this results in the transformer's cost is almost as much as the laminated iron core transformer. In order to reduce the cost, an optimization method must be used to design the transformer's core.

The problem belongs to a multi-objective optimization. The multi-objective optimization problems in an electrical device were generally transformed to a single-objective optimization problem by taking some weights of objective functions. Consequently, some man-made factors are added into the optimal results. The results will be subject to the weights. However, Pareto theory, which is effective to the multi-objective optimization problems, can give optimal sets emphasizing particularly on different objective functions.

Pareto theory had ever been used in the multi-objective

MATHEMATIC MODEL

Multi-objective optimization problem can be described as follows,

$$\text{Min } f(x) \tag{1}$$

$$x \in R^m \mid g(x) \geq 0, h(x) \leq 0 \tag{2}$$

In (1) and (2), $x = [x_1, x_2, \dots, x_n]^T$, $f(x) = [f_1(x), f_2(x), \dots, f_n(x)]^T$, $g(x) = [g_1(x), g_2(x), \dots, g_n(x)]^T$, $h(x) = [h_1(x), h_2(x), \dots, h_n(x)]^T$. When there isn't any point in R^m satisfied $f_i(x) \leq f_i(x^*)$, x^* is the optimal point. And the points have to fail the other objective functions, when they improve an objective function. Genetic Algorithm find the optimal point in a group, so it is suitable for searching Pareto points.

CALCULATED RESULTS

A level 10kV, 30kVA 3-phase roll-iron core transformer shown in fig.1 is optimized, according to above mathematical model. The formula is as follows,

Maximum: The magnetic flux density

Minimum: The iron core cost

Constraint: Magnetic flux density is less than 1.8T, and the core diameter is less than 107mm, the core window width is less than 227mm, height is less than 495mm. These variables are coded by binary system in the genetic algorithm. The optimization results are shown as Fig.2 and Fig.3.

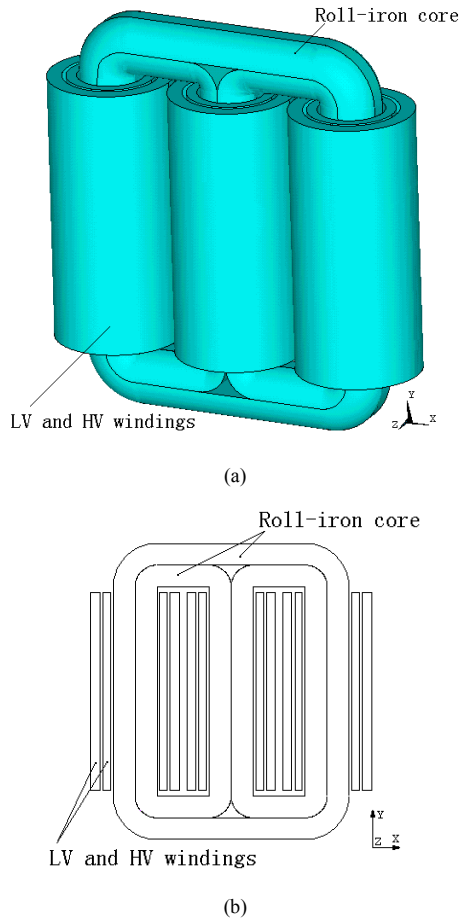


Fig.1 Illustration of a roll-iron core transformer

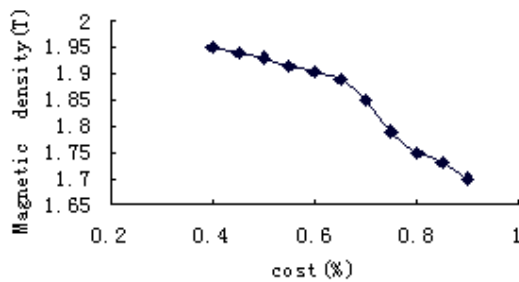


Fig.2 Pareto optimal set of the cost versus the magnetic flux density

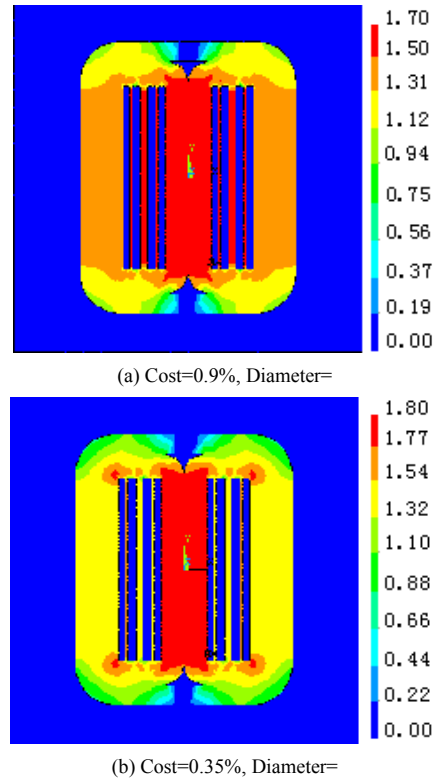


Fig.3 Distributions of magnetic flux densities at different optimal schemes

CONCLUSIONS

The combination method of Pareto genetic algorithm and electromagnetic field numerical calculation is successfully used to optimize a roll-iron core transformer. From the Pareto optimal sets, the transformer designers can obtain different optimal schemes emphasizing particularly on different objective functions.

REFERENCES

- [1] D. S. Weile and E. Michielssen, "Genetic Algorithm design of Pareto optimal broadband microwave absorbers", *IEEE Transaction on Electromagnetic Compatibility*, vol.38, Issue 3, pp518-525, 1996.
- [2] A.E.Raino, Makinen, Periaux Jacques, Toivanen Jari, "Multidisciplinary Shape Optimization in Aerodynamics and Electromagnetics Using Genetic Algorithms", *International Journal for Numerical Methods in Fluids*, vol.30, No.2, pp149-159,1999.

A new Tabu Search Method for Optimization with Continuous Parameters

O. Hajji, S. Brisset, and P. Brochet

L2EP

Ecole Centrale de Lille – Cité Scientifique – BP 48 – 59651 Villeneuve d’Ascq cedex - France

E-mail: omessaad.hajji@ec-lille.fr, stephane.brisset@ec-lille.fr, pascal.brochet@ec-lille.fr

Abstract— A new tabu search algorithm for global optimization of multimodal functions with continuous variables is presented. The tabu list contains all points and a prohibited zone around each point that depends on the value of its objective function and decreases as the number of iteration increases. The numerical results obtained by solving the problem 22 benchmark of the TEAM workshop demonstrates the speed effectiveness of the proposed method. It is compared favorably with Hu’s tabu search, genetic algorithm, and simulated annealing.

NEW TABU METHOD

Tabu search is now a well known method. Details on the main implementation are referred in [1,2]. Differences with Hu’s TS (HuTS) and universal TS (UTS) are pointed out.

INTRODUCTION

Generating new points

The optimal design of electromagnetic structures using global optimization techniques is a wide field of research. This is due to the fact that objective functions of this kind of problem are generally multimodal, non linear and non-derivable ones, and classical optimization algorithms lead to poor results.

As no information on the location of optimum is available at the first iteration, points are generated in the whole design space using an uniform density of probability.

Recently, probabilistic heuristic algorithms have been used as efficient and general approaches for the global optimization of multimodal functions with continuous variables in electromagnetic. These algorithms include simulated annealing (SA), genetic algorithms (GA), and tabu search (TS) methods.

For the next iterations, points are generated using the normal law. The density of probability is defined with:

$$p(x_i) = \frac{1}{\sigma_i \sqrt{2\pi}} \exp\left(-\frac{(x_i - x_i^{best})^2}{2\sigma_i^2}\right) \quad i = 1, \dots, n \quad (1)$$

Only a few applications of tabu algorithm have been found in electromagnetic compared to SA and GA [1-4]. Nevertheless, lots of stochastic methods use memory table to avoid generating points too close to already existing points, especially when FE simulations are used.

Where σ_i is the standard deviation, x_i^{best} is the coordinate of the best point at previous iteration, and n is the number of design variables. The standard deviation is chosen initially equal to 10% of design space in order to proceed to the intensification phase. This way, new points have more probability to be close to the best point. The standard deviation will be increased during the diversification process.

TS is based on the use of prohibition-based techniques and basic heuristic algorithms. Therefore, the main advantage of TS with respect to GA and SA, lies in the intelligent use of the past history of the search to influence its future search procedures. Since the method uses a tabu list for storing the past history of the search, the efficient structure of the tabu list is important for fast computation.

To do that, points are generated using a random number between 0 and 1, and the function of repartition $P(x)$:

$$x_i = x_i^{best} + \sigma_i P^{-1}(rand) \quad i = 1, \dots, n \quad (2)$$

with $P(x) = \int_{-\infty}^x p(u) du$ and $0 \leq rand \leq 1$

In the proposed TS method, the tabu list contains all points and a prohibited zone around each point that depends on the value of its objective function and decreases as the number of iteration increases. Alternation of intensification and diversification phases allows to find the global optimum with a good accuracy.

HuTS and UTS use several neighborhoods, i.e. intervals and uniform densities of probability to generate points around the best one. It can be shown that this process is similar to our with an hyperbolic density of probability.

The first section presents the new tabu search method and details the generation of points, the tabu list properties, the intensification and diversification phases, and the algorithm parameters. The second section apply the new TS method to the problem 22 benchmark of the TEAM workshop and compare it with standard GA, SA and TS.

Tabu list

The tabu list contains all tabu areas. These areas are hyper-rectangles defined with a center and sides lengths for each direction, i.e. design variable. The center is a point already generated. The difficulty which arises is how to

determine the sides lengths of these hyper-rectangles. Some heuristic rules are proposed. As the probability to find the global optimum near good points is assumed to be higher than bad points, the side lengths depend on the value of the objective function. Also, the sum of tabu areas is chosen to be roughly the same whatever the number of iteration is. This means that the sides lengths $l(X, g)$ of a tabu hyper-rectangle is computed with:

$$l(X, g) = \frac{x_i^U - x_i^L}{c} \frac{f(X)}{f(X_{g-1}^{best})} \frac{2}{\sqrt[n]{g}} \quad (3)$$

Where X is the center of the hyper-rectangle, x_i^U and x_i^L are respectively the upper and lower limits of the design variables, f is the objective function to be minimized, g is the number of iteration, c is a constant and X_{g-1}^{best} is the best point at previous iteration.

The tabu list and side lengths have to be updated each time a new point is generated. No tabu area is removed from the tabu list but the areas sizes decrease when the number of iteration increases.

Intensification and diversification

Intensification and diversification are two interesting techniques to improve the power of TS. They make this method an effective one. Intensification allows exploring areas of search space, near of those characterizing the configurations of good quality visited before. Intensification enables the location of optimum with a good precision. Diversification seeks to search towards unexplored areas of the design space and generate configurations significantly different from those met before. That allows to find global optimum and not only local one.

The algorithm proposed here begin with intensification. Indeed, at the beginning of each iteration, the standard deviation is set to 1/10 of the design space, i.e. $\sigma_i = (x_i^U - x_i^L)/10$ and the normal law assume that 68% of generated points are between $x_i^{best} - \sigma_i$ and $x_i^{best} + \sigma_i$.

As many points are generated close to the best one, the neighborhood of the best point becomes tabu and lots of points are rejected because they are inside tabu areas. If the rejected points represent more than 95% of generated points, the standard deviation is increase. This way, points are generated farer from best one and diversification begins.

Algorithm parameters

Four parameters, characterizing the new TS algorithm, have an great influence on its convergence. They are the number of points generated at each iteration N_p , the

maximum number of iterations G , the constant c , and the relative accuracy of the optimum location. The following relations can be proved:

$$c = \frac{1}{\text{relative accuracy} \cdot \sqrt[n]{G}} \quad \text{and} \quad N_p < c^n \quad (4)$$

SMES OPTIMIZATION

To show the feasibility of the proposed algorithm in solving electromagnetic optimization problems, it is applied to the optimization of a superconducting magnetic energy storage (SMES), i.e. benchmark problem 22 described in [5].

Table I shows the results achieved with the new TS algorithm and other well-known stochastic methods. It can be seen that the proposed method uses less time, i.e. number of FE simulations, and reach almost the same optimum as HuTS.

TABLE I. OPTIMIZATIONS RESULTS

Method	OF	B ² _{strav}	Energy	R ₂	h ₂₂	d ₂	Time
GA	0.090	7.668	179.19	3.04	0.24	0.386	2400
SA	0.087	7.59	179.36	3.078	0.237	0.39	5025
HuTS	0.0864	7.67	179.79	3.08	0.246	0.381	3821
new TS	0.0864	7.78	179.99	3.08	0.254	0.37	1800

CONCLUSION

A new tabu search algorithm for global optimization with continuous variables has been presented. The numerical results on problem 22 benchmark show that the proposed method not only obtains better optimal, but is also time saving compared with other stochastic methods.

REFERENCES

- [1] N.Hu, "Tabu search method with random moves for globally optimal design", *Int. J. Num. Meth. Engineering*, Vol. 35, pp. 1055-1070, 1992.
- [2] Y. Shiyou, L. Yan, "An universal Tabu Search Algorithm for Global Optimization of Multimodal Functions with Continuous Variables in Electromagnetics", *IEEE Trans. Mag.*, Vol. 34, No. 5, pp. 2901-2904, September 1998.
- [3] C. Xudong, N. Guangzheng, and Y. Shiyou, "An Improved Tabu Algorithm Applied to Global Optimizations of Inverse Problems in Electromagnetics", *IEEE Trans. Mag.*, Vol. 38, No. 2, pp. 1069-1072, March 2002.
- [4] P.J. Leonard and A.M. Connor, "Pole Shape Optimization Using a Tabu Search Scheme", *IEEE Trans. Mag.*, Vol. 36, No. 4, pp. 1115-1118, July 2000.
- [5] SMES Optimization Benchmark, definition of the 3 parameter problem, discrete case, <http://www-igte.tu-graz.ac.at/team/team3dis.htm>.

Treating Constraints as Objectives in Multiobjective Optimization Problems using Niche Pareto Genetic Algorithm

Douglas A. G. VIEIRA¹, Ricardo L. S. ADRIANO¹, Laurent KRÄHENBÜHL² and João A. VASCONCELOS¹

¹Federal University of Minas Gerais, 31270-901 Belo Horizonte, Minas Gerais, Brazil (e-mail: joao@cpdee.ufmg.br).

²L. Krähenbühl is with CEGELY – ECL – Lyon – France (e-mail: Laurent.Krahenbuhl@ec-lyon.fr).

Abstract – In this paper, a novel approach based on handling constraints as objectives together with a modified Parks & Miller elitist technique, to solve constrained Multiobjective optimization problems, is analyzed with Niche Pareto Genetic Algorithm. The performance of this approach is compared with the classical procedure of handling constraints that is the exterior penalty function method. Results are obtained applying both procedures of handling constraints, with and without elitism. Especially when using the modified elitist technique, simulation results suggest the effectiveness of the proposed technique.

INTRODUCTION

When genetic based algorithms are used, the most common way of handling constraints is by using penalty techniques like the exterior penalty method. There is a weakness in this classical approach because good values for the penalty parameters are not known.

In this paper, constraints in constrained multiobjective optimization problems (CMOPs) are handled as objectives and the resulting problem is solved by the Niche Pareto Genetic Algorithm (NPGA). The original NPGA was modified by incorporating the Parks & Miller elitist technique (P&M) [1], which needed some changes when constraints were treated as objectives. The required changes were essential to avoid convergence toward an infeasible space.

Two analytical test problems, TBU [2] and CPT7 [3], that were designed with special features to difficult the PO front search, are chosen to compare both approaches of handling constraints as objectives and using penalty function. The methodology adopted here to compare the results from both approaches made use of three quantitative metrics: generational distance (GD), coverage relationship (CR) and timing analyses [4]. This choice enabled a realistic sight of the techniques discussed, pointed out the advantages of the new approach. After that, both classical and new procedures were applied to find the nondominated front by solving a CMOP based on the TEAM22 [5].

MATHEMATICAL FORMULATION

The multiobjective optimization involves a set of k decision variables, m objective functions and n constraints. In terms of minimization we can write this problem as:

minimize:

$$\bar{f} = \{f_1(\bar{x}), f_2(\bar{x}), \dots, f_m(\bar{x})\}^T \quad (1)$$

subjected to:

$$\bar{g} = \{g_1(\bar{x}), g_2(\bar{x}), \dots, g_n(\bar{x})\}^T \leq \{0, 0, \dots, 0\}^T \quad (2)$$

where $\bar{x} = \{x_1, x_2, \dots, x_k\}^T$.

As NPGA is not capable to deal directly with constrained problems, some way must be found to handle the constraints. In this paper, two approaches are considered. First, the constraints are incorporated to the fitness function by using penalty functions. This procedure will be denoted here as classical approach (CA). Initially, the original optimization problem is rewritten as an unconstrained one. As an example, for the i^{th} objective, a pseudo-objective function ff_i can be written as:

$$ff_i(\bar{x}) = f_i(\bar{x}) + \rho \sum_{j=1}^n (g_j(\bar{x}))_+^2, \quad (3)$$

where ρ is a penalty parameter associated and $()_+$ denotes that only violated constraints are considered.

Second, the n constraints are transformed in n more objectives. To avoid confusion, this approach will be denoted here as objective approach (OA). Mathematically, the original problem is rewritten as:

minimize:

$$\bar{f} = \{f_1(\bar{x}), \dots, f_m(\bar{x}), g_1(\bar{x}), \dots, g_n(\bar{x})\}^T. \quad (4)$$

MODIFIED PARKS & MILLER ELITISM

To improve the NPGA performance the Parks & Miller elitist technique [1] was used. It consists in incorporating the efficient individuals of the on-line population (P_{on}) to the off-line population (P_{off}), at each generation. When P_{off} size exceeds a threshold, the dominance criterion is applied, eliminating all dominated solutions. If P_{off} size continues bigger than the threshold, a distance criterion is applied. It is based on measuring the distance between the off-line individuals, taking two per turn, and if they are within some distance one of them is discarded, chosen randomly. This distance is measured in the objective space. The individuals of P_{off} are reinserted in P_{on} , when the size of P_{off} is bigger than a threshold, to improve the convergence. This approach works well when the constraints are considered in the classical approach. Although infeasible individuals do not represent the wished PO front, keeping them in the on-line population seems to be a good idea because infeasible points near the PO front might be lost during the optimization process. When using constraints as objectives, P&M elitism does not work properly because sometimes the P_{off} may be composed by a great deal of infeasible points,

guiding the search in a wrong way. To avoid this drawback, P&M was modified by two additional procedures to avoid convergence to the infeasible region: *i*) when eliminating individuals of P_{off} by the distance criterion, infeasible points are discarded if they are near to a feasible one and *ii*) when P_{off} size is bigger than a threshold, all infeasible points are discarded. This modified P&M will be denoted by M-P&M. The nondominated set without these procedures can partially converge toward an infeasible region due to reinserting many infeasible individuals of P_{off} in P_{on} . So, in the elitism process the constraints are not always viewed as objectives. When using the classical approach (penalty functions) these procedures are not needed because just feasible individuals are placed in P_{off} .

ANALYTICAL TEST FUNCTIONS

The first test function, TBU [2], has the following properties: *i*) the feasible region is non-convex and *ii*) some feasible PO solutions lie on boundaries between the feasible and infeasible regions. This problem was simulated with population size and generation number equal to 80 and 100, respectively. The main property of the second test function, CPT7 [3], is the disconnected PO front. This problem was simulated with population size and generation number equal to 40 and 400, respectively. The NPGA was executed twenty times for each test problem. The arithmetic mean of these results using the metrics as used in [4] are shown in Table I and II, respectively, where OA denotes the approach of handling constraints as objectives, CA the classical penalty approach, P&M the Parks&Miller elitism and M-P&M the modified Parks&Miller elitism as described before. The comparisons between OA and CA were done with and without elitism separately.

TABLE I - RESULTS OF TBU PROBLEM.

Metric	With Elitism		Without Elitism	
	OA (M-P&M)	CA (P&M)	OA	CA
CR	100%	99.33%	100%	57.01%
(Mean)	(27.66)	(22.40)	(16)	(6.30)
GD	0.0155	0.0152	0.0190	0.0328
Time	1.72	1.28	1.78	1.16

TABLE II - RESULTS OF CPT7 PROBLEM

Metric	With Elitism		Without Elitism	
	OA (M-P&M)	CA (P&M)	OA	CA
CR	100%	0.0%	100%	0.0%
(Mean)	(12.5)	(0.0)	(0.1)	(0.0)
GD	0.0025	0.0615	0.2506	0.9315
Time	1.27	1.23	1.15	1.02

The results in Table I with elitism (second and third columns) show that both approaches present comparable results. This can be seen from the CR and GD metric values. However, the front was better represented (see the mean of nondominated solutions found) when using the constraints as objectives. In the other situation, without elitism (fourth and fifth columns), the advantages of using constraints as objectives are clear. It is observed that the

computing time for OA increases proportionally with the number of constraints, but it is not significant for real world problems.

For the second test problem, an adequate front was only found by using the new approach, that is, OA together with the M-P&M technique. This is clearly shown in Table II.

CONSTRAINED MULTIOBJECTIVE OPTIMIZATION IN ELECTROMAGNETICS

The TEAM'22 problem with three continuous variables was chosen to demonstrate the performance of the new approach in CMOP in electromagnetics, for further details see [5]. This problem was solved using NPGA with both new and classical approaches. In both cases the modified and standard P&M were used and the population size and generation number were fixed to 30. The results are presented in Fig. 1. The front found using constraint as penalty function was completely dominated by that obtained using constraint as objective.

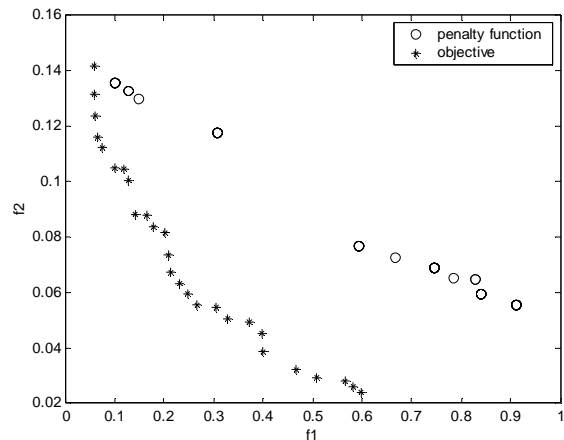


Fig. 1 – Nondominated sets found for the TEAM22 problem.

The results obtained by handling constraints as objectives when solving both test and TEAM'22 problems demonstrate that the new approach works better than the classical method of handling constraints using penalty functions. A complete analysis and more results will be given in the full paper.

REFERENCES

- [1] G. T. Parks and Miller, 'Selective breeding in a multiobjective genetic algorithm'. *Parallel Problem Solving From Nature PPSN V*, pp. 250-259, Holland, Springer-Verlag, 1998.
- [2] To Thanh Binh and Ulrich Korn. 'MOBES: A multiobjective evolution strategy for constrained optimization problems', *The Third International Conference on Genetic Algorithms (Mendel 97)*, pp. 176-182, Brno, Czech Republic, 1997.
- [3] K. Deb, A. Pratap, and T. Meyarivan, 'Constrained Test Problems for Multi-objective Evolutionary Optimization'. *First Intern. Conference on Evolutionary Multi-Criterion Optimization*, pp. 284-298. Springer-Verlag. Lecture Notes in Computer Science No. 1993, 2001.
- [4] David A. Van Veldhuizen and Gary B. Lamont, 'On measuring multiobjective evolutionary algorithm performance'. *2000 Congress on Evolutionary Computation*, v. 1, pp. 204-211, New Jersey, 2000.
- [5] 'TEAM Optimization Benchmark Problem 22'. Internet edition: <http://www-igte.tu-graz.ac.at/team/team3dis.htm>.

Extracting Sensitivity Information of Electromagnetic Device Models from a Modified ANFIS Topology

Douglas A. G. Vieira, Walmir M. Caminhas, Jaime A. Ramirez and João A. Vasconcelos

Federal University of Minas Gerais, 31270-010 Belo Horizonte, Minas Gerais, Brazil

jramirez@cpdee.ufmg.br , joao@cpdee.ufmg.br

Abstract – This paper addresses the extraction of sensitivity information from a modified ANFIS model. The modified ANFIS topology was designed to avoid the dimensionality problem of the classical ANFIS. The modified ANFIS topology is more appropriate for optimization problems, particularly when dealing with problems with a high number of variables. An analytical and an electromagnetic optimization problem are discussed. The results show the effectiveness of this new approach.

INTRODUCTION

The main problem of the classical ANFIS model is its computational effort [1]. The rules are generated with all possible combinations of *premises*, thus the ANFIS model has a spatial exponential complexity. The number of generated rules N for a system with n inputs and P *premises* is $N = P^n$.

In the modified ANFIS topology, a layer of *perceptrons* replaces the classical ANFIS first layer, changing the rules by weights that must be adjusted. In the classical ANFIS case the number of adjustable parameters is a function of P^n . So, for a given number of inputs the possible number of adjustable parameters is defined. On the other hand, in the modified ANFIS case the numbers of *perceptrons* is not a function of the number of variables. In this case it is possible to generate a network better adjusted with the problem to be solved.

In this paper, the extraction of the sensitivity information when using the modified ANFIS topology is addressed. This sensitivity information can be used to improve the convergence process of deterministic optimization algorithms avoiding the high cost of derivative evaluations. The formulation concerning sensitivity extraction using the classical ANFIS can be found in [2,3].

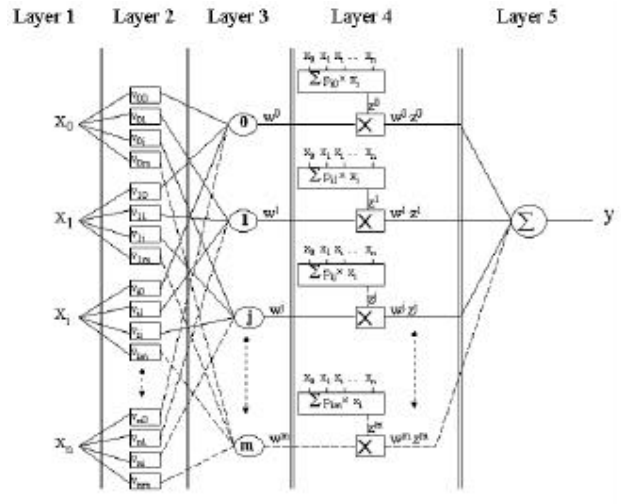
MATHEMATICAL FORMULATION

The output y of the modified ANFIS considering n inputs and m *perceptrons* is calculated as:

$$y = \sum_{j=1}^m \left[\phi \left(\sum_{i=0}^n X_i v_{ij} \right) \times \left(\sum_{i=0}^n p_{ij} X_i \right) \right] \quad (1)$$

where $\phi(\cdot)$ is the activation function (e.g. hyperbolic tangent, gaussian function, ...), p is a matrix of *consequent* parameters, v is a matrix of *perceptron* weights and X is the

vector of input variables. Figure 1 shows the topology of the modified ANFIS model.



Calculating the first derivative of (1) with respect to each input variable X_i , the following equation can be obtained:

$$\frac{\partial y}{\partial X_i} = \sum_{j=1}^m \left[\left(\frac{\partial \phi}{\partial X_i} v_{ij} \right) \times \left(\sum_{i=0}^n p_{ij} X_i \right) + \phi \left(\sum_{i=0}^n X_i v_{ij} \right) p_{ij} \right] \quad (2)$$

Finally, the gradient of the output y can be found using Eq. (3).

$$\nabla_x y = \left[\frac{\partial y}{\partial X_1} \quad \frac{\partial y}{\partial X_2} \quad \dots \quad \frac{\partial y}{\partial X_n} \right]^T \quad (3)$$

Then, it is straightforward to extract the sensitivity information from the proposed modified ANFIS network. A detailed analysis of the structure of the modified ANFIS network and the sensitivity extraction will be given in the full paper.

ANALYTICAL PROBLEM

The formulation presented before was applied to evaluate the derivatives of the Rosenbrock's function, which is mathematically stated as:

$$F(x, y) = 100(y - x^2)^2 + (1 - x)^2 \quad (4)$$

where $x \in [-2, 2]$ and $y \in [-2, 2]$. The analytical derivatives are given by:

$$\frac{\partial F}{\partial x} = 400x^3 - 400xy + 2x - 2 \quad (5)$$

$$\frac{\partial F}{\partial y} = 200y - 200x^2 \quad (6)$$

To represent the surface accurately, a modified ANFIS with 20 neurons is trained using 144 evenly sampled points. The root mean squared errors (RMSE) for the Rosenbrock's function and both the derivatives were respectively 0.03, 0.76 and 0.37. The approximated derivative surfaces are presented in Fig. 2. It is observed the superposition of the analytical and extracted values, showing the effectiveness of the modified ANFIS model.

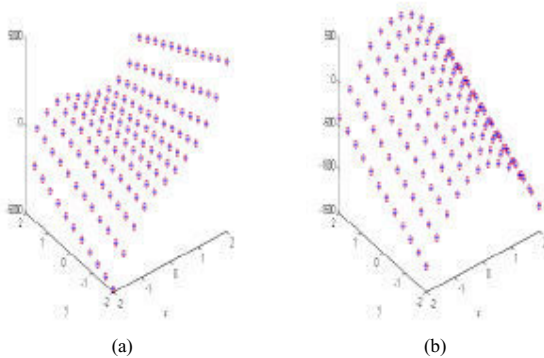


Fig. 2 Gradient Surface (analytical (o), extracted (+)) for (a) $\partial F/\partial x$ and (b) $\partial F/\partial y$.

SENSITIVITY INFORMATION OF AN ELECTROMAGNETIC DEVICE

A loudspeaker magnet assembly unit with seven design variables is investigated as described in [2]. The magnetic flux density is calculated using the finite element method. The function and its derivatives were extracted using 169 points. Table 1 show the results achieved using both classical (as in [2]) and the modified ANFIS topology.

TABLE I - ERROR ON THE RESULTS FOR THE LOUDSPEAKER.			
ANFIS Model	RMSE		
	F	$\partial F/\partial x_1$	$\partial F/\partial x_2$
Modified	0.00041	0.067	0.001
Classical [2]	0.00056	0.682	0.837

Both models give good results when compared with the numerical derivatives as given in [2]. However, it can be seen

that the error using the modified ANFIS model is lower than that given by the classical model, confirming the effectiveness of the modified ANFIS. This technique for sensitivity extraction, which has a lower cost if compared with gradient evaluation, can be helpful in the optimization process. The surfaces for the approximated derivatives are presented in Fig. 3.

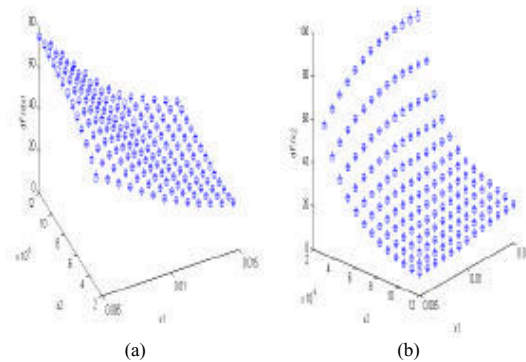


Fig. 3 Gradient Surface (numerical (o), extracted (+)) for (a) $\partial F/\partial x_1$ and (b) $\partial F/\partial x_2$.

CONCLUSION

The results obtained show the effectiveness of the modified ANFIS model to extract sensitivity information. This information can be used in deterministic optimization process. One of the disadvantages of deterministic methods is the cost to evaluate the gradient that sometimes can be prohibitive. However, using this formulation the gradient information is not directly evaluated, decreasing computational effort. Moreover, one of the advantages of the modified ANFIS topology is that it does not have the spatial complexity of the ANFIS topology. In the case of dealing with problems that have high number of optimization variables, the modified ANFIS topology should be more effective.

REFERENCES

- [1] Jang, J. S. R., "ANFIS: Adaptive-Network-Based Fuzzy Inference System", IEEE Transactions on Systems, Man and Cybernetics, pp. 665-685, May 1993.
- [2] Rashid, K, Ramirez, J. A. and Freeman, E. M., "A General Approach for Extracting Sensitivity Analysis from a Neuro-Fuzzy Model", IEEE Transactions on Magnetics, pp. 1066-1070, vol. 36, no. 4, July 2000.
- [3] Rashid, K, Ramirez, J. A. and Freeman, E. M., "Optimization of Electromagnetic Devices Using Sensitivity Information from Clustered Neuro-Fuzzy Models", IEEE Transactions on Magnetics, pp. 3575-3578, vol. 37, no. 5, September 2001.

Design Optimization for Cogging Torque Minimization using Response Surface Methodology

J. T. Li, Z. J. Liu, M. A. Jabbar, and X. K. Gao
Data Storage Institute, 5 Engineering Drive 1,
Singapore 117608
dsiliuzj@dsi.a-star.edu.sg

Abstract—This paper discusses the application of Response Surface Methodology (RSM) to design optimization for brushless dc permanent magnet motors to reduce cogging torque. The feasibility of using RSM with finite element method (FEM) in the practical engineering problems is investigated by the computational examples and the comparison between the fitted response and the results obtained from an analytical solution.

INTRODUCTION

Cogging torque is introduced by the interaction between the slot and the magnets. It has an undesirable effect on the performance of the spindle motor, especially in the high precision systems such as spindle motor for Hard Disk Drive (HDD). Suppression the cogging torque to an acceptable smoothness level through the appropriate combination of the structure parameters can be an effective way.

Response surface methodology (RSM) is a collection of statistical and mathematical techniques useful to find the “best” value of the response [1]. It is now recognized as an effective optimization approach for design of electrical devices when used in combination of the numerical method for product performance simulation [2][3]. Generally, a polynomial model is constructed to simulate the relationship between the performance and the design parameters. Therefore this model is used to predict product performance with certain design variables to carry out the optimization design process. The quality of the fitted model is then evaluated by checking the statistics index which are based on the experimental data from the required investigation points in RSM. The approach is expected to produce useful results for optimization tasks. However, report on the feasibility of the method has been rare in the literature although there is awareness to certain degree that the fitting quality of the response surface is vital to get meaningful results using the method and the quality depends on the size of the region in which the design parameters may vary. This paper reports a study of the feasibility of the method based on comparison of the fitted response surface against the performance response obtained from a closed form analytical solution [4] which can produce performance response in wide ranges of parameter variations. Computational examples are given in this paper.

DESCRIPTION OF DESIGN PROBLEM

In this paper, the motor under investigation is a 6-pole and 9-slot BLDC spindle motor used in HDD. In original design, the airgap is 0.2mm, the thickness of the surface mounted

magnet is 1.05mm and the iron yoke outside is 1.17mm thick. The slot opening is 1.18mm.

The pole arc to pole pitch ratio (α_p) and the tooth face angle (α_t) are the main control factors (design parameters) influencing the cogging torque. First a relatively large design space is selected, in which α_p varies from 0.5 to 1 and α_t from 32 deg to 35 deg. The flux density distribution obtained from FEM is showed in Figure 1.

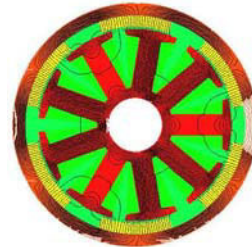


Figure 1. Flux distribution of 6-pole 9-slot motor

The maximum cogging torques are computed. The ‘true’ response surface, obtained from the analytical solution, for the cogging torque with respect to the design parameters are plotted in Figure 2. Within the given design space, a valley near $\alpha_p \approx 0.7$ can be clearly observed. The optimum setting of the design parameters be easily found as $\alpha_t = 35$ deg, and $\alpha_p = 0.73$.

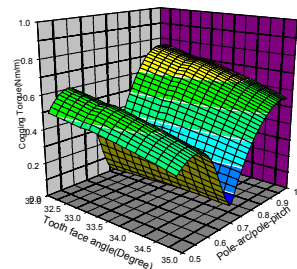


Fig. 2. Response surface of cogging torque

DESIGN, SIMULATION AND ANALYSIS

In this stage, RSM is used to fit the response model. A quadratic approximation model is commonly used to construct the fitted response surface. In general, the response model can be written as Equ. 1.

$$y = \alpha_0 + \sum_{i=1}^2 \beta_i x_i + \sum_{i=1}^2 \gamma_i x_i^2 + \varepsilon \quad (1)$$

where α_i , β_i and γ_i are coefficients for the control variables.

The central composite design (CCD) is applied to construct the above second order polynomial model [2]. CCD consists of three portions: a complete 2^k or fractional 2^{k-m} first order factorial design which the factor levels are coded into -1 and 1; axial points at a distance α from the center point and one design center point. Assume the initial design point is $\alpha_t=32.5$ and $\alpha_p=0.9$. The center design point is at $\alpha_t=33.5$ degree, $\alpha_p=0.75$. The control variable matrix is showed in Table I (In this CCD scheme, $k=2$, so $\alpha=\sqrt{2}$). FEM based simulation is used to obtain the responses with respect to the CCD experimental design. In the FEM analysis the permeability of the soft-magnetic components are set to be extremely large to imitate the conditions under which the closed form analytical solution is derived.

TABLE I. DESIGN PARAMETERS

Control factors		$-\alpha$	-1	0	1	α
x_1	α_t	32.44	32.75	33.5	34.25	34.56
x_2	α_p	0.644	0.675	0.75	0.825	0.856

The second-order regression model is fitted as:

$$\hat{y}=56.026-2.589x_1 - 32.563x_2 + 0.0382x_1^2 + 22.020x_2^2 \quad (2)$$

The fitted response surface is showed Fig. 3.

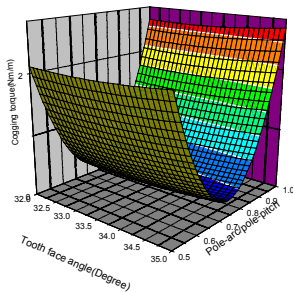


Fig. 3. The fitted second-order model

To check the quality of the fitted response surface, the analysis of variance (ANOVA) is computed as given in Table2.

Table 2. Analysis Of Variance

Source	DF	SS	MS	F	R^2	R_A^2
Regression	4	0.2307	0.0577	10.38	0.9157	0.8311
Residual	4	0.0222	0.0056			
Total	8	0.2531	0.0316			

The R^2 value of 0.9157 means that 91.75% of the total variation in torque performance may be explained by the regression surface relating it to the design variables. R_A^2 of 0.8311 indicates that the estimate of the error variance provided by the residual mean square is 16.89% of the error variance estimate using the total mean square. Compare the fitted response with the original response, it can be observed that the fitted response surface cannot adequately reflect the dip in the original response surface even though the statistics data shows the fitting is particularly 'bad'.

When focusing on a smaller region in the design space as shown in Fig. 4, such that $\alpha_t \in [32 \text{ deg}, 35 \text{ deg}]$ and $\alpha_p \in [0.75, 1]$, redo the surface fitting using RSM, the fitted model is given in equation (3) and the fitted surface is showed in Fig. 5.

$$\hat{y} = -31.948 + 1.568x_1 + 14.442x_2 - 0.0242x_1^2 - 7.19x_2^2 \quad (3)$$

The analysis of variance is given in Table 4.

Table 4. Analysis Of Variance

Source	DF	SS	MS	F	R^2	R_A^2
Regression	4	0.4270	0.1067	31.354	0.9709	0.9381
Residual	4	0.0136	0.0034			
Total	8	0.4398	0.0549			

From the Table 4, we can see that, 97.09% of the total variation can be explained by the regression model. Apparently the quality of the fitting surface has improved. Using the fitted model the optimal design point (optimal setting of design parameters) can be easily obtained as $\alpha_t=35$ deg, and $\alpha_p=0.75$ which coincides with the optimal settings obtained from the original response surface.

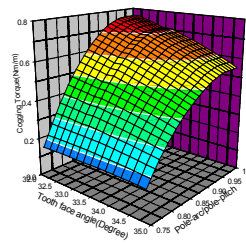


Fig. 4 Response of a given region

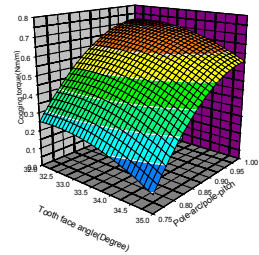


Fig. 5. Fitted response for the given region

CONCLUSION

The present work demonstrate that the RSM approach relies critically on the quality of fitted model in the area of interests, and it can be difficult for a given RSM scheme to achieve necessary quality when the true response in the given region is complex. Caution must be taken in the application of RSM in conjunction with FEM or other numerical techniques for digital validation when the true response is unknown to the designers.

REFERENCE

- [1] Andre. I. Khuri, John A. Cornell, *Response Surface: Designs and Analyses*, Marcel Dekker, Inc., New York, 1996.
- [2] X. K. Gao, T. S. Low, S. X. Chen, Z. J. Liu, *Structural Robust Design for Torque Optimization of BLDC Spindle Motor Using Response Surface Methodology*, *IEEE Trans. Magn.*, Vol. 37, NO 4, July 2001.
- [3] D. Dyck, D. A. Lowther, Z. Malik, R. Spence, J. Nelder, *Response Surface Models of Electromagnetic Devices and Their Application to Design*, *IEEE Trans. Magn.* Vol. 35, NO 3, May, 1999.
- [4] Z. J. Liu, et al, 'Electromagnetic design for hard disk drive spindle motors with fluid film lubricated bearings', *IEEE Trans. Magnetics*, 32, 5, 3893-3895, 1996.

A high-order, high-frequency method for surface scattering by convex obstacles

Oscar P. Bruno and Christophe A. Geuzaine

Applied and Computational Mathematics, California Institute of Technology, MC 217-50

Pasadena, California 91125, USA

E-mail: {bruno,geuzaine}@acm.caltech.edu

Abstract— We present a new algorithm for the numerical solution of problems of electromagnetic or acoustic scattering by large, convex obstacles. This algorithm combines the use of an ansatz for the unknown density in a boundary integral formulation of the scattering problem with an extension of the ideas of the method of stationary phase. We present results showing the high order convergence of the algorithm as well as its asymptotically bounded computational complexity as the frequency increases.

I. INTRODUCTION

However efficient they may be, direct numerical methods for solving scattering problems require a fixed number of discretization points per wavelength λ , and thus exhibit an $\mathcal{O}(k^n)$ computational complexity for an n -dimensional discretization (where $k = 2\pi/\lambda$ is the wavenumber).

This paper introduces a solver with an asymptotic $\mathcal{O}(1)$ computational complexity for surface-scattering problems by convex obstacles in two or three dimensions, using a combined-field integral equation [1]. Our approach relies on two main results.

Firstly, the boundary integral equation is transformed to explicitly capture the rapidly oscillating phase progression of the scattered waves. For this purpose, the original unknown in the boundary integral formulation is replaced by the product of an ansatz derived from the asymptotic theory [2] and a slowly varying residual. This residual can then be represented by a number of degrees of freedom independent of the frequency. This idea is similar to those presented by Ling [3] for partial differential equations and by James [4] and others for integral equations.

Secondly, an extension of the method of stationary phase is used to reduce the support of integration to a subset of the scatterer boundary. This localized integration scheme can be seen as a natural link between high-frequency approximate, *non-convergent* methods such as the Kirchhoff approximation and a direct method of moment method. The reduced integration support is shown in Section IV to be proportional to the wavelength, leading to a number of integration points also independent of frequency. The resulting *convergent* integral method can evaluate accurately in a personal computer scattering problems throughout the electromagnetic spectrum; see Tables I and II.

II. BOUNDARY INTEGRAL FORMULATION

We consider the scattering of an incident plane wave $\psi^{\text{inc}}(\mathbf{r}) = e^{ik\boldsymbol{\alpha}\cdot\mathbf{r}}$ on a convex impenetrable obstacle D ($\boldsymbol{\alpha}$ is

Work supported by AFOSR, DARPA and NSF. C. Geuzaine is a Postdoctoral Researcher with Caltech's Applied and Computational Mathematics Dept. and with the Belgian National Fund for Scientific Research, University of Liège, Montefiore Dept. B28, B-4000 Liège, Belgium.

the direction of propagation). This problem, which is governed by the Helmholtz equation, can be treated by using the following single layer potential and its normal derivative:

$$(S\varphi)(\mathbf{r}) = \int_{\partial D} \Phi(\mathbf{r}, \mathbf{r}')\varphi(\mathbf{r}') ds(\mathbf{r}'), \quad (1)$$

$$(K'\varphi)(\mathbf{r}) = \int_{\partial D} \frac{\partial\Phi(\mathbf{r}, \mathbf{r}')}{\partial\nu(\mathbf{r})}\varphi(\mathbf{r}') ds(\mathbf{r}'). \quad (2)$$

Here $\Phi(\mathbf{r}, \mathbf{r}') = e^{ik|\mathbf{r}-\mathbf{r}'|}/(4\pi|\mathbf{r}-\mathbf{r}'|)$ in three dimensions and $\Phi(\mathbf{r}, \mathbf{r}') = i/4 H_0^{(1)}(k|\mathbf{r}-\mathbf{r}'|)$ in two dimensions, and $\nu(\mathbf{r})$ is the external normal to the surface at point \mathbf{r} . Explicitly, given the values of the incoming wave $\psi^{\text{inc}}(\mathbf{r})$ on ∂D , the scattered field can be easily found once the integral equation

$$\frac{1}{2}\varphi(\mathbf{r}) - (K'\varphi)(\mathbf{r}) - i\gamma(S\varphi)(\mathbf{r}) = \frac{\partial\psi^{\text{inc}}(\mathbf{r})}{\partial\nu(\mathbf{r})} + i\gamma\psi^{\text{inc}}(\mathbf{r}) \quad (3)$$

has been solved for $\mathbf{r} \in \partial D$. In (3), γ is an arbitrary positive constant.

III. ANSATZ

In the present convex case the high frequency ansatz is given by

$$\varphi(\mathbf{r}) = \varphi_{\text{slow}}(\mathbf{r})e^{ik\boldsymbol{\alpha}\cdot\mathbf{r}}, \quad (4)$$

where the new unknown $\varphi_{\text{slow}}(\mathbf{r})$ is assumed to be a slowly varying function of $\mathbf{r} \in \partial D$. Note that in the case of an electromagnetic TE formulation, this ansatz is precisely the current of the physical optics approximation. Introducing (4) in (3), and dividing by $e^{ik\boldsymbol{\alpha}\cdot\mathbf{r}}$, we obtain a new boundary integral formulation involving the operators

$$(\tilde{S}\varphi)(\mathbf{r}) = \int_{\partial D} \Phi(\mathbf{r}, \mathbf{r}')e^{ik\boldsymbol{\alpha}\cdot(\mathbf{r}'-\mathbf{r})}\varphi(\mathbf{r}') ds(\mathbf{r}'), \quad (5)$$

$$(\tilde{K}'\varphi)(\mathbf{r}) = \int_{\partial D} \frac{\partial\Phi(\mathbf{r}, \mathbf{r}')}{\partial\nu(\mathbf{r})}e^{ik\boldsymbol{\alpha}\cdot(\mathbf{r}'-\mathbf{r})}\varphi(\mathbf{r}') ds(\mathbf{r}'). \quad (6)$$

The kernels in (5) and (6) are the only highly-oscillatory functions in this new formulation. Being a slowly varying function, the unknown density φ_{slow} can be represented, to within any prescribed tolerance, by a *fixed* set of discretization points, independent of frequency.

IV. LOCALIZED INTEGRATION

To apply the ideas of the method of stationary phase [5] we obtain the critical points of the integrals in (5) and (6). The details of such an evaluation depend on the particular kernels

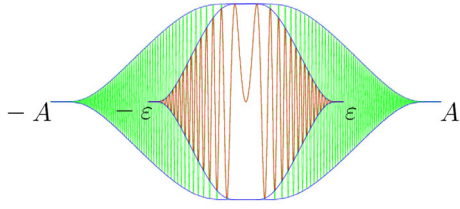


Fig. 1. Functions $f_A(x)e^{ikx^p}$ and $f_\varepsilon(x)e^{ikx^p}$ with envelopes f_A and f_ε , respectively.

under consideration, but in the present case, for $r \neq r'$, both kernels in (5) and (6) behave asymptotically as

$$e^{ik[|r-r'|+\alpha\cdot(r'-r)]} = e^{ik\phi}, \quad (7)$$

i.e. as the kernel of a generalized Fourier integral with phase ϕ . The critical points are

- the target (observation) point r itself;
- the stationary points, i.e. the points where the phase ϕ in the integrals has a vanishing gradient. Note that these stationary points vary as a function of the target point;
- the shadow boundaries, where the second derivative of the phase vanishes.

The method of stationary phase then tells us that, *asymptotically*, the only relevant contributions arise from the critical points. In order to build a *convergent* method for the whole frequency range, we introduce a localized integration procedure around these critical points.

As an example, let us consider the problem of integration of the one-dimensional smooth function $f_A(x)e^{ikx^p}$ (see Figure 1). For the smooth cutoff $f_\varepsilon(x)e^{ikx^p}$ in the interval $[-\varepsilon, \varepsilon]$, one can show that [6]:

$$\int_{-A}^A f_A(x)e^{ikx^p} = \int_{-\varepsilon}^{\varepsilon} f_\varepsilon(x)e^{ikx^p} + \mathcal{O}((k\varepsilon^p)^{-n}), \quad \forall n, p \geq 2.$$

A similar error estimate for the integrals (5) and (6) can be obtained by expanding ϕ in (7) around the critical points. This provides a criterion for the localized integration: the target point is to be covered by a region U_t of radius proportional to the wavelength λ ; for each target point, the ℓ -th stationary point is then covered by a region U_{st}^ℓ of radius proportional to $\sqrt{\lambda}$, while the shadow-boundary set is covered by U_{sb} : the set of points whose distance to the boundary is less than a radius proportional to $\sqrt[3]{\lambda}$. A partition of unity (POU) [7] is used to smoothly split the integral over ∂D into a number of integrals over the subsets $U_t \cup U_{st}^\ell \cup U_{sb}$ of ∂D . The integral outside these subsets is neglected.

In order to obtain a high-order algorithm, the (singular) integrals in the region U_t is evaluated in two dimensions as in [8] and in three dimensions as in [7]. Note that the number of integration points in U_t , U_{st}^ℓ and U_{sb} being proportional to λ , $\sqrt{\lambda}$ and $\sqrt[3]{\lambda}$ respectively, the total number of integration points is independent of the frequency.

V. NUMERICAL RESULTS

Tables I and II show results of a preliminary version of the two-dimensional high-frequency integral algorithm, as applied

TABLE I
SCATTERING BY A CIRCULAR CYLINDER OF RADIUS a , USING
100 UNKNOWNNS.

ka	GMRES Iter.	Mean Square Err.	CPU (s)
1	9	$8.8e-12$	< 1
10	17	$9.2e-12$	< 1
100	31	$2.5e-5$	8
1000	30	$2.1e-4$	84
10000	33	$6.6e-4$	83

TABLE II
SCATTERING BY A CIRCULAR CYLINDER OF RADIUS a , WITH
 $ka = 150$: ERROR CONVERGENCE.

Unknowns	GMRES Iter.	Max. Error
25	13	$4.4e-3$
50	23	$1.2e-3$
100	31	$1.2e-4$
200	34	$4.4e-6$
400	39	$1.0e-9$
800	44	$1.0e-12$

to a circular cylinder of radius a . Errors were computed by comparison with an exact solution for the integral equation. This example illustrates the asymptotic bounded complexity (the error for $k = 1000$ is roughly equal to the error for $k = 10000$, using the same number of unknowns and the same number of integration points, leading to identical computation times) as well as the high order convergence of the solver. As illustrated by Table I, the high-frequency solver is well conditioned and requires a small number of GMRES iterations for arbitrarily large wave numbers.

Generalizations of the ansatz (4) which are valid for non-convex scatterers have been given [9]. Extensions of our high-frequency methods to non-smooth geometries (containing singularities such as corners and edges) will be presented in the full paper.

REFERENCES

- [1] J. R. Mautz and R. F. Harrington, "A combined-source solution for radiation and scattering from a perfectly conducting body," *IEEE Transactions on Antennas and Propagation*, vol. AP-27, no. 4, pp. 445–454, 1979.
- [2] J. B. Keller and R. M. Lewis, *Asymptotic methods for partial differential equations: the reduced wave equation and Maxwell's equations*, vol. 1 of *Surveys in Applied Mathematics*, pp. 1–82, Plenum Press, New York, 1995.
- [3] R. T. Ling, "Numerical solution for the scattering of sound waves by a circular cylinder," *AIAA Journal*, vol. 25, no. 4, pp. 560–566, 1987.
- [4] R. M. James, "A contribution to scattering calculation for small wavelengths—the high frequency panel method," *IEEE Transactions on Antennas and Propagation*, vol. 38, no. 10, pp. 1625–1630, 1990.
- [5] C. M. Bender and S. A. Orszag, *Advanced Mathematical Methods for Scientists and Engineers*, McGraw-Hill, 1978.
- [6] O. P. Bruno, J. A. Monro, and C. A. Geuzaine, "Rigorous high-frequency solvers for electromagnetic and acoustic scattering: convex scatterers," In preparation.
- [7] O. P. Bruno and L. A. Kunyansky, "High-order algorithm for the solution of surface scattering problems: Basic implementation, tests, and applications," *Journal of Computational Physics*, vol. 169, pp. 80–110, 2001.
- [8] D. Colton and R. Kress, *Inverse Acoustic and Electromagnetic Scattering Theory*, Springer-Verlag, Berlin/Heidelberg, 1998.
- [9] O. P. Bruno and F. Reitich, "Rigorous high-frequency solvers for electromagnetic and acoustic scattering: non-convex scatterers and multiple scattering," In preparation.

Computation of HF Currents in Opened Shells

Badr Kebaili, Bernard Bandelier, Françoise Rioux-Damidau
U2R2M, Université Paris XI, ESA CNRS 8081
Bat 220, 91405 Orsay, FRANCE
E-mail: Bernard.Bandelier@u2r2m.u-psud.fr

Abstract—We consider a dielectric material partially covered by a conducting thin shell put into a high frequency source field. In order to compute the current density that appears in the shell we here present a variational formulation based on an integral representation which needs only a surface meshing.

INTRODUCTION

The problem of thin shells immersed into an electromagnetic field has been solved in the low frequency domain by introducing a scalar potential [1] or a vector potential [2]. But those methods do not permit to treat high frequencies; moreover, they cannot take into account opened shells. In this paper, we present a formulation suited to this problem.

PHYSICAL PROBLEM

We consider a dielectric material Ω of permittivity ($\varepsilon = \varepsilon_0 \varepsilon_r$) and permeability μ_0 . Its surface Γ is partially covered with a conducting shell of very small thickness d and conductivity σ . The outside domain is the air. The part of Γ covered by the shell is called Γ_c and the rest of Γ is called Γ_d ; then $\Gamma = \Gamma_c \cup \Gamma_d$. The line between Γ_c and Γ_d is γ_0 . n is the outside normal to Γ .

When the system is put into a high frequency electromagnetic source field (e^s, h^s) at frequency ω , there appears a current density in the shell. In order to compute it, we assume that current density j and electric field e are constant over the thickness d and we consider that the shell is geometrically confused with Γ_c . Then we define the surface current J_c as the total current in the shell and we have :

$$\tilde{J}_c = \begin{cases} J_c = \sigma d e & \text{on } \Gamma_c \\ 0 & \text{on } \Gamma_d \end{cases} \quad (1)$$

Using the definition above, the jumps across Γ of the tangential electric and magnetic fields, total solutions of Maxwell's equations, are :

$$[n \times e]_{\Gamma} = 0. \quad (2)$$

$$[n \times h]_{\Gamma} = \tilde{J}_c. \quad (3)$$

In order to compute J_c we will take as unknown quantities only the tangential components of e and h on Γ . We

here present a variational formulation implying surface Γ alone.

VARIATIONAL FORMULATION

In the case of a dielectric material completely covered with a conducting thin shell we have proposed a variational formulation to compute the current density in the shell [3] which uses the integral representation of the electromagnetic fields at high frequencies by Stratton-Chu's formulae. In the present case where the shell is not closed, the above variational formulation cannot be applied to compute the current density because the lineic charges appearing on γ_0 need to be taken into account. In order to establish a new variational formulation we will take the equations of the previous integral representation as the beginning point :

$$\begin{aligned} \frac{1}{2} n(x) \times e^a(x) &= n(x) \times e^s(x) \\ -\frac{1}{i\omega\varepsilon_0} n(x) \times \text{grad}_x \int_{\Gamma} \text{div}_{\Gamma}(n(y) \times h^a(y)) G_a(x, y) d\gamma_y \\ &+ i\omega\mu_0 n(x) \times \int_{\Gamma} (n(y) \times h^a(y)) G_a(x, y) d\gamma_y \\ n(x) \times \int_{\Gamma} \text{grad}_x G_a(x, y) \times (n(y) \times e^a(y)) d\gamma_y & \quad (4) \end{aligned}$$

and a similar one for h^a , where e^a, h^a are the tangential components of the electromagnetic fields by the side of the air. We have also two similar equations for the tangential components of the electromagnetic fields, e^d and h^d , by the side of Ω with a Green function in the dielectric.

For the following we define the unknown quantities e and h as :

$$n \times h = n \times h^a = n \times h^d + \tilde{J}_c \quad (5)$$

$$n \times e = n \times e^a = n \times e^d \quad (6)$$

By writting (2) and (3) under a variational form with e' and h' as test functions defined on Γ and using the integral representation of the electromagnetic fields in the air and the dielectric, we obtain the equations :

$$\int_{\Gamma} (n(x) \times e'(x)) \cdot (n(y) \times e(y)) (G_a + \varepsilon_r G_d)$$

$$\begin{aligned}
& -\frac{1}{i\omega\mu_0} \int_{\Gamma} \int_{\Gamma} \operatorname{div}_{\Gamma}(n(x) \times e'(x)) \operatorname{div}_{\Gamma}(n(y) \times e(y)) (G_a + G_d) \\
& + \int_{\Gamma} \int_{\Gamma} (n(x) \times e'(x)) \times (n(y) \times h(y)) \cdot \operatorname{grad}_y (G_a + G_d) \\
& \quad - \int_{\Gamma} \int_{\Gamma_c} (n(x) \times e'(x)) \times J_c(y) \cdot \operatorname{grad}_y G_d \\
& \quad + \frac{1}{2} \int_{\Gamma_c} J_c \cdot e' = \int_{\Gamma} n \times h^s \cdot e', \quad (7)
\end{aligned}$$

$$\begin{aligned}
& \text{and } i\omega\mu_0 \int_{\Gamma} \int_{\Gamma} (n(x) \times h'(x)) \cdot (n(y) \times h(y)) (G_a + G_d) \\
& + \frac{1}{i\omega\varepsilon_0} \int_{\Gamma} \int_{\Gamma} \operatorname{div}_{\Gamma}(n(x) \times h'(x)) \operatorname{div}_{\Gamma}(n(y) \times h(y)) (G_a + \frac{G_d}{\varepsilon_r}) \\
& + \int_{\Gamma} \int_{\Gamma} (n(x) \times h'(x)) \times (n(y) \times e(y)) \cdot \operatorname{grad}_y (G_a + G_d) \\
& \quad - i\omega\mu_0 \int_{\Gamma} \int_{\Gamma_c} (n(x) \times h'(x)) \cdot J_c(y) G_d \\
& \quad - \frac{1}{i\omega\varepsilon_0} \int_{\Gamma} \int_{\Gamma} \operatorname{div}_{\Gamma}(n(x) \times h'(x)) \operatorname{div}_{\Gamma} \tilde{J}_c(y) \frac{G_d}{\varepsilon_r} \\
& \quad = \int_{\Gamma} n \times e^s \cdot h', \quad (8)
\end{aligned}$$

We notice that we can not replace J_c by its value (1) and limit the problem to two unknown quantities because the problem will then be badly defined. When σ is constant on whole Γ_c we have :

$$\operatorname{div}_{\Gamma} \tilde{J}_c = [\tilde{J}_c \cdot N]_{\gamma_0} \delta_{\gamma_0} \quad (9)$$

where N is the normal to γ_0 , on Γ . The jump of the normal component of \tilde{J}_c is equal to :

$$[\tilde{J}_c \cdot N]_{\gamma_0} = 0 - J_c \cdot N = -J_c \cdot N$$

In order to have a well defined problem, we first replace integral

$$\begin{aligned}
& -\frac{1}{i\omega\varepsilon_0} \int_{\Gamma} \int_{\Gamma} \operatorname{div}_{\Gamma}(n(x) \times h'(x)) \operatorname{div}_{\Gamma} \tilde{J}_c(y) \frac{G_d}{\varepsilon_r} \text{ in (8) by} \\
& + \frac{1}{i\omega\varepsilon_0} \int_{\Gamma} \int_{\gamma_0} \operatorname{div}_{\Gamma}(n(x) \times h'(x)) J_{\Gamma} \cdot N \frac{G_d}{\varepsilon_r}
\end{aligned}$$

and we write (1) under a variational form with J' as a test function defined only on Γ_c :

$$\int_{\Gamma_c} J_{\Gamma} \cdot J' - \int_{\Gamma_c} \sigma d e \cdot J' = 0, \quad (10)$$

The final formulation is made of (7), (8) and (10). Equation (10) is very important because it permits to have the unicity of the solution of the formulation.

For the discretization, surface Γ is meshed into triangles. Fields e and h , which appear in (7), (8) and (10) by their tangential components, are discretized with Nédélec's edge elements; current J_c is discretized with edge elements rotated by $\pi/2$ so that the degrees of freedom are fluxes.

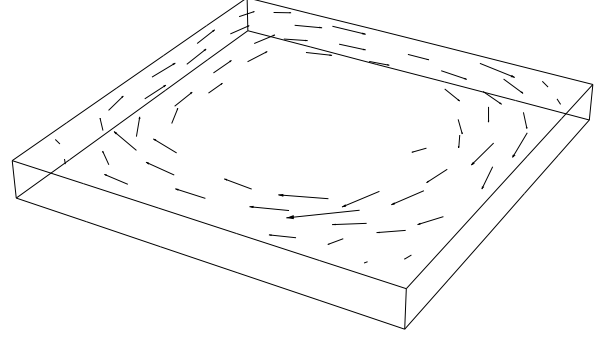


Fig. 1. Surface current in an annulus

NUMERICAL RESULTS

The present variational formulation has been applied to many examples. In this paper we present only one. Some other interesting examples will be given in the full paper.

As a first test, we put a dielectric plate ($L = 1 \text{ cm}$, $H = 1 \text{ mm}$, $\varepsilon_r = 2$), on which there is a conducting annulus ($\sigma = 2.10^8 \text{ Sm}$), in an homogeneous source field h^s at frequency ($\omega = 2.10^6 \text{ Hz}$).

Γ is meshed into 228 triangles, 342 edges and 116 vertices and Γ_c is meshed into 60 triangles and 106 edges. Figure 1 shows surface current J_c which appears in the annulus with the thickness $d = 1 \mu\text{m}$ and the penetration depth $\delta = 63 \mu\text{m}$. The obtained results show that surface current is well presented.

CONCLUSION

The presented variational formulation describes well the currents in closed or opened shells. It can be applied to printed circuits and, in particular, to antennas used in MRI.

REFERENCES

- [1] L. Krähenbühl, and D. Müller, "Thin layers in electrical engineering. Example of shell models in analysing eddy-currents by boundary and finite element methods," *IEEE Transactions on Magnetics*, vol 29, 1993, pp. 1450-1455.
- [2] I. D. Mayergoyz, and G. Bedrosian, "On calculation of 3-D eddy currents in conducting and magnetic shells," *IEEE Transactions on Magnetics*, vol 31, 1995, pp. 1319-1324.
- [3] B. Kebaili, B. Bandelier and F. Rioux-Damidou "Modelling a thin shell submitted to an electromagnetic wave" *IEEE Transactions on Magnetics*, vol 37, 2001, (Sep).

Using Star Loop Method of Moment to Model Arbitrary Shaped Microstrip Antennas

Kezhong Zhao, Jin-Fa Lee

ElectroScience Lab
1320 Kinnear Rd.

Columbus, Ohio 43212, USA

Zhao.74@osu.edu, Jinlee@ee.eng.ohio-state.edu

Abstract. A full solution to the radiation problem of the microstrip antenna of arbitrary shape using loop star basis function is presented. The solution begins by the formation of mix-potential integral equation. The integral equation is solved by method of moment using loop star basis functions and layered medium's Green's functions. A new "mesh-neighboring" preconditioner is implemented to solve the resulting matrix equations efficiently. Few numerical examples are presented to validate the present approach.

I. INTRODUCTION

INTERGRAL equation formulation in conjunction with the method of moment (MoM) has become a popular approach for the electromagnetic analysis of microstrip antenna and monolithic millimeter and microwave integrated circuits (MMIC) over the years. The electrical field integral equation (EFIE) is the preferred choice for microstrip problems. However because EFIE contains derivatives, it becomes important to employ proper basis functions for the MoM, otherwise fictitious charges will be induced. The Rao-Wilton-Glisson (RWG) basis functions [1] have been famous of their property of being free of fictitious charges, but they are ill posed at low frequency [2]. On the contrary, it has been shown that even at the DC limit, using loop star basis functions the MoM matrix is still well conditioned [2]. Loop star basis functions are the linear combination of the RWG basis functions. Therefore loop star basis functions "inherit" all the properties of the RWG, while the use of loop star basis function circumvents the RWG's low frequency instability.

II. THEORY

First the electric field integral equation is derived to be

$$\bar{e}_z \times \left[k_o^2 \int_D \bar{G}_A \cdot \bar{J}_s ds' - \nabla \int_D G_v \nabla' \cdot \bar{J}_s ds' \right] = -\frac{jk_o}{Z_o} \bar{e}_z \times \bar{E}^i \quad (1)$$

(1) is solved with Galerkin's MoM, where both basis function and testing function are expressed in term of loop star basis functions. The assembly process is in fashion used in FEM (finite element method) community. Namely,

$$[Z] = \sum_m \sum_n Z^{(mn)}, \text{ where} \quad (2)$$

$$\begin{aligned} [Z^{(mn)}]_{pq} = & k_o^2 \int_{\Delta_m} \bar{\alpha}_p(\bar{r}) \cdot \int_{\Delta_n} \bar{G}_A \cdot \bar{\alpha}_q(\bar{r}') ds' ds \\ & - \int_{\Delta_m} \nabla \cdot \bar{\alpha}_p(\bar{r}) \int_{\Delta_n} G_v \nabla' \cdot \bar{\alpha}_q(\bar{r}') ds' ds \end{aligned} \quad (3)$$

and $\bar{\alpha}_p, \bar{\alpha}_q$ are the p-th and q-th basis function, respectively.

Furthermore, it is important to recognize that without an effective preconditioner, the matrix equations result from (3) will be difficult to solve using iterative matrix solution such as Conjugate Gradient (CG) like methods. In the paper, we propose a "mesh-neighboring" preconditioner that is both effective and efficient when used together GMRES to solve the final matrix equations. The "mesh-neighboring" preconditioner starts by constructing a sparse version of the impedance matrix $[Z^s]$, which includes only "strong" coupling of triangle pairs, viz.

$$[Z^s] = \sum_m \sum_{n \in S(m)} [Z^{(mn)}]$$

$$S(m) = \left\{ n \mid D(\Delta_m, \Delta_n) \leq \frac{h_{avg}}{\min(h_m, h_n)} \times N^{0.05} \times \max(h_m, h_n) \right\} \quad (4)$$

$S(m)$ denotes the set of triangles that have "strong" couplings with respect to triangle, Δ_m . $D(\Delta_m, \Delta_n)$ is the distance between Δ_m and Δ_n , from center to center; h_m is the characteristic length for Δ_m ; h_{avg} is the average characteristic length of the mesh and N is the number of the unknowns. Once the sparse matrix is formed, then the preconditioner is generated by

$$[M] = D^{-1/2} [Z^s] D^{-1/2}, \text{ where } D = \text{diag}(Z). \quad (5)$$

II. NUMERICAL RESULTS

For the first example considered in this section, the structure is situated on the infinite dielectric slab of the dielectric constant $\epsilon_r = (2.62, 0.0)$, and of thickness 0.007λ . It deals with a circular patch antenna with two stubs, as in figure 1. The various components of far fields are compared with [3], as shown in figures 2 and 3. The results agree very well. Furthermore we note that the proposed preconditioner results in superior convergence of GMRES. For this example, with the tolerance of 10^{-4} , it only takes 13 iterations, as opposed to more than 500 iterations without preconditioner.

The second example deals with a series-fed microstrip antenna arrays, with the parameters specified in fig. 4. We compare our result with both theoretical solution [4] and experimental measurement [5], as shown in fig. 5. As seen from figure, they agree quite well.

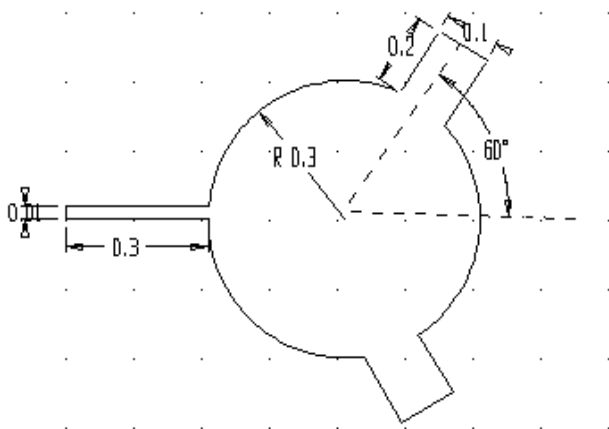


Fig. 1 A circular patch antenna with two stubs

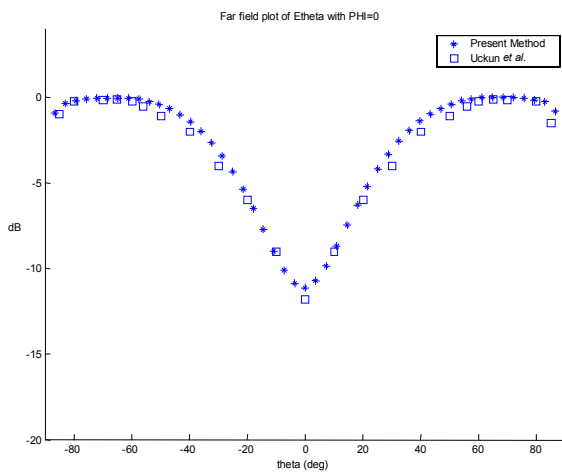


Fig. 2 $20 \log_{10} |E_{\theta}|$ at $\phi = 0$ for $-90 \leq \theta \leq 90$.

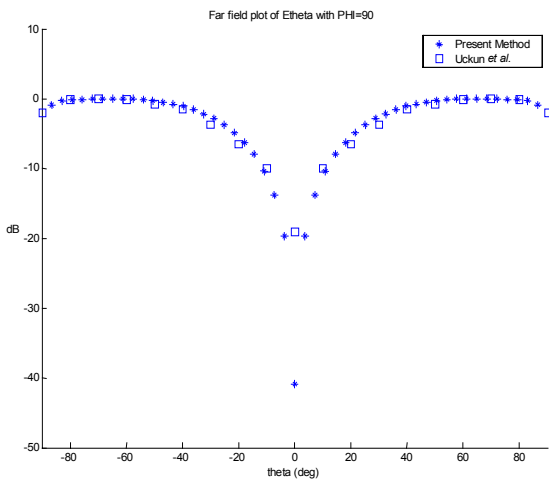


Fig. 3 $20 \log_{10} |E_{\theta}|$ at $\phi = 90$ for $-90 \leq \theta \leq 90$.

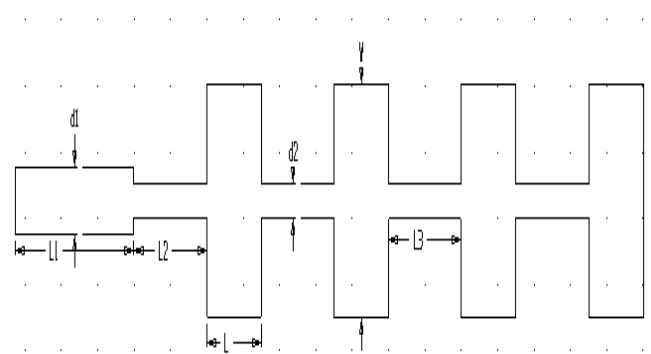


Fig. 4 A series-fed microstrip array $L = 10.06$ mm, $W = 11.79$ mm, $L_1 = 23.6$ mm, $L_2 = 13.4$ mm, $L_3 = 12.32$ mm, $d_1 = 3.93$ mm, $d_2 = 1.3$ mm, thickness of substrate $h = 1.5748$ mm, $\epsilon_r = 2.1$, $f = 9.42$ GHz.

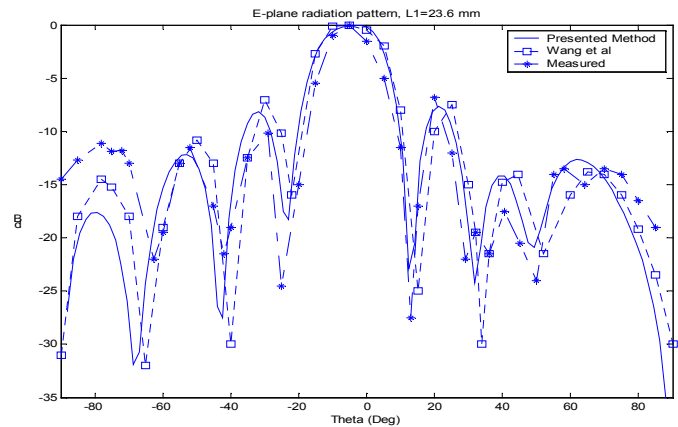


Fig. 5 The E-plane radiation pattern of the series-fed microstrip array

REFERENCES

- [1] S. M. Rao, D. R. Wilton, and A. W. Glisson, "Electromagnetic Scattering by Surfaces of Arbitrary Shape," *IEEE Trans. Antennas Propagat*, vol.AP-30, pp. 409-418, May 1982.
- [2] J. F. Lee, R. Lee, and R. Burkholder, "Loop Star Basis Functions and a Robust Preconditioner for EFIE Scattering Problems," *IEEE Trans. Antennas Propagat*, to be published.
- [3] S. Uckun, T. Sarkar, S. M. Rao, and M. Salazar-Palma, "A Novel Technique for Analysis of Electromagnetic Scattering from Microstrip Antennas of Arbitrary Shape," *IEEE trans. Microwave Theory tech*, vol.45, pp.485-491, April 1997.
- [4] C. F. Wang, F. Ling, and J. M. Jin, "A Fast Full-Wave Analysis of Scattering and Radiation from Large Finite Arrays of Microstrip Antennas," *IEEE Trans. Antennas Propagat.*, vol. 46, pp. 1467-1474, Oct. 1998.
- [5] K. L. Wu, M. Spenuk, J. Litva, and D. G. Fang, "Theoretical and Experimental Study of Feed Network Effects On the Radiation Pattern of Series-fed Microstrip Antenna Arrays," *Proc. Inst. Elect. Eng.*, vol. 138, pt. H, pp. 238-242, June 1991.

Optimal Design of Planar Microwave Filter Structure of Arbitrary Shape by the FEM-GA Approach

Wen Wang, Yilong Lu[†] and Jeffrey S Fu

School of Electrical and Electronic Engineering, Nanyang Technological University
Nanyang Avenue, Singapore 639798

[†] Corresponding author: eylu@ntu.edu.sg

Abstract--The traditional design methods restrict planar microwave filter structure to regular shapes so that the results may not be optimal. In this paper, we present a novel design approach that can take into account of arbitrary planar structures. This approach is based on the powerful and flexible finite element method (FEM) as the 3-dimensional field simulator and the genetic algorithm (GA) as the optimization engine. Using this design approach, new filter structures can be invented automatically with the enhanced performance.

INTRODUCTION

Planar microwave filters play a very important role in many microwave applications. Emerging applications such as wireless communications continue to challenge microwave filter design with ever more stringent requirements—higher performance, smaller size, lighter weight, and lower cost. The traditional design is based on the network synthesis techniques [1]-[3]. After frequency transformation and prototype selection, the normalized lumped elements of lowpass prototype can be determined according to the desired specifications. Then, the planar distributed elements of simple shapes are used to approximate the lumped elements. This method restricts the distributed elements to regular shapes, in most cases, rectangular strips. Since the equivalent circuit analysis of irregular shapes is very complicated, only some simple shapes can be used as building blocks to design filters. Often higher performance filters require higher orders structure but higher orders structures results in larger size, higher power loss and higher cost. It is always desirable to achieve higher selective performance within a smaller structure and with a smaller loss.

In this paper, a novel design approach is proposed for optimal planar filter design. In this approach, the three-dimensional finite element method (FEM) [4],[5] is used for accurate computation of electric fields and the genetic algorithm (GA) [6] is as the optimization engine. Both FEM and GA are powerful and flexible for their tasks. FEM is very popular and powerful for problems with arbitrary structures and material profiles. GA is a stochastic search and optimization technique modeled on the mechanics of biological genetics and natural evolution. GA can be used to optimize large and complicated problems.

In this work, GA is used to optimize the shape of filter. For each shape, FEM is utilized to computer propagation

response. The combination of FEM and GA would greatly increase the design capability. The new design approach will be much more flexible than traditional ones and novel filters can be designed with improved performance which cannot be achieved before.

FEM/GA DESIGN APPROACH

As illustrated in Fig. 1, the filter model is an planar structure with arbitrary metal patch shape enclosed in a metallic rectangular box except two ports. In the enclosed domain, the lower part is the substrate, and the upper part is air. The conducting structure includes two section 50 Ω strips connected with two ports and a filter section of arbitrary shape. Fig. 1(b) illustrates a possible shape of the filter section of the model. We divide the whole model into a number of rectangular finite elements. The filter section will be automatically created and optimized by genetic algorithm that only needs to optimize a vector with 1's and 0's, for examples, 1 means with metal deposition and 0 means no metal on the substrate surface of an particular element.

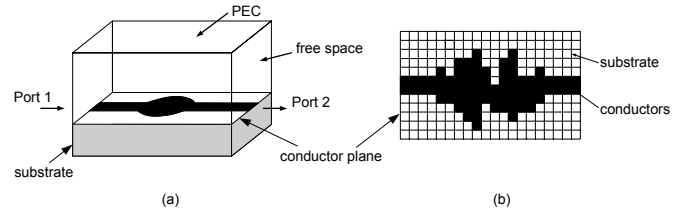


Fig. 1: Structure of Planar Filter (a) Planar Filter (b) Conductor Plane

For the fitness evaluation, it relies on the output to input response against frequencies from the FEM simulator. The FEM simulator calculates the electric fields for each particular shape and sends S-parameters back to the GA optimizer for fitness calculations. As the GA iteration goes on, the optimal filter structure may be automatically invented without human interference.

FEM FORMULATIONS

A. 2.5D Modal Pattern

In order to get the modal patterns at the input port, one may solve an eigenvalue problem based a 2.5D model. From Maxwell's equations, one can easily establish a variational formulation (1)

NUMERICAL RESULTS

$$\begin{cases} \delta F(\mathbf{E}) = 0 \\ \hat{n} \times \mathbf{E} = 0 \end{cases} \quad \text{on } \Gamma \quad (1)$$

where

$$F(\mathbf{E}) = \frac{1}{2} \int_{\Omega} [\mu_r^{-1} (\nabla \times \mathbf{E}) \cdot (\nabla \times \mathbf{E})^* - k_0^2 \epsilon_r \mathbf{E} \cdot \mathbf{E}^*] d\Omega \quad (2)$$

Ω denotes the cross section of the structure whose boundary is comprised by the electric wall Γ .

Using the transformations mentioned by Lee et al. [4],

$$\begin{aligned} \mathbf{e}_t &= k_z \mathbf{E}_t \\ \mathbf{e}_z &= -j \mathbf{E}_z \end{aligned} \quad (3)$$

one may obtain

$$\begin{aligned} F(\mathbf{e}) &= \frac{1}{2} \int_{\Omega} \{ \mu_r^{-1} (\nabla_t \times \mathbf{e}_t) \cdot (\nabla_t \times \mathbf{e}_t)^* - k_0^2 \epsilon_r \mathbf{e}_t \cdot \mathbf{e}_t^* \\ &+ k_z^2 [\mu_r^{-1} (\nabla_t \mathbf{e}_z + \mathbf{e}_t) \cdot (\nabla_t \mathbf{e}_z + \mathbf{e}_t)^* - k_0^2 \epsilon_r \mathbf{e}_z \mathbf{e}_z^*] \} d\Omega. \end{aligned} \quad (4)$$

After applying the edge and nodal finite element discretization, the eigenvalue problem can be obtained and solved.

$$\begin{bmatrix} A_{tt} & 0 \\ 0 & 0 \end{bmatrix} \begin{Bmatrix} e_t \\ e_z \end{Bmatrix} = -k_z^2 \begin{bmatrix} B_{tt} & B_{tz} \\ B_{zt} & B_{zz} \end{bmatrix} \begin{Bmatrix} e_t \\ e_z \end{Bmatrix} \quad (5)$$

B. 3D formulation

For the 3-D boundary-value problem, the equivalent variational problem is

$$F(\mathbf{E}^*) = F_1(\mathbf{E}^*) + F_2(\mathbf{E}^*) \quad (6)$$

where

$$F_1(\mathbf{E}^*) = \int_V [\mu_r^{-1} (\nabla \times \mathbf{E})^* \cdot (\nabla \times \mathbf{E}) - k_0^2 \epsilon_r \mathbf{E} \cdot \mathbf{E}^*] dv \quad (7)$$

$$F_2(\mathbf{E}^*) = - \int_{s_p} \mu_r^{-1} [\mathbf{E}^* \times (\nabla \times \mathbf{E})] \cdot \hat{n} ds \quad (8)$$

By using the transfinite element method mentioned by Lee [5], the electric field at each port surface can be described as

$$\begin{aligned} \mathbf{E}^{(1)} &= M_{11} e^{-\gamma_1 z} + \sum_{j=1}^{\infty} a_{1j} M_{1j} e^{\gamma_j z} \\ \mathbf{E}^{(2)} &= \sum_{j=1}^{\infty} a_{2j} M_{2j} e^{-\gamma_j z} \end{aligned} \quad (9)$$

The final system of 3D problem is expressed in matrix form as

$$\begin{bmatrix} [\mathbf{K}_i] & [\mathbf{K}_{s_1}] \{M_1\} & [\mathbf{K}_{s_2}] \{M_2\} \\ \{M_1\}^T [\mathbf{K}_{s_1}] & \{M_1\}^T [\mathbf{K}_{s_1}] \{M_1\} + j\alpha \mathbf{M} [s_1] & \{M_1\}^T [\mathbf{K}_{s_2}] \{M_2\} \\ \{M_2\}^T [\mathbf{K}_{s_2}] & \{M_2\}^T [\mathbf{K}_{s_1}] \{M_1\} & \{M_2\}^T [\mathbf{K}_{s_2}] \{M_2\} + j\alpha \mathbf{M} [s_2] \end{bmatrix} \begin{Bmatrix} \{E\} \\ \{a_1\} \\ \{a_2\} \end{Bmatrix} = \begin{Bmatrix} -[\mathbf{K}_{s_1}] \{M_1\} \\ -\{M_1\}^T [\mathbf{K}_{s_1}] \{M_1\} + j\alpha \mathbf{M} \\ -\{M_2\}^T [\mathbf{K}_{s_1}] \{M_1\} \end{Bmatrix} \quad (10)$$

where

$$[\mathbf{K}] = \int_V \left[\frac{1}{\mu_r} (\nabla \times \{\mathbf{N}\}) \cdot (\nabla \times \{\mathbf{N}\})^* - k_0^2 \epsilon_r \{\mathbf{N}\} \cdot \{\mathbf{N}\}^* \right] dv \quad (11)$$

Substituting the modal pattern obtained in the 2.5D problem into the system above, one can solve for the electric field distribution and S-parameters simultaneously.

Fig.2 shows the numerical result of the field distribution of the dominant quasi-TEM mode of the shielded microstrip line on the cross section at the input port. The electric field distribution is calculated by using the formulation of 2.5D problem.

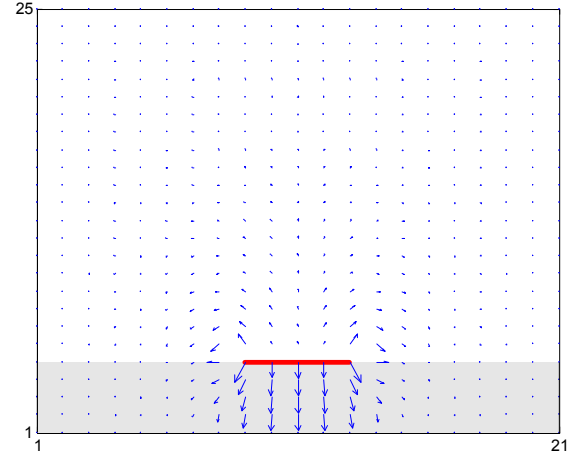


Fig. 2: Vector plot for the dominant mode on ports

We will present the 3D FEM solution and optimal design results for the filter structures.

CONCLUSIONS

This paper present a novel approach for innovative microwave planar filter design. The powerful FEM and GA tools are combined together to search for the optimal filter structures. Complete solution and design results will be presented at the conference and shown in the full paper.

REFERENCE

- [1] G. L. Matthaei, L. Young, and E. M. T. Jones, *Microwave Filters, Impedance-Matching Networks, and Coupling Structures*, Artech House, Dedham, Mass., 1980.
- [2] D. M. Pozar, *Microwave Engineering*, Wiley, 1998.
- [3] Jia-Sheng Hong and M. J. Lancaster, *Microstrip Filters for RF/Microwave Applications*, Wiley, 2001.
- [4] J. F. Lee, D. K. sun, and Z. J. Cendes, "Full-wave analysis of dielectric waveguides using tangential vector finite elements," *IEEE Trans. MTT*, Vol. 39, Aug., 1991, pp. 1262-1271.
- [5] J. F. Lee, "Analysis of passive microwave devices by using three-dimensional tangential vector finite elements," *Int. J. Num. Modeling*, 3, pp.235-246, 1990.
- [6] B K Yeo and Y Lu, "Array failure correction by using the genetic algorithm," *IEEE Trans. on Antennas and Propag.*, Vol. 47, May 1999, pp.823-828.

Rapid Simulation of Laser Scattering from Dielectric Cylinders of Arbitrary Cross-Section

Meng H. Lean

Palo Alto Research Center Inc
Device Hardware Laboratory
Palo Alto, CA 94304 USA
e-mail: mlean@parc.com

Abstract - Boundary integral formulations are implemented for the electromagnetic scattering of laser radiation from dielectric cylinders of arbitrary cross-section. Because of the optical frequencies involved, problem size is controlled by a judicious choice of element size. Results for the more compute intensive Galerkin method are generated for comparison against the less time consuming Moment method using linear isoparametric boundary elements. Singular kernels are integrated numerically using a technique that converges rapidly. Scattered intensities generated for both TE and TM polarizations on circular cylinders compare extremely well with analytic far field predictions.

INTRODUCTION

The boundary integral equation method has been shown to be a powerful simulation tool to compute radiation phenomena from conducting scatterers of arbitrary shape [1]. Problem dimension is significantly reduced by defining the problem in terms of the dependent variable distribution on the boundary rather than within the domain as in the volume integral method. The use of the Galerkin method for matrix discretization ensures a more accurate averaged solution rather than the discrete point-collocation philosophy of the Moment method [2]. The major difference is that the fields computed in the inter-nodal regions may show oscillations using the latter method if the maximum element size is exceeded. This criterion is typically $\lambda/10$, although it may be relaxed at lower frequencies. With the Galerkin method and proper treatment of the kernel singularity, this criterion can be further relaxed to $\lambda/4$. At optical frequencies, this improvement leads to significant reduction in overall problem size.

In this paper, we consider a laser scattering application where the backward scattered intensities within a 25-degree range are used to infer important *in-situ* diagnostic information on scatterer cross-sections. Due to the geometric aspect ratio, the problem is simplified to consideration of 2D integral formulations for dielectric cylinders with orthotropic material properties. The TE (transverse electric) polarization case is formulated in terms of a coupled set of two MFIE (magnetic field integral equation) using Green's theorem. The corresponding TM (transverse magnetic) polarization case is posed in the EFIE (electric field integral equation). Kernel singularities involve Hankel functions of the first and second kind, and are treated using a tailored numerical quadrature scheme that converges to the analytic result in the limit of increasing radius of curvature [3]. Large argument

expansions of the Hankel functions for far-field calculations are evaluated using a highly convergent series representation [4]. Scattered intensities or RCS (radar cross section) generated for circular dielectric cylinders with both TE and TM polarizations are compared against analytic predictions. Poynting vector calculations within the cylinder are used to indicate regions of localized power dissipation. This model is used as a tool for parametric studies of the sensitivity of scattered intensities to geometric perturbations about the circular cross-sectional shape.

PROBLEM FORMULATION

The time-harmonic wave equation, with suppressed $e^{j\omega t}$ time dependence, for homogeneous source-free media is the complex Helmholtz equation given by:

$$(\nabla^2 + k^2) \psi(\mathbf{r}) = 0 \quad (1)$$

where k is the wave number. The integral solution is synthesized from Green's function satisfying:

$$(\nabla^2 + k^2) G(\mathbf{r}, \mathbf{r}') = -\delta(\mathbf{r} - \mathbf{r}') \quad (2)$$

so that

$$\psi(\mathbf{r}) = \gamma \int_{S'} [G(\mathbf{r}, \mathbf{s}') \partial \psi(\mathbf{s}') / \partial n' - \psi(\mathbf{s}') \partial G(\mathbf{r}, \mathbf{s}') / \partial n'] ds' \quad (3)$$

where γ is the Cauchy Principal Value (CPV) integral; and equals 0, 1, or 2, depending on whether \mathbf{r} is respectively, outside, inside, or on contour S' . Kernel $G(\mathbf{r}, \mathbf{s}')$ is the zero-order Hankel function of the second kind:

$$G(\mathbf{r}, \mathbf{r}') = -j/4 H_0^{(2)}(k|\mathbf{r} - \mathbf{r}'|) \quad (4a)$$

with normal derivative given by:

$$\partial G(\mathbf{r}, \mathbf{r}') / \partial n' = -jk/4 H_1^{(2)}(k|\mathbf{r} - \mathbf{r}'|) \cos(\mathbf{n}', \mathbf{r} - \mathbf{r}') \quad (4b)$$

Together with $\psi(\mathbf{r})$, the wave function, boundary conditions are satisfied on S' and in the far-field where the Sommerfeld radiation condition:

$$\lim_{r \rightarrow \infty} r[\partial \psi / \partial r + jk\psi] = 0 \quad (5)$$

ensures the finiteness of the solutions at infinity.

TM Polarization

Equations for TM polarization are obtained by setting $\psi=E_z$, where the incident wave is TEM to x, the direction of propagation. The H and E field vector components are respectively, perpendicular to and aligned with the z-axis. Equation (3) is written separately for both exterior and interior regions, denoted by subscripts '1' and '2'. Enforcing continuity of tangential **E** and normal **D**(= $\underline{\epsilon}\mathbf{E}$), where ($\underline{\epsilon}=\epsilon_r\epsilon_0-j\sigma/\omega$), and noting that the surface normals have opposite polarity, the resulting two equations for the common set of dependent variables on the surface S' are:

$$\int_{S'} [G_1(\mathbf{r},s') \partial E_z(s')/\partial n' - E_z(s')\partial G_1(\mathbf{r},s')/\partial n'] ds' + E_z(s)/2 = E_z^1(s) \quad (6)$$

$$\int_{S'} [G_2(\mathbf{r},s') \partial E_z(s')/\partial n' - E_z(s')\partial G_2(\mathbf{r},s')/\partial n'] ds' - E_z(s)/2 = 0$$

These equations have to be solved simultaneously.

TE Polarization

The corresponding equations for TE polarization are derived by setting $\psi=H_z$, with all else following a similar procedure as before. The E and H field vector components are respectively, perpendicular to and aligned with the z-axis. Enforcing continuity of tangential **H** and normal **D**(= $\underline{\epsilon}\mathbf{E}$), and noting that the surface normals have opposite polarity, the resulting two equations for the common set of dependent variables on the surface S' are:

$$\int_{S'} [G_1(\mathbf{r},s') \partial H_z(s')/\partial n' - H_z(s')\partial G_1(\mathbf{r},s')/\partial n'] ds' + H_z(s)/2 = H_z^1(s) \quad (7)$$

$$\int_{S'} [G_2(\mathbf{r},s') \partial H_z(s')/\partial n' - (\underline{\epsilon}/\epsilon_0)H_z(s')\partial G_2(\mathbf{r},s')/\partial n'] ds' - H_z(s)/2 = 0$$

Far Field Scattered Intensities (RCS)

The corresponding far field normalized scattered intensities or radar cross section (RCS) are given by:

$$\sigma_{TM}(\phi) = \lim_{r \rightarrow \infty} 2\pi r |E_z^s|^2 / |E_z^i|^2 \quad (8)$$

$$\sigma_{TE}(\phi) = \lim_{r \rightarrow \infty} 2\pi r |H_z^s|^2 / |H_z^i|^2$$

SAMPLE RESULTS

To verify the algorithm, sample RCS calculations are performed for the circular dielectric cylinder subject to TM and TE polarized waves incidences. These results are for 400 boundary elements ($\lambda/4$) using the Galerkin method. They are compared to the analytic solution to determine the accuracy of the numerical technique. For He-Ne lasers, a wavelength of 0.6328 μm is used. The cylinders are 9.75 μm in radius, implying a very large ka value of 97. The back scattered RCS in the 155-180 degree range is used to compare the accuracy of the two solutions. Results for the TM and TE polarized

waves are shown in Figs. 1 and 2, respectively. Agreement is clearly seen to be excellent. More detailed results will be shared in the full paper.

REFERENCES

- [1] Lean, M.H., "Boundary integral solution of wave effects in laser-annealed silicon", *Computational Electromagnetics*, Z.J. Cendes (Ed.) Elsevier Science Publishers, B.V., EMACS, 1986.
- [2] Harrington, R.F., *Field Computation by Moment Methods*, Kriedger Publishing Co. Inc., Florida, 1982.
- [3] Lean, M.H., and Wexler, A., "Accurate numerical integration of singular boundary element kernels over boundaries with curvature", *Int.J.Num.Meth.Engng.*, vol.21, no.2, 211-228, 1985.
- [4] Abramovitz, A., and Stegun, I.A. (Eds.), *Handbook of Mathematical Functions*, Dover Publications, New York, 1968

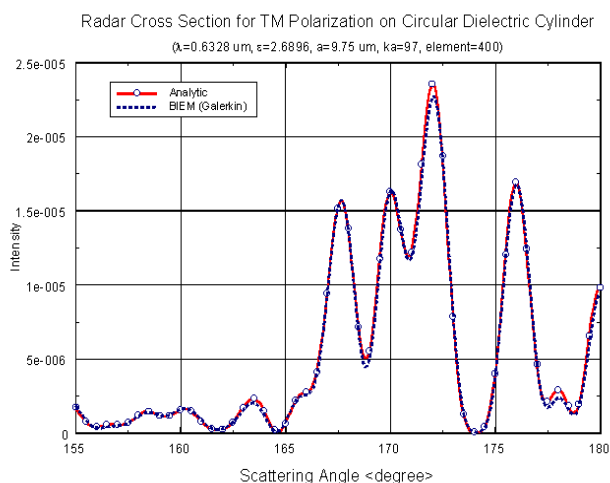


Fig. 1. Analytic and numerical RCS for TM polarized wave incident on circular dielectric cylinder.

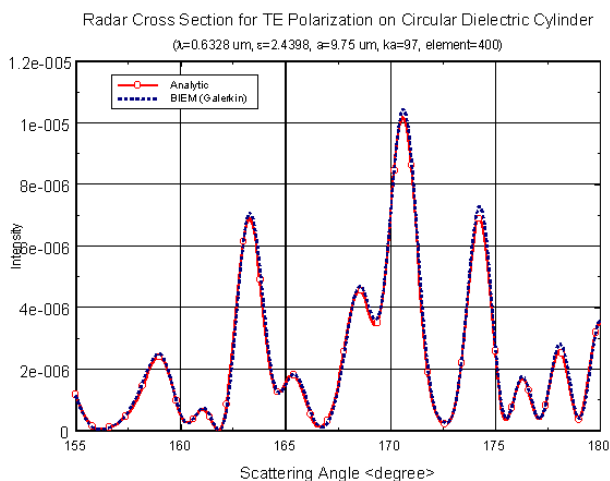


Fig. 2. Analytic and numerical RCS for TE polarized wave incident on circular dielectric cylinder.

Finite Element Modelling for the Design of Microwave Filters

S. Bila⁽¹⁾, D. Bariant⁽¹⁾, D. Baillargeat⁽¹⁾, M. Aubourg⁽¹⁾, S. Verdeyme⁽¹⁾,
F. Seyfert⁽²⁾, L. Baratchart⁽²⁾, C. Boichon⁽³⁾, F. Thevenon⁽³⁾, J. Puech⁽⁴⁾, C. Zanchi⁽⁴⁾

(1). IRCOM, 123 avenue Albert Thomas, 87060 Limoges, France

(2). INRIA, 2004 route des Lucioles, 06902 Sophia Antipolis, France

(3). CADOE, 11 avenue Albert Einstein, 69100 Villeurbanne, France

(4). CNES, 18 avenue Edouard Belin, 31401 Toulouse, France.

Email : bila@ircom.unilim.fr

Abstract: This paper outlines a frequency parameterised finite element technique. The analysis method is used in an optimisation procedure dedicated to the design of microwave filters. The frequency parameterisation enables to compute an approximation of the field in a given frequency range. The scattering parameters of the filter are deduced from the field approximation. The analysis method is described in the first part and a numerical investigation compares the frequency parameterised technique with the standard approach. The second section presents the electromagnetic optimisation procedure and the design of a microwave filter.

1. INTRODUCTION

Electromagnetic methods have for many years been applied to the rigorous analysis of microwave circuits. Generally, these methods show a good accuracy, but present a great disadvantage in term of computation time; particularly when the considered circuit includes a lot of discontinuities. Consequently, the design of complex microwave circuits applying both a global electromagnetic analysis method and a classical optimisation method is unrealisable. The trends in microwave computer aided design are now to develop specific optimisation procedures, in order to reduce the number of analyses, and powerful analysis techniques [1]-[2], to reduce the overall computation time.

In this paper, a frequency parameterised finite element method is presented. Applying this technique, an approximation of the electromagnetic field is computed in the frequency range of interest. The scattering parameters are finally determined from the approximated field. The analysis technique is described in the first section. The frequency parameterised technique and the standard approach are compared in term of computation time. In the second section, an electromagnetic optimisation procedure that uses the frequency parameterised technique is presented. The optimisation procedure is applied to the design of a microwave filter.

2. FINITE ELEMENT MODELLING

The finite element method is based on the fact that the structure geometry may be divided into sub-elements. In the case of electromagnetism, Maxwell's equations are solved element by element in order to determine the electric field or the magnetic field, taking into account the boundary conditions. The linear system to solve is the following one:

$$A(f).X(f) = B(f) \quad (1)$$

where f is the frequency,
 A is the structure discretisation,
 B is the set of sources,
 X is the electric or magnetic field.

The system is solved either in free oscillations or in forced ones. In the case of free oscillations, the second member of (1) equals zero by imposing a short-circuit at the input and output ports (no signal source). Solving the system eigenvalues enables to know the distributions of the electromagnetic field and the resonant frequencies. In the second case, the second member is different from zero and propagating and evanescent modes are computed thanks to a modal decomposition. The elementary solutions $X_i(f)$ of this linear system enables to compute the electromagnetic field inside the structure and the scattering parameters.

Frequency parameterisation – In the standard approach, since matrices A and B depend on the frequency, they are computed at each desired frequency. Applying a frequency parameterisation, an explicit formulation of $X(f)$ is built in the range $[f_{\min}, f_{\max}]$. The frequency formulation is based on the computation of a polynomial function from the high order derivatives of the linear system (1) : matrices A , B and X are computed at the centre frequency f_0 , then, the n-order derivatives of $X(f)$ are deduced from the n-order derivatives of (1). These derivatives enable to compute the Padé approximation of $X(f)$ around the centre frequency f_0 :

$$X(f_0 + \Delta f) \approx \frac{\sum_{i=0}^{n_p} P_i \Delta f^i}{\sum_{i=0}^{n_q} Q_i \Delta f^i} \quad (2)$$

Then, the poles of (2) provides the resonant frequencies f_i . The polynomial is evaluated at these frequencies to determine the modes ϕ_j . Then, for any frequency in the range $[f_{\min}, f_{\max}]$, the sources are computed, and the electromagnetic field is calculated from the modal basis (f_j, ϕ_j) . The approximated field is finally used to compute the scattering parameters.

Numerical results – The frequency parameterised method and the standard one are compared by analysing the 5-pole dual

mode filter presented in figure 1. The scattering parameters computed applying the parameterised method are compared, in figure 2, with the parameters computed applying the standard approach. The spectral analyses are in good agreement. The total CPU time, applying the frequency parameterisation, is 8 min in order to obtain the spectral response with 251 frequency samples on a HP9000/785 workstation. Applying the standard approach, the total CPU time is 2.5 min at each frequency, that is equivalent to 10.5 hours for 251 frequency samples.

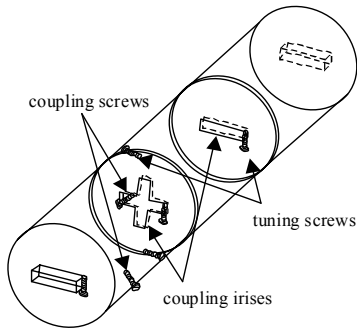


Fig.1. Dual mode microwave filter

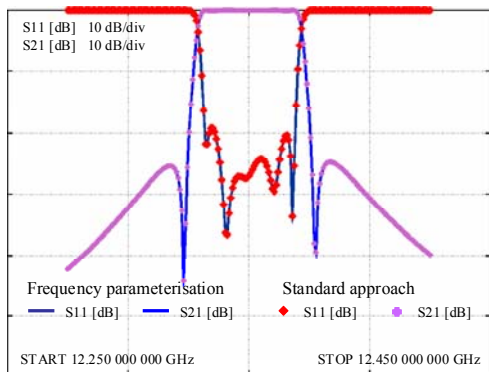


Fig.2. Scattering parameters applying the frequency parameterised method (lines) and the standard method (dots)

3. ELECTROMAGNETIC OPTIMISATION

The frequency parameterised finite element method is used in an optimisation procedure [3] dedicated to the design of microwave filters. The purpose is to determine precisely the optimal dimensions of the electromagnetic model. The proposed procedure consists in extracting the lumped elements of the equivalent circuit from the electromagnetic model, then to converge the ideal values by adjusting the geometrical dimensions. The synthesis of the equivalent circuit provides ideal values for the lumped elements.

Optimisation loop – The global electromagnetic model of the filter is analysed applying the frequency parameterised method. The scattering parameters are then approximated as rational polynomials. The lumped elements of the equivalent circuit are extracted from these polynomials, and comparing the ideal and extracted values, the geometrical dimensions of

the filter are corrected. The optimisation loop is repeated as long as the extracted elements do not match the ideal ones.

Application – A 5-pole dual mode filter is designed applying the optimisation procedure. The centre frequency is at 12.35 GHz and the pass band is 37.5 MHz-wide. The electromagnetic model is tuned applying the optimisation procedure. The scattering parameters of the optimised model are presented in figure 3. An experimental model has been built. The spectral response is presented in figure 4.

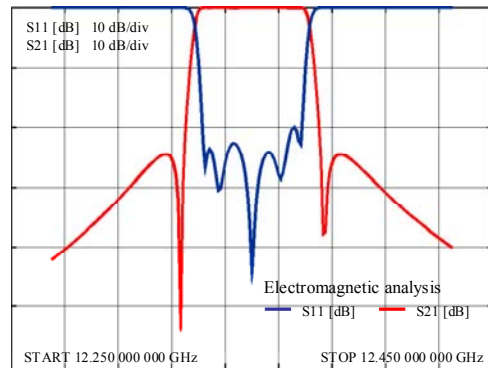


Fig.3. Scattering parameters of the optimised finite element model

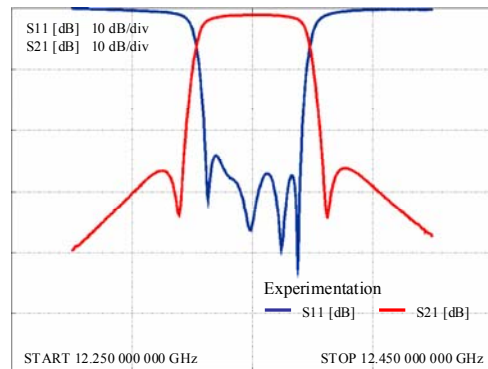


Fig.4. Scattering parameters of the experimental model

4. CONCLUSION

This paper presents a frequency parameterised finite element modelling. The analysis technique provides improved results in term of computation time. The technique is applied in this paper to the design of dual mode band pass filters.

REFERENCES

[1] D.K. Sun, J.F. Lee, Z. Cendes, "ALPS- A new fast frequency-sweep procedure for microwave devices", *IEEE Trans. Microwave Theory and Tech.*, vol. MTT-49, no. 2, pp. 398-402, Feb 2001.
 [2] A.Gati, M.F.Wong, V.Fouad Hanna, "New technique using poles and modes derivatives for frequency and geometry parameterization of microwave structures", *Int. Microwave Symposium Digest*, Phoenix, AZ, USA, May 2001.
 [3] S.Bila, D.Baillargeat, M.Aubourg, S.Verdeyme, P.Guillon, F.Seyfert, J.Grimm, L.Baratchart, C.Zanchi, J.Sombrin, "Direct electromagnetic optimization of microwave filters", *IEEE Microwave Magazine*, vol. 2, n°1, pp 46-51, Mar 2001.

3D Ray Tracing Propagation Model in Urban Environments

A.Barabino, P.Girdinio, M.Nervi

Dept. Of Electrical Engineering, University of Genova

Via Opera Pia 11a - 16145 Genova - Italy

e-mail: barabino@die.unige.it, girdinio@die.unige.it, nervi@die.unige.it

Abstract—This paper proposes an efficient 3-dimensional model to predict wave propagation within urban environments for frequencies between 900MHz and 2GHz, using ray-tracing techniques together with the Uniform Theory of Diffraction (UTD). This model takes into account multiple reflected rays by walls and ground and diffracted by corners and edges of buildings and their combinations.

INTRODUCTION

The continuing evolution of land mobile radio communication systems lead to high capacity networks with small cell sizes (micro- and pico-cells) especially in densely built up areas. The planning of these modern mobile systems requires highly sophisticated planning tools.

The models used for network planning can be distinguished in two categories: the empirical ones (Fig.1) and the deterministic ones (Fig.2).

The first ones assume straight propagation between transmitter and receiver neglecting any obstacle (walls or buildings). They offer short computation time but suffer from limited accuracy.

Deterministic propagation models are generally based on ray optical techniques.

They could be used when the wavelengths are smaller than the surrounding obstacles. In these cases electromagnetic waves can be approximated by rays, applying the laws of optics. Their idea is to describe the wave propagation with rays launched from the transmitting antenna. These rays are reflected and diffracted at walls and similar obstacles. Unlike the empirical models, deterministic models consider the actual physical rays and their interaction with obstacles (reflection and diffraction). If the number of interactions is high, the accuracy of ray optical propagation models is very good.

The main disadvantage of ray optical models is the high computational effort and therefore the very long computation times for the predictions.

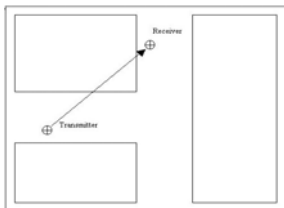


Fig. 1. Empirical Models.

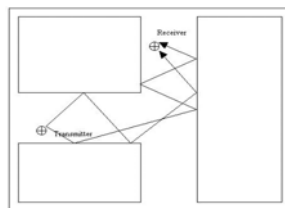


Fig. 2. Deterministic Models.

This problem is essentially due to the diffraction effects produced by edges, wedges and rooftops of buildings. In case of reflection, in fact, one ray generates one ray, following Snell's law; when a ray hits a corner, it generates a bundle of rays (Keller's cone), as visible in Fig.3.

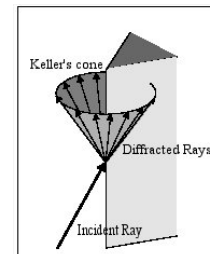


Fig. 3. Diffracted Rays.

To avoid this problem it's possible to consider only the significant rays, sampling in a proper way the cone. In this way, the number of diffracted rays decreases and the error on electromagnetic field value is acceptable [3].

To evaluate the contribution of each ray Fresnel's equations are used for the reflected ones while UTD's equations are used for the diffracted ones [1].

RAY TRACING TECHNIQUES

There are two basic approaches to searching propagation paths. The 'ray tracing' algorithm looks for valid ray paths between transmitter and a fixed receiving station. Therefore, ray tracing is a point-to-point algorithm. For coverage calculation, the receiver has to be moved all around the prediction area. Computation time goes directly with the number of receiving points. Besides, there is an exponential dependency on the number of buildings and the number of subsequent interaction points considered in the calculation.

An alternative technique is the 'ray launching' algorithm. Rays are launched from a fixed transmitting station in various directions, discretized into small angular increments. Field strength is summed up at all potential receiver points and the ray search is stopped, when energy falls below a minimum or a given maximum number of interactions is reached. Ray launching is basically an area oriented algorithm and therefore very well suited for coverage prediction. Computation time is almost independent on the number of receivers. It has a linear dependency on the number of subsequent interaction points and an inversely proportional behaviour with the dimensions of the angular increments.

The ray tracing technique used in this model is the ray launching one. The target of the model is the EMF coverage in an urban area. For this purpose, various types of rays are taken into account: direct, reflected by ground, reflected by walls, diffracted by corners, diffracted by wedges, reflected-diffracted, diffracted-reflected, multiple reflected and multiple diffracted.

Unlike other models, this is a full 3D model where buildings have a finite height; in this case, it's impossible to ignore the contributions of rays diffracted by rooftops.

A simple example of urban scenario is taken into account to predict the coverage when a GSM antenna is placed on a building rooftop. An upper view of this scenario is shown in Fig.4.



Fig. 4. Urban Scenario.

One of the critical aspects using ray-tracing techniques is the database accuracy. If the urban environment isn't well described, some intersections could be missed with the consequent loose of accuracy on the prediction.

In the model presented in this paper, in order to find accurately all the possible intersection between rays and buildings, the urban scenario is meshed and divided in triangles as big as desired. Fig.5 shows the 3D scenario in which each edge is divided into 5 parts. In this case we don't need to make a dense meshing because the buildings are described as big blocks.

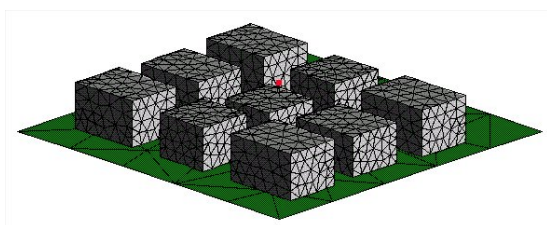


Fig. 5. Meshed scenario.

The meshing process allows us to take into account more complex urban environments, i.e. with domes or curvilinear surfaces.

The complexity of the algorithm is almost linear, due to the very limited impact of the advancing front section of the algorithm (Fig.6).

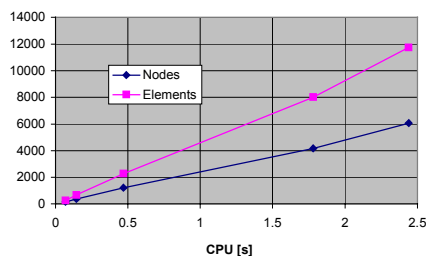


Fig.6. Algorithm complexity.

Then the radiation diagrams of the antenna are considered (an example in Fig.7). They are discretized along the vertical and the horizontal plane into small angular increments.

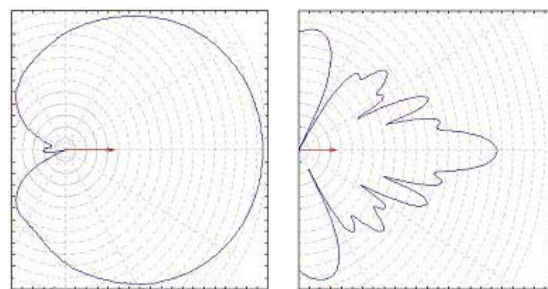


Fig 7. Horizontal (Left) and vertical (Right) radiation planes.

Each ray path is followed until it reaches the fixed maximum number of interactions. Then, using UTD equations, the electric field is calculated along each path.

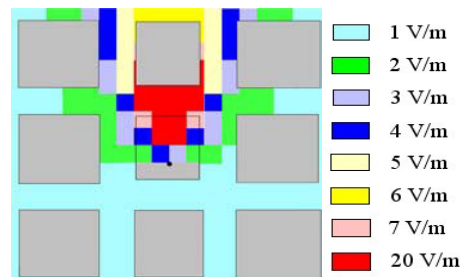


Fig 8. Electric field values

CONCLUSION

A new model for field strength prevision in urban environments is here presented. The proposed method has a CPU time and accuracy appropriate for this purpose. It also allows considering real and complex environments, without any approximation on shapes of buildings.

REFERENCES

[1] D.A.McNamara, C.W.I.Pistorius, J.A.G.Malherbe "Introduction to the Uniform Theory of Diffraction", *Artech House, 1990*.
 [2] A.S.Glassner, "An Introduction to Ray Tracing", *Morgan Kaufmann Publishers In., 1989*

EMIR – A Numeric Processor for the Analysis and Simulation of Radiated Electromagnetic Fields due to Electric Cabling Systems

Carlos F. R. Lemos Antunes and António Paulo Coimbra

ISR / DEEUC, Univ. of Coimbra
Pólo II, 3030-290 Coimbra, Portugal
lemos.antunes@deec.uc.pt and acoimbra@deec.uc.pt

Abstract— The paper presents a numeric processor for the analysis and simulation of radiated electromagnetic fields due to conductors of electric cabling systems of arbitrary shape and length carrying sinusoidal currents. It allows the computation of the steady state electromagnetic field components for any point in free space irrespective of the distance to the source, by emulating the classical standing wave pattern, with the propagation delay taken into account. The program also allows the calculation of the wave impedance and the visualization of the amplitudes of each component in the form of contour plots in the plane of analysis, as well as the variation of these amplitudes along lines.

INTRODUCTION

The electric cabling systems can be considered as unintentional antennas and are important sources of radiated interference as these can cause degradation in the performance of nearby electromagnetic devices. These interferences are commonly known as EMI radiated emissions. It is then important to predict the electric and magnetic fields radiated from these sources. The objective of the paper is the presentation of EMIR- A numeric processor for the analysis and simulation of radiated electromagnetic fields due to conductors of electric cabling systems. It allows the computation of the steady state field components of \vec{E} and \vec{H} for any point $P(r, \theta, \phi)$ due to a cabling system of arbitrary shape and length carrying sinusoidal currents, by emulating the classical standing wave pattern. The total field components are obtained irrespective of the distance of $P(r, \theta, \phi)$ to the source, so there are no simplifications for far field or near field zones and the propagation delay is taken into account. The program is very easy to use. As computer aided education is becoming increasingly popular, this program EMIR can also be used as a computer aided teaching tool that allows a quick and easy insight into the mechanism of radiation either for practical engineers or engineering students.

FORMULATION

The electromagnetic field structure radiating from an infinitesimal electrical short length conductor dl carrying a phasor current \hat{I} , can be represented by the following components \hat{E}_θ , \hat{E}_r , \hat{H}_ϕ at an observation point $P(r, \theta, \phi)$ in a spherical coordinate system (see Fig.1):

$$\hat{E}_\theta = \frac{\hat{I}dl}{4\pi} \eta_0 \beta_0^2 \sin \theta \left(j \frac{1}{\beta_0 r} + \frac{1}{\beta_0^2 r^2} - j \frac{1}{\beta_0^3 r^3} \right) e^{-j\beta_0 r} \quad (1)$$

$$\hat{E}_r = \frac{2\hat{I}dl}{4\pi} \eta_0 \beta_0^2 \cos \theta \left(\frac{1}{\beta_0^2 r^2} - j \frac{1}{\beta_0^3 r^3} \right) e^{-j\beta_0 r} \quad (2)$$

$$\hat{H}_\phi = \frac{\hat{I}dl}{4\pi} \beta_0^2 \sin \theta \left(j \frac{1}{\beta_0 r} + \frac{1}{\beta_0^2 r^2} \right) e^{-j\beta_0 r} \quad (3)$$

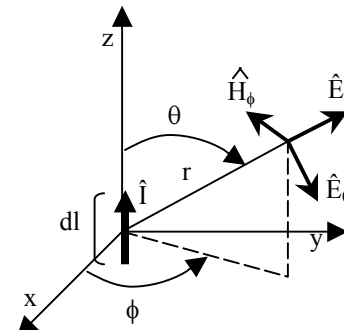


Fig. 1. Radiation field components from an electric dipole.

The observation point is assumed to be in free space. This infinitesimal current element is known as the electric (Hertzian) dipole [1].

The parameters in the field components represent:

- r is the distance from the source to the observation point P.
- $\eta_0 = \sqrt{\frac{\mu_0}{\epsilon_0}}$ is the intrinsic impedance of free space in Ohm.
- $\beta_0 = \omega \sqrt{\mu_0 \epsilon_0}$ is the phase constant of the wave in rad/m.
- $\omega = 2\pi f$ is the radian frequency, with f in Hz.

The term $e^{-j\beta_0 r}$ represents the propagation delay.

In order to meet the conditions of electrically small, $dl \ll r$ and $dl \ll \lambda$ (λ is the wavelength at the frequency f) and the current does not vary in amplitude and phase along the length dl .

For analysis purposes, the conductors of the cabling system are divided into a series of n connected segments with length l_n each carrying a current \hat{I}_n , each segment at a distance r_n to the observation point $P(r, \theta, \phi)$.

The conditions for considering each segment electrically small must be met, and the total field at $P(r, \theta, \phi)$ is found by summing the individual fields from each of the segments using the expressions described in eq.1-3. The total field components are thus obtained for far field or near field zones, without the need to do any simplifications.

STRUCTURE OF THE PROGRAM

The program EMIR is written in C. The program takes as input data the consecutive end points of line segments that describe the geometry of the source conductors as well as the phasor complex amplitude of the currents carried out by each segment. For a point or grid of points defined by the user it computes the individual contributions due to each segment and the total field components by summing these contributions.

The program also allows the calculation of the wave impedance \hat{Z}_w i.e the ratio of the amplitudes of \hat{E}_θ to \hat{H}_ϕ at a given point. The amplitudes of each component \hat{E}_θ , \hat{E}_r , \hat{H}_ϕ can be plotted in the form of contour plots in the plane of analysis, and it is also possible to plot a variation of these amplitudes along lines.

APPLICATION EXAMPLE

The application example chosen is the calculation of the radiated emissions at 100 MHz, of a two wire cable, with length of 2 m separated by 5 cm carrying the currents of 104 mA (wire 1) and -96 mA (wire 2) respectively. The conductors are placed in the $x=0$ plane centered at the origin, aligned in the OZ direction. In table I it is presented the field components in amplitude and phase at four points at distances of 0.1 m, 1 m, 10 m and 100 m for $\phi=90^\circ$, $\theta=90^\circ$, as well as the wave impedance \hat{Z}_w .

TABLE I
FIELD COMPONENTS FOR $r=0.1$ m-100 m $\phi=90^\circ$, $\theta=90^\circ$

r	\hat{E}_θ	\hat{E}_r	\hat{H}_ϕ	$ \hat{Z}_w $	$\frac{ \hat{E}_\theta }{ \hat{E}_r }$
0.1 m	8.5501 └ -81°	3.481e-13 └ -90°	0.096906 └ 1°	88.23	2.46e+13
1 m	1.2176 └ -16°	4.626e-16 └ -133°	4.024e-3 └ -32°	302.54	2.63e+15
10 m	0.16788 └ 15°	2.967e-17 └ -101°	4.474e-4 └ 15°	375.2	5.65e+15
100 m	0.01659 └ 14°	2.565e-19 └ 103°	4.404e-5 └ 14°	376.7	6.47e+16

In Fig. 2 it is presented a contour plot of the amplitudes of \hat{E}_θ in the plane $y=\text{const}=9$ m and in Fig. 3 the variation of \hat{Z}_w along $\frac{r}{\lambda}$ in the y axis.

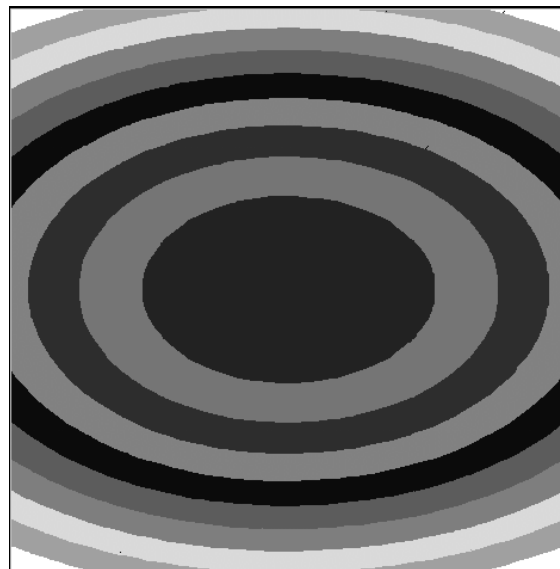


Fig. 2. Amplitudes of \hat{E}_θ in the plane $y=9$ m.

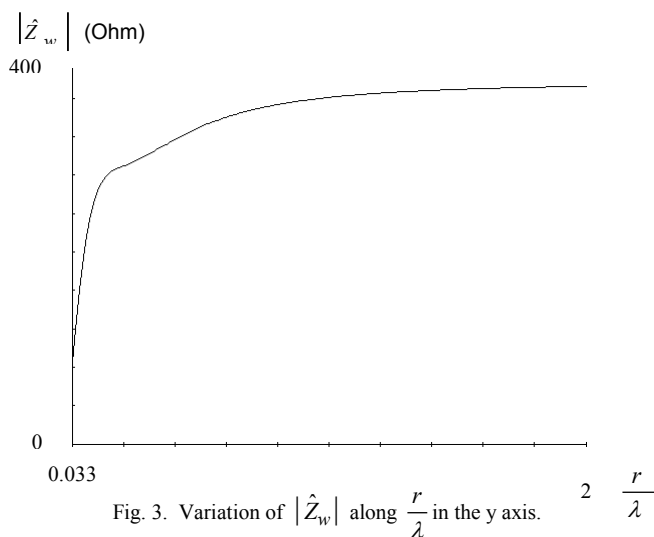


Fig. 3. Variation of $|\hat{Z}_w|$ along $\frac{r}{\lambda}$ in the y axis.

The wave impedance varies with r and thus it is important to know the boundaries between the near fields and the far fields as this will affect the choice of adequate shielding materials.

In the full version of the paper it will be presented a more complete set of results, including the contributions to the field components of the common mode and differential equivalent currents, regarding two application examples, not shown here due to length limitations of this summary.

REFERENCES

[1] C. R. Paul, *Introduction to Electromagnetic Compatibility*, John Wiley & Sons Inc., U.S.A., 1992.

Multiobjective Optimization of Wire Antennas

R. M. Ramos¹, R. R. Saldanha², R. H. C. Takahashi³, F. J. S. Moreira⁴

¹Faculdade de Ciências Exatas de Pedro Leopoldo – UNIPEL - Dept. Computer Science
 R. Teófilo Calazans de Barros, 100 – 33600-000 – Pedro Leopoldo – MG- Brazil
 Universidade Federal de Minas Gerais - ²Dept. Electrical Eng., ³Dept. Mathematics, ⁴Dept. Electronics Eng.
 Av. Antônio Carlos, 6627 – 31270-010 – Belo Horizonte – MG – Brazil
 e-mail: ramos@cpdee.ufmg.br; rodney@cpdee.ufmg.br; rtakahashi@ufmg.br, fernando@eee.ufmg.br

Abstract - This work presents a multiobjective optimization of wire antennas using the real biased multiobjective genetic algorithm (RBMGA) with a novel feature: the real biased crossover operator. The procedure leads to better estimates of the *Pareto-set* during the multiobjective search. The novel algorithm is further applied to the optimization of a Yagi-Uda antenna, where the element's length and separation between elements are varied. The multiobjective approach provides an antenna geometry with superior performance than those presented in the available literature.

MULTIOBJECTIVE GA

INTRODUCTION

The optimal design of wire antennas has attracted the attention of many researchers in the past decades, specially for wireless applications demanding a relatively large spectrum. Several optimization techniques have been applied to the design of wire antennas [1 - 4]. For instance, in [1,2] deterministic methods were used to solely reach the maximum gain, while [3] also deals with the input impedance, in order to maximize the matching with a given transmission line.

Due to the amount of variables to be optimized (specially for a large number of dipole elements) and restrictions imposed upon the antenna electrical characteristics, a better strategy for designing wire antennas should account for several objectives, in particular due to the sensitivity of the electrical characteristics with the frequency variation through the operating spectrum. This suggests the application of multiobjective techniques.

This paper presents the application of a multiobjective optimization using RBMGA, leading to antenna designs that are superior to former ones found in the literature.

MULTIOBJECTIVE PROBLEM

The multiobjective optimization problem can be defined as follows. Given a set of objective functions to be minimized, f_i , $i = 1, \dots, m$, one should find the set P of solutions defined as follows:

$$P = \{ x \in F \mid \text{not exists } y \in F \text{ such that } f(y) \leq f(x) \text{ and } f(y) \neq f(x) \}, \quad (1)$$

in which F denotes the feasible set. The set P contains the *efficient solutions* of the problem, and is called the *Pareto-optimal set*.

In the present work, a novel real-biased crossover operator will be used for the construction of the multiobjective genetic algorithm. The operator uses information about the difference among the two parents fitness values in the generation of new individuals [5]. Such measure can be interpreted as a *long-term gradient* information. The Pareto-set is found with high resolution and low computational effort.

The algorithm employed is described as follows. Initially, the population is divided in two sets and for each one of them the occurrence of crossover is verified. So, let $J(x)$ denote the fitness function and lets consider the vectors x_1 and x_2 representing two individuals, such that $J(x_2) < J(x_1)$. The real biased crossover is then defined as:

$$x_g = \alpha x_1 + (1 - \alpha)x_2, \quad (2)$$

with α chosen in the interval $[-0.1; 1.1]$, according to the probability distribution defined by

$$\alpha = 1.4\beta_1\beta_2 - 0.2, \quad (3)$$

where β_1 and β_2 are random variables with uniform probability distribution inside the domain $[0; 1]$. Such conditions are so to provide a quadratic probability distribution for α . The application of a new genetic crossover operator (the real-biased crossover), adds the feature of producing new individuals that are *probably* closer to the best parent than to the *worst* one. The remaining operators are as usual [6].

In case of one individual being out of the admissible range as will be explored later, the reflection method is applied to force the individual inside the feasible region [5]. Afterwards, the mutation operator is applied. In case of occurrence, this operation is defined by $\delta + x$, where x represents the individual inside the admissible range and the vector δ is defined as:

$$\delta_i = 0.05 \beta_i (x_r)_i, \quad (4)$$

where β_i is a random number with Gaussian distribution, zero mean, and variance equal to one and i denotes that its vector is different at each mutation. The x_r vector is a range vector between lower and upper limits for the variables.

In this section, will be done an optimization of a 6-element Yagi-Uda antenna, as illustrated in Fig. 1. The element centered at the origin is the reflector, followed by the centered-fed driven element and the 4 directors. The distances between consecutive elements and the lengths of each element are the parameters to be optimized. The cross-section radius is the same for all elements.

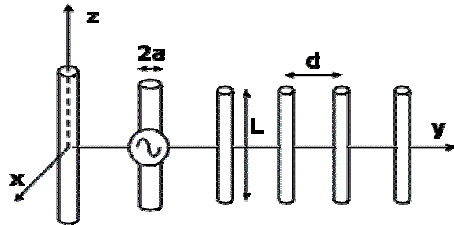


Fig. 1 – 6-element Yagi-Uda antenna configuration

The electrical characteristics of the antenna, necessary to the establishment of the objective functions, are attained by a numerical analysis based on the method of moments (MoM) [7].

The desired objectives were the highest possible directivity and front-to-back ratio, while sustaining narrow half-power beam-widths on both E- and H-planes with an input resistance close to 50 Ω over a 5% bandwidth, for a 6-element Yagi.

NUMERICAL RESULTS

An important issue in a multiobjective optimization is to pick the best solution among several candidates (the Pareto-set). Next, the designer chooses the best group of antennas, based on their individual characteristics.

In the Table I we will present three antennas selected from the Pareto-Optimal set, in order to discuss the results obtained with RBMGA. The optimized results are summarized in Table II, where they are compared against some found in the literature [3,4]. Figure 2 shows results for directivity and input resistance across the band, which are compared against those provided by the NEC2 code.

TABLE I
LENGTHS AND INTER-SEGMENT DISTANCES OF THE ANTENNAS CHOSEN IN THE PARETO OPTIMAL SET . RESULTS IN λ (AT 300 MHZ).

RBMGA					
Lengths	Distances	Lengths	Distances	Lengths	Distances
0.5084	-	0.5089	-	0.5184	-
0.4890	0,2450	0.4824	0.2208	0.4943	0.2445
0.4382	0,1486	0.4331	0.1428	0.4383	0.1480
0.4047	0,2830	0.4018	0.2542	0.4070	0.2794
0.4325	0,3844	0.4149	0.3705	0.4254	0.3627
0.4198	0,2438	0.3903	0.2699	0.4123	0.2657

TABLE II
(1) NORMALIZED FREQUENCY, (2) DIRECTIVITY (dB), (3) FRONT-TO-BACK RATIO (dB), HALF POWER BEAM WIDTH (DEGREES) IN THE (4) E- AND (5) H-PLANES, (6) INPUT RESISTANCE (Ω).

	RBMGA			Ref. [3]			Ref. [4]		
(1)	0.975	1	1.025	0.975	1	1.025	0.975	1	1.025
(2)	11.00	11.65	11.50	11.79	12.66	11.60	9.475	9.702	10.02
(3)	21.42	17.55	12.37	16.86	10.52	10.33	14.31	15.47	15.55
(4)	48.40	44.60	39.54	44.72	40.53	35.96	56.75	55.23	53.23
(5)	55.28	49.86	43.09	50.15	44.47	40.05	69.15	66.33	62.92
(6)	52.02	49.64	49.94	21.02	49.49	1.849	54.44	62.05	68.33

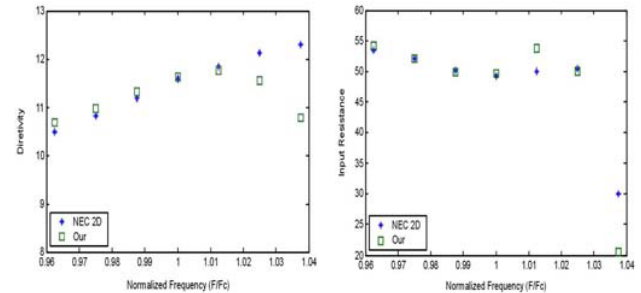


Fig. 2 – Directivity and input resistance along the band.

CONCLUSIONS

The RBMGA has presented a good performance in the design of wire antennas. The usage of a multiobjective approach in this problem was a key issue in getting high performance antennas, that feature good parameters in a broad frequency range.

The Pareto Optimal set was well mapped, showing that this novel feature applied to Genetic Algorithms, i.e., Biased Crossover, can be an efficient tool to reach better results when its applied at one specific goal.

REFERENCES

- [1] D. K. Cheng and C. A. Chen, "Optimum spacings for Yagi-Uda arrays", *IEEE Trans. Antennas Propagat.*, vol. AP-21, pp. 615—623, Sept. 1973.
- [2] C. A. Chen and D. K. Cheng, "Optimum element lengths for Yagi-Uda arrays", *IEEE Trans. Antennas Propagat.*, vol. AP-23, pp. 8—15, Jan. 1975.
- [3] E. A. Jones and W. T. Joines, "Design of Yagi-Uda antennas using genetic algorithm", *IEEE Antennas Propagat. Magazine*, vol. 39, pp. 1386—1391, Sept. 1997.
- [4] D. Correa, A. J. M. Soares, and M. A. B. Terada, "Optimization of gain, impedance and bandwidth in Yagi-Uda antennas using genetic algorithm", in *SBMO/IEEE MTT-S IMOC'99 Proceedings*, pp. 41—44, Rio de Janeiro, Brazil, 1999.
- [5] R. M. Ramos, "Utilization of Genetic Algorithms in Multiobjective Optimization of Yagi Uda Antennas" (In Portuguese), Master's Dissertation, PPGEE - UFMG, Belo Horizonte, Brasil, 2002.
- [6] D. E. Goldberg, *Genetic Algorithms in Search, Optimization and Machine Learning*. Reading, MA: Addison-Wesley Publishing Co., 1989.
- [7] J. H. Holland, *Adaptation in Natural and Artificial Systems*, Ann Arbor, MI: University of Michigan Press.
- [7] G. A. Thiele, "Calculation of the current distribution on a thin linear antenna", *IEEE Trans. Antennas Propagat.*, vol. AP-14, pp. 648—649, Sept. 1966.

Conceptual Framework for Numerical Wave Propagation Schemes

Timo Tarhasaari, Lauri Kettunen

Abstract—In this paper a conceptual background for wave propagation schemes is presented. The framework enables one to classify well known numerical techniques according to the approximations they involve. Such a understanding is needed in further development of these approaches.

I. INTRODUCTION

THE finite element method and Yee-like schemes [1] have similarities [2], [3], [4] but as well they may be viewed as separate approaches, see for instance [5], [6], [7]. The similarities and differences between the two families of numerical approaches are not easily recognizable as the language employed in the finite element and in the finite difference literature is not alike. However, the true nature of a numerical approach is not the same thing as how the main ideas are typically explained, and thus, to state precisely the possible relationship between finite elements and Yee-like schemes a conceptual framework powerful enough to explain the essential features of both techniques is needed.

In this paper we aim to introduce such a framework especially for the needs of computational electromagnetism and electromagnetic wave propagation problem.

II. COCHAINS AND CHAINS

Evidently the basic observations we make of the electromagnetic phenomena has to do with real numbers related to (oriented) lines, surfaces and volumes, and this is also the starting point of the so called finite integration technique (FIT) [5] and finite formulation approach [6], [7].

The geometrical objects involved in the observations can be recognized as *chains*, and the real numbers –such as currents, voltages, emf’s, mmf’s etc.– are images yielded by *cochains* when they act on these chains. In unformal words, if integration of field f over chain c is denoted by $\int_c f$, then $\int f$ (notice, without the c) as a compound object can be interpreted as cochain F . In general, cochain F may well exist without field f , and our starting point is precisely to express the information behind Maxwell’s equations in terms of cochains without employing fields at all at the first place.

Let E, D, J, B, H be the cochains whose counterparts are the familiar e, d, j, b and h fields, respectively. The real number E yields when it acts on 1-chain c is denoted by $(E|c)$. In more simple words, $(E|c)$ is the emf along c , and therefore, in terms of cochains Faraday’s law is given by: $(E|\partial s) = -\partial_t(B|s)$ holds for all 2-chains s .

This work is supported by the Academy of Finland, project 53972. T. Tarhasaari and L. Kettunen are with the Tampere University of Technology, Inst. of Electromagnetics, P.O.Box 692, FIN-33101 Tampere, Finland. E-mail: {timo.tarhasaari,lauri.kettunen}@tut.fi

Writing Maxwell’s equations in this style involves already some assumptions as otherwise the model would not make sense. At first, the *boundary operator* ∂ is defined as a linear map between certain *chain spaces*, and chains themselves are made of formal sums of *cells* and to define cells, r -planes are needed calling for an *affine structure* [8]. The chain spaces also make it meaningful to state that Faraday’s law holds “for all” chains.

Cochains themselves must also have some properties. Let $|c|$ denote the measure of cell c . We’ll assume, that:

Property I: Given a cochain F there is a real number α such that $|(F|c)| \leq \alpha|c|$, holds for all cells c of proper degree.

Property II: Given a cochain G there is a real number β such that $|(G|\partial c)| \leq \beta|c|$, holds for all cells c of proper degree.

From the electromagnetic point of view these assumptions are well motivated: For instance, property I implies that voltage $(E|l)$ and magnetic flux $(B|s)$ is bounded by the (affine, i.e. relative) length of path l and area of surface s , respectively. Correspondingly, in case of Faraday’s law, property II implies that the emf $(E|\partial s)$ over the boundary of surface s is bounded by the area of s . A cochain fulfilling properties I and II is called a *flat cochain* [8].

The power of the cochain approach lies in the *geometrical* interpretation. The real numbers cochains yield depend only on the geometrical objects called chains, and the notion of chains is easy to grasp and visualize.¹ This results in a clear intuitive interpretation of the linear operators involved in cochain approaches such as, for instance, the “Maxwell’s grid equations” in FIT [5].

III. FIELDS AND EXTERIOR DERIVATIVE

Cochains yield numbers on chains, and very small ones are also allowed. But, the very limit of a chain decreasing to zero changes things. This is what a *field* is about: A field is obtained as the limit of a sequence of a (flat) cochain acting on cells whose measure converges towards zero. More precisely, the fields are (flat) *differential forms* which map r -vectors to real numbers. For example, if F is a cochain representing the electrostatic force on point charge q , then $(F|l)$ is the *work* needed to move q along path l . Correspondingly, if f represents the same force but now as a field, then the real number $(f|\{l\})$ of f acting on 1-vector $\{l\}$ is known as the *virtual work*. (Vector $\{l\}$ is just an ordinary vector which is typically denoted by \mathbf{l} .)

¹Still, simple interpretation does not imply that the conceptual framework of cochain formulations were more trivial than that of other approaches.

In the same spirit, the *exterior derivative* dg of a field g is defined as the limit of cochain G acting on $\partial c/|c|$, when $|c|$ approaches 0. Be aware, cochains are *not* “discrete differential forms”. The cochain spaces are of infinite dimension, and the cochains do even fulfill two *continuity conditions*: The first one is, in fact, property I, which enables one to define the notion of a field, and the second one, property II, makes it possible to introduce the exterior derivative of a field.

IV. WAVE PROBLEM AND NUMERICAL SCHEMES

The electromagnetic wave propagation problem is a solution of the Faraday and the Ampère laws which can *either* be expressed in terms of cochains or fields. In addition, the constitutive laws are needed, but they can *only* be given as a relation between fields.²

The very idea of the numerical schemes designed to solve the electromagnetic wave problem is to construct a finite dimensional counterpart of the “continuous” problem. The finite nature of the numerical approach can be developed in many ways. In the well known FDTD, FIT and FEM schemes the finiteness follows from the need of a *cell complex* (or complexes), and the conceptual differences between the approaches follow from the approximations made along the way in developing the schemes.

A. Finite integration technique

The main modeling decision behind the FIT approach is to describe the electromagnetic phenomena in terms of cochains. Cochains themselves call for chains and cells (relying on the affine structure), and the finite nature of FIT is obtained by *restricting* the domain of the cochains and the boundary operator to cell complexes. (At this stage no approximation is made yet.³)

The restriction implies one is no longer able to talk of fields, as the notion of field needed the limiting sequence of chains, and this is not available in the restricted space. Thus, one may neither employ the constitutive laws, but instead, an approximation has to be introduced.

Assuming the measure $|c|$ of cell c is available, the limit process

$$\frac{(g|\{c\})}{||\{c\}||} = \lim_{|c| \rightarrow 0} \frac{(G|c)}{|c|}. \quad (1)$$

provides one with an apparent approximation of p -form g in terms of cochain G : In the center point of cell c $(g|\{c\}) \approx (G|c)$ holds. (The smaller $|c|$, the better is the approximation.) Thereafter the definition of the *Hodge operator* yields, for instance, $(B|f)/|f| \approx \mu(H|\tilde{e})/|\tilde{e}|$, as an approximation of the relation between magnetic flux b and field h , at the *center points* where the primal faces f and

²In formal terms, the so called Hodge (star) operator cannot be introduced to cochains. It is only defined as a pointwise map between differential forms of proper degree.

³A restriction of the domain an operator does not introduce any kind of approximation. All what is said, is that the operator may not act on all elements of the domain. This is, for instance, why “Maxwell’s grid equations” [5] are exact.

the dual side edges \tilde{e} intersect. Furthermore, the definition of the Hodge implies also that 1-vector $\{\tilde{e}\}$ needs to be orthogonal to the vectors of the plane of $\{f\}$.

B. Finite difference time domain

The constitutive laws are relations between fields which hold (almost) everywhere in the domain. The FDTD approach starts from the constitutive laws, which are assumed to hold only at certain points of the domain. (Eventually, these points will be the intersections of the dual pairs of edges and faces.)

Next, the very idea is to approximate cochains in terms of fields and thereafter exterior derivatives with cochains. That is, one has $(G|c) \approx (g|\{c\})$ which together with the definition of d and (1) yields

$$\frac{(dg|\{c'\})}{||\{c'\}||} \approx \frac{(G|\partial c')}{|c'} \quad (2)$$

at the center point of cell c' .

The two grids of FDTD define the finite amount of intersection points where the constitutive laws should hold, and the tools presented above enable to approximate the Faraday and Ampère laws in terms of fields at these points.

So, in FIT the approximation lies in the constitutive laws, whereas in case of FDTD in the differential equations. Notice, that both approaches employ the same first order approximation of the one-to-one relation between cochains and fields. This is why on the algorithm level the two techniques become related.

C. Finite elements

In the finite element approach the constitutive laws are included in the *inner product* (related to energy or power) which has to do with the *whole* domain. For this reason finite elements is another kind of approach not that similar to FDTD and FIT in which the constitutive laws are related to the *local* Hodge operator. The full paper will describe this issue in details.

REFERENCES

- [1] K. S. Yee, “Numerical solution of initial boundary value problems involving Maxwell’s equations in isotropic media,” *IEEE Trans. Antennas Propagat.*, vol. 14, pp. 302–307, May 1966.
- [2] T. Tarhasaari, L. Kettunen, and A. Bossavit, “Some realizations of a discrete Hodge operator: A reinterpretation of finite element techniques,” *IEEE Trans. Magn.*, vol. 35, no. 3, 1998.
- [3] A. Bossavit and L. Kettunen, “Yee-like schemes on staggered cellular grids: A synthesis between FIT and FEM approaches,” *IEEE Trans. Magn.*, vol. 36, no. 4, pp. 861–867, 2000.
- [4] A. Bossavit, “Generalized finite difference in electromagnetic wave propagation problems,” *PIER, Geometric Methods for Computational Electromagnetics*, pp. 45–63, 2001.
- [5] T. Weiland, “Time domain electromagnetic field computation with finite difference methods,” *Int. J. Num. Modell.*, vol. 9, pp. 295–319, 1996.
- [6] E. Tonti, “Algebraic topology and computational electromagnetism,” in *Proc. of 4th Int. Workshop on Elec. and Magn. Fields*, (Marseilles, France), pp. 285–294, 1998.
- [7] E. Tonti, “Finite formulation of electromagnetic field,” *IEEE Trans. Magn.*, vol. 38, pp. 333–336, March 2002.
- [8] H. Whitney, *Geometric Integration Theory*. Princeton University Press, 1957.

Current and Near Field Calculations for Cellular Base-Station Collinear Array Antennas

Federico Delfino, Renato Procopio, Mansueto Rossi
Department of Electrical Engineering, University of Genoa
Via Opera Pia 11a
I-16145 Genova – ITALY

federico.delfino@die.unige.it; rprocopio@epsl.die.unige.it; mansueto@die.unige.it

Abstract—In this paper we present a new formulation for the evaluation of the electromagnetic field levels in the near zone of a cellular radio base-station (RBS) collinear array antenna. The algorithm allows to determine the real current distribution along each half-wave dipole forming the array for a given exciting function and it enables to take into account the effects of mutual coupling among array elements. Once the antenna current distribution has been determined, the radiated field in the near zone is reconstructed using the integro-differential equation relating field and current. As preliminary result, the simulation of a 4-element collinear array antenna operating at 900 MHz is presented.

INTRODUCTION

This paper addresses the issue of electromagnetic field calculations in proximity of cellular RBSs [1-2] and proposes a new formulation for the determination of the current distribution in a collinear array antenna made up of N half-wave dipoles. The approach is based on the assumption that the presence of people near the installation does not affect significantly the current on each element of the array. This hypothesis is satisfied if the region of interest for the field observation is in the vicinity of the antenna, but at distances greater or equal than $\lambda/2$ (i.e. the element size) [2]. With such position, the antenna can be modelled as an array of dipoles radiating in free space (Fig. 1b).

The main feature of the developed algorithm is that it allows to take into account the effects of the mutual interaction among array elements, which is usually neglected by simplified approaches on the subject [2-3]. Furthermore, it represents a viable alternative to the widely adopted antenna code NEC [4] for the study of radiation from collinear array antennas, with the significant improvement of not exhibiting the numerical inaccuracies affecting this latter approach when, as the number of subdivisions increases, the length of the segments in which each radiating element is divided becomes comparable to its radius.

THEORY

Let us consider the situation depicted in Fig. 1a, where N radiating elements lie in free space. The notations x_i , y_i and z_i are used to identify the coordinates of the i^{th} element centre, while a_i represents the element radius. The z -coordinate is parameterized on each element by a local abscissa ζ :

$$z = z_i + \zeta \cdot h, \quad \zeta \in (-1, 1). \quad (1)$$

Each element is modelled as a perfect conductor. The governing equation is derived imposing that the tangential component of the electric field vanishes on each element surface:

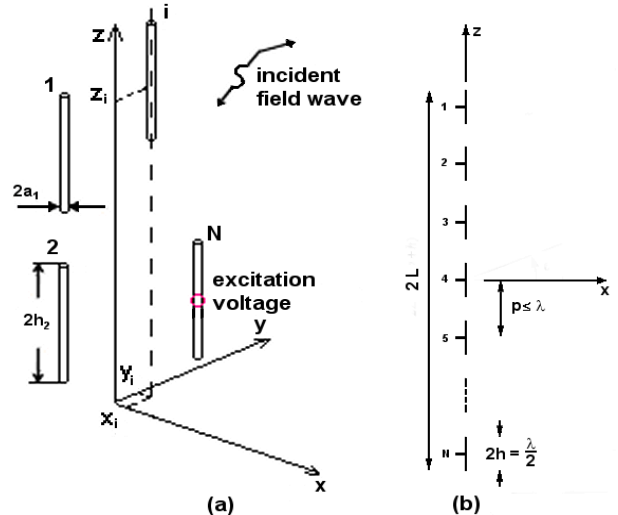


Fig. 1. Geometry of the model problem (a) and an example of application: a collinear array antenna for cellular base-stations (b).

$$\left[\frac{d^2}{d\zeta^2} + \hat{k}^2 \right] \sum_{i=1}^N \int_{-1}^1 I_i(\zeta') g_{il}(\zeta - \zeta') d\zeta' = F_l(\zeta)/4, \quad l=1..N, \quad (2)$$

where $I_i(\zeta)$ is the current on the generic dipole, ξ_0 is the free space impedance, $\hat{k} = kh$, being k the wave number, g_{il} are suitable Green functions and $F_l(\zeta) = -j(16\pi kh/\xi_0)E_{inc,l}(\zeta)$, being $E_{inc,l,z}$ the z -component of the incident field on each element, due to an e.m. wave or to an applied potential.

Two new set of function are now introduced:

$$\tilde{I}_l(\zeta) = \begin{cases} I_l(\zeta), & |\zeta| < 1, \\ 0, & 1 < |\zeta| < 2, \\ \tilde{I}_l(\zeta - 4), & \text{in general,} \end{cases} \quad \tilde{g}_{il}(\zeta) = \begin{cases} g_{il}(\zeta), & |\zeta| < 2, \\ \tilde{g}_{il}(\zeta - 4), & \text{in general.} \end{cases} \quad (3)$$

Inserting (3) into the governing equation (2) and adopting a vector notation, it results in:

$$\left[\frac{d^2}{d\zeta^2} + \hat{k}^2 \right] \int_{-2}^2 [\tilde{g}(\zeta - \zeta')] [\tilde{I}(\zeta')] d\zeta' = F(\zeta)/4, \quad (4)$$

where the integrations, extended in the interval $(-2, 2)$, take the form of convolution. Expanding $[\tilde{I}(\zeta)]$ and $[\tilde{g}(\zeta)]$ in Fourier series and applying the convolution theorem, one has:

$$\sum_{r=-\infty}^{+\infty} \left(\hat{k}^2 - \frac{r^2 \pi^2}{4} \right) [G_r] [I_r] e^{jr \frac{\pi}{2} \zeta} = [F(\zeta)], \quad (5)$$

It can be shown that $[I_r]$ can be expanded in the following Neumann series:

$$[I_r] = \sum_{n=0}^{\infty} [s_n] (r\pi/2)^{-1} J_{n+1}(r\pi/2). \quad (6)$$

Now, the coefficient $[s_n]$ are the new unknowns of the problem. Substituting (6) into (5) and expanding both sides of this expression in Gegenbauer polynomials C_n^1 , the following system is obtained:

$$\begin{bmatrix} [B_{00}] & [B_{01}] & \cdot \\ [B_{10}] & [B_{11}] & \cdot \\ \cdot & \cdot & \cdot \end{bmatrix} \begin{bmatrix} [s_1] \\ [s_2] \\ \cdot \end{bmatrix} = \begin{bmatrix} [F_1] \\ [F_2] \\ \cdot \end{bmatrix}, \quad (7)$$

where $[F_n]$ is the n^{th} coefficient of the expansion of $[F(\zeta)]$ in Gegenbauer polynomials and

$$[B_{qn}] = \frac{2\pi\alpha_n\beta_q}{\gamma_q} \sum_{r=-\infty}^{+\infty} \left(\hat{k}^2 - \frac{r^2\pi^2}{4} \right) \frac{J_{n+1}(r\pi/2)J_{q+1}(r\pi/2)}{(r\pi/2)^2} [G_r], \quad (8)$$

being $\alpha_n, \beta_q, \gamma_q$ suitable constants. Once the coefficients $[s_n]$ have been evaluated, it can be proved that the currents on each radiating dipole can be obtained by the following expansion:

$$[\tilde{I}(\zeta)] = (1-\zeta^2)^{\frac{1}{2}} \sum_{n=0}^{+\infty} (\pi\alpha_n)^{-1} [s_n] C_n^1(-\zeta) \quad (9)$$

It should be noticed that if a voltage is applied to an element l at the point ζ_0 , a corresponding term of the form $F_l(\zeta) = -j(16\pi\hat{k}/\xi_0)(V/h)\delta(\zeta - \zeta_0)$ must be added at the r.h.s. of equation (2).

NUMERICAL EXPERIMENTS

We considered as a first test case for the proposed formulation a typical omni-directional antenna: a *Celwave PDI610* 4-element collinear half-wave dipole array [5] operating at 900 MHz, with each element fed in phase by a unit voltage source. The vertical component of the electric field has been evaluated along x-axis (referring to the notation of Fig. 1b) at the fixed quote corresponding to the antenna centre. The good agreement between the proposed approach (using 25 Gegenbauer polynomials for the current expansion) and the NEC solution (with 25 subdivisions for each dipole) can be observed in Fig. 2.

As a second test case, we calculated the current for a single half-wave dipole working at 900 MHz and characterized by a radius $a = 0.005$ m and a length $2h = 0.16$ m. As far as NEC solution is concerned, it can be seen (Fig. 3) that it is not able to correctly reconstruct the behaviour of the imaginary part of the current distribution on the dipole. This is due to the fact that the length of the single segment becomes comparable to the dipole radius, when the subdivisions are increased in order to get more accuracy.

CONCLUSIONS

In this short paper a new algorithm for the computation of the antenna current and the near field of collinear half-wave

arrays has been presented and tested on practical configurations. First results show that the algorithm is effective also in cases where other more popular approaches fail.

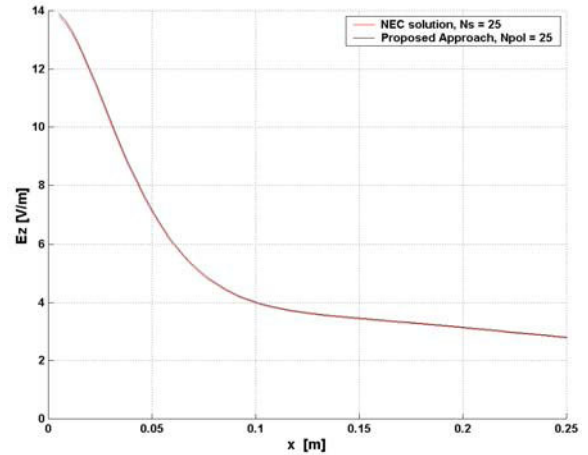


Fig. 2. Vertical component of the electric field in the near zone.

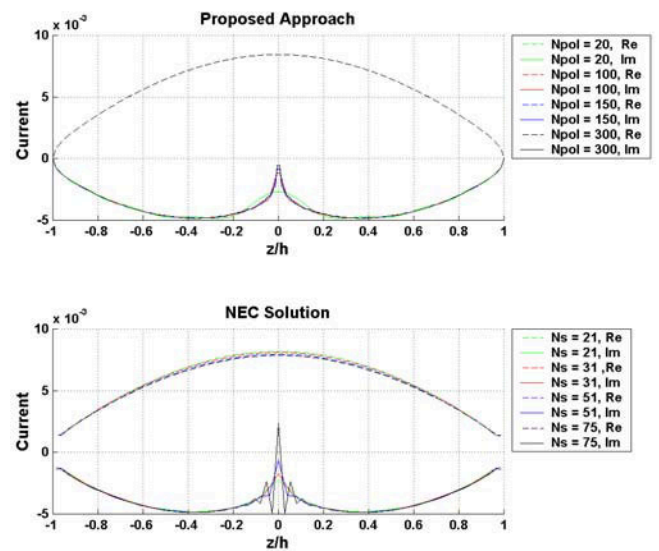


Fig. 3. Current spectrum on the half-wave dipole: failure in NEC solution.

REFERENCES

- [1] S. Blanch, J. Romeu, A. Cardama, "Near field in the vicinity of wireless base-station antennas: an exposure compliance approach," *IEEE Trans. on AP*, vol. 50, n. 5, May 2002, pp. 685-692.
- [2] A. Faraone, R. Yew-Siow Tay, K. H. Joyner, Q. Balzano, "Estimation of the average power density in the vicinity of cellular base-station collinear array antennas," *IEEE Trans. on Vehic. Techn.*, vol. 49, n. 3, May 2000, pp. 984-996.
- [3] D. Forigo, P. Gianola, R. Scotti, R. Vallari, "Measurements and numerical evaluation of the electric field in the near-zone of radio base station antennas," *Proc. of the IEEE Int. Symp. AP Society*, vol. 3, March 2001, pp. 338-341.
- [4] G. J. Burke, A. J. Poggio, "Numerical electromagnetic code (NEC) – Method of moments," *Naval Ocean Systems Center*, Technical Document 116, January 1981.
- [5] C. A. Balanis, *Antenna Theory: Analysis and Design*, John Wiley & Sons, New York, 1997.

Finite Element Waveguide Solvers Revisited

Ortwin Farle, Volker Hill, and Romanus Dyczij-Edlinger
Lehrstuhl fuer Theoretische Elektrotechnik, Saarland University
P.O. Box 15 11 50, D-66041 Saarbrücken, Germany
E-Mail: edlinger@lte.uni-saarland.de

Abstract—A general analysis of potential- or field-based finite element solvers for axially uniform electromagnetic waveguides is presented. We show that the partial discretization performed by such methods results in certain constraints on the set of permissible gauge transformations. We demonstrate that these side effects may affect the reliability of present formulations and propose a particular choice of gauge to overcome such limitations.

I. PRELIMINARIES

In the following, k_0 denotes the wavenumber, η_0 the characteristic impedance, and c_0 the speed of light in free space. For simplicity, let the waveguide be lossless and the electric permittivity ϵ_r and magnetic permeability μ_r be scalar quantities. Then the Maxwell equations for time-harmonic fields can be written as

$$\nabla \times \vec{H} = jk_0/\eta_0 \epsilon_r \vec{E}, \quad (1)$$

$$\nabla \times \vec{E} = -jk_0 \eta_0 \mu_r \vec{H}, \quad (2)$$

$$\nabla \cdot \vec{B} = 0, \quad (3)$$

$$\nabla \cdot \vec{D} = 0. \quad (4)$$

Thanks to uniformity along the waveguide axis z , we may factorize all modal fields v in the form

$$v(x, y, z) = w(x, y)e^{-\gamma z}, \quad (5)$$

where γ denotes the propagation constant. Similarly, the operator ∇ is decomposed into

$$\nabla = \nabla_t - \gamma \hat{e}_z, \quad (6)$$

where subscript t stands for transversal components, and \hat{e}_z for the unit vector in axial direction.

II. POTENTIAL FORMULATION

In view of (2) and (3), we define a magnetic vector potential \vec{A} and an electric scalar potential ϕ by

$$\vec{B} = \nabla \times \vec{A}, \quad (7)$$

$$\vec{E} = -c_0 \nabla \phi - jk_0 c_0 \vec{A}. \quad (8)$$

From (1), we obtain the fundamental equations

$$\nabla \times \mu_r^{-1} \nabla \times \vec{A} - k_0 \epsilon_r (k_0 \vec{A} - j \nabla \phi) = 0, \quad (9)$$

$$\nabla \cdot \epsilon_r (k_0 \vec{A} - j \nabla \phi) = 0. \quad (10)$$

We have stated (10) because in the static case (9) does not impose (4) anymore.

For waveguide analysis, we factorize the potentials as in (5) and split \vec{A}_t into a transverse gradient $\nabla_t \psi$ plus a function \vec{A}_t^c of non-vanishing circulation,

$$\vec{A} = e^{-\gamma z} \left(\vec{A}_t(x, y) + A_z(x, y) \hat{e}_z \right), \quad (11)$$

$$\phi = e^{-\gamma z} V(x, y), \quad (12)$$

$$\vec{A}_t(x, y) = \vec{A}_t^c(x, y) + \nabla_t \psi(x, y). \quad (13)$$

By plugging (13) into (7) and (8), we obtain for the behavior of \vec{B} and \vec{E} in the transverse plane

$$\vec{B}(x, y) = \nabla_t \times \vec{A}_t^c - \hat{e}_z \times [\gamma \vec{A}_t^c + \nabla_t(\gamma \psi + A_z)], \quad (14)$$

$$\vec{E}(x, y) = -jc_0 [k_0 \vec{A}_t^c + \nabla_t(k_0 \psi - jV)] - jc_0 [k_0(\gamma \psi + A_z) - \gamma(k_0 \psi - jV)] \hat{e}_z. \quad (15)$$

With the help of (1), we arrive at a set of equations that is equivalent to the vector wave equation (9),

$$\begin{aligned} \nabla_t \times \mu_r^{-1} \nabla_t \times \vec{A}_t^c \\ + \gamma^2 \hat{e}_z \times \mu_r^{-1} \hat{e}_z \times \vec{A}_t^c - k_0^2 \epsilon_r \vec{A}_t^c \\ + \gamma \hat{e}_z \times \mu_r^{-1} \hat{e}_z \times \nabla_t(\gamma \psi + A_z) \\ - k_0 \epsilon_r \nabla_t(k_0 \psi - jV) \end{aligned} = 0, \quad (16)$$

$$\begin{aligned} - \gamma \hat{e}_z \cdot (\nabla_t \times \mu_r^{-1} \hat{e}_z \times \vec{A}_t^c) \\ - \hat{e}_z \cdot (\nabla_t \times \mu_r^{-1} \hat{e}_z \times \nabla_t(\gamma \psi + A_z)) \\ - k_0^2 \epsilon_r (\gamma \psi + A_z) + \gamma k_0 \epsilon_r (k_0 \psi - jV) \end{aligned} = 0. \quad (17)$$

As before, we must state (4) explicitly to prevent ambiguities for $k_0 \rightarrow 0$. Using (10), we obtain

$$\begin{aligned} \nabla_t \cdot \epsilon_r [k_0 \vec{A}_t^c + \nabla_t(k_0 \psi - jV)] \\ + \gamma \epsilon_r [\gamma(k_0 \psi - jV) - k_0(\gamma \psi + A_z)] \end{aligned} = 0. \quad (18)$$

Eqs. (16)-(18) provide a common basis for a broad variety of waveguide solvers. Specific implementations differ mainly in the choice of gauge.

III. FINITE ELEMENT IMPLEMENTATION

In case of lowest order elements, we represent \vec{A}_t^c by the co-tree variables of edge elements [1] and the scalar-valued functions A_z , ψ , and V by the corresponding nodal basis. By applying a Galerkin process to (16)-(18), we arrive at a second order generalized algebraic eigenvalue problem of the form

$$\begin{pmatrix} A_{11} & A_{12} & 0 & A_{14} \\ A_{21} & A_{22} & 0 & A_{24} \\ 0 & 0 & A_{33} & 0 \\ A_{41} & A_{42} & 0 & A_{44} \end{pmatrix} - \gamma \begin{bmatrix} 0 & 0 & B_{13} & 0 \\ 0 & 0 & B_{23} & 0 \\ B_{31} & B_{32} & 0 & B_{34} \\ 0 & 0 & B_{43} & 0 \end{bmatrix}$$

$$-\gamma^2 \begin{pmatrix} C_{11} & C_{12} & 0 & 0 \\ C_{21} & C_{22} & 0 & 0 \\ 0 & 0 & 0 & 0 \\ 0 & 0 & 0 & C_{44} \end{pmatrix} \begin{bmatrix} \bar{x}(A_t^c) \\ \bar{x}(\psi) \\ \bar{x}(A_z) \\ \bar{x}(jV) \end{bmatrix} = \begin{bmatrix} 0 \\ 0 \\ 0 \\ 0 \end{bmatrix}, \quad (19)$$

where \bar{x} stands for an unknown coefficient vector. We do not give specific expressions for the submatrices in (19) but mention that some of them are wavenumber-dependent.

IV. PERMISSIBLE GAUGE TRANSFORMATIONS

Since the formulation (16)-(18) contains three different types of scalar functions, we ought to clarify what constraints one may impose on the system without affecting the generality of the field approximation. Eqs. (14) and (15) show that the EM fields just depend on two independent linear combinations of V , ψ , and A_z rather than all three scalars. By substituting

$$\alpha(x, y) = \gamma \psi(x, y) + A_z(x, y), \quad (20)$$

$$\beta(x, y) = k_0 \psi(x, y) - jV(x, y) \quad (21)$$

for the relevant terms, we obtain

$$\vec{B}(x, y) = \nabla_t \times \vec{A}_t^c - \hat{e}_z \times (\gamma \vec{A}_t^c + \nabla_t \alpha), \quad (22)$$

$$\vec{E}(x, y) = -j c_0 (k_0 \vec{A}_t^c + \nabla_t \beta) - j c_0 (k_0 \alpha - \gamma \beta) \hat{e}_z. \quad (23)$$

The differential equations now take the form

$$\begin{aligned} \nabla_t \times \mu_r^{-1} \nabla_t \times \vec{A}_t^c - k_0^2 \epsilon_r \vec{A}_t^c - k_0 \epsilon_r \nabla_t \beta \\ + \gamma \hat{e}_z \times \mu_r^{-1} \hat{e}_z \times (\gamma \vec{A}_t^c + \nabla_t \alpha) = 0, \end{aligned} \quad (24)$$

$$\begin{aligned} -\hat{e}_z \cdot [\nabla_t \times \mu_r^{-1} \hat{e}_z \times (\gamma \vec{A}_t^c + \nabla_t \alpha)] \\ - k_0^2 \epsilon_r \alpha + \gamma k_0 \epsilon_r \beta = 0, \end{aligned} \quad (25)$$

$$\nabla_t \cdot \epsilon_r (k_0 \vec{A}_t^c + \nabla_t \beta) + \gamma \epsilon_r (\gamma \beta - k_0 \alpha) = 0. \quad (26)$$

Eqs. (22) and (23) imply that, in order to avoid non-physical restrictions on the electromagnetic fields, the gauge must not impose any constraints on the scalar functions $\alpha(x, y)$ and $\beta(x, y)$. We propose to either formulate in (α, β) directly or, for more physical insight, use (A_z, V) and set

$$\psi(x, y) = 0. \quad (27)$$

We mention one disadvantage of the proposed formulation. By plugging $\psi = 0$ into the algebraic system (19), one can see that the linear term in γ does not vanish.

In the following, we will show that constraints on A_z or V lead to less general formulations.

V. ANALYSIS OF AXIAL GAUGE

In [2], it was proposed to impose a gauge by setting

$$A_z(x, y) = 0, \quad (28)$$

which is equivalent to deleting the third row and column in the algebraic system (19). The fact that (19) reduces to a linear eigenvalue problem for γ^2 makes this choice of gauge very appealing.

However, note that (20) now reads

$$\alpha = \gamma \psi. \quad (29)$$

At $\gamma = 0$, the scalar function α fails to serve as an independent variable, and we have

$$\alpha(x, y) = 0, \quad (30)$$

$$\vec{B}(x, y) = \nabla_t \times \vec{A}_t^c \quad \parallel \hat{e}_z, \quad (31)$$

$$\vec{E}(x, y) = -j c_0 (k_0 \vec{A}_t^c + \nabla_t \beta) \quad \perp \hat{e}_z. \quad (32)$$

For (31) and (32) imply $\vec{B} \parallel \hat{e}_z$ and $\vec{E} \perp \hat{e}_z$, the formulation will have trouble with transverse magnetic (TM) modes close to cut-off. In addition, the method supports wavenumber-independent null field solutions [2] of the form

$$\gamma = 0; \psi \text{ arbitrary}, jV = k_0 \psi, A_t^c = 0; \vec{B} = 0, \vec{E} = 0. \quad (33)$$

VI. V-GAUGE AND FIELD FORMULATION

Let us impose the gauge by constraining V . We now have

$$V(x, y) = 0, \quad (34)$$

$$\beta(x, y) = k_0 \psi(x, y). \quad (35)$$

Since $k_0 \rightarrow 0$ enforces $\beta \rightarrow 0$, the scalar function $\beta(x, y)$ fails to serve as an independent variable in the static limit. As a result, the formulation may lead to numerical instabilities in the low frequency case.

To eliminate the linear term in the eigenvalue problem (19), one may perform a transformation of variables [3]. However, close to cut-off it may prove difficult to undo the transformation. Moreover, the modified formulation supports wave-number independent null field solutions [3] of the form

$$\gamma = 0; \vec{A}_z \text{ arbitrary}, \psi = 0, A_t^c = 0; \vec{B} = 0, \vec{E} = 0. \quad (36)$$

Eq. (8) shows that the field formulation is equivalent to the present method but for a scaling factor of $-j c_0 k_0$. Hence field-based algorithms [3] [4] [5] are expected to exhibit similar behavior as the V-gauge approach.

VII. CONCLUSION AND OUTLOOK

Our analysis of potential- or field-based waveguide solvers has shown that the use of a particular gauge can overcome the shortcomings of existing finite element formulations. In the full paper, we will detail the underlying theory and present numerical examples to validate our findings.

REFERENCES

- [1] R. Albanese and R. Rubinacci, "Solution of three dimensional eddy current problems by integral and differential methods," *IEEE Trans. Magn.*, vol. 24, pp. 98 - 101, 1988.
- [2] S.V. Polstyanko, R. Dyczij-Edlinger, and J.F. Lee, "Fast Frequency Sweep Technique for the Efficient Analysis of Dielectric Waveguides," *IEEE Trans. Microwave Theory Tech.*, vol. 45, no. 7, pp. 1118 - 1126, 1997.
- [3] J.F. Lee, D.K. Sun, Z.J. Cendes, "Full-Wave Analysis of Dielectric Waveguides Using Tangential Vector Finite Elements," *IEEE Trans. Microwave Theory Tech.*, vol. 39, pp. 1262 - 1271, 1991.
- [4] I. Bardi et al., "Nodal and Edge Element Analysis of Inhomogeneously Loaded Waveguides," *IEEE Trans. Magn.*, vol. 29, pp. 1466 - 1469, 1993.
- [5] B.M. Dillon, A.A.P. Gibson, and J.P. Webb, "Cut-off and Phase Constants of Partially Filled Axially Magnetized, Gyromagnetic Waveguides Using Finite Elements," *IEEE Trans. Microwave Theory Tech.*, vol. 41, pp. 803 - 808, 1993.

Microwave Drying of Cylindrical Products

Dr.M.A.Saber

21 BLDG 1560 , Road 625, Manama Town 306
State of Bahrain

Abstract: Application of microwave power for drying of products in cylindrical form is presented . Numerical analysis of mass and heat transfer of the processed material using microwave energy and hot air , is carried out. The system is nonlinear one. Three dimensional finite difference using the polar coordinate system(curved boundaries) is the cornerstone of the solution of the system. To avoid physical and chemical or biological changes during manipulation, such technique possess implicit energy balance and control.

Keywords: Cylindric Products , Microwave applicator, Finite difference , Hot air, Microwave power , Hybrid drying , energy control.

Introduction

Recent attention has been given to the spatial distribution of temperature (due to microwave energy processing)within the product . The advantages and suitability of microwaves and hot air are related to their unique volumetric drying and the effects that produces. Hybrid drying phenomena has been analyzed by the author [1] .

This paper is devoted for drying out moisture contents of products of cylindric shapes. Microwave power required for drying is related to the quantity of moisture contained in the processed material. The profile of the power is determined by repartition of the water contents in the porous medium and its evolution with time. The waves , then dissipate their energy , preferentially, in the regions of higher humidity and so they have the tendency to behave as a factor of auto regulation of the humidity distribution. Change of mass m and temperature T , as a functions of the material thickness z , during hybrid drying is already analyzed [1]. Simulation is performed for a material of isothermal moisture content and mass transfer analogue of temperature.

Mathematical Formulation

(a) The Governing Equation

The heat and mass transfer equations which describe the drying process can be respectively expressed by the following equations[1-2] :

$$dT/dt = (1/\rho_0 c') [(d/dt)A_q dT/du] + (e'L/c')dm/dt + P_{m.w} \quad (1)$$

$$dm/dt = d/du \{a_m[dm/du + \eta dT/du]\} \quad (2)$$

Where A_q is the coefficient of thermal conductivity in the coordinate directions (r, Θ and z) and it is measured as a nonlinear function of humidity[2], L is the latent heat of evaporation of free water , e' is the coefficient of phase change , c' is the specific heat of the processed material and ρ_0 is its bulk density , a_m is the mass diffusion coefficient (in r, Θ and z directions), $m=M/M_0$, M and M_0 are respectively masses of humidity and dried body, η is the coefficient of thermo migration (in r, Θ and z directions). For the

underlying case η and a_m are the same in all the coordinate directions. T is the absolute temperature, t is the time and $P_{m.w}$ is the microwave power. Equation (1) represents conservation of energy for the system, d/du is the derivative with respect to polar coordinates.

(b) The Solution Technique and Finite Difference Formulation: Using CRANK-NICHOLSON finite difference relation[3] , for polar coordinates , in equations (1) and (2) , and after some mathematical arrangements the results can be written in the following form :

$$A \begin{vmatrix} m \\ T \end{vmatrix}^{n+1} = B \begin{vmatrix} m \\ T \end{vmatrix}^n \quad (3)$$

Where $n+1$ and n denote new and old iterated values, $[A]$ and $[B]$ are the coefficient matrices.

Boundary Conditions

The total surface boundary conditions[1] must satisfy the following requirements :

- 1- Continuity of the heat flux .
- 2- The total mass flux that reaches the surface must be equal to the vapor flux.

For the material cross-section, the used finite difference calculation grid must be suitable for the curved boundaries shown in fig.1 . And therefore, polar coordinate form of the finite difference technique is applied to get the solution of the problem. Fig.2 shows the geometry of calculation of a point (i, j) in the calculating grid shown in fig. 1 .

As for the material center the difference between the fiction line, surface and interior of the product can be expressed as follows:

$$dT_1^n/dz = (T_2^n - T_0^n) / 2 HZ \quad (4)$$

$$dm_1^n/dz = (m_2^n - m_0^n) / 2 HZ \quad (5)$$

Where HZ is the step length in z direction, 0 , 1 and 2 respectively denote fiction line , surface and interior of the product (as shown in fig. 3).

Determination of Dissipated Microwave Power

The microwave power term, in equation1 illustrates the power dissipated into the processed material. It is important to precise such term in order to obtain good results. From equations 1 and 2 , using boundary, central and initial conditions, the humidity $m(r, \Theta)$ can be determined and hence from the known measured curves between m and the dielectric constant ϵ , and the loss $\tan \delta$, the corresponding values of ϵ and $\tan \delta$ can be determined. The length d of the cylindrical material is divided into n parallel dielectric discs as shown in fig.4 . Each has a number i ($i=1, 2, 3, \dots, n$), thickness equal to d/n , permittivity ϵ_i , conductivity O_i , and constant humidity m_i . Each disc is separated from the others by infinitesimal air cell. Repartition of sources of radiation is done in the two directions of

z axis in such a way that the radiation is symmetric with respect to the middle plane of the material and this is means it is a bilateral one [1]. The dimensions of the product inside the applicator and the distribution of the electromagnetic sources maintain constant dissipated power during manipulation. The power dissipated in one dielectric disc is determined as the difference between the incident and reflected ones and the total bilateral dissipated power per unit surface area can be written[1] as follows :

$$P_t = (1/2) ([A_1]^2 - [B_1]^2) \times 2 \quad (6)$$

Where A_1 and B_1 are respectively amplitude of the incident and reflected waves at the interface between the air and the dielectric .

Simulation Results

Due to the temperature results caused by the microwave power $P_{m.w}$ the values of both m^n and T^n can be known . Then by iteration and use of equation 3 , the new iterated values could be determined. Iteration process is repeated until the required object is reached . The profile of the dissipated microwave power is calculated and it is contained in the main program with the help of sub – program (Hyper).

To get rapid drying the cylinder is exposed to microwave power radiations from its two sides (i.e +ve and –ve directions of its longitudinal axis z), and this is called bilateral radiation . The obtained profile of the total used microwave power as a function of z has oscillating shape and this is due to standing wave phenomena which occurs with the bilateral radiation (more details exist in reference1).

Simulation is done for drying of solid cylinder of sand with diameter equals to 30 cm, length of 10 cm and other data given in table 1. The evolution of temperature (fig. 5) as a function of the radial distance R and angular coordinate Θ of the cylinder is

Table 1
Data Used in Simulation

Initial Profile of Humidity, m	15%
Initial Profile of Temperature, T	293 ⁰ K
Ambient Air Temperature, T _a	363 ⁰ K
Humidity of Drying Air,	0.1 m _{sat}
Frequency of Operation, F	2.45 GHz
Step Length in r direction, HR	0.25 cm
Step Length in Θ direction, H Θ	3 deg
Step of Time, HT	30 sec
Saturated Humidity, m _{sat}	0.4
Heat Capacity of Dry Body, CP ₀	5 J/gk
Heat Capacity of Water,, CPE	4.18 J/gk
Bulk Density of the Material, ρ_0	1 g/cm ³
Latent Heat Generation Source, L	2200 W/m ³
Biot Number, NB	0.5
Transformed Biot Number, NBT	1000
Velocity of Light, C	3x10 ¹⁰ cm/sec
Loss Tang δ of Water	0.1
Loss Tang δ of Dried Sand	0.013
Relative Dielectric Constant Of Dried Sand, ϵ_{r1}	2.4
Relative Dielectric Constant Of Water, ϵ_r	40
Step Length in z Direction, HZ	0.5 cm

illustrated for drying time equals 1.5 hours , ambient temperature $T_a = 90^{\circ}C$, with hot air and without microwave power. Simulation is carried out for hybrid drying (i.e. drying with hot air and microwave power) of the same mentioned specimen. Evolution of temperature T(⁰C) is given as a function of cylindrical coordinates as shown in fig. 6.

The obtained results displayed on the temperature surfaces of fig. 5 and 6 assure that microwave energy is dissipated in the regions where the humidity is higher and so temperature rise occurs.

Conclusions

Hybrid drying is more faster than conventional one, besides it gives products which meet the user requirements. Standing wave phenomena has been occurred due to bilateral radiation. Microwave energy permits more and rapid migration of humidity from the heart to the surface of the cylindric product and therefore more water are obtained on the surface of the material. Simulation of 3-D hybrid drying , for cylindric products is more difficult than that for cubic ones studied in reference [1].

References

- [1]-M.A.Saber “ Three Dimensional Heat and Mass Transfer Using Microwave Energy” 26 th conference of Microwave Power and microwave Technology, Aug 1991 BUFFALO, NY, U.S.A.
- [2]-Presi.A.”Etude de l’amelioration du rendement des techniques de Sechage des materiaux epais par apport d’energie electromagnetique conception d’applicateur” These I.N.P , Toulouse ,French 1998
- [3]-J.Crank, “Numerical Solutions of Partial Differential Equations-Finite Difference Methods” 2nd edition, ch.5 .Oxford, 1978.
- [4]-Bruce W.Arden “Numerical Algorithms: Origins and Applications” Addison Wesley Comp,1970.

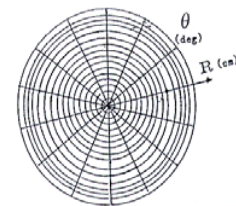


Fig. 1 Cross section of the processed material as a calculating grid.

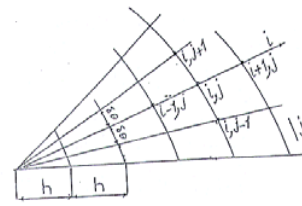


Fig. 2 Geometry of a calculated point (node i, j) in the grid shown in the fig. 1.

Proposal of Detecting Method of Plural Cracks and Their Depth by Alternating Flux Leakage Testing

- 3-D Nonlinear Eddy Current Analysis and Experiment -

Yuji Gotou* and Norio Takahashi**

*Department of Electronics Engineering, Chugoku Polytechnic College,
1242-1 Nagao, Tamashima, Kurashiki, 710-0251, Japan
e-mail: gotou@eplab.elec.okayama-u.ac.jp

**Department of Electrical and Electronic Engineering, Okayama University,
3-1-1 Tsushima, Okayama 700-8530, Japan
e-mail: norio@eplab.elec.okayama-u.ac.jp

Abstract— The alternating magnetic flux leakage testing is used for the detection of cracks on the surface of steel plate. In this paper, a new technique of how to detect plural cracks and their depth, which are located at very short distance each other, is proposed. The leakage flux density of the parallel (x-) component is used for the distinction of the plural cracks. Moreover, the depth of plural cracks is obtained by changing the exciting frequency and by detecting the perpendicular (z-) component of leakage flux. The behavior of leakage flux is examined using 3-D edge-based hexahedral FEM and compared with experiment.

evolution strategy.

The condition of analysis is shown in Table I. In order to get the steady state periodic result, the calculation is carried out during 2.5 period (=40 steps). The yoke is assumed to be linear (relative permeability: 60,000) and the eddy current in it is neglected. The condition of evolution strategy is shown in Table II.

I. INTRODUCTION

The alternating magnetic flux leakage testing has been applied in the inspection process for detecting cracks on the surface of steel. We have already reported that the detection of the parallel component (B_x) of the leakage flux density is effective in inspecting plural cracks[1]. However, the detection technique of depth of plural cracks is not established yet. There may be some possibility to detect the depth of the crack by the amplitude of B_x or B_z . But, the depth of the cracks cannot be inspected when plural cracks are located at very short distance, because the amplitude is influenced by the adjacent cracks.

In this paper, a technique of how to detect plural cracks and their depth, which are located at very short distance, is investigated by 3-D edge-based hexahedral FEM. In order to detect plural adjacent cracks, a differential type search coil for detecting B_x is proposed. The dimension of the search coil is optimized by the evolution strategy. Moreover, a new method for detecting the depth of plural cracks using the perpendicular component (B_z) of leakage flux, which is detected by changing the exciting frequency, is proposed. The experimental investigation is also carried out.

II. MODEL AND METHOD OF ANALYSIS

Fig.1 shows a model of testing apparatus. The ac field from the electromagnet magnetizes the steel. The search coils shown in Fig.1(b) is used. These coils consist of the differential type search coil of B_x , and single coil of B_z . The dimension of the differential type coil is optimized using the

TABLE I
CONDITIONS OF ANALYSIS AND EXPERIMENT

Exciting coil	1A(rms), 30turns×2
Steel	SS400, $\mu_{r,max}=1500$, $\sigma = 7.51 \times 10^6$ S/m
Nodes and elements	88095, 83232
Convergence criterion	N-R method 0.01T ICCG method 1.0×10^{-3}

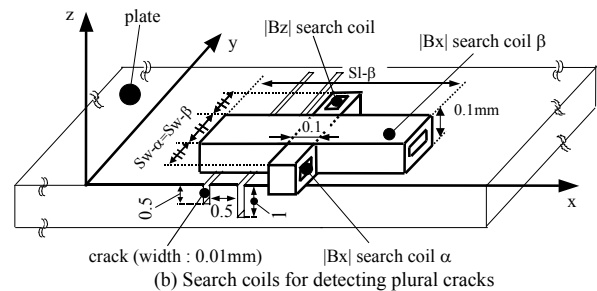
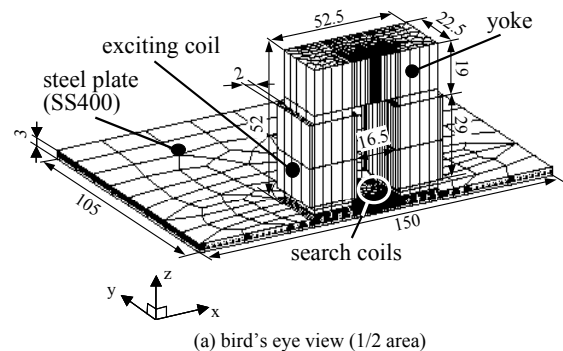


Fig.1. Model for alternating flux leakage testing of plural cracks.

TABLE II
CONDITIONS OF EVOLUTION STRATEGY

Design variable	SI- β , Sw- α (=Sw- β)
Optimization condition	The differential value of $ B_x $ should be maximum. SI- β should be minimum.
Restrictions condition	1mm < SI- β < 150mm 1mm < Sw- α (=Sw- β) < 15mm
Initial value	SI- β =1mm, Sw- α (=Sw- β)=5mm
Convergence criterion	standard deviation σ : 0.5 (Initial value : 75)

III. RESULTS OF ANALYSIS AND EXPERIMENT

Fig.2 shows the distribution of $|B_x|$ when the depth of two cracks is different. The depth of a left-side crack and that of a right-side crack are 0.5mm and 1mm, respectively. The exciting frequency is 1kHz. The width (x-direction, C_w) and the length (y-direction, C_l) of both two cracks are 0.01mm and 100mm, respectively. The figure denotes that two cracks can be detected by the differential type search coil. The result obtained by the optimal design method is also shown in the figure. $|B_x|$ detected by the optimal coil is increased about 8% compared with the initial coil.

Fig.3 shows the distribution of B_x of one, two and four cracks detected using the optimal coil. The crack width (C_w), depth (C_d) and distance (L) of plural cracks are 0.5mm, 1mm and 0.5mm, respectively. The figure illustrates that even if C_d is constant, the amplitude of $|B_x|$ changes with the number of cracks. Therefore, it is difficult to presume C_d from the amplitude of $|B_x|$. The figure also denotes the agreement between calculation and measurement.

Fig.4 shows the effect of the skin depth δ , which corresponds to the exciting frequency, on $|B_z|$. In this case, the exciting current is kept constant (=1A(rms)). The frequency is changed from 100Hz to 10kHz. The skin depth δ is calculated using $\mu_s \max = 1500$ of steel. $\delta = 1.06\text{mm}$ and 0.047mm correspond to 20Hz and 10kHz, respectively. The figure denotes that if δ becomes smaller than C_d , $|B_z|$ is increased rapidly. Fig.5 shows the distribution of flux density near the crack. The figure illustrates that if δ (=0.047mm) becomes smaller than C_d (=0.1mm), the flux in steel is suppressed by the crack. Then, the leakage flux ($|B_z|$)

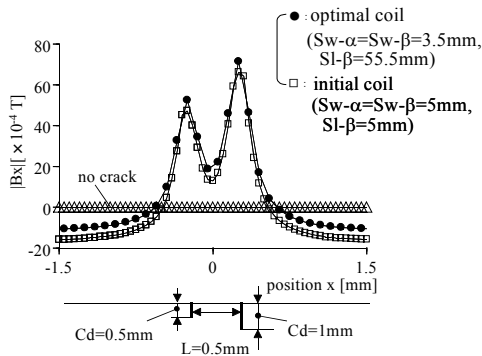


Fig.2. $|B_x|$ detected by initial and optimal coils ($f=1\text{kHz}$).

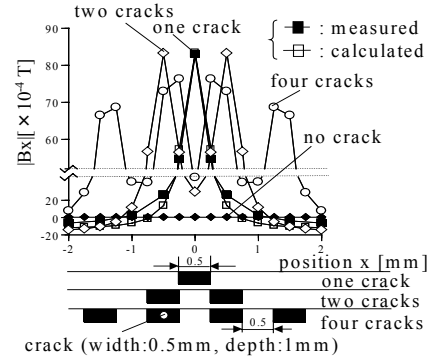


Fig.3. Detection of $|B_x|$ using differential search coils ($C_w=0.5\text{mm}$, $C_d=1\text{mm}$, $L=0.5\text{mm}$).

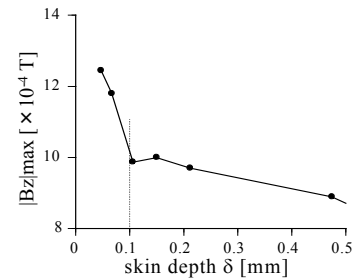


Fig.4. Relation between $|B_z|_{\max}$ and skin depth δ ($C_w=0.01\text{mm}$, $C_d=0.1\text{mm}$, $L=0.5\text{mm}$, exciting current=1A (rms)).

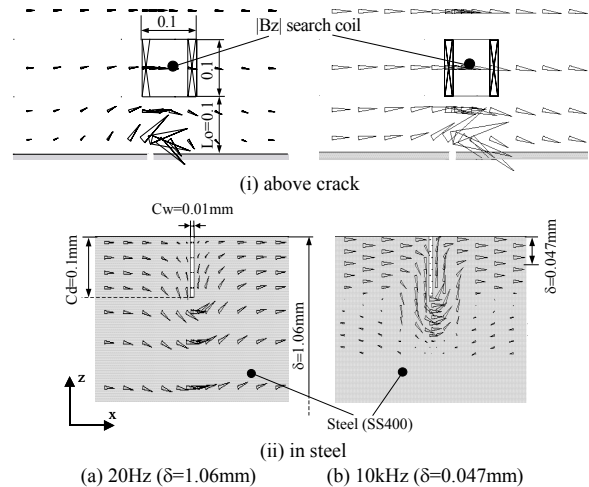


Fig.5. Distribution of flux density near the crack ($C_w=0.01\text{mm}$, $C_d=0.1\text{mm}$).

increases rapidly at the point of $\delta=C_d$.

The possibility of distinguishing the number of plural cracks and their depth will be discussed in detail by examining the distribution of leakage flux and experiment in the full paper.

REFERENCE

[1]Y.Gotoh, and N.Takahashi, "3-D nonlinear eddy current analysis of alternating flux leakage testing -analysis of one crack and two cracks-", *IEEE Trans., Magn.* vol.38, no.2, pp.1209-1212, 2002.

Eigenmode Simulation of Electromagnetic Resonator Cavities with Gyrotropic Materials

Stefan Feigh, Markus Clemens, Rolf Schuhmann and Thomas Weiland

Technische Universität Darmstadt, FB 18 Elektrotechnik und Informationstechnik,
Computational Electromagnetics Laboratory (TEMF), Schloßgartenstr. 8, D-64289 Darmstadt, Germany
email: feigh/clemens/schuhmann/weiland@temf.tu-darmstadt.de.

Abstract— For the numerical solution of complex eigenvalue problems, arising with gyrotropic materials in resonators, the Jacobi-Davidson method is considered. In this paper the correction equation, which has to be solved within the Jacobi-Davidson method, is simplified and several preconditioning strategies, including also a multigrid scheme, are compared for the approximate solution of this correction equation.

I. INTRODUCTION

Gyrotropic materials such as ferrites are used in modern cavity design for tuning and vacuum isolation purposes [1]. For most practical cavities the geometry is sufficiently complicated such that analytical solutions for the eigenmodes inside these cavities do not exist. The geometry of the test problem which is used for the further analysis of our numerical eigenvalue solver is sketched in Fig. 1. The simulation of electromagnetic fields in

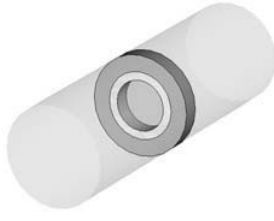


Fig. 1. Cylindrical resonator including a dielectric ring covered with a gyrotropic material

gyrotropic materials is not straightforward, since their material tensors typically are non-symmetric and complex-valued. Using the Finite Integration Technique (FIT) [2] for the simulation of electromagnetic waves in structures including gyrotropic materials leads to complex-valued, non-symmetric algebraic eigenvalue problems. For this task the Jacobi-Davidson subspace iteration method is adapted.

II. GYROTROPIC MATERIALS

Gyrotropic materials represent a subgroup of anisotropic materials with a second order material tensor. Those magnetic and electric tensor material characteristics are central to a broad class of complex materials such as plasmas and ferrites. The gyrotropic material properties are due to an electric or magnetic material tensor and thus such a material is either referred to as gyroelectric or gyromagnetic, respectively.

S. Feigh is supported by the graduate student programme 'Physik und Technik von Teilchenbeschleunigern' of the Deutsche Forschungsgemeinschaft (DFG) under grant GK-GRK 410/1.

In accelerator technique ferrites represent the most important gyrotropic material. Their magnetic material tensor for gyrotropic coupling is given by the Polder Tensor [3], which consists of complex diagonal and non-diagonal elements. For the further analysis it is of importance to note that $\vec{\mu}$ is complex and non-symmetric. The dielectric tensor of ferrite is diagonal.

III. NUMERICAL MODELING

Using the FIT for the numerical modeling the analytical eigenvalue equation $(\nabla \times \vec{\mu}^{-1} \nabla \times - \omega^2 \vec{\epsilon}) \vec{e} = 0$ results in the discrete algebraic eigenvalue equation:

$$(\tilde{\mathbf{C}} \mathbf{M}_{\mu^{-1}}(\omega) \mathbf{C} - \omega^2 \mathbf{M}_{\epsilon}(\omega)) \vec{e} = 0. \quad (1)$$

Where \mathbf{C} and $\tilde{\mathbf{C}}$ are symmetric matrices and represent the discrete curl operators. The operators $\mathbf{M}_{\mu^{-1}}$, \mathbf{M}_{κ} and \mathbf{M}_{ϵ} are the material-matrices and in case of gyrotropic materials they are non-diagonal, non-symmetric, complex and frequency dependent [4]. These matrices are obtained by introducing a grid on which the primary field components are allocated. The material distribution is discretized with respect to this grid and represented in the material matrices. Neglecting the frequency dependence of $\mathbf{M}_{\epsilon}(\omega)$ and $\mathbf{M}_{\mu^{-1}}(\omega)$ (1) by using an estimation frequency yields a linear generalized eigenvalue problem. For gyromagnetic materials \mathbf{M}_{ϵ} is diagonal and can be inverted easily. In this case a standard eigenvalue problem

$$\mathbf{A} \vec{e} = \omega^2 \vec{e}, \quad (2)$$

with the system-matrix $\mathbf{A} = \mathbf{M}_{\epsilon}^{-1} \tilde{\mathbf{C}} \mathbf{M}_{\mu^{-1}} \mathbf{C}$, has to be solved. For most applications in accelerator technology only the smallest dynamical eigenvalues are of interest. The solutions of (2) also include the static solutions with $\omega = 0$. Since these static solutions will be a problem when trying to find the lowest dynamical eigenvalues, a gauging can be performed by adding a grad-div augmentation [5] to (1).

IV. JACOBI-DAVIDSON METHOD

The Jacobi-Davidson (JD) subspace iteration method [6] is applicable to non-symmetric and complex matrices \mathbf{A} . In this approach a search subspace is generated onto which the given eigenvalue problem is projected. The projected eigenvalue problem is solved and this leads to an approximation for the original much larger eigenvalue problem. In each iteration step the search subspace is expanded by a correction vector \mathbf{v} which is computed by solving the correction equation

$$(\mathbf{I} - \mathbf{q}\mathbf{q}^T)(\mathbf{A} - \lambda\mathbf{I})(\mathbf{I} - \mathbf{q}\mathbf{q}^T)\mathbf{v} = -\mathbf{r}, \quad (3)$$

where \mathbf{q} is the estimated eigenvector, \mathbf{q}^T is the transposed vector of \mathbf{q} , λ is the approximated eigenvalue and \mathbf{r} is the residual vector of the eigenvalue problem, approximately.

$$\mathbf{r} = (\mathbf{A} - \lambda\mathbf{I})\mathbf{q}. \quad (4)$$

The correction equation (3) has to be solved only approximately. However, for large problems as they commonly arise with 3D simulations the computation of (3) is the most time consuming part in this algorithm. For the test problems it is found, that also a solution of

$$\mathbf{A}\mathbf{v} = -\mathbf{r} \quad (5)$$

would result in a convergence of the JD method. For the test problem the convergence history computing the 3 lowest eigenvalues is plotted in Fig. 2 using (3) and (5). The solution of the

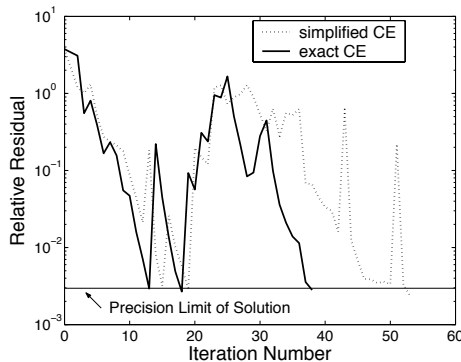


Fig. 2. Relative residual versus iteration step for the solution of the exact and simplified correction equation (CE), computing the 3 lowest eigenvalues of the test problem.

exact correction equation (3) indeed shows faster convergence in terms of the required number of iterations. The more important criterion, namely the time consumption, will be discussed in the next section.

V. INTERIOR SOLVERS

For the solution of (3) and (5) in the JD algorithm the iterative BICGSTAB method is used. It is found that a relative residual of 10^{-2} results in the fastest convergence of the JD algorithm. Solutions with a smaller residual do not result in sufficiently smaller numbers of iterations, whereas more inaccurate solutions will increase the number of iterations or may lead to a stagnation of the exterior JD method.

The number of iterations and the computation time for the JD method computing the lowest eigenvalue using (3) and (5) (solved with BICGSTAB) are stated in Table I.a and Table I.b respectively. Different preconditioners such as the incomplete LU factorization, Jacobi and SSOR were applied to the BICGSTAB-solver. As Table I shows, the best results can be obtained using the incomplete LU factorization. However, for large systems the ILU factorization itself is extremely time consuming and therefore not suitable for our problems. A different possibility to solve (5) approximately is to replace \mathbf{A} with an easily invertible approximation of itself, such as the incomplete LU factorization (Table I.d) and the Gauss-Seidel decomposition (Table I.e) of

Correction Equation	Mv=-r	Iter.	Time
a.) $\mathbf{M} = (\mathbf{I} - \mathbf{q}\mathbf{q}^T)(\mathbf{A} - \lambda\mathbf{I})(\mathbf{I} - \mathbf{q}\mathbf{q}^T)$ - BICGSTAB(tol= 10^{-2})		16	65s
b.) $\mathbf{M} = \mathbf{A}$ - BICGSTAB(tol= 10^{-2}) - BICGSTAB(tol= 10^{-2} , ILU(0)) - BICGSTAB(tol= 10^{-2} , JACOBI) - BICGSTAB(tol= 10^{-2} , SSOR)		21 10 20 19	31s 20s 38s 36s
c.) $\mathbf{M} = \mathbf{I}$ - exact		542	212s
d.) $\mathbf{M} = \tilde{\mathbf{L}}\tilde{\mathbf{U}} + \mathbf{R}$ - exact: $\mathbf{v} = \tilde{\mathbf{U}}^{-1}\tilde{\mathbf{L}}^{-1}(-\mathbf{r})$		114	48s
e.) $\mathbf{M} = (\mathbf{D} + \mathbf{L})\mathbf{D}^{-1}(\mathbf{D} + \mathbf{U})$ - exact		143	70s
f.) Multigrid-solver $\mathbf{M} = \mathbf{A}$ (tol= 10^{-2})		21	25s

TABLE I

Computation time and number of inner iteration steps, calculating the lowest eigenvalue of the test problem (10^4 gridpoints), for different correction equations and solvers on a 1.8GHz PC using a MATLAB implementation. The first argument of the BICGSTAB solver refers to the tolerance of the solution (relative residuum) and the second argument refers to the applied preconditioner. The matrix \mathbf{L} represent the lower triangular part respectively \mathbf{U} the upper triangular part of the matrix \mathbf{A} . \mathbf{D} is the diagonal of \mathbf{A} .

A. Once \mathbf{A} is substituted in this way, an exact solution of the obtained approximation can be derived. Even the approximation $\mathbf{A}=\mathbf{I}$ leads to convergence of the JD method (Table I.c), but the convergence is rather slow.

A new promising method lies in the approximate solution of the algebraic system $\mathbf{A}\mathbf{x} = -\mathbf{r}$ by using a multigrid scheme [7]. A geometrical multigrid method solving $\mathbf{A}\mathbf{x} = -\mathbf{r}$ was developed and implemented in MATLAB. Using this multigrid solver in the JD method a competitive computation time was achieved (see Table I.f) for this small problem size. Since the asymptotic complexity of multigrid solvers are superior to that of standard solvers it seems to be best suited for this task.

REFERENCES

- [1] I.S.K. Gardner, "Ferrite Dominated Cavities", CERN Accelerator School Vol. II, Geneva, p.349-347, 1992.
- [2] T. Weiland, "Time Domain Electromagnetic Field Computation with Finite Difference Methods", International Journal of Numerical Modelling, Vol. 9, pp. 295-319 (1996).
- [3] D. Polder, "On the Theory of Ferromagnetic Resonance", Philosophical Magazine, Vol. 40, p.99-115, 1949.
- [4] Holm Krüger, H.Spachmann, T.Weiland, "FIT-Formulation for Gyrotropic Media", Proceedings ICEEA Conference, Turin, Italy, S.737-740, 2000.
- [5] T. Weiland, "On the Unique Numerical Solution of Maxwellian Eigenvalueproblems in Three Dimensions", Particle Accelerators Vol. 17 (1985), pp. 227-242.
- [6] Diederik R. Fokkema, Gerard L.G. Sleijpen, and Henk A. Van der Vorst, "Jacobi-Davidson style QR and QZ algorithms for the partial reduction of matrix pencils", Preprint 941, Department of Mathematics, University Utrecht (January, 1996), SIAM J. Sc. Comput., 20:1 (1998), pp. 94-125.
- [7] Ulrich Trottenberg, Cornelius Oosterlee, Anton Schüller, "Multigrid", Academic Press, New York, 2001.

Approximate Methods for the Calculation of the ECT Signal of a Crack in a Plate Coated by Conducting Deposit

József Pávó

Department of Electromagnetic Theory, Budapest University of Technology and Economics
H-1521 Budapest, Hungary, e-mail: pavo@evtsz1.evt.bme.hu

Abstract— Approximate methods for the calculation of the interaction of a pancake type exciting coil and a crack in a non-ferromagnetic conducting plate covered by a thin layer of conducting deposit are presented. The perturbations caused by the presence of the crack and the deposit are represented by secondary sources that actual values are obtained by the solution of a set of integral equations. Using different approximations, the coupling between these integral equations can be reduced, as a result, fast calculation methods are obtained for the prediction of the signal of the investigated eddy current testing (ECT) arrangement.

INTRODUCTION

The eddy current testing (ECT) signal of a crack is significantly modified if various deposits are accumulated on the surface of the tested specimen. In fact, in most cases the signal due to the presence of a deposit is considerably larger than the signal of the crack, so the real question in such situations is the detection of the crack that signal is shaded by the signal of the deposit. This statement is especially true for the situations when the deposit and the crack are located on the same side of the plate that is actually inspected from the opposite side by a conventional pancake type induction probe (OD type crack and deposit). Limited number of experimental results are available on such configurations among the JSAEM Benchmark Problems #5 [1]. One possible way to detect cracks in plates coated by deposits might be the application of some inversions technique that can be based on optimization or neural networks. For the implementation of such methods, the fast solution of the forward problem plays an important role that is used either for the evaluation of the function calls in the optimization loop or for the generation of data base for teaching the neural network.

General purposes codes developed for electromagnetic field calculation (such as finite element or boundary element codes) cannot be easily applied without modification for ECT because of the spatially concentrated nature of the defects compared to the rest of the arrangements. If, however, the mentioned techniques are applied, special effort should be made to decompose the small field perturbation caused by the defect from the large electromagnetic field due to the defect-free configuration [2], [3]. Previously, for plate specimens, we published calculation methods used for the fast evaluation of the ECT signal of crack type defects [4] (for time harmonic excitations) and thin, uniform thickness deposits [5], [6] (for time harmonic and time dependent excitations, respectively). The combination of these results leads to the development of a method that can be used for the calculation of the ECT signal of cracks in a plate coated by thin uniform thickness deposit. In the following this calculation model is outlined.

NUMERICAL MODEL

Consider the configuration shown in Fig. 1, where an arbitrary shape cylindrical ECT coil scans above a non-ferromagnetic infinite plate that thickness and conductivity are h and σ , respectively. The exciting field vary in time as the real part of $\exp(j\omega t)$. The metal deposit is located on that surface of the conductor that is on the opposite side where the excitation is. The shape of the deposit in the x - y plane is arbitrary, while it is assumed that its thickness, d , is uniform and considerably smaller than the thickness of the plate. The deposit is modeled as a linear material that conductivity and permeability are σ_d and μ_d , respectively. The plane of the assumed infinitesimally thin crack is perpendicular to the plane of the plate and its conductivity is zero.

According to the crack and deposit models [4-7], secondary sources are used for the representation of the presence of these objects in the otherwise homogeneous plate. Specifically, the infinitesimally thin crack is represented by an x -directed current dipole layer distribution, $p(y,z)$, concentrated on the surface of the crack, S_c (see Fig. 1). The thin deposit is represented by tangential surface electric, $\mathbf{K}(x,y)$, and magnetic, $\mathbf{M}(x,y)$, current distributions on surface S_d that is the surface occupied by the deposit on the surface of the plate (see Fig. 1). Considering the linearity of the outlined problem, the total electromagnetic field generated by the interaction of the exciting coil and the described arrangement can be written as the sum of three electromagnetic fields as,

$$\begin{aligned} \mathbf{H} &= \mathbf{H}^e + \mathbf{H}^d + \mathbf{H}^c \\ \mathbf{E} &= \mathbf{E}^e + \mathbf{E}^d + \mathbf{E}^c \end{aligned} \quad (1)$$

where superscript, e , denotes the electromagnetic field calculated from the interaction of the exciting coil and the plate (here the presences of the deposit and the crack are neglected). Superscripts, d and c , stand for the electromagnetic fields that are generated by the secondary sources representing the deposit ($\mathbf{K}(x,y)$, $\mathbf{M}(x,y)$) and the crack ($p(y,z)$), respectively. Assuming the infinite plate geometry, the electromagnetic field due to the secondary sources (\mathbf{E}^d , \mathbf{H}^d , \mathbf{E}^c , \mathbf{H}^c) can be expressed with the help

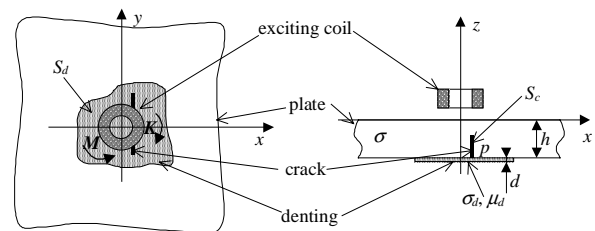


Fig. 1. The investigated ECT arrangement.

of dyadic Green's functions. The field of the excitation (\mathbf{E}^e , \mathbf{H}^e) can be obtained by any field calculation method, in most cases it is given analytically.

The already known secondary sources can be obtained from the boundary conditions applicable at the given object, namely the impedance type boundary conditions at the deposit and the requirement that there is no current flowing across the surface of the crack. From these requirements we obtain that the total electromagnetic field, \mathbf{E} and \mathbf{H} , must satisfy the following conditions,

$$\begin{aligned} \frac{\eta}{\sigma_d} \coth\left(\frac{d\eta}{2}\right) [\mathbf{H}_t^+(\mathbf{r}) - \mathbf{H}_t^-(\mathbf{r})] &= -\hat{z} \times [\mathbf{E}^+(\mathbf{r}) + \mathbf{E}^-(\mathbf{r})], \quad \mathbf{r} \in S_d, \quad (2) \\ \frac{\sigma_d}{\eta} \coth\left(\frac{d\eta}{2}\right) [\mathbf{E}_t^+(\mathbf{r}) - \mathbf{E}_t^-(\mathbf{r})] &= \hat{z} \times [\mathbf{H}^+(\mathbf{r}) + \mathbf{H}^-(\mathbf{r})] \\ \mathbf{E}(\mathbf{r}) \cdot \hat{x} &= 0, \quad \mathbf{r} \in S_c, \quad (3) \end{aligned}$$

where $\eta = (1 + j)\sqrt{\omega\mu_d\sigma_d/2}$ and \hat{x} , \hat{y} , \hat{z} are the unit vectors of the co-ordinate directions. Subscript t denotes the tangential components of the vectors, while superscripts + and - stand for the field components on the upper side ($z=h+0$) and lower side ($z=h-0$) of the surface S_d , respectively.

Writing the Green's function expression of the field of the secondary sources into (2) and (3), a system of integral equations is obtained that numerical solution provides the actual distribution of the secondary sources. Knowing this, the impedance variation, ΔZ , of the exciting coil can be expressed based on the reciprocity theory as,

$$I^2 \Delta Z = - \int_{S_d} [\mathbf{E}^e(\mathbf{r}) \cdot \mathbf{K}(\mathbf{r}) - \mathbf{H}^e(\mathbf{r}) \cdot \mathbf{M}(\mathbf{r})] d\mathbf{r} - \int_{S_c} \mathbf{E}^e(\mathbf{r}) \cdot \hat{x} p(\mathbf{r}) d\mathbf{r}, \quad (4)$$

where I is the amplitude of the exciting current of the coil.

APPROXIMATION METHODS

Assume that the deposit and the crack are not interacting with each other, that is,

$$\mathbf{H}^c(\mathbf{r}) \ll \mathbf{H}^e(\mathbf{r}), \mathbf{H}^d(\mathbf{r}), \quad \mathbf{E}^c(\mathbf{r}) \ll \mathbf{E}^e(\mathbf{r}), \mathbf{E}^d(\mathbf{r}), \quad \mathbf{r} \in S_d, \quad (5)$$

$$\mathbf{H}^d(\mathbf{r}) \ll \mathbf{H}^e(\mathbf{r}), \mathbf{H}^c(\mathbf{r}), \quad \mathbf{E}^d(\mathbf{r}) \ll \mathbf{E}^e(\mathbf{r}), \mathbf{E}^c(\mathbf{r}), \quad \mathbf{r} \in S_c. \quad (6)$$

In this case (2) and (3) are decoupled, consequently their solution provides the simple superposition of the perturbations caused by the deposit on the homogeneous plate and the crack in the otherwise homogeneous plate. This approximation can be surely used if the crack and the deposit are not on the same sides of the plate.

A better approximation can be obtained if we neglect only the field perturbation due to the crack on the surface of the deposit, that is we assume only (5). In this case (2) will not depend on the solution of (3). If we first solve (2) and then knowing \mathbf{E}^d and \mathbf{H}^d we solve (3), the computational effort does not increase compared to the previous case, on the other hand the accuracy of the result is significantly improved. We believe that this approximation is acceptable for most of the situations of practical interest.

NUMERICAL EXAMPLE

In Fig. 2 the impedance changes of the exciting coil scanning along the $x=0$ line are plotted when the not interacting crack and deposit approximation is assumed. The

frequency of the excitation is 150 kHz. The deposit is centrally positioned and its size is 8mm×8mm. The crack is in the $x=0$ plane and it is opened to that side of the plate where the excitation is located, its length and depth are 4mm and 0.25mm (ID 20%). The other parameters of the arrangement are (see Fig. 1), $h=1.25$ mm, $\sigma=9.7$ MS/m, $d=80$ μ m, $\sigma_d=58.1$ MS/m and $\mu_d=1.0$. In Fig. 2 the signal without the presence of the crack (deposit only) is also shown.

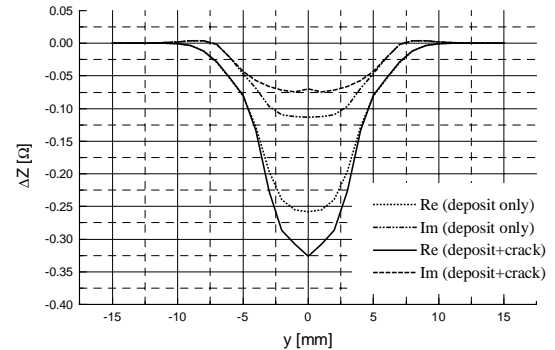


Fig. 2. Impedance variation versus location of the middle of the ECT probe.

CONCLUSIONS

Efficient approximation methods for the calculation of the ECT signal due to a crack in a plate covered by thin conducting deposit have been presented. The accuracy and the efficiency of the presented methods suggest their applicability for the solution of the inverse problem of shape reconstruction of cracks in plates covered by deposit. A numerical example demonstrating one of the methods has been also shown. In the extended version of the paper numerical results obtained by both methods will be compared and the error of the approximations in the case of practically important situations will be investigated.

ACKNOWLEDGMENT

This work was supported in part by the Hungarian Scientific Research Funds under Grant No. T-035264.

REFERENCES

- [1] T. Takagi and H. Fukutomi, "Benchmark activities of eddy current testing for steam generator tubes," in: *Electromagnetic Nondestructive Evaluation (IV)*, S.S. Udpa et al. (Eds.), pp. 235-252, IOS Press: Amsterdam, 2000.
- [2] Z. Badics et al., "Rapid Reconstruction Scheme for 3D Inverse Problems in Eddy Current NDE," in: *Electromagnetic Nondestructive evaluation*, T. Takagi et al. (Eds.), pp. 303-309, IOS Press: Amsterdam, 1997.
- [3] R. Albanese, G. Rubinacci, A. Tamburrino, F. Villone, "Phenomenological approaches based on an integral formulation for forward and inverse problems in eddy current testing," *International Journal of Applied Electromagnetics and Mechanics*, vol. 12, No. 3-4, pp. 115- 37, 2002
- [4] J. Pavo and K. Miya, "Reconstruction of crack shape by optimization using eddy current field measurement," *IEEE Transaction on Magnetics*, vol. 30, pp.3407-3410, September 1994.
- [5] J. Pavo, "Forward Solution Method for the Reconstruction of the Shape of Thin Metal Deposit on Plate Specimen," *International Journal of Applied Electromagnetics and Mechanics* (accepted for publication)
- [6] J. Pavo, "Numerical Calculation Method for Pulsed Eddy Current Testing," *IEEE Transaction on Magnetics*, vol. 38, pp.1169-1172, March 2002.
- [7] J.R. Bowler, "Eddy current field theory for flawed conducting half space," in *Review of Progress in Quantitative Nondestructive Evaluation*, vol. 13, eds. D.O. Thompson and D.E. Chimenty, Plenum, New York, pp.149-155, 1986.

An Optimum Design and Analysis of A Multi-Port Microwave Cavity using 3D FEM with a Sensitivity Method

Pan Seok Shin, Changyul Cheon and Sheppard J. Salon

Abstract—This paper presents an application of the 3-dimensional vector finite element analysis for design and analysis of multi-port microwave cavities with a sensitivity optimization algorithm. To verify the method, 2-port microwave cavities are analyzed and compared with the test results. Also, several types of cavities have been analyzed by the method to demonstrate the validity and accuracy of the program.

Index Terms— Microwave cavity, Vector finite element method, Edge element.

I. INTRODUCTION

We present a vector finite element method with a sensitivity method to analyze and to design a multi-source microwave cavity. The 3D FEM using edge elements can overcome the various difficulties of microwave cavity analysis such as long computing time and large memory requirements.

A vector wave equation for the electric field, E , is derived from Maxwell's equation,

$$\nabla \times (\mu_r \times E) - k_0^2 \epsilon_r E = 0 \quad (1)$$

where, k_0 is the propagation constant ($k_0 = \omega \sqrt{\epsilon_0 \mu_0}$), ω is angular frequency, μ_r is a relative permeability and ϵ_r is a dielectric constant, and all the walls of the cavity are assumed to be perfect conductors. The FEM formulation of the vector wave equation (1) is performed by using the Galerkin Weighted Residual method using 3-D tetrahedral edge elements[1] as follows:

$$\int_{\Omega} \bar{N}_i \cdot \left(\nabla \times \left(\frac{1}{\mu_r} \nabla \times \bar{E} \right) - k_0^2 \epsilon_r \bar{E} \right) d\Omega = 0 \quad (2)$$

where \bar{N}_i is used as a weighting function. The boundary integration over the conducting wall becomes zero by choosing the appropriate basis function.

II. EXAMPLES OF APPLICATIONS

A. One-port Microwave Cavity Model

For verifying the 3D FEM formulation of (2), a one-port cavity is analyzed as shown in Fig.1. The cavity size is 405 x 450x 55 mm with a port, whose width is 109 mm. TE₁₀ mode (f=2.45

GHz) is imposed on the boundary surface of the waveguide port, and its E-field distribution is calculated as shown in Fig.1. The E-field is well distributed as expected.

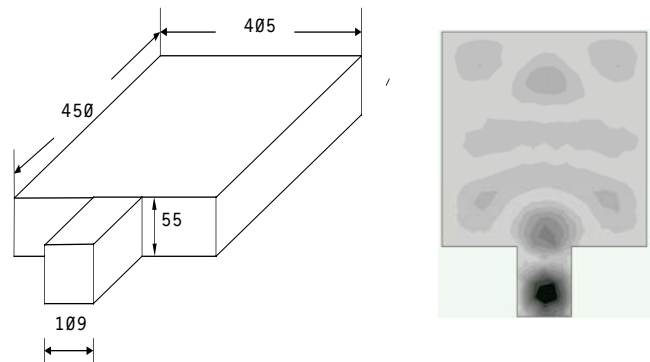


Fig. 1 One-port microwave cavity model and its E-field distribution

B. Sensitivity Algorithm to Optimize a Cavity

A sensitivity method is employed to optimize a microwave cavity for making the incident power maximum. If the coefficients of the reflection and transmission of the cavity were minimum, the incident power would be maximum. To minimize the reflection coefficient an objective function is set as follows:

$$F(p, H) = \left(|R(p, H)|^2 - |R_0|^2 \right)^2 \quad (3)$$

where, p is a design variable vector, H is the state variable, and $|R_0|$ is a reflection coefficient, which is zero with no reflection.

When (3) is minimum, the reflection coefficient of the cavity will be minimum. The sensitivity of the variable is calculated as dF/dp .

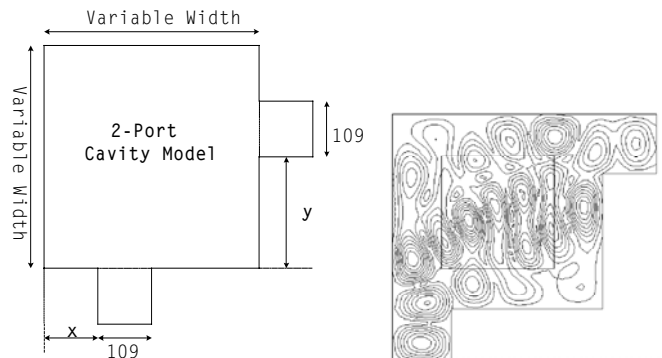


Fig. 2. Simulation model of the 2-port MW cavity and E-field contour lines.

Pan Seok Shin is with the Hongik University, Jochiwon, Chungnam 339-701, S. Korea (e-mail: psshin@hongik.ac.kr / yangjer@hongik.ac.kr).

Sheppard J. Salon is with the Rensselaer Polytechnic Institute, Troy, New York 12180, USA (e-mail: salons@rpi.edu).

Fig. 2 shows the simulation model of the 2-port MW cavity model. There are 3 variables, x, y, and the cavity width. Fig. 3 shows the power dissipation of the simulation model as functions of x and y. The maximum point occurs at x = 0 and y = 131 mm. Fig. 4 shows the reflection and transmission coefficient of the model. The minimum reflection and the maximum power dissipation occurs at the width = 355 mm. The final model is determined using the variables x=0, y=131 and width= 355 mm.

The optimized 2-port microwave cavity was manufactured as a test model to verify the 3D FE program. The scattering parameters are also calculated by using the 2-port network method to compare with the measured values. The 2 values are compared as shown in TABLE I. The agreement is fairly good, within a tolerance of 5 %.

TABLE I
Comparison of S-parameters for the 2-port cavity

S-parameters	Calculated	Measured
S11 amplitude	0.9121	0.9051
S21 amplitude	0.4981	0.5145
S22 amplitude	0.8921	0.8762
S12 amplitude	0.5020	0.5019

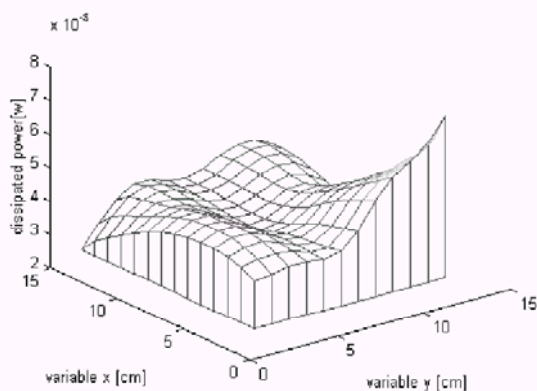


Fig.3. Power dissipation of the simulation model as functions of x and y.

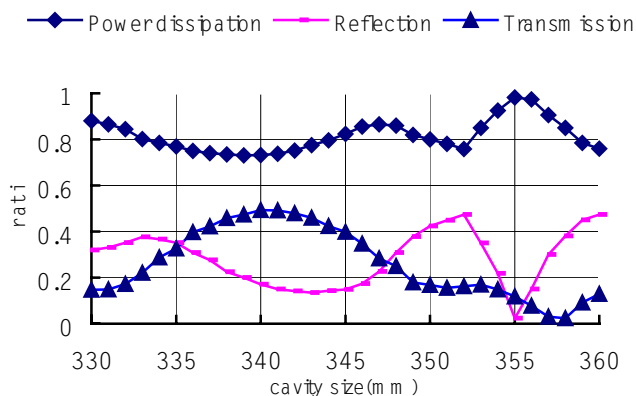


Fig. 4. Reflection and transmission coefficient of the simulation model

C. Optimal distance between 2 Ports

Fig. 5 shows a simulation model to optimize the distance (x variable) between 2-ports using the sensitivity algorithm for calculating the power dissipation. The dissipated power, P_{dis} ,

of the cavity is calculated by the following equation.

$$P_{dis} = \frac{1}{2} \operatorname{Re} \int_{\Gamma} \frac{-j}{\omega \epsilon} j \gamma (\hat{n} \times \bar{H}) \cdot (\hat{n} \times \bar{H}^T) d\Gamma \quad (4)$$

Fig. 6 shows the power dissipation of the simulation model as a function of distance between 2 ports. The maximum power dissipation occurs at x= 9.5 mm.

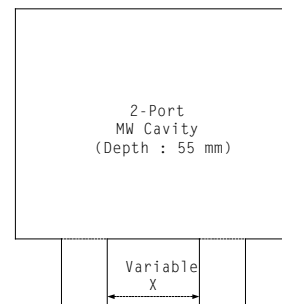


Fig. 5 A simulation model to optimize the distance between 2-ports

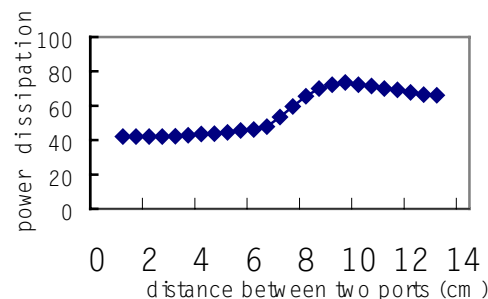


Fig.6. Power dissipations as a function of distance between 2 ports

III. CONCLUSION

This paper proposes an application of the 3-dimensional vector finite element analysis for design and analysis of multi-port microwave cavities with a sensitivity optimization algorithm. The 3D FEM formulation of the vector wave equation is performed by using the Galerkin's Weighted Residual method using 3-D tetrahedral edge elements. For verifying the program, one and two-port microwave cavities are analyzed by the method as the case studies. The sensitivity algorithm is also applied to the model for optimization of the 2-port MW cavity size and port distance. The optimized model was manufactured for testing, and the test results agreed well with the calculations.

Consequently, the proposed program can be a very useful tool to design and analyze a multi-port microwave cavity.

REFERENCES

- [1] J.W Shin, P. S Shin and C.Y Cheon, "Analysis of Circulator Using Hybrid Finite Element Method", Journal of KIEE, vol. 46, no. 5. May 1997, pp. 68-73.
- [2] Hong-bae Lee, *Computer Aided Optimal Design Methods for Waveguide Structures*, Ph.D Dissertation, Seoul Nation University, Seoul, Korea 1955, pp. 9-24.

TLM and FEM Analysis of a Mode Stirred Chamber Excited by Wires

D. Weinzierl, R. Jacobs, A. Kost

Lehrstuhl Allgemeine Elektrotechnik und Numerische Feldberechnung
Brandenburgische Technische Universität Cottbus
Postfach 101344, D-03013 Cottbus, Germany
weinzierl/jacobs/kost@aet.tu-cottbus.de

A. Raizer

Departamento de Engenharia Elétrica
Universidade Federal de Santa Catarina
Caixa Postal 476, CEP 88040-900, Florianópolis, SC, Brasil
raizer@eel.ufsc.br

Abstract— A Mode Stirred Chamber excited by wires is analysed using the Transmission Line Modelling (TLM) method. The TLM method solves the chamber problem in the time domain and computed results are compared to calculations using the Finite Element Method (FEM). Agreement with previously published Moment Method results will be shown.

I. INTRODUCTION

Mode stirred chambers are electrically large, highly conductive enclosed cavities equipped with mechanical stirring devices. When the chamber is excited with RF energy the resulting multi-mode electromagnetic environment can be stirred by the mechanical tuners. The cavity is employed to perform electromagnetic measurements (both emissions and immunity) on electronic equipment. The chamber mode density and the effectiveness of the mechanical tuner determine the lowest usable frequency [1]. A different method to excite and stir the fields in the chamber at low frequencies using wires has been proposed in [2]. This procedure of excitation is analysed in this work using the TLM method. As transmission lines support TEM fields, the method not only excites the common modes but also the TEM mode in the chamber. This widens the range of generated frequencies below the lowest resonance frequency [3]. In order to validate the TLM calculations, results will be compared to Finite Element computations and Method of Moment results.

II. CAVITY STRUCTURE

Fig. 1 shows the chamber under investigation which is excited by two transmission lines. The lines are parallel to the z -axis and are located at $x_1 = 0.8$ m, $y_1 = 1.8$ m and $x_2 = 3.2$ m, $y_2 = 2.1$ m. The width, height and length of the cavity are given by $a = 4.6$ m, $b = 2.7$ m and $c = 5.2$ m, respectively. The resonance frequency is determined by [4]:

$$f_{mnp} = \frac{1}{2\sqrt{\epsilon\mu}} \sqrt{\left(\frac{m}{a}\right)^2 + \left(\frac{n}{b}\right)^2 + \left(\frac{p}{c}\right)^2}, \quad (1)$$

where m , n and p determine the mode in the cavity. There is no maximum irradiation frequency, but the lowest fre-

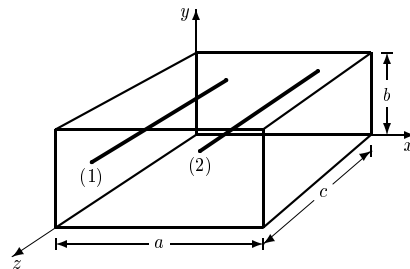


Fig. 1. Chamber with two parallel wires

quency is determined by the dimensions of the chamber. Transverse electric TE_{mnp} and transverse magnetic TM_{mnp} modes can be generated in the chamber.

III. TLM METHOD

The Transmission Line Modelling (TLM) method is a differential technique for the computation of electromagnetic fields. The problem domain is discretized and the fields in a subdomain are computed using a Symmetrical Condensed Node (SCN). Each port of a SCN is associated with two voltages, and the fields are calculated from these voltages. The excitation of the chamber is implemented applying magnetic fields at adjacent nodes around the wires as shown in Fig. 2. The path around the con-

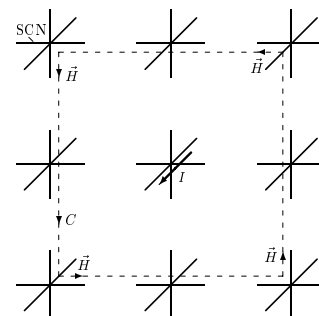


Fig. 2. Symmetrical Condensed Nodes around wire

ducting wire is denoted C , \vec{H} is the magnetic field at the adjacent nodes, and I is the current in the wire. A detailed description of the TLM method, its applications and computational requirements can be found in [5].

IV. FINITE ELEMENT PROCEDURE

The finite element formulation is derived using the weighted residual method. Weighting the wave equation for a time-harmonic electric field \vec{E} with $e^{j\omega t}$ time dependency with a set of weighting functions \vec{v}_i and integrating over the cavity domain Ω , leads after application of Green's first integral theorem to:

$$\begin{aligned} & \iint_{\Omega} \iint \frac{1}{\mu_r} (\nabla \times \vec{E}) \cdot (\nabla \times \vec{v}_i) - k_0^2 \epsilon_r \vec{E} \cdot \vec{v}_i \\ & + jk_0 Z_0 \sigma \vec{E} \cdot \vec{v}_i d\Omega - jk_0 Z_0 \iint_{\Gamma} \vec{v}_i \cdot [\vec{n} \times \nabla \times \vec{E}] d\Gamma \\ & = -jk_0 Z_0 \iint_{\Omega} \vec{J} \cdot \vec{v}_i d\Omega, \quad \forall i \in [1, N], \end{aligned} \quad (2)$$

where k_0 and Z_0 denote the wavenumber and impedance of free space, \vec{n} the normal vector on the bounding surface $\Gamma = \partial\Omega$, \vec{J} the current density in the wire, and the constitutive parameters σ , ϵ_r and μ_r the conductivity, relative permittivity and relative permeability, respectively. Approximation of the electric field $\vec{E} = \sum_{j=1}^N a_j \vec{v}_j$ with a set of vectorial basis functions \vec{v} associated with the edges of the elements leads to a system of linear equations which can be solved for the unknown coefficient a_j .

V. SIMULATED RESULTS

Fig. 3 shows the spectrum of the chamber. Both wires were excited simultaneously with a rectangular pulse of 1 V magnitude and a duration of $83.3 \cdot 10^{-12}$ s. The lowest resonance frequency of the chamber is at

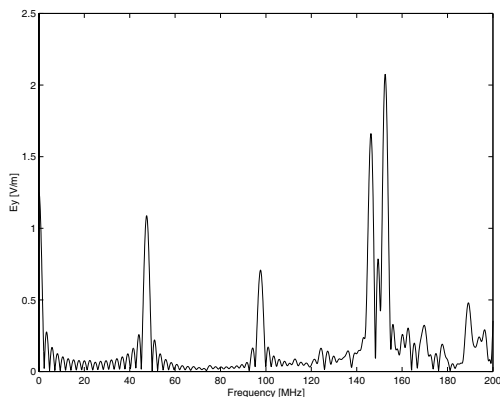


Fig. 3. Spectrum of the chamber

45.5 MHz, where the total electric field is defined as

$E = (|E_x|^2 + |E_y|^2 + |E_z|^2)^{1/2}$. Fig. 4 displays the total electric field along the z -coordinate at $x = 2.3$ m and $y = 1.0$ m for a sinusoidal current signal with a frequency of 2 MHz and phase differences of 0° and 180° between the two lines. The TLM simulations have been performed with a cell size of 5.0 cm and time steps of $83.3 \cdot 10^{-12}$ s. Good agreement can be observed between

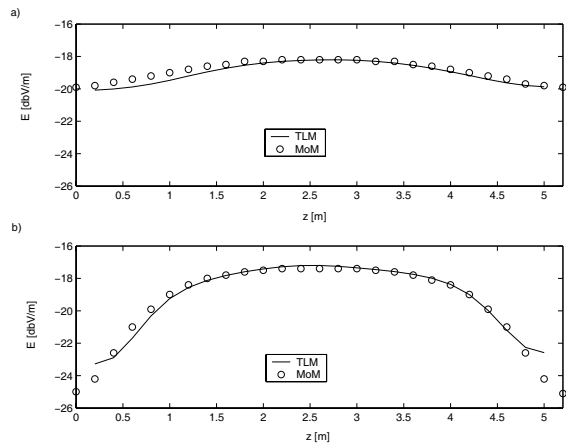


Fig. 4. Total electric field along z -coordinate, a) $\phi = 0^\circ$ b) $\phi = 180^\circ$ (log. scaling with reference to an electric field of 1 V m^{-1})

the TLM calculations and the Method of Moment (MoM) results from [2], and similar good agreement will be shown with finite element computations.

VI. DISCUSSION

In contrast to mechanically mode stirred chambers, the wire excitation allows to set-up the TEM mode. The TEM mode lowers the minimum usable frequency of a mode stirred chamber below the lowest resonance frequency, and it has been shown that the Transmission Line Modelling method is capable of accurately predicting the field distribution in the chamber.

REFERENCES

- [1] *Electromagnetic Compatibility (EMC), Part 4: Testing and Measurement Techniques - Section 21: Reverberation Chamber Test Methods*, International Electrical Commission, IEC 61000-4, 2000.
- [2] J. Perini and L.S. Cohen, "Extending the frequency of mode stirred chambers to low frequencies," in *IEEE International Symposium on Electromagnetic Compatibility*, Washington D.C., Aug. 2000, pp. 633-637.
- [3] D. Weinzierl, A. Raizer, A. Kost, and G.S. Ferreira, "Simulation of a mode stirred chamber excited by wires using the TLM method," in *10th International IGTE Symposium on Numerical Field Calculation in Electrical Engineering*, Graz, Austria, Sept. 2002, p. 98.
- [4] C.R. Paul, *Introduction to Electromagnetic Compatibility*, Wiley Interscience, New York, 1992.
- [5] C. Christopoulos, *The Transmission-Line Modeling Method TLM*, IEEE Press and Oxford University Press, New York, 1996.

A Combined Method for Fast 3-D FEM Modeling of NDT Signal

LIN Heyun, S.L. HO¹, H.C. WONG²

Department of Electrical Engineering, Southeast University, Nanjing 210096, P. R. China

¹Department of Electrical Engineering, ²Industrial Centre, Hong Kong Polytechnic University, Kowloon, Hong Kong

Email: hyling@seu.edu.cn; eeslho@polyu.edu.hk

Abstract—A combined method for the fast 3-D Finite Element Method (FEM) modeling of defect responses in non-destructive testing (NDT) of electromagnetics is presented. The method consists of three numerical techniques including, namely, ‘zoom-in’ technique, ‘difference field’ technique and ‘iterative solution’ technique. With the ‘zoom-in’ technique, the computational zone focuses onto a relatively small domain around the defect. Using the ‘difference field’ technique, the 2-D field solution corresponding to the case with no defect can be used to obtain the 3-D modeling results quickly. With the ‘iterative solution’ technique, the matrix equation system from the 3-D FEM modeling of NDT probe signals can be solved readily. Significant computer resources can thus be saved.

INTRODUCTION

Numerical methods, such as Finite Element Method (FEM) and Boundary Element Method (BEM), have been applied successfully to study many NDT problems in the past decades [1]. Most of these methods focus on the development of effective formulations instead of calculation techniques. However better effects can be realized if efficient techniques and effective formulations are developed together. In the 3-D modeling of defect response prediction and defect reconstruction, a large linear algebraic equation is generated and most algorithms require enormous computer resources when evaluating the multiple solutions of the governing equations. The development of effective and efficient calculation techniques to simplify the numerical modeling would be highly useful. Indeed a very successful ‘zoom-in’ technique that requires very limited computer resource when studying the defect responses of 3-D remote eddy current effect has been reported [2]. The ‘difference field’ technique has also been applied in the fast simulation of eddy current testing signals [3]. Subsequent studies by the authors recently show that these techniques can be enhanced further to save additional computer resources in most 3-D FEM modeling of NDT problems by combining an iterative solution technique as described below.

This paper presents a combined method that saves a significant amount of computation cost in modeling 3-D NDT problems. The basic principles of the technique are described in details in the full paper. The modeling of a benchmark problem provided by JSAEM shows that the proposed combined method is very promising in the simulation of electromagnetic NDT problems.

BASIC PRINCIPLES

In most cases, the size of the real defect is very small compared with that of the specimen being studied. Hence the influence of the defect is only noticeable in the vicinity of the defect. Fig.1 shows the relative amplitude variation

of the circumferential component of the magnetic vector potential A in an eddy current test system comprising of a tube having a 50% inner diameter (ID) defect. Hence a ‘zoom-in’ technique can be used to confine the 3-D modeling to a relatively small domain around the defect. This technique has successfully been applied to study the 3-D remote field eddy current effects with relatively few computer resources [2].

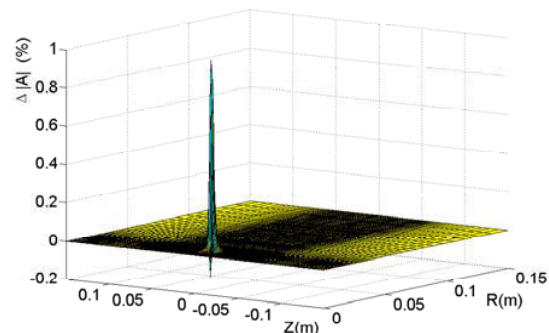


Fig.1 Relative Variation of $|\Delta A|$ Due to a 50% ID Defect

If the difference between the fields with and without defect is chosen as the unknown variable, the ‘difference field’ can be obtained by solving the following FEM matrix equation:

$$[K + \Delta K][\Delta u] = -[\Delta K][u] \quad (1)$$

where K is the FE stiffness matrix and u denotes the potential functions employed, ΔK and Δu are, respectively, the variation of K and u due to the defect. Note that u can easily be obtained by extending the 2-D or axial-symmetric solutions to 3-D in many cases such as in, for example, the inspections of large plates and long tubes/rods using pancake and co-axis coils. The other advantages to choose the ‘difference field’ as the unknown is to avoid the re-meshing procedure, which is normally required when modeling the impedance of coils moving over a period of time.

Since the real defect is usually very small, ΔK is typically a slight perturbation to K . Example calculations have shown that if an iterative algorithm is applied to the FEM equation system (1), the iteration process is rapidly convergent. Besides, the solution of whole matrix equation system stemming from 3-D FEM modeling can be avoided by applying an iterative algorithm.

APPLICATION IN A BENCHMARK PROBLEM

A benchmark problem provided by JSAEM has been studied in order to validate the proposed method. In the problem a pancake coil is used to inspect cracks with different depths in a square Inconel plate as shown in Fig.2 [4]. The inner and outer diameters of the coil are 1.2mm and 3.2mm respectively. The coil height is 0.8mm. The coil lift-off is 1.0mm. The frequency of the applied current is 300kHz.

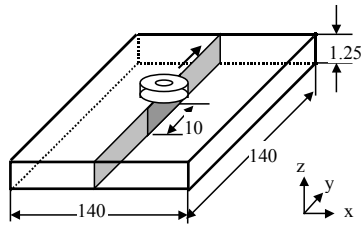


Fig. 2 The analyzed model

The objective of the modeling is to compute the change in impedance as the coil moves along the cracks and to compare the values with the corresponding experimental results provided by JSAEM. Fig.3 shows the eddy current distributions on the surface of the metal plate for four coil positions: $y=0.0, 2.5, 5.0$ and 10mm . It can be seen that the eddy current distributions are quite reasonable.

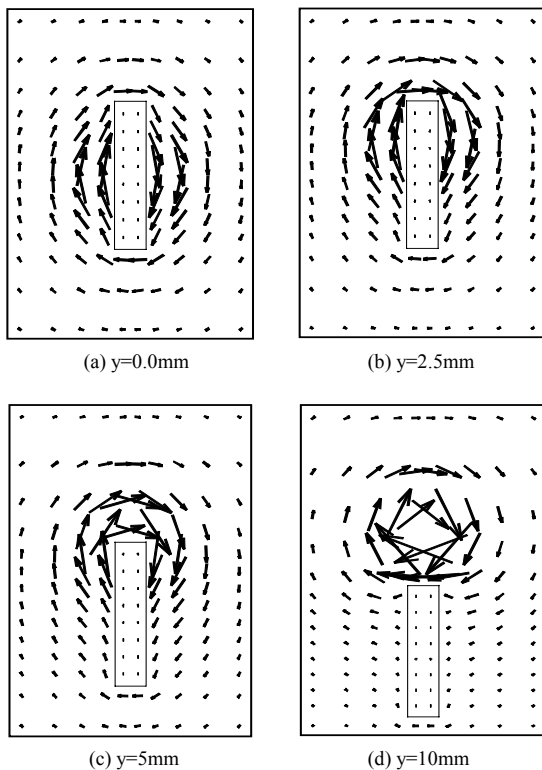


Fig.3 The eddy currents on the surface of the plate

Fig. 4 and Fig.5 show the impedance perturbations for cases with inner defects and outer defects, respectively. All the calculated results will be explained and reported in the full paper.

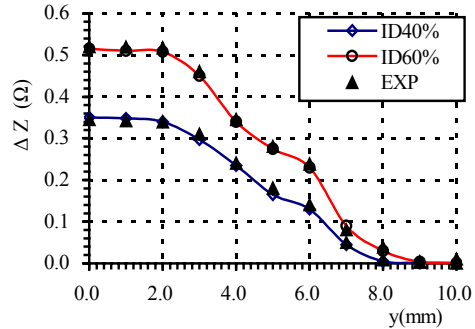


Fig. 4 Impedance perturbation for inner diameter defects

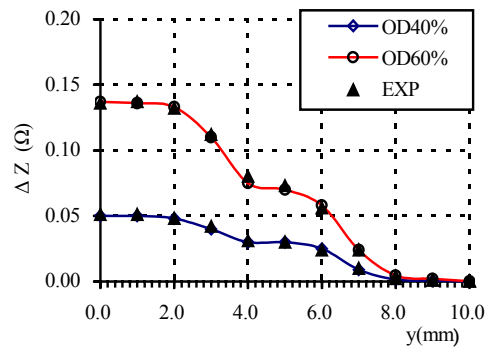


Fig. 5 Impedance perturbation for outer diameter defects

CONCLUSIONS

A combined calculation method for fast 3-D FEM modeling of NDT probe signals has been successfully presented. Based the combined method, the calculated region can be confined to a relatively small domain around the defect, instead of examining the entire field domain in the conventional methods. Furthermore, an iterative algorithm can be used to obtain the solution of the matrix equation system quickly. With the proposed algorithm significant computer resources can be saved. The proposed method has been applied in the derivation of the 3-D solution of a benchmark problem with relatively few computer resources. It has been shown that the proposed combined method is highly effective and efficient in electromagnetic NDT simulations, particularly for problems having small perturbations only.

REFERENCES

- [1] T. Sakai et al., "Development of 3D electromagnetic field FE code specialized for the numerical simulation of eddy current testing," *Electromagnetic Nondestructive Evaluation*, pp. 23-29, IOS Press, 1997, pp. 23-29.
- [2] H. Y. Lin et al., "Application of "zoom-in" technique in 3D remote eddy current effect computation," *IEEE Transactions on Magnetics*, Vol. 26, No.2, March 1990, pp. 881-884.
- [3] M. Tanaka et al., "Fast Simulation Method for Eddy Current Testing," *IEEE Transactions on Magnetics*, Vol. 36, NO. 4, July 2000, pp.1728-1731
- [4] T. Takagi et al., "Benchmark models of eddy current testing for steam generator tube: experiment and numerical analysis," *Int. J. of Appl. Electromagnetics in Material*, vol. 5, 1994, pp. 149-162.

Minimum Norm Reconstruction of Vicinal Defects in Magnetic Flux Leakage Pipeline Data

J. Haueisen¹, M. Seitz^{1,2}, T. Beuker³, M. E. Bellemann²

¹ Biomagnetic Center, Department of Neurology, Friedrich-Schiller-University, Philosophenweg 3, 07743 Jena, Germany
e-mail: haueisen@biomag.uni-jena.de

² Department of Biomedical Engineering, University of Applied Sciences, Carl-Zeiss-Promenade 2, 07745 Jena, Germany

³ H. ROSEN Engineering GmbH, Am Seitenkanal 8, 49811 Lingen (Ems), Germany

Abstract—The analysis of magnetic flux leakage pipeline data involves both a scanning part for defect recognition and an analysis part to describe the defects found. In the analysis part, it is often important to discriminate between vicinal (close-by) defects and to examine these defects separately. We applied an inverse method (L_2 minimum norm reconstruction) and a novel post-processing technique based on equivalent ellipsoids to resolve vicinal defects measured in a test pipeline. The magnetic fields were computed with the help of a boundary element model. We found that using inverse algorithms, thresholding, and post-processing techniques, the automatic discrimination of vicinal defects was possible in 15 out of 16 cases.

INTRODUCTION

Worldwide about three million kilometers of oil and gas pipelines are in use. This number increases each year by approximately 25,000 km. Inspection of these pipelines is of crucial importance to avoid large financial losses and environmental damages.

Data sets from oil and gas pipeline inspections, such as magnetic flux leakage (MFL) data, are typically scanned with the help of automated algorithms. Nevertheless, a validation of the findings after scanning has to be performed by a visual crosscheck on a regular basis. Especially for the detailed analysis of flaws that are in close vicinity to each other, it would be highly desirable to perform an automated computer-based analysis. This analysis should give a discrimination of these flaws and an estimate of their respective size and position.

The goal of our work is to develop a technique capable to discriminate vicinal defects in pipelines on the basis of inverse algorithms applied to MFL data.

METHODS

The basic principle of the MFL method is the application of a static, uniform magnetic field that is coupled into the metallic wall of the pipeline. Flaws in the pipe wall generate magnetic field perturbations, which are called leakage fields when they leak out of the pipe. The measured leakage of the magnetic flux is analyzed off-line in order to extract the prop-

erties of the flaws in the pipe wall such as the extent and the depth.

The analysis in this paper is based on a measurement data set of a test pipeline with given flaw geometries provided by H. Rosen Engineering. Measurements were carried out on a set of flaws (defects) in the pipe wall. The flaws were located on the outside of the pipe and had a depth of 50 % of the wall thickness. For the detection of the stray field, two different types of sensors were used simultaneously: a Hall sensor measured the axial magnetic field (in the following indicated by B_z) and a coil sensor measured the axial derivative of the radial magnetic field component (in the following indicated by B_ρ). For the inverse computations, we assumed stationarity and we restricted the number of measuring points included in each inverse computation so that this number was as small as possible (reduced computation time) while still covering the relevant field information.

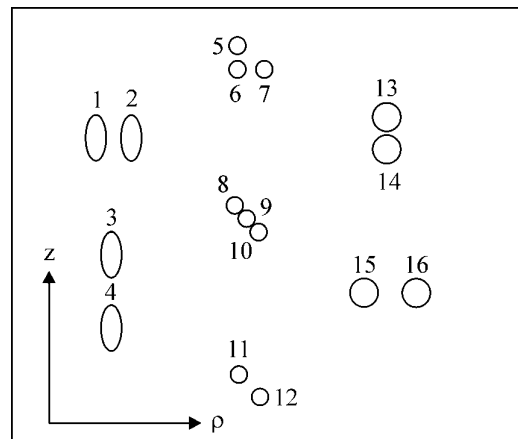


Fig. 1. Defect geometries with numbering (approximate length in z-direction: 180 cm).

For the numerical field computation (forward problem), we applied the analogy of the current sheet convention (as opposed to the pole sheet convention) [1]. The current sheet convention employs currents (often line-like current elements) to approximate the magnetic field produced by a magnetized body, while the pole sheet convention does so with the help of a pole density. Line-like current elements can generally be approximated by current dipoles. Thus, the

sources of the magnetic stray field were modeled employing a sheet of electric current dipoles in an electric volume conductor. We have chosen this approach because of the software available. A section of the pipe wall was modeled with the help of the boundary element method (BEM). A total of 5768 linear triangular elements (triangle side length of 6 mm) were used. In the area, where the highest potential gradients were expected, a local refinement was applied and the triangle side length was approximately halved.

For our inverse solutions, we used the L_2 minimum norm least squares, which was found to be a very robust method in previous investigations [2,3]. The source (dipole) positions were predefined on a quadratic grid with an extent of approximately $280 \text{ mm} \times 280 \text{ mm}$ that was located below the array of the measuring points in the middle of the BEM model.

A novel post-processing technique based on equivalent ellipsoids [4] was used to extract the flaw extent from the thresholded current density distribution and to automatically discriminate the vicinal flaws. An equivalent ellipsoid was defined as a 3D ellipsoidal object fitted (using a principal component approach) to a current density distribution region in which the magnitude of the currents was above a predefined threshold. The crucial parameter for this procedure is the threshold value, which was set here to a fixed value (70% of the maximum dipole strength).

RESULTS AND DISCUSSION

Fig. 2 shows the results of the inverse computations for defects #15 and #16. The inverse algorithm is able to discriminate both defects and the equivalent ellipsoids describe the extent of the defects quantitatively.

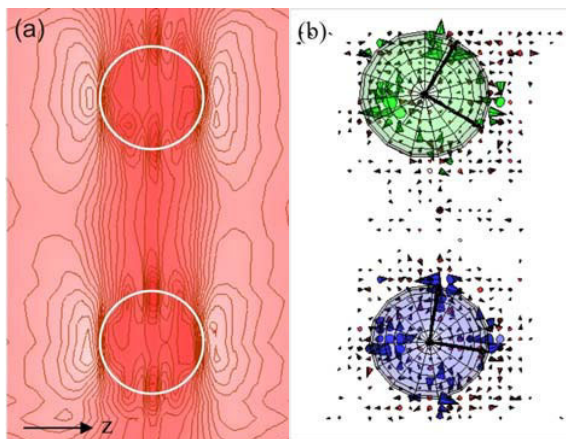


Fig. 2. Magnetic stray fields of two circular flaws (#15 and #16) and their original size (white line) (a) and reconstructed dipole distribution with estimated equivalent ellipsoids (b).

Except for flaw #10 from the defect group #8 / #9 / #10, all flaws were automatically discriminated. The estimated extent error is given in Fig. 3. Here it is important to note that the minimum norm mesh for the reconstruction had a resolution of 7 mm.

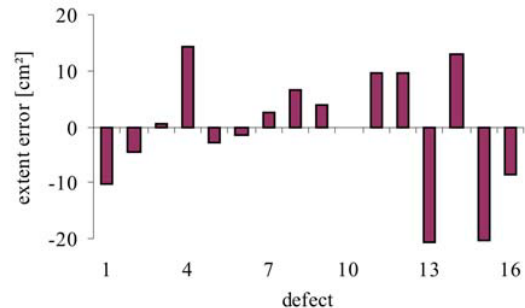


Fig. 3. Estimated extent error for all flaws. Flaw #10 was not resolved.

Since the threshold value applied to the current distribution is crucial for the extent estimation, current research is focused on the automatic and adaptive estimation of this threshold.

Unlike in our previous study [2], we found that the estimation of the defect extent in z -direction (along the pipe) was more accurate than in circumferential direction. The overlapping leakage fields of the vicinal defects can at least partially explain this effect. Axially oriented defect groups (e.g. #13 / #14) showed better circumferential extent estimation, and circumferentially oriented defect groups (e.g. #15 / #16) showed better axial extent estimation.

In conclusion, inverse algorithms in combination with equivalent ellipsoids post-processing allow the automated discrimination of vicinal flaws in MFL data.

REFERENCES

- [1] D. Craik, "Magnetism: Principles and Applications," John Wiley & Sons, Chichester, 1995.
- [2] J. Haueisen, R. Unger, T. Beuker, M. E. Belleman, "Evaluation of inverse algorithms in the analysis of magnetic flux leakage data," *IEEE Transactions on Magnetics*, vol. 38, pp. 1481-1488, 2002.
- [3] A. C. Bruno, L. C. Miranda, C. H. Barbarosa, G. S. Kühner, "Image reconstruction of spherical inclusions in ferromagnetic structures using the generalized inverse," *IEEE Transactions on Magnetics*, vol. 34, pp. 2912-2915, 1998.
- [4] M. Ziolkowski, J. Haueisen, U. Leder, "Postprocessing of 3D current density reconstruction results with equivalent ellipsoids," *IEEE Transactions on Biomedical Engineering*, vol. 49, pp. 1379-1384, 2002.

Analysis of the Velocity Induced Eddy Current in MFL Type NDT

G. S. Park, S. H. Park

Dept. of Electrical Engineering, Korea Maritime University
Youngdo-Ku, Dongsam-Dong, Pusan 606-791, South Korea
e-mail: gspark@hanara.kmaritime.ac.kr

Abstract— MFL (Magnetic Flux Leakage) type NDT (Non-destructive testing) is one of the remote sensing systems. In the system, defect signals are measured under the running of the sensing module consisted of permanent magnet, yoke, and sensors. Because of the strong magnetic field of the PIG, there could be velocity induced eddy current during the sensing, which could cause the distortion of the defect signals. In this paper, the velocity induced eddy currents of the running sensors in MFL type NDT are analyzed by 3D FEM. The distortions of the sensing signals are analyzed and the method to deduce the velocity speed of the sensors are suggested.

I. INTRODUCTION

In the magnetic flux leakage (MFL) type non-destructive testing (NDT) system, sensor modules are consisted with permanent magnet, magnetic yoke and sensors to detect the corrosion defect and any other damages of the gas pipeline. In the system, the object pipeline is magnetically saturated by the magnetic system with permanent magnet and yokes. The defect signals are measured during the sensor modules are running inside the underground pipeline. So, there could be distortion of the sensing signals because of the velocity induced eddy current.

To detect the defects precisely, the sensing signals are need to be compensated to eliminate the distortions coming from the velocity induced eddy current, media hysteresis, magnetic anisotropy, and so on. During the sensing, the velocity of the modules are from 1 m/s up to 10 m/s, and average velocity is 4 m/s. In this paper, velocity induced eddy current are analyzed by 3D finite element analysis. The distortion of the measured signals are analyzed and compensation scheme to eliminate the velocity induced eddy currents are presented.

II. ANALYSIS OF THE VELOCITY INDUCED EDDY CURRENT

From the Maxwell equations including time and space dependent eddy current, the following equations could be obtained.

$$\nabla \times \nu \nabla \times A = J_o - \sigma \frac{\partial A}{\partial t} + \sigma \nu \times B \quad (1)$$

where σ is the conductivity of material and ν is the velocity of the conductor. The first term on the right of eq. (1) represents the current density due to the applied source, the

second term represents the induced current density, and the third team represents current density produced by the speed voltage. By employing a frame of reference and Galerkin method, integration by parts yields

$$\begin{aligned} & \iiint \nu \left[\frac{\partial W}{\partial x} \frac{\partial A}{\partial x} + \frac{\partial W}{\partial y} \frac{\partial A}{\partial y} + \frac{\partial W}{\partial z} \frac{\partial A}{\partial z} \right] dv \quad (2) \\ & + \iiint \sigma W \frac{\partial A}{\partial t} dv - \iiint W J_o dv - \oint \nu W \frac{\partial A}{\partial n} d\Gamma = 0 \end{aligned}$$

where W is weighting function, n is an outward normal to the boundary. As the shape functions are equal to the weighting functions, eq. (2) could be represented in matrix form,

$$\sum_e \left[\nu [S]_e [A(t)]_e + \sigma [T]_e \left[\frac{\partial A(t)}{\partial t} \right]_e - [Q]_e J_o \right] = [0] \quad (3)$$

where the subscript e means that the matrices refer to a particular element and

$$S_{e,ij} = \iiint \nu \left[\frac{\partial N_i}{\partial x} \frac{\partial N_j}{\partial x} + \frac{\partial N_i}{\partial y} \frac{\partial N_j}{\partial y} + \frac{\partial N_i}{\partial z} \frac{\partial N_j}{\partial z} \right] dv \quad (4)$$

$$T_{e,ij} = \iiint N_i N_j dv \quad (5)$$

$$Q_{e,ij} = \iiint N_i dv \quad (6)$$

In this equation, the eddy current induced by flux changes in time and space are both included.

III. DISTORTION OF THE SENSING SIGNALS

Fig. 1 shows the eddy current on the pipe surface in 3D analysis. Eddy current vortex is produced to prevent the change of the flux on the pipe. As the speed increases in Fig. 2, the radial component of the magnetic field on the pipe is decreasing while the axial component of the magnetic field is increasing. The change of the magnetic flux causes the distortion of the sensing signals. In the metal loss region, MFL signals are also distorted as in Fig. 3. As the speed

increasing, the maximum signals are decreased and the slopes of the signals are increasing. So the speed of the PIG could be estimated from the maximum field and the slope of the field by using Fig. 4. The velocity of the sensing module could be deduced by this curve from the measured signals. So, the pure defect signals could be obtained by eliminating the distortion signals according to the sensor velocity.

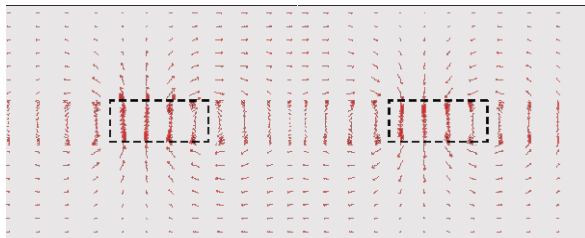
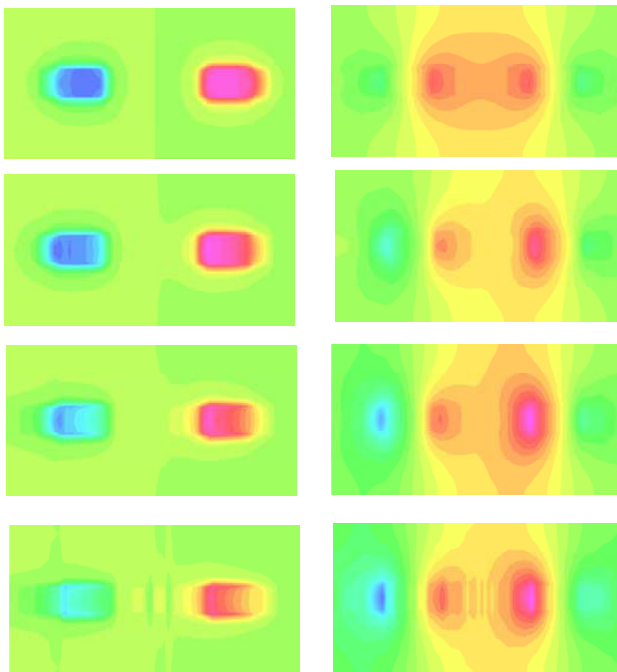
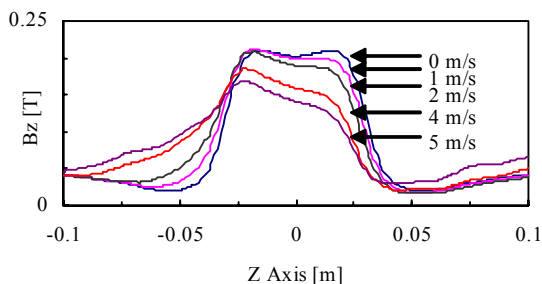


Fig. 1. Eddy current on the pipe surface ($v = 4\text{m/s}$)

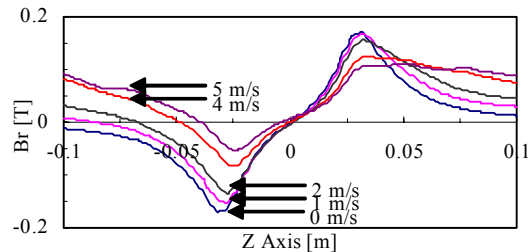


(a) Radial component (b) Axial component

Fig. 2 Changes of the magnetic fields according sensor speed



(a) Axial component of the MFL signals



(b) Radial component of the MFL signals

Fig. 3 Effect of the PIG speed in the defect region

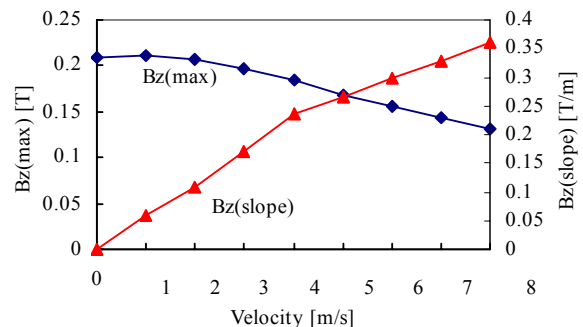


Fig. 4 Maximum field and slope according to the sensor speed

IV. CONCLUSIONS

In this paper, the velocity induced eddy current in MFL type NDT system are analyzed by 3D finite element method. As the magnetic field is strong enough to saturate the sensing object and the sensing modules are running in high speed, there are strong eddy current induced by running velocity, which causes the distortion of the sensing signals inevitably. The distortion of the sensing signals are analyzed according to the running velocities. As the velocity increased, the peak values of the sensing signals are decreased and the slope of the peak value are increased. So the velocities of the sensing module could be deduced from the sensing signals. The scheme to eliminate the velocity induced distortion could be applied successfully.

V. REFERENCES

- [1] D. L. Atherton and M. G. Daly, "Finite Element Calculation of Magnetic Leakage Detector Signals", *NDT International*, vol. 20, no. 4, pp. 235-238, August 1987.
- [2] J. Bruce Nestleroth, Steven W. Rust, and David A. Burgoon, "Determining Corrosion Defect Geometry from Magnetic Flux Leakage PIG Data", *The NACE International Annual Conference and Exposition CORROSION 96*, Paper No. 44, pp. 1-11, 1996.
- [3] G.S.Park, P.W.Jang, Y.W.Rho, "Optimum Design of a Non-Destructive Testing System to Maximize Magnetic Flux Leakage", *Journal of Magnetism*, vol.6, no. 1, pp. 31-35, March 2001.

Transmission Line Matrix Model for Detection of Local Changes in Permeability Using a Microwave Technique

Razvan Ciocan, Nathan Ida,
Electrical Engineering Department,
The University of Akron, OH 44325-3904, USA
rc17@uakron.edu

Abstract - A 3D transmission-line matrix (TLM) model was developed to simulate the microwave detection of local changes in permeability. The technique can be used to map local non-uniformities in magnetization. Numerical modeling was carried out for frequencies that are commonly used in microwave nondestructive testing (1GHz). A comparison between experimental and numerically generated curves is provided. This comparison validated the numerical model proposed. A numerical implementation of scanning microwave microscopy based on model the proposed was performed.

INTRODUCTION

The first microwave probe capable of measuring the spatial variation of magnetic properties was proposed in 1962 by Sahoo [1]. The possibility to perform microwave measurements on thin ferromagnetic layers in magnetic field was demonstrated recently [2,3]. A full theoretic model for these techniques in various geometries is almost impossible to obtain. This is the reason why a numerical model that is unconditionally stable and that works for different geometries is very attractive and very useful for future development of these investigation techniques.

The Transmission Line Matrix (TLM) is a time domain numerical technique that was found to be most suitable for complex geometries [4]. The method is a direct numerical implementation of the Huygens principle. The wave front at each iteration for a certain mesh node is a result of the waveforms generated at neighboring nodes in the previous iteration. The TLM is a physical discretization approach and this method does not require the solution of the differential equation in whole space being modeled. The solution of differential equation is implemented in the scattering matrix formulation. This matrix gives the time and spatial solution for the smallest entity (called node) that can be modeled using TLM method. The coefficients of this matrix are obtained in such a way that charge conservation rule is obeyed for the node. This method is recognized for his unconditional convergence [5] that is achieved for dimensions of nodes less than one tenth of a wavelength. Numerical results were obtained based on the General Symmetrical Condensed Node [6].

ALGORITHM IMPLEMENTATION

The main steps of a TLM algorithm are initialization, scattering and connection. A supplementary part called scanning was added to these components. This part involves changing the position of excitation according to the experimental scanning pattern whereby the TLM algorithm is repeated for each new position. The time response for each position is saved in an output file for further processing. In the initialization step a Gaussian modulated pulse is injected in the TLM mesh in the position of the microwave probe. The voltage injected is given by:

$$V^i(x, y) = Ae^{-\frac{(t-t_o)^2}{2\sigma^2}} \cos(2\pi f(t-t_o) + \varphi) \quad (1)$$

In relation (1) the following notations were used: A -amplitude; σ standard deviation; t -time; t_o -delay; f -frequency; φ -phase. The pulse parameters have been modified to obtained the best fit with a reflected signal from a material with known permeability. In further experiments these parameters were kept the same.

The scattering matrix was implemented according to the methodology proposed by Trenkic [7]. This method is based on an algorithm that explores the symmetry of the scattering matrix and decreases the number of operations associated with this step. The voltages at all ports can be obtained using the following equations:

$$V_{inj}^r = V_{temp} - V_{dif} \quad (2)$$

$$V_{ipj}^r = V_{temp} \quad (3)$$

In relations (2) and (3) the following notations were used:

$$V_{temp} = \frac{1}{2}(V_{kni} + V_{kpi} + V_{dif}) \quad (4)$$

$$V_{dif} = V_{ipj} - V_{inj} \quad (5)$$

The voltages are obtained considering all circular permutations of indices (x, y, z) denoted in general form as (i, j, k). The S11 parameter cannot be obtained directly from the TLM algorithm because an incident field cannot be separated. To solve this problem two successive runs of the program are

needed. The first run is performed with excitation without a reflecting object. This run will provide data for the reference port.

RESULTS

An experimental set-up was designed for this application [8]. In this set-up the magnetic sample was placed over an electromagnet that was energized by a dc current. The sample and the electromagnet assembly were located underneath the microwave probe. The electromagnet used in the present work produced 250 Gauss at 100 mA (16 Volts) and its B versus I characteristics were approximately linear in that range as determined with a Gauss-meter. The microwave probe was operated in reflection mode [9]. The probe position over the sample could be changed using various micrometers and stepping motors. Figure 1 shows a comparison between numerical and experimental resonance curves obtained for a CO-NETIC alloy sample [10]. The graph shows a good agreement between experimental and numerical data. The relative change in S_{11} parameter determined by permeability variations has the same value for both cases (1dB). A 5 % shift that exists between the numerical and experimental curves has been generated mainly by the difference in frequency step that exists between the two methods ($\Delta f_{exp} = 10\text{kHz}$, $\Delta f_{num} = 200\text{kHz}$)

CONCLUSIONS

A numerical model for scanning microwave microscopy for magnetic materials was implemented. The model is based on the TLM algorithm. The experimental results obtained by authors validate the numerical model proposed. The dimensional characterization of structures with different

permeabilities can be numerically simulated. The scanning process was also implemented into the numerical model. The results obtained show that the numerical model can be run in parallel with the experimental scanning. This allows a better characterization of discontinuities in magnetic permeability detected using microwave techniques.

REFERENCES

- [1] Soohoo R.F. "A microwave Magnetic Microscope", *Journal of Applied Physics* vol.33 (3) pp.1276-1277,1962.
- [2] Acher O., Baclet P., Perin G. "Investigation of the microwave permeability of ferromagnetic film laminations under a magnetic field" *Journal of Magnetism and Magnetic Materials* vol157/158, pp. 480-481 1996.
- [3] Ustinov V.V., Rinkevich A. B., and Romashev L.N., "Microwave magnetoresistance of Fe/Cr multilayers in current-perpendicular to plane geometry" *Journal of Magnetism and Magnetic Materials* vol. 198/199, pp. 82-84,1999.
- [4] Johns, P. B. Beurle, R. L. " Numerical solution of Two-Dimensional Scattering Problems Using a Transmission-Line Matrix" *Proc. IEEE*, vol 118, pp 1203-1209, 1971.
- [5] Rebel, J.R., Aidam M., Russer,P. "On the convergence of the Classical Symmetrical Condensed Node-TLM scheme" *IEEE transaction on Microwave theory and techniques* No.49 No.5 pp954-963, 2001.
- [6] Trenkic, V., Christopoulos, C. Benson T.M. " Development of a general Symmetrical condensed node for the TLM method" *IEEE Trans. Microwave Theory Tech.* Vol MTT-44 , No.12 pp. 2129-2135, 1996
- [7] Trenkic, V., Christopoulos, C. Benson T.M. "Simple and elegant formulation of scattering in TLM nodes " *Electronics Letter*, 29, pp 1651-1652, 1993
- [8] Ciocan R. "*Evanescence Microwave microscope: a novel nondestructive, high resolution method for quantitative evaluation of materials*", MS thesis, pp.39-46, CWRU, 2000
- [9] Ida N. "*Microwave NDT*" Kluwer Press, pp201-273 1992
- [10] CO-NETIC & NETIC Magnetic shielding Alloys obtained from Magnetic Shield Corporation, 740 North Thomas Drive, Bensenville, IL 60106, 1999.

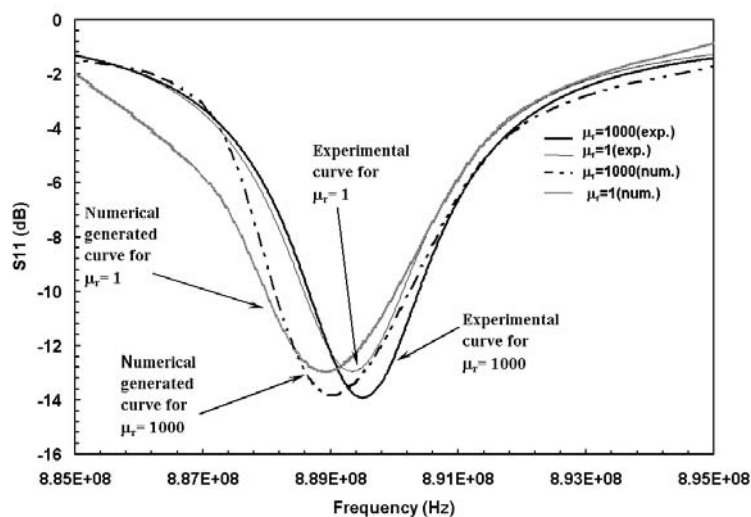


Figure 1. The experimental and numerical curves obtained for S_{11} parameter that validates the TLM model proposed for detection of local variation in permeability using microwave techniques

Extending the Operation of Mode Stirred Chambers to Low Frequencies

Prof. Jose Perini

ECE Dept Syracuse University
Daytona Beach Shores, FL, USA
jperini@ieee.org

Lawrence S. Cohen

Naval Research Laboratory.
Washington, DC, USA
cohen@radar.navy.mil

Abstract: In this paper a new technique is presented to excite the fields inside a mode stirred chamber down to very low frequencies. The proposed approach is then simulated using the Method of Moments (MoM). In a previous paper [1] it was shown that this type of simulation agrees very well with actual measurements. The proposed technique is based on the use of wires parallel to the coordinate axis of the chamber. Each wire and the walls parallel to them form a coaxial transmission line that can support a transverse electromagnetic (TEM) wave also called a transmission line mode. The TEM wave has no frequency limitation being capable of exciting fields from DC to any frequency.

INTRODUCTION

The conventional mode stir chamber is a rectangular cavity, which uses an antenna to excite the fields inside of it. In order to homogenize the fields throughout the volume of the chamber it uses a metallic stirrer similar to a large paddle wheel. When the paddle wheel turns, being metallic, it changes the boundary conditions inside of the chamber producing a homogenization of the fields. This is a technique used by some microwave ovens to eliminate hot spots. The mode stirring approach only works when there is a substantial number of propagating modes inside the cavity, thus restricting the low frequency operation of these chambers. This is discussed in detail in a previous paper [1]. That paper proposes the use of two wires, parallel to one of the rectangular axis of the chamber. These wires and the four walls parallel to them form a coaxial transmission line, which supports a TEM wave, also known as the transmission line mode. The fields inside of the chamber can be stirred by changing the relative excitation between the two wires in phase, in amplitude or both. It was shown that with a very small amount of power substantial fields can be excited inside the chamber down to very low frequencies. In theory the frequency can be extend to DC. The antenna used in the present excitation method is not capable of exciting the TEM mode of propagation.

THE PROPOSED METHOD

As mentioned before in the previous paper [1] two wires parallel to one of the coordinate axis was used. The fields were stirred by changing the phase between the wires. The field at any point inside the chamber is the result of the two components produced by the excitation of each of the wires. Since there are only two components, and if the phase between the wires is changed from 0° to 180° , in a reasonable number of steps, it is expected that the fields should cover all possibilities from being in phase to out of phase. In this way, at all points within the chamber, it is reasonable to expect that the fields have attained their maximum value at some phase on the 180° interval. This maximization of field levels within a 180° phase interval does not necessarily occur with the use of a paddle wheel. The simulations and measurements demonstrated that, as expected, the fields transversal to the wires were stronger than the longitudinal components because of their TEM nature. If the wires were parallel to the x-axis, then the E_y and E_z components were larger than the E_x . Therefore a more uniform field can be obtained if three wires, one parallel to each coordinate axis, is used. Now there will be always two large TEM components parallel to each of the coordinate axis. This is proposed in the discussion section

at the end of the paper [1]. The present paper demonstrates that indeed this occurs.

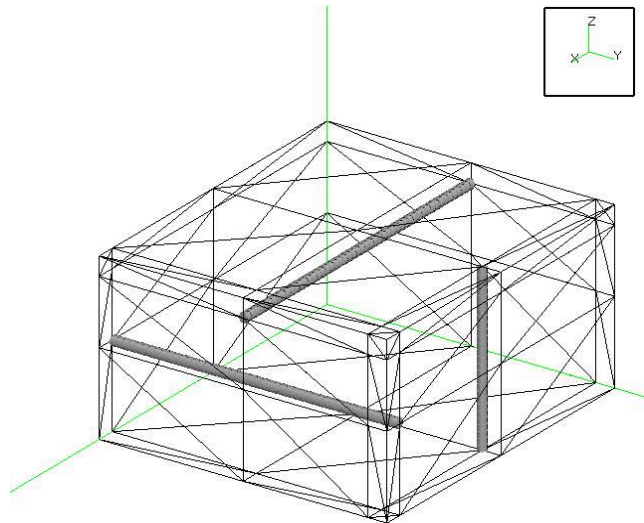


Fig 1 illustrates the geometry of the chamber. The triangles are the patches used by the MoM simulation program for the low frequencies. The three wires are shown by the orthogonal thick gray rod-like structures. They are situated about 40cm from the closest wall placed midway along the wall extent in order to create a more uniform field. The chamber dimensions are 5.2m x 4.6m x 2.7m in the x, y, and z coordinates respectively. Each wire is fed by an independent amplifier at one end, and is terminated with a 50-Ohm load at the other end. The simulation program calculates the fields inside the chamber at the vertices of cubes 20cm on a side

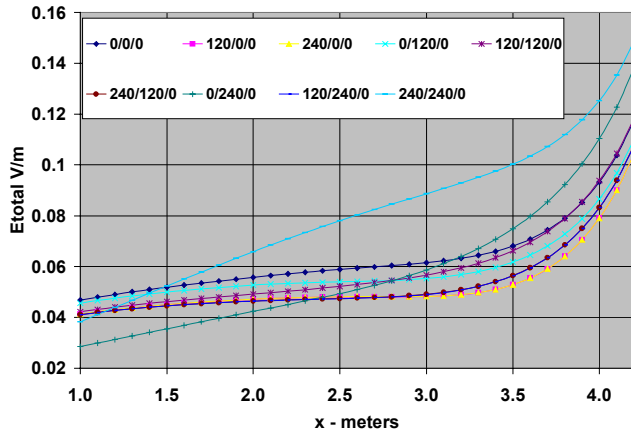
SIMULATION RESULTS

The simulation results shown below were obtained by using a MoM program. The wire parallel to the z-axis was used as reference and the phases of the other two wires were changed in steps of 120° . The reason for this choice was that three parallel vector phasors having the same amplitude and phases 0° , 120° , and 240° would add to zero. This is the case for each of the rectangular components of the vector phasors throughout the chamber. In each of the plots there are nine plots corresponding to the phases of 0/0/0, 120/0/0, 240/0/0, 0/120/0, 120/120/0, 240/120/0, 0/240/0, 120/240/0, and 240/240/0. The first phase is between the x-axis parallel wire and the z-axis parallel wire. The second is between the wire parallel to the y-axis and the wire parallel to the z-axis. The plots are for the total Electric field at different points along a line parallel to x-axis, 1m above the cavity floor ($z=1m$) and in the middle of the yz face ($y=2.3m$). For the chamber used this corresponds to $(x,2.3m,1.0m)$. The simulation

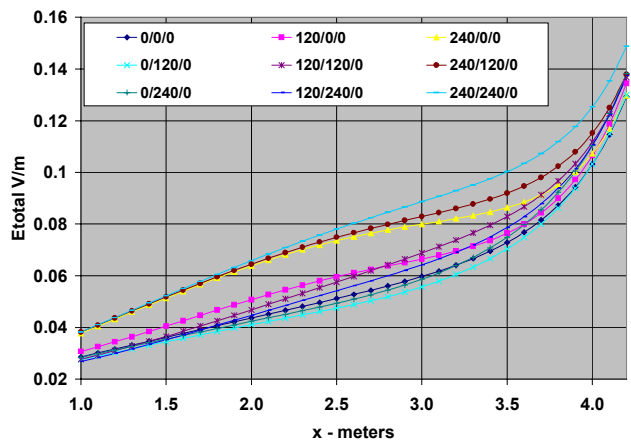
calculates all three rectangular components of the fields. The estimated “total field” given by:

$$E_t = \sqrt{|E_x|^2 + |E_y|^2 + |E_z|^2}$$

may be as much as 3 dB larger than the actual maximum field. This maximum can be achieved only if the phases of the three components are equal. Keeping this in mind Eq.1 gives an indication of the overall field strength. Fig 2 shows the result for the frequency of 10 kHz. The next two figures are for 10 MHz and 100 MHz. The chamber cut off frequency is 43.5 Mhz. Therefore only at 100 MHz there are propagating modes present.

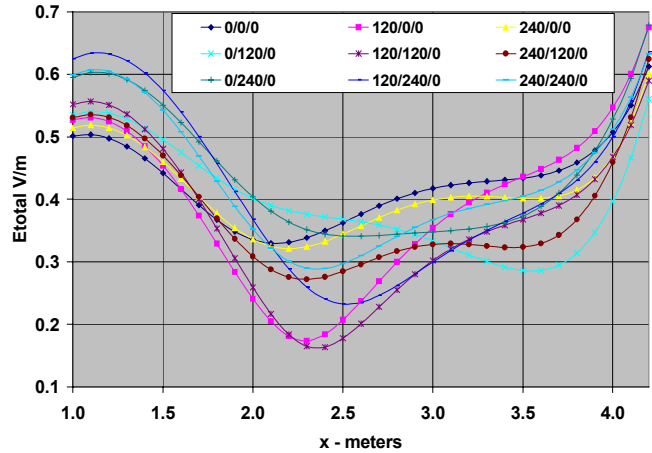


What is important in these plots is to observe the maximum value



of the Etotal-Field when the phases are changed since this is the maximum EUT exposure level. In the first two plots, Fig.2 and Fig.3, the maximum field is attained for the phases 240/240/0 most of the time. Only for low values of x, between 1.0 and 1.5 m that other phases produce a larger field in Fig.2. In Fig.4, for 100 MHz, different phases combinations contribute for the maximum field along the x-axis.

Notice that the total input power for all three plots is only a few mW. Multiplying the power by 10000 multiplies the fields by 100. Therefore for 10 kHz, with 150W total input power, an average field of 10 V/m can be expected. For 10 MHz, with 31W



again an average field of about 10 V/m can be expected.

At 100 MHz, with 81W the average field is about 50 V/m. This decrease of the power with the frequency is expected since now more of the modes excited in the cavity are becoming propagating modes.

Conclusion and Recommendations

The present configuration of three wires was an improvement over the two wires discussed in [1]. In the low frequency plots it is clear that the fields increase monotonically as x increases. At x = 4.2m the fields increase substantially because of the proximity to the y directed wire as can be seen in Fig.1. Presently different wire configurations and positions are under study and will be reported in the future as they become available.

The fact that more power is required for low frequencies to produce high field strength can be attributed to the fact that, although many cavity modes are excited at any frequency, only the transmission line mode propagates at the frequencies below the cavity fundamental resonance. Many cavity modes are necessary to satisfy the local boundary condition near the walls where the wires are attached. However these modes are all evanescent and cannot be felt throughout the cavity. This is discussed in detail in [1] and explains why the chamber cannot operate at low frequencies when excited by the antennas used today. As the frequency increases above the fundamental cavity resonance many of the excited cavity modes become propagating and start to contribute to the fields inside the chamber. Since high power amplifiers are substantially less expensive for low frequencies this fact may not be a problem.

REFERENCES

[1] Perini, J. and Cohen, L.S., “An Alternative Way to Stir The Fields in A Mode Stirred Chamber”, Proceedings of The 2000 IEEE International Symposium on Electromagnetic Compatibility, Pages 633-637, Aug. 2000, Washington, DC.

Working Nonlinear Transient Eddy Current Problems with Time Harmonic Solutions

Kent R. Davey

2275 Turnbull Bay Rd., New Smyrna Beach, FL 32168-5941, USA

Abstract - The classical approach to solving transient problems is a finite difference based time stepping procedure. A powerful alternative when motion is not involved is to use time harmonic solutions to build the transfer function of the system, appropriate for a spectrum of source excitations. This paper shows how nonlinear problems are approached with this method, and how the transfer function is derived using variable metrics and multivariate splines.

Index terms - Transient, eddy current, time harmonic, Laplace.

I. INTRODUCTION

Nearly all transient field problems are solved using a time stepping procedure in which the incremental changes are either explicitly or implicitly determined. These approaches are without doubt, the most general, but not necessarily the most efficient, especially when velocity effects are not involved. This paper discusses the use of time harmonic solutions to build a transfer function, and then to employ Laplace transform theory to generate the time transient. Among the advantages of this approach are the following:

1. Once the transfer function is known, the computation of the complete transient response is usually rapid.
2. No cumulative error accrues with time as is true in all time stepping procedures.
3. The solution to a multitude of source excitations is available, not simply the one obtained with the time stepping approach.

The technique is only valid when no velocity is involved. Within this context, however, even nonlinear effects can be taken into account. Nonlinearities get incorporated into the transfer function through the choice of excitation strength throughout the harmonic analysis.

II. Explanation of the Technique

The steps involved in this procedure are as follows:

1. Estimate the characteristic time constant for the system. This is usually accomplished by looking at the L/R time constant. Of importance is the shortest time constant for the system.
2. Execute a parametric analysis of the system over the complete spectrum of frequencies from 0 Hz to twice the

reciprocal of the shortest characteristic system time.

- a. If the excitation is current specified, this step is a simple loop incrementing frequency.
 - b. If the excitation is a voltage specification, a nested loop must be employed, the outer loop being incremented over the frequencies required, and the inner loop over the current range expected. The current range follows immediately at dc through the ratio of the voltage and the resistance. At every computation, both the flux linkage with the excitation coil(s) is required in addition to the desired output quantities, e.g., torque, force, etc.
3. A functional fit between the desired output quantities and the current must be computed. Bivariate splines and radial basis functions are two candidates for realizing this function fit.
 4. For a general voltage excitation, a nonlinear inverse algorithm must be employed to link the output quantities and the current to the voltage at any frequency. This nonlinear inversion is how saturation effects are incorporated into the solution. If the problem is linear, this step is trivial since any output is directly related to the voltage through the resulting current.
 5. The current or torque frequency dependence allows an estimate of the system transfer relation. Many choices for the number of poles and zeros are possible; the rule is to begin with one pole and to add additional poles and zeros as necessary consistent with the frequency response.
 6. Substitute the Laplace s domain parameter for the frequency.
 - a. Multiple by the Laplace transform of the source signal if available, and perform the inverse to get the time domain response for the parameter of interest.
 - b. If the Laplace transform of the signal does not exist, either multiply by $1/s$ and invert to get the unit step response, or invert directly to get the impulse response. An estimate of the output parameters follows by convolution.

III. THREE DIMENSIONAL NONLINEAR TRANSIENT EDDY CURRENT PROBLEM

Team problem 24 and problem 27 serve as a good test bed for this theory. Fig. 1 shows the geometry of problem 24. A solid steel hub and rotor are fixed at an angle of 22° from the vertical. Two series wound 350 turn coils are excited with a step voltage of 23.1 V at time zero. The output flux, desired current, and torque are desired as a function of time. The

conductivity of the steel is $4.54 \cdot 10^6$ S/m. Details of the measurements and the nonlinear material are discussed in [1]. A time stepping finite element procedure has been successfully employed in the solution [2].

IV. ANALYSIS RESULTS

Since voltage is impressed on the coils, an analysis of the device was required for a spread of currents and frequencies, computing the coil flux linkage at every step. Since the resistance of the coil is 3.09Ω , the current was allowed to change from 1 A to 8 A in 8 steps, varying the frequency from 0 Hz to 100 Hz in 12 steps. A 3D boundary element analysis was employed for this task [3].

The Bode plot function is determined by hypothesizing possible options, then determining the constants in those options using algorithm is based on Golden Section search and parabolic interpolation, also found in [4]. It is recommended that the simplest Bode function involving only one pole be attempted. It is useful to force the Bode relation to be correct at frequency f equal 0.

$$\frac{I(f)}{V(f)} = \frac{c I(f=0)}{f + c} \quad (1)$$

The unknown c is established by determining the minimum of a functional over the complete frequency spectrum, from $f=0$ to the final frequency f_N ,

$$\mathcal{F} = \sum_{j=0}^{f_N} \sqrt{\left\{ I(f_j) - \frac{c I(1)}{f_j + c} \right\}^2} \quad (2)$$

A double pole, one zero approximation would involve two unknowns,

$$\frac{I(f)}{V(f)} = \frac{f + C_1 C_2 I(f=0)}{\{ (f + C_1) (f + C_2) \}} \quad (3)$$

Single and double pole models are investigated. The double pole approximation is only slightly improved; if the single pole approximation is close, adding the second pole will introduce a faster response decay constant, a result that is not normally desired.

Once the Bode relation is determined, the Laplace transform for the system is found by substituting the Laplace variable s for frequency f . This is multiplied by the source Laplace transform, and the resulting expression inverted. For example, given (3), the current's step response to a voltage signal is

$$I(t) = \frac{1}{(C_1 - C_2)} \left\{ C_1 I(f_0) - C_2 I(f_0) + e^{-C_1 t} [C_2 I(f_0) - 1] + e^{-C_2 t} [1 - C_1 I(f_0)] \right\} \quad (4)$$

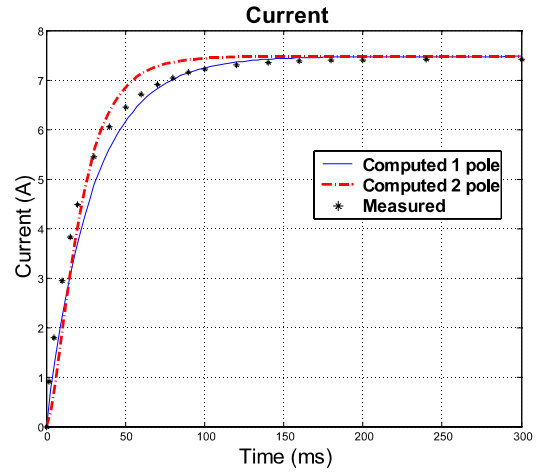


Fig. 1 Computed Current with one and two pole models.

Shown in Fig. 5 is the computed time response for the current. The two pole model does indeed add in an unwanted faster time constant. The two pole system more closely models the experiment at the beginning of the transient than does the single pole model. However, the single pole model exhibits a better overall fit.

V. CONCLUSIONS

For problems that do not involve velocity, deriving the transfer function from time harmonic solutions affords a useful way of investigating a multitude of responses. Evaluations of the responses with time is fast, and no accumulation of errors surfaces, as with the more typical time stepping procedures. If possible, the time harmonic responses should be registered close to the actual source values to incorporate nonlinear effects. The simpler Bode relations with one or two poles is recommended. The form of the Bode relation is different for every variable of interest, but the form, i.e., the number of poles and zeros) should not change much.

VI. REFERENCES

- [1]. M. Burnet Fauchez, "Calculation of eddy currents in N. Allen and D. Rodger, "Description of Team workshop problem 24: Nonlinear time transient rotational test rig", pp. 1-4, <http://ics.ec-lyon.fr/problems/problem24.pdf>.
- [2]. D. Rodger, N. Allen, H.C. Lai, and P.J. Leonard, "Calculation of Transient 3D eddy currents in nonlinear media - Verification Using a Nonlinear Test Rig," *IEEE Trans. Magn.*, vol. 30, no. 5, pp. 2988-2991, 1994.
- [3]. Dalian Zheng, "Three dimensional eddy current analysis by the boundary element method", *IEEE Trans. Magn.*, vol. 33, no. 2, March 1997, pp. 1354-1357.
- [4]. Forsythe, G. E., M. A. Malcolm, and C. B. Moler, *Computer Methods for Mathematical Computations*, Prentice-Hall, 1976.
- [5]. Kent R. Davey, "Use of Tensor Product Splines in Magnet Optimization", *IEEE Transactions on Magnetics*, Vol. 35, No. 3, pp. 1714-1717, May 1999.

Numerical Analysis of Thin Skin Depth of 3-D Eddy Current Problems Using a Combination of Finite Element and Meshless Methods

Shiyong YANG¹, S. L. HO², Guangzheng NI¹, H.C. WONG³, Yuhuai WANG¹

¹EE College, Zhejiang University, China

²EE Department, ³Industrial Centre, The Hong Kong Polytechnic University, Hong Kong

Email : eeslho@polyu.edu.hk

Abstract—To alleviate the difficulties encountered in the generation of meshes for the FE method in solving thin skin depth problems involving 3-D eddy current, particularly in cases in which the eddy current region is only a fraction of the entire domain, a new technique based on a combination of FE and meshless methods is proposed. Numerical approach to uphold the mathematical properties of the combined shape functions in terms of consistency and linear independence is also investigated. It is shown that a very coarse mesh is sufficient with the proposed algorithm. To validate and demonstrate the advantages of the proposed method, typical numerical results on a prototype high frequency 3-D eddy current problem are reported.

COMBINED METHOD OF FE AND MESHLESS METHOD FOR THIN SKIN DEPTH
3-D EDDY CURRENT PROBLEMS

Although finite element (FE) methods are widely used and recognized as the most powerful numerical technique by academics and engineers alike in solving 3-D electromagnetic field problems, they are not equally applicable to all kinds of field problems such as in, for example, large scale thin skin depth 3-D eddy problems in which the eddy current region is only a fraction of the entire domain. For these thin skin depth problems using 3-D FE methods, one normally has to make a compromise on the need for fine meshes (to ensure the solutions in the eddy current regions are sufficiently accurate) and the need for minimizing the computer resources. Thus, a flexible method to add or remove meshes or nodes irrespective the connectivity of the existing meshes or nodes is highly desirable. In this regard, meshless methods are ideal. On the other hand, meshless methods are notorious in enforcing boundary and interface conditions when they are used to solve boundary value problems. To make full use of the advantages of FE and meshless methods, a combined FE and meshless method is proposed in the numerical study of large scale 3-D eddy current problems to allow one to obtain sufficiently accurate numerical solutions from coarse meshes. In order to separate the meshless and the FE shape functions, the bridging scales are added to modify the meshless shape functions to preserve the desirable mathematical properties of the resulting function space in terms of consistency and linear independence.

Shape Function of Meshless Methods

The development of the shape function of the proposed meshless method is based on the moving least squares approximation. For any function $\dot{A}(x, y, z)$, its approximation based entirely on the meshless method in terms of a set of nodes in the solution domain is

$$\dot{A}(x, y, z) = \sum_{j=1}^n \Phi_j^{\text{meshless}}(x, y, z) \dot{c}_j \quad (1)$$

where $\Phi_j^{\text{meshless}}(x, y, z)$ is the shape function of the meshless method, and its details are referred to [1].

Shape Function of the Combined Method

For the proposed method, the meshless method is only used to refine the FE solutions in the eddy current regions. Thus, the approximation of the solution variable in most of the solution domain is expressed in the standard form of FE methods. For the eddy current regions, the general interpolation formula using both FE and meshless shape functions is

$$\dot{A}(x, y, z) = \sum_i \dot{A}_i N_i^{\text{FEM}}(x, y, z) + \sum_j \Phi_j^{\text{Meshless}}(x, y, z) \dot{c}_j \quad (2)$$

where, $N_i^{\text{FEM}}(x, y, z)$ is the FE shape function.

To uphold the mathematical properties of the entire bases regarding consistency and linear independence, the bridge scales as proposed in [2] is used. The basic concept of the bridging scales is based on a hierarchical decomposition of a function \dot{A} which is dependent on some projection operator P to represent, for example, the projection of \dot{A} onto the span of FE shape functions. To decompose the solution variable into two different parts, i.e., the first one that is approximated by meshless shape functions and the second one being represented by the FE shape functions, one employs the property of a projection operator such that multiple projections of the function will leave the function unchanged, i.e., $PP\dot{A} = P\dot{A}$. By using this concept, the total function \dot{A} of (2) can now be reformulated as

$$\begin{aligned} \dot{A}(x, y, z) = & \sum_i \dot{A}_i N_i^{\text{FEM}}(x, y, z) + \sum_j \Phi_j^{\text{Meshless}}(x, y, z) \dot{c}_j \\ & - \sum_i \sum_j N_i^{\text{FEM}}(x, y, z) \Phi_j^{\text{Meshless}}(x_i, y_i, z_i) \dot{c}_j \end{aligned} \quad (3)$$

The last term on the right hand side of (3) is called the bridging scales. The reason for including the bridging scale term is to make the term that is approximated by the meshless shape functions to contain only the parts of the solution variable which are not included in FE interpolations. Accordingly, the meshless shape function based on the bridging scales is modified as

$$\begin{aligned} \overline{\Phi}_j^{\text{Meshless}}(x, y, z) = & \Phi_j^{\text{meshless}}(x, y, z) \\ & - \sum_i N_i^{\text{FEM}}(x, y, z) \Phi_j^{\text{meshless}}(x_i, y_i, z_i) \end{aligned} \quad (4)$$

Thus, the general interpolation formula for the proposed combined FE and meshless methods is

$$\dot{A}(x, y, z) = \sum_i \dot{A}_i N_i^{FEM}(x, y, z) + \sum_j \dot{\Phi}_j^{meshless}(x, y, z) \dot{c}_j \quad (5)$$

The details about the discrete mathematical model and the numerical implementation of the proposed combined FE and meshless method will be given in the full paper.

NUMERICAL APPLICATIONS

To validate the feasibility of the proposed algorithm for solving practical thin skin depth eddy current problems, the electromagnetic fields around a circular conductor carrying a 20kHz harmonic current flowing in the z-coordinate direction as shown in Fig. 1 is investigated. The radius of the circular conductor is 2mm. By setting a cylindrical surface, S_1 , which is co-centered with the conductor and is sufficiently far from the conductor surface, S_3 , so that the field on S_1 can be approximated as zero, this pseudo-3D eddy current problem is formulated as

In the conductor

$$\begin{aligned} \nabla \times (\nu \nabla \times \dot{A}) - \nabla (\nu \nabla \cdot \dot{A}) + j\omega \dot{A} + \sigma \nabla \dot{V} &= \dot{J}_z \\ \nabla \cdot (-j\omega \sigma \dot{A} - \sigma \nabla \dot{V}) &= 0 \end{aligned} \quad (6)$$

In the residual regions

$$\begin{aligned} \nabla \times (\nu \nabla \times \dot{A}) - \nabla (\nu \nabla \cdot \dot{A}) &= 0 \\ \dot{A}_x|_{S_1} = \dot{A}_y|_{S_1} = \dot{A}_z|_{S_1} &= 0 \\ \dot{V}|_{S_3} &= 0 \end{aligned} \quad (7)$$

In the numerical implementation, the entire domain is firstly discretized into a coarse FE mesh. Some nodes are then added into the thin skin depth eddy current region (the conductor) as shown in Fig. 2. The comparison on the accuracy of the computed results using the proposed method and those obtained from a close-form expression is given in Fig. 3. The distribution of the magnetic flux density along the radial direction is shown in Fig. 4. From these numerical results, it is very clear that (1) the results of the computed eddy current distribution of the proposed method and those obtained from the close-form expression are nearly the same, and they are indeed indistinguishable in the figure; (2) besides producing nearly exact solutions of the eddy current fields in the conductor where both FE mesh and meshless nodes are used, the proposed algorithm also produces very accurate far end magnetic flux density results even if very coarse FE meshes are used. Thus these numerical results positively confirm the feasibility of the proposed algorithm for solving practical large scale 3-D eddy current problems.

REFERENCES

- [1] T. Belytschko, Y.Y. Lu, and L. Gu, "Element-free Galerkin Methods," *Int. J. Numer. Meth. Engng.*, vol. 37, pp. 229-254, 1994.
- [2] G.J. Wagner, W.K. Liu, "Hierarchical enrichment for bridging scales and mesh-free boundary conditions," *Int. J. Numer. Meth. Engng.*, vol.50, pp.507-524, 2001.

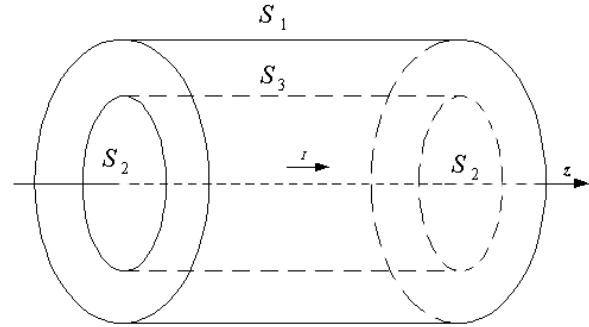


Fig. 1. A circular conductor carrying a 20kHz harmonic current flowing in the z-coordinate direction

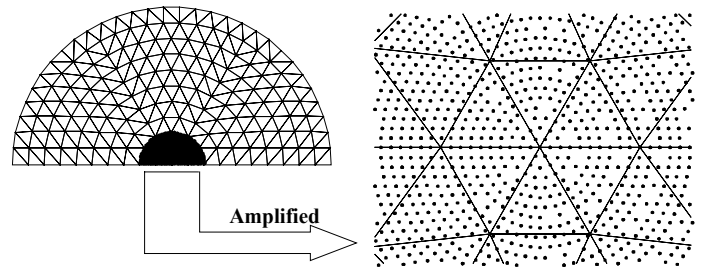


Fig. 2. The finite element mesh and the node arrangement of the proposed method Surface S_2 . Left: global survey of the FE meshes and meshless nodes, Right: amplified view of the conductor region

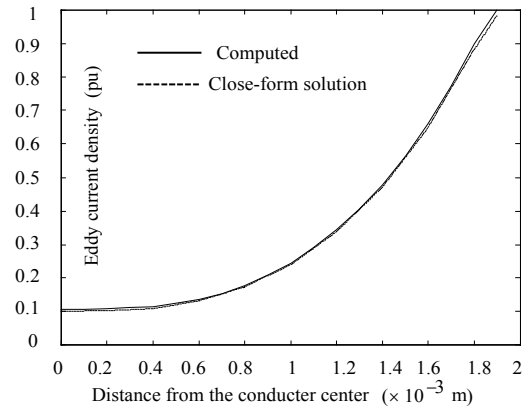


Fig. 3 The distribution of the eddy current density in the conductor

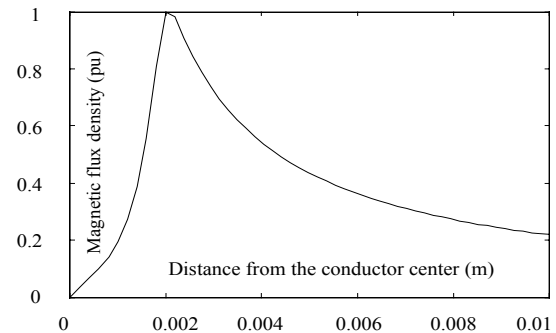


Fig. 4. The distribution of the magnetic flux density along radial direction

A Single-Source Surface Integral Formulation for Eddy-Current Problems

I.R.Ciric, *Fellow, IEEE*, and R.Curiac, *Student Member, IEEE*

Department of Electrical and Computer Engineering
The University of Manitoba, Winnipeg, Manitoba, Canada R3T 5V6
e-mail: irciric@ee.umanitoba.ca; rcuriac@ee.umanitoba.ca

Abstract – An integral equation satisfied by a single unknown surface current density is formulated for the analysis of the quasistationary field of a cylindrical conductor immersed in a transverse time-harmonic magnetic field. This is an alternative to the classical boundary integral equations formulated in terms of two unknowns, the magnetic vector potential and its normal derivative over the conductor surface. The accuracy of the results computed by the proposed solution method is demonstrated by comparison with results from an exact analytical method.

I. INTRODUCTION

Various finite difference and finite element techniques have been developed for computing eddy currents in homogeneous and nonhomogeneous solid conductors [1]. In these techniques, the entire conducting region is discretized and the respective nodal unknowns have to be determined throughout the region. Eddy currents in homogeneous conductors can also be analyzed by using boundary integral equations formulated in terms of two unknowns, for instance, the magnetic vector potential and its normal derivative distributed over the surface of the conducting bodies [2].

In this paper, a formulation of a single-source surface integral equation (SSSIE) is presented for the analysis of eddy currents induced in two-dimensional conductors. The vector potential in the region inside the conductor is expressed in terms of a single unknown surface current density distributed over the surface of the conductor, while the potential outside the conductor is obtained from the formula of the three potentials for Laplacian fields. In order to evaluate the accuracy of the proposed method, numerical results have been generated using a circular cylindrical conductor and are compared with those obtained from the eigenfunction solution.

II. FORMULATION

Consider a cylindrical conductor of arbitrary cross section immersed in a transverse time-harmonic magnetic field of flux density B_0 . The material inside the body is characterized by a conductivity σ and a permeability μ , while the region outside is a free space.

The magnetic vector potential has only a component parallel to the conductor. Inside the conducting region D , it satisfies a homogeneous Helmholtz equation,

$$(\nabla^2 + k^2)A(\mathbf{r}) = 0, \quad \mathbf{r} \in D \quad (1)$$

where $k^2 \equiv -j\omega\mu\sigma$, ω is the angular frequency, and \mathbf{r} is the position vector of the observation point. In the free-space region D_e , the quasistationary magnetic vector potential is decomposed as $A_e = A_0 + A'$, where A_0 corresponds to the external field B_0 and A' satisfies the Laplace equation

$$\nabla^2 A'(\mathbf{r}) = 0, \quad \mathbf{r} \in D_e \quad (2)$$

The following continuity conditions across the interface S between the conducting and the nonconducting regions are to be imposed:

$$A(\mathbf{r}) = A_e(\mathbf{r}), \quad \mathbf{r} \in S \quad (3)$$

$$\frac{1}{\mu} \frac{\partial A(\mathbf{r})}{\partial n} = \frac{1}{\mu_0} \frac{\partial A_e(\mathbf{r})}{\partial n}, \quad \mathbf{r} \in S \quad (4)$$

with $\partial/\partial n$ denoting the normal derivative and μ_0 the permeability of free space.

In order to construct a single-source surface integral equation, we first assume to have everywhere conducting material identical with that in the region D and that the actual potential A in D is produced by a single layer of electric surface current parallel to the vector potential, of density J_s , distributed over the conductor surface, while the potential in D_e is left undefined, i.e.

$$A(\mathbf{r}) = \mathcal{A}J_s, \quad \mathbf{r} \in D \cup S \quad (5)$$

where the integral operator \mathcal{A} is given from

$$\mathcal{A}J_s = -\frac{j\mu}{4} \int_C J_s(\mathbf{r}') H_0^{(2)}(kR) dl' \quad (6)$$

with C being the conductor cross-sectional contour, $H_0^{(2)}$ the Hankel function of second kind and zero order, $R = |\mathbf{r} - \mathbf{r}'|$ and \mathbf{r}' the position vector of the source point. The tangential component of the actual magnetic field intensity just inside the conductor surface is

$$H_t(\mathbf{r}) = -\frac{1}{\mu} \frac{\partial A}{\partial n} = -\frac{1}{2} J_s + \mathcal{H}J_s \quad (7)$$

where the integral operator \mathcal{H} is defined from

$$\mathcal{H}J_S = \oint_C J_S(\mathbf{r}') \frac{\partial}{\partial n} H_0^{(2)}(kR) dl' \quad (8)$$

with the integral taken in principal value.

On the other hand, the potential A_e in the region D_e , outside the conductor, can be represented by applying the Green theorem. Assuming that the potential and the magnetic field vanish at infinity,

$$A_e(\mathbf{r}) = A_0(\mathbf{r}) - \frac{1}{2\pi} \left[\int_C \frac{\partial A_e(\mathbf{r}')}{\partial n'} \ln \frac{1}{R} dl' - \int_C A_e(\mathbf{r}') \frac{\partial}{\partial n'} \left(\ln \frac{1}{R} \right) dl' \right], \quad \mathbf{r} \in D_e \cup S \quad (9)$$

Taking into account (3), (4) and (7), the actual potential just outside the conductor surface S is

$$A_e(\mathbf{r}) = A_0(\mathbf{r}) + \mathcal{A}_0^e H_t + \left(\frac{1}{2} I + \mathcal{A}_0^m \right) A, \quad \mathbf{r} \in S \quad (10)$$

where I is the identity operator and with the operators \mathcal{A}_0^e and \mathcal{A}_0^m acting as

$$\mathcal{A}_0^e H_t = \frac{\mu_0}{2\pi} \int_C H_t(\mathbf{r}') \ln \frac{1}{R} dl' \quad (11)$$

$$\mathcal{A}_0^m A = \frac{1}{2\pi} \int_C A(\mathbf{r}') \frac{\partial}{\partial n'} \left(\ln \frac{1}{R} \right) dl' \quad (12)$$

and the integral in (12) evaluated in principal value.

Imposing the continuity condition in (3) and substituting H_t from (7) and A from (5) yields a single-source surface integral equation in J_s ,

$$\left[\mathcal{A}_0^e \left(-\frac{1}{2} I + \mathcal{H} \right) + \left(-\frac{1}{2} I + \mathcal{A}_0^m \right) \mathcal{A} \right] J_s = -A_0, \quad \mathbf{r} \in S \quad (13)$$

Once the unknown current density J_s is determined from (13), the magnetic vector potential in D and D_e is obtained, respectively, from (5) and (9), i.e.

$$A(\mathbf{r}) = \mathcal{A} J_s, \quad \mathbf{r} \in D \quad (14)$$

$$A_e(\mathbf{r}) = A_0 + \left[\mathcal{A}_0^e \left(-\frac{1}{2} I + \mathcal{H} \right) + \mathcal{A}_0^m \mathcal{A} \right] J_s, \quad \mathbf{r} \in D_e \quad (15)$$

III. NUMERICAL RESULTS

The single-source surface integral equation has been implemented numerically for a circular cylindrical conductor by employing a point-matching method of moments. The cylinder cross-sectional contour was discretized into a number of about 60 straight segments, with a constant current density J_s over each segment. In order to test the accuracy of

the SSSIE solution, the induced eddy-current density was calculated for several frequencies and compared with the corresponding analytical solution.

Numerical results shown in Fig.1 are for a cylinder of a conductivity $\sigma = 5.8 \times 10^7$ S/m (copper) and a permeability $\mu = \mu_0$, immersed in a uniform magnetic field of flux density B_0 with a time-harmonic variation. The magnitude of the induced current density normalized to $B_0 / (\mu_0 r_c)$, where r_c is the cylinder radius, is plotted versus the distance r from the cylinder center along the direction perpendicular to the direction of the external field for various depths of penetration δ .

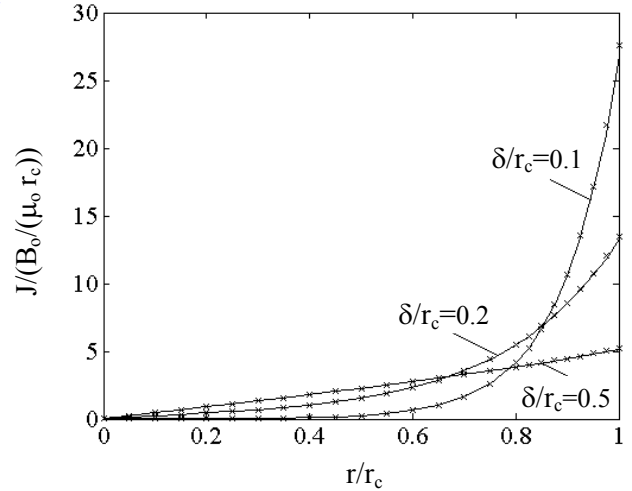


Fig.1. Magnitude of the normalized induced current density versus the normalized distance from the cylinder center for various skin depths: — SSSIE ; x exact analytical solution.

IV. CONCLUSIONS

A single-source surface integral equation has been formulated for the analysis of eddy currents in cylindrical conductors, all the field quantities of interest being determined in terms of only one surface current distributed over the conductor boundary. It was tested for a conductor immersed in a transverse time-harmonic magnetic field.

The computational accuracy of the SSSIE method has been demonstrated by comparison with the exact analytical solution for a large range of frequencies.

REFERENCES

- [1] M.V.K.Chari, G.Bedrosian, J.D'Angelo, and A.Konrad, "Finite element applications in electrical engineering", *IEEE Trans. Magn.*, vol.29, pp.1306-1314, March 1993.
- [2] W.M.Rucker and K.R.Richter, "Calculation of two-dimensional eddy current problems with the boundary element method", *IEEE Trans. Magn.*, vol.19, pp.2429-2432, November 1983.
- [3] D.R.Swatek and I.R.Ciric, "Single source integral equation for wave scattering by multiply-connected dielectric cylinders", *IEEE Trans. Magn.*, vol.32, pp.878-881, May 1996.

Performance of Surface Impedance Integral Equation for Quasistationary Field Analysis in Axisymmetric Systems

Himal C. Jayatilaka and Ioan R. Ciric, *Fellow, IEEE*

Department of Electrical and Computer Engineering
The University of Manitoba, Winnipeg, MB R3T 5V6, Canada
e-mail: himal@ee.umanitoba.ca

Abstract – Surface integral equations satisfied by the induced current density are formulated for axisymmetric solid conductors by applying the surface impedance model. Their performance is investigated employing prolate and oblate conducting spheroids with a large range of geometric parameters. Numerical results generated are compared with available analytical results and with experimental data.

INTRODUCTION

Boundary integral equations are used for solving approximately a wide range of electromagnetic field problems. They have the advantage of requiring less computation than methods based on the discretization of the entire conducting region. The perfect conductor model is commonly used in the formulation of surface integral equations for solid conductors, especially at high frequencies. The validity of this model has been analyzed in [1] for spheroids of various axial ratios by comparison with experimental results.

In this paper, we formulate surface integral equations for axisymmetric conductors in the presence of quasistationary magnetic fields using both the surface impedance and the perfect conductor models. These integral equations are solved numerically for the unknown surface current density by applying a point matching procedure [2]. Power losses and forces are derived from the induced current and computed results are compared with available measured data. The minimum number of necessary unknowns for a desired accuracy is determined for various prolate and oblate spheroidal conductors.

INTEGRAL EQUATION FORMULATION

Consider an arbitrarily shaped axisymmetric good conductor, as depicted in Fig. 1, in the presence of a quasistationary magnetic field produced by coaxial turns carrying sinusoidal with time currents of same frequency. At sufficiently small depths of penetration, the electromagnetic field can be analyzed by determining the equivalent surface current density \mathbf{J}_s which has an azimuthal φ -direction. An integral equation satisfied by \mathbf{J}_s is constructed by imposing

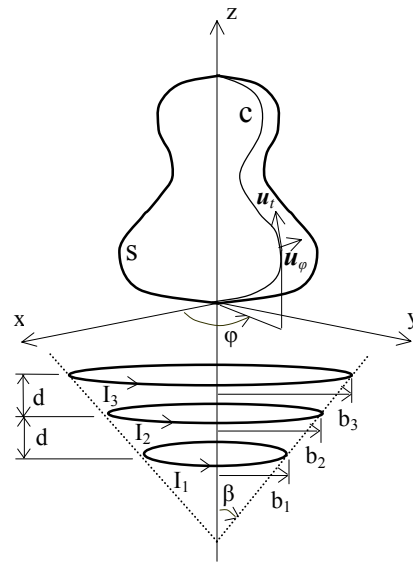


Fig. 1. Solid conductor in the presence of current-carrying turns.

the condition that the tangential electric field intensity at the conductor surface S ,

$$E_\varphi = -\frac{j\omega\mu_0}{4\pi} \left[\mathbf{u}_\varphi \cdot \int_S \frac{\mathbf{J}_s(\mathbf{r}')}{R} ds' + \sum_{k=1}^N I_k \mathbf{u}_\varphi \cdot \int_{C_k} \frac{d\mathbf{l}'}{R} \right] \quad (1)$$

is related to the tangential magnetic field intensity,

$$H_t = \frac{1}{4\pi} \left[\mathbf{u}_t \cdot \int_S \frac{\mathbf{J}_s(\mathbf{r}') \times \mathbf{R}}{R^3} ds' + \sum_{k=1}^N I_k \mathbf{u}_t \cdot \int_{C_k} \frac{d\mathbf{l}' \times \mathbf{R}}{R^3} \right] \quad (2)$$

through the surface impedance Z_s ,

$$E_\varphi|_S = -Z_s H_t|_S \quad (3)$$

Here, $\mathbf{R} = \mathbf{r} - \mathbf{r}'$, with \mathbf{r} and \mathbf{r}' being the position vectors of the observation point and the source point, respectively, $d\mathbf{l}'$ is the vector length element in the direction of the current along the respective inducing turn C_k , N is the total number of current-carrying turns, \mathbf{u}_t and \mathbf{u}_φ are unit vectors along the

generator curve C of the conductor and along the azimuthal direction, respectively, I_k is the current carried by the k -th turn, and $Z_s = R_s(1+j)$, with $R_s = (\omega\mu_0/(2\sigma))^{1/2}$ and $j \equiv \sqrt{-1}$, ω , μ_0 and σ being the angular frequency, the permeability and the conductivity of the conductor, respectively. The formulation for the perfect conductor model is obtained by taking $Z_s=0$.

The surface integrals in (1) and (2) are taken in principal values and the singularities in the integrands are evaluated by considering separately the contributions of each rectangular self-patch of dimensions $g \times h$ to the fields at its center, namely

$$E'_\varphi = -\frac{j\omega\mu_0 J_s}{\pi} \left[g \ln \left(\frac{h}{g} + \sqrt{1 + \frac{h^2}{g^2}} \right) + h \ln \left(\frac{g}{h} + \sqrt{1 + \frac{g^2}{h^2}} \right) \right] \quad (4)$$

and

$$H'_t = -\frac{J_s}{2} \quad (5)$$

NUMERICAL RESULTS AND CONCLUSION

To illustrate the performance of the surface integral equation in (3), we consider an Aluminum ($\sigma = 3.77 \times 10^7$ S/m) prolate spheroid of major and minor semi-axes a_0 and b_0 , respectively, in the presence of three coaxial turns connected in series and carrying a current I_0 . The three turns are placed on the surface of a cone of opening 2β , as shown in Fig.1, the distance between the plane of the lower turn and the spheroid center being d_1 . Due to the axisymmetry of the system, the induced current density has a component only in the φ -direction. The conductor surface is discretized into a number of M coaxial rings and their vector potential and magnetic field intensity are computed by employing Biot-Savart formulas. Each ring and each external current-carrying turn is divided into a number of elements to evaluate their vector potential and magnetic field intensity. The current density of each ring is considered to be constant and concentrated on the centerline of the ring, except wherever the source point coincides with the observation point, when the contributions in (4), (5) are used. The integral equation is finally reduced to a system of M linear equations with M unknowns, which are the current densities of the rings. The force acting upon the spheroid is evaluated by computing the force upon the inducing turns, which is the same in magnitude but opposite in direction. The accuracy of the numerical results for the forces and for the power loss in the conductor is increased to a desired level by increasing the number of elements on the conductor surface and by comparison with available analytical results and experimental data. The force normalized to $\mu_0 I_0^2$ for two frequencies and various geometric

parameters is plotted in Figs. 2 and 3 as a function of d_1/b_1 . A good agreement with experimental data is achieved in the cases considered when using a number of about forty rings and one hundred elements on each ring. The improvement brought by the surface impedance model over the perfect conductor one, especially at smaller distances between the inducing turns and the induced body, is shown in Fig. 3.

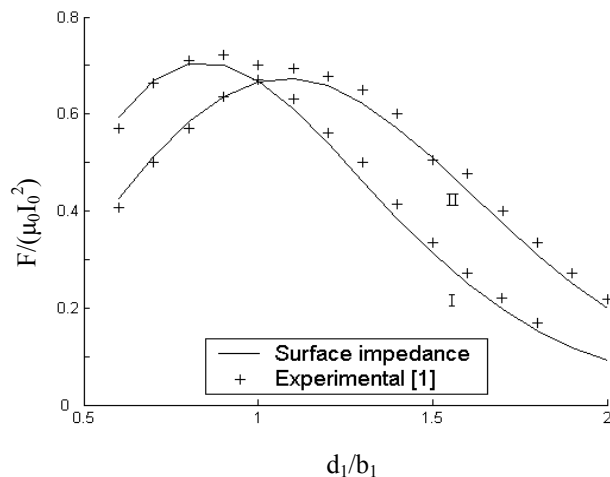


Fig. 2. Normalized force versus d_1/b_1 for an Aluminum conducting spheroid at 8 KHz, with $N=3$, $\tan\beta=0.4$, $d/b_1=0.25$, $b_0/b_1=0.5$ and $b_0=2$ cm: (I) $b_0/a_0=0.6$; (II) $b_0/a_0=0.4$.

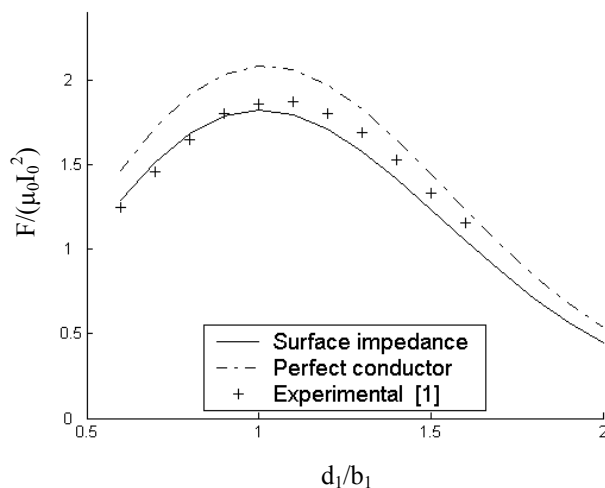


Fig. 3. Normalized force versus d_1/b_1 for an Aluminum conducting spheroid at 2 KHz, with $N=3$, $\tan\beta=0.4$, $d/b_1=0.25$, $b_0/b_1=0.75$, $b_0/a_0=0.6$ and $b_0=2$ cm.

REFERENCES

- [1] I.R. Ciric, "Electromagnetic levitation in axially symmetric systems," *Rev. Roum. Sci. Techn.-Electrotechn. et Energ.*, vol.15, pp. 35-73, 1970.
- [2] R.F. Harrington, *Field Computation by Moment Methods*. New York: Macmillan, 1968.

The Weighted Wavelet-Based Multiresolution Time-Domain Analysis in the MOM Solutions for Transient Eddy Current Problems

K. R. Shao, L. R. Li

Department of Electrical Engineering, Huazhong University of Science & Technology, Wuhan, 430074 China

J. D. Lavers

Department of Electrical & Computer Engineering, University of Toronto, Toronto, M5S 3G4 Canada

Abstract — A novel method of moments approach to the solutions of time-domain integral-equation formulation of transient eddy current problems is presented. The method is based on a time-domain multiresolution analysis. The wavelets are biorthogonal with respect to a weighted inner product and are used as basis functions in MoM solutions. The TEAM benchmark problem 4 is analyzed as a sample problem to show the validity of the technique. The matrix obtained by the proposed approach is rendered sparsely populated.

FOUNDATION OF WAVELET AND WEIGHTED MULTIREOLUTION ANALYSIS

The basic formulation of wavelet theory for electric and magnetic field computations can be found in [1]. The weighted multiresolution analysis technique was fully described in [5] and will be briefly outlined in the full paper.

INTRODUCTION

The wavelet-based multiresolution analysis (MRA) has been applied to many problems in Electromagnetics [1]-[3]. The matrix obtained by MRA is rendered sparsely populated.

In this paper, we take a novel approach to build a wavelet system, referred to as the lifting scheme [4]. In this approach, we use a new biorthogonal wavelet system as basis and weighting functions in the method of moments (MoM) for transient eddy current problems. The weight function in the scalar product of basis functions speeds up the convergence of the algorithm while preserving the sparse matrix structure. The validity of the proposed technique is examined by using the TEAM benchmark problem 4, the FELIX brick, and the calculated results are compared with those obtained by using other methods.

BASIC FORMULATION

Combining the definition of electric field $\mathbf{E}(\mathbf{r},t)$ and Ohm's law inside the conducting material we have:

$$\mathbf{E} = -\partial\mathbf{A} / \partial t - \nabla\phi = \mathbf{J} / \sigma . \quad (1)$$

The magnetic vector potential \mathbf{A} can be expressed as:

$$\mathbf{A} = \frac{\mu}{4\pi} \int_{\Omega} \frac{\mathbf{J}(\mathbf{r}', t')}{|\mathbf{r} - \mathbf{r}'|} d\Omega \quad (2)$$

Using the Lorentz gauge $\nabla \cdot \mathbf{A} = -\mu\epsilon \frac{\partial\Phi}{\partial t}$ and considering a causal system we obtain :

$$\Phi = -\frac{1}{\mu\epsilon_0} \int_{\Omega} \nabla \cdot \mathbf{A} d\tau \text{ and consequently:}$$

$$\begin{aligned} \frac{\mathbf{J}(\mathbf{r}, t)}{\sigma} = & -\frac{\mu}{4\pi} \int_{\Omega} \frac{\partial\mathbf{J}(\mathbf{r}', t')}{\partial t} \frac{1}{|\mathbf{r} - \mathbf{r}'|} d\Omega \\ & + \nabla \frac{1}{\mu\epsilon_0} \int_{\Omega} \left(\nabla \cdot \frac{\mu}{4\pi} \frac{\mathbf{J}(\mathbf{r}', t')}{|\mathbf{r} - \mathbf{r}'|} d\Omega \right) d\tau \end{aligned} \quad (3)$$

NUMERICAL SAMPLE AND RESULTS

The TEAM benchmark problem 4, 3D transient eddy currents in a rectangular aluminum brick with a hole shown in Fig. 1, is analyzed. The brick is 0.1524mx0.1016mx0.0508m. A rectangular hole 0.0889mx0.0381m penetrates the brick through the centers of the large faces. The applied magnetic field is uniform and decays exponentially with time as follows:

$$B_z = 0.1 \exp(-t/0.0119).$$

The resistivity of aluminum $\rho=3.94 \times 10^{-8} \Omega m$. Due to the symmetry, the solution region is the 1/8 brick shown in Fig.2.

Fig. 3 and Fig. 4 show the good agreement between the calculated results obtained with the proposed weighted MRA and FEM.

REFERENCES

- [1] K. R. Shao, J. C. Yang, J.D. Lavers, "Wavelet-based multiresolution algorithm for integral and boundary element equations in electric and magnetic field computations," *IEEE Transactions on Magnetics*, Vol.38, pp. 2373-2375, September 2002
- [2] Y. Shifman, Y. Leviatan, "On the use of spatio-temporal multiresolution analysis in method of moment solutions of transient electromagnetic scattering," *IEEE Transactions on Antennas and Propagation*, Vol. 49, pp. 1123-1129, August 2001
- [3] Ben Zion Steinberg, Yehuda Leviatan, "On the use of wavelet expansions in the method of moments," *ibid*, Vol. 41, pp. 610-619, May 1993
- [4] W. Sweldens, "The lifting scheme: A construction of second generation wavelets," *Siam J. Math. Anal.*, Vol.29, No.2, pp. 511-546, 1997
- [5] Mikhail Toupikov, Guang-Wen Pan, Barry K.Gilbert, "Weighted wavelet expansion in the method of moments," *IEEE Transactions on Magnetics*, Vol.35, pp. 1550-1553, May 1999

This work was supported by NSFC under Grant No. 50077009.

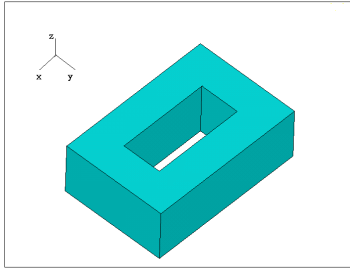


Fig. 1 The geometry of FELIX brick.

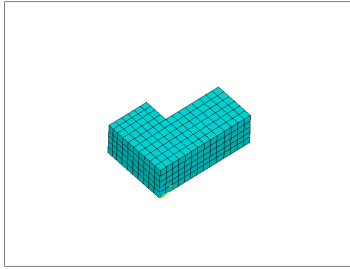


Fig. 2 The solution region: the 1/8 of the brick.

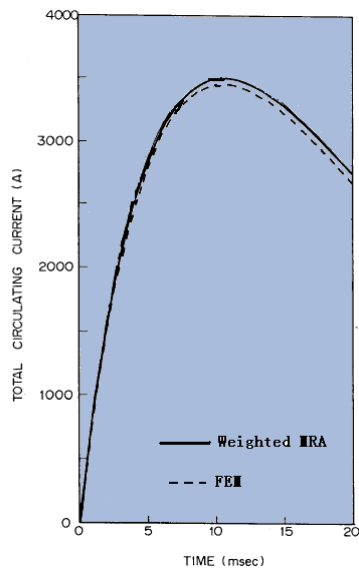


Fig. 3 Total circulating current vs. time.

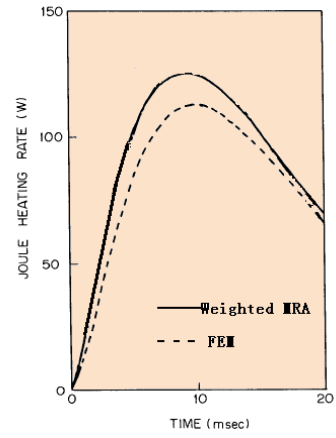


Fig. 4 Joule heating rate vs. time.

Transient Eddy Current Analysis of Pulsed Eddy Current Testing by Finite Element Method

Hajime Tsuboi, Norio Seshima

Department of Information Engineering,
Fukuyama University,
Fukuyama 729-0292, Japan.
tsuboi@fuip.fukuyama-u.ac.jp,
seshima@fucc.fukuyama-u.ac.jp

Imre Sebestyén, Josef Pávó,
Szabolcs Gyimóthy

Department of Electromagnetic Theory,
Budapest University of Technology and Economics,
H-1521 Budapest, Hungary.
si@evtsz1.evt.bme.hu, pavo@evtsz1.evt.bme.hu,
gyimothy@evtsz1.evt.bme.hu

Antal Gasparics

Research Institute for Technical
Physics and Material Sciences,
H-1525 Budapest,
PO. Box. 49, Hungary.
gaspari@mfa.kfki.hu

Abstract - Transient eddy current analysis of pulsed eddy current testing was performed by time-stepping method and Fourier transform method based on finite element method. The characteristics of two methods were evaluated by using a simple model. The accuracy was examined by the comparison of calculated and measured data. The calculated results of the two methods provided good agreement with measured data. However it was clear that the Fourier transform method provided higher accuracy of amplitude than the time stepping method. As a three-dimensional problem of pulsed eddy current testing, the TEAM Workshop Problem 27 was analyzed.

ALUMINUM PLATE MODEL

In order to evaluate time-stepping method and Fourier transform method [1] for transient analysis, we chose a simple pulsed ECT (Eddy Current Testing) model: an aluminum plate model shown in Fig. 1. In this case, there is no flaw in the aluminum plate. The numbers of turns of the exciting coil and pick-up coil are 350 and 35. The waveform of excitation is a half of sinusoidal wave whose width is 100 μsec .

An axisymmetric finite element method using first order nodal element is used for the analysis. A coarse mesh and a fine mesh were used to examine the two methods for transient analysis. The numbers of elements are 1,426 and 12,998 for the coarse mesh and the fine mesh, respectively.

In the time-stepping method, the time step is fixed to 5 μsec . In the Fourier transform method, the basic period and basic frequency are 1,600 μsec and 625 Hz. The number of divisions is 512 and the time step becomes 3.125 μsec .

Fig. 2 shows the comparison of the measured data [2] and the calculated results. When the fine mesh is used, the calculated results by the time-stepping method are almost same as the results by the Fourier transform method. And both calculated results fit for the measured data. When the coarse mesh is used, amplitude error of the results by the time-stepping method becomes large compared with the Fourier transform method as shown in Fig. 2.

As a result, it was clear that the Fourier transform method was suitable to pulsed ECT problems because accuracy of amplitude is important for the detection of flaws.

TEAM WORKSHOP PROBLEM

The TEAM Workshop problem 27 [3] was analyzed by a three-dimensional finite element method using the Fourier

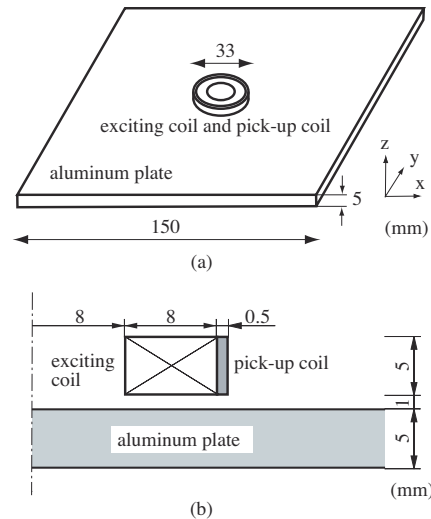


Fig. 1 Aluminum plate model, (a) overview, (b) exciting coil and pick-up coil.

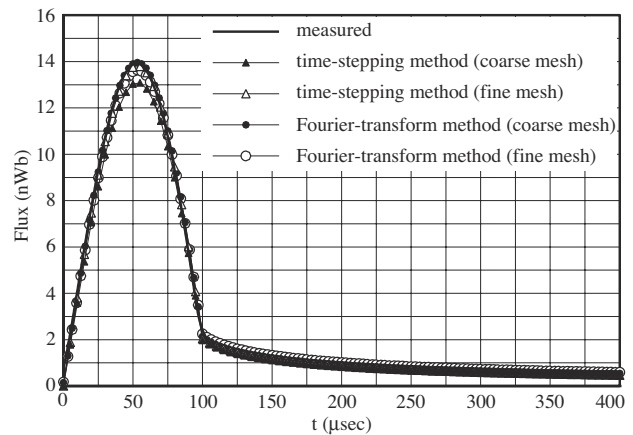


Fig. 2 Comparison of the measured data and the calculated results of the aluminum plate model.

transform method for transient analysis. In the finite element method, a second order tetrahedral edge-element [4] is used and magnetic vector potential is introduced as unknown variable. The problem 27 has three variations which modeled dif-

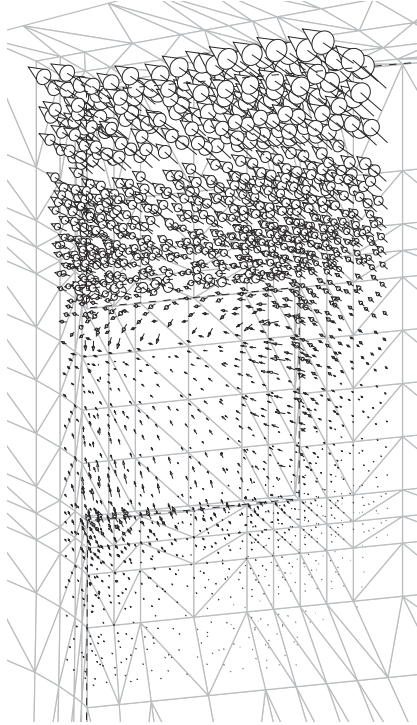


Fig. 3 Eddy current distribution at $t=39.0625 \mu\text{sec}$ around the flaw 2 of the TEAM Workshop problem 27,

ferent shapes of flaw: flaw 1, flaw 2 and flaw 3 [3]. The three models have a plane symmetry with respect to the x - z plane. The periodic excitation waveform is rectangle.

In the case of flaw 2, a half of the region to be analyzed was divided into 61,920 tetrahedra. In this case, the number of unknowns is 92,344.

For the transient analysis, we used 50 Hz for the basic frequency and 512 for the number of divisions in frequency domain. Therefore, the calculations were performed for 256 frequencies. And the time step becomes $39.0625 \mu\text{sec}$ in time domain.

Fig. 3 shows the eddy current distribution around the flaw 2 at $t= 39.0625 \mu\text{sec}$. The origin of time for the measurement is the time when the exciting current turns off.

The output signal of the model is difference between output of the hall effect sensor on the flaw and that on a region without flaw. In the analysis, calculations were performed twice: one is for the model with flaw and the other is for the model without flaw. The output signal ΔB is calculated by the following equation:

$$\Delta B = B_{\text{flaw}} - B_0 \quad (1)$$

where B_{flaw} is calculated magnetic flux density at the sensor location in the model with flaw and B_0 calculated magnetic flux density at same location without flaw.

The comparison of calculated results and measured output

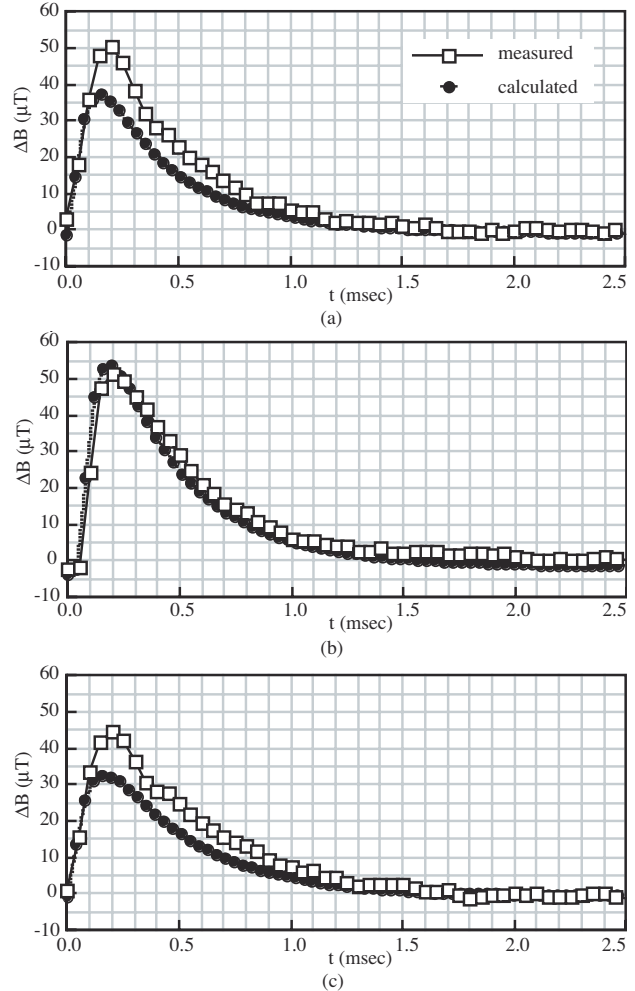


Fig. 4 Comparison between calculated and measured data of detected signal in the TEAM Workshop problem 27, (a) flaw 1, (b) flaw 2, (c) flaw 3.

signals [3] are shown in Fig. 4. The calculated results almost agree with measured data.

Considering stated above, the developed method can be utilized for the evaluation of pulsed ECT probes.

REFERENCES

- [1] Hajime Tsuboi, "Finite element analysis of pulsed eddy current testing," *Electromagnetic Nondestructive Evaluation (V)*, J. Pavo et al. (Editors), pp. 38-45, IOS Press, Amsterdam, 2001.
- [2] Sz. Gyimóthy, I. Sebestyén, J. Pávó, A. Gasparics, H. Tsuboi, "Comparison of some transient eddy-current codes and measured data," *Proc. 13th Conference on the Computation of Electromagnetic Fields (COMPUMAG)*, Evian (France), July 2-5, 2001, Vol. 2, pp. 212-213.
- [3] F. Thollon, "Eddy current NDT and deep flaws," TEAM Workshop Problem 27, *TEAM Workshop web site*.
- [4] Hajime Tsuboi, Motoo Tanaka, Kazumasa Ikeda, Kentaro Nishimura, "Computational results of the TEAM workshop problem 7 by finite element methods using tetrahedral and hexahedral elements," *Journal of Materials Processing Technology*, Elsevier, vol. 108, pp. 237-240, 2001.

Efficient Technique for 3-D Finite Element Analysis of Skin Effect in Current-Carrying Conductors

H.K. Kim¹, K.Y. Park¹, C.H. Im² and H.K. Jung²

Advanced Power Apparatus Group, KERI, P.O. Box 20, Changwon, 641-600, South Korea¹
E-mail : kimhk@keri.re.kr
Electromechanics Lab., School of Electrical Engineering, Seoul National University, San 56-1,
Shirrimdong, Seoul 151-742, South Korea²

Abstract — In this paper, an efficient method for the 3-D computation of steady-state skin effect problem in current-carrying conductors is presented. It is assumed that the total current is composed of the source current and eddy current and source current density is proportional to the electric field intensity. To calculate the source current density, the iterative procedure is employed. The proposed method can be easily implemented in the existing 3-D finite element code with slight modification. The proposed method is validated by comparison to known solutions of slot-embedded model and applied to the analysis of current distribution in vacuum interrupter.

density, \vec{J}_s source current density, \vec{J}_e eddy current density, ϕ electric scalar potential.

The source current density could be calculated if the potential difference between the two end sides of conductor is known. However, the only measurable known quantity is the total current J_t . The source current density can be expressed as (3) under the condition that the electric conductivity in a conductor is constant.

INTRODUCTION

If the skin depth of current-carrying conductor in AC system is shorter than the thickness of conductor, the current density is higher towards the surface of conductor. To find the dynamic impedance of such system, the current distribution in the conductor should be known accurately. General approach to calculate the current distribution starts from the assumption that the total current is composed of the source current and eddy current. For 2-D case, smart formulations for finite element analysis of skin effect problem were proposed [1,2,3]. However, for 3-D case the number of unknowns increases dramatically and the discretization procedure is complicated compared with 2-D case.

This paper presents the efficient iterative method for computing the current distribution in the harmonic current-carrying conductors with 3-D finite element method. Main idea of the method is that the source current density is proportional to the pre-calculated electric field intensity. The additional variable for the source current density is the proportional coefficient which is constant in each conductor. The method is applied to the simple validation problem to check the accuracy and efficiency.

$$\vec{J}_s = -\sigma \nabla \phi = \lambda \vec{e} \quad (3)$$

where \vec{e} is the electric field intensity within the conductor when the potential difference is 1[V] and λ is the coefficient which is constant for one conductor.

From (3), (1) is rewritten as (4).

$$\nabla \times \nabla \times \vec{A} = -j\omega \sigma \vec{A} + \lambda \vec{e} \quad (4)$$

To find the unknown variable λ , following equation is used.

$$I_t = \int_{S_c} \vec{J}_t \cdot d\vec{S} = \int_{S_c} (-j\omega \sigma \vec{A} + \lambda \vec{e}) \cdot d\vec{S} \quad (5)$$

where I_t [A] is the known total current and S_c is the cross section of a conductor.

The final equations to be solved are (4) and (5) with the boundary conditions and total current condition. If (1) and (2) are used as the governing equations, the unknown variables increase considerably compared to the pure harmonic magnetic field problem because of the addition of ϕ in each finite element located in the conductor. However if (4) and (5) are used, the unknown variable λ is added just by one for one conductor. Therefore the computational cost of proposed method can be reduced fairly compared to solving the full equations of (1) and (2).

GOVERNING EQUATIONS

For 3-D quasi-stationary eddy current problems, the governing equation and current composition equation are expressed as followings :

$$\nabla \times \nabla \times \vec{A} = \vec{J}_t \quad (1)$$

$$\vec{J}_t = \vec{J}_e + \vec{J}_s = -j\omega \sigma \vec{A} - \sigma \nabla \phi \quad (2)$$

where \vec{A} is magnetic vector potential, \vec{J}_t total current

ITERATIVE PROCEDURE

The simultaneous system matrix obtained from the finite element discretization of (4) and (5) by Galerkin method is non-symmetric because the unknown variable λ is only related to the elements contained in S_c and general symmetric algorithm of finite element method can not be used. To overcome the problem and reduce the computational cost, the iterative method is proposed. Fig. 1

shows the flow chart for iterative calculation. First, the electric field intensity is computed with the potential difference of 1[V] for each conductor. Then equation (4) is solved with assumed value of λ . The new value of λ for each conductor is then calculated from (5). The computation time of (5) is ignorable. If $\lambda \vec{e}$ of (4) is known, then solving (4) by FEM is the common A -method for 3-D harmonic eddy current problem. The implementation of A -method is easy compared to $A-\phi$ formulation [4] in solving 3-D eddy current problems. By the iteration process, the converged value of vector potential A and coefficient λ can be obtained. In updating λ , under-relaxation method is used.

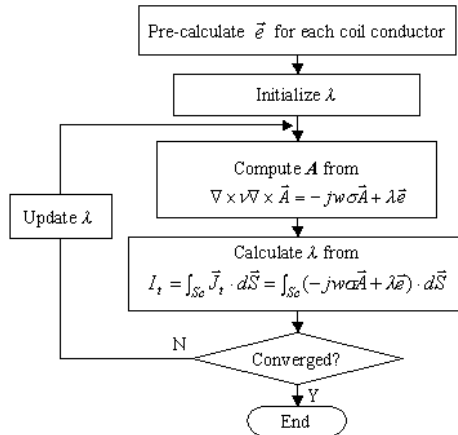


Fig.1. Analysis procedure for proposed method.

NUMERICAL EXAMPLES

The proposed method is applied to the slot-embedded conductor model for the validation. The 3-D model for the conductor is shown in Fig. 2(a) and the current flows along the z -direction. In this case, the number of conductor is one and only one λ is added as the unknown variable. To verify the method, simulation results are compared with the results obtained from the 2-D integro-differential method [2]. Fig. 2(b) shows the flux distribution and Fig. 3 shows the comparison of the real part of source current density according to the frequency. As shown in the figure, good agreement can be achieved. If the frequency is low, then converged solution can be obtained within a few iterations. However, it is found that the higher the frequency is, the more iteration steps are required. Another analyzed model is the vacuum interrupter used for circuit breakers. The magnetic field in the interrupter is very important for extinguishing the vacuum arc. To compute the magnetic field accurately, the current distribution within the current path should be calculated precisely [5]. Fig. 4(a) shows the analyzed vacuum interrupter model. The current is 20[kA] and frequency is 60[Hz]. Fig. 4(b) shows the distribution of real part of the current on the contact surface. The pattern of the expected current flow was obtained. More analysis results for other models and the efficiency of the method will be shown in the full paper.

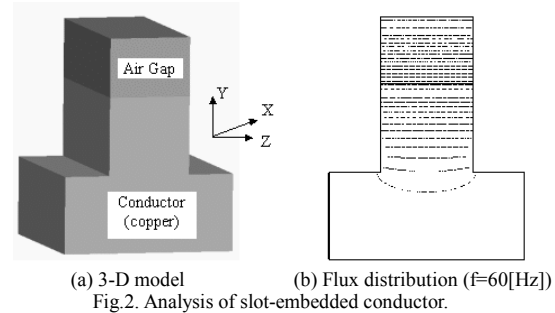


Fig.2. Analysis of slot-embedded conductor.

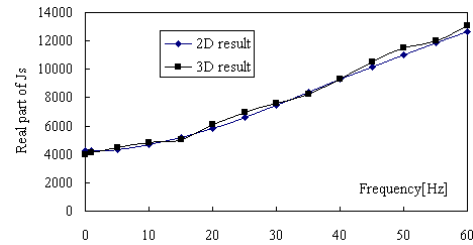


Fig.3. Comparison of the real part of the source current density for slot-embedded problem.

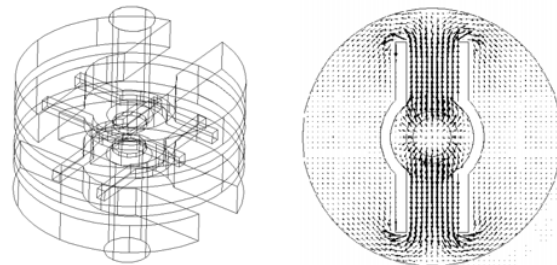


Fig. 4. Analysis of current distribution in the vacuum interrupter.

CONCLUSIONS

In this paper, the efficient iterative method for the calculation of 3-D skin effect problem in current-carrying conductor is presented. The method requires less computational cost than the direct solution of full equations and easy to implement.

REFERENCES

- [1] J.Weiss, Z.J.Csendes, "A One -Step Finite Element Method for Multiconductor Skin Effect Problems", *IEEE Trans., Power App. Syst.*, Vol. PAS-101, No. 10, pp. 3796-3800, October 1982.
- [2] A.Konrad, "Integrodifferential Finite Element Formulation of Two-Dimensional Steady - State Skin Effect Problems," *IEEE Trans., Magn.*, Vol. MAG-18, No.1, pp.284-292,1982.
- [3] R. Jafari-Shapoorabadi, A.Konrad,A.N. Sinclair, "Comparison of Three Formulations for Eddy-Current and Skin Effect Problems," *IEEE Trans., Magn.*, vol 38. No.2, pp.617-620, March 2002.
- [4] O. Biro and K. Preis, " On the Use of the Magnetic Vector Potential in the Finite Element Analysis of Three-Dimensional Eddy Currents," *IEEE Trans., Magn.*, vol 25. No.4, pp.3145-3159, 1989.
- [5] Y.Kawase *et al.*, "Numerical Analysis of Axial Magnetic Field Acting on the Arc in Vacuum circuit Breakers by 3-D Finite Element Method Taking into Account Eddy Currents," *IEEE Trans., Magn.*, Vol. 34, No.3, pp.2668-2671, 1998.

Algebraic MultiGrid Preconditioner for Harmonic Eddy Current Problems in 3D

¹M.Kaltenbacher, ²S.Reitzinger

¹Department of Sensor Technology, University of Erlangen, Germany

²CST - Computer Simulation Technology, Darmstadt, Germany

Abstract— The focus of this paper is on the efficient solution - both in CPU time and memory - for harmonic eddy current problems in 3D. The magnetic vector potential is used as the field variable and Nédélec (edge) finite elements are used for the space discretization. The resulting system of equations is solved by applying a Quasi Minimal Residual solver with an appropriate Algebraic MultiGrid (AMG) preconditioner.

I. FORMULATIONS

Restricting Maxwell's equations to the problem class of quasi-static (eddy current) electromagnetic fields yields for the magnetic vector potential \mathbf{A}

$$\gamma \frac{\partial \mathbf{A}}{\partial t} + \nabla \times \nu \nabla \times \mathbf{A} = \mathbf{J}_i \quad (1)$$

with boundary condition $\mathbf{n} \times \mathbf{A} = 0$ and \mathbf{n} the unit outward normal vector. In (1) \mathbf{J}_i denotes the impressed current density, ν the magnetic reluctivity and γ the electric conductivity. Furtheron, the following interface conditions have to be fulfilled

$$[\mathbf{A} \times \mathbf{n}] = 0 ; \quad [\nu \mathbf{n} \times \nabla \times \mathbf{A}] = 0 ; \quad \left[\gamma \frac{\partial \mathbf{A}}{\partial t} \right] = 0 \quad (2)$$

with $[\mathbf{Z}] = \mathbf{Z}_{\text{right}} - \mathbf{Z}_{\text{left}}$. For further discussions let Ω be a bounded single connected convex domain with boundary $\partial\Omega = \Gamma$. In the harmonic case the time derivative of the magnetic vector potential is substituted by

$$\frac{\partial \mathbf{A}}{\partial t} \rightarrow j\omega \hat{\mathbf{A}}$$

with j the complex number, ω the angular frequency and $\hat{\mathbf{A}}$ the complex magnetic vector potential.

The function spaces $L^2(\Omega)$ and $H_0^1(\Omega)$ are defined as usual, see e.g. [1]. Therewith, the variational formulation for (1) in the function space

$$\mathbf{H}_0(\text{curl}) = \{ \mathbf{u} \in (L^2(\Omega))^3 \mid \nabla \times \mathbf{u} \in (L^2(\Omega))^3, \mathbf{u} \times \mathbf{n}|_{\Gamma} = 0 \} \quad (3)$$

reads as follows: Find $\hat{\mathbf{A}} \in \mathbf{H}_0(\text{curl})$ such that

$$\begin{aligned} \int_{\Omega} j\omega \gamma \hat{\mathbf{A}}' \cdot \hat{\mathbf{A}} \, d\Omega + \int_{\Omega} \nabla \times \hat{\mathbf{A}}' \cdot \nu \nabla \times \hat{\mathbf{A}} \, d\Omega \\ = \int_{\Omega} \hat{\mathbf{A}}' \cdot \mathbf{J}_i \, d\Omega \end{aligned} \quad (4)$$

The edge finite elements approximate the magnetic vector potential $\hat{\mathbf{A}}$ by

$$\hat{\mathbf{A}} \approx \sum_{k=1}^{N_h} \hat{A}_k \mathbf{N}_k. \quad (5)$$

In (5) N_h defines the number of edges in the finite element mesh, \mathbf{N}_k the edge shape function associated with edge e_k , and \hat{A}_k the corresponding degree of freedom, namely the line integral of the magnetic vector potential along e_k

$$\hat{A}_k = \int_{e_k} \hat{\mathbf{A}} \cdot d\mathbf{s}. \quad (6)$$

Therewith, the spatial discretization of (4) leads to an algebraic system of equations

$$K_h \hat{\mathbf{A}}_h = \underline{\mathbf{f}}_h \quad (7)$$

with the complex system matrix K_h .

At this point we want to emphasize, that an edge FE-discretization of (4) is $\mathbf{H}_0(\text{curl})$ -conform [6]. However, the solution of the algebraic system requires special care in order to obtain an optimal MultiGrid solver (see e.g. [2], [4]). We suggest to add a fictive electric conductivity γ' to regions with zero electric conductivity to obtain a variational form, which is elliptic [10]. Of course, this fictive conductivity γ' has to be chosen small as compared to the reluctivity of the material. The proof of convergence even in the case of $\gamma' \rightarrow 0$ is given in [8].

A. Algebraic MultiGrid

We have to apply the AMG method to a complex valued and symmetric algebraic system of equations (see (7)) with system matrix

$$K_h = K_h^{re} + jK_h^{im}. \quad (8)$$

In (8) K_h^{re} denotes the real part and K_h^{im} the complex part of the system matrix.

AMG methods are very similar to geometric MG methods, but are based on the information available on a given single grid (for the pioneer work on AMG see [9]). Therewith, the main components of an AMG algorithm are as follows [5]:

- Coarsening Process

Coarsening Process: The first task within an AMG solver is to perform the coarsening process to extract from the given system matrix K_h matrices with decreasing dimensions. The complexity of this task is, that an appropriate and fast coarsening can just be guaranteed, if K_h is an M-matrix. Since in general this is not the case, we construct an auxiliary matrix B_h on which the coarsening is performed. We define B_h to be real valued, and construct it FE-element wise by [7]

$$B_{h,ij} = \begin{cases} b_{ij} \leq 0 & \text{if } i \neq j, \\ 1 - \sum_{j \neq i} b_{ij} \geq 0 & \text{if } i = j. \end{cases} \quad (9)$$

$$b_{ij}^r = -\frac{\nu_r}{\|\mathbf{a}_{ij}\|_2} \quad i \neq j \text{ and } (i, j) \in \omega_h^e. \quad (10)$$

In (10) ν_r denotes the reluctivity of element r , $\|\mathbf{a}_{ij}\|_2$ the length of the geometric edge vector defined by the nodes i and j and ω_h^e the set of edges within the FE-mesh. Now the coarsening is performed on B_h , e.g. as described in [7].

Construction of coarse FE-spaces: For the construction of a coarse grid operator K_H we define the system prolongation operator P_h to be real valued. Therewith, we obtain

$$K_H = P_h^T K_h P_h = P_h^T K_h^{re} P_h + j P_h^T K_h^{im} P_h = K_H^{re} + j K_H^{im}.$$

Smoothing operator: In the case of an algebraic system of equations arising from the edge FE-discretization we apply the complex version of the smoother proposed by D. Arnold, R. Falk and R. Winther in [2].

B. Results

We present results of 3D magnetic field computations for an electric transformer as shown in Fig. 1. The arising

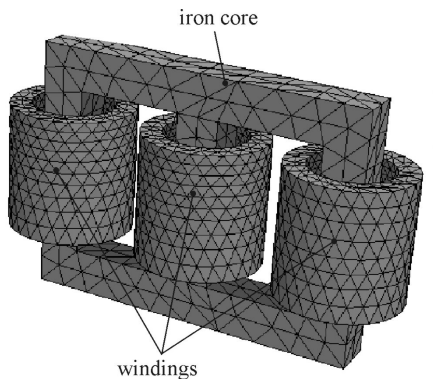


Fig. 1. FE-mesh of an electric transformer (no air region is displayed)

algebraic system of equations have been solved by a Quasi Minimal Residual method (see e.g. [3]) with the presented AMG as preconditioner. For the stopping criteria of the iterative solver we used

$$\|\underline{f}_h - K_h \hat{A}_h\|_2 \leq 10^{-6} \|\underline{f}_h\|_2.$$

All computations have been performed on a PC Pentium Record of the 14th Compumag Conference on the Computation of Electromagnetic Fields, July 2003
 and of the 14th Compumag Conference on the Computation of Electromagnetic Fields, July 2003
 ations and the CPU-times can be found.

N_h	MB	Iter	Setup [s]	Solver [s]
4.786	9	19	0.1	1.5
37.390	72	30	1.1	22.5
296.064	580	51	9.6	319

TABLE I

Electric Transformer: Performance for different FE-meshes

II. OUTLOOK

In the full paper, we will give a detailed discussion on all components of the presented AMG method as well as detailed numerical studies of different problem cases.

REFERENCES

- [1] R.A. Adams, *Sobolev Spaces*, Pure and Applied Mathematics, Academic Press, 1975.
- [2] D. Arnold, R. Falk, and R. Winther, *Multigrid in $H(\text{div})$ and $H(\text{curl})$* , Numer. Math. **85** (2000), 197–218.
- [3] R. Barrett, M. Berry, T.F. Chan, J. Demmel, J. Donato, J. Dongarra, V. Eijkhout, R. Pozo, C. Romine, and H. Van der Vorst, *Templates for the Solution of Linear Systems: Building Blocks for Iterative Methods*, SIAM, 1994.
- [4] R. Hiptmair, *Multigrid method for Maxwell's equations*, SIAM J. Numer. Anal. **36** (1999), no. 1, 204–225.
- [5] M. Kaltenbacher and S. Reitzinger, *Algebraic MultiGrid Methods for Nodal and Edge based Discretizations of Maxwell's Equations*, International Compumag Society Newsletter **9** (2002), no. 3, 15–23.
- [6] J. Nédélec, *A new family of mixed finite elements in R^3* , Numer. Math. **50** (1986), 57–81.
- [7] S. Reitzinger, *Algebraic Multigrid Methods for Large Scale Finite Element Equations*, Reihe C - Technik und Naturwissenschaften, no. 36, Universitätsverlag Rudolf Trauner, 2001.
- [8] S. Reitzinger and J. Schöberl, *An Algebraic Multigrid Method for Finite Element Discretizations with Edge Elements*, Numer. Linear Algebra Appl. **31** (2002), no. 3, 223 – 238.
- [9] J. W. Ruge and K. Stüben, *Algebraic multigrid (AMG)*, Multigrid Methods (S. McCormick, ed.), Frontiers in Applied Mathematics, vol. 5, SIAM, Philadelphia, 1986, pp. 73–130.
- [10] M. Schinnerl, J. Schberl, M. Kaltenbacher, and R. Lerch, *Multigrid Methods for the 3D Simulation of Nonlinear Magneto-Mechanical Systems*, IEEE Transactions on Magnetics **38** (2002), no. 3, 1497–1511, accepted.

Magnetic scalar potential formulation using a 3D complex permeability for proximity losses computation

M. Joan^(1,2), O. Moreau⁽¹⁾, G. Meunier⁽²⁾, T. Chevalier⁽²⁾

⁽¹⁾ EDF R&D - 1 avenue Général de Gaulle 92141 CLAMART FRANCE

(E-mail: Michael.Joan@leg.ensieg.inpg.fr, Olivier.Moreau@edf.fr).

⁽²⁾ LEG - ENSIEG (INPG-UJF, CNRS UMR 5529) BP 46, 38402 Saint-Martin d'Hères Cedex, FRANCE

(E-mail: Gerard.Meunier@inpg.fr, Thierry.Chevalier@inpg.fr).

Abstract—The FEM computation of eddy current losses in transformers (specially in the conductor winding) at high frequencies remains unrealistic with standard material models (huge meshes). However, this difficulty can be overcome by using the complex permeability concept. So, 3D FEM magnetodynamic simulations (Flux3D) with anisotropic complex permeability applied to coil give accurate results for proximity effects losses. These 3D simulations have been done with the magnetic scalar potential formulation (T_0 - ϕ) using the complex permeability to overcome the problem of the huge mesh.

INTRODUCTION

To predict Very Fast Overvoltage Transients in transformer windings we have to be able to compute the eddy currents in the conductors. The FEM eddy currents losses computation at high frequencies is unfortunately unrealistic in the case of industrial wounded equipments (transformer, rotating machine...). As a matter of fact, taking into account properly the skin depth at high frequencies (from kHz up to several MHz) would involve huge meshes due to 2 finite elements in the skin depth (0.1 mm at 150 kHz). For proximity effects accounting (skin effect can be analytically post-processed [1]), this difficulty can be overcome by using the complex permeability concept which consists in substituting a non conductive ferromagnetic material (featuring an elliptical loop described with a complex permeability) in place of a conductive material, based on active and reactive power equivalency. Complex permeability method applied to 2D problems have shown a very good accuracy in the loss approximation and made possible an important reduction of the mesh size. The present work deals with the 3D extension of the method and specially with the magnetic scalar potential formulation [2].

DEFINITION OF THE 3D COMPLEX PERMEABILITY

Dealing with a rectangular unsupplied conductor and applying the superposition principle (linear materials), the assumption of a locally uniform external magnetic field source enables to define an anisotropic complex permeability with respect to the x, y and z axis [3]. The complex permeability x and y components derive from the analytical calculation of the magnetic field in an infinite conductive plate submitted to a homogeneous harmonic field. Whereas the third component calculation assumes

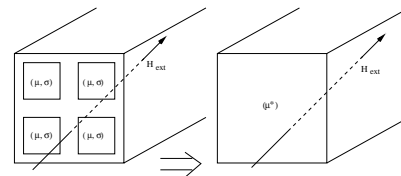


Fig. 1. a bundles of conductor, homogenization

that the third dimension is much larger than the planar dimensions considering the field along the z axis. In addition, since a coil may be constituted of several turns wrapped with insulation (Fig. 1), a homogenization based on reluctance considerations has been applied to set one complex anisotropic permeability for a chosen conductive area.

MAGNETIC SCALAR POTENTIAL FORMULATION

Up to now, the transformer simulations have to take into account several physical domains: insulator, conductors and ferromagnetic materials.

In our approach the conductors have for unique physical prop-

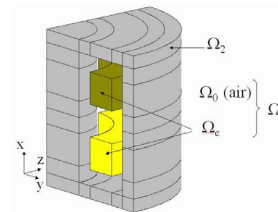


Fig. 2. Typical physical problem which implies two conductors set.

erty, the complex permeability, and so the simulation space is compound of three distinct regions (Fig. 2):

- Ω_0 : insulator region, the air,
- Ω_c : “conductor” region (μ^*),
- Ω_2 : ferromagnetic region.

For that we use the magnetic scalar total and reduced potential formulation derived from the Maxwell's equations:

$$\vec{\nabla} \cdot \vec{B} = 0 \quad \text{and} \quad \vec{\nabla} \times \vec{H} = J \quad (1)$$

In $\Omega_1 = \Omega_0 \cup \Omega_c$, we use the reduced scalar potential:

$$\vec{H} = \vec{T}_0 - \vec{\nabla} \phi \quad \text{in } \Omega_1 \quad (2)$$

$$\vec{T}_0 \times \vec{n} = 0 \quad \text{on } \Gamma_{12} = \Omega_1 \cap \Omega_2 \quad (3)$$

where T_0 is deduced from $\vec{\nabla} \times \vec{T}_0 = \vec{J}$ [4].

In Ω_2 , we use the total magnetic scalar potential. This requires the introduction of a cut to insure the Ampere's theorem (to overcome the problem of connexity). On the cut, in Ω_2 , the scalar potential jump verifies the relation:

$$\delta\phi_{total} = I \quad \text{surrounded current the coil} [2] \quad (4)$$

For a network simulation [5] the transformer has to be characterized by their electrical parameters R, L, C and G. That's why, by post-processing, we recover the currents and voltages of the coils (conductors set). The current-voltage relation is given by the following expression [6]:

$$U_k = R_k I_k + \int_{\Omega_1} \vec{t}_{0k} \cdot \vec{B} \cdot d\Omega \quad (5)$$

\vec{t}_{0k} is the unitary \vec{T}_0 calculated for the k^{th} coil supplied at 1A from that is following the expression of the voltage:

$$U_k = R_k I_k + \int_{\Omega_1} \vec{t}_{0k} \cdot \frac{\partial}{\partial t} \left[\mu \left(\sum_l I_l \vec{t}_{0l} - \vec{\nabla} \phi \right) \right] \cdot d\Omega \quad (6)$$

With $\mu = \mu_0$ in air and $\mu = \mu^*$ in the "conductor" (Ω_c). The alliance between the complex permeability concept and the magnetic scalar potential formulation has been validated by comparison with the standard case, where we take into account a massive conductors (μ, σ). For that we use the $T - T_0 \phi$ formulation, which takes into account the eddy currents by:

$$\vec{\nabla} \times \vec{E} = - \frac{\partial \vec{B}}{\partial t} \quad (7)$$

And we have the potential definition: $\vec{H} = \vec{T} + \vec{T}_0 - \vec{\nabla} \phi$. The validation is based on the resistance called of "proximity", they are mainly due to the induced effects.

VALIDATION - 3D TEST-CASES

In a previous work we have validated the anisotropic μ^* concept on a single conductor in an external magnetic field [3]. Now, we are focus on 3D of R and L computation on a two conductors set (shown in Fig. 3) using μ^* concept incorporate

in 3D formulation. This validation is based on the calculation of the terms of the (R) and (L) matrix, by comparison between the (μ, σ) and the (μ^*) numerical simulations without ferromagnetic core to compare to the 2D axi simulation. The coil geometry (shown in Fig. 3) implies a local complex permeability tensor regard to each node. R and L are deduced from U and I variables provided by Flux3D post-processing.

Considering that the actual configuration (2 conductors set) is

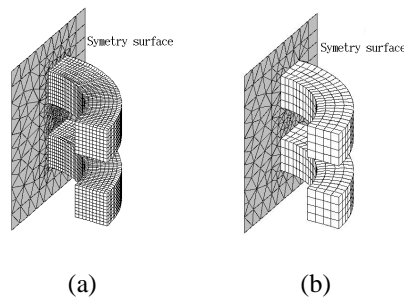


Fig. 3. Geometry and mesh density for (a) the (μ, σ), (130000 nodes) and (b) the (μ^*), (28900 nodes). Notice that in the case of (μ, σ) we have to increase the mesh density with respect to the frequency.

unfavourable since H is not uniform around the coil, the results are encouraging (see Table I) at the view of the error on the R diagonal elements which is less than 7%. Then, dealing with much more conductors, results will be better. Similar results have been obtained in presence of ferromagnetic core.

F(Hz)		(μ, σ) axi	3D (μ, σ)	3D (μ^*)
3000	(R) $\times e^{-4}$	3.26	3.25	3.41
5000	(R) $\times e^{-4}$	3.46	3.45	3.68

Table I: Diagonal elements of the R matrix.

CONCLUSION AND PROSPECTS

The substitution by the 3D complex magnetic permeability is validated for the computation of the losses and for the determination of the R and L parameters on simple test-cases (two conductors set). Integration of the complex permeability in cases nearer of real electrical devices like transformer, multi-conductors set cases with ferromagnetic core, is now in progress.

References

- [1] Stoll R.L., "The analysis of eddy current", Clarendon Press Oxford, 1974.
- [2] LeFloch Y.; Meunier G.; Guerin C.; Labie P.; Brunotte X.; Boudaud D., "Coupled problem computation of 3D multiply connected magnetic circuits and electric circuits", CEFC 2002 proceeding, pp 277.
- [3] Joan M.; Moreau O.; Meunier G.; Chevalier., "Proximity losses computation using a 3D complex permeability", CEFC 2002 proceeding, pp 40.
- [4] LeFloch Y.; Guerin C.; Boudaud D.; Meunier G.; Brunotte X., "A current transformer modeling", COMPEL, Vol. 21 No 4, 2002
- [5] Moreau O.; Guillot Y., "SUMER: A Software For Overvoltage Surges Computation Inside Transformers", ICEM 1998 Proc. pp. 965-970.
- [6] Meunier G.; Luong H.T.; Marchal Y., "Computation of coupled problem of 3D eddy current and electrical circuit by using $T - T_0 \phi$ formulation", IEEE Trans. Mag., Vol. 34 No 5, pp 3047-7, 1998

Field-Circuit Coupling for Time-Harmonic Models Discretized by the Finite Integration Technique

Herbert De Gersem, Thomas Weiland

Technische Universität Darmstadt, Computational Electromagnetics Laboratory (TEMF),
Schloßgartenstraße 8, D-64289 Darmstadt, Germany
Email: degersem/weiland@temf.tu-darmstadt.de

Abstract—This paper develops the coupling between a 3D modified magnetic vector potential formulation discretized by the Finite Integration Technique (FIT) and a circuit including solid and stranded conductors. The conductor models relate local quantities defined at primal edges or dual facets and the global circuit unknowns. Two possible couplings are derived affecting either the edges perpendicular to a reference cross-section or all edges inside the conductor. To preserve the sparsity and the structure of the discrete system, the circuit analysis is based on a circuit tree, incorporates both voltage drops and currents as additional unknowns and results in a symmetric coupling.

INTRODUCTION

Field-circuit coupled models are applied for simulating electrical energy transducers. The geometry of the device is discretized in order to consider local effects such as ferromagnetic saturation and eddy currents, whereas the electrical supply and loads are represented by lumped parameters. Field-circuit coupling schemes have been established for finite element models (see [1] and the references therein). In this paper, a field-circuit coupling mechanism is developed for the Finite Integration Technique (FIT). It is shown that the use of integrated quantities as is common in FIT, yields incidence matrices as field-circuit coupling operators which substantially simplifies the treatment of field-circuit coupled models.

DISCRETIZATION

The field-circuit coupled formulation is developed for a time-harmonic model. The generalization to transient models is straightforward. The quasistatic subset of Maxwell's equations discretized by FIT reads

$$\left(\underbrace{\tilde{\mathbf{C}}\mathbf{M}_\nu\mathbf{C} + j\omega\mathbf{M}_\kappa}_{\mathbf{K}} \right) \hat{\mathbf{a}} = \hat{\mathbf{j}}_s \quad (1)$$

where \mathbf{C} and $\tilde{\mathbf{C}}$ are the discrete curl operators at the primal and dual grid respectively, $\hat{\mathbf{a}}$ is the component vector of the path integrated modified vector potential, $\hat{\mathbf{j}}_s$ is the vector of source currents, ω is the pulsation, underlined quantities indicate phasors and \mathbf{M}_ν and \mathbf{M}_κ are the reluctivity and conductivity material matrices which are diagonal in the case of orthogonal grids and isotropic materials [2].

H. De Gersem is working in the cooperation project "DA-WE1 (TEMF/GSI)" with the "Gesellschaft für Schwerionenforschung (GSI)", Darmstadt.

SOLID CONDUCTORS

The current density in a solid conductor is

$$\hat{\mathbf{j}} = \mathbf{M}_\kappa (\mathbf{G}\hat{\phi} - j\omega\hat{\mathbf{a}}) \quad (2)$$

where \mathbf{G} is the gradient operator defined on the primal grid and $\hat{\phi}$ is the vector of nodal voltages. Given the voltage drop ΔV_{sol} along the solid conductor, a divergence-free source current $\hat{\mathbf{j}}_s = -\mathbf{M}_\kappa\mathbf{G}\hat{\phi}$ can be computed from

$$\tilde{\mathbf{S}}\mathbf{M}_\kappa\tilde{\mathbf{S}}^T\hat{\phi} = \tilde{\mathbf{S}}\mathbf{M}_\kappa\hat{\mathbf{e}}_{app} \quad (3)$$

where $\tilde{\mathbf{S}} = \mathbf{G}^T$ is the divergence operator on the dual grid and the voltage excitation $\hat{\mathbf{e}}_{app} = \mathbf{Q}\Delta V_{sol}$ is constructed by putting ΔV_{sol} as electric voltage at the primal edges perpendicular to one reference cross-section of the solid conductor. The field-circuit incidence matrix \mathbf{Q} consists of 0, 1 and -1 [3]. The solution of (3) renders a relation between each primal edge in the solid conductor and the applied voltage drop. As a consequence, if ΔV_{sol} is unknown, coupling terms appear for primal edge in the solid conductor volume. A more sparse coupling is possible and is preferred here. The term $\mathbf{M}_\kappa\hat{\mathbf{e}}_{app}$ can serve as a non-divergence-free source current excitation in (1) [4]. The current density (2) is, however, divergence-free due to (1) and the topological property $\tilde{\mathbf{S}}\tilde{\mathbf{C}} = 0$ [2]. The total current I_{sol} through the solid conductor is measured at the reference cross-section:

$$I_{sol} = \mathbf{Q}^T\mathbf{M}_\kappa (\hat{\mathbf{e}}_{app} - j\omega\hat{\mathbf{a}}) \quad (4)$$

The coupled system of equations for a model with a current-driven solid conductor is

$$\begin{bmatrix} \mathbf{K} & -\mathbf{M}_\kappa\mathbf{Q} \\ -\mathbf{Q}^T\mathbf{M}_\kappa & \chi G_{sol} \end{bmatrix} \begin{bmatrix} \hat{\mathbf{a}} \\ \Delta V_{sol} \end{bmatrix} = \begin{bmatrix} 0 \\ \chi I_{sol} \end{bmatrix} \quad (5)$$

where G_{sol} is the DC conductance of the solid conductor and $\chi = 1/j\omega$ symmetrizes the system. The field-circuit coupling represented by the incidence operator \mathbf{Q} is purely topological and does not require any metric information.

STRANDED CONDUCTORS

In analogy to the solid conductor case, the coupling between a stranded conductor and an external circuit can be introduced at all dual facets in the conductor volume or at the dual facets of a reference cross-section Γ_{str} . In the

second case, the stranded conductor current \underline{I}_{str} is homogeneously distributed at Γ_{str} :

$$\hat{\underline{j}}_{app} = \mathbf{D}_{\hat{A}} \mathbf{Q} \underline{I}_{str} N_t / S_{str} \quad (6)$$

with $\mathbf{D}_{\hat{A}}$ the dual facet areas, N_t the number of turns and S_{str} the area of Γ_{str} . The current distribution is forced to be homogeneous by defining an anisotropic conductivity aligned with the winding direction in the stranded conductor [5]. Since an anisotropic conductivity matrix \mathbf{M}_κ is not diagonal, the efficiency of the FIT matrix-vector product decreases significantly. Therefore, here, the first approach is preferred. In a first step, a divergence-free source current field is computed from $\mathbf{S} \mathbf{M}_\kappa \mathbf{S}^T \underline{\phi} = \hat{\mathbf{S}} \hat{\underline{j}}_{app}$ yielding the relation $\hat{\underline{j}}_s = \mathbf{P} \underline{I}_{str}$ between the applied winding current and the source current field. For windings without small curves, an isotropic material matrix \mathbf{M}_κ can be used. The voltage drop $\Delta \underline{V}_{str}$ along the winding is found by averaging the voltage drops across cross-sections and summing them along the winding. This corresponds to

$$\Delta \underline{V}_{str} = R_{str} \underline{I}_{str} + \mathcal{I} \omega \mathbf{P}^T \hat{\underline{a}} \quad (7)$$

with $R_{str} = \mathbf{P}^T \mathbf{M}_\kappa^{-1} \mathbf{P}$ the DC resistance of the winding. The coupled system for a voltage-driven stranded conductor is

$$\begin{bmatrix} \tilde{\mathbf{C}} \mathbf{M}_\nu \mathbf{C} & -\mathbf{P} \\ -\mathbf{P}^T & -\chi R_{str} \end{bmatrix} \begin{bmatrix} \hat{\underline{a}} \\ \underline{I}_{str} \end{bmatrix} = \begin{bmatrix} 0 \\ -\chi \Delta \underline{V}_{str} \end{bmatrix}. \quad (8)$$

CIRCUIT DESCRIPTION

The sparsity of the FIT system part is preserved if for solid and stranded conductors, voltage drops and currents exist as unknowns, respectively. Conform to this requirement, a circuit model is developed combining both types of unknowns without loosing the symmetry of the system [1]. A tree is traced through the circuit by selecting branches favouring, in order of priority, voltage sources, solid conductors, impedances, stranded conductors and current sources. The voltage drops \underline{v}_{tro} and the currents \underline{i}_{ino} are assigned as unknowns to the tree branches and the links respectively. The excitations due to voltage and current sources are collected in \underline{v}_{trv} and \underline{i}_{ini} respectively. The *fundamental cut-set* associated with a tree branch contains the tree branch and a number of links such that removing the set would result in two disconnected circuit parts [1]. The *fundamental loop* associated with a link consists of the link and a unique path through the tree. For the fundamental cut-sets and links corresponding to tree branches and links at which the voltage drops or currents are unknown, Kirchhoff's current and voltage laws, respectively, are written which results in the field-circuit coupled system of equations

$$\begin{bmatrix} \mathbf{K} & -\mathbf{M}_\kappa \mathbf{Q} & -\mathbf{P} \\ -\mathbf{Q}^T \mathbf{M}_\kappa & \mathbf{Y} & -\mathbf{B}_{\text{ino,two}}^T \\ -\mathbf{P}^T & -\mathbf{B}_{\text{ino,two}} & -\mathbf{Z} \end{bmatrix} \begin{bmatrix} \hat{\underline{a}} \\ \underline{v}_{tro} \\ \underline{i}_{ino} \end{bmatrix} \quad (9)$$

$$= \begin{bmatrix} 0 \\ \mathbf{B}_{\text{ini,two}}^T \underline{i}_{ini} \\ \mathbf{B}_{\text{ino,two}} \underline{v}_{trv} \end{bmatrix} \quad (10)$$

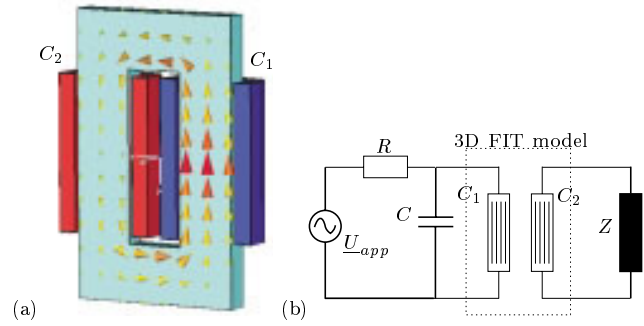


Fig. 1. (a) Magnetic flux in a single-phase transformer connected to (b) an inductive load and a voltage source with compensation. The circuit tree is indicated by thick lines.

where \mathbf{Y} is the tree branch admittance matrix, \mathbf{Z} the link impedance matrix and \mathbf{B} the fundamental loop matrix. This field-circuit coupling mechanism is applicable to each electric interconnecting of solid and stranded conductors. The coupled system preserves the sparsity and the structure of the FIT operator \mathbf{K} , is complex symmetric and can be solved conveniently by preconditioned bi-conjugate gradient or quasi-minimal residual methods for complex symmetric matrices [6].

APPLICATION

The field-circuit coupled formulation is used to simulate a single-phase transformer with an inductive load, excited by a voltage source (Fig. 1).

CONCLUSIONS

The topological treatment of both the field discretization and the circuit description results in a non-metric field-circuit coupling scheme. Global voltage drops and currents are computed as combinations from the local integrated quantities that represent the state variables in the FIT discretization. A single-phase transformer model illustrates the method. A larger three-phase transformer model is described in the full paper.

REFERENCES

- [1] H. De Gersem, R. Mertens, U. Pahner, R. Belmans, and K. Hameyer, "A topological method used for field-circuit coupling," *IEEE Transactions on Magnetics*, vol. 34, no. 5, pp. 3190–3193, Sept. 1998.
- [2] M. Clemens and T. Weiland, "Transient eddy current calculation with the FI-method," *IEEE Transactions on Magnetics*, vol. 35, no. 3, pp. 1163–1166, 1999.
- [3] L. Kettunen, "Fields and circuits in computational electromagnetism," *IEEE Transactions on Magnetics*, vol. 37, no. 5, pp. 3393–3396, Sept. 2001.
- [4] P. Dular, F. Henrotte, and W. Legros, "A general and natural method to define circuit relations associated with magnetic vector potential formulations," *IEEE Transactions on Magnetics*, vol. 35, no. 3, pp. 1630–1633, May 1999.
- [5] P. Dular, N. Sadowski, J.P.A. Bastos, and W. Legros, "Dual complete procedures to take stranded inductors into account in magnetic vector potential formulations," *IEEE Transactions on Magnetics*, vol. 36, no. 4, pp. 1600–1605, July 2000.
- [6] M. Clemens, U. van Rienen, and T. Weiland, "Comparison of Krylov-type methods for complex linear systems applied to high-voltage problems," *IEEE Transactions on Magnetics*, vol. 34, no. 5, pp. 3335–3338, Sept. 1998.

Experimental Validation for Numerical Simulation of Eddy Current in Iron Structures

Tatsuei Nomura and Yoshihiro Tani

Osaka Electro-Communication University
18-8 Hatsucho, Neyagawa City
572-8530 Osaka Prefecture, Japan
t-nomura@isc.osakac.ac.jp

Mitsubishi Electric Corporation, R&D
8-1-1 Tsukaguchi-honmachi,
Amagasaki, 661-8661 Hyogo, Japan
Tani.Yoshihiro@wrc.melco.co.jp

Abstract –A forced flow experiment is proposed for validation of the numerical simulation of eddy current in iron structures. The eddy current is forcedly flowed in a short sample bar with a round cross-section by the alternating current source. Because the source impedance is comparable to the sample load, not only the current but the voltage wave are distorted. Therefore the current and voltage waves are compared with the simulated waves, and the tests are in good agreement with the simulation. The simulated loss-density is in good agreement with the tested. However the phase angle is considerably larger than the tested. This may be based on ignoring hysteresis. It is concluded that this evaluating experiment is applicable to the validation.

Introduction

As high speed CPU and large memory are popular now, we can daily use 3D finite element methods for determining the magnetic field with eddy current in solid iron structures. And those are usually numerical simulation using explicit finite-difference for time varying term. Those methods are useful, but it must be validated by using experiments.

Test Method

Test specimens of ring iron were used in most of presented papers such as [1]. The rings were excited with sinusoidal current forced in the exciting coil. Lim and Hammond used rectangular steel blocks with laminated iron yokes[2]. The magnetic circuit was excited by sinusoidal voltage source which was maintained by feedback techniques. The author proposes a forced flow test method where the specimen is short sample bar with round cross-section and the eddy-current is forced by a current source as shown in Fig. 1. If the rectangular cross-section is

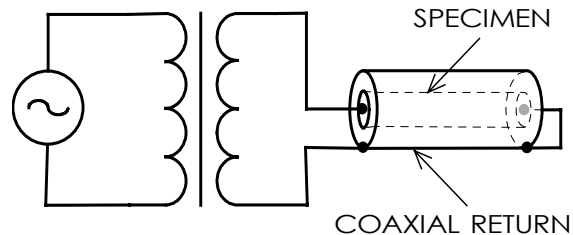


Fig. 1 Test method

used, the edge effect of iron bar may be checked. The specimen can be made easily. The coaxial return bus is necessary for uniform boundary condition over the surface of specimen. Test specimen is SS400 iron bars annealed in vacuum chamber and the conductivity is 5.3E6 S/m. The diameter is 8mm, and the length about 400mm. The ring specimen for measuring BH curve and the short sample for testing eddy-current are cut out from an iron rod with 80 mm diameter.

The distortion of current and voltage waves may give an important problem in this method, because the specimen is so short that its load impedance is comparable of current source. The author, however, has discovered that the distortion of excitation current or voltage is not an important matter. This fact is mentioned below.

Simulation Method

A popular simulation method is used, where 3D edge element A-phi method [3] is 2-dimensionally applied to a quarter of bar cross-section. The time step is 1/64 per a cycle, 10 cycles are calculated and the last 1 cycle is treated as a result. Hysteresis is neglected and the initial exciting BH curve is used.

Fig. 2 shows the loss density at 60 Hz . The curve CALC is the simulation where the impedance of the source is taken into consideration. The curves Sin_E and Sin_H correspond to the sinusoidal electric and the sinusoidal magnetic fields, respectively. These simulation results are almost on the same curve and somewhat larger than of the test. This is an important result. This figure shows the fact that the distortion is not a matter of discuss. In passing the results of references[1] and [2] are on this TEST line. This fact has never been pointed out.

The field is the smaller, the test results are the larger than the simulation. This must be caused by neglecting hysteresis in the simulation.

Fig. 3 and 4 show the surface impedance defined by the surface fields; E/H. The test result of phase angle is much less than the simulation results. The distortion dose not affected these simulation results also. This fact is remarkable. Neglecting hysteresis in the simulation is a reason of these results.

When the measured distortion factors of the current and the voltage waves are compared with the CALC results, it can be concluded that the wave forms are similar to the measured.

Conclusions

- (1) The proposed experimental method for validation of the simulation of eddy-current may gives reasonable results.
- (2) The distortion of electric voltage and current waves is not essential in the experiment for the validation.
- (3) The simulation for eddy-current in iron gives good results about loss value, but the simulated result of phase angle is much larger than of the test.

References

- [1] P.D. Agrwal, "Eddy Current Losses in Solid and Laminated Iron," Trans. Amer. Inst. Elect. Engrs., vol. 78, Pt. II, pp. 169-181, 1959
- [2] K.K.Lim and P.Hammond, "Numerical method for determining the electromagnetic field in saturated steel plates," Proc.IEE, Vol. 119, No.11, pp.1667-1675, 1972
- [3] A. Kameari, "Calculation of Transient 3-D Eddy Current using Edge Elements," IEEE Trans. on Magn. Vol. 26, No.2, 1990

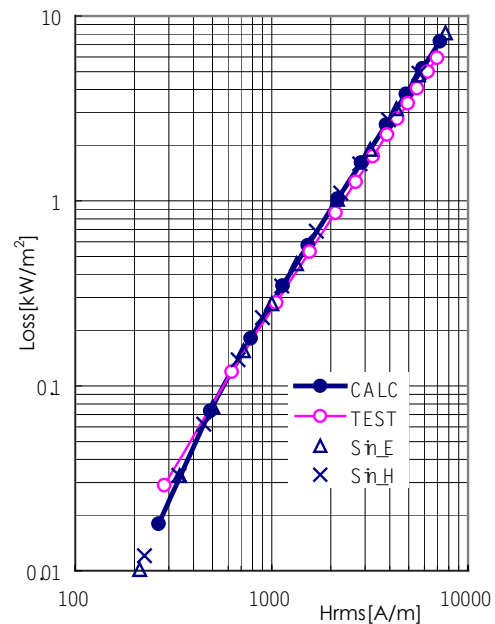


Fig. 2 Loss density

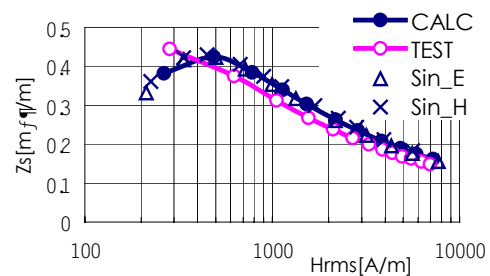


Fig. 3 Surface impedance

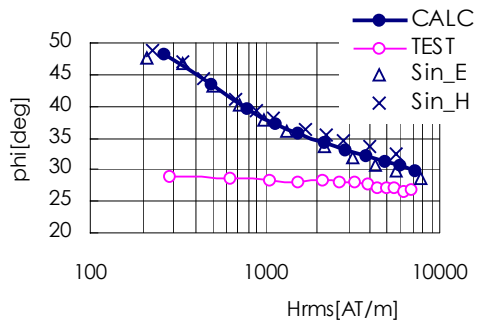


Fig. 4. Phase angle

Time-domain analysis of proximity effect current driven problems

M. Vitelli

Seconda Università di Napoli
DII, Real Casa dell'Annunziata, Aversa (CE), Italy
vitelli@unina.it

Abstract – An efficient FEM-based approach for the solution of 2-D proximity effect transient problems is presented. Both computer execution times and memory storage requirements can be consistently reduced by employing a suitable formulation leading to a sparse linear system of equations with a (slightly) higher dimensionality with respect to the corresponding much more dense system resulting from the standard formulation.

I. INTRODUCTION

Different formulations have been proposed in the literature in order to study proximity effect problems [1-2]. In this paper the method presented in [3] is generalized in order to study current-driven proximity problems and an efficient approach for the solution of the FEM formulation of the problem is also provided.

II. FORMULATION

Consider N adjacent, infinite (along z), homogeneous and linear conductors Ω_{ck} ($k=1,2,\dots,N$), with permeability $\mu=\mu_0$ and conductivity σ , carrying currents $i_k(t)$, surrounded by an unbounded nonconducting domain Ω_n of permeability μ_0 . Since we consider currents $i_k(t)$ directed along the z -axis, the electric field \mathbf{E} and the current density \mathbf{J} are z -directed while the flux density \mathbf{B} lies in the x - y plane. On the basis of such considerations, the magnetoquasistatic approximation of Maxwell equations after a discretization based on the backward Euler method, leads to:

$$\nabla^2 A_z - \mu_0 \sigma \frac{A_z(t)}{\Delta t} + \frac{\mu_0 \sigma \iint_{S_{ck}} A_z(t) dS}{\Delta t S_{ck}} = f_k(t) \quad \text{in } \Omega_{ck} \quad (k=1,\dots,N) \quad (1)$$

$$\nabla^2 A_z = 0 \quad \text{in } \Omega_n$$

where S_{ck} is the cross section of conductor k , and

$$f_k(t) = -\mu_0 \frac{i_k(t)}{S_{ck}} - \mu_0 \sigma \frac{A_z(t-\Delta t)}{\Delta t} + \frac{\mu_0 \sigma \iint_{S_{ck}} A_z(t-\Delta t) dS}{\Delta t S_{ck}}. \quad \text{The FEM}$$

solution of eq. (1) is based on the construction of a triangular mesh with n_t triangles and n_n nodes ($n_n=n_D+n_p$ where n_D is the number of Dirichlet points placed on $\partial\Omega$ and n_p is the number of mesh nodes where A_z is unknown) and on the choice of a test-function space [4]. There are many choices for the test-function spaces; we have used continuous functions that are linear on each triangle of the mesh. A suitable basis for such function space is the set of functions v_i which are linear on each triangle of the mesh and take the value 0 at all nodes except node i where they are equal to one. By labeling with \mathbf{A}_n the column vector of the unknown nodal values of A_z , a FEM variational formulation of (1) would lead to the following linear system of equations [4]:

$$(\mathbf{K} + \mathbf{M})\mathbf{A}_n + \mathbf{D} = \mathbf{F} \quad (2)$$

where \mathbf{K} and \mathbf{M} are n_p -by- n_p matrices and \mathbf{D} and \mathbf{F} are n_p -vectors defined as it follows:

$$K(i,j) = \iint_{\Omega_k} \nabla v_i \cdot \nabla v_j d\Omega; \quad M(i,j) = \iint_{\Omega_k} \frac{\mu_0 \sigma}{\Delta t} v_i v_j d\Omega; \quad (2.1)$$

$$D(i) = -\frac{\mu_0 \sigma}{\Delta t} \sum_{k=1,N} \iint_{\Omega_{ck}} v_i \left(\frac{\iint_{S_{ck}} A_z dS}{S_{ck}} \right) d\Omega; \quad F(i) = -\sum_{k=1,N} \iint_{\Omega_{ck}} f_k v_i d\Omega; \quad (2.2)$$

The integrals in (2) can be computed by using the mid-point rule; this approximation is optimal since it has the same order of accuracy of the piecewise linear interpolation. On the basis of such consideration, $D(i)$ can be rewritten as:

$$D(i) = -\frac{\mu_0 \sigma}{\Delta t} \sum_{k=1,N} \iint_{\Omega_{ck}} v_i \sum_{m=1,n_k} \frac{S_{ckm}}{S_{ck}} |x_{km} y_{km} 1| \begin{pmatrix} x_{km1} y_{km1} 1 \\ x_{km2} y_{km2} 1 \\ x_{km3} y_{km3} 1 \end{pmatrix} |A_n(m_l)| d\Omega; \quad (3)$$

where n_k is the number of mesh triangles in Ω_{ck} , Ω_{ckm} represents the m -th mesh triangle belonging to Ω_{ck} , S_{ckm} and P_{km} are respectively the area and the center of mass (barycenter) of Ω_{ckm} , x_{kml} and y_{kml} ($l=1, 2, 3$) are the coordinates of the three nodes of Ω_{ckm} , x_{km} and y_{km} are the coordinates of P_{km} ($x_{km} = \sum_{l=1,3} \frac{x_{kml}}{3}$, $y_{km} = \sum_{l=1,3} \frac{y_{kml}}{3}$), m_l

($l=1, 2, 3$) are the indices of the nodes of Ω_{ckm} and $A_n(m_l)$ are the values assumed by A_z in such nodes. Therefore vector \mathbf{D} can be written as: $\mathbf{D} = \mathbf{C}\mathbf{A}_n$ where \mathbf{C} is a n_p -by- n_p matrix; the entries $C(i, m_l)$ ($i=1,\dots,n_p$; $l=1, 2, 3$) are given by the coefficients of $A_n(m_l)$ in eq. (3). System (2) can thus be rewritten as:

$$(\mathbf{K} + \mathbf{M} + \mathbf{C})\mathbf{A}_n = \mathbf{H}\mathbf{A}_n = \mathbf{F} \quad (4)$$

The chosen basis function v_i vanishes on all the triangles that do not contain the node i ; therefore $K(i,j)$ and $M(i,j)$ are zero unless nodes i and j are vertices of the same triangle. Thus \mathbf{K} and \mathbf{M} are very sparse matrices, instead \mathbf{C} , and consequently \mathbf{H} , is much more dense since, when i and j are nodes belonging to the same conducting region Ω_{ck} then entry $C(i, j)$ is different from zero even if i and j are not vertices of the same triangle. Due to the dense nature of \mathbf{H} the solution of (4) is very onerous in terms of execution times and memory storage requirements. A more efficient approach to take into account the integral term in the left-hand side of the first of eqs. (1) is the following. Eq. (1) can be rewritten as:

$$\nabla^2 A_z - \mu_0 \sigma \frac{A_z(t)}{\Delta t} + \frac{\mu_0 \sigma A_{ck}(t)}{\Delta t} = f_k(t) \quad \text{in } \Omega_{ck} \quad (5)$$

$$\nabla^2 A_z = 0 \quad \text{in } \Omega_R - \Omega_c$$

where $A_{ak}(t) = \frac{\iint_{S_{ck}} A_z(t) dS}{S_{ck}}$ (5.1)

$A_{ak}(t)$ ($k=1, \dots, N$) represents the spatial average value of the magnetic vector potential A_z on S_{ck} . In place of an unknown n_p -vector \mathbf{A}_n , in the following it will be considered a fictitious unknown (n_p+N) -vector \mathbf{A}_n' such that the first n_p components of \mathbf{A}_n' coincide with the corresponding components of \mathbf{A}_n , while the further N components of \mathbf{A}_n' represents the N average values A_{ak} collected in the N -vector \mathbf{A}_a . The variational formulation of (5) coupled with the set of N linear equations expressing the dependence of A_{ak} on \mathbf{A}_n leads to:

$$\mathbf{H}' \mathbf{A}_n' = \begin{bmatrix} \mathbf{B}_n & \mathbf{B}_a \\ \mathbf{G}_n & \mathbf{G}_a \end{bmatrix} \begin{bmatrix} \mathbf{A}_n \\ \mathbf{A}_a \end{bmatrix} = \begin{bmatrix} \mathbf{F} \\ \mathbf{0} \end{bmatrix} \quad (6)$$

$\mathbf{B}_n, \mathbf{B}_a, \mathbf{G}_n$ and \mathbf{G}_a are defined as it follows:

$$B_n(i, j) = K(i, j) + M(i, j) \quad \begin{cases} i = 1, 2, \dots, n_p \\ j = 1, 2, \dots, n_p \end{cases} \quad (6.1)$$

$$B_a(i, j) = -\frac{\mu_0 \sigma}{\Delta t} \iint_{\Omega_q} v_i d\Omega \quad \begin{cases} i = 1, 2, \dots, n_p \\ j = 1, 2, \dots, N \end{cases} \quad (6.2)$$

$$G_a(i, j) = 0 \quad \begin{cases} i = 1, 2, \dots, N \\ j = 1, 2, \dots, N \\ j \neq i \end{cases} \quad G_a(i, j) = -1 \quad \begin{cases} i = 1, 2, \dots, N \\ j = i \end{cases} \quad (6.3)$$

The entries $G_n(k, m_l)$ ($k=1, 2, \dots, N; l=1, 2, 3$) of \mathbf{G}_n are given by the coefficients of $A_n(m_l)$ in eq. (7) that describes, with the usual meaning of symbols, the dependence existing among A_{ak} and \mathbf{A}_n :

$$A_{ak} = \sum_{m=1, n_k} \frac{S_{ckm}}{S_{ck}} \begin{bmatrix} x_{km1} & y_{km1} & 1 \\ x_{km2} & y_{km2} & 1 \\ x_{km3} & y_{km3} & 1 \end{bmatrix} \begin{bmatrix} A_n(m_1) \\ A_n(m_2) \\ A_n(m_3) \end{bmatrix}; \quad k=1, \dots, N \quad (7)$$


It is worth noting that, thanks to the very sparse nature of \mathbf{K} and \mathbf{M} , \mathbf{B}_n which is by far the largest of the four submatrices of \mathbf{H}' is a very sparse matrix. Instead matrices \mathbf{B}_a and \mathbf{G}_n are more dense but they are very small (as long as $n_p \gg N$) with respect to the overall size of \mathbf{H}' . Therefore \mathbf{H}' is a very sparse matrix too so that it is far less expensive to solve system (6) rather than system (4).

III. RESULTS AND DISCUSSION

We will refer to the case of two adjacent conductors ($N=2$) of rectangular cross section ($0.1 \text{ mm} \times 10 \text{ mm}$), conductivity $\sigma=5.8 \cdot 10^{17} \text{ S/m}$, placed at a distance $d=1 \text{ mm}$. As an example, the analysis has been carried out by using the periodic current waveform c_t typical in dc-dc converters (Table 1). The duty-ratio D indicates the interval during which $i(t) \neq 0$, normalized with respect to the period $T=1/f$. In figs. 1 the spatial distributions of the r.m.s. volume current densities, at steady state, are shown for currents flowing in the same direction ($i_1(t)=i_2(t)=c_t(t)$) and in opposite directions ($i_1(t)=-i_2(t)=c_t(t)$) respectively. The simulations have been carried out in MATLABTM environment by exploiting its built-in computational linear algebra on sparse matrices. The adopted mesh is characterized by the following parameters: $n_t=6206$, $n_n=3138$, $n_D=68$, $n_p=3070$; the

memory requirements to store \mathbf{H} and \mathbf{H}' as MATLAB sparse matrices are equal to 28295 kB for \mathbf{H} and to 363 kB for \mathbf{H}' . It is evident the considerable saving of computer memory which can be obtained by using formulation (6). The sparsity ratios q (the ratio between the number n_z of nonzero elements and the total number of entries) of \mathbf{H} and \mathbf{H}' are respectively $q(\mathbf{H})=0.245$ and $q(\mathbf{H}')=0.0027$. In spite of its higher dimensionality (3072 instead of 3070), the very sparse system (6) can be solved in a much more computationally efficient way than system (4). The execution times needed by MATLABTM to solve the linear sparse systems of equations (6) and (4) on an Intel Pentium III at 1 GHz are equal to 20.4 and 0.9 s respectively.

Table 1

current	Shape	D	f [kHz]	I _{max} [A]
c_t		0.3	200	1

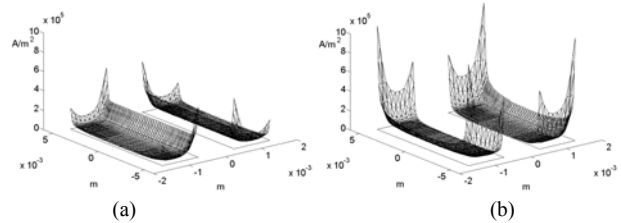


Fig. 1: r.m.s. volume current densities at steady state: (a) $i_1(t)=i_2(t)=c_t(t)$; (b) $i_1(t)=-i_2(t)=c_t(t)$

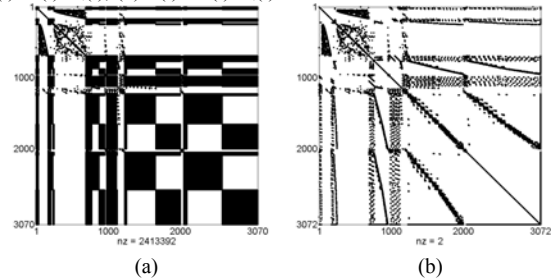


Fig. 2: sparsity patterns: (a) \mathbf{H} , (b) \mathbf{H}'

IV. CONCLUSIONS

In spite of the (slightly) higher dimensionality of system (6) (n_p+N unknowns) with respect to that of system (4) (n_p unknowns), since $n_p \gg N$, it is possible to exploit advantageously the lower computational complexity required by arithmetic operations on very sparse matrices with respect to that one required by the corresponding operations on more dense matrices.

REFERENCES

- [1] O. Bíró, K. Preis, W. Renhart, G. Vrisk, K. R. Richter "Computation of 3-D current driven skin effect problems using a current vector potential", IEEE Trans. On Mag., Vol. 29, N. 2, March 1993.
- [2] J. P. Webb, B. Forghani, D. A. Lowther "An approach to the solution of 3D voltage driven and multiply connected eddy current problems", IEEE Trans. On Mag., Vol. 28, N. 2, March 1992.
- [3] M. Vitelli "Calculation of per unit length resistance and internal inductance in 2-D skin-effect current driven problems", in print on IEEE Trans on EMC.
- [4] P. P. Silvester, R. L. Ferrari: Finite elements for electrical engineering, Cambridge University Press, Cambridge (UK).

Simulation of a three-phase transformer using an improved anisotropy model

H. Vande Sande¹, T. Boonen², I. Podoleanu¹, F. Henrotte¹ and K. Hameyer¹

¹ Katholieke Universiteit Leuven, Dept. ESAT, Div. ELECTA, Kasteelpark Arenberg 10

² Katholieke Universiteit Leuven, Dept. Computer Science, Celestijnenlaan 200A
B-3001 Heverlee-Leuven, Belgium

Email: hans.vandesande@esat.kuleuven.ac.be

Abstract—The numerical modelling of electromagnetic devices with non-linear and anisotropic materials requires the knowledge of the reluctivity tensor. Its entries generally depend both on the magnitude and the direction of the flux density. They can be obtained from measurements with a single sheet tester by considering an improved anisotropy model. The paper discusses how this model can be integrated in the finite element method. It is successfully applied for simulating a three-phase transformer.

I. INTRODUCTION

NON-LINEAR magnetostatic systems are described by the equation

$$\text{curl}(\nu \text{curl}A) = J, \quad (1)$$

where A is the vector potential [Vs/m], ν the reluctivity [Am/Vs] and J the applied current density vector [A/m²]. The reluctivity is represented by a symmetric second-rank tensor. It relates the flux density B [Vs/m²] to the field strength H [A/m] according to $H = \nu B$. In its principal coordinate system {PQ}, all off-diagonal entries are zero. In order to obtain the tensor in the global coordinate system {XY}, the following transformation rule is used [1]:

$$\begin{pmatrix} \nu_{xx} & \nu_{xy} \\ \nu_{yx} & \nu_{yy} \end{pmatrix} = \mathbf{T}^{-1} \begin{pmatrix} \nu_p & 0 \\ 0 & \nu_q \end{pmatrix} \mathbf{T}, \quad (2)$$

with

$$\mathbf{T} = \begin{pmatrix} \cos \phi & \sin \phi \\ -\sin \phi & \cos \phi \end{pmatrix} \quad (3)$$

the matrix of direction cosines and ϕ the angle between the X-axis and the P-axis. In the general case of non-linear anisotropic materials, the diagonal entries are not equal and depend on the magnitude and the direction of B . This behaviour can be analyzed by the improved anisotropy model presented in [2]. This paper shows how this hybrid model can be integrated in the finite element method. It is demonstrated for the simulation of a three-phase transformer.

II. IMPROVED ANISOTROPY MODEL

Silicon steels that are widely used in transformers exhibit a considerable non-linear anisotropy, originating from their Goss-texture [3], [4]. Physical considerations and measurements show that B and H are aligned if the applied field is directed along the rolling direction (RD) or transverse direction (TD). Hence, these directions are the principal axes of the

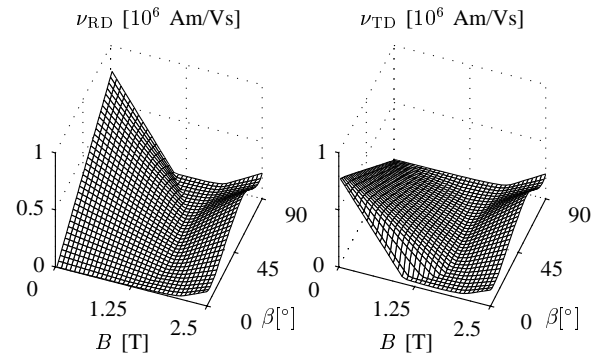


Fig. 1. The tensor reluctivity components of a Goss-textured ferromagnetic material as a function of the magnitude and the direction of B .

reluctivity tensor. By combining the laws of ferromagnetism with measurements from a single sheet tester, it is possible to determine the reluctivity in the RD (ν_{RD}) and TD (ν_{TD}), as a function of the magnitude of B and the angle β it makes with the RD [2]. Their shape is plotted in Fig. 1. These characteristics reveal that the hardest magnetization occurs for a certain angle between 0° and 90° (Theoretically at 54.7°). At lower flux density levels, this improved anisotropy model yields an area in the $B - \beta$ plane in which ν_{RD} and ν_{TD} are undefined. The corresponding B -vectors are never reached during the measurements because B tends to stay close to the RD or TD. As the finite element method may require to evaluate the reluctivity in this area, it is supposed that $\nu_{RD}(0, 90^\circ)$ and $\nu_{TD}(0, 0^\circ)$ equal the reluctivity of air, and that the reluctivity components increase linearly towards this value over the empty region.

III. NON-LINEAR COMPUTATION

Convergence is not easily achieved when simulating devices with non-linear anisotropic material characteristics such as the ones presented in Fig. 1. Several simulations have shown that reliable solutions are obtained by applying a fixed-point iteration (successive substitution), in which the reluctivity tensor is initialized as linear isotropic

$$\nu_{RD} = \nu_{TD} = \text{constant}, \quad (4)$$

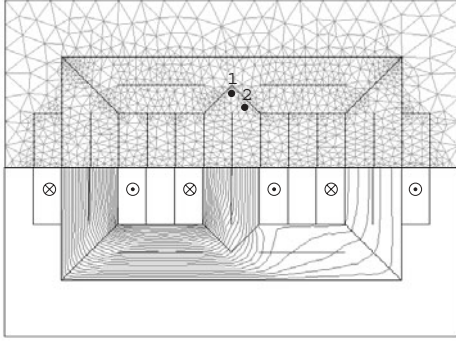


Fig. 2. The mesh and a field solution, for a particular instant of time, obtained by applying the improved anisotropy model. The RD is indicated by lines in the ferromagnetic parts.

followed by a smooth transformation into non-linear isotropic

$$\nu_{RD} = \nu_{TD} = f(\|B\|) \quad (5)$$

and eventually into non-linear anisotropic.

$$\nu_{RD} = f_1(\|B\|, \beta) \quad \nu_{TD} = f_2(\|B\|, \beta) \quad (6)$$

For the applied finite element analysis, the mathematical software libraries PETSc (Portable Extensible Toolkit for Scientific Computing) and TAO (Toolkit for Advanced Optimization) have been used [5], [6].

IV. EXAMPLE

The hybrid model is used for simulating the three-phase transformer of Fig. 2. Obviously, the bending of the flux lines is located close to the joints. This is not observed with isotropic materials. In order to demonstrate the improvement which can be achieved, when compared to anisotropy models of the type

$$\nu_{RD} = f_1(\|B\|) \quad \nu_{TD} = f_2(\|B\|) \quad (7)$$

as e.g. discussed in [7], the B -loci in points 1 and 2 of Fig. 2 are plotted in Fig. 3. The applied current varies sinusoidally over one period. For a fair comparison, $f_1(\|B\|, 0^\circ)$ and $f_2(\|B\|, 90^\circ)$ of Fig. 1 have been used. The smooth loci obtained with the latter model are in contrast with the complicated loci of the improved anisotropy model. Both models show a preferred orientation of the flux density in the rolling direction. However, the improved model additionally accounts for the more difficult magnetization along the hard axis of the material ($\beta = 54.7^\circ$). Similar B -loci have been measured and presented in [8].

V. CONCLUSIONS

Anisotropy of magnetic materials can be implemented in numerical simulations by means of a reluctivity tensor. Its diagonal entries generally depend on both the magnitude and

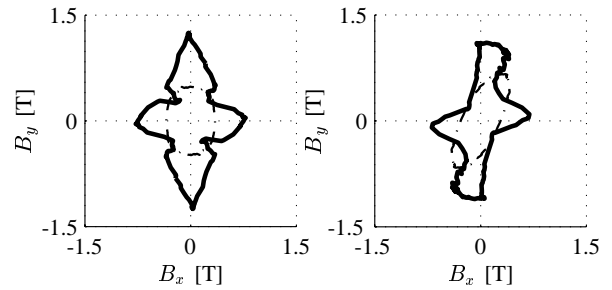


Fig. 3. The B -loci obtained by applying an improved (solid) and a traditional (dashdot) anisotropy model, at points 1 (left) and 2 (right) indicated in Fig. 2.

the direction of the flux density. This dependency can be obtained from an improved anisotropy model. However, the shape of the resulting reluctivity surfaces impedes the convergence of the numerical simulation method. Therefore, a fixed-point method, which gradually increases the non-linearity and the anisotropy, is adopted. By the simulation of a three-phase transformer it is shown that the improved anisotropy model yields a solution which better corresponds with the physical phenomenon, compared to the solution obtained by applying an anisotropy model which ignores the angle dependency of the tensor entries.

ACKNOWLEDGMENTS

The authors are grateful to the Belgian “Fonds voor Wetenschappelijk Onderzoek Vlaanderen” (project G.0427.98) and the Belgian Ministry of Scientific Research (IUAP No. P5/34).

REFERENCES

- [1] J.F. Nye, *Physical Properties of Crystals*, Oxford Science Publications, Clarendon Press, Oxford, UK, 2nd edition, 1985.
- [2] H. Vande Sande, F. Henrotte, L. Froyen, and K. Hameyer, “A hybrid method for determining the reluctivity tensor components of Goss textured ferromagnetic materials,” in *Proceedings of the 17th Symposium on Electromagnetic Phenomena in Nonlinear Circuits (EPNC’02)*, Leuven, Belgium, July 2002, pp. 1–4.
- [3] D.N. Lee and H.T. Jeong, “The evolution of Goss texture in silicon steel,” *Scripta Materialia*, vol. 38, no. 8, pp. 1219–1223, 1998.
- [4] G.H. Shirkoohi and M.A.M. Arikat, “Anisotropic properties in high-permeability grain-oriented 3.25% Si-Fe electrical steel,” *IEEE Transactions on Magnetics*, vol. 30, no. 2, pp. 928–930, Mar. 1994.
- [5] S. Balay, W.D. Gropp, L. Curfman McInnes, and B.F. Smith, “PETSc users manual,” Tech. Rep. ANL-95/11 - Revision 2.1.2, Mathematics and Computer Science Division, Argonne National Laboratory, 2002. See <http://www.mcs.anl.gov/petsc>.
- [6] S. Benson, L. Curfman McInnes, J. Moré, and J. Sarich, “TAO users manual,” Tech. Rep. ANL/MCS-TM-242, Mathematics and Computer Science Division, Argonne National Laboratory, 2002. See <http://www.mcs.anl.gov/tao>.
- [7] P.P. Silvester and R.L. Ferrari, *Finite Elements for Electrical Engineers*, Cambridge University Press, Cambridge, UK, 2nd edition, 1996.
- [8] A.J. Moses and J. Liu, “Quantification of the accuracy of different approaches to modelling anisotropy of grain oriented electrical steel,” *Journal de Physique IV*, vol. 8, no. 2, pp. 595–598, 1998.

A Time Domain Homogenisation Technique for Laminated Iron Cores in Three-Dimensional Finite Element Models

J. Gyselinck, P. Dular, and W. Legros

Department of Electrical Engineering, Institut Montefiore, University of Liège,
Sart Tilman Campus, Building B28, B-4000 Liège, Belgium, johan.gyselinck@ulg.ac.be

Abstract – The authors present a novel homogenisation technique for laminated iron cores in 3D FE models of electromagnetic devices. It takes into account the eddy currents in the individual laminations and the ensuing skin effect. The insulating layers of finite width between the laminations (fill factor < 1) are considered as well. The method is successfully applied to the 3D FE model of a laminated ring core.

INTRODUCTION

When modelling electromagnetic devices comprising laminated iron cores by means of the FE method, it is for practical reasons impossible to discretise each lamination separately. Homogenisation techniques are to be used in order to account for the induced eddy currents, the associated losses and the ensuing skin effect.

In [1] a homogenisation technique for 2D FE models has been proposed. It is based on the 1D eddy current model of a lamination, neglecting skin and edge effects, and has been extended to 3D FE models in [2]. In the linear case, skin effect can be easily included in a frequency domain analysis, adopting a frequency dependent complex equivalent relativity [2].

In this paper, we present the time domain extension of the latter frequency domain method. It is briefly elaborated in the following section, and then applied to a test case.

LUMPED 1D LAMINATION MODEL

We consider a single lamination of thickness d ($-d/2 \leq z \leq d/2$), carrying a time varying induction $b(z, t)$ along e.g. the x -axis. The governing 1D differential equation in terms of $b(z, t) = b(-z, t)$ and the magnetic field $h(z, t) = h(-z, t) = \nu b(z, t)$ reads:

$$\frac{\partial^2 h}{\partial z^2} = \sigma \frac{\partial b}{\partial t}, \quad (1)$$

where the permeability μ , the relativity $\nu = \mu^{-1}$, and the electrical conductivity σ are constant. The resolution of (1) can be developed either in the frequency domain [2] or the time domain [1], [2].

The quantities to be used in homogenisation techniques are the average induction $b_a(t) = \frac{1}{d} \int_{-d/2}^{d/2} b(z, t) dz$ and the magnetic field $h_s(t) = h(z = \pm d/2, t)$ on the surface of the lamination [1].

In the frequency domain, with frequency f and pulsation $\omega = 2\pi f$, an equivalent complex relativity ν_{eq} can be defined:

$$\frac{\nu_{eq}}{\nu} = \frac{h_s}{\nu b_a} = \frac{d^*}{2} \left(\frac{\sinh d^* + \sin d^*}{\cosh d^* - \cos d^*} + j \frac{\sinh d^* - \sin d^*}{\cosh d^* - \cos d^*} \right), \quad (2)$$

with h_s and b_a the complex representation of the sinusoidal $h_s(t)$ and $b_a(t)$ respectively, j the imaginary unit, $\delta = \sqrt{2/\sigma\mu\omega}$ the penetration depth, and $d^* = d/\delta$ the relative lamination thickness [1].

An approximate time domain solution of (1) can be obtained by considering a polynomial expansion of $b(z, t)$ comprising even basis functions $\alpha_0(z)=1, \alpha_2(z) = -\frac{1}{2} + 6(z/d)^2, \dots$, which are orthogonal, $\frac{1}{d} \int_{-d/2}^{d/2} \alpha_i(z)\alpha_j(z) dz = 0$ if $i \neq j$, and have unit value on the lamination surface:

$$b(z, t) = \alpha_0(z) b_a(t) + \alpha_2(z) b_2(t) + \dots \quad (3)$$

The work has been carried out in the frame of the Interuniversity Attraction Poles IAP P5/34, funded by the Belgian federal government. P. Dular is a Research Associate with the Belgian National Fund for Scientific Research (F.N.R.S.).

Then, on account of (1), the magnetic field $h(z, t)$ is expanded as

$$h(z, t) = h_s(t) - \sigma d^2 \beta_2(z) \frac{db_a}{dt} - \sigma d^2 \beta_4(z) \frac{db_2}{dt} - \dots, \quad (4)$$

with $\beta_2(z) = \frac{1}{8} - \frac{1}{2}(z/d)^2, \beta_4(z) = -\frac{1}{32} + \frac{1}{4}(z/d)^2 - \frac{1}{2}(z/d)^4$.

When considering a finite number of basis functions, up to order n for $b(z, t)$ and order $n+2$ for $h(z, t)$, the linear (or nonlinear) constitutive law $h(b) = \nu b$ cannot be fulfilled exactly. Its weak formulation is given by

$$\int_{-d/2}^{d/2} (h(z, t) - h(b(z, t))) \alpha_k(z) dz = 0, \quad k = 0, 2, \dots \quad (5)$$

This leads for e.g. $n = 2$ to a system of two linear differential equations in terms of $b_a(t), b_2(t)$ and $h_s(t)$:

$$\begin{bmatrix} h_s \\ 0 \end{bmatrix} = \nu \begin{bmatrix} 1 & 0 \\ 0 & \frac{1}{5} \end{bmatrix} \begin{bmatrix} b_a \\ b_2 \end{bmatrix} + \sigma d^2 \begin{bmatrix} \frac{1}{12} & \frac{-1}{60} \\ \frac{-1}{60} & \frac{1}{210} \end{bmatrix} \frac{d}{dt} \begin{bmatrix} b_a \\ b_2 \end{bmatrix}, \quad (6)$$

where either $b_a(t)$ or $h_s(t)$ are given functions of time. The equivalent complex relativity (2) is thus approximated as:

$$\frac{\nu_{eq}}{\nu} = \left(1 + \frac{49d^{*4}}{8820 + 20d^{*4}} \right) + j \left(\frac{d^{*2}}{6} - \frac{7d^{*6}}{26460 + 60d^{*4}} \right). \quad (7)$$

The zero order model, $n = 0$, considered in [1], [2], yields the first term in both real and imaginary part of (7).

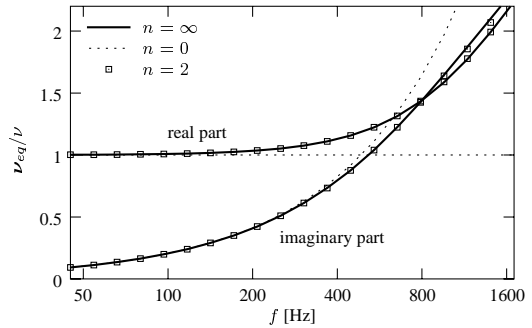


Fig. 1: Equivalent complex relativity as a function of frequency, with $d = 0.5$ mm, $\sigma = 5e6$ S/m, $\mu_r = \mu/\mu_0 = 2500$

In Fig. 1, the zero and second order approximation, $n = 0$ and $n = 2$ respectively, are compared to the analytical expression (2), $n = \infty$. Allowing a maximum error of 5% for real and imaginary part, the zero order model is valid up to $d^* = 1.76$ (250 Hz), the second order model up to $d^* = 5.8$ (2700 Hz).

Note that the above linear analysis also holds for a rotational flux excitation. The superposition principle applies to the induction along x and y axis, inducing eddy currents along y and x axis respectively.

In this 1D model, an infinitely wide lamination is considered. In laminations of finite width, the eddy current loss density is lower. For a width to thickness ratio of 20, e.g., the reduction is about 5% [1].

IMPLEMENTATION IN 3D FE MODEL

We consider a linear 3D eddy current problem, and its formulation in terms of the magnetic vector potential \underline{a} , with $\underline{b} = \text{curl } \underline{a}$. The weak

form of Ampère's law $\text{curl } \underline{h} = \underline{j}$ reads

$$(\nu \text{curl } \underline{a}, \text{curl } \underline{a}')_{\Omega} + (\sigma \partial_t \underline{a}, \underline{a}')_{\Omega_i} = (\underline{j}, \underline{a}')_{\Omega_s}, \forall \underline{a}' \in F_a(\Omega), \quad (8)$$

with $\underline{j}(t)$ the imposed current density in the subdomain Ω_s and $\underline{j} = -\sigma \partial_t \underline{a}$ the induced current density in the conducting subdomain Ω_l . $F_a(\Omega)$ is the function space defined on Ω containing the basis functions for \underline{a} as well as for the test functions \underline{a}' ; $(\cdot, \cdot)_{\Omega}$ denotes the volume integral in Ω of the product of its vector field components [2].

We consider the case where Ω_l consists of the laminations of a stacked core (conductivity σ , thickness d , magnetic reluctivity $\nu \ll \nu_0$). The insulating nonmagnetic and nonconducting layers, of thickness e , between the laminations constitute a domain Ω_i , which belongs to $\Omega \setminus \Omega_l$. The fill factor of the stacked core thus is $\lambda = \frac{d}{d+e}$.

The formulation (8), as is, requires a fine discretisation of all laminations and is likely to result in an unworkably large number of unknowns. As an approximation, Ω_l and Ω_i can be replaced by a homogeneous but magnetically and electrically anisotropic domain $\Omega_h = \Omega_l \cup \Omega_i$, for which a "normal" discretisation level suffices.

The induction and the magnetic field in Ω_h can be decomposed in two components which are either parallel or perpendicular to the plane of the laminations: $\underline{b} = \text{curl } \underline{a} = \underline{b}_{\parallel} + \underline{b}_{\perp}$ and $\underline{h} = \underline{h}_{\parallel} + \underline{h}_{\perp}$. In absence of eddy currents, the \underline{b} and \underline{h} components are related as follows: $\underline{h}_{\parallel} = \nu_{\parallel} \underline{b}_{\parallel}$ with $\nu_{\parallel} = \frac{\nu \nu_0}{(1-\lambda)\nu + \lambda \nu_0} \approx \frac{\nu}{\lambda}$ and $\underline{h}_{\perp} = \nu_{\perp} \underline{b}_{\perp}$ with $\nu_{\perp} = \lambda \nu + (1-\lambda)\nu_0$. This amounts to a reluctivity tensor $\underline{\nu}_h = \nu_{\parallel} \underline{1}_{\parallel} + \nu_{\perp} \underline{1}_{\perp}$, and $\underline{h} = \underline{\nu}_h \underline{b}$.

Let us now consider eddy currents in the laminations associated with $\underline{b}_{\parallel}$ and \underline{h}_{\perp} . The corresponding fields in the above presented 1D lamination model are $\underline{b}_a \approx \frac{\nu_{\perp}}{\nu} \underline{b}_{\parallel}$ and $\underline{h}_s = \underline{h}_{\parallel}$. The system (6) thus becomes in terms of the average fields $\underline{b} = \frac{\nu_{\perp}}{\nu} \underline{b}_a + \underline{b}_{\perp}$, $\underline{h} = \underline{h}_s + \nu_{\perp} \underline{b}_{\perp}$ and $\underline{b}_2^* = \frac{\nu_{\perp}}{\nu} \underline{b}_2$:

$$\begin{bmatrix} \underline{h} \\ 0 \end{bmatrix} = \underline{\nu}_h \begin{bmatrix} 1 & 0 \\ 0 & \frac{1}{\lambda} \end{bmatrix} \begin{bmatrix} \underline{b} \\ \underline{b}_2^* \end{bmatrix} + \underline{\sigma}_{h1} d^2 \begin{bmatrix} \frac{1}{12} & \frac{-1}{60} \\ \frac{-1}{60} & \frac{1}{210} \end{bmatrix} \frac{d}{dt} \begin{bmatrix} \underline{b} \\ \underline{b}_2^* \end{bmatrix}, \quad (9)$$

with $\underline{\sigma}_{h1} = \frac{\nu_{\perp}}{\nu} \sigma \underline{1}_{\parallel} \approx \frac{1}{\lambda} \sigma \underline{1}_{\parallel}$ a conductivity tensor.

Induced eddy currents due to \underline{b}_{\perp} , resulting in a net current parallel to the laminations, can be readily taken into account in (8) by replacing the integral over Ω_l by one over Ω_h , and by considering the conductivity tensor $\underline{\sigma}_{h2} = \lambda \sigma \underline{1}_{\parallel}$.

Combining (8) and the first equation of (9), the weak form of $\text{curl } \underline{h} = \underline{j}$ is:

$$(\nu \text{curl } \underline{a}, \text{curl } \underline{a}')_{\Omega \setminus \Omega_h} + (\underline{\nu}_h \text{curl } \underline{a}, \text{curl } \underline{a}')_{\Omega_h} + (\underline{\sigma}_{h2} \partial_t \underline{a}, \underline{a}')_{\Omega_h} + \left(\frac{\underline{\sigma}_{h1} d^2}{12} \partial_t \text{curl } \underline{a}, \text{curl } \underline{a}' \right)_{\Omega_h} - \left(\frac{\underline{\sigma}_{h1} d^2}{60} \partial_t \underline{b}_2^*, \text{curl } \underline{a}' \right)_{\Omega_h} = (\underline{j}, \underline{a}')_{\Omega_s}, \quad (10)$$

while the weak form of the second equation in (9) is:

$$\left(\frac{\underline{\nu}_h}{5} \underline{b}_2^*, \underline{b}_2^{*'} \right)_{\Omega_h} - \left(\frac{\underline{\sigma}_{h1} d^2}{60} \partial_t \text{curl } \underline{a}, \underline{b}_2^{*'} \right)_{\Omega_h} + \left(\frac{\underline{\sigma}_{h1} d^2}{210} \partial_t \underline{b}_2^*, \underline{b}_2^{*'} \right)_{\Omega_h} = 0. \quad (11)$$

A piecewise constant interpolation of the vector quantity \underline{b}_2^* in Ω_h can be obtained as follows. Two vector interpolation functions are assigned to each element of Ω_h , in which they have unit length and are directed along either of two perpendicular directions in the plane of the laminations; in the other elements they are identically zero. Note that the continuity of (the normal component of) \underline{b}_2^* , through e.g. a magnetic vector potential \underline{a}_2 , should not be imposed.

APPLICATION EXAMPLE

By way of illustration we consider an axisymmetric problem which comprises a laminated ring core (20 laminations, $d = 0.5$ mm, inner radius 40 mm, outer radius 50 mm, $\sigma = 5e6$ S/m, $\mu_r = 2500$, sepa-

rated by 0.02 mm airgaps, i.e. $\lambda = 0.96$), a toroidal 100 turn coil and the air between the ring core and the coil (Fig. 2). A volume mesh of hexahedral and prismatic elements is obtained by circularly extruding a 2D mesh of half of a radial cross-section (with the xy -plane) over an angle $\Delta\theta$ (around the z -axis) in m steps.

Two meshes are considered. In the first one, with $\Delta\theta = 2\pi/64$ and $m = 1$, each of the 10 laminations is finely discretised, allowing the direct modelling of the eddy currents. In the second one, to be used when applying the proposed homogenisation technique, with $\Delta\theta = 2\pi/4$ and $m = 16$, the discretisation of Ω_h is much coarser.

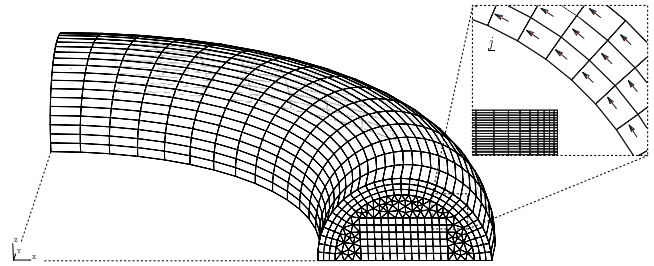


Fig. 2: FE models of the laminated ring core (with zoom of the fine discretisation of the laminations)

Several dynamic simulations with an imposed triangular current waveform of the same peak value but with different frequencies f , ranging from 50 Hz to 2000 Hz, and with both FE meshes are carried out. One period, $[0, T]$ with $T = 1/f$, is time stepped with backward Euler and $\Delta t = T/100$. The flux linkage of the coil is calculated by integrating $\underline{j} \cdot \underline{a}$ over Ω_s . The flux vs. time curves obtained with the fine FE model (with direct inclusion of the eddy currents) serve as reference. Fig. 3 shows all obtained flux vs. time curves. The second order homogenisation technique is shown to give quite satisfactory results for all frequencies considered, while the zero order model is only accurate up to 250 Hz.

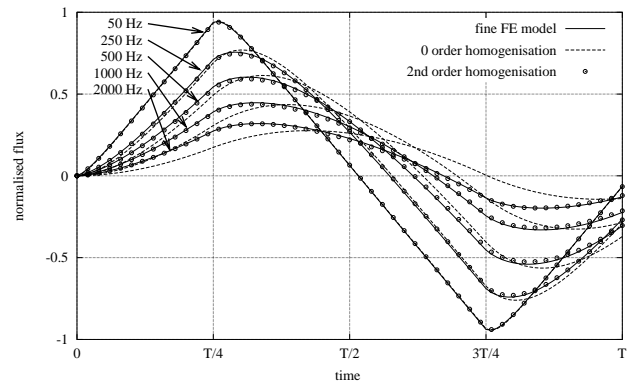


Fig. 3: Flux vs. time curves obtained with direct inclusion of the eddy currents and with zero and second order homogenisation

In the extended paper, the proposed method will be elaborated in more detail and more results will be given.

REFERENCES

- [1] J. Gyselinck et al., Calculation of eddy currents and associated losses in electrical steel laminations, *IEEE Trans. on Magn.*, Vol. 35, pp. 1191–1194, May 1999.
- [2] P. Dular et al., A 3D magnetic vector potential formulation taking eddy currents in lamination stacks into account, *Proc. of CEFC2002*, June 16–19, Perugia, Italy, p. 123.

Iron Losses Analysis in Magnetic Circuits supplied by PWM Converters

Konstantinos V. Tatis, Antonios G. Kladas and John A. Tegopoulos

Electric Power Division, Department of Electrical & Computer Engineering

National Technical University of Athens

9, Iroon Polytechniou Street, 15780 Athens, Greece

e-mail: tegopoul@power.ece.ntua.gr

Abstract — This paper presents a methodology for determination of harmonic iron losses in laminated iron cores under non sinusoidal excitation. The methodology adopted is based on a particular 3D finite element model by using a reduced scalar potential formulation. Eddy currents in iron laminations are considered by means of convenient surface current densities. Experimental verification is performed by comparing computed and measured leakage field in an E-shape laminated core case. A convenient modification of induction motor equivalent circuit parameters is proposed enabling consideration of switching frequency iron losses in case of inverter supply.

METHODOLOGY

Harmonic iron losses consideration due to eddy currents in laminated iron cores constitutes a complicated task, even in cases of cores with simple geometry. Such phenomena are even more complex in cases of electrical motors supplied by converters [1].

Adjustable frequency drives operating over a wide range of frequencies require accurate determination of the motor behavior in order to avoid possible consequences on the motor drive system and control units involved [3,4]. This can be implemented by combining equivalent circuit and detailed field calculations by means of utilizing appropriate finite element techniques [2,6].

However, the motor representation by the standard equivalent circuit may lead to inaccurate results, due to inappropriate evaluation of harmonic response and associated iron losses [9,10].

A first model for the consideration of harmonic iron losses in PWM inverter fed induction motors has been proposed [7], by using harmonic decomposition and superposition principle. This model is limited to steady state operating conditions and off line analysis. In the present work the authors present models appropriate for dynamic phenomena consideration and on line analysis.

The methodology adopted is based on an approximate representation of eddy currents developed in iron laminations due to tangential magnetic field variation at switching frequency by using analytical formulae. Eddy currents in rotor cages as well as in iron laminations caused by time variations of leakage field oriented perpendicularly to the lamination position are simulated by convenient finite element techniques [5]. The proposed model enables harmonic iron losses representation as well as motor

equivalent circuit parameter variations with switching frequency.

Three dimensional eddy current problems have been successfully modeled by means of finite element formulations involving vector quantities [8]. On the other hand scalars, involving only one unknown per node of the mesh, seem to be more efficient. We have developed a particular scalar potential formulation enabling treatment of 3D magnetostatics as well as 3D eddy currents developed in well defined paths [5].

According to our method the magnetic field strength H is conveniently partitioned to a rotational and an irrotational part as follows :

$$\mathbf{H} = \mathbf{K} - \nabla\Phi \quad (1)$$

where Φ is a scalar potential extended all over the solution domain while \mathbf{K} is a vector quantity (fictitious field distribution), defined in a simply connected subdomain comprising the conductor, that satisfies Ampere's law and is perpendicular on the subdomain boundary.

This technique can be applied in cases involving eddy currents developed in iron laminations due to harmonic frequencies, where the skin effect enables to express the corresponding induced surface current density \mathbf{J}_1 as follows:

$$\mathbf{J}_1 = \frac{\partial(\nabla T \times \mathbf{n})}{\partial t} \quad (2)$$

where T is a scalar quantity existing only on the lamination surface while \mathbf{n} is the unit normal to the lamination surface.

RESULTS AND DISCUSSION

The new method's efficiency and precision are checked by comparing the computed leakage field to the measured one in the case of an electromagnet formed by E and I shape parts separated by an air-gap of 1mm. When the excitation winding is supplied by a 50 Hz sinusoidal supply with 1000 A-t the measured losses are 22.5 W while the calculated ones are 19.75 W. In case of supply by a PWM inverter with fundamental frequency 50 Hz and switching frequency 1 kHz

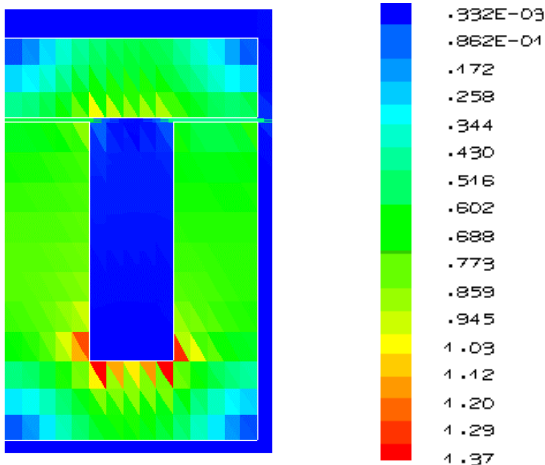


Fig. 1. Flux density distribution (half core configuration)

TABLE I
COMPARISON OF MEASURED AND CALCULATED FLUX DENSITIES AND LOSSES

Waveform	Meas. B (mT)	Calc. B (mT)	Meas. Losses (W)	Calc. Losses (W)
sinusoidal	438	445	22.5	19.75
$F_s=1$ kHz	471	463	40	38.5
$F_s=2$ kHz	512	503	35	33.2

the losses are almost doubled while a small reduction is obtained for a switching frequency of 2 kHz. The calculated losses for the same regimes are in quite good agreement with the measured ones, as shown in Table I. The flux density distribution on the surface of the magnetic circuit is given in Fig. 1. Table I compares also the computed and measured values of the flux density in the middle of the air gap.

In a second case a three phase, two pole, 20 kW, 220 V squirrel cage induction motor has been considered. The high order harmonic losses are taken into account by conveniently modifying the two axes motor equivalent circuits. These circuits include newly defined resistances representing iron losses associated with stator and rotor leakage fluxes, placed in parallel with the corresponding leakage inductance terms.

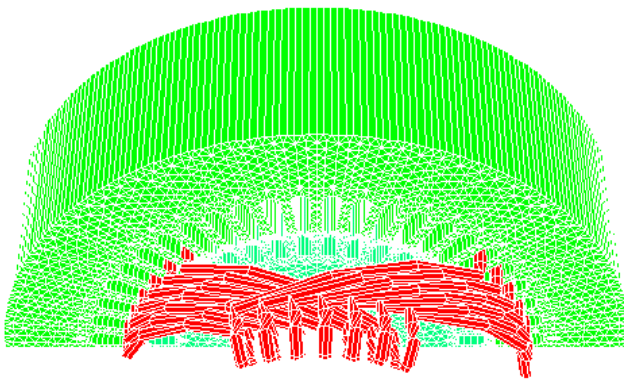


Fig. 2. One phase windings configuration at the end part of the machine.

Their determination involves evaluation of eddy currents developed at the end parts due to leakage fluxes. This can be obtained by using the proposed technique. The configuration of the windings at this region is shown in Fig. 2. Figure 3 compares the measured no load current time variation with the simulated waveforms by using the classical and modified equivalent circuits, respectively. This figure illustrates that the modified equivalent circuit enables better representation of the iron saturation in the motor magnetic circuit.

REFERENCES

- [1] J.M.D. Murphy and V.B. Honsinger, "Efficiency of inverter-fed induction motor drives", *Proceedings of 13th Annual IEEE Power Electronics Specialists Conference*, 1982 Record, pp. 544-552.
- [2] A. Yahoui, F. Bouillault, "2D and 3D numerical computation of electrical parameters of an induction motor", *IEEE Transactions on Magnetics*, vol. 30, no. 5, Sept. 1994, pp. 3690-3692.
- [3] E. Levi, M. Sokola, A. Boglietti and M. Pastorelli, "Iron loss in rotor-flux-oriented induction machines: identification, assessment of detuning, and compensation", *IEEE Transactions Power Electronics*, vol. 11, no. 5, Sept. 1996, pp. 698-709.
- [4] S.C. Mukhopadhyay, S.K. Pal, D. Roy, S. Bose, "Software Aided Derating and Performance Prediction of Cage-rotor Induction Motors under Distorted Supply Conditions", *Proceedings of 1996 International Conference on Industrial Growth*, vol. 1, pp. 452-457.
- [5] A. Kladas, J. Tegopoulos, "3D eddy currents modeling by means of a particular reduced scalar potential technique", *IEEE Transactions on Magnetics*, vol. 33, no 2, pp. 1350-1353, March 1997.
- [6] P. Dziwniel, F. Piriou, J.P. Ducreux and P. Thomas, "A time-stepped 2D-3D Finite Element Method for Induction Motors with skewed slots modeling", *IEEE Transactions on Magnetics*, Vol. 35, no 3, May 1999, pp. 1262-1265.
- [7] A. Vamvakari, A. Kandianis, A. Kladas and S. Manias, "High fidelity equivalent circuit representation of induction motor determined by finite elements for electrical vehicle drive applications", *IEEE Transactions on Magnetics*, Vol. 35, no 3, May 1999, pp. 1857-1860.
- [8] Z. Ren and A. Razek, "Comparison of some 3D eddy current formulations in dual systems", *IEEE Transactions on Magnetics*, Vol. 36, no 4, July 2000, pp. 751-755.
- [9] E. N. Hildebrand and H. Roehrad, "Losses in Three-Phase Induction Machines Fed by PWM Inverter", *IEEE Transactions on Energy Conversion*, Vol. 16, no 3, Sept. 2001, pp. 228-233.
- [10] J. Hur, H. A. Toliyat, "3-D time-stepping analysis of induction motor by new equivalent magnetic circuit network method", *IEEE Transactions on Magnetics*, Vol. 37, no 5/1, Sept. 2001, pp. 3225 -3228.

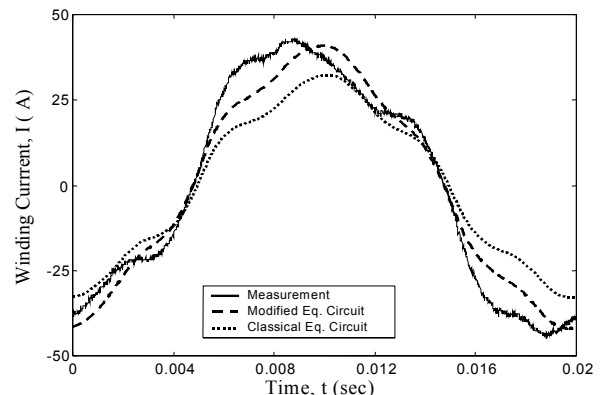


Fig. 3. No load current time variation

Field Errors in SC Magnets Due to Persistent Currents Generated by Arbitrary Field Changes in the Transverse Plane

Martin Aleksa, Bernhard Auchmann, Stephan Russenschuck, Christine Völlinger

Abstract— Magnetic field changes in the coils of superconducting magnets are shielded from the filaments' core by so-called persistent currents which can be modeled by means of the critical state model. This paper presents a semi-analytical 2-dimensional model of the filament magnetization due to persistent currents for changes of the magnitude of the magnetic induction and its direction while taking the field dependence of the critical current density into account. The model is combined with numerical field computation methods for the calculation of field errors in superconducting magnets. The filament magnetization and the field errors in a nested orbit corrector magnet have been calculated as an example.

Keywords— Bean model, Filament magnetization, Persistent currents.

I. INTRODUCTION

THE Large Hadron Collider (LHC), will consist of about 8400 superconducting (SC) magnet units of different types. The applied magnetic field induces currents in the filaments of the SC coils that screen the external field changes (so-called persistent currents). The filaments are made of type II hard SC material with the property that the magnetic field penetrates into the filaments with a gradient that is proportional to the magnitude of the persistent currents. Macroscopically, these currents are the source of a magnetization $\vec{M}(\vec{B})$ in the strands. One way to calculate this would be to mesh the coil with finite elements and solve the resulting non-linear field problem numerically by making use of a measured $\vec{M}(\vec{B})$ -curve. This approach has two main drawbacks: The numerical field computation has to be combined with a hysteresis model for hard superconductors, and the coil has to be discretized with highest accuracy also accounting for the existing gradient of the current density due to the trapezoidal shape of the cables, the conductor alignment on the winding mandrel, and the insulation layers. Hence, we aimed for computational methods that avoid the meshing of the coil by combining a semi-analytical magnetization model with the BEM-FEM coupling method [3]. In order to account for the feed-back of the filament magnetization on the magnetic field, an $\vec{M}(\vec{B})$ -iteration is performed. To describe the persistent currents, the critical state model [2] is applied, which states that any external field change is shielded from the filament's core by layers of screening currents at critical density $j_c(B, T)$. The presented model differs from other attempts to describe a SC filament's response to arbitrary field changes as, e.g., in [6]. It takes into account the dependence of the critical current density on the applied external field and the resulting field distribution in

the filament cross-section. As a consequence, also low field effects such as the peak-shifting (asymmetry in the magnetization curve for vanishing external field), magnetizations due to minor loops and rotating external fields are reproduced by the model. The model introduced in [1] has been extended to account for filament magnetizations due to arbitrary field changes in the transverse plane.

II. EXTENDED PERSISTENT CURRENT MODEL

Field changes on the surface of SC filaments induce layers of shielding currents of critical density $j_c(B)$ (B is the magnitude of the penetrated magnetic induction inside the filament). As in author's paper [1], the induction shielded by such layers is modelled by the integral over intersecting circles, each carrying currents of critical density $j_c(B)$ of opposite direction, compare Fig. 1. The relative penetration q parameterizes linearly the filament cross-section, assuming values between 0 on the outside and 1 in the center of the filament. Thus, the magnitude of the shielding induction vector $\Delta\vec{t}$, generated by a layer between q_1 and q_2 is given by

$$|\Delta\vec{t}| = \frac{\mu_0 r}{2} \int_{q_1}^{q_2} j_c(B(q)) dq, \quad (1)$$

with r the filament radius. Let \vec{B}_{out} (or \vec{B}_{new} or \vec{B}_{old}) denote the external magnetic field after an excitation step, and $\vec{B}(q) = \vec{B}_{\text{out}} + \vec{t}(q)$ the course of the magnetic induction inside the filament. Note that, with $|\vec{t}| = t$ and $q_1 = 0$, the differential of the shielding reads $dt(q) = \frac{\mu_0 r}{2} j_c(B(q)) dq$, compare (1) for $(q_2 - q_1) \rightarrow 0$ and (4). The mathematical task to resolve consists in the determination of: (a) the vector function of the shielded induction (shielding vector) $\vec{t}(q)$ for a given excitation; (b) the penetration depth q^* of a new shielding current layer, given a persistent current distribution from preceding excitation steps, respecting the continuity requirements:

$$\vec{B}(0) = \vec{B}_{\text{new}} + \underbrace{\vec{t}_{\text{new}}(0)}_0 = \vec{B}_{\text{new}}, \quad (2)$$

$$\vec{B}(q^*) = \vec{B}_{\text{new}} + \vec{t}_{\text{new}}(q^*) = \vec{B}_{\text{old}} + \vec{t}_{\text{old}}(q^*); \quad (3)$$

and (c) the resulting magnetization from a set of shielding current layers. With the approximation of the critical current density around the working point given in [1], $j_c(B) = \frac{\mathcal{F}(B_{\text{out}})}{\sqrt{B(q)}}$, a differential equation is derived for $t(q)$

$$dt \sqrt{B_{\text{out}}^2 - 2B_{\text{out}}t(q)\cos(\alpha) + t(q)} = \mu_0 \mathcal{F}(B_{\text{out}}) \mathcal{H} dq, \quad (4)$$

where the geometrical factor $\mathcal{H} = 2r(1 - \ln 2) = 0.614r$ is explained in [1] and the angle α between the external field and the shielding vector is illustrated in Fig. 1. A solution is found with the mathematica program [4] for the inverse relation:

$$q(B_{\text{out}}, \alpha, t) = \frac{1}{3\mu_0\mathcal{F}(B_{\text{out}})\mathcal{H}} \left[B_{\text{out}} \cos(\alpha) \left(2\sqrt{B_{\text{out}}} \right. \right. \quad (5)$$

$$+ \sqrt{B_{\text{out}}|\sin(\alpha)|} {}_2F_1 \left(\frac{1}{2}, \frac{3}{4}, \frac{3}{2}, -\cot^2 \alpha \right) \left. \right)$$

$$+ (t - B_{\text{out}} \cos \alpha) \left(2 \left(B_{\text{out}}^2 + t^2 - 2B_{\text{out}}t \cos \alpha \right)^{1/4} \right.$$

$$\left. \left. + \sqrt{B_{\text{out}}|\sin \alpha|} {}_2F_1 \left(\frac{1}{2}, \frac{3}{4}, \frac{3}{2}, -\frac{(t - B_{\text{out}} \cos \alpha)^2}{\sin^2 \alpha B_{\text{out}}} \right) \right) \right],$$

where ${}_2F_1$ denotes the Gauss' Hypergeometric function. The function for $t(B_{\text{out}}, \alpha, q)$ is obtained by a Newton algorithm.

An equation system to solve task (b) is derived from the continuity equations (2-3) and from geometric considerations. A 3-dimensional Newton algorithm yields $\alpha_{\text{new}}, t_{\text{new}}(q^*)$, and $t_{\text{old}}(q^*)$, so that, with (4) and (5), the course of the magnetic induction is defined:

$$\vec{B}(q) = \begin{cases} \vec{B}_{\text{new}} + \vec{t}_{\text{new}}(B_{\text{new}}, \alpha_{\text{new}}, q), & 0 \leq q < q^* \\ \vec{B}_{\text{old}} + \vec{t}_{\text{old}}(B_{\text{old}}, \alpha_{\text{old}}, q), & q^* \leq q < 1. \end{cases} \quad (6)$$

The magnetization of one shielding layer between penetration depths q_i and q_{i+1} is given by $\vec{M}_i = \frac{4r}{\pi} \int_{q_i}^{q_{i+1}} j_c(B(q))(1-q)^2 \vec{e}_{t_i} dq$, where \vec{e}_{t_i} denotes the direction of the corresponding shielding vector $\vec{t}_i(q)$. Figure 1 illustrates the transition from a field change in only one direction, discussed in [1], to field changes in arbitrary directions.

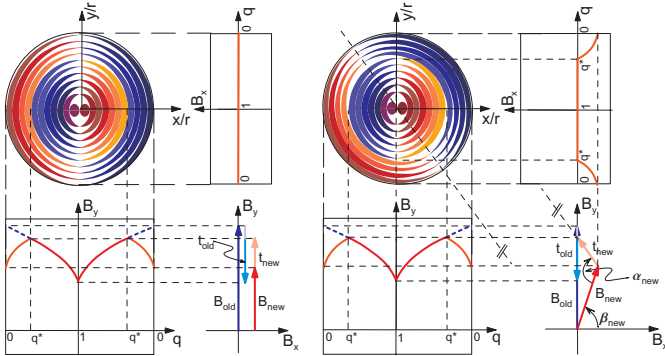


Fig. 1. SC filament exposed to a (left): 1-dimensional field change and (right): a 2-dimensional field change. In both cases, the field change was preceded by an up-ramp of magnetic induction on the outside. The course of the current density over the cross-section is parameterized by the shading of the individual layers. For the continuous model, the thickness of these layers thrives to zero.

III. COMBINING THE MODEL WITH NUMERICAL FIELD CALCULATION

For the calculation of persistent current induced field errors in SC accelerator magnets with a ferromagnetic yoke,

the magnetization model is combined with the BEM-FEM coupling method, which accounts for the local saturation effects in the yoke [3]. In order to calculate global shielding effects in the coil (in particular at low excitations), the feed back of the persistent currents on the excitational field is calculated by means of an $\vec{M}(\vec{B})$ -iteration on the strand level.

The MCBXA is a combined single aperture concentric (nested) dipole corrector, with one horizontal MCBXH (inside) and one vertical MCBXV (outside) associated to the quadrupoles Q1 and to Q2 in the insertion regions of the LHC. Inside the aperture of the nested dipole an insert with a nested sextupole and dodecapole is installed, see fig. 2 left. A somewhat academic excitational cycle is considered (which will serve the purpose of validating the model with measurements). First the outer layer coil is powered to a fifth of its nominal current and then the outer layer dipole follows a cosine and the inner layer dipole a sine like excitation. This way the resulting field rotates clockwise with about constant magnitude. The insert with the sextupole and dodecapole coil is not powered. Fig. 2 right shows the amplitude of the sextupole field component (the first higher multipolar field error in a dipole coil) as a function of the field direction in the aperture. Measurements of a prototype magnet are underway and will be used for the validation of the model presented in the paper.

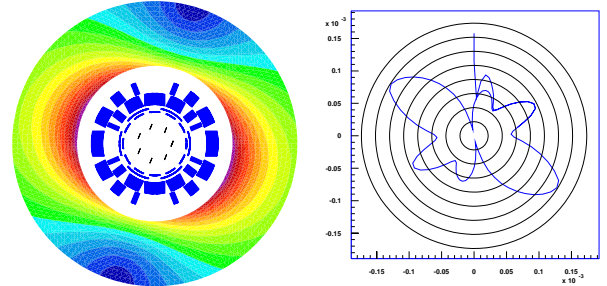


Fig. 2. Left: MCBXA orbit corrector with multipole insert (display of field modulus in the iron yoke). Right: Amplitude of the sextupole field component (in T) as a function of the field direction in the aperture of the MCBXA magnet.

REFERENCES

- [1] M. Aleksa, C. Völlinger and S. Russenschuck, *Magnetic Field Calculations Including the Impact of Persistent Currents in Superconducting Filaments* IEEE Trans. on Magn., Vol. 38, No. 2, 2002.
- [2] C.P. Bean, *Magnetization of High Field Superconductors*, Review of Modern Physics, vol. 36, 1964.
- [3] S. Kurz and S. Russenschuck, *The Application of the BEM-FEM Coupling Method for the Accurate Calculation of Fields in Superconducting Magnets*, Electrical Engineering - Archiv für Elektrotechnik, vol. 82, no. 1, Berlin, Germany, 1999.
- [4] Wolfram Research, *Mathematica 4.1*
- [5] W.H. Press et al., *Numerical Recipes in C: The Art of Scientific Computing*, 2nd edition, Cambridge University Press, 1992
- [6] M. Pekeler et al., *Coupled Persistent-Current Effects in the Hera Dipoles and Beam Pipe Correction Coils*, Desy Report no. 92-06, Hamburg, 1992

Author Index

- Adamiak, Kazimierz I - 88
 Adriano, Ricardo L.S. II - 126
 Adriano, U. III - 62
 Afonso, M.M. III - 26
 Aiello, G. III - 34
 Akduman, Ibrahim I - 110
 Akyel, Cevdet II - 78
 Al Aawar, N. III - 48
 Albanese, R. IV - 42
 Albert, Laurent II - 102
 Aleksa, Martin II - 208
 Alloto, P. III - 18
 Amrani, Djamel III - 78
 An, Kwang-Ok I - 66
 An, Yuejun IV - 116
 Andrei, P. II - 8
 Antunes, Carlos F.R. Lemos II - 146, IV - 194
 Antunes, O.J. I - 54
 Ara, Takahiro II - 62
 Arjona, Marco I - 56
 Arkadan, A.A. III - 48
 Arkkio, Antero II - 66
 Arturi, Cesare Mario I - 68, I - 128, IV - 90
 Ashiho, Kohei II - 90
 Askour, R. I - 184
 Atienza, E. III - 116
 Aubourg, M. II - 142
 Auchmann, Bernhard II - 208, III - 106
 Avdeev, Ilya II - 42
 Avila, S.L. III - 200, IV - 202
 Babic, Slobodan II - 78
 Badics, Zsolt I - 192, III - 4
 Bae, Sung-Woo II - 68, IV - 66
 Baillargeat, D. II - 142
 Bakopoulos, J. II - 98
 Bandelier, Bernard II - 80, II - 134, IV - 128
 Barabino, A. II - 144
 Barakat, K. IV - 16
 Baratchart, L. II - 142
 Bariant, D. II - 142
 Barmada, Sami III - 36
 Barros, Paulo H.L. IV - 170
 Bastos, J.P.A. I - 54, III - 172, III - 200
 Batistela, N.J. III - 200
 Baumgartner, Ulrike II - 110
 Bayada, G. III - 176
 Beitelman, L. IV - 52
 Bellemann, M.E. II - 170
 Bellina, Fabrizio II - 100
 Beltrame, Philippe IV - 190
 Benmansour, Amor IV - 182
 Benrejeb, M. III - 126, III - 128
 Bensetti, M. I - 206
 Bernard, Y. II - 12
 Besbes, M. II - 54
 Beuker, T. II - 170
 Biddlecombe, C.S. III - 14
 Bila, S. II - 142
 Bíró, Oszkár I - 204, I - 220, III - 10, IV - 146
 Boichon, C. II - 142
 Bondeson, Anders III - 212, IV - 204
 Boonen, T. II - 202
 Borghi, Carlo A. IV - 36, IV - 54
 Bossavit, Alain I - 2
 Bottauscio, O. I - 44, I - 186, III - 62, III - 130
 Bouchilloux, Philippe II - 12
 Bouillault, F. II - 54, IV - 192
 Bouzo, Marta Costa IV - 22
 Brandstätter, Bernhard II - 110, IV - 10
 Brauer, Hartmut IV - 122, IV - 160
 Brauer, J.R. I - 46
 Brisset, S. II - 124, IV - 166
 Brochet, P. II - 124, III - 126, III - 128, IV - 26, IV - 166
 Bruno, Oscar P. II - 132
 Brunotte, Xavier I - 52
 Buchgraber, G. III - 10
 Bullo, M. II - 28
 Burais, Noël I - 60, II - 104, IV - 190
 Buret, F. I - 200
 Butrylo, Boguslaw I - 16, III - 206
 Byun, Jin-Kyu III - 124
 Cabral, Sérgio H. L. III - 188
 Camberos, José A. IV - 174
 Caminhas, Walmir M. II - 128
 Cangellaris, Andreas II - 40
 Canova, A. I - 186, III - 138
 Cao, Shuying II - 44
 Cao, Yundong I - 122, IV - 46, IV - 200
 Capizzi, G. I - 218
 Cardelli, E. III - 180, III - 186
 Cardoso, José Roberto I - 138, III - 146
 Carlson, R. II - 74
 Carpes Jr., W.P. III - 200, IV - 202
 Carraro, Mario R. IV - 36, IV - 54
 Cavallo, A. III - 184
 Cehan-Racovita, Mircea I - 90
 Cendes, Zoltan J. I - 192, III - 4, IV - 88
 Chadebec, O. IV - 188
 Chai, Jianyun II - 30, III - 82
 Chang, G. III - 154
 Chang, Song Chu III - 156
 Chari, M.V.K. IV - 64
 Chen, C. III - 120
 Chen, Haiyan II - 92
 Chen, Xiangyong III - 76
 Chen, Yinchao I - 142
 Chen, Zhifei IV - 116
 Cheng, K.W.E. I - 178, II - 106, IV - 144
 Cheng, S.P. III - 154, III - 156
 Cheng, Z. IV - 156
 Cheon, Changyul II - 164

Author Index

- Chevalier, Thierry II - 194
Chiampi, M. I - 44, I - 186, III - 130
Chiang, Tsung-Shiun IV - 70
Chien, X.Y. III - 154
Chillet, Christian II - 94
Cho, Han Wook IV - 76, IV - 78, IV - 80
Cho, J.H. IV - 72
Cho, Seong Kook IV - 80
Cho, Sung Kook IV - 76, IV - 78
Choi, B.Y. I - 124
Choi, Charles T.M. I - 76, II - 34, II - 36
Choi, In-Ho IV - 92
Choi, Jae-Hak IV - 112, IV - 140
Choi, Kyeong-Ho IV - 66
Choi, Kyung IV - 110
Chong, T.C. III - 96
Christopoulos, Christos III - 182
Chung, Tae-Kyung III - 56
Chung, Young-Ki IV - 96
Cingoski, Vlatko III - 84
Ciocan, Razvan II - 174
Cioffi, M. IV - 198
Ciric, Ioan R. II - 182, II - 184
Clavel, E. III - 94
Clemens, Markus I - 10, I - 198, II - 160, IV - 18
Clénet, S. III - 164, IV - 32
Coco, Salvatore I - 132, I - 218
Codecasa, Lorenzo II - 32, III - 202
Cogitore, Bruno III - 86
Cohen, Lawrence S. II - 176
Coimbra, António Paulo II - 146
Cornic, D. III - 132
Costa, Maurício Caldora III - 118
Coulomb, Jean-Louis II - 94, III - 118, IV - 22,
IV - 164
Cowan, A. III - 100
Cristofolini, Andrea IV - 36, IV - 54
Cros, J. III - 164
Cui, Xiang I - 86, I - 98, I - 112, I - 114, II - 20
Curiaç, Paul IV - 74
Curiaç, R. II - 182
Davey, Kent R. I - 4, II - 178, IV - 158
Decoster, J. I - 194
Defour, Olivier III - 92
De Gersem, Herbert I - 48, I - 198, II - 196, III - 64
Delale, Augustin II - 102
Delfino, Federico II - 152
Deliège, Geoffrey II - 56
Delinchant, Benoit III - 86, III - 116
Della Torre, Edward III - 190
de Loos, Marieke I - 100
Deprez, W. I - 194
Desideri, D. I - 102
De Vasconcelos, João A. I - 200, II - 126, II - 128,
III - 26, IV - 202, IV - 206
De Vivo, B. IV - 148
De Wulf, Marc A.C. II - 50, III - 62
Dias, Guilherme III - 136
Dibben, David I - 26
Di Fraia, S. III - 186
Dilettoso, E. III - 34
Di Rienzo, Luca I - 68, I - 128, IV - 90
Dolinar, Drago IV - 62
Domeki, Hideo IV - 56
Domínguez, H. I - 162
Dorica, Mark I - 24
Ducharme, B. III - 20, III - 176
Dufour, S. IV - 44
Dughiero, F. II - 28, III - 108
Dular, Patrick I - 208, I - 210, II - 74, II - 204, III - 6,
III - 172, IV - 154
Dumetz, E. I - 184
Dupré, L. I - 120, III - 62
Dyck, Derek N. II - 86, IV - 168
Dyczij-Edlinger, Romanus I - 14, II - 154
Egawa, Akira I - 20
Egiziano, L. I - 108
El Amraoui, L. III - 126, III - 128
Endo, Hisashi III - 174, III - 192, IV - 2
Engdahl, G. IV - 130
Enokizono, Masato I - 202, III - 196
Eon, Yannick III - 30
Ergene, Lale T. II - 76
Erraki, A. IV - 52
Escarela-Perez, Rafael I - 56
Fabrègue, O. I - 60
Falqueto, T.S. III - 90
Fan, C. IV - 156
Farle, Ortwin I - 14, II - 154
Farschtschi, Abbas IV - 182
Fei, M.N. II - 106
Feigh, Stefan II - 160, IV - 18
Ferreira, G.S. III - 136
Ferreira da Luz, M.V. III - 172
Filho, Mário Leite Pereira III - 146
Finocchio, G. III - 180
Fireteanu, V. III - 66
Flemisch, B. II - 6
Forghani, Behzad IV - 168
Formisano, A. I - 134, IV - 198
Forster, Hermann II - 4
Fresa, R. I - 130
Fu, Jeffrey S. II - 138
Fu, W.N. I - 192, IV - 88
Fujimoto, Yukio II - 46
Fujisaki, Keisuke III - 52, IV - 50
Fujitsu, Hidefumi IV - 152
Fujiwara, Koji II - 90
Fujiwara, Naoya II - 90
Fukuda, T. IV - 48
Furukawa, Tatsuya IV - 50, IV - 162
Furuki, Syuji II - 46

Author Index

- Gao, X.K. II - 130
 Gao, Y.Q. III - 142
 Gasparics, Antal II - 188
 Georgilakis, P. II - 98
 Gerbaud, Laurent II - 102
 Gergam, E. Dufour I - 206
 Geuzaine, C. I - 210, III - 6
 Geuzaine, Christophe A. II - 132
 Giannacopoulos, Dennis I - 22, I - 24, I - 212, IV - 38
 Gibson, A.A.P. I - 104
 Gilbert, Geoff IV - 168
 Gilles, J.-P. I - 206
 Gillon, F. III - 126, III - 128
 Girdinio, P. II - 144
 Giuffrida, C. I - 218
 Glière, Alain III - 30
 Gotoh, Yuji II - 158
 Grabner, Christian II - 48
 Gruosso, G. I - 186, III - 138
 Guarnieri, M. I - 102, II - 28
 Guérin, Christophe I - 52, IV - 22
 Guichon, J.M. III - 94
 Guimaraes, Frederico G. II - 120, IV - 170
 Guo, J. III - 142
 Gyimesi, Miklos II - 42
 Gyimóthy, Szabolcs II - 188, IV - 146
 Gyselinck, Johan I - 208, I - 210, II - 50, II - 204,
 III - 6, IV - 194
 Ha, Kyung-Ho II - 70, III - 50
 Hadjali, M. II - 54
 Hahn, Song-Yop III - 56, III - 68
 Hahn, Sung-Chin I - 170, III - 68
 Hajji, O. II - 124, IV - 166
 Hameyer, Kay I - 194, II - 56, II - 202, III - 58, IV - 62
 Hamouda, Leila II - 80
 Han, G.P. II - 38
 Han, Sang-Joon III - 98
 Hanawa, Toshihiro I - 34
 Hao, R. IV - 156
 Haruishi, Yoshihisa II - 62
 Hashimoto, S. III - 120
 Haueisen, Jens I - 68, II - 170, IV - 4
 Hayano, Seiji III - 174, III - 192, IV - 2
 He, J.L. I - 118, III - 134, III - 142
 Hecquet, M. IV - 26
 Henneberger, Gerhard II - 58, II - 64, III - 88,
 IV - 180
 Henneron, T. I - 184, III - 164, IV - 32
 Henrotte, François I - 194, II - 56, II - 202
 Heyun, Lin II - 168
 Hill, Volker I - 14, II - 154
 Hill-Cottingham, R.J. IV - 82
 Hino, Noriaki IV - 68
 Ho, S.L. I - 116, I - 138, I - 178, II - 16, II - 106,
 II - 168, II - 180, III - 38, IV - 84, IV - 86,
 IV - 144
 Hoa, X. IV - 172
 Hollaus, K. I - 80, I - 140
 Holler, Gert IV - 10
 Holopainen, Timo P. II - 66
 Hong, J.P. I - 170
 Hong, Jung-Pyo I - 164, II - 70, III - 50, III - 152,
 IV - 108
 Hong, Sam-Nyol IV - 92
 Hong, Wei III - 80
 Honma, Toshihisa I - 28, I - 126, IV - 34, IV - 48
 Horibe, Toyomi III - 196
 Hou, Chunguang I - 122
 Houston, P. III - 2
 Hsieh, His-Kuang III - 156
 Hu, Q. IV - 156
 Hu, Yan II - 122, III - 28, III - 44, IV - 116
 Huang, Haoyu IV - 8, IV - 186
 Huang, Q. II - 84
 Hue, Yik-Kiong I - 154
 Hung, S.L. III - 72
 Hur, Jin I - 164, III - 150, III - 152
 Hur, Yoon IV - 108
 Hwang, C.C. III - 154, III - 156
 Hwang, Don-Ha II - 68, II - 70, IV - 66
 Hyder, H.R. McK. II - 2
 Ida, Nathan I - 128, II - 174
 Igarashi, Hajime I - 28, I - 126, IV - 34, IV - 48
 Ikuno, Soichiro I - 34, IV - 30, IV - 138
 Im, Chang-Hwan I - 66, II - 24, II - 190, III - 68,
 IV - 6, IV - 110
 Imada, Toshiaki I - 74
 Ingelstrom, Par III - 212
 Ionescu, Bogdan III - 4
 Ishihara, Yoshiyuki IV - 56
 Ishikawa, T. III - 120
 Ito, T. IV - 48
 Iványi, Amália III - 194, IV - 24
 Jabbar, M.A. II - 130
 Jacobs, R. II - 166
 Jagiela, M. III - 42, IV - 100
 Jajczyk, Jaroslaw IV - 114
 Janet, Fleur II - 94
 Jang, Ki-Bong II - 26
 Jang, Seok Myeong IV - 74, IV - 76, IV - 78, IV - 80
 Jayatilaka, Himal C. II - 184
 Jenkins, David II - 60
 Jeon, H.J. I - 124
 Jeong, Y.H. IV - 74
 Joan, Michael II - 194
 Johnen, Markus II - 58
 Jonson, Michael II - 60
 Joo, S.W. I - 170
 Jun, H.D. IV - 94
 Junak, Jacek III - 70
 Jung, Hyun-Kyo I - 66, I - 180, II - 24, II - 190,
 III - 68, IV - 6, IV - 110, IV - 124

Author Index

- Jung, S.J. IV - 74
Jung, Sang-Yong I - 180
Jung, T. III - 122
Kaehler, Christian II - 58, III - 88, IV - 180
Kahler, G.R. III - 190
Kaido, Chikara IV - 56
Kaltenbacher, M. II - 192
Kameari, Akihisa I - 188
Kamitani, Atsushi I - 34, IV - 28, IV - 30, IV - 138
Kanai, Yasushi I - 144
Kang, D.H. I - 170, IV - 74
Kang, Do-Hyun IV - 66
Kang, Dong-Sik II - 68
Kang, Gyu-Hong III - 150, III - 152
Kang, J. III - 122
Kang, Mi-Hyun IV - 124
Kang, S.I. I - 124
Kangas, Jari I - 216
Kanki, Takashi IV - 40
Kantartzis, Nikolaos V. I - 148
Kashiwa, Tatsuya I - 144
Kawase, Yoshihiro I - 18, IV - 56, IV - 184
Kawashima, Takuji I - 202
Kebaili, Badr II - 134
Kebbas, Mounir III - 78
Keradec, Jean-Pierre III - 86
Keranen, Janne I - 158
Kettunen, Lauri I - 158, I - 216, II - 150
Kildishev, Alexander V. II - 82, III - 160
Kim, B.S. I - 124
Kim, B.T. I - 182, III - 168
Kim, C. III - 122
Kim, D.W. II - 22
Kim, Dong-Hee II - 68, IV - 66
Kim, Dong-Hun II - 112
Kim, Gina IV - 92
Kim, Gyu-Tak I - 172, I - 174, I - 176, II - 118
Kim, H.K. II - 22
Kim, H.S. I - 182
Kim, Hong-Kyu II - 24, II - 190, IV - 110
Kim, Hyeong-Seok III - 56
Kim, J.K. I - 170
Kim, Jae-Kwang I - 180
Kim, Ji-Hoon III - 68
Kim, Jin-Yong IV - 92
Kim, K.Y. I - 124
Kim, Ki-Chan III - 166, III - 170
Kim, M.C. I - 124
Kim, Mi-Yong I - 172, II - 118
Kim, S. I - 124
Kim, T.H. III - 162
Kim, Y.S. II - 22
Kim, Y.Y. II - 38
Kim, Yong-Chul I - 172
Kim, Yong-Joo II - 68, IV - 66
Kim, Young-Kyoun I - 164, III - 50, IV - 108
Kim, Young-Kyun II - 70
Kim, Youn-hyun IV - 140
Kirk, A. IV - 172
Kis, Peter III - 194
Kitamura, Masashi IV - 68
Kitamura, Shingo IV - 56
Kladas, Antonios G. II - 98, II - 206
Knight, Andrew M. III - 8
Kocer, Fatma III - 110
Koch, Wigand I - 198
Koh, Chang Seop I - 30, II - 114, III - 112, III - 114
Koljonen, Emmi I - 158
Koltermann, P.I. I - 196
Koo, D.H. I - 170
Kost, Arnulf I - 82, II - 166
Kotiuga, P. Robert IV - 12
Krähenbühl, Laurent I - 200, II - 126, IV - 154
Krawczyk, Andrzej I - 72
Krozer, Viktor I - 142
Kuczmann, Miklós IV - 24
Kuilekov, Milko IV - 122
Kuo-Peng, P. II - 74, III - 200
Kurz, Stefan II - 88
Kwon, B.I. I - 182, III - 168, IV - 72, IV - 94
Kwon, Hyuk-Chan I - 66, IV - 6
Kwon, O-Mun IV - 64
Labie, Patrice I - 52, IV - 188
Lage, C. I - 106
Lai, Changxue I - 122
Lai, H.C. I - 58, IV - 82
Laporte, B. II - 72, IV - 44
Laskar, J. I - 150
Laudani, Antonio I - 132, I - 218
Lavers, J.D. II - 186, III - 72, IV - 52
Lean, Meng H. II - 140
Lebensztajn, Luiz III - 118, IV - 164
Le Bihan, Y. I - 206
Leconte, Vincent I - 36
Lee, C.K. III - 168
Lee, Cheol-Gyun I - 180, IV - 124
Lee, Dong-yeup I - 176
Lee, Dong-Yeup I - 174
Lee, Erping IV - 120
Lee, Eun Woong I - 166, I - 168
Lee, Geun-Ho I - 164, III - 50
Lee, J. III - 162
Lee, J.F. II - 18
Lee, J.W. I - 182
Lee, Jeong-Jong II - 70, IV - 108
Lee, Jin-Fa I - 214, II - 136
Lee, Joon-Ho III - 98, III - 124, IV - 96
Lee, Ju II - 26, III - 166, III - 170, IV - 112, IV - 140
Lee, Jung Ho I - 166, I - 168
Lee, Kab-Jae III - 166, III - 170
Lee, Min Myung I - 166, I - 168
Lee, Se-Hee III - 98

Author Index

- Lee, Sung Ho IV - 76, IV - 78, IV - 80
 Lee, Y.J. I - 124
 Lee, Yong-Ho I - 66, IV - 6
 Le Floch, Yann I - 52, IV - 188
 Legros, W. II - 204, III - 6
 Leite, J.V. III - 200
 Le Menach, Y. I - 184
 Lemercier, Guillaume I - 36
 Lengsfield, Byron II - 4
 Leonard, Paul J. IV - 136
 Leonardi, Franco III - 148
 Li, Erping I - 156, III - 24, III - 32
 Li, Huaishu IV - 58
 Li, J.T. II - 130
 Li, L.R. II - 186, III - 72
 Li, Langru IV - 58
 Li, Le-Wei I - 156
 Li, Li I - 94
 Li, Lin I - 86, I - 98, I - 114
 Li, Pei Pei I - 92
 Li, R.L. I - 150
 Li, Y. IV - 84, IV - 86
 Li, Ying I - 70
 Liang, Zhenguang III - 44
 Lim, Ki-Chae I - 174
 Lin, D. I - 192, IV - 88
 Lin, X. IV - 84
 Lipo, Thomas A. III - 148, IV - 124
 Lissorgues, G. I - 206
 Liu, Cheng-Tsung IV - 70
 Liu, Dong IV - 200
 Liu, En-Xiao I - 156
 Liu, Fuigui II - 44
 Liu, Jianxin II - 20
 Liu, S. II - 52
 Liu, Suzhen II - 92
 Liu, Xiaoming I - 122, IV - 46, IV - 200
 Liu, Z.J. II - 130, III - 96, IV - 126
 Liu, Zhenhua II - 20
 Lo, W.C. IV - 84
 Lowther, D. III - 100, III - 102, IV - 172
 Lu, Mai IV - 136
 Lu, Yilong I - 142, II - 138, IV - 120
 Łukaniszyn, M. IV - 100
 Lupi, S. III - 108
 Ma, Donglin I - 38, I - 40, I - 42
 Ma, X.S. I - 112, II - 14, II - 84, IV - 176
 Maday, Y. II - 6
 Maeda, Toshihiro I - 32
 Magalhaes, A.L.C.C. III - 90
 Magele, Christian I - 80, I - 140, II - 96, II - 110,
 IV - 196
 Magot, David III - 86
 Mahmoud, M. III - 144
 Manzin, A. I - 44, I - 186, III - 130
 Marashdeh, Q. III - 104
 Marchand, C. I - 206
 Maréchal, Yves I - 36, III - 30, III - 92
 Marinova, Iliana III - 174, III - 192, IV - 2
 Marretto, Carina A. Rondini III - 118
 Marrone, Massimiliano III - 204
 Martone, R. I - 134, IV - 198
 Mas, Patrick II - 94
 Masidlover, A.R. I - 104
 Massé, Philippe III - 30, III - 92
 Masson, J.P. II - 104, III - 20, III - 176
 Matsubayashi, Yutaka III - 84
 Matsumoto, Hirokazu II - 10
 Matsunami, M. III - 120
 Matsuo, T. III - 178
 Matsutomo, Shinya IV - 118
 Mayergoyz, Isaak D. I - 46, II - 8
 Mazauric, Vincent I - 6, I - 36, III - 94, IV - 188
 Mazzurco, Letizia I - 132
 McDevitt, Timothy II - 60
 McFee, Steve I - 38, I - 40, I - 42, I - 212
 Melgoza, Enrique I - 56
 Melkebeek, Jan A.A. II - 50, III - 62
 Mendrela, E.A. III - 42
 Merwa, R. I - 80
 Mesquita, R.C. III - 26, III - 90
 Meunier, Gérard I - 52, II - 194, III - 132, IV - 188
 Meyer, Luiz H. III - 188
 Mezani, S. II - 72
 Minerva, Vito II - 32, III - 202
 Miwa, Masahiko I - 26
 Miyagi, Daisuke IV - 132
 Mohammed, O.A. II - 52
 Mohellebi, Hassane III - 78
 Mol, C.L.L. III - 90
 Monzel, C. III - 88
 Moon, Jae-Yun I - 176, II - 118
 Moreau, Olivier II - 194
 Moreira, F.J.S. II - 148
 Morel, L. III - 20
 Moretti, R. IV - 44
 Morin, Eric III - 132
 Muramatsu, Kazuhiro IV - 152
 Musolino, Antonino III - 36
 Mustafa, Thair I.A.H. III - 188
 Musy, François III - 22, IV - 14
 Nabeta, Silvio Ikuyo III - 58
 Nagaya, Yoshiaki IV - 8
 Nair, D. III - 210
 Nakagawa, Seiji I - 74
 Natale, C. III - 184
 Nawrowski, Ryszard IV - 114
 Nemetz, José III - 136
 Nenonen, Jukka IV - 4
 Nervi, M. II - 144
 Neuls, Flavio III - 136
 Ni, Guangzheng I - 116, II - 180, III - 38, IV - 106

Author Index

- Ni, Peihong I - 138, III - 76
Nicolas, Alain I - 16, I - 60, IV - 206
Nicolas, Laurent I - 16, I - 60, III - 26, III - 206,
IV - 14, IV - 206
Noguchi, So I - 32, III - 84, IV - 118
Nomura, Tatsuei II - 198
Nowak, Lech III - 40
Nunes, C.R.S. III - 90
Ohchi, Masashi IV - 162
Ohtani, Tadao I - 144
Okamoto, Yoshifumi IV - 102
Okitsu, Takashi IV - 152
Oliveira, A.M. II - 74
Ono, Tomohiro IV - 184
Ooi, K. I - 126
Ortega, J.M. I - 196
Osowski, Stanislaw II - 116
Ostergaard, Dale II - 42
Ozdemir, N.A. II - 18
Palaniswamy, K. I - 96, III - 16
Palma, Rodolfo III - 110
Pang, Da-Chen IV - 70
Papapolymerou, J. I - 150
Paparigas, D. II - 98
Park, Gwan Soo II - 38, II - 172, IV - 150
Park, Il-Han III - 98, III - 124, IV - 96
Park, K.Y. II - 24, II - 190
Park, S.H. II - 172
Paul, John III - 182
Pávó, József II - 162, II - 188, IV - 146
Paya, Bernard III - 66, III - 74
Pereira, V.M. I - 196
Pereirinha, P.G. IV - 194
Perini, Jose II - 176
Perrussel, Ronan IV - 14
Perugia, I. III - 2, III - 18
Pham, Tan H. III - 158
Pichon, Lionel III - 140
Pinzaglia, E. III - 180
Piriou, Francis I - 184, IV - 32
Pirozzi, S. III - 184
Pitsilis, C. II - 98
Podoleanu, I. II - 202
Polajžer, Boštjan IV - 62
Poli, E. I - 102
Politi, Marco II - 32, III - 202
Popa, M. III - 66
Pöplau, Gisela I - 100
Popović, Branko I - 78
Popović, Milica I - 78
Preis, K. I - 204, II - 96, III - 10
Procopio, Renato II - 152
Proekt, Leonid B. II - 40
Puech, J. II - 142
Rain, Oliver II - 88
Raizer, Adroaldo I - 162, II - 166, III - 136, III - 140,
III - 188
Ramírez, Jaime A. II - 120, II - 128, IV - 170
Ramos, R.M. II - 148
Rapetti, F. II - 6, IV - 192
Raugi, Marco III - 36
Raulet, M.A. III - 20, III - 176
Razek, A. IV - 192
Reitzinger, S. II - 192
Rekanos, I.T. III - 208
Ren, Z. I - 106
Renhart, W. II - 96, II - 110
Repetto, M. I - 186, III - 138
Retière, N. III - 132
Righi, L.A. I - 196
Rioux-Damidau, Françoise II - 80, II - 134, IV - 128
Rischmuller, Volker II - 88
Ritonja, Jože IV - 62
Rjasanow, Sergej II - 88
Rodger, D. I - 58, IV - 82
Rosa, A.D. I - 162
Rossi, Mansueto II - 152
Roudet, James III - 94, III - 132
Rubinacci, Guglielmo III - 12, IV - 42, IV - 134
Rüncos, F. II - 74
Russenschuck, Stephan II - 208, III - 106
Ryu, Jae Seop III - 112, III - 114
Sabariego, R.V. III - 6
Saber, M.A. II - 156
Sadowski, N. I - 54, II - 74, III - 172, III - 200
Şahintürk, Hülya I - 136
Sahraoui, H. II - 108
Saito, Yoshifuru III - 174, III - 192, IV - 2
Saitoh, Ayumu IV - 28, IV - 30, IV - 138
Saldanha, R.R. II - 148
Salon, Sheppard J. II - 12, II - 76, II - 78, II - 164,
IV - 64
Samora, H.F.M. III - 90
Sano, Shinya I - 18, IV - 184
Santandrea, L. IV - 192
Sartori, Carlos A. França III - 146
Sato, Y. IV - 130
Satoh, Shouji IV - 50
Sawicki, Bartosz I - 72
Schabes, Manfred E. II - 4
Scharfetter, H. I - 80
Schimmanz, Klaus I - 82
Schlensok, Christoph II - 64, III - 88
Schmidt, Erich II - 48, IV - 60
Schotzau, D. III - 2
Schrefl, Thomas II - 4
Schreiber, Jörg IV - 4
Schuhmann, Rolf I - 10, I - 160, II - 160
Scorretti, R. I - 60, II - 104
Sebestyén, Imre II - 188, IV - 146
Seitz, M. II - 170

Author Index

- Seo, Kang IV - 150
 Seo, Seung Mo I - 214
 Sergeant, P. III - 62
 Serra, Enrico II - 100
 Seshima, Norio II - 188
 Seyfert, F. II - 142
 Shao, K.R. II - 186, III - 72
 Shao, Zhenhai III - 24, III - 80
 Shen, Xueqin I - 62
 Shen, Zhongxiang III - 24, III - 32, III - 80
 Shi, Hongyan IV - 116
 Shim, H. III - 122
 Shimasaki, M. III - 178
 Shimoji, Hiroyasu III - 196
 Shimomura, Tohru IV - 56
 Shin, Hyun-Hun II - 26
 Shin, Pan-Seok II - 164, III - 112
 Shinagawa, Kiminari II - 90
 Shintaku, Eiji II - 46
 Ship, K.S. II - 112
 Shiu, M.Y. III - 154
 Siauve, N. IV - 206
 Silva, Viviane Cristine III - 146
 Silveira, Jony L. III - 136, III - 140
 Simkin, J. I - 8, I - 84, III - 14
 Sivasubramaniam, Kiruba IV - 64
 Sixdenier, F. III - 20
 Slodicka, M. I - 120
 Smółka, Krzysztof IV - 98
 Sommer, Egon IV - 104
 Song, Seunghyun III - 56
 Souflaris, A. II - 98
 Spagnuolo, G. I - 108, IV - 148
 Stanton, S. IV - 88
 Starzyński, Jacek I - 72, II - 116
 Steiner, Gerald IV - 196
 Štumberger, Gorazd IV - 62
 Sun, Changzhi IV - 116
 Sun, Shu-Hai II - 34, II - 36
 Sun, W.M. I - 118
 Sun, Xianjing I - 64
 Supancic, P. I - 204
 Suuriniemi, Saku I - 216
 Sykulski, Jan K. II - 112
 Szmurło, Robert I - 72
 Szymanski, G. IV - 178
 Taguchi, Kenji I - 144
 Tajima, Fumio IV - 68
 Takagi, Toshiyuki III - 198, IV - 8, IV - 186
 Takahashi, N. IV - 156
 Takahashi, Norio II - 90, II - 158, IV - 56, IV - 102, IV - 132
 Takahashi, R.H.C. II - 148
 Takorabet, Norio II - 72
 Tallbäck, G. IV - 52
 Tamburrino, A. I - 130, III - 12
 Tanaka, Shin-ichiro IV - 162
 Tanaka, Shinya III - 198
 Tanaka, Yoshikazu II - 46
 Tang, R.Y. IV - 86
 Tang, Renyuan II - 122, III - 28, III - 44, III - 46
 Tani, Yoshihiro II - 198
 Tanimoto, Shigeya IV - 118
 Tao, Rui Min I - 92
 Tapia, Juan A. III - 148
 Tarhassari, Timo II - 150
 Tasseti, C.-M. I - 206
 Tatis, Konstantinos V. II - 206
 Taylor, S.C. I - 84
 Tegopoulos, John A. II - 206
 Teixeira, Fernando L. I - 152, I - 154, III - 104
 Tellini, B. III - 186
 Telló, Marcos III - 136
 Tenhunen, Asmo II - 66
 Tentzeris, E.M. I - 150
 Terada, Y. III - 178
 Thevenon, F. II - 142
 Thomas, David W.P. III - 182, III - 188
 Tian, Y. I - 130
 Tičar, I. I - 204, III - 10
 Tittonel, E. II - 28, III - 108
 Toledo, T. I - 200
 Toliyat, H. A. II - 108
 Tong, Ming-Sze I - 142
 Tonoike, Mitsuo I - 74
 Torii, Shinji IV - 132
 Tounzi, A. I - 184
 Trevisan, Francesco I - 190
 Trowbridge, C.W. II - 2
 Tsiboukis, Theodoros D. I - 146, I - 148, III - 208
 Tsili, M. II - 98
 Tsuboi, Hajime II - 188
 Tsukerman, Igor I - 12
 Tucci, V. IV - 148
 Tudorache, T. III - 66
 Uchimoto, Tetsuya IV - 8, IV - 186
 Udayakumar, K. I - 96, III - 16
 Udpa, S.S. I - 130
 Ueda, Kiyotaka IV - 132
 Ueno, Shoogo I - 74
 van der Geer, Bas I - 100
 Vander Heiden, M.J.J. III - 48
 Vande Sande, Hans I - 194, II - 56, II - 202
 Vandavelde, Lieven I - 210, II - 50
 van Rienen, Ursula I - 100, III - 70
 van Riesen, Dirk III - 88
 Vauhkonen, M. I - 124
 Ventre, S. III - 12
 Verdeyme, S. II - 142
 Viarouge, P. III - 164
 Vieira, Douglas A.G. II - 126, II - 128
 Villone, Fabio III - 12, IV - 42, IV - 134

Author Index

- Vincent, Grégory IV - 22
Vinsard, G. IV - 44
Visbal, Miguel R. I - 222
Visone, C. III - 184
Vitelli, M. I - 108, II - 200, IV - 148
Vivier, S. III - 126, IV - 26
Vollaire, Christian I - 16, III - 22, III - 26, III - 206, IV - 206
Vollinger, Christine II - 208
Wakatsuki, Tomohiro IV - 132
Wang, Bowen II - 44
Wang, Erzhi I - 92, I - 94, I - 122, IV - 46, IV - 200
Wang, H.T. IV - 126
Wang, Jinming IV - 20
Wang, S. III - 122
Wang, S.H. IV - 86
Wang, Shumin I - 152
Wang, Wen II - 138
Wang, Xiulian II - 122, III - 28
Wang, Yanting I - 50
Wang, Youhua III - 60, IV - 104
Wang, Yuhuai II - 180, III - 76, IV - 106
Waszak, M. IV - 178
Watanabe, Hiroko III - 198
Watanabe, K. IV - 48
Watanabe, Kota IV - 34
Watari, Shinjiro I - 20
Watzenig, Daniel IV - 10
Webb, J.P. II - 86, III - 210, IV - 16, IV - 168
Weber, Andreas IV - 196
Weicker, P. III - 102
Weiland, Thomas I - 10, I - 48, I - 160, I - 198, II - 160, II - 196, III - 64, IV - 18
Weinerfelt, P. IV - 204
Weinzierl, D. II - 166
Weiß, B. I - 220
Wen, J. IV - 172
Weng, Ling II - 44
White, Michael D. I - 222
Wiak, Sławomir IV - 98
Wilke, Markus I - 10, I - 198
Wincenciak, Stanisław I - 72, II - 116
Wohlmuth, B.I. II - 6
Won, H. II - 38
Wong, H.C. I - 116, II - 16, II - 106, II - 168, II - 180, III - 38, IV - 84, IV - 86
Woo, K.I. IV - 72, IV - 94
Wróbel, R. IV - 100
Wu, Duolong III - 32
Wu, Qing I - 62, I - 70
Wu, Qingying I - 212
Wu, Y.H. IV - 126
Wurtz, Frédéric II - 102, III - 86, III - 116
Xia, Pingchou I - 64
Xie, Dexin I - 30, I - 64, II - 114, III - 46, III - 114, IV - 20
Xie, Y.Q. I - 112, II - 14, IV - 176
Xie, Z. III - 96
Xu, E.X. I - 8, I - 84
Xu, Guizhi I - 70
Xu, J.Y. IV - 84
Xue, X.D. I - 178
Yamada, Takahiro III - 52
Yamada, Takashi I - 26, IV - 56
Yamaguchi, Katsuhiko III - 198
Yamaguchi, Tadashi I - 18, IV - 184
Yamamoto, A. I - 28
Yamashita, Hideo I - 32, III - 84, IV - 118
Yamazaki, Katsumi I - 20, II - 62, IV - 56
Yan, L. IV - 144
Yan, Rongge II - 44
Yan, Weili I - 50, I - 62, I - 70, II - 44, II - 92, IV - 104
Yan, Xiuke III - 46
Yan, Xixin II - 30
Yang, Qingxin I - 70, II - 92
Yang, Rui IV - 120
Yang, Shiyu I - 116, I - 138, II - 16, II - 180, III - 38, III - 76, IV - 106
Yang, Xiaoguang III - 60, IV - 104
Yang, Y. IV - 204
Yao, Yingying I - 30, I - 64, II - 114, III - 112, III - 114, IV - 20
Yioultsis, T.V. III - 208
Yoshida, Kinjiro II - 10
You, D. IV - 126
You, Y.M. IV - 72
Yu, G. I - 118
Yuan, J.S. I - 112, II - 14, II - 84, IV - 176
Yuferev, Sergey I - 128
Zamboni, Walter IV - 134
Zanchi, C. II - 142
Zeidan, Tarek IV - 154
Zeng, R. I - 118, III - 134
Zeroug, H. II - 108
Zhang, Bo I - 86, I - 98, I - 114
Zhang, Huijuan I - 50
Zhang, Yihuang III - 46
Zhang, Yongjie III - 76
Zhao, Kezhong II - 136
Zhao, Liangyun II - 122
Zhao, Yu III - 82
Zhao, Zhibin I - 86, I - 98
Zhilichev, Y. III - 54, IV - 142
Zhou, H. III - 96
Zhou, P. I - 192, IV - 88
Ziolkowski, Marek IV - 122, IV - 160
Zou, J. I - 112, I - 118, II - 14, II - 84, III - 134, III - 142, IV - 176
Zucca, M. III - 62
Zygiridis, Theodoros T. I - 146, I - 148
Zyss, Tomasz I - 72

THE 14TH COMPUMAG
CONFERENCE ON THE
COMPUTATION OF
ELECTROMAGNETIC FIELDS
WILL BE HELD IN
SARATOGA SPRINGS, NY
USA, FROM
JULY 13 TO 18, 2003.



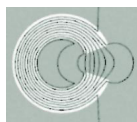
PREVIOUS COMPUMAG
CONFERENCES WERE HELD AT
OXFORD, UK · 1976
GRENOBLE, FRANCE · 1978
CHICAGO, USA · 1981
GENOA, ITALY · 1983
FORT COLLINS, USA · 1985
GRAZ, AUSTRIA · 1987
TOKYO, JAPAN · 1989
SORRENTO, ITALY · 1991
MIAMI, USA · 1993
BERLIN, GERMANY · 1995
RIO DE JANEIRO, BRAZIL · 1997
SAPPORO, JAPAN · 1999
EVIAN, FRANCE · 2001

WWW.COMPUMAG2003.COM

FOR MORE INFORMATION,
PLEASE E-MAIL THE
SECRETARIAT FOR
COMPUMAG 2003
AT [SECRETARIAT@
COMPUMAG2003.COM](mailto:SECRETARIAT@COMPUMAG2003.COM)



CHAIRMAN
DR. SHEPPARD SALON,
RENSSELAER POLYTECHNIC
INSTITUTE



© 2002 Gregory N. Montgomery

COMPUMAG 2003

Conference on the
Computation of
Magnetic Fields

SARATOGA SPRINGS, NY, USA
JULY 13-18, 2003